



Titanium-based Bulk Metallic Glasses : Glass Forming Ability and Mechanical Behavior

Jinna Mei

► To cite this version:

Jinna Mei. Titanium-based Bulk Metallic Glasses : Glass Forming Ability and Mechanical Behavior. Mechanics [physics.med-ph]. Université Joseph-Fourier - Grenoble I, 2009. English. NNT: . tel-00515163

HAL Id: tel-00515163

<https://theses.hal.science/tel-00515163>

Submitted on 5 Sep 2010

HAL is a multi-disciplinary open access archive for the deposit and dissemination of scientific research documents, whether they are published or not. The documents may come from teaching and research institutions in France or abroad, or from public or private research centers.

L'archive ouverte pluridisciplinaire **HAL**, est destinée au dépôt et à la diffusion de documents scientifiques de niveau recherche, publiés ou non, émanant des établissements d'enseignement et de recherche français ou étrangers, des laboratoires publics ou privés.

Joseph Fourier University – Grenoble
Northwestern Polytechnical University – Xi'an

PhD Thesis

To obtain the grades of

Doctor of the Joseph Fourier University, Spécialité Matériaux, Mécanique, Génie civil,
Electrochimie
Doctor of the Northwestern Polytechnical University

Presented by

MEI Jinna

**Titanium-based Bulk Metallic Glasses :
Glass Forming Ability and Mechanical Behavior.**

November 20th, 2009

Jury :

KOU Hongchao	Professor at NPU	Rapporteur
PELLETIER Jean-Marc	Professor at INSA-Lyon	Rapporteur
LI Yulong	Professor, dean of Graduate School at NPU	Examinator
WEI Bingbo	Professor at NPU, vice president at NPU	Examinator
LI Jinshan	Professor at NPU	Examinator
TOURNIER Robert	Research Director at CRETA	Examinator
FU Hengzhi	Professor at NPU	Supervisor
BLANDIN Jean-Jacques	Research Director at SIMAP	Supervisor
SOUBEYROUX Jean-Louis	Research Director at Néel Institut	Supervisor

PhD thesis prepared at the Institut Néel and the CRETA, CNRS Grenoble, France
and at the Northwestern Polytechnical University (NPU), Xi'an, China
in the framework of the French-Chinese International Associated Laboratory LAS2M.

ACKNOWLEDGEMENTS

This work would not have been possible without the support from the Sino-French Doctoral College Program, French-Chinese International Associated Laboratory LAS2M and ÉGIDE scholarship.

I want to express my outmost gratitude to my supervisors, Dr. Hengzhi FU, Dr. Jean-louis SOUBEYROUX and Dr. Jean-Jacques BLANDIN for their support, both intellectual and emotional, throughout the years of my Ph.D studies. They have taken me from my infantile knowledge of materials science and introduced me to a whole new world. Performing experiments with them left me in both joy and awe and I hope to retain this excitement in any future research endeavor. It was through their encouragement and understanding that I am standing here today, about to embark on a career in academia. I want to thank them for all the time they have spent with me explaining the most obscure concepts, for helping me view results with a whole new light and for teaching me how to think by myself. Even in the rainiest of days, they have guided me with wisdom and care. I hope that one day I may be able to repay them for all the good they have done for me.

A special note of thanks goes to Dr. Lian ZHOU, Dr. André SULPICE and Dr. Eric BEAUGNON, for their enthusiasm and support for my study in France as well as in China. Dr. Lian ZHOU recommended me to study in France. Dr. André SULPICE and Dr. Eric BEAUGNON gave me help in many ways, and with their support, I had a chance to learn French in CUEF and Alliance Française in Grenoble. They were always there when I needed them.

My work would not have been possible without the collaboration and assistance from many individuals. I owe lots of love to all of my professors, colleagues, and friends in China and France. Dr. Jinshan LI and Dr. Hongchao KOU were on my Ph.D candidacy exam committee, and I thank them for guidance on research and academic discussions, and Dr. Rui HU also gave me helpful advices on my thesis. A special note of thanks goes to Dr. Qing WANG, Dr. Sylvain PUECH and Antoine VOLLAND (GPM2), for their enthusiasm when working on the mechanical properties testing, to Dr. Meibo TANG (Shanghai Institute of Ceramics, CAS) for his guidance in low-temperature physics properties of metallic glasses, and to Dr. Ping WEN (Institute of Physics, CAS) for his advice on structural relaxation of metallic glasses. I would like to express my gratitude to Philippe PLAINDOUX who is in charge of the thermal analysis equipment in Institut Néel for his friendship, to Paul CHOMETON for his help in SEM testing, and to Ying ZHANG, who has ever been my roommate for her discussion on numerical calculation. I appreciate all of the members in the laboratories of CRETA, Intitut Néel, GPM2 in Grenoble France, and Institute of Rare Metal Materials & Processing in Xi'an China, for their friendship, cooperation in the labs and many discussions on various topics. A partial list would include Xavier CHAUD, Patricia DE RANGO, Daniel FRUCHART, Philippe ODIER, Laureline PORCAR, Marie-Dominique BERNARDINIS, Sophie RIVOIRARD, Albin CHAISE, Tristan CAROFF, Thomas GARCIN, Sylvain GARRIER, Sophie ROTH, Jérémy TILLIER, Alexandre VASSA, Stéphanie MORLENS, Cheikh BIRAHIM, Jaemyung CHANG, Jennifer CHEVY, Weidong QIN, Weifeng MA, Shengyin ZHOU, Jun WANG, Lei HUANG, Xiao JIA, et al.

Especially, I am grateful to Gildas DIGUET and Dr. Cyril MILLON, they are my best friends in

France, they take care of me like my brothers, give me lecture about French culture and teach me French, make my life in France more happy and meaningful.

I also want to thank my Chinese friends who accompany with me in France: Jianjun LUO (CRETA), Cuiping ZHANG (CRETA), Haixia ZHANG (MCMF), Qingyang WANG (MCBT), Dr. Lin Dong (GPM2), Dr. Xiaoxin LIU (GPM2) and Dejiang LI (GPM2), Tieren GAO (NANO), Liang LI (CEA), Haitao CAO (CRISMAT).

Finally, I would like to express my deepest gratitude to my parents for their unconditional love and encouragement. I would not be where I am today without the support of them. I am also grateful to Dr. Ye TAO for being with me and sharing together all the moments.

TABLE OF CONTENTS

ACKNOWLEDGEMENTS	I
TABLE OF CONTENTS	III

CHAPTER 1

INTRODUCTION	1
1.1 Critical Review about Metallic Glass.....	1
1.1.1 Glassy State	1
1.1.2 Formation of Glassy State	2
1.1.3 Formation of Metallic Glasses	4
1.2 Critical Review about Ti-based Bulk Metallic Glasses.....	11
1.2.1 Interest of Ti-based BMGs	11
1.2.2 Exploration for New Ti-based BMGs	14
1.2.3 Application of Ti-based BMGs	15
1.3 Motivation	16

CHAPTER 2

STRUCTURE OF TI-BASED BULK METALLIC GLASSES	18
2.1 Selection of Alloy Composition.....	18
2.1.1 Ti-Zr-Ni (Be-containing) System	18
2.1.2 Ti-Cu-Ni (Be-free) System.....	22
2.1.3 Comparison between $\text{Ti}_{40}\text{Zr}_{25}\text{Ni}_8\text{Cu}_9\text{Be}_{18}$ and $\text{Ti}_{41.5}\text{Cu}_{37.5}\text{Ni}_{7.5}\text{Zr}_{2.5}\text{Hf}_5\text{Sn}_5\text{Si}_1$ BMGs	28
2.2 Background and Motivation.....	30
2.3 Experiment.....	30
2.4 Results.....	32
2.4.1 Characteristics of Structure	32
2.4.2 Thermal Analysis	38
2.5 Discussion on the Identification of Microstructure and the Structural Stability	46
2.6 Conclusion	51

CHAPTER 3

LOW-TEMPERATURE PHYSICAL PROPERTIES FOR TI-BASED BULK METALLIC GLASSES	52
3.1 Background and Motivation.....	52
3.1.1 Low-temperature Specific Heat	53
3.1.2 Transport Properties	56
3.1.3 Motivation	59
3.2 Experiment.....	60
3.3 Results and Discussion.....	60
3.3.1 Specific Heat at Low Temperature.....	60

3.3.2 Electrical Resistivity	78
3.4 Conclusion	91
 CHAPTER 4	
THERMALLY INDUCED STRUCTURAL TRANSFORMATIONS.....	93
4.1 Background and Motivation.....	93
4.1.1 Structural Relaxation.....	95
4.1.2 Crystallization	99
4.1.3 Motivation.....	104
4.2 Experiment.....	105
4.3 Kinetics for Structural relaxation	107
4.3.1 Theory of Enthalpy Relaxation	107
4.3.2 Experimental Results of Enthalpy Relaxation.....	109
4.3.3 Characteristics of Enthalpy Relaxation.....	114
4.3.4 Mechanism of Enthalpy Relaxation	118
4.3.5 Discussion on the Comparison of Enthalpy Relaxation between $\text{Ti}_{41.5}\text{Cu}_{37.5}\text{Ni}_{7.5}\text{Zr}_{2.5}\text{Hf}_5\text{Sn}_5\text{Si}_1$ and $\text{Ti}_{40}\text{Zr}_{25}\text{Ni}_8\text{Cu}_9\text{Be}_{18}$ BMGs	119
4.4 Kinetics of Crystallization.....	122
4.4.1 Comparison of Theoretical kinetics Analysis based on the JMA and Starink Kinetics Models	123
4.4.2 Kinetics Analysis of Crystallization for $\text{Ti}_{41.5}\text{Cu}_{37.5}\text{Ni}_{7.5}\text{Zr}_{2.5}\text{Hf}_5\text{Sn}_5\text{Si}_1$ BMG	127
4.4.3 Kinetics Analysis of Crystallization for $\text{Ti}_{40}\text{Zr}_{25}\text{Ni}_8\text{Cu}_9\text{Be}_{18}$ BMG	134
4.5 Thermally Induced Structural Transformations	136
4.5.1 Thermally Induced Structural Transformations for $\text{Ti}_{41.5}\text{Cu}_{37.5}\text{Ni}_{7.5}\text{Zr}_{2.5}\text{Hf}_5\text{Sn}_5\text{Si}_1$ BMG	137
4.5.2 Thermally Induced Structural Transformations for $\text{Ti}_{40}\text{Zr}_{25}\text{Ni}_8\text{Cu}_9\text{Be}_{18}$ BMG	146
4.6 Conclusion	153
 CHAPTER 5	
EFFECTS OF PRE-ANNEALING NEAR GLASS TRANSITION TEMPERATURE ON THE THERMODYNAMICS AND KINETICS OF THE FOLLOWING GLASS TRANSITION AND CRYSTALLIZATION	155
5.1 Background and Motivation.....	155
5.1.1 Background	155
5.1.2 Motivation	156
5.2 Experiment.....	156
5.3 Effects of Thermally Induced Transformation of BMGs on Their Thermodynamic Properties of Glass Transition and Crystallization.....	157
5.4 Effects of Pre-annealing of BMGs on Their Kinetics Properties of Glass Transition and Crystallization	161
5.4.1 Non-isothermal Kinetics of Glass Transition and Crystallization.....	161
5.4.2 Isothermal Kinetics of Crystallization.....	164
5.5 Conclusion	170

CHAPTER 6

EFFECTS OF THERMALLY INDUCED STRUCTURAL TRANSFORMATIONS ON ROOM TEMPERATURE MECHANICAL PROPERTIES OF TI-BASED BMGS

6.1 Background and Motivation.....	171
6.1.1 Characteristics and Mechanisms for Room-temperature Deformation and Fracture of Metallic Glasses	172
6.1.2 Effects of Thermally Induced Structural Transformations on Room-temperature Mechanical Properties of Metallic Glasses	173
6.1.3 Main Issues Related to Room-temperature Deformation.....	173
6.1.4 Motivation.....	174
6.2 Experiment.....	175
6.3 Behavior and Mechanism of Deformation and Fracture for Ti-based BMGs.....	176
6.3.1 Characteristics of Deformation and Fracture for Ti-based BMGs	176
6.3.2 Deformation and Fracture Mechanisms of Ti-based BMGs.....	180
6.3.3 Discussion on Intrinsic Plasticity or Brittleness Ti-based BMGs	189
6.4 Effects of Thermally Induced Structural Transformations on the Mechanical Properties	191
6.4.1 Structurally Relaxed and Crystallized States	191
6.4.2 Effects of Structural Relaxation and Crystallization on Mechanical Properties ..	192
6.5 Conclusion	198

CHAPTER 7

HOMOGENEOUS DEFORMATION BEHAVIOR IN THE SUPERCOOLED LIQUID REGION.....

7.1 Background and Motivation.....	200
7.1.1 Review on the High-temperature Deformation Behavior of BMGs.....	201
7.1.2 Motivation.....	206
7.2 Experiment.....	207
7.3 Characteristics of High-temperature Deformation of Ti-based BMGs	210
7.3.1 $\text{Ti}_{41.5}\text{Cu}_{37.5}\text{Ni}_{7.5}\text{Zr}_{2.5}\text{Hf}_5\text{Sn}_5\text{Si}_1$ BMG	210
7.3.2 $\text{Ti}_{40}\text{Zr}_{25}\text{Ni}_8\text{Cu}_9\text{Be}_{18}$ BMG.....	214
7.4 Rheology Behavior of $\text{Ti}_{41.5}\text{Cu}_{37.5}\text{Ni}_{7.5}\text{Zr}_{2.5}\text{Hf}_5\text{Sn}_5\text{Si}_1$ BMG Deformed in the SLR	215
7.4.1 Transition from Newtonian Flow to Non-Newtonian Flow	215
7.4.2 Analysis on the Transition from Newtonian Flow to Non-Newtonian Flow.....	221
7.5 Effects of Deformation on the Structural Stability of Ti-based BMGs.....	226
7.6 Evaluation of Hot Workability and Optimization of Processing Conditions	230
7.6.1 Characteristic of Deformation of $\text{Ti}_{41.5}\text{Cu}_{37.5}\text{Ni}_{7.5}\text{Zr}_{2.5}\text{Hf}_5\text{Sn}_5\text{Si}_1$ BMG	231
7.6.2 Deformation Map of $\text{Ti}_{41.5}\text{Cu}_{37.5}\text{Ni}_{7.5}\text{Zr}_{2.5}\text{Hf}_5\text{Sn}_5\text{Si}_1$ BMG	232
7.6.3 Power Dissipation Map of $\text{Ti}_{41.5}\text{Cu}_{37.5}\text{Ni}_{7.5}\text{Zr}_{2.5}\text{Hf}_5\text{Sn}_5\text{Si}_1$ BMG	233
7.7 Conclusion	235

CONCLUSIONS.....

REFERENCES

CHAPTER 1

INTRODUCTION

1.1 Critical Review about Metallic Glass

1.1.1 Glassy State

A glass is defined as an amorphous solid which does not possess the long-range order (periodicity) characteristic (Fig. 1-1) and which exhibits a glass transition. In other words, a glass is a vitrified liquid, formed by continuous cooling of a cooled liquid.

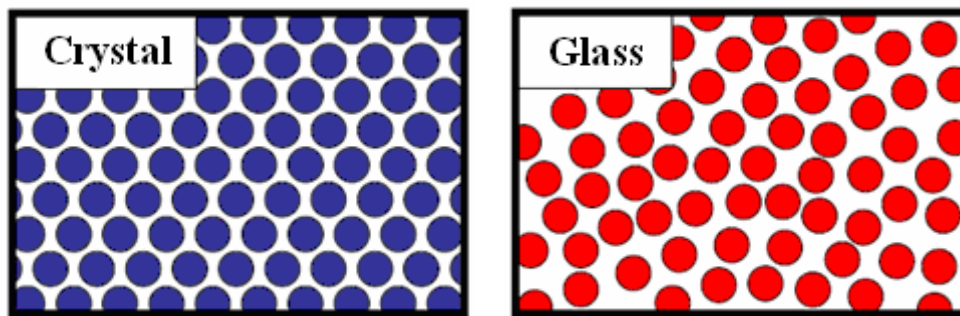


Fig. 1-1 Sketch map showing crystal and glass structure

The absence of long-range order characteristic of an amorphous solid is most clearly evidenced in a diffraction experiment such as X-ray diffraction (XRD) or with a transmission electron microscopy (TEM). When using X-rays, one observes a broad bump instead of the sharp Bragg diffraction peaks corresponding to crystals (Fig. 1-2). While the typical “salt and pepper” contrasts and the broad diffuse halo rings are shown in the high-resolution TEM image and its corresponding selected area electron diffraction pattern (SADP) (Fig. 1-3).

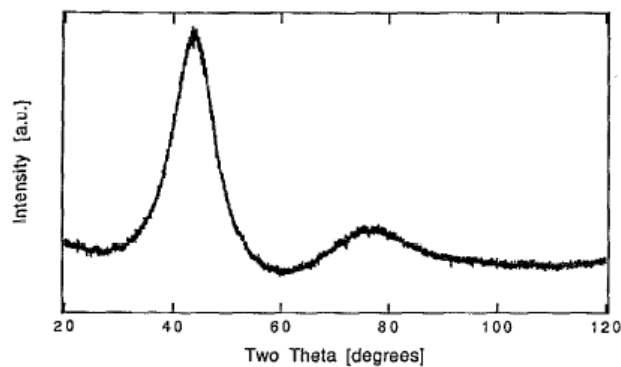


Fig. 1-2 XRD pattern taken from the cross-sectional surface of 12.6-mm-diam rod for $\text{Zr}_{41.2}\text{Ti}_{13.8}\text{Cu}_{12.5}\text{Ni}_{10.0}\text{Be}_{22.5}$ metallic glass [Peker et al., 1993]

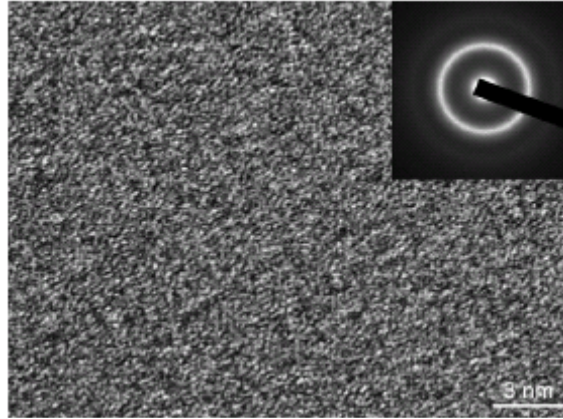


Fig. 1-3 HRTEM image of the as-cast $Zr_{60}Al_{15}Ni_{25}$ ribbon. The inset is the corresponding SADP [J.F. Li et al., 2007]

Polycrystalline materials of a grain size less than 25 nm are called nanocrystalline materials. They demonstrate quite different physical properties from both the conventional polycrystalline materials and amorphous materials. Nanocrystalline materials are characterized by their small crystallite-size in the range of a few nanometers which are separated by high-angle grain or interphase boundaries and, consequently, by their large volume fraction of disordered regions, the grain boundaries. Sometimes the distinction between an amorphous structure and a nanocrystalline structure becomes difficult [Liu, 1998].

1.1.2 Formation of Glassy State

The term “metallic glass” is commonly used to describe an amorphous solid formed by continuous cooling from the liquid state. On cooling, a liquid must be undercooled below the equilibrium crystallization temperature in order to begin to crystallize (Fig. 1-4). This can be explained by the existence of an energy barrier preventing the formation of nuclei. The degree of undercooling, a very important factor in obtaining an amorphous state, depends on several factors, including the viscosity of the liquid, the rate of viscosity increase with decreasing temperature, the interfacial energy between melt and crystal, the volume density of heterogeneously nucleating particles and the cooling rate. If the liquid metal is cooled rapidly, the influence of heterogeneous nucleation is delayed for metastable crystalline phases. When the cooling rate is sufficiently high, crystallization is suppressed because of insufficient time for growth. In the extreme case, even nucleation is suppressed. In such a case, the shear viscosity of the melt (η), increases continuously. With increasing undercooling, the driving force for nucleation is increased; however this is opposed by the rapid decrease in atomic mobility, which dominates for high undercoolings. As a consequence, the atomic configuration of the liquid deviated from equilibrium and becomes homogeneously frozen at the glass transition temperature T_g . The shear viscosity at the structural freezing point is, by convention, considered to be about 10^{12} Pa.s [Tlomag, 1988].

The glass transition temperature T_g , is generally defined as the inflection point of the rising curve of specific heat as a function of temperature. The reduced glass temperature T_{rg} , is defined as $T_{rg} = T_g / T_l$, where T_l is the liquidus temperature of the alloy. This ratio is always less than unity and it has been observed that for the metallic glasses $0.45 < T_{rg} < 0.70$. The T_g and the glass

structure are both cooling rate dependent (Fig. 1-4, 1-5). Variations in the structure are manifested by different structural relaxation behavior during annealing or crystallization of the glasses. Fig. 1-4 shows the temperature dependence of the enthalpy H , and the specific heat C_p , corresponding to crystallization and freezing of a molten metal. At T_g , a discontinuous decrease of the enthalpy causes a marked drop of the specific heat C_p , as a consequence of fewer degrees of freedom existing in a “frozen” configuration of the metallic glass [Tlomag, 1988].

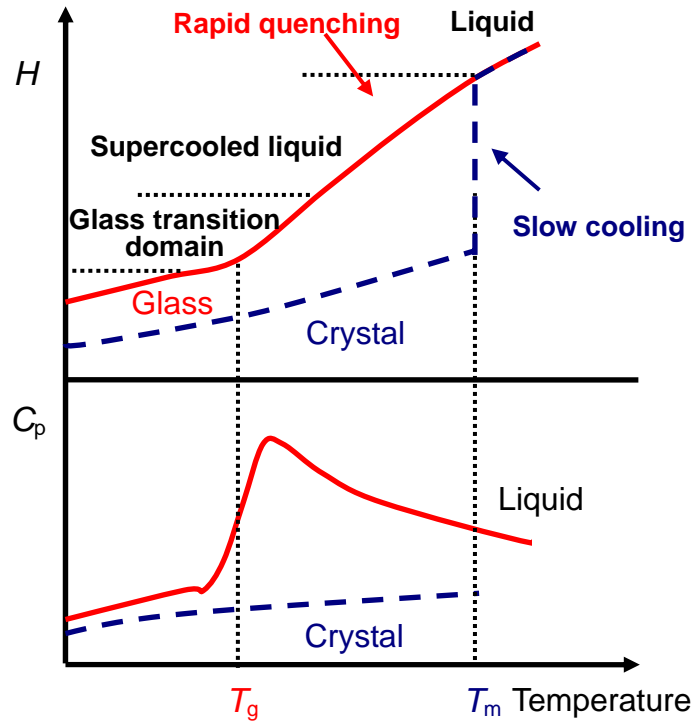


Fig. 1-4 Temperature dependences of the enthalpy H and specific heat C_p corresponding to crystallization and vitrification of a metallic melt

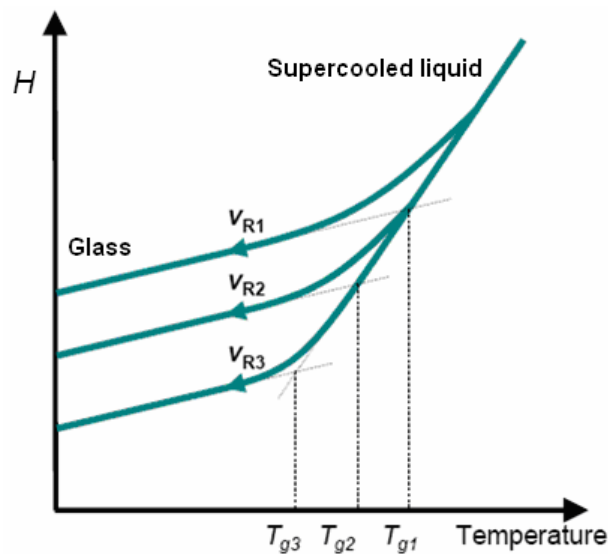


Fig. 1-5 Enthalpy H for various cooling rates $V_{R1} > V_{R2} > V_{R3}$ on molten liquid leading to the formation of glass

1.1.3 Formation of Metallic Glasses

1.1.3.1 History

Since the pioneering work of Duwez et al. [Klement et al., 1960] on the synthesis of Au-Si system metallic glasses by a rapid solidification technique for the first time in 1960, tremendous effort has been devoted to decrease the critical cooling rate with which an alloy melt can be frozen into glassy state, because through such rapid solidification techniques it was possible to produce metallic glasses only in the form of ribbons only a few microns thick. A series of multi-component amorphous alloys have been produced in a number of systems. Conventionally, in order to produce amorphous metallic alloys in the various techniques, a high cooling rate is required and the resulting amorphous products are generally very thin, less than 50 μm , in at least one dimension [Chen, 1980]. Such a small physical size has so far limited industrial/commercial applications of this class of materials. Over the past two decades, there has been a large advancement in the synthesis of bulk amorphous alloys via direct casting method through lower cooling rates (of the order of 1–100 K/s) [Inoue, 2000; Peker et al., 1993]. In this method, the composition of alloys is designed to gain the large glass formation ability (GFA) so that ‘bulk’ amorphous alloys with a dimension ≥ 1 mm in all directions can be prepared at a low cooling rate. Recently, a series of bulk amorphous alloys such as Pd-, Zr-, Mg-, Ln-, Ti-, Fe-, and Ni-based bulk glasses have successfully been prepared by the direct casting method.

The first alloy termed “bulk metallic glass” (BMG) was the $\text{Pd}_{40}\text{Ni}_{20}\text{P}_{20}$ reported by Drehman, Greer and Turnbull [Drehman et al., 1982]. Two decades have passed since Kui et al. [Kui et al., 1984] prepared in 1984, in the flux of boron oxide, the first bulk ingot of glassy alloy $\text{Pd}_{40}\text{Ni}_{20}\text{P}_{20}$ with a diameter of 10 mm. Since that, many new systems of BMGs were developed, originally based on expensive elements such as Pd, Pt, Au and then on less expensive ones such as Zr, Ni, Ti and La. Recently cheaper Fe-, Cu-, and Mg-based BMGs were prepared and now extensive research has been conducted on these alloys due to their potential applications. Researchers have shown that the glass forming ability of BMGs is sensitive to composition and many BMGs undergo phase separation, such as, $\text{Zr}_{41.2}\text{Ti}_{13.8}\text{Cu}_{12.5}\text{Ni}_{10}\text{Be}_{22.5}$ [Löffler et al., 2001], $\text{La}_{27.5}\text{Zr}_{27.5}\text{Al}_{25}\text{Cu}_{10}\text{Ni}_{10}$ [Kündig et al., 2004], $\text{Ti}_{28}\text{Y}_{28}\text{Al}_{24}\text{Co}_{24}$ [B.J. Park et al., 2004], $\text{Ni}_{58.5}\text{Nb}_{20.25}\text{Y}_{21.25}$ [Mattern et al., 2005] and $\text{Cu}_{46}\text{Zr}_{22}\text{Al}_7\text{Y}_{25}$ [Park et al., 2006] alloys. Metallic glasses become more and more attractive because of their excellent chemical, electrical, mechanical and magnetic properties: high mechanical strength and hardness, good resistance to corrosion, reduced sliding friction and improved wear resistance, excellent soft and hard magnetic properties, and unique optical or electrical properties. The deformation of metallic glasses exhibits homogeneous, superplastic behavior in the supercooled liquid region (SLR) between the glass transition temperature T_g and the onset crystallization temperature T_x at high temperatures even if the superplasticity was initially defined as a mechanism of deformation associated to grain boundary sliding, although they are very brittle at room temperature due to the inhomogeneous deformation behavior. For instance, previous studies have reported excellent plasticity in Pd-, Cu-, and Zr-based metallic glasses when deformed in SLR. Moreover, the deformed behaviors in SLR exhibited Newtonian and non-Newtonian flows, depending upon the temperature and applied strain rates [Chu et al., 2006].

In contrast to traditional glassy alloys, BMGs exhibit an extended supercooled liquid region. It

allows shaping the glass under a small applied pressure in supercooled liquid region, which is of practical importance [Shen et al., 1999; Lu et al., 2003; Kawamura et al., 2001]. However, the maximum size of bulk metallic glasses prepared by means of direct casting method is still confined to its glass formation ability. They have quite limited glass forming ability and normally their critical thickness value is less than 5 mm. For example, for important bulk magnetic Fe-, Ni- and Co-based amorphous alloys, the maximum size is restricted to less than 10 mm. Thus, the optimization of composition is still in need.

1.1.3.2 Structure

Some physical and mechanical properties of crystalline metals are explained by their inherent crystal structures and defects. However, the inherent structures and defects of metallic glasses are not clearly defined, making it difficult to understand the origin of their properties. Local atomic structure of metallic glasses is one of the interesting and open issues in the amorphous area. Recently, several pioneering works have attempted to define the atomic-scale structures and defects of amorphous alloys. Spaepen [Spaepen, 1977] and Argon and Kuo [Argon et al., 1980], in their free volume model, suggested that the free volume can be regarded as a structural defect in amorphous alloys and the origin of the local plastic deformation. Miracle [Miracle, 2004], in his dense cluster-packing model, evidenced for the first time that amorphous alloys consist of various types of short-range ordered (SRO) atomic clusters. Very recently, some studies indicated that an icosahedral short-range order (ISRO) prevails in metallic glasses and undercooled metallic melts [Xing et al., 2000; Hufnagel et al., 2003; Sheng et al., 2006]. However, other studies proposed that the chemical short-range order (CSRO) is predominant in the amorphous state [Mattern et al., 2002; Asoka-Kumar et al., 2000; Kramer et al., 2004]. Even in the same alloy systems, different researchers have advanced different viewpoints. Xing et al. [Xing et al., 2000], for example, have found that the SRO is ISRO in undercooled melts and metallic glasses of $Zr_{62-x}Ti_xCu_{20}Ni_8Al_{10}$ ($0 < x < 10$) glass forming alloys. Mattern et al. [Mattern et al., 2002], nevertheless, have found that the SRO of $Zr_{62-x}Ti_xCu_{20}Ni_8Al_{10}$ ($2 < x < 7.5$) bulk metallic glasses belongs to CSRO rather than ISRO by performing synchrotron X-ray diffraction experiments. The fact indicates that the local atomic structure of amorphous alloys is still a matter of debate.

Sheng et al. [Sheng et al., 2006] reported that these SRO atomic clusters affect the atomic packing state, which in turn may influence the properties. Although the values of these findings are significant in revealing the existence of various types of SRO structures that comprise amorphous alloys, there is little understanding of the connection between the macroscopic properties of amorphous alloys and their quantifiable structural characteristics. Many early studies implicitly suggested that the properties of amorphous alloys are intimately related to the free volume fraction, i.e. the packing density [Cao et al., 2006; Wen et al., 2003; Suh et al., 2003]. Fundamental questions arise as to what determines the packing density and how the properties are affected by it.

1.1.3.3 Glass forming ability

Despite their superior properties, their industrial availability is restricted due to their low toughness at room temperature and maximum thickness for fabrication. In order to overcome these limitations, a great deal of research has focused on increasing their glass forming ability and

optimizing their microstructures. Great efforts have also been made to understand the mechanism of amorphization for the prediction of alloy compositions with better glass forming ability. In this regard, according to traditional nucleation theory, Turnbull [Turnbull, 1969], linked nucleation ratio of crystals in amorphous with temperature and viscosity, and got conclusion that a so-called reduced temperature T_{rg} ($= T_g / T_m$, here T_g and T_m represent glass temperature and melting temperature, respectively) must be close to 2/3 to obtain the amorphous state. Inoue et al. [Inoue et al., 1998-a] proposed three empirical rules, which suggests that the composition of a glass former generally should satisfy the following conditions: (a) three or more elements; (b) a difference of atomic size ratios higher than about 12% among the three main constituent elements; and (c) negative heats of mixing among the three main constituent elements. Points (a) and (b) indicate the importance of topology in glass formation and (c) is supported by the experimental fact that the glass formation composition range generally coincides with an eutectic region. Egami et al. [Egami et al., 1984; Egami, 1996; Egami, 1997] proposed a correlation between the minimum solute concentrations required for glass formation and the extent of the atomic size mismatch in binary alloys:

$$C_s^{\min} = 0.1 / |(R_B / R_A)^3 - 1| \quad (1-1)$$

where R_A and R_B are the atomic radii of the solvent A and the solute B, respectively. Miracle and Senkov [Miracle et al., 2003] developed the above topological criterion for glass formation in binary and multicomponent alloy systems. This criterion indicated that fractions of a solute in interstitial and substitutional sites and the internal strain were functions of the radius ratio of solute and matrix elements, their elastic moduli, and absolute temperature. According to the criterion, the critical concentration initially decreases, reaches a minimum at $R \sim 0.8$ and then increases as the radius ration decreases from 1 to ~ 0.5 . Additionally, there are also many thermodynamic [Whang, 1983] and electronic [Nagel et al., 1975] models proposed. Unfortunately, there exists no universal model to predict the families of alloy compositions which are likely to possess good GFA. Even though these rules above can offer some useful guidelines for alloy design, development of new alloy with large GFA is mainly dependent on the necessity of carrying out a series of experiments where compositions are changed step by step.

1.1.3.4 Properties

The interest for bulk metallic glasses has been increasing during recent years, triggered in part by their unique physical, chemical and mechanical properties, in many cases superior to their crystalline counterparts.

1. Corrosion resistance

The amorphous structure is known to improve the corrosion resistance of an alloy, which can be explained with respect to the lack of defects like dislocations or grain boundaries, the optimized composition (not available as a single crystalline phase) and the chemical homogeneity of the metallic glass.

Gebert et al. [Gebert et al., 2008] reported the corrosion behavior of Mg-based BMGs in aqueous environments and found a superior corrosion resistance and passivation ability compared to that of Mg and the conventional AZ31 alloys (Fig. 1-6). Also, Liu et al. [L. Liu et al., 2006] showed that the corrosion resistance of Zr-based alloys was better than 316L stainless steel and Ti-6Al-4V alloy in different artificial body fluids and was significantly enhanced by the addition of

Nb (Fig. 1-7).

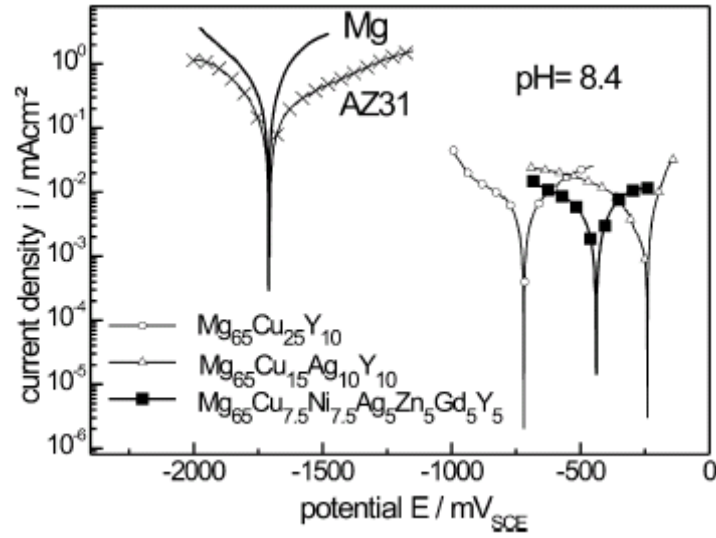


Fig. 1-6 Current density vs. potential curves of glassy Mg-based alloys in comparison to Mg and AZ31 recorded in borate buffer solution with pH 8.4 (sr = 0.5 mV/s) [Gebert et al., 2008]

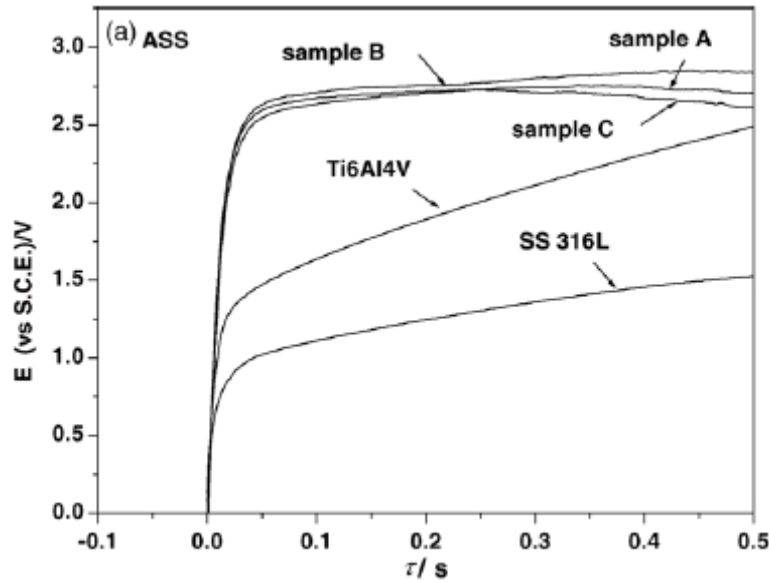


Fig. 1-7 Potential-time ($E-t$) curves of $Zr_{65}Cu_{17.5}Ni_{10}Al_{7.5}$ (sample A), $(Zr_{60}Nb_5)Cu_{17.5}Ni_{10}Al_{7.5}$ (sample B) and $(Zr_{60}Nb_5)Cu_{17.5}(Ni_5Pd_5)Al_{7.5}$ (sample C) alloys in comparison to 316L stainless steel and Ti-6Al-4V alloy in artificial saliva solution [L. Liu et al., 2006]

2. Mechanical properties

The yield stress and hardness of BMGs can be twice as those of steels, in addition, they exhibit more elastic strain and fracture toughness than ceramics and be less brittle than conventional oxide glasses [Telford, 2004]. Fig. 1-8 shows the relationship between σ_f or H_v and E for Mg-Cu-Y, La-Al-Ni, La-Al-Co-Ni-Cu, Zr-Ti-Al-Ni-Cu, Pd-Cu-Ni-P and Ti-Zr-Ni-Cu-Sn bulk metallic glasses together with the data of conventional crystalline alloys. It shows that the mechanical properties for the BMGs is significantly different from that for the crystalline alloys: the BMGs exhibit higher σ_f and H_v than those of any kinds of crystalline alloys. The BMGs have high σ_f of

840-2100 MPa combined with E of 47-102 GPa which depend on alloy compositions.

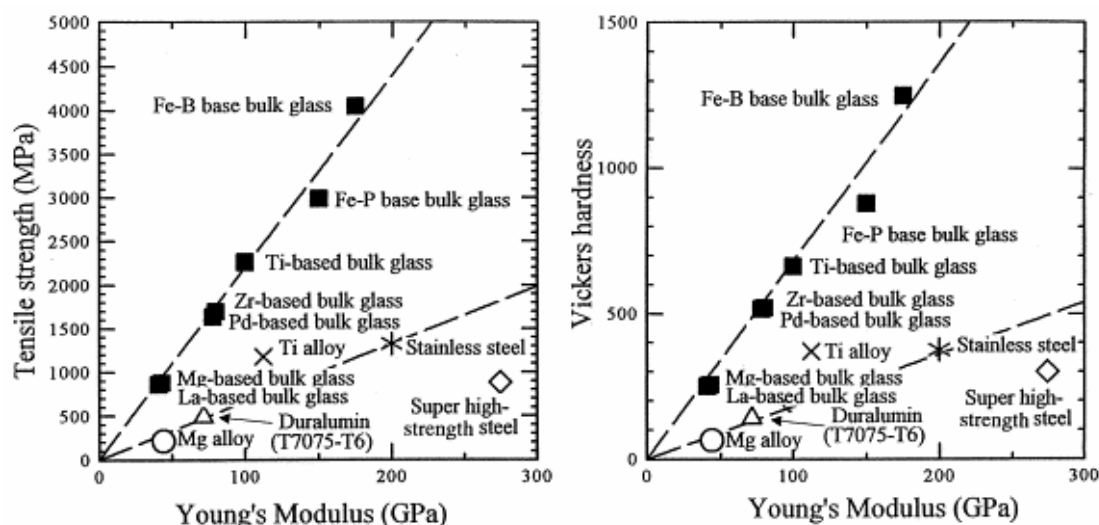


Fig. 1-8 Relationship between tensile strength σ_f or Vickers hardness H_v and Young modulus E_y for various BMGs [Inoue, 2000]

3. Net shape forming ability

It is well known that the homogeneous deformation of bulk metallic glasses usually takes place at temperatures in the supercooled liquid region, and presents usually a large ductility (over 300%). In this region, whether a BMG behaves in the Newtonian manner or not, depends on the strain rate; a slow strain rate usually favors Newtonian flow. Active study on homogeneous deformation of bulk metallic glasses began in the late 1990s, only several years after the materials could be reliably made. A brief summary of deformation data from several different metallic glass systems in the supercooled liquid region is listed in Table 1-1 [Nieh et al., 2006]. For example, Kawamura et al. investigated the superplastic deformation of $\text{Pd}_{40}\text{Ni}_{40}\text{P}_{20}$ metallic glass in ribbon form having a wide supercooled liquid region of 72 K. The maximum elongation to failure was more than 1260% at a strain rate of $1.7 \times 10^{-1} \text{ s}^{-1}$ and at 620 K with a low flow stress of about 70 MPa [Kawamura et al., 1998]. Surprisingly, $\text{La}_{55}\text{Al}_{25}\text{Ni}_{20}$ BMG, when deformed in the supercooled liquid region, exhibits extraordinarily large elongation of up to 20,000% (Fig. 1-9) [Nieh et al., 2006]. Accordingly, BMGs are considered as promising structural materials, e.g. in the field of near-net-shape fabrication of structural components.

Table 1-1

Deformation data of some BMGs in the supercooled liquid region [Nieh et al., 2006]

Alloys (in at.%)	T_g (K)	T_x (K)	m value	Ductility ^a
$\text{La}_{55}\text{Al}_{25}\text{Ni}_{20}$	480	520	1	1800 (T)
$\text{Zr}_{65}\text{Al}_{10}\text{Ni}_{10}\text{Cu}_{15}$	652	757	0.8–1.0	340 (T)
$\text{Pd}_{40}\text{Ni}_{40}\text{P}_{20}$	578–597	651	0.4–1.0	1260 (T)
$\text{Zr}_{52.5}\text{Al}_{10}\text{Ti}_5\text{Cu}_{17.9}\text{Ni}_{14.6}$	358	456	0.45–0.55	650 (T)
$\text{Zr}_{55}\text{Cu}_{30}\text{Al}_{10}\text{Ni}_5$	683	763	0.5–1.0	N/A (C)
$\text{La}_{60}\text{Al}_{20}\text{Ni}_{10}\text{Co}_5\text{Cu}_5$	451	523	1.0	N/A
$\text{Pd}_{40}\text{Ni}_{40}\text{P}_{20}$	589	670	0.5–1.0	0.94 (C)
$\text{Zr}_{65}\text{Al}_{10}\text{Ni}_{10}\text{Cu}_{15}$	652	757	0.83	750 (T)
$\text{Zr}_{55}\text{Al}_{10}\text{Cu}_{30}\text{Ni}_5$	670	768	0.5–0.9	800 (T)
$\text{Ti}_{45}\text{Zr}_{24}\text{Ni}_{17}\text{Cu}_8\text{Be}_{16}$	601	648	N/A	1.0 (T)
$\text{Cu}_{60}\text{Zr}_{20}\text{Hf}_{10}\text{Ti}_{10}$	721	766	0.3–0.61	0.78 (C)
$\text{Zr}_{52.5}\text{Al}_{10}\text{Cu}_{22}\text{Ti}_{2.5}\text{Ni}_{13}$	659	761	0.5–1.0	>1.0 (C)
$\text{Zr}_{41.25}\text{Ti}_{13.75}\text{Ni}_{10}\text{Cu}_{12.5}\text{Be}_{22.5}$	614	698	0.4–1.0	1624 (T)

^a “T” and “C” stand for tension and compression, respectively.

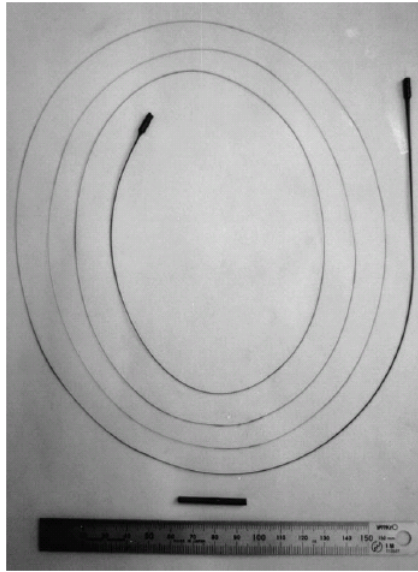


Fig. 1-9 A $\text{La}_{55}\text{Al}_{25}\text{Ni}_{20}$ alloy is deformed to 20,000% in the supercooled liquid region [Nieh et al., 2006]

1.1.3.5 Application

Bulk metallic glasses have been extensively explored owing to their fundamental scientific importance and engineering applications. BMGs exhibit unique properties, e.g. high strength (about 2–3 times of its counterpart crystalline material), large elastic limit (about 2%) which is very near to some polymer materials, high corrosion resistance, high wear resistance, etc. These properties, which can be rarely found in crystalline materials, are attractive for the practical application as a new class of structural and functional materials.

Due to the fact that new glass-forming compositions have been found that have a critical cooling rate of less than 100 K/s and can be made glassy with dimensions of 10 mm or more, which makes them attractive for applications. Recently, several families of amorphous alloys have been developed, commercialized, or tested for some potential applications. For example, Cu-based amorphous alloys have attracted more and more attention due to their good mechanical properties [Inoue et al., 2002]. They are considered one of the potential structural materials for sporting goods, defense related applications, and micro-electromechanical systems (MEMS). Meanwhile, Mg-based amorphous alloys have attracted increasing interest as promising hydrogen storage and engineering materials because of their absorbability of hydrogen in large quantities, lower specific gravity, richer mineral resources, low glass transition temperature and so on [L.J. Huang et al., 2008]. Ti-based amorphous alloys have attracted increasing attention owing to their high specific strength as a potential structural materials [Duan et al., 2008; Ma et al., 2004-a; Ma et al., 2004-b; Kim et al., 2004; J.M. Park et al., 2005; Guo et al., 2005; K.B. Kim et al., 2008]. Among the BMGs produced so far, the Zr-based alloys exhibit excellent mechanical properties and good glass forming ability, and have been used to fabricate sporting goods (Fig. 1-10 (a)), medical devices, springs, parts of cellphones (Apple i-phone), parts of precision instruments (Fig. 1-10 (b)) and so on [Johnson, 1999; Inoue et al., 2000-b]. Meanwhile, Fe-based amorphous alloys, such as $\text{Fe}_{40}\text{Ni}_{38}\text{B}_{18}\text{Mo}_4$, are already utilized in many commercial applications, such as power switchings, signal transformers, composites, brazing foil, and magnetic devices [Wu et al., 2008].

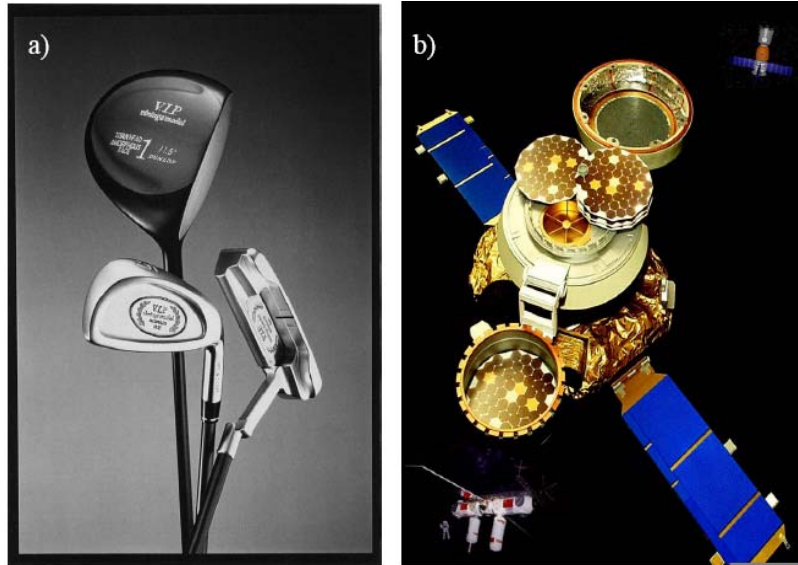


Fig. 1-10 (a) Outer shapes of commercial golf clubs where the face materials are composed of Zr-Al-Ni-Cu bulk metallic glasses. (b) The Genesis spaceship and her solar wind collector, the materials of which are composed of Zr-Nb-Cu-Ni-Al bulk metallic glasses [Xi, 2005]

1.1.3.6 Limits for applications as structural materials

1. Maximum dimension

Although the functional application of metallic glasses is well established, the prospect of structural applications of metallic glass has brightened with the discovery of a large number of bulk metallic glasses. However, the sample dimensions achievable during processing restrict the application of BMGs as structural materials, and also prevent detailed studies of mechanical properties under different loading conditions.

2. Brittleness at ambient temperature

In contrast to traditional glassy alloys, BMGs are characterized by a high glass forming ability with a large supercooled liquid region before crystallization. This provides new opportunities for high temperature forming and near-net-shape fabrication of structure components by using the superplasticity of BMGs in the supercooled liquid region. However, monolithic BMGs, without crystalline structure, dislocation contribution to ductile deformation is impossible, usually they exhibit very limited globe plasticity at room temperature. Even for ductile Zr- or Pd-based BMGs, the commercial application is still limited due to the lack of sufficient plasticity. As a result of the highly localized shear band formation, BMG specimens often shear off at $\sim 45^\circ$ with respect to the loading axis along the major shear plane with a remarkably little plastic strain of $< 2\%$ in compression and essentially naught ductility in tension at room temperature, which limits their widespread applications as promising structural materials [H.M. Chen et al., 2009].

The deformation of metallic glasses generally conforms to elastic-perfectly plastic flow behavior. The inhomogeneous plastic flow in that case is related to a local change in viscosity leading to a softening of the glass and the localization of plastic strain. There exist two hypotheses aimed to explain the local softening of the glass. In one it was suggested that the deformation can lead to a change in free volume which results in a lowering of the density and is responsible for flow softening due to lowering of the resistance to deformation. The second model invokes flow

softening due to adiabatic heating during shear deformation. Although most of the current work conforms to an explanation based on the concept of excess free volume, evidence also points to a substantial temperature rise near the fracture surface. Electron microscopy of the shear band in recent time has revealed that nanocrystals can form in the shear bands during deformation in several glasses and the origin of these nanocrystals is the subject of debate [Chang et al., 2006].

Intensive efforts have been made to enhance the plasticity of BMGs and two promising approaches have been developed [H.M. Chen et al., 2009]. One approach is the intrinsic toughening by increasing the Poisson's ratio or the amount of free volume in BMG, and another approach is the extrinsic toughening by developing a BMG-based composite by introducing the second ductile crystalline phase or by in situ formation of ductile crystalline phase within the glassy matrix or phase-separated dual phase glasses. These approaches are designed with the goal to block or confine the propagation of shear bands during deformation. For example, strength and ductility of the BMG can be enhanced by precipitation of nanoscale quasicrystalline phase in the amorphous matrix [Inoue et al., 2000-a; Kim et al., 2003].

Very recently, new approaches have been proposed to develop simple and feasible methods that could enhance the plasticity of the BMGs including the known BMG systems [Y. Zhang et al., 2006; Yu et al., 2007; L.Y. Chen et al., 2008]. Although there are only few reports about the low-temperature mechanical behaviors of metallic glasses, and the plasticity of those BMGs at cryogenic temperatures was not distinctly improved [H. Li et al., 2006; Takeuchi et al., 2000]; however, Huang et al. [Huang et al., 2008-a] found a significant enhancement in both compressive strength and plasticity of a Ti-based BMG ($\text{Ti}_{40}\text{Zr}_{25}\text{Ni}_3\text{Cu}_{12}\text{Be}_{20}$) deformed at low temperature far below the ambient temperature. The compressive maximum fracture strength increases from 1710 MPa to 1908 MPa and the plasticity also increases from 6.9% to 14.5% with the temperature decrease from 298 K to 123 K, which provides us a new way to resolve the limited plasticity problem of BMGs.

1.2 Critical Review about Ti-based Bulk Metallic Glasses

1.2.1 Interest of Ti-based BMGs

Bulk metallic glasses and their composites have attracted a great deal of attention due to the excellent properties they possess compared with their crystalline counterparts. Of particular importance are those metallic glasses based on lightweight elements such as Al, Mg and Ti that exhibit high specific strength. Among them, Ti-based metallic glasses are promising as a new family of lightweight materials (e.g. automotive or aerospace industries) due to their relatively low-cost, low density, high specific strength, large compressive strength and reasonable Young's modulus and good corrosion resistance [Duan et al., 2008; Ma et al., 2004-a; Ma et al., 2004-b; Kim et al., 2004; J.M. Park et al., 2005; Guo et al., 2005; K.B. Kim et al., 2008]. Accordingly, a number of studies on amorphization of Ti-based alloys have been carried out for the last three decades presumably because the amorphization is expected to cause remarkable increases in mechanical strength and corrosion resistance, etc.

Although Ti-based metallic glasses were reported as early as 1977 [Tanner et al., 1977], during a long period the Ti-based metallic glasses were found only in rapidly solidified Ti-M

(M=transition metal) [Polk et al., 1978], Ti-Al-M [T. Zhang et al., 1993], Ti-Ni-Cu [T. Zhang et al., 1994], Ti-Ni-Cu-Al [Inoue et al., 1994] and Ti-Cu-Ni-Sn [T. Zhang et al., 1998-a]. No BMGs were formed in these alloys due to their poor glass forming ability, so that a fully amorphous structure was available only in the form of ribbon. Until 1994, Ti-based BMGs were first reported in the Ti-Zr-Ni-Be system by Peker and Johnson [Peker et al., 1994]. To day, a number of Ti-based bulk metallic glasses, such as Ti-Cu-Ni-(Sn or Sb) [T. Zhang et al., 1998-a], Ti-Cu-Ni-Si-B [T. Zhang et al., 1999; T. Zhang et al., 2001], Ti-Zr-Ni-Cu-Sn [Louzguine et al., 1999], Ti-Cu-Ni-Zr-Al-Si-B [Xia et al., 2005-a], (Ti, Zr)-(Cu, Ni) [Men et al., 2005], Ti-Zr-Ni-Cu-Be [Kim et al., 2004], Ti-Cu-Ni-Al-Si-M-B (M = Sc, Hf, Ta, Nb) [Xia et al., 2005-b], Ti-Cu-Ni-Sn-B-Si [T. Zhang et al., 2001] and Ti-Cu-Ni-Zr-Hf-Sn-Si [Huang et al., 2007-a], ect. have been synthesized among the multi-component alloys by the copper mold casting method. For example, Recently, Zhang and Inoue [T. Zhang et al., 2001] reported that a fully amorphous rod of a $\text{Ti}_{50}\text{Cu}_{20}\text{Ni}_{24}\text{Sn}_3\text{B}_1\text{Si}_2$ alloy with a diameter of 1 mm was fabricated by injection casting. BMGs with a diameter of 2 mm have been reported in the more complex multi-component Ti-Cu-Ni-Al-Si-M-B (M = Sc, Hf, Ta, Nb) system [Xia et al., 2005-b]. More recently, several BMGs have been successfully fabricated in a ternary system, such as, $\text{Ti}_{50}\text{Cu}_{42}\text{Ni}_8$ [X.F. Wu et al., 2008] and $\text{Ti}_{45}\text{Zr}_{20}\text{Be}_{35}$ [Duan et al., 2008] with diameters of 2 and 6 mm, respectively.

Indeed, the Ti-based metallic glasses have already shown to form glassy rods with maximum diameters up to 6-14 mm [Guo et al., 2005; Kim et al., 2003; Kim et al., 2004]. However, these metallic glasses with critical thickness larger than 5 mm usually contain toxic beryllium element. It is of scientific and technological interest to synthesize new Ti-based bulk amorphous alloys free of toxic element, but with low density and high strength. Ma et al. [Ma et al., 2004-b] have recently tried to improve the glass forming ability of a eutectic alloy $\text{Ti}_{50}\text{Cu}_{42.5}\text{Ni}_{7.5}$ by substituting Ti with appropriate amounts of Zr and Hf as well as a minor amount of Si and succeeded in synthesizing Ti-based BMG with maximum diameters up to 5 mm for $\text{Ti}_{41.5}\text{Zr}_{2.5}\text{Hf}_5\text{Cu}_{42.5}\text{Ni}_{7.5}\text{Si}_1$ by using the copper mold casting. More recently, based on the work of Ma et al., Huang et al. [Huang et al., 2007-a] successfully fabricated $\text{Ti}_{41.5}\text{Cu}_{37.5}\text{Ni}_{7.5}\text{Zr}_{2.5}\text{Hf}_5\text{Sn}_5\text{Si}_1$ BMG with maximum diameter up to 6 mm by partial replacement of Cu by Sn. At the same time, new Ti-based bulk metallic glasses without toxic elements in Ti-Zr-Cu-Pd-Sn [Qin et al., 2006] and Ti-Zr-Cu-Pd [Zhu et al., 2007] systems have been synthesized by Inoue et al. In particular, the Ti-Zr-Cu-Pd alloy system has high glass forming ability leading to glassy alloy rods with diameters up to 6 mm ($\text{Ti}_{40}\text{Zr}_{10}\text{Cu}_{36}\text{Pd}_{14}$) [Qin et al., 2007].

Ti-based metallic glasses can be generally classified into two classes: Be-free and Be-containing alloys, which show different GFA and mechanical properties. The maximum size (D_{max}) of the Be-free Ti-based BMGs is 6 mm [Huang et al., 2007-a], while the Be-containing Ti-based BMGs can be up to 10 mm [J.M. Park et al., 2005]. With regard to the mechanical properties, the Be-free, Ti-based BMGs exhibit a high fracture strength (σ_f) exceeding ~ 2300 MPa but unfortunately they suffer from a lack of plasticity ($<0.5\%$) [Huang et al., 2007-a; T. Zhang et al., 2001; Ma et al., 2004-a] (Fig. 1-11). The poor plasticity renders these alloys prone to catastrophic failure in load-bearing applications. Catastrophic early failure can occur if most of the plastic deformation becomes localized in one or a few dominant shear bands. In contrast, the Be-containing Ti-based BMGs display a larger plastic strain (ϵ_p) of about 2-7% but show a relatively lower σ_f of ~ 1900 MPa [J.M. Park et al., 2005; Guo et al., 2005] (Fig. 1-12). However, their plasticity does not originate from the glassy phase itself but is closely related to the amount

of nanocrystals embedded in the metallic glass matrix, which means that Be-containing Ti-based BMGs are actually nanocrystalline/metallic glass matrix composites rather than monolithic metallic glasses.

As mentioned in the above section, one of the main technological drawbacks of BMGs is that they typically show limited plasticity at room temperature, which actually hinders further advancement in the applicability of these materials. Nevertheless, compared to other BMGs, Be-containing Ti-based metallic glasses exhibit moderate plastic deformation, not far from the commercially available Zr-, Ni-, Cu- or Pd-based metallic glasses [Kim et al., 2004; J.M. Park et al., 2005; J. Zhang et al., 2007; Lewandowski et al., 2005; Wang, 2006; Fornell et al., 2009].

Very recently, Ti-based bimodal composites [He et al., 2003-a; Louzguine et al., 2005; C.L. Zhang et al., 2007] have been developed with the aim of obtaining high strength Ti alloys with large plasticity. The Ti-based bimodal composites display much higher σ_f of ~2000-2600 MPa and larger $\varepsilon_p > 2\%$ compared with the Ti-based metallic glasses. For example, the $\text{Ti}_{60}\text{Cu}_{14}\text{Ni}_{22}\text{Sn}_4\text{Nb}_{10}$ alloy reaches a strength of 2400 MPa and 14.5% plastic strain [He et al., 2003-a], and $\text{Ti}_{63.375}\text{Fe}_{34.125}\text{Sn}_{2.5}$ has $\sigma_f = 2650$ MPa and $\varepsilon_p = 12.5\%$ [C.L. Zhang et al., 2007]. The strategy of using a composite or non-uniform microstructure formed in situ is a common thread linking several recent successful attempts to enhance the plasticity or toughness of high-strength nanocrystalline alloys and metallic glasses.

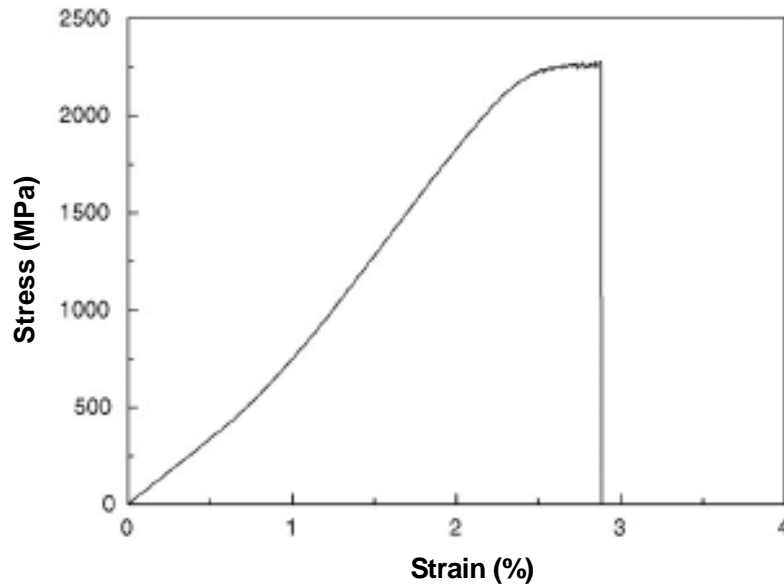


Fig. 1-11 Nominal compressive stress-strain curve of the $\text{Ti}_{41.5}\text{Cu}_{37.5}\text{Ni}_{7.5}\text{Hf}_5\text{Sn}_5\text{Zr}_{2.5}\text{Si}_1$ glassy alloy rod under an initial strain rate of $4 \times 10^{-4} \text{ s}^{-1}$ [Huang et al. 2007]

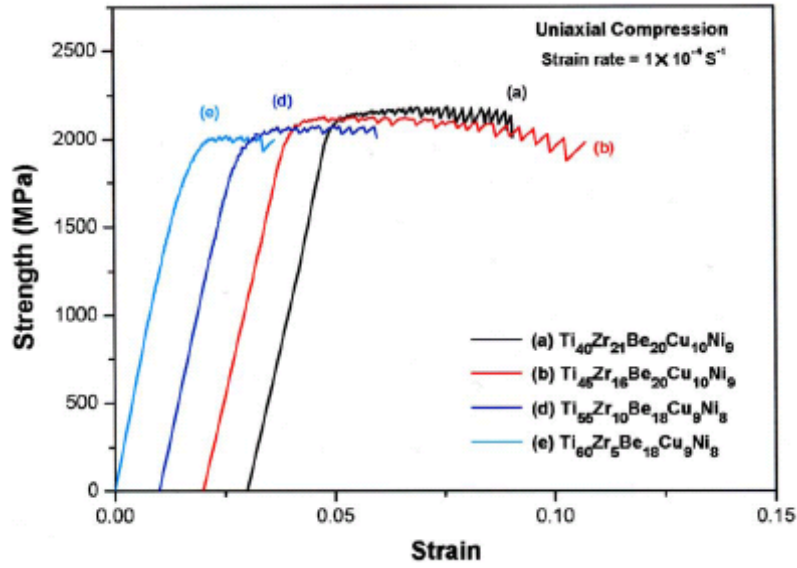


Fig. 1-12 Compressive stress-strain curves obtained from the typical Ti-Zr-Be-Cu-Ni bulk metallic glasses [J.M. Park et al., 2005]

1.2.2 Exploration for New Ti-based BMGs

The glass forming ability of Ti alloys is still poor compared with other easy glass forming alloys. Moreover, they usually contain a low Ti concentration (40-50 at.%), and so do not fully exploit the benefits attributed to the Ti element. Many theoretical models exist to aid in the design of metallic glass compositions. As there is no universal model to explain the vitrification behavior of all alloy systems, significant “experimental trial and error” is still required to design good glass forming alloys (possessing a critical thickness above one millimeter). The design challenge becomes more difficult when a cost constraint is considered, such that only low-cost alloying elements must be used.

In order to design low-cost alloys, Cheney et al. [Cheney et al., 2009] combined three separate models: chemical short range order model, structural model and deep eutectics model, to effectively analyze the composition space of Ti-Ni-Cu-Si-Sn system studied for the presence of potential good glass forming alloys, and successfully produced a series of Ti-based BMGs over a wide compositional space with only cost-effective alloying elements, Ni, Cu, Si, and Sn (Fig. 1-13). The best glass former in this composition space, $\text{Ti}_{48}\text{Ni}_{32}\text{Cu}_8\text{Si}_8\text{Sn}_4$, demonstrates a supercooled liquid region in excess of 100 K, and was successfully cast into fully amorphous rods, 3 mm in diameter, with a compressive fracture strength of ~ 1.8 GPa.

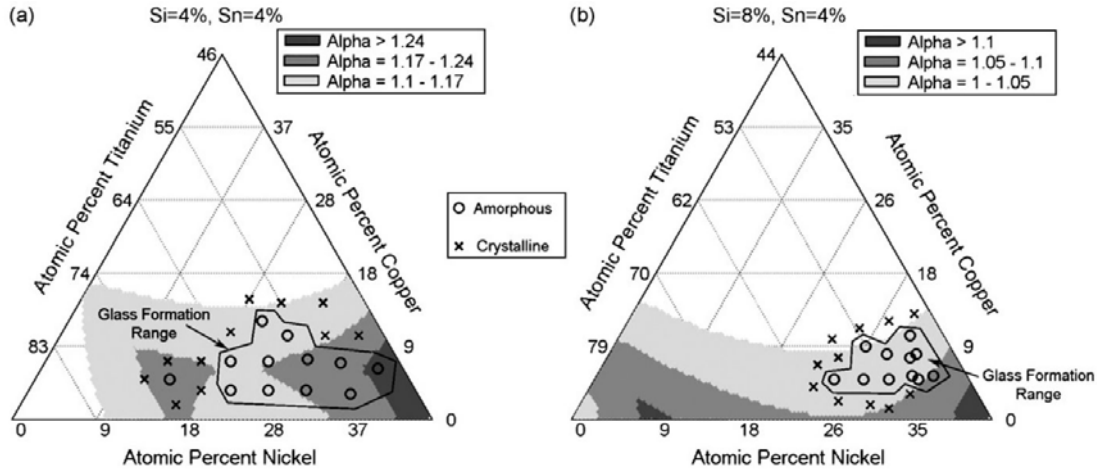


Fig. 1-13 Pseudo-ternary phase diagrams showing successful glass forming compositions in the circled regions. a) Si = 4% and Sn = 4%, b) Si = 8% and Sn = 4% [Cheney et al., 2009]

During the composition design of Ti-based BMGs, density should be significantly considered. As we know, conventional titanium alloys have been widely used in the aerospace industry due to their availability, low density and high specific strength. However no Ti-based BMGs with density comparable to that of pure Ti or Ti6Al4V (4.42 g/cm^3) alloy are reported until the occurrence of Ti-Zr-Be BMGs with low density of around 4.6 g/cm^3 produced by Johnson et al. by the elimination of late transition metals (LTMs) in the Be-containing Ti-based BMGs [Duan et al., 2008], although researchers have developed several Ti-based glass-forming systems. Unfortunately, although these amorphous alloys exhibit very high specific strength, at the same time, they significantly loose plasticity compared with Ti-Zr-Ni-Cu-Be BMGs.

1.2.3 Application of Ti-based BMGs

The combination of properties of crystalline titanium and its alloys, low density, high strength, high specific strength, a relatively low modulus and excellent biocompatibility with outstanding corrosion resistance, has resulted in the widespread use of titanium and Ti-based alloys in the industrial, aerospace and biomedical industries. But with the development of science and technology, aerospace and biomedical materials are faced more and more critical request. The ease of fabrication and the excellent mechanical properties found in Ti-based BMGs could be advantageous in aerospace and biomedical applications. In my opinion, biomedical devices are the most promising application for Ti-based BMGs so far, such as pacemaker cases, housings for ventricular-assist devices, implantable infusion drug pumps, screws and bone plates, etc. [Morrison et al., 2007].

Two problems are needed to be considered: some elements, such as Cu, Ni, Al and Be, as one of compositions of biomaterials, are not compatible with human body, which may lead to cytotoxicity and neurotoxicity. Another problem is the very limited plasticity before fracture at room temperature. Great efforts have been made to produce Ti-based biomaterials which can fulfil these two requests mentioned above. Ti-based amorphous alloys $\text{Ti}_{70}\text{Zr}_{16}\text{Fe}_7\text{Si}_{17}$ and $\text{Ti}_{64}\text{Zr}_{15}\text{Fe}_6\text{Si}_{17}\text{Mo}_6\text{Nb}_2$ were fabricated by Bai et al. [Bai et al., 2008]. By introducing Nb into the Ti-Zr-Cu-Pd bulk metallic glass, Qin et al. [Qin et al., 2008] obtained a good biomaterial with

enhanced plasticity by in situ forming ductile bcc phase.

1.3 Motivation

In this study, after an exhaustive search for new alloys, we have chosen 2 alloys that we were able to produce in a bulk form. We select $\text{Ti}_{40}\text{Zr}_{25}\text{Ni}_8\text{Cu}_9\text{Be}_{18}$ and $\text{Ti}_{41.5}\text{Cu}_{37.5}\text{Ni}_{7.5}\text{Zr}_{2.5}\text{Hf}_5\text{Sn}_5\text{Si}_1$ BMGs as an objective, and focus our work on the following 5 aspects, aiming to find the applicability of Ti-based BMGs as a structural material. The reason why we choose these two compositions will be clarified in the Chapter 2.

1. Glassy state is the most fundamental and essential scientific question, it is necessary to identify the microstructure of these two Ti-based BMGs firstly, monolithic glass, embedded with nuclei in the quenched matrix or there exist nanocrystals in the glass matrix.
2. Little is known about the appearance of glass transition and supercooled liquid region for Ti-based metallic glasses. The appearance of the supercooled liquid region before crystallization is important because of the expectation that the metallic glasses have high glass forming ability and can be net shape formed in the supercooled liquid region. The ease of net shape forming in the supercooled liquid region is dependent on the temperature interval of the supercooled liquid region. So it is necessary to clarify the structural relaxation, glass transition behavior and the appearance of supercooled liquid region.
3. It is known that an annealing treatment of glassy alloy precursors is an useful method to prepare bulk nano-crystalline alloys. Inoue [Inoue, 1994] indicated that the formation of a nano-crystalline structure should satisfy the following criteria: (1) multistage crystallization processes; (2) high nucleation frequency; (3) low growth rate; and (4) enhancement of the thermal stability of the remaining glassy phase caused by the redistribution of a solute element at the nano-crystalline/glassy interface. However, two different effects will occur in different alloy systems after annealing of glassy precursors. Some glassy alloys become very brittle after partial crystallization, such as Fe-Si-B-Nb alloy [Sakamoto et al., 1996]. While both the mechanical strength and ductility of the bulk glassy alloy can be significantly improved by the formation of the nano-structures as compared with the corresponding glassy single phase alloys in Zr-Al-Cu-Pd [Inoue et al., 2000-b] and Zr-Ti-Ni-Cu-Al [Xing et al., 1998] alloys. Therefore, it is necessary to investigate the crystallization behavior, mechanism and the influence of annealing on the microstructure and mechanical properties of Ti-based BMGs.
4. In order to develop the applicability of BMGs as structural materials, there has been intensive investigation of the mechanical behavior of bulk metallic glasses. It should be noted that, in spite of the interesting properties, some aspects of the mechanical behavior of BMGs have not been systematically addressed yet. In addition, universal agreement on the deformation mechanism of metallic glasses has yet to be attained. For example, Sergueeva et al. [Sergueeva et al., 2004] reported that the ductility increases and the fracture strength decreases with increasing strain rate in tension in Dy_3Al_2 ribbon and bulk Vitreloy-1 ($\text{Zr}_{41.2}\text{Ti}_{13.8}\text{Cu}_{12.5}\text{Ni}_{10}\text{Be}_{22.5}$) amorphous alloys. On the contrary, Mukai et al. [Mukai et al., 2002] found that the fracture strength and strain of $\text{Pd}_{40}\text{Ni}_{40}\text{P}_{20}$ BMG were independent of the strain rate in tension. Similarly, during compression testing Bruck et al. [Bruck et al., 1996] and Subhash et al. [Subhash et al., 2002] found that the fracture strength and plastic strain of Vitreloy-1 alloy were independent of strain rate. However, negative rate sensitivity was found in Zr/Hf-based BMG by Li et al. [H. Li et al., 2003]. These

conflicting results suggest that many factors, such as chemical compositions, level of amorphization, loading mode, and sample geometry of the metallic glasses, can significantly influence the mechanical behavior under different strain rates. Therefore, more experimental data are required to fully understand the deformation nature in metallic glasses.

5. Previous studies have reported excellent plasticity in Pd-, Cu-, and Zr-based metallic glasses when deformed in the supercooled liquid region. Moreover, the deformed behaviors in SLR exhibited Newtonian and non-Newtonian flows, depending upon the temperature and applied strain rates. To my knowledge, no report is about the deformation behavior in the SLR and associated mechanisms of Ti-based BMGs. So it could be a pioneering work in this aspect.

CHAPTER 2

STRUCTURE OF TI-BASED BULK METALLIC GLASSES

2.1 Selection of Alloy Composition

As mentioned in Chapter 1, Ti-based metallic glasses can be generally classified into two classes: Be-free and Be-containing alloys, which show different GFA and mechanical properties. The detail difference between these two systems was shown in Chapter 1. In addition, in this regard, the researchers usually classify Ti-based metallic glass into another two classes: Ti-Zr-Ni and Ti-Cu-Ni system. Ti-Zr-Ni system is related to quasicrystalline system, which means the quasicrystals can form easily in this system, while Ti-Cu-Ni system is related to titanium primary phase. In my opinion, these two taxonomies can be unified under a certain condition when Ti-Zr-Ni-Be-(M) and Ti-Cu-Ni-(M) (M represents the element except Be) system are considered. The most typical BMGs alloy system of these two systems are Ti-Zr-Ni-Cu-Be and Ti-Cu-Ni-Zr-(M), respectively. So, we plan to select one alloy amongst each systems mentioned above. In the next part, first we will select two alloys by considering the general research work and some of our experiments. Next, we will summarize the difference between two alloys from various points: cost, density, with or without toxic element, microstructure, thermal stability, GFA, plasticity, crystallization product, ect., to clarify the significance of our study work.

2.1.1 Ti-Zr-Ni (Be-containing) System

Since the great efforts that have been made by D.H. Kim et al. to develop Ti rich bulk metallic glasses through considering the high GFA of Be containing Zr-based alloy [Peker et al., 1993] and pseudo ternary phase diagram representation of the alloy with axes of Ti, Zr and NCB(Ni-Cu-Be alloy) [Szuecs et al., 2001]. A series of Ti-rich (containing Ti above 40 at.%) Ti-Zr-Ni-Cu-Be system BMGs were obtained. Fig. 2-1 shows the schematic pseudo Ti-Zr-(Be, Cu, Ni) ternary diagram [J.M. Park et al., 2005]. The maximum diameter and compressive properties of the as-cast Ti-Zr-Ni-Cu-Be BMGs are listed in Table 2-1. They exhibit outstanding GFA and excellent mechanical properties, high strength, large elastic limit, especially the moderate plasticity comparable to Zr- and Pd-based commercial metallic glasses.

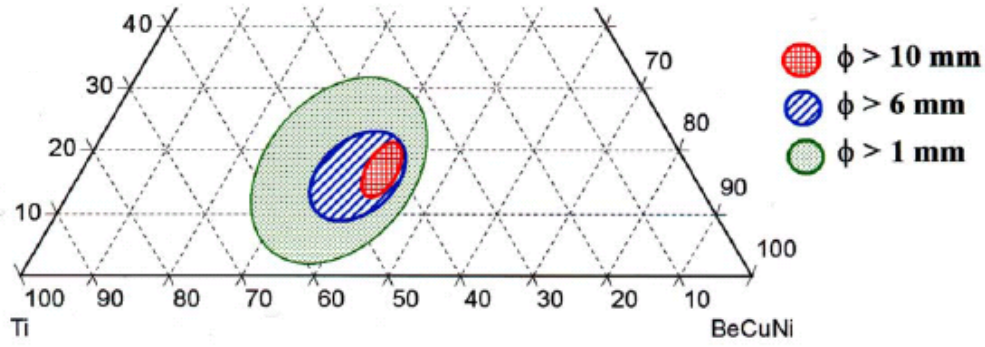


Fig. 2-1 Schematic pseudo Ti-Zr-(Be, Cu, Ni) ternary diagram showing outline of composition range for maximum diameter for glass formation of 1, 6 and 10 mm [J.M. Park et al., 2005]

Table 2-1

Mechanical properties of the as-cast Ti-Zr-Be-Cu-Ni BMG samples (ultimate compressive stress: σ_{\max} , total strain: ε_t , and plastic strain: ε_p for glass formation), maximum diameter: D_{\max} , Φ and $\dot{\varepsilon}$ represent the diameter of the sample and strain rate for compression test

Composition (at.%)	D_{\max} (mm)	Φ (mm)	$\dot{\varepsilon}$ (s ⁻¹)	σ_{\max} (MPa)	ε_t (%)	ε_p (%)	Ref.
Ti ₄₀ Zr ₂₁ Ni ₉ Cu ₁₀ Be ₂₀	10	1	1×10^{-4}	2176	6.0	4.0	[J.M. Park et al., 2005]
Ti ₄₅ Zr ₁₆ Ni ₉ Cu ₁₀ Be ₂₀	10	1	1×10^{-4}	2105	8.9	6.9	[J.M. Park et al., 2005]
		1	1×10^{-4}	1900	6.3	4.7	[J. Zhang et al., 2007]
Ti ₄₀ Zr ₂₅ Ni ₈ Cu ₉ Be ₁₈	8	1	1×10^{-4}	1900	5.2	4	[Kim et al., 2004]
		1	1×10^{-4}	1600	24	22	[W.F. Ma et al., 2009]
		3	1×10^{-4}	1750	10	8	[W.F. Ma et al., 2009]
		3	1.8×10^{-4}	1720	5.6	3.4	[Fornell et al., 2009]
Ti ₅₀ Zr ₁₅ Ni ₈ Cu ₉ Be ₁₈	6	1	1×10^{-4}	2072	4.9	2.9	[J.M. Park et al., 2005]
Ti ₅₅ Zr ₁₀ Ni ₈ Cu ₉ Be ₁₈	6	1	1×10^{-4}	2097	4.8	2.8	[J.M. Park et al., 2005]
Ti ₆₀ Zr ₅ Ni ₈ Cu ₉ Be ₁₈	2	1	1×10^{-4}	2010	3.7	1.7	[J.M. Park et al., 2005]
Ti ₄₀ Zr ₂₉ Ni ₈ Cu ₉ Be ₁₄	2	1	1×10^{-4}	1978	9.3	7.4	[J.M. Park et al., 2005]
Ti ₄₅ Zr ₂₈ Ni ₆ Cu ₇ Be ₁₄	2	1	1×10^{-4}	1684	4.0	2.0	[J.M. Park et al., 2005]
Ti ₅₅ Zr ₁₈ Ni ₆ Cu ₇ Be ₁₄	2	1	1×10^{-4}	1753	3.2	1.2	[J.M. Park et al., 2005]
Ti ₄₀ Zr ₂₅ Ni ₃ Cu ₁₂ Be ₂₀	6 (12)	3	4×10^{-4}	1710	8.9	6.9	[Guo et al., 2005; Ohkubo,
		1	4×10^{-4}	1651		12.5	et al., 2007; Huang et al.,
		2	4×10^{-4}	1680		10	2007-b; Huang et al.,
		4	4×10^{-4}	1784		2.5	2008-a]
		6	4×10^{-4}	1858		1.2	

Amongst these Ti-based BMGs, Ti₄₀Zr₂₁Ni₉Cu₁₀Be₂₀, Ti₄₅Zr₁₆Ni₉Cu₁₀Be₂₀ and Ti₄₀Zr₂₅Ni₈Cu₉Be₁₈ exhibit the best GFA resulting in the maximum diameter of sample obtained by conventional casting (up to 8-10 mm), combining with obvious plastic deformation under the condition of compression test at room temperature. Although Ti₄₀Zr₂₉Ni₈Cu₉Be₁₄ BMG exhibit excellent plasticity, however it fails to fabricate a sample with the diameter larger than 2 mm. In addition, we found that Ti₄₅Zr₁₆Ni₉Cu₁₀Be₂₀ and Ti₄₀Zr₂₅Ni₈Cu₉Be₁₈ were relatively extensively investigated so far due to their excellent GFA and mechanical properties, however, there exists

debate about the strength as well as the plasticity, especially for $\text{Ti}_{40}\text{Zr}_{25}\text{Ni}_8\text{Cu}_9\text{Be}_{18}$ BMG, the strength obtained is in the range of 1600-1900 MPa and the difference of plasticity obtained from different measurements is even larger, the best and the worst one are 22% and 3.4%, respectively, which make us to think about and be of great interest in clarifying the intrinsic reason. So we try to prepare the samples with the nominal compositions of $\text{Ti}_{45}\text{Zr}_{16}\text{Ni}_9\text{Cu}_{10}\text{Be}_{20}$ and $\text{Ti}_{40}\text{Zr}_{25}\text{Ni}_8\text{Cu}_9\text{Be}_{18}$ in diameter of 2 mm and then check their mechanical properties. Fig. 2-2 shows the compressive stress-strain curves of these two alloys, we use the strain rate, $5 \times 10^{-4} \text{ s}^{-1}$, which is generally used in the literature for easy comparison with results of the literature. For each alloy, we measured three times to get an average result, because as we know there maybe pores originated from the conventional cast process. The compressive stress-strain curve of another amorphous alloy, with the nominal composition of $\text{Ti}_{42}\text{Zr}_{16}\text{Ni}_{12}\text{Cu}_{13}\text{Be}_{17}$ which is located in the center of the red region in the schematic pseudo Ti-Zr-(Be, Cu, Ni) ternary diagram which is considered to be able to fabricate large dimension Ti-based BMGs, was also shown in the Fig. 2-2. The compressive properties are listed in Table 2-2.

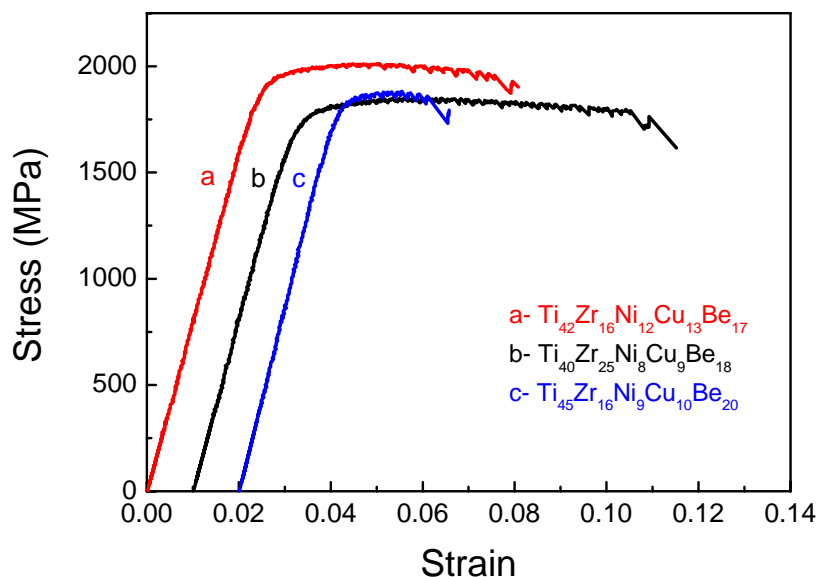


Fig. 2-2 Compressive stress-strain curves under the constant strain rate of $5 \times 10^{-4} \text{ s}^{-1}$ at room temperature for as-cast $\text{Ti}_{45}\text{Zr}_{16}\text{Ni}_9\text{Cu}_{10}\text{Be}_{20}$, $\text{Ti}_{40}\text{Zr}_{25}\text{Ni}_8\text{Cu}_9\text{Be}_{18}$ and $\text{Ti}_{42}\text{Zr}_{16}\text{Ni}_{12}\text{Cu}_{13}\text{Be}_{17}$ BMGs

Table 2-2

Compressive mechanical properties of as-cast $\text{Ti}_{45}\text{Zr}_{16}\text{Ni}_9\text{Cu}_{10}\text{Be}_{20}$, $\text{Ti}_{40}\text{Zr}_{25}\text{Ni}_8\text{Cu}_9\text{Be}_{18}$ and $\text{Ti}_{42}\text{Zr}_{16}\text{Ni}_{12}\text{Cu}_{13}\text{Be}_{17}$ BMGs

Composition	σ_y (MPa)	σ_{\max} (MPa)	ε_t (%)	ε_p (%)
$\text{Ti}_{45}\text{Zr}_{16}\text{Ni}_9\text{Cu}_{10}\text{Be}_{20}$	1810	1880	4.2	2.4
$\text{Ti}_{40}\text{Zr}_{25}\text{Ni}_8\text{Cu}_9\text{Be}_{18}$	1770	1850	10.5	8.0
$\text{Ti}_{42}\text{Zr}_{16}\text{Ni}_{12}\text{Cu}_{13}\text{Be}_{17}$	1910	2010	7.7	5.5

According to our experiment, we found that amongst $\text{Ti}_{45}\text{Zr}_{16}\text{Ni}_9\text{Cu}_{10}\text{Be}_{20}$, $\text{Ti}_{40}\text{Zr}_{25}\text{Ni}_8\text{Cu}_9\text{Be}_{18}$ and $\text{Ti}_{42}\text{Zr}_{16}\text{Ni}_{12}\text{Cu}_{13}\text{Be}_{17}$ BMGs, $\text{Ti}_{40}\text{Zr}_{25}\text{Ni}_8\text{Cu}_9\text{Be}_{18}$ alloy exhibit outstanding mechanical properties as well as good GFA compared with the other two alloys. In this regard, we think it worthwhile being investigated deeply to clarify the microstructure, thermal stability, GFA, structural relaxation, glass transition, crystallization behavior and corresponding mechanism,

deformation behavior and mechanism at both room temperature and high temperature.

Ti₄₀Zr₂₅Ni₈Cu₉Be₁₈ BMG was first reported by Kim et al. in 2004 [Kim et al., 2004]. After that, Ma et al [W.F. Ma et al., 2009] and Fornell et al. [Fornell et al., 2009] carried out some work on this alloy, mainly focused on trying to explain the intrinsic plasticity at room temperature. According to the literature [Kim et al., 2004], the thermal properties of this alloy obtained by the measurement of continuous heating DSC and DTA with the heating rate of 40 K/min, are listed in Table 2-3. The Ti₄₀Zr₂₅Ni₈Cu₉Be₁₈ alloy showed high GFA, enabling the fabrication of fully amorphous alloy rods of diameter 8 mm, as can be inferred from the high value of T_{rg} and γ parameter. However, the Ti₄₀Zr₂₅Ni₈Cu₉Be₁₈ amorphous alloy showed ΔT_x of 47 K, which is much smaller than the reported value of 80 K in Zr_{41.2}Ti_{13.8}Cu_{12.5}Ni_{10.0}Be_{22.5} bulk metallic glass [Peker et al., 1993].

Table 2-3

Thermal properties of melt-spun Ti₄₀Zr₂₅Ni₈Cu₉Be₁₈ metallic glass and Zr_{41.2}Ti_{13.8}Cu_{12.5}Ni_{10.0}Be_{22.5} BMG. T_g : glass transition temperature; T_{x1} : onset temperature of first crystallization; T_{x2} : onset temperature of second crystallization; T_{x3} : onset temperature of third crystallization; T_l : liquidus temperature; $\Delta T_x = T_{x1} - T_g$; $T_{rg} = T_g / T_l$; $\gamma = T_x / (T_g / T_l)$. [Kim et al., 2004; Peker et al., 1993]

Composition	T_g (K)	T_{x1} (K)	T_{x2} (K)	T_{x3} (K)	T_m (K)	T_l (K)	ΔT_x (K)	T_{rg}	γ
Ti ₄₀ Zr ₂₅ Ni ₈ Cu ₉ Be ₁₈	621	668	776	813	948	1009	47	0.62	0.41
Zr _{41.2} Ti _{13.8} Cu _{12.5} Ni _{10.0} Be _{22.5}	625	705	735		937	996	80	0.63	0.43

With regard to crystallization behavior upon heating, the two step crystallization process of the amorphous Ti₄₀Zr₂₅Ni₈Cu₉Be₁₈ phase can be summarized as follows: primary icosahedral phase precipitation from amorphous matrix, followed by the remaining amorphous phase crystallized into the hexagonal Laves phase. The icosahedral phase transformed into a Laves phase at high temperature through an endothermic reaction [Kim et al., 2004]. And after heat treatment at 753 K, icosahedral phase particles with the average size of about 10 nm were precipitated in amorphous matrix in the Ti₄₀Zr₂₅Ni₈Cu₉Be₁₈ alloy, as maybe leading to the enhancement of strength and plasticity.

Park et al. [J.M. Park et al., 2005] reported that a higher plastic strain can be observed when the first crystallization product is a quasicrystalline phase, which maybe due to the existence of quenched-in icosahedral nuclei embedded in the amorphous matrix, as is found in Ti₄₀Zr₂₉Ni₈Cu₉Be₁₄ alloy. However, Ohkubo et al. [Ohkubo, et al., 2007] argued that the plasticity of Ti₄₀Zr₂₅Cu₁₂Ni₃Be₂₀ alloy does not originate from the glassy phase itself but is closely related to the amount of nanocrystals embedded in the metallic glass matrix, which means that Be-containing Ti-based BMGs are actually nanocrystalline/metallic glass matrix composites rather than monolithic metallic glasses. So it is necessary and of interest to identify the real microstructure and to clarify the correlation between the microstructure and the mechanical properties, thermal stability.....

2.1.2 Ti-Cu-Ni (Be-free) System

The design of Ti-Cu-Ni metallic glasses was performed mainly on the base of two alloy compositions, $\text{Ti}_{50}\text{Cu}_{25}\text{Ni}_{25}$ and a eutectic alloy $\text{Ti}_{50}\text{Cu}_{42.5}\text{Ni}_{7.5}$. It is clear that the difference between these two compositions is that the latter one is rich in Cu while poor in Ni while the former one has the equal proportion between Cu and Ni, so the latter one is heavier than the former one while has the advantage of lower cost.

So far, many existing glassy samples that were obtained by adding some selected alloying elements, Zr, Al, Sn, Be, Hf, Si, B etc. are based on these two compositions. The maximum diameter and thermal properties of the as-cast Ti-Cu-Ni system metallic glasses are listed in [Table 2-4](#). We found that the GFA for ternary Ti-Cu-Ni system is good for Cu-rich compositions and poor for Ni-rich compositions, as the evidence of large maximum diameter of 3-6 mm for $\text{Ti}_{41.5}\text{Cu}_{42.5}\text{Ni}_{7.5}\text{Zr}_{2.5}\text{Hf}_5\text{Si}_1$, $\text{Ti}_{41.5}\text{Cu}_{37.5}\text{Ni}_{7.5}\text{Zr}_{2.5}\text{Hf}_5\text{Sn}_5\text{Si}_1$, $\text{Ti}_{45}\text{Zr}_5\text{Cu}_{45}\text{Ni}_5$, $\text{Ti}_{42.5}\text{Zr}_{7.5}\text{Cu}_{45}\text{Ni}_5$ and $\text{Ti}_{42.5}\text{Zr}_{7.5}\text{Cu}_{40}\text{Ni}_5\text{Sn}_5$ except $\text{Ti}_{50}\text{Ni}_{15}\text{Cu}_{25}\text{Sn}_5\text{Zr}_5$, as is accordance with the early study [\[Murty et al., 1995\]](#).

Table 2-4

The maximum diameter and thermal properties of the as-cast Ti-Cu-Ni system metallic glasses

Composition	T_g (K)	T_{x1} (K)	T_m (K)	T_l (K)	ΔT_x (K)	T_{rg}	γ	D_{\max} (mm)	Ref.
$\text{Ti}_{50}\text{Cu}_{42.5}\text{Ni}_{7.5}$	670	708	1199	1226	38	0.55		~200 μm	[Ma et al., 2004-b]
$\text{Ti}_{47.5}\text{Cu}_{42.5}\text{Ni}_{7.5}\text{Zr}_{2.5}$	673	720	1143	1225	47	0.56		1-1.5	
$\text{Ti}_{42.5}\text{Cu}_{42.5}\text{Ni}_{7.5}\text{Zr}_{2.5}\text{Hf}_5$	677	726	1143	1203	49	0.56		2-2.5	
$\text{Ti}_{41.5}\text{Cu}_{42.5}\text{Ni}_{7.5}\text{Zr}_{2.5}\text{Hf}_5\text{Si}_1$	680	730	1143	1199	50	0.57		~5	
$\text{Ti}_{41.5}\text{Cu}_{37.5}\text{Ni}_{7.5}\text{Zr}_{2.5}\text{Hf}_5\text{Sn}_5\text{Si}_1$	693	758	1117	1176	65	0.59	0.41	6	[Huang et al., 2007-a]
$\text{Ti}_{50}\text{Cu}_{25}\text{Ni}_{25}$	713	753			40			μm scale	[T. Zhang et al., 1998-a; Inoue, 1999]
$\text{Ti}_{50}\text{Ni}_{22}\text{Cu}_{25}\text{Sn}_3$	715	765			50			μm scale	
$\text{Ti}_{50}\text{Ni}_{20}\text{Cu}_{25}\text{Sn}_5$	710	770	1229		60			μm scale	
$\text{Ti}_{50}\text{Ni}_{20}\text{Cu}_{23}\text{Sn}_7$	710	759			49			μm scale	
$\text{Ti}_{50}\text{Ni}_{24}\text{Cu}_{25}\text{Sb}_1$	707	740			33			μm scale	
$\text{Ti}_{50}\text{Ni}_{22}\text{Cu}_{25}\text{Sb}_3$	763	718			45			μm scale	
$\text{Ti}_{50}\text{Ni}_{15}\text{Cu}_{25}\text{Sn}_5\text{Zr}_5$	~690	~750			~60			~6	
$\text{Ti}_{50}\text{Cu}_{20}\text{Ni}_{24}\text{Si}_4\text{B}_1$	735	800	~1185		65			1	[T. Zhang et al., 1999]
$\text{Ti}_{50}\text{Zr}_5\text{Cu}_{42.5}\text{Ni}_{2.5}$								1	[Men et al., 2005]
$\text{Ti}_{50}\text{Zr}_5\text{Cu}_{40}\text{Ni}_5$	634	685		1155	51	0.55		2	
$\text{Ti}_{50}\text{Zr}_5\text{Cu}_{37.5}\text{Ni}_{7.5}$								1	
$\text{Ti}_{45}\text{Zr}_5\text{Cu}_{45}\text{Ni}_5$	673	715		1203	43	0.56		3	
$\text{Ti}_{42.5}\text{Zr}_{10}\text{Cu}_{42.5}\text{Ni}_5$	651	695		1213	45	0.54		2	
$\text{Ti}_{42.5}\text{Zr}_{7.5}\text{Cu}_{45}\text{Ni}_5$	~675	~720			45			3	
$\text{Ti}_{50}\text{Cu}_{42}\text{Ni}_8$	657	713	1114	1168	56	0.563	0.391	2	[Wu et al., 2008]
$\text{Ti}_{42.5}\text{Zr}_{7.5}\text{Cu}_{40}\text{Ni}_5\text{Sn}_5$					64	0.561	0.393	4	[Huang et al., 2008-b]
$\text{Ti}_{53}\text{Cu}_{27}\text{Ni}_{12}\text{Zr}_3\text{Al}_3\text{Si}_3\text{B}_1$	685	754	1105		69			2	[Xia et al., 2005-a]
$\text{Ti}_{53}\text{Cu}_{15}\text{Ni}_{18.5}\text{Al}_7\text{Si}_3\text{Sc}_3\text{B}_{0.5}$	709	767		1240	58	0.619	0.394	2	[Xia et al., 2005-b]

Ti ₅₃ Cu ₁₅ Ni _{18.5} Al ₇ Si ₃ Hf ₃ B _{0.5}	695	749		1230	54	0.609	0.389	2	
Ti ₅₃ Cu ₁₅ Ni _{18.5} Al ₇ Si ₃ Ta ₃ B _{0.5}	675	760		1254	85	0.606	0.394	<1.5	
Ti ₅₃ Cu ₁₅ Ni _{18.5} Al ₇ Si ₃ Nb ₃ B _{0.5}	669	747		1252	78	0.597	0.389	<1.5	
Ti ₅₃ Cu ₁₅ Ni _{18.5} Al ₇ Si ₃ Zr ₃ B _{0.5}	703	765		1237	62	0.57		2.5	[Ma et al., 2004-a]
Ti ₅₀ Cu ₂₀ Ni ₂₄ B ₁ Si ₂ Sn ₃	726	800	1230	1310	74	0.554		1	[T. Zhang et al., 2001]
Ti ₅₀ Cu ₂₀ Ni ₂₄ B ₂ Si ₄	742	807	1178		65			2	[Inoue, 1999]
Ti ₄₃ Zr ₇ Cu ₄₃ Ni ₇	677	700			23			2	[K.B. Kim et al., 2006-a]
Ti ₄₅ Zr ₅ Cu ₄₀ Ni _{7.5} Sn _{2.5}	690	720			30			2	

Considering the early study of exploiting Ti-based BMGs, Ti₅₀Ni₁₅Cu₂₅Sn₅Zr₅, Ti_{41.5}Cu_{42.5}Ni_{7.5}Zr_{2.5}Hf₅Si₁ and Ti_{41.5}Cu_{37.5}Ni_{7.5}Zr_{2.5}Hf₅Sn₅Si₁ show excellent GFA, whose maximum diameter are ~6, ~5 and 6 mm, respectively. So, it is of interest to know their mechanical properties. The compressive mechanical properties at room temperature obtained from the literature are listed in Table 2-5. Little is known about these BMGs, especially for the mechanical properties, maybe due to the low GFA of Be-free Ti-based BMGs. Unlike Be-containing Ti-based BMGs which show moderate plasticity, Be-free Ti-based BMGs show a relatively high fracture strength exceeding ~2000 MPa but unfortunately they suffer from a lack of plasticity (<2%). The poor plasticity renders these alloys prone to catastrophic failure in load-bearing applications. So it is necessary to investigate the intrinsic reason of brittleness and the method to enhance the plasticity.

Table 2-5

Compressive mechanical properties of typical Ti-Cu-Ni BMGs

Composition	σ_{\max} (MPa)	ϵ_t (%)	ϵ_p (%)	$\dot{\epsilon}$ (s ⁻¹)	Ref.
Ti ₅₀ Ni ₁₅ Cu ₂₅ Sn ₅ Zr ₅	2090				[Inoue, 1999]
Ti _{41.5} Cu _{42.5} Ni _{7.5} Zr _{2.5} Hf ₅ Si ₁	2080	6	1.5	3×10 ⁻⁴	[Ma et al., 2004-b]
Ti _{41.5} Cu _{37.5} Ni _{7.5} Zr _{2.5} Hf ₅ Sn ₅ Si ₁	2260	2.8	0.5	4×10 ⁻⁴	[Huang et al., 2007-a]

Although, according to the literature these three compositions can be fabricated as BMGs with large dimension up to 5-6 mm, however, as we know the critical size of the BMGs is dependent on different fabrication conditions. Namely, even though under the experimental condition described in the literature, they can successfully fabricate these three alloys with diameters of 5-6 mm, it does not mean that we can obtain the same size of critical diameter as reported in the literature. It is generally believed that the critical diameter for a certain amorphous alloy composition is dependent on fabrication condition (solidification cooling rate) and purity of the element. So we fabricated rod samples with the nominal composition of Ti₅₀Ni₁₅Cu₂₅Sn₅Zr₅, Ti_{41.5}Cu_{42.5}Ni_{7.5}Zr_{2.5}Hf₅Si₁ and Ti_{41.5}Cu_{37.5}Ni_{7.5}Zr_{2.5}Hf₅Sn₅Si₁ and diameter in 2 and 4 mm to identify the glassy state of these alloys. Fig. 2-3, 2-4 and 2-5 show the XRD patterns and SEM (or TEM) images for Ti₅₀Ni₁₅Cu₂₅Sn₅Zr₅ (rod sample with diameter in 2 mm), Ti_{41.5}Cu_{42.5}Ni_{7.5}Zr_{2.5}Hf₅Si₁ (2 mm) and Ti_{41.5}Cu_{37.5}Ni_{7.5}Zr_{2.5}Hf₅Sn₅Si₁ (2 mm and 4 mm), respectively. As a result, under the condition of our experiment, Ti_{41.5}Cu_{37.5}Ni_{7.5}Zr_{2.5}Hf₅Sn₅Si₁ metallic glass with diameter in the range of 2-4 mm can be fabricated, for 4 mm sample, only limited crystals are precipitated in the amorphous matrix; however, for the other two compositions even for 2 mm sample, it is almost fully crystalline phase. Based on the experiments above, Ti_{41.5}Cu_{37.5}Ni_{7.5}Zr_{2.5}Hf₅Sn₅Si₁ was selected for our study due to its relatively high GFA.

The maximum diameter achievable in this study is smaller than that reported in the literature. The decrease of maximum diameter for the same alloy may be attributed to the unlike casting conditions.

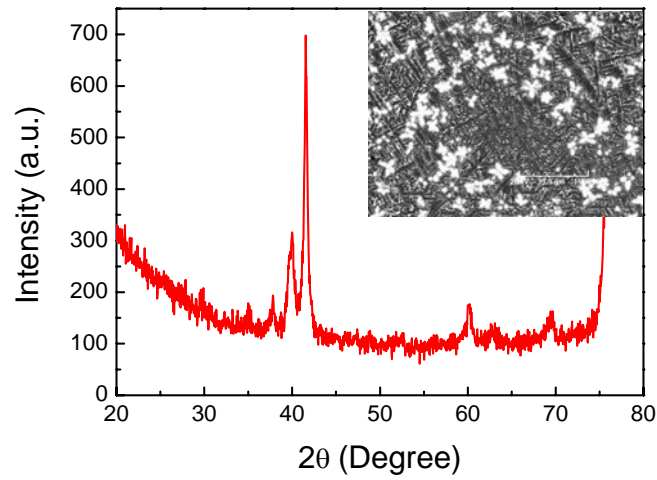


Fig. 2-3 XRD pattern and SEM image for as-cast $\text{Ti}_{50}\text{Ni}_{15}\text{Cu}_{25}\text{Sn}_5\text{Zr}_5$ rod sample ($\Phi 2$ mm)

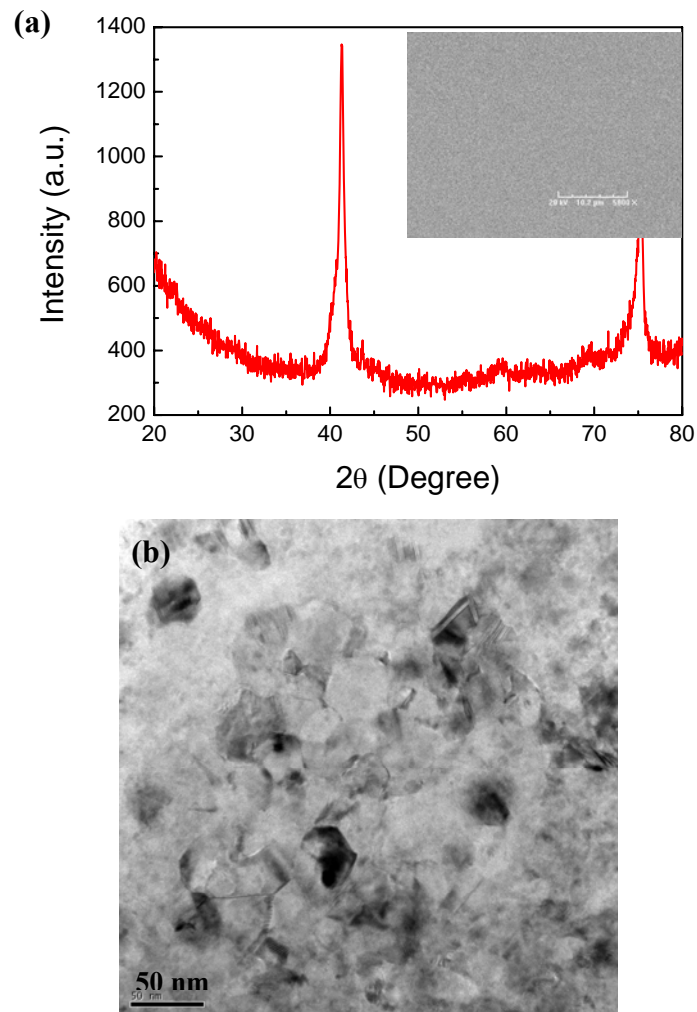


Fig. 2-4 (a) XRD pattern, SEM image and (b) TEM image for as-cast $\text{Ti}_{41.5}\text{Cu}_{42.5}\text{Ni}_{7.5}\text{Zr}_{2.5}\text{Hf}_5\text{Si}_1$ rod sample ($\Phi 2$ mm)

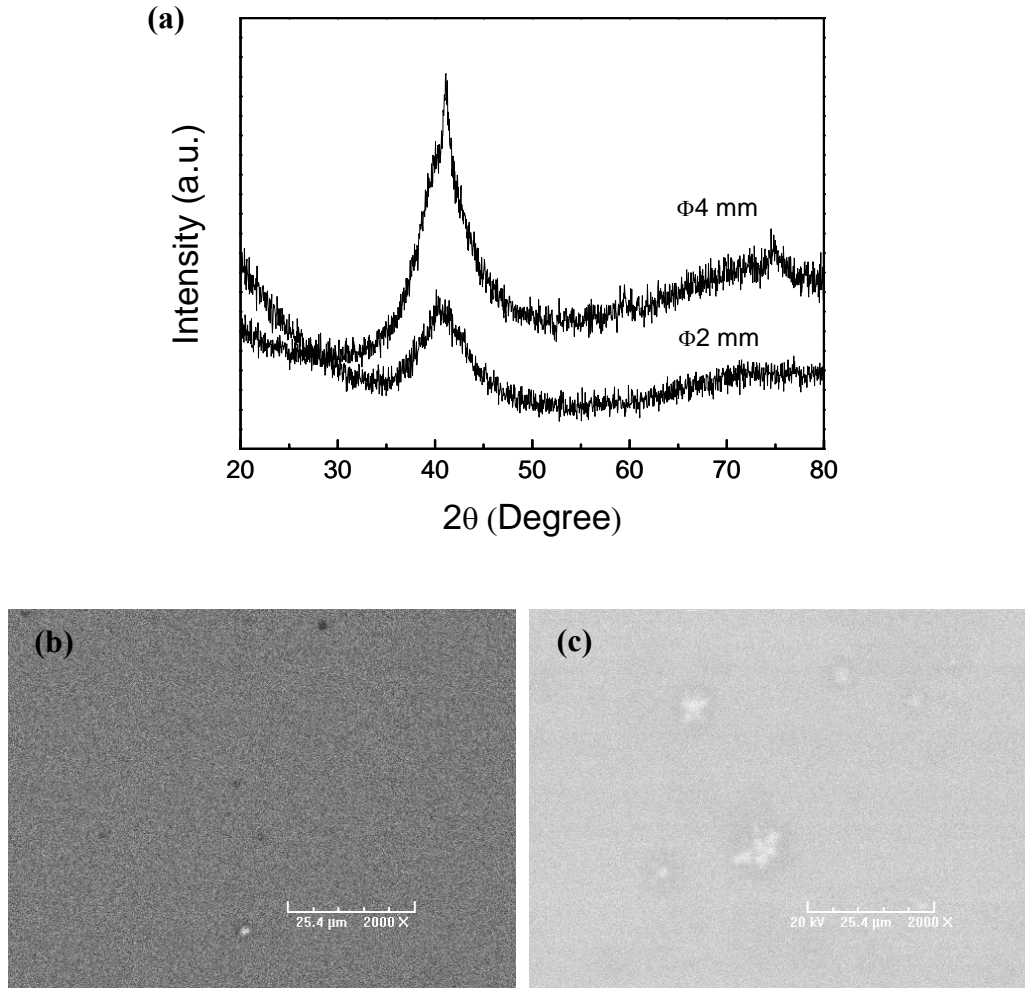


Fig. 2-5 (a) XRD patterns and SEM images for as-cast $\text{Ti}_{41.5}\text{Cu}_{37.5}\text{Ni}_{7.5}\text{Zr}_{2.5}\text{Hf}_5\text{Sn}_5\text{Si}_1$ rod samples ((b) $\Phi 2$ mm and (c) $\Phi 4$ mm)

In order to further improve the GFA and get Ti-based BMGs with larger critical size, we have made great efforts to develop Be-free Ti rich bulk metallic glasses through considering pseudo ternary phase diagram representation of the alloy with axes of (Ti, Zr, Hf), (Cu, Ni) and (Sn, Si). A series of Ti-rich (containing Ti above 40 at.%) Ti-Cu-Ni system alloy were obtained whose composition are summarized in [Table 2-6](#). [Fig. 2-6](#) shows the alloy composition distribution diagram with x axis of Cu content and y axis of Ti content. [Fig. 2-7](#) shows the schematic pseudo (Ti, Zr, Hf)-(Cu, Ni)-(Sn, Si) ternary diagram. Here we should point out the original idea of composition design. For high GFA Ti-based BMGs, they usually contain a low Ti concentration (40-50 at.%), and so do not fully exploit the benefits attributed to the element Ti. For Ti-Cu-Ni system alloy, from the point of density decrease (the most important problem is the higher density than Be-containing Ti-Zr-Ni-Cu-Be BMGs), Cu content should be decreased to a low level as well as the Ti content should be improved to more than 50%; on the other hand, if the low cost is to be considered while the density is without being considered, one should make an effort to improve the content of Cu.

Table 2-6

Alloy composition of Ti-Cu-Ni (Be-free) system prepared

NO.	Ti	Zr	Ni	Cu	Sn	Si	Hf	BMG?	Ref.
1	50	5	15	25	5			N	[Inoue, 1999]
2	49	5	15	25	5	1		N	This work
3	50	5	14	25	5	1		N	This work
10	50	5	15	27	2	1		N	This work
4	52.5	7.5	12.5	22.5	5			N	This work
5	52.5	7.5	11.5	22.5	5	1		N	This work
7	52.5	7.5	14	25		1		N	This work
8	52.5	7.5	13	24	2	1		N	This work
12	41.5	2.5	7.5	42.5		1	5	N	[Ma et al., 2004-b]
13	41.5	2.5	7.5	37.5	5	1	5	Y	[Huang et al., 2007-a]
14	41.5	2.5	12	33	5	1	5	N	This work
15	41.5	2.5	20	25	5	1	5	N	This work
16	44	2.5	12	33	5	1	2.5	N	This work
17	44	2.5	20	25	5	1	2.5	N	This work
18	46.5	2.5	12	33	5	1		N	This work
19	46.5	2.5	20	25	5	1		N	This work
20	44	2.5	3	42	5	1	2.5	N	This work
21	46.5	2.5	3	42	5	1		N	This work
26	41.5		7.5	40	5	1	5	Y	This work
28	40	4	7.5	37.5	5	1	5	Y	This work
29	41.5	5	7.5	35	5	1	5	Y	This work
30	43	1	7.5	37.5	5	1	5	Y	This work
31	41.5	7.5	7.5	37.5	5	1		Y	This work
32	46.5	2.5	15	25	5	1	5	N	This work

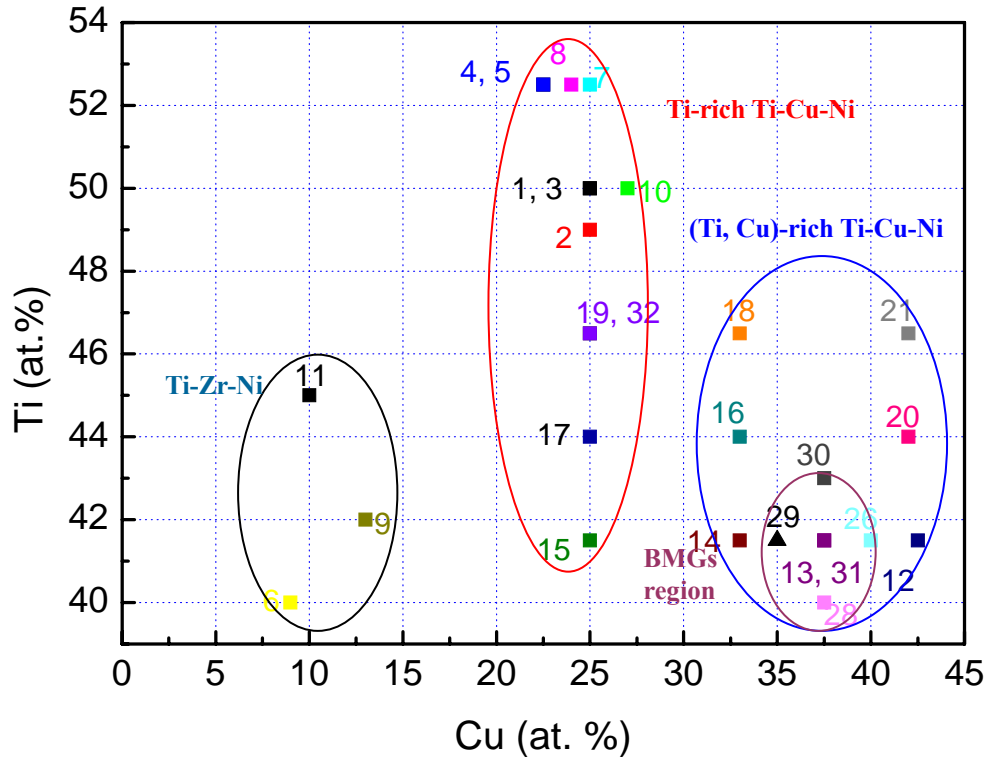


Fig. 2-6 The alloy composition distribution diagram with x axis of Cu content and y axis of Ti content (alloy compositions listed in Table 2-6, and 6: $\text{Ti}_{40}\text{Zr}_{25}\text{Ni}_8\text{Cu}_9\text{Be}_{18}$; 9: $\text{Ti}_{42}\text{Zr}_{16}\text{Ni}_{12}\text{Cu}_{13}\text{Be}_{17}$; 11: $\text{Ti}_{45}\text{Zr}_{16}\text{Ni}_9\text{Cu}_{10}\text{Be}_{20}$)

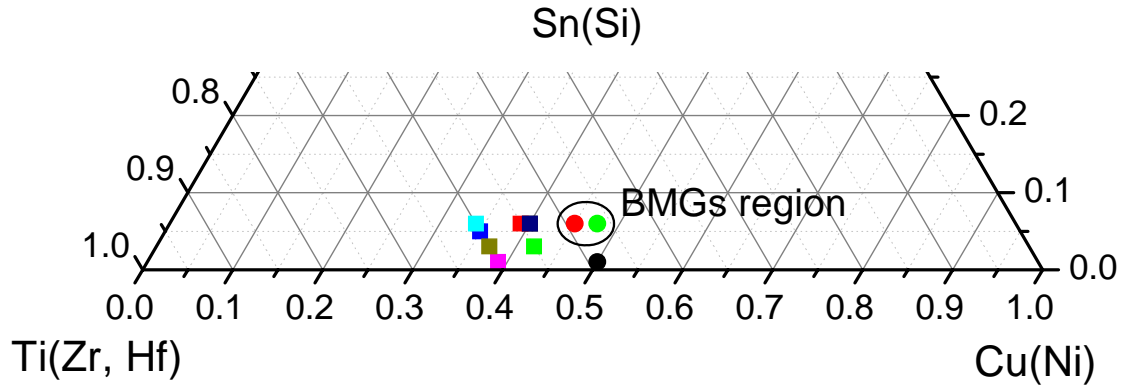


Fig. 2-7 The schematic pseudo (Ti, Zr, Hf)-(Cu, Ni)-(Sn, Si) ternary diagram (alloy compositions listed in Table 2-6, circled composition range for bulk metallic glasses)

The BMG-forming region was determined around the eutectic point, which is shown in Fig. 2-7. The composition regions in which bulk glass rods with diameters of at least 2 mm can be made by the injection casting method are presented here. It is noted that the largest GFA is slightly off eutectic point, which may be caused by non-equilibrium solidification. We found that the composition which can form glassy alloy restricted in a limited region where $\text{Ti}(\text{Zr, Hf}) \text{ at. \%} / \text{Cu}(\text{Ni}) \text{ at. \%} \approx 1$. So from this point of view, this series of Ti-based BMGs can be regarded as Ti-Cu-based alloys.

In this study, $\text{Ti}_{41.5}\text{Cu}_{37.5}\text{Ni}_{7.5}\text{Zr}_{2.5}\text{Hf}_5\text{Sn}_5\text{Si}_1$ was chosen as a typical representation of Ti-Cu-Ni

(Be-free) BMGs for further study. While we were studying this alloy, a report was also made by Huang et al. [Huang et al., 2007-a]. We review the research work about this alloy. $\text{Ti}_{41.5}\text{Cu}_{37.5}\text{Ni}_{7.5}\text{Zr}_{2.5}\text{Hf}_5\text{Sn}_5\text{Si}_1$ was first reported by Huang et al. [Huang et al., 2007-a] based on the work of Ma et al. [Ma et al., 2004-b]. In details, Ma et al. [Ma et al., 2004-b] improved the GFA of an eutectic alloy $\text{Ti}_{50}\text{Cu}_{42.5}\text{Ni}_{7.5}$ which is located on an eutectic groove of $\text{L} \rightarrow \text{TiNi} + \text{TiCu}$ in Ti-Cu-Ni system [Villars et al., 1997] by substituting Ti with appropriate amounts of Zr and Hf as well as a minor amount of Si and succeeded in synthesizing a new high GFA alloy in a multi-component (Ti, Zr, Hf)-(Cu, Ni)-Si system with maximum diameters up to 5 mm for $\text{Ti}_{41.5}\text{Zr}_{2.5}\text{Hf}_5\text{Cu}_{42.5}\text{Ni}_{7.5}\text{Si}_1$ by using the copper mold casting. Then, by investigating the effects of partial replacement of Cu by Sn on the GFA of (Ti, Zr, Hf)-(Cu, Ni)-Si system in $\text{Ti}_{41.5}\text{Cu}_{42.5}\text{Ni}_{7.5}\text{Zr}_{2.5}\text{Hf}_5\text{Si}_1$ alloy, $\text{Ti}_{41.5}\text{Cu}_{37.5}\text{Ni}_{7.5}\text{Zr}_{2.5}\text{Hf}_5\text{Sn}_5\text{Si}_1$ BMG with diameter up to 6 mm was found. Thermal properties have been listed in Table 2-4, and the crystallization behavior process by two events, activation energies E_g (for glass transition) and E_{Tp1} (for first crystallization) for this alloy are calculated to be 409.51 and 302.30 kJ/mol, respectively [Huang et al., 2007-a], indicating a high GFA and thermal stability. It exhibits good room temperature compressive properties which are listed in Table 2-5. In addition, the Vickers hardness (H_v) and the density are measured to be 676 kg/mm² and 7.0 g/cm³, respectively [Huang et al., 2007-a]. The specific strength of the alloy is 3.31×10^5 Nm/kg, as is worthwhile to notice that the amorphous $\text{Ti}_{41.5}\text{Zr}_{2.5}\text{Hf}_5\text{Cu}_{37.5}\text{Ni}_{7.5}\text{Si}_1\text{Sn}_5$ alloy exhibits a higher specific strength value than Zr- [Das et al., 2005; T. Zhang et al., 1998-b], Pd- [Ma et al., 2002] and Cu- [Xu et al., 2004] based amorphous alloys [Huang et al., 2007-a].

2.1.3 Comparison between $\text{Ti}_{40}\text{Zr}_{25}\text{Ni}_8\text{Cu}_9\text{Be}_{18}$ and $\text{Ti}_{41.5}\text{Cu}_{37.5}\text{Ni}_{7.5}\text{Zr}_{2.5}\text{Hf}_5\text{Sn}_5\text{Si}_1$ BMGs

In order to clarify the significance of this study, it is necessary to compare these two alloys from the following aspects: cost, density, with or without toxic element, microstructure, thermal stability, GFA, plasticity, crystallization product, etc. (see Table 2-7).

Table 2-7

Properties comparison between $\text{Ti}_{40}\text{Zr}_{25}\text{Ni}_8\text{Cu}_9\text{Be}_{18}$ and $\text{Ti}_{41.5}\text{Cu}_{37.5}\text{Ni}_{7.5}\text{Zr}_{2.5}\text{Hf}_5\text{Sn}_5\text{Si}_1$ BMGs

Composition	Toxic element (Y/N)	Cost	Density (g/cm ³)	Microstructure	Thermal stability	Crystallization	Plasticity
$\text{Ti}_{40}\text{Zr}_{25}\text{Ni}_8\text{Cu}_9\text{Be}_{18}$	Y	High	5.6	May be quenched-in nuclei?	Not good?	Multistep Primary phase: I-phase	Obvious
$\text{Ti}_{41.5}\text{Cu}_{37.5}\text{Ni}_{7.5}\text{Zr}_{2.5}\text{Hf}_5\text{Sn}_5\text{Si}_1$	N	Low	7.0		Good	Multistep ?	Limited

In my opinion, $\text{Ti}_{40}\text{Zr}_{25}\text{Ni}_8\text{Cu}_9\text{Be}_{18}$ and $\text{Ti}_{41.5}\text{Cu}_{37.5}\text{Ni}_{7.5}\text{Zr}_{2.5}\text{Hf}_5\text{Sn}_5\text{Si}_1$ BMGs are typical representation in Ti-Zr-Ni (Be-containing) and Ti-Cu-Ni (Be-free) systems, respectively. There exist significant differences between them.

1. It is obvious that Be element is added into $\text{Ti}_{40}\text{Zr}_{25}\text{Ni}_8\text{Cu}_9\text{Be}_{18}$ BMG, and it possesses a relatively high percentage of up to 18%, while $\text{Ti}_{41.5}\text{Cu}_{37.5}\text{Ni}_{7.5}\text{Zr}_{2.5}\text{Hf}_5\text{Sn}_5\text{Si}_1$ is Be-free alloy. So the high percentage of Be leads to the restrictive application of the former alloy.
2. From the viewpoint of cost, compared with $\text{Ti}_{40}\text{Zr}_{25}\text{Ni}_8\text{Cu}_9\text{Be}_{18}$, $\text{Ti}_{41.5}\text{Cu}_{37.5}\text{Ni}_{7.5}\text{Zr}_{2.5}\text{Hf}_5\text{Sn}_5\text{Si}_1$ consists of higher proportion of Cu and lower proportion of Zr as well as without Be. It is believed that BMGs containing certain LTMs (e.g. Fe, Ni, Cu) have better GFA, higher strength and elastic modulus, and lower materials cost. So due to the limited Zr resources and the high cost of Be, development of bulk metallic glasses containing common metals as the major constituent is strongly desired for extensive practical applications.
3. The densities are 5.6 and 7.0 g/cm³ for $\text{Ti}_{40}\text{Zr}_{25}\text{Ni}_8\text{Cu}_9\text{Be}_{18}$ and $\text{Ti}_{41.5}\text{Cu}_{37.5}\text{Ni}_{7.5}\text{Zr}_{2.5}\text{Hf}_5\text{Sn}_5\text{Si}_1$, respectively. Although $\text{Ti}_{41.5}\text{Cu}_{37.5}\text{Ni}_{7.5}\text{Zr}_{2.5}\text{Hf}_5\text{Sn}_5\text{Si}_1$ has large density of 7.0 g/cm³, the specific strength of this alloy, 3.31×10^5 Nm/kg, still higher than that of Zr-, Pd- and Cu-based glassy alloys. Obviously, the specific strength of $\text{Ti}_{40}\text{Zr}_{25}\text{Ni}_8\text{Cu}_9\text{Be}_{18}$ is 3.39×10^5 Nm/kg, which is a little higher than that of $\text{Ti}_{41.5}\text{Cu}_{37.5}\text{Ni}_{7.5}\text{Zr}_{2.5}\text{Hf}_5\text{Sn}_5\text{Si}_1$ alloy. Although there exists a large difference of density between these two alloys, no significant difference of specific strength existed due to the higher strength of $\text{Ti}_{41.5}\text{Cu}_{37.5}\text{Ni}_{7.5}\text{Zr}_{2.5}\text{Hf}_5\text{Sn}_5\text{Si}_1$ compared with $\text{Ti}_{40}\text{Zr}_{25}\text{Ni}_8\text{Cu}_9\text{Be}_{18}$.
4. The nature of these two glassy alloys is not so clear. As we know, the thermal properties, physical properties and mechanical properties, etc. are associated with the microstructure of the as-cast sample. So it is crucial to identify the nature of as-cast sample. For as-cast $\text{Ti}_{40}\text{Zr}_{25}\text{Ni}_8\text{Cu}_9\text{Be}_{18}$ BMG, we consider it to be fully of quenched-in nuclei and contribute to the lower thermal stability, the only growth process for isothermal crystallization, the enhancement of compressive plasticity and impossibility of homogeneous deformation in the supercooled liquid region. However, for as-cast $\text{Ti}_{41.5}\text{Cu}_{37.5}\text{Ni}_{7.5}\text{Zr}_{2.5}\text{Hf}_5\text{Sn}_5\text{Si}_1$, we think its microstructure to be different from $\text{Ti}_{40}\text{Zr}_{25}\text{Ni}_8\text{Cu}_9\text{Be}_{18}$ BMG, as is the reason why it shows high thermal stability and high compressive strength with limited plasticity obtained according to the literature. We can daringly image that the glassy state in the supercooled liquid region is stable enough to realize net shape forming.
5. The similarity of these two BMGs is that they both possess multistep crystallization. The crystallization behavior and the corresponding crystallization products for $\text{Ti}_{41.5}\text{Cu}_{37.5}\text{Ni}_{7.5}\text{Zr}_{2.5}\text{Hf}_5\text{Sn}_5\text{Si}_1$ are unclear; while for $\text{Ti}_{40}\text{Zr}_{25}\text{Ni}_8\text{Cu}_9\text{Be}_{18}$ BMG, icosahedral quasicrystals have been found to precipitate during the first step of crystallization. As mentioned in chapter 1, nanocrystals will significantly affect the corresponding mechanical properties, two different effects will occur in different alloy systems after annealing of glassy precursors: enhancement of strength or not, improvement of plasticity or not. In addition, it is known that an annealing treatment of glassy alloy precursors is an effective method to prepare nanocrystalline/amorphous composites. Therefore, it is necessary to investigate the influence of annealing on the microstructure and mechanical properties of these two alloys. Moreover, considering the low GFA of $\text{Ti}_{41.5}\text{Cu}_{37.5}\text{Ni}_{7.5}\text{Zr}_{2.5}\text{Hf}_5\text{Sn}_5\text{Si}_1$ alloy and its low plasticity with respect to $\text{Ti}_{40}\text{Zr}_{25}\text{Ni}_8\text{Cu}_9\text{Be}_{18}$ alloy, it would be desirable to tailor the microstructure through annealing, with the aim of achieving large plasticity without sacrificing the high strength.

Accordingly, in this work, $\text{Ti}_{40}\text{Zr}_{25}\text{Ni}_8\text{Cu}_9\text{Be}_{18}$ and $\text{Ti}_{41.5}\text{Cu}_{37.5}\text{Ni}_{7.5}\text{Zr}_{2.5}\text{Hf}_5\text{Sn}_5\text{Si}_1$ BMGs were chosen due to their highest GFA in Ti-Zr-Ni and Ti-Cu-Ni system, respectively, as well as the serious difference between each other which has shown above, nature state of as-cast sample,

physical properties, thermal induced structural transformations and their effects on the mechanical properties at ambient temperature, and homogeneous deformation in the supercooled liquid region will be investigated, aiming to clarify the microstructure-property correlations.

2.2 Background and Motivation

Once the composition is selected and the sample is synthesized, the challenge is to confirm (or deny) the glassy structure of these materials, as well as making a determination as to the processing stability.

BMG was thought to lack plasticity, but many recent investigations reported considerable plastic deformation in compression at room temperature. Cu-Zr-Ti based BMG was one of the earliest metallic glasses that was claimed to show a plasticity of about 1.6% in compression [Inoue et al., 2001], but it was later found that the cast rod was composed of nanocrystalline particles embedded in a glassy matrix [Jiang et al., 2003; Inoue et al., 2004]. Recently, the enhancement of plasticity was explained as being due to the existence of quenched-in icosahedral nuclei embedded in the as-cast amorphous matrix in $\text{Ti}_{40}\text{Zr}_{29}\text{Be}_{14}\text{Cu}_9\text{Ni}_8$ alloy by Park et al. [J.M. Park et al., 2005]. Similarly, Guo et al. [Guo et al., 2005] reported a $\text{Ti}_{40}\text{Zr}_{25}\text{Be}_{20}\text{Cu}_{12}\text{Ni}_3$ monolithic BMG with 12 mm in diameter and it exhibited a large compressive plastic strain of 5%. However, Ohkubo et al. [Ohkubo, et al., 2007] proved the existence of nanocrystals in the amorphous matrix which contribute to the enhancement of plasticity. It means that the actually nanocrystalline/metallic glass matrix structure rather than monolithic metallic glass of this alloy. In addition, $\text{Ti}_{41.5}\text{Zr}_{2.5}\text{Hf}_3\text{Cu}_{42.5}\text{Ni}_{7.5}\text{Si}_1$ metallic glass was reported by Ma et al. which can fabricate in large dimension of 5 mm in diameter, then the latter research by Ishimaru et al. [Ishimaru et al., 2005] revealed that the as-cast sample with 3 mm in diameter contained Cu-rich nanocrystals with $L1_2$ -type ordered structure and a size of 10 nm. So it is crucial to identify the original microstructure of BMGs before carrying out the following research.

Accordingly, to understand the microstructure-properties correlation in the Ti-based BMGs, we should investigate the microstructure. The microstructural characterizations were carried out by XRD, HRTEM and neutron diffraction. The thermal stability and GFA were also discussed in this chapter based on the DSC measurement upon heating.

2.3 Experiment

Two BMGs with the nominal compositions of $\text{Ti}_{40}\text{Zr}_{25}\text{Ni}_8\text{Cu}_9\text{Be}_{18}$ and $\text{Ti}_{41.5}\text{Cu}_{37.5}\text{Ni}_{7.5}\text{Zr}_{2.5}\text{Sn}_5\text{Hf}_5\text{Si}_1$ (at.%) were used in this study. The ingots of master alloy with mass of 30 g were prepared by melting elements of 99.8 to 99.999 wt.% purity with high frequency electromagnetic induction in a water-cooled copper crucible under a high purity argon atmosphere (Fig. 2-8 (a)). The ingot alloys (Fig. 2-9 (a)) were remelted at high temperature several times to ensure the compositional homogeneity. Particularly, for $\text{Ti}_{41.5}\text{Cu}_{37.5}\text{Ni}_{7.5}\text{Zr}_{2.5}\text{Sn}_5\text{Hf}_5\text{Si}_1$, in order to ensure the homogeneous distribution of Si which is a nonmetallic element, a two-step melting process was carried out: the raw elements of Cu and Si were first melted together to get an homogenous master alloy with the nominal composition of $\text{Cu}_{80}\text{Si}_{20}$; the binary alloy ingots were then remelted with the remained metals (Ti, Cu, Ni, Zr, Hf and Sn) to obtain a master alloy with the desired composition. Cylindrical specimens (Fig. 2-9 (b)) with 40 mm in length and 2, 3 and 4 mm

in diameter, respectively, were prepared by injection casting (Fig. 2-8 (b)) into a water-cooled copper mould via an electromagnetic levitation-melt state under a high purity argon atmosphere before casting to obtain a completely melted state. Alloy's oxygen content was measured <400 ppm.

The glassy state of alloy was examined by X-ray diffractometry (XRD, Philips PW3830) using monochromatic Cu-K α radiation ($\lambda=1.5406$ Å), in-situ neutron diffraction ($\lambda=2.524$ Å, D1B-CRG diffractometer, Institute Laue Langevin, Grenoble, France). Data treatment was done with the LAMP and FULLPROF programs of ILL. The glass transition and crystallization behavior were studied using differential scanning calorimetry (DSC, Netzsch DSC 404s) with the heating rates in the range of 5-40 K/min in a flowing argon atmosphere. After each continuous heating, a second scan of the crystallized sample was made for the baseline correction. Scanning electron microscopy (SEM, JEOL-JSM6400) coupled with an energy-dispersive X-ray spectrometry (EDS) and high-resolution transmission electron microscopy (HRTEM, JEM-3010 and JEM-2010F) were used for crystal structure/microstructure analysis. Specimens used for TEM observation were jet polished in a 10% HClO₄+90% ethanol solution at 25 V and -30 °C. Final thinning was conducted with ion milling with a less than 10° milling angle, at 4 kV and 5 mA in a Fishbone ion milling. A liquid nitrogen cold stage was used.

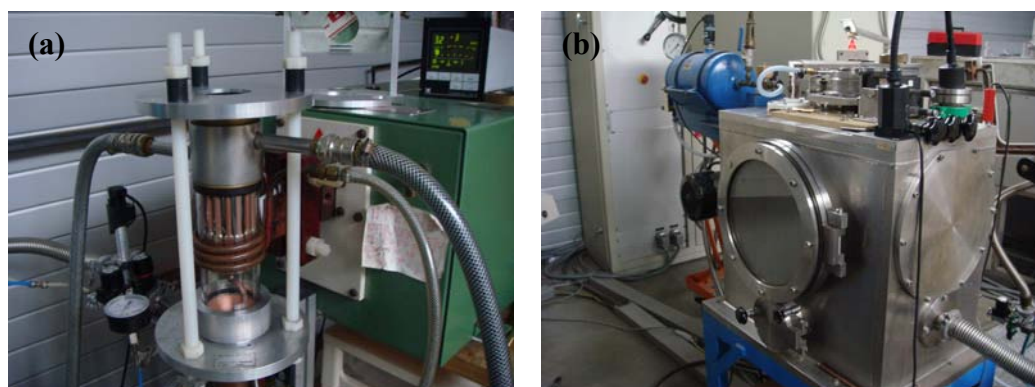


Fig. 2-8 (a) Induction furnace with cold crucible for obtaining master alloys, (b) injection casting furnace for obtaining as-cast samples

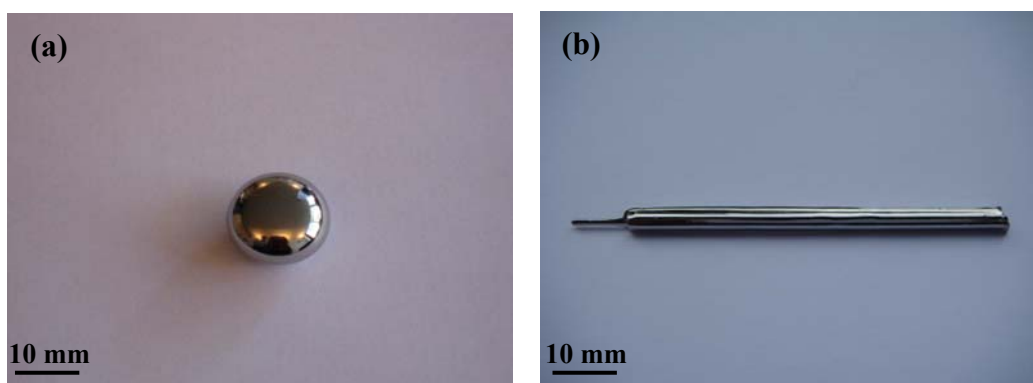


Fig. 2-9 (a) Master alloy, (b) as-cast cylindrical sample

2.4 Results

2.4.1 Characteristics of Structure

Fig. 2-10 (a) and (b) show the XRD patterns of as-cast $\text{Ti}_{40}\text{Zr}_{25}\text{Ni}_8\text{Cu}_9\text{Be}_{18}$ and $\text{Ti}_{41.5}\text{Cu}_{37.5}\text{Ni}_{7.5}\text{Zr}_{2.5}\text{Hf}_5\text{Sn}_5\text{Si}_1$ BMGs both with 2 and 4 mm in diameter, respectively. Only a broad band with absence of well-defined peaks was observed for the as-cast $\text{Ti}_{40}\text{Zr}_{25}\text{Ni}_8\text{Cu}_9\text{Be}_{18}$ sample of both 2 and 4 mm, and the optical microscope (OM) and scanning electron microscope (SEM) observations of samples, taken from the central part of the ingots, revealed featureless surface, which indicate the amorphous nature without detectable crystalline phases of this alloy with the diameter of up to 4 mm. The microstructures of $\text{Ti}_{41.5}\text{Cu}_{37.5}\text{Ni}_{7.5}\text{Zr}_{2.5}\text{Hf}_5\text{Sn}_5\text{Si}_1$ alloy with 2 and 4 mm in diameter are shown in Fig. 2-11. Similar results were found in $\text{Ti}_{41.5}\text{Cu}_{37.5}\text{Ni}_{7.5}\text{Zr}_{2.5}\text{Hf}_5\text{Sn}_5\text{Si}_1$ alloy with 2 mm in diameter. However, for $\Phi 4$ sample of $\text{Ti}_{41.5}\text{Cu}_{37.5}\text{Ni}_{7.5}\text{Zr}_{2.5}\text{Hf}_5\text{Sn}_5\text{Si}_1$ alloy, the XRD patterns and SEM show tiny crystals of an extra phase that were attributed to a bcc $\text{TiNi}(\text{Cu})$ or β -Ti phase quenched from high temperature and a second phase ($\text{Ti}_5\text{Sn}_3\text{Cu}$). The bcc ($\text{Ti}, \text{Cu}, \text{Ni}$) phase has been found in a great number of Ti-based BMGs and reported as a β -Ti phase [He et al., 2003-b; Sun et al., 2006] or a TiNi (CsCl-type) phase [Woodcock et al., 2005; Calin et al., 2007]. In the SEM images of $\Phi 4$ sample shown in Fig. 2-11 (b), white particles are observed in back scattering mode (average typical size is 5 μm) with a “flower-like” shape and are not very widespread in the glassy matrix with a darker grey zone around, the chemical element percentages of these small crystals measured by EDS are given in Table 2-8. The white flowers are enriched in Sn and could correspond to the $\text{Ti}_5\text{Sn}_3\text{Cu}$ crystallized phase not observed by XRD. The dark grey zone is lower in Sn and should correspond to the $\text{TiNi}(\text{Cu})$ structure, the light grey zone (matrix) has a composition very close to the initial glass composition.

Neutron diffraction patterns have been recorded on $\Phi 4$ samples of both $\text{Ti}_{40}\text{Zr}_{25}\text{Ni}_8\text{Cu}_9\text{Be}_{18}$ and $\text{Ti}_{41.5}\text{Cu}_{37.5}\text{Ni}_{7.5}\text{Zr}_{2.5}\text{Hf}_5\text{Sn}_5\text{Si}_1$ alloys. The neutron diffractograms will be shown in chapter 4. Neutron diffraction technique measures the whole volume of the sample, so it is possible to observe three different components of diffraction. It is found that the neutron diffraction pattern of $\text{Ti}_{40}\text{Zr}_{25}\text{Ni}_8\text{Cu}_9\text{Be}_{18}$ BMG shows a characteristic diffraction pattern of an amorphous compound with short-range order: an unique bump maximum at $2\theta=68^\circ$; $d=2.514 \text{ \AA}$.

For $\text{Ti}_{41.5}\text{Cu}_{37.5}\text{Ni}_{7.5}\text{Zr}_{2.5}\text{Hf}_5\text{Sn}_5\text{Si}_1$ alloy, a bump centered at $2\theta=73^\circ$ corresponding to the amorphous part of the sample, small lines around $2\theta=22$ and 42° and indexed as the $\text{Ti}_5\text{Sn}_3\text{Cu}$ phase and 3 stronger lines indexed as (100), (110) and (111) of a cubic phase. The neutron diffraction pattern and the corresponding X-ray diffraction pattern have been both refined with a model of two phases, $\text{Ti}_5\text{Sn}_3\text{Cu}$ (SP= $\text{P6}_3/\text{mmc}$; $a=0.8117(7) \text{ nm}$, $c=0.5605(8) \text{ nm}$) and $\text{TiNi}(\text{Cu})$ (SP= Pm-3m ; $a=0.3117(1) \text{ nm}$) with Ti at the 0,0,0 position and Ni, Cu at the $1/2, 1/2, 1/2$ position. The result of these refinements gives a good refinement with the 3 peaks (100), (110) and (111) and X-ray diffraction pattern with the (110) peak only (see Fig. 2-12). Copper, nickel and titanium have a too close number of electrons to observe this ordering by X-ray, but the high neutron contrast between scattering lengths of titanium (-0.34) compared to copper (0.77) and nickel (1.03) evidences this ordering.

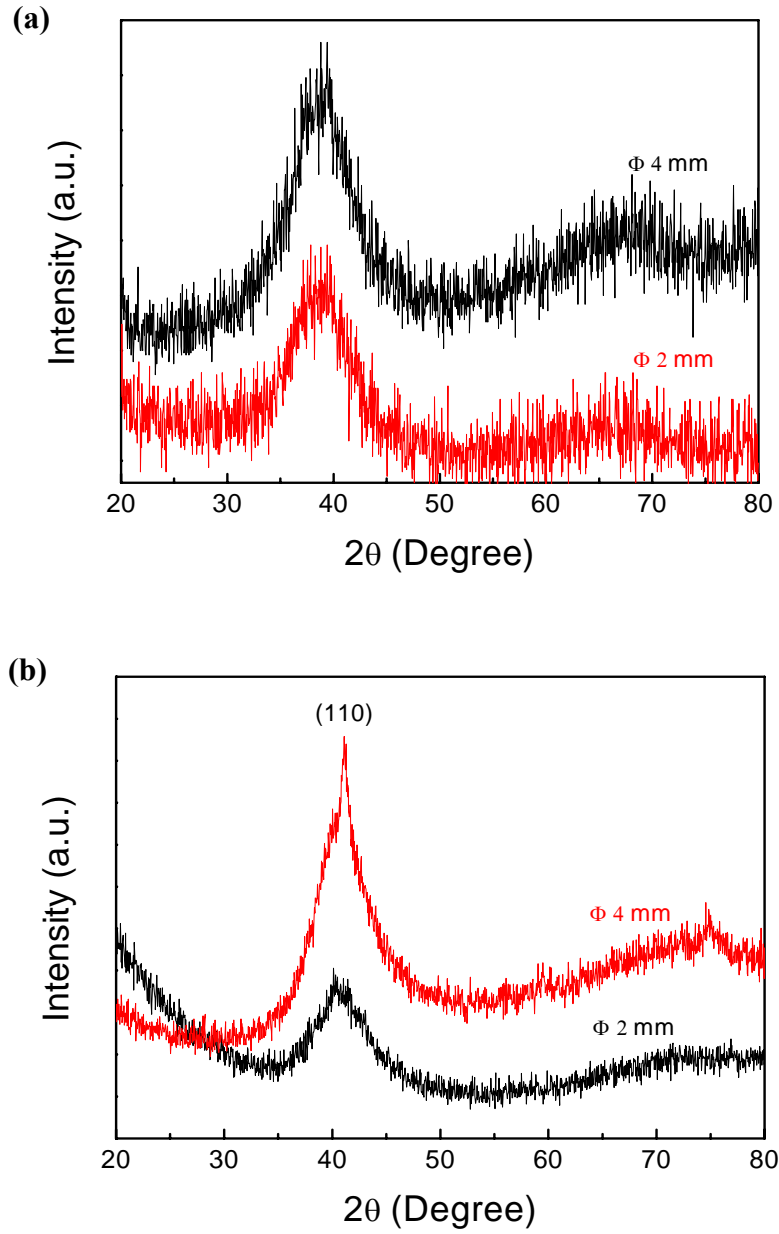


Fig. 2-10 XRD patterns of (a) $\text{Ti}_{40}\text{Zr}_{25}\text{Ni}_8\text{Cu}_9\text{Be}_{18}$ and (b) $\text{Ti}_{41.5}\text{Cu}_{37.5}\text{Ni}_{7.5}\text{Zr}_{2.5}\text{Hf}_5\text{Sn}_5\text{Si}_1$ BMGs with 2 and 4 mm in diameter

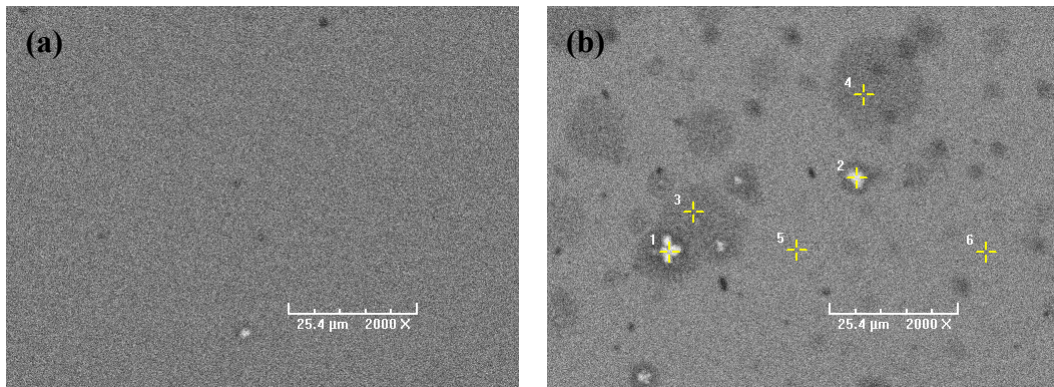


Fig. 2-11 SEM of $\text{Ti}_{41.5}\text{Cu}_{37.5}\text{Ni}_{7.5}\text{Zr}_{2.5}\text{Hf}_5\text{Sn}_5\text{Si}_1$ BMGs with (a) 2 mm and (b) 4 mm in diameter

Table 2-8

EDS analysis of the different grey zones of $\text{Ti}_{41.5}\text{Cu}_{37.5}\text{Ni}_{7.5}\text{Zr}_{2.5}\text{Hf}_5\text{Sn}_5\text{Si}_1$ alloy with 4 mm in diameter (the overlap of the energies of Si and Hf lowers the Hf content and enhance the Si content)

Element	Ti	Cu	Ni	Zr	Hf	Sn	Si
Nominal composition	41.5	37.7	7.5	2.5	5	5	1
While flowers	42.05	29.35	5.35	3.85	2.65	12.25	4.5
Dark grey zone	43.15	36.7	7.9	2.78	2.48	3.35	3.65
Light grey zone	42.6	35.9	6.6	2.65	3.45	5.45	3.35

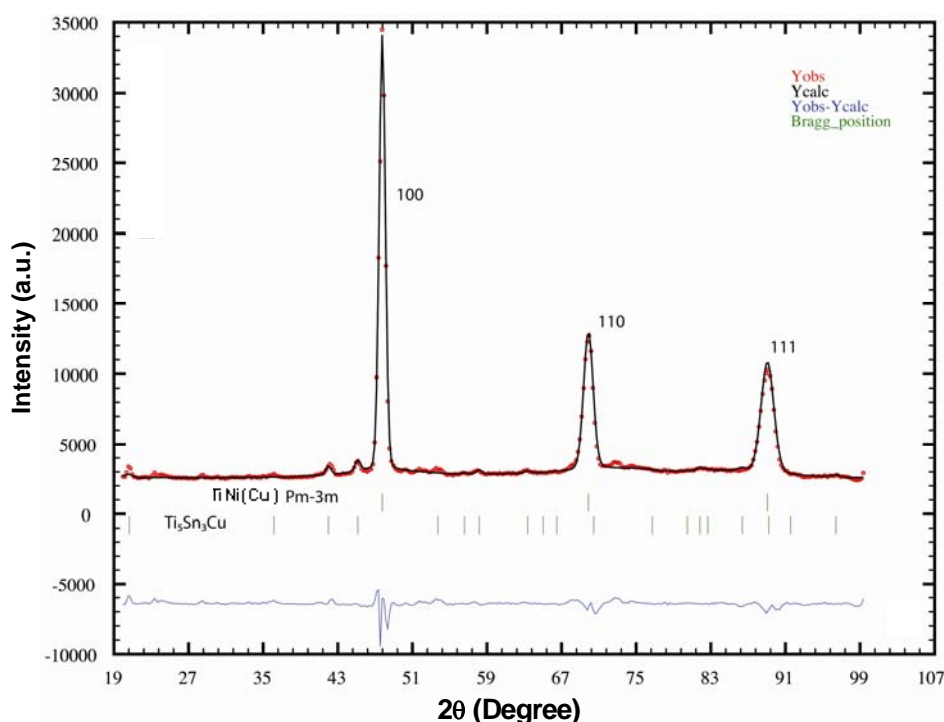


Fig. 2-12 Neutron diffractogram recorded at $\lambda=0.2518$ nm of the $\text{Ti}_{41.5}\text{Cu}_{37.5}\text{Ni}_{7.5}\text{Zr}_{2.5}\text{Hf}_5\text{Sn}_5\text{Si}_1$ alloy with 4 mm in diameter

Further evidences for the amorphous character of these two alloys were obtained from the HRTEM observation and the corresponding SADP which were operated on the sample with 2 mm in diameter, and combined with DSC measurement.

DSC measurements of both $\Phi 2$ and $\Phi 4$ samples were performed in the present work. **Fig. 2-13 (a)** and **(b)** show the DSC scans of $\text{Ti}_{40}\text{Zr}_{25}\text{Ni}_8\text{Cu}_9\text{Be}_{18}$ and $\text{Ti}_{41.5}\text{Cu}_{37.5}\text{Ni}_{7.5}\text{Zr}_{2.5}\text{Hf}_5\text{Sn}_5\text{Si}_1$, respectively. All samples exhibit an endothermic heat event characteristic of the glass transition, followed by characteristic exothermic transformations from the undercooled liquid to the equilibrium crystalline phases. The glass transition temperature T_g and the onset crystallization temperature T_{x1} are marked with arrows in **Fig. 2-13**.

As shown in **Fig. 2-13 (a)**, for $\text{Ti}_{40}\text{Zr}_{25}\text{Ni}_8\text{Cu}_9\text{Be}_{18}$ alloy, both samples show nearly identical DSC scans, no obvious differences were detected except the first crystallization peak of the $\Phi 4$ sample shifts slightly to high temperature as compared with $\Phi 2$ sample and the crystallization enthalpies for the second crystallization reaction of $\Phi 4$ sample is a little smaller than that of $\Phi 2$

sample, however, such differences between them are negligible within experimental uncertainty. One of the most interesting finding is that the glass transition for $\text{Ti}_{40}\text{Zr}_{25}\text{Ni}_8\text{Cu}_9\text{Be}_{18}$ alloy is not so clear that no glass transition temperature is detected in our experiment, which indicates the special glassy state of this alloy, as will be discussed in the section of discussion.

As shown in Fig. 2-13 (b), different from $\text{Ti}_{40}\text{Zr}_{25}\text{Ni}_8\text{Cu}_9\text{Be}_{18}$ alloy, obvious glass transition can be observed in the DSC scans of $\text{Ti}_{41.5}\text{Cu}_{37.5}\text{Ni}_{7.5}\text{Zr}_{2.5}\text{Hf}_5\text{Sn}_5\text{Si}_1$ alloy with both diameters, and DSC scans of $\text{Ti}_{41.5}\text{Cu}_{37.5}\text{Ni}_{7.5}\text{Zr}_{2.5}\text{Hf}_5\text{Sn}_5\text{Si}_1$ alloy show slight difference between $\Phi 2$ and $\Phi 4$ sample, in detail, the whole DSC curve of the $\Phi 4$ sample shifts to low temperature as compared with $\Phi 2$ sample and the crystallization enthalpies for the first crystallization reaction of $\Phi 4$ sample is smaller than that of $\Phi 2$ sample, which indicates the different original microstructure between $\Phi 2$ and $\Phi 4$ sample. Compared with $\Phi 2$ sample, more crystals are formed in $\Phi 4$ sample, which is in accordance with the former analysis of XRD and neutron diffraction.

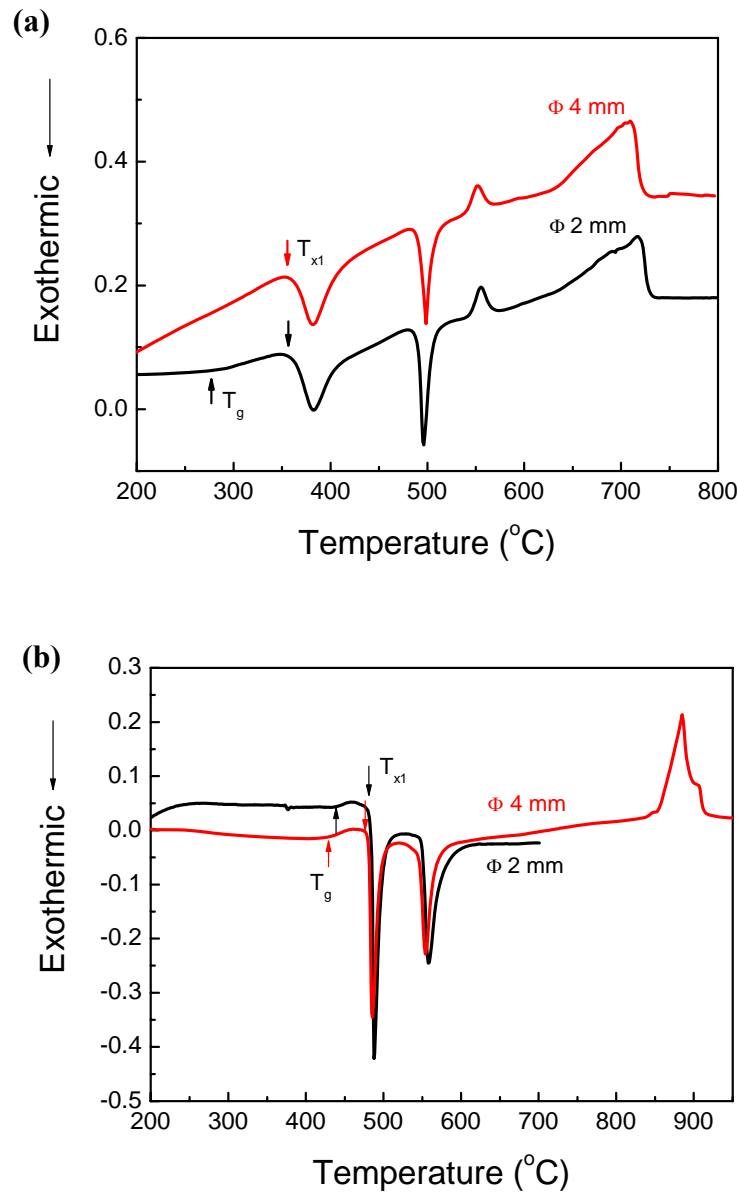


Fig. 2-13 Continuous heating DSC curves of (a) $\text{Ti}_{40}\text{Zr}_{25}\text{Ni}_8\text{Cu}_9\text{Be}_{18}$ and (b) $\text{Ti}_{41.5}\text{Cu}_{37.5}\text{Ni}_{7.5}\text{Zr}_{2.5}\text{Hf}_5\text{Sn}_5\text{Si}_1$ alloys with diameter of 2 and 4 mm at heating rate of 10 K/min

TEM observation was performed on 2 mm sample for both $\text{Ti}_{40}\text{Zr}_{25}\text{Ni}_8\text{Cu}_9\text{Be}_{18}$ and $\text{Ti}_{41.5}\text{Cu}_{37.5}\text{Ni}_{7.5}\text{Zr}_{2.5}\text{Hf}_5\text{Sn}_5\text{Si}_1$ alloy. Fig. 2-14 shows a bright-field HRTEM image with inset of selected-area electron diffraction pattern from the as-cast $\text{Ti}_{40}\text{Zr}_{25}\text{Ni}_8\text{Cu}_9\text{Be}_{18}$ alloy with a diameter of 2 mm, reveals a uniform, featureless homogeneous contrast, lacking any long-range topological order, no regularity of the lattice fringes and a series of diffuse halo rings, respectively, indicating a monolithic amorphous phase.

In contrast, the TEM bright-field image in Fig. 2-15 obtained from the as-cast $\text{Ti}_{41.5}\text{Cu}_{37.5}\text{Ni}_{7.5}\text{Zr}_{2.5}\text{Hf}_5\text{Sn}_5\text{Si}_1$ BMG, reveals a homogeneously distributed contrast, however, the inset selected-area diffraction pattern shows only halo diffraction intensity, similar to $\text{Ti}_{40}\text{Zr}_{25}\text{Ni}_8\text{Cu}_9\text{Be}_{18}$ BMG. Dark grey regions are homogeneously distributed in the light grey matrix, and no obvious crystal lattice was found in the dark grey region and no sharp interface (boundary) between the dark grey region and the light grey matrix which can be observed from the HRTEM image. Only from the observation of bright field image, one was easy to consider it to be nanocrystals/amorphous composite structure. However, by accounting for the absence of electronic diffraction patterns, continuous and spotty or strong diffuse rings superimposed on a dim amorphous halo pattern, another structure not nanocrystals/amorphous composite structure has to be considered. The contrast between the bright regions and the dark grey regions are believed to be attributed to the chemical composition fluctuation, as has been reported for $\text{Cu}_{47.5}\text{Zr}_{47.5}\text{Al}_5$ [K.B. Kim et al., 2006-b; Yao et al., 2006] and $\text{Ti}_{45}\text{Cu}_{40}\text{Ni}_{7.5}\text{Zr}_5\text{Sn}_{2.5}$ BMGs [K.B. Kim et al., 2006-a]. To confirm the chemical heterogeneity in as-cast BMG, chemical analysis should be carried out using EDS with a nanobeam spot size of several nanometer; however, limited within our experimental technique, we failed to analyze the chemical composition of both the bright grey region and dark grey regions. It is well known that liquid phase separation of BMGs easily occurs upon solidification when the constituent elements have a positive heat of mixing [Kündig et al., 2004; B.J. Park et al., 2004]. However, numerous BMGs, which consist of elements with negative heat of mixing, also often develop chemical fluctuations upon solidification [K.B. Kim et al., 2006-a; K.B. Kim et al., 2006-b; Yao et al., 2006; Löffler et al., 2000]. Furthermore, recent investigations on the microstructure of $\text{Cu}_{47.5}\text{Zr}_{47.5}\text{Al}_5$ and $\text{Ti}_{45}\text{Cu}_{40}\text{Ni}_{7.5}\text{Zr}_5\text{Sn}_{2.5}$ BMGs revealed that the degree of nano-scale chemical fluctuations can be macroscopically heterogeneous throughout the material [K.B. Kim et al., 2006-b; K.B. Kim et al., 2006-a]. This suggests that the occurrence of liquid phase separation in alloys, consisting of constituent elements with negative heat of mixing, can be considered to be linked to the formation of CSRO leading to a drastic reduction of the free enthalpy of the melt with decreasing temperature. In this scenario, the addition of Sn in the $\text{Ti}_{41.5}\text{Cu}_{42.5}\text{Ni}_{7.5}\text{Zr}_{2.5}\text{Hf}_5\text{Si}_1$ BMG possibly plays a role in producing a local miscibility gap upon solidification, thus creating Ti- and Cu-rich areas. The addition of minority elements, such as Sn in the present case, possibly enhances local ordering of the undercooled liquid, as recently demonstrated by both simulation and experiments [Sheng et al., 2006; K.B. Kim et al., 2006-a]. The microstructure of the as-cast $\text{Ti}_{41.5}\text{Cu}_{37.5}\text{Ni}_{7.5}\text{Zr}_{2.5}\text{Hf}_5\text{Sn}_5\text{Si}_1$ BMG is needed to be clarified deeply in the future work.

HRTEM was also performed on $\Phi 3$ sample. As a result, limited in our TEM observation region, we found several nanocrystals which appear with the same morphology as the dark grey regions in the matrix of $\Phi 3$ sample as that in $\Phi 2$ sample (see Fig. 2-16), and the corresponding SADP shows a dim diffraction ring around a broad hale pattern, revealing the coexistence of phase separation-like structure and the nanocrystals.

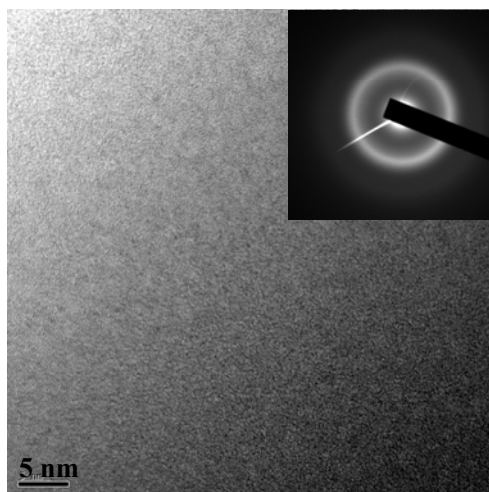


Fig. 2-14 HRTEM image and corresponding SADP of $\text{Ti}_{40}\text{Zr}_{25}\text{Ni}_8\text{Cu}_9\text{Be}_{18}$ alloy with a diameter of 2 mm

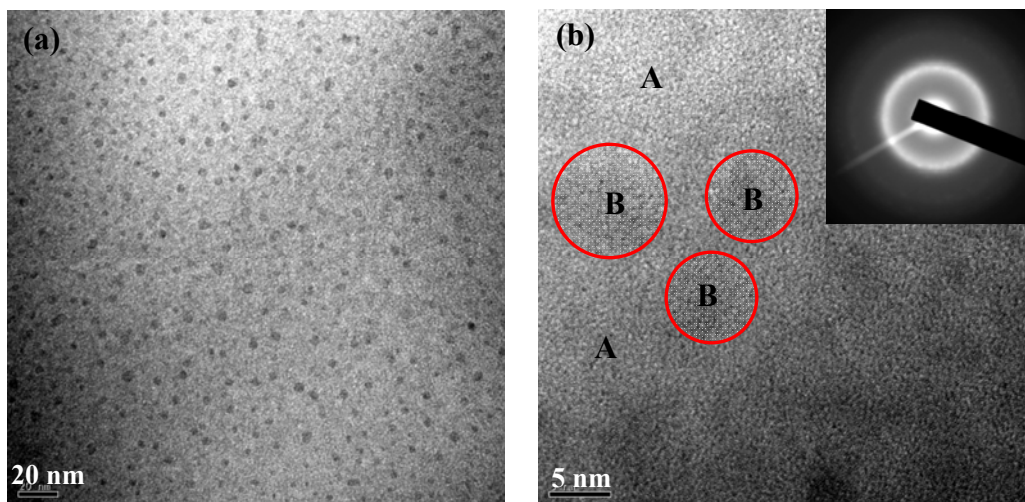


Fig. 2-15 (a) TEM image, (b) HRTEM image and corresponding SADP of $\text{Ti}_{41.5}\text{Cu}_{37.5}\text{Ni}_{7.5}\text{Zr}_{2.5}\text{Hf}_5\text{Sn}_5\text{Si}_1$ alloy with a diameter of 2 mm

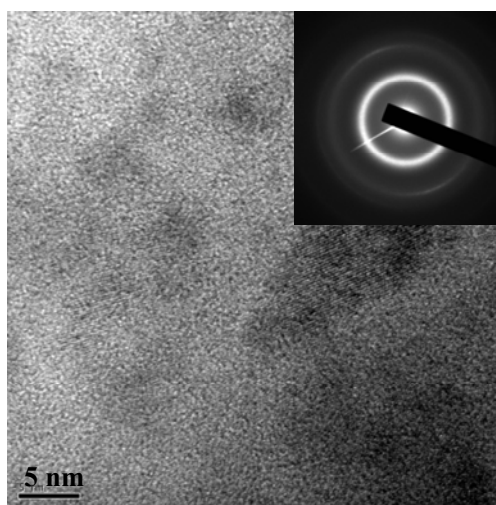


Fig. 2-16 HRTEM image and corresponding SADP of $\text{Ti}_{41.5}\text{Cu}_{37.5}\text{Ni}_{7.5}\text{Zr}_{2.5}\text{Hf}_5\text{Sn}_5\text{Si}_1$ alloy with a diameter of 3 mm

2.4.2 Thermal Analysis

In general, DSC measurement at a heating rate of 20 K/min is performed to obtaining thermal parameters of glassy alloys. Fig. 2-17 shows a typical DSC curve of $\text{Ti}_{40}\text{Zr}_{25}\text{Ni}_8\text{Cu}_9\text{Be}_{18}$ glassy alloy with a diameter of 2 mm at a heating rate of 20 K/min. In addition, DSC curve obtained at a heating rate of 40 K/min was also added into Fig. 2-17 in order to compare thermal parameters of $\text{Ti}_{40}\text{Zr}_{25}\text{Ni}_8\text{Cu}_9\text{Be}_{18}$ glassy alloy extracted from our experiments with previous study on the same alloy with a diameter of 8 mm at a heating rate of 40 K/min reported by Kim et al [Kim et al., 2004]. Similarly, Fig. 2-18 shows a DSC trace obtained from $\text{Ti}_{41.5}\text{Cu}_{37.5}\text{Ni}_{7.5}\text{Zr}_{2.5}\text{Hf}_5\text{Sn}_5\text{Si}$ glassy alloy at a heating rate of 20 K/min, and the DSC trace obtained from the same composition alloy however with diameter of 4 mm is included for comparison with the study in the literature [Huang et al., 2007-a].

It is seen that upon heating, all the DSC traces undergoes the sequence in endothermic event, characteristic of glass transition to undercooled liquid, followed by exothermic reactions corresponding to crystallization of the undercooled liquid, then melting. They both exhibit multi-step crystallization reactions. Table 2-9 and 2-10 give the thermal parameters, the onset temperature of glass transition T_g , the onset temperature of crystallization T_{x1} , the liquidus temperature T_l , the supercooled liquid region ΔT_x , the reduced glass transition temperature T_{rg} , the reduced crystallization temperature T_{x1}/T_l [J. Guo et al., 2007] which is a parameter estimating GFA when T_g is not available, parameter γ and parameter δ , obtained from DSC traces in Fig. 2-17 and 2-18, respectively, and the relevant previous studies [Kim et al., 2004; Huang et al., 2007-a] on each alloy are also listed in Table 2-9 and 2-10, respectively, for comparison.

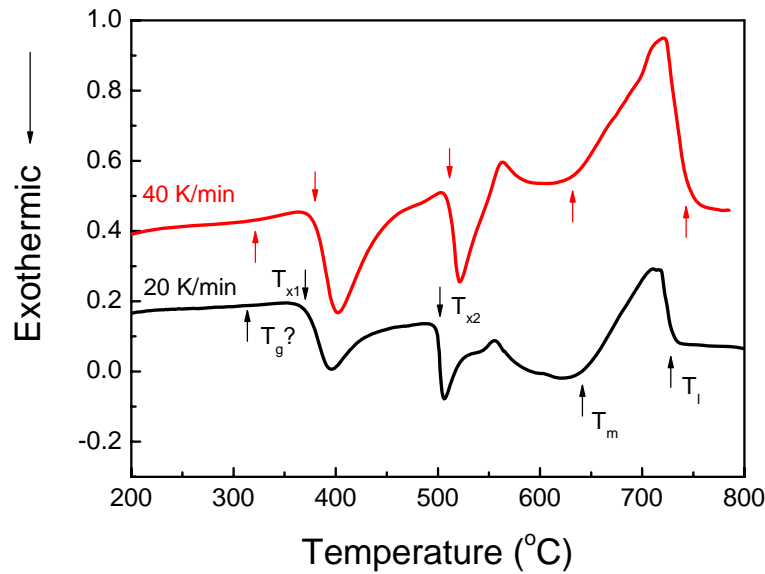


Fig. 2-17 Continuous heating DSC curves of $\text{Ti}_{40}\text{Zr}_{25}\text{Ni}_8\text{Cu}_9\text{Be}_{18}$ alloy with a diameter of 2 mm with various heating rates

Table 2-9

DSC thermal parameters of $\text{Ti}_{40}\text{Zr}_{25}\text{Ni}_8\text{Cu}_9\text{Be}_{18}$ alloy extracted from experiments performed on $\Phi 2$ mm sample

Alloy	T_g (K)	T_{x1} (K)	T_l (K)	ΔT_x (K)	T_{rg}	T_{x1}/T_l	γ	δ	Ref.
$\Phi 2$ mm (20 K/min)	586	645	1004	59	0.584	0.642	0.406	1.539	This study
$\Phi 2$ mm (40 K/min)	590	654	1016	64	0.581	0.644	0.407	1.535	This study
$\Phi 8$ mm (40 K/min)	621	668	1009 (20 K/min)	47	0.615	0.662	0.410	1.722	[Kim et al., 2004]

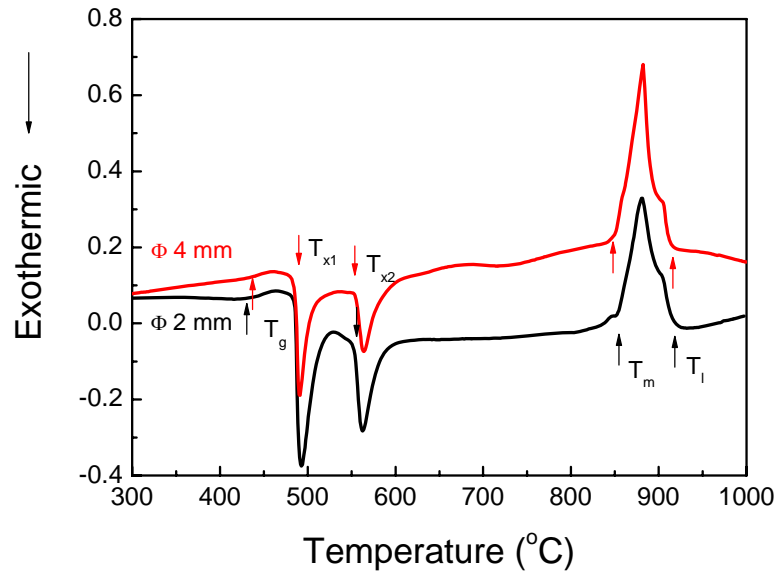


Fig. 2-18 Continuous heating DSC curves of $\text{Ti}_{41.5}\text{Cu}_{37.5}\text{Ni}_{7.5}\text{Zr}_{2.5}\text{Hf}_5\text{Sn}_5\text{Si}_1$ glassy alloy at a heating rate of 20 K/min

Table 2-10

DSC thermal parameters of $\text{Ti}_{41.5}\text{Cu}_{37.5}\text{Ni}_{7.5}\text{Zr}_{2.5}\text{Hf}_5\text{Sn}_5\text{Si}_1$ glassy alloy extracted from experiments performed on $\Phi 2$ mm and $\Phi 4$ mm samples.

Alloy	T_g (K)	T_{x1} (K)	T_m (K)	T_l (K)	ΔT_x (K)	T_{rg}	T_{x1}/T_l	γ	δ	Ref.
$\Phi 2$ mm (20 K/min)	705	758	1123	1190	53	0.592	0.637	0.400	1.563	This study
$\Phi 4$ mm (20 K/min)	698	757	1123	1186	59	0.589	0.638	0.402	1.551	This study
$\Phi 1$ mm (20 K/min)	693	757	1116	1176	64	0.590	0.644	0.405	1.569	[Huang et al., 2007-a]

Now we compare the thermal parameters obtained from our experiments with that obtained from literature. We chose the same heating rate for getting the information about T_g and T_{x1} , however different size of sample for $\text{Ti}_{40}\text{Zr}_{25}\text{Ni}_8\text{Cu}_9\text{Be}_{18}$ glassy alloy, 2 mm and 8 mm, respectively. Here we should pay attention that we got the liquidus temperature T_l from the DSC trace at a heating rate of 40 K/min, however, it was obtained from the DTA trace at a heating rate of 20 K/min in the study of Kim et al, which effected the following calculation about T_{rg} , γ and δ .

The value of T_g shows much more difference between our study and that of Kim et al. which results from the blurry glass transition reaction leading to the difficulty in locating the onset glass transition temperature. In regard to the value of T_g , Fornell et al. [Fornell et al., 2009] also found

the fact that the value of T_g measured from the DSC trace at the same heating rate however obtained from $\Phi 3$ sample was 610 K which was lower than that reported by Kim et al. However, if we compare the onset crystallization temperature with that in the literature, we found only that a difference of 14 K existed between $\Phi 2$ sample in our investigation and $\Phi 8$ sample in the work of Kim et al. We should think about the microstructure differences originating from different sizes of sample. The former investigation in the last section showed that the typical temperatures shift to a high temperature with increase in the diameter of sample, which was in good accordance with the investigation reported in the literature by Kim et al., in which the onset crystallization temperature of the rod sample in 8 mm diameter shifted to a higher temperature compared with that of ribbon sample. In addition, the investigation of Fornell et al. showed that the value of T_{x1} obtained from $\Phi 3$ sample was around 650 K, which was lower than that obtained from $\Phi 8$ sample. So it is reasonable to deduce that if the diameter of the sample used in our study was 8 mm, the onset crystallization temperature should be larger than 654 K and further close to 668 K as shown in the literature.

In regard to the thermal parameters of $\text{Ti}_{41.5}\text{Cu}_{37.5}\text{Ni}_{7.5}\text{Zr}_{2.5}\text{Hf}_5\text{Sn}_5\text{Si}_1$ glassy alloy, we found some inconsistency compared with the study of Huang et al [Huang et al., 2007-a]. In detail, the investigation in the last section revealed that the typical temperatures, T_g and T_{x1} , shifted to lower temperatures with increase in sample size due to the change of microstructure. So, according to this conclusion, $\Phi 1$ sample in the literature with fully glassy phase should exhibit higher typical temperatures. In addition, we found that the melting temperature and liquidus temperature obtained from our study are much higher than that reported by Huang et al., which maybe due to two possible reasons: slight alloy composition deviation and DSC measurement errors. As we know, the melting point and liquidus temperature are dependent on the alloy composition, and also glass forming ability is significantly affected by the purity of alloy. So, high pure elements were chosen for fabricating samples and the levitation melting with cold crucible technique was adopted to avoid ignition loss during melting and confirm homogeneous melting. However, arc melting technique which was applied by Huang et al. can not ensure the final alloy composition, in regards to the nominal composition. Accordingly, it is understandable that the difference in the final sample compositions may lead to the temperature difference between our study and Huang's study. So, the DSC curves obtained from our measurement were believed to be reasonable.

2.4.2.1 Glass forming ability

The GFA of metallic glasses can be represented by the critical cooling rate (R_c); however, R_c is generally difficult to be measured directly, and therefore other criteria have been used to indicate relative GFA. The correlation in metallic glass forming systems between GFA and the reduced glass transition temperature (T_{rg}) defined by Turnbull as the ratio between the glass transition (T_g) and liquidus (T_l) temperature [Turnbull, 1969] has been confirmed in many experiments. For some systems it has been demonstrated that larger values of ΔT_x tend to be associated with low values of critical cooling rate [Inoue, 2000]. As a result, the thermal stability, represented by ΔT_x , has also served as an indicator of GFA in some alloy systems. So far, several indicators have been used to evaluate GFA besides T_{rg} and ΔT_x . For example, Lu et al. proposed a parameter $\gamma = T_{x1} / (T_l + T_g)$, which was obtained by simple additive assumption of devitrification tendency of a glass and suppression of crystallization during solidification, to predict the GFA for various glass forming systems [Lu et al., 2002]. Chen et al. defined a parameter $\delta = T_{x1} / (T_l - T_g)$, derived from the

classical nucleation and growth theory, to evaluate the GFA of a metallic glass [Q.J. Chen et al., 2005].

In order to evaluate the GFA of the alloys, the values of ΔT_x , T_{rg} , γ parameter and δ parameter for these two alloys were calculated according to the thermal parameters obtained from DSC measurement and listed in the Table 2-9 and 2-10. The comparatively large parameters, ΔT_x , T_{rg} , γ and δ , indicate that both $Ti_{40}Zr_{25}Ni_8Cu_9Be_{18}$ and $Ti_{41.5}Cu_{37.5}Ni_{7.5}Zr_{2.5}Hf_5Sn_5Si_1$ glassy alloys possess high glass forming ability. Due to the ambiguity in glass transition temperature determination in $Ti_{40}Zr_{25}Ni_8Cu_9Be_{18}$ glassy alloy, the values of T_{rg} and δ were calculated to be lower than those of $Ti_{41.5}Cu_{37.5}Ni_{7.5}Zr_{2.5}Hf_5Sn_5Si_1$ glassy alloy, however, the values of these other two indicators were not. So, it is unbelievable to evaluate the GFA of glassy alloys simply by considering the GFA indicators mentioned above. In our study, the critical thickness and corresponding critical cooling rate were regarded as believable parameters to evaluate the GFA. The experimental results indicate that the fully amorphous $Ti_{40}Zr_{25}Ni_8Cu_9Be_{18}$ alloy with a diameter of 4 mm can be obtained, however, $Ti_{41.5}Cu_{37.5}Ni_{7.5}Zr_{2.5}Hf_5Sn_5Si_1$ glassy alloy with 4 mm in diameter have been verified to be crystalline/amorphous composite, this indicates the higher GFA of $Ti_{40}Zr_{25}Ni_8Cu_9Be_{18}$ alloy than that of $Ti_{41.5}Cu_{37.5}Ni_{7.5}Zr_{2.5}Hf_5Sn_5Si_1$ alloy.

It is well known that the critical cooling rate, R_c , is an important parameter for determining the GFA of a glass former, which can be determined by using the Barandiaran-Colmenero expression [Barandiaran et al., 1981]

$$\ln R = \ln R_c - \frac{B}{(T_l - T_{xc})^2} \quad (2-1)$$

where B is a material constant, and T_{xc} the onset solidification temperature of the melt at a cooling rate (R). The DSC curves of the $Ti_{40}Zr_{25}Ni_8Cu_9Be_{18}$ glassy alloy at the cooling rates of 10, 20, 30 and 40 K/min and at a heating rate of 20 K/min are shown in Fig. 2-19 (a). The plot of $\ln R$ vs. $-10000 / (T_l - T_{xc})^2$, obtained by linear fitting the data points determined in the DSC measurements, is shown in Fig. 2-19 (b). R_c can be calculated from the intercept of the linear fitting curve. The critical cooling rate of the $Ti_{40}Zr_{25}Ni_8Cu_9Be_{18}$ alloy for glass formation is determined to be 1.5 K/s, and the critical cooling rate of $Ti_{41.5}Cu_{37.5}Ni_{7.5}Zr_{2.5}Hf_5Sn_5Si_1$ glassy alloy, 28 K/s, was evaluated by the same method (see Fig. 2-20). The rather low critical cooling rate of $Ti_{41.5}Cu_{37.5}Ni_{7.5}Zr_{2.5}Hf_5Sn_5Si_1$ glassy alloy confirms the high GFA for it, and the even lower critical cooling rate of $Ti_{40}Zr_{25}Ni_8Cu_9Be_{18}$ glassy alloy, up to 1.5 K/s, indicates the even higher GFA than $Ti_{41.5}Cu_{37.5}Ni_{7.5}Zr_{2.5}Hf_5Sn_5Si_1$ glassy alloy, which is in accordance with the former conclusion.

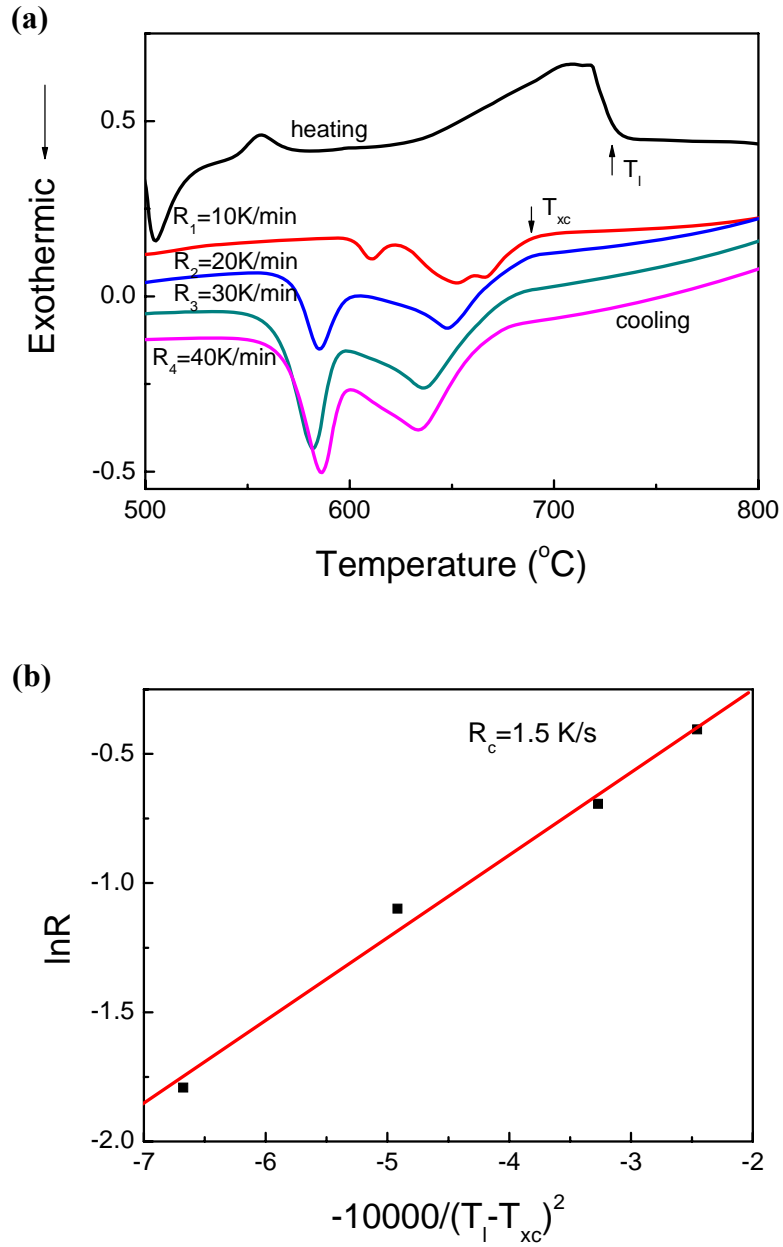


Fig. 2-19 (a) DSC heating and cooling curves of $\text{Ti}_{40}\text{Zr}_{25}\text{Ni}_8\text{Cu}_9\text{Be}_{18}$ alloy at heating rate of 20 K/min and various cooling rates of 10-40 K/min; (b) the plot of $\ln R$ vs. $-10000 / (T_1 - T_{xc})^2$.

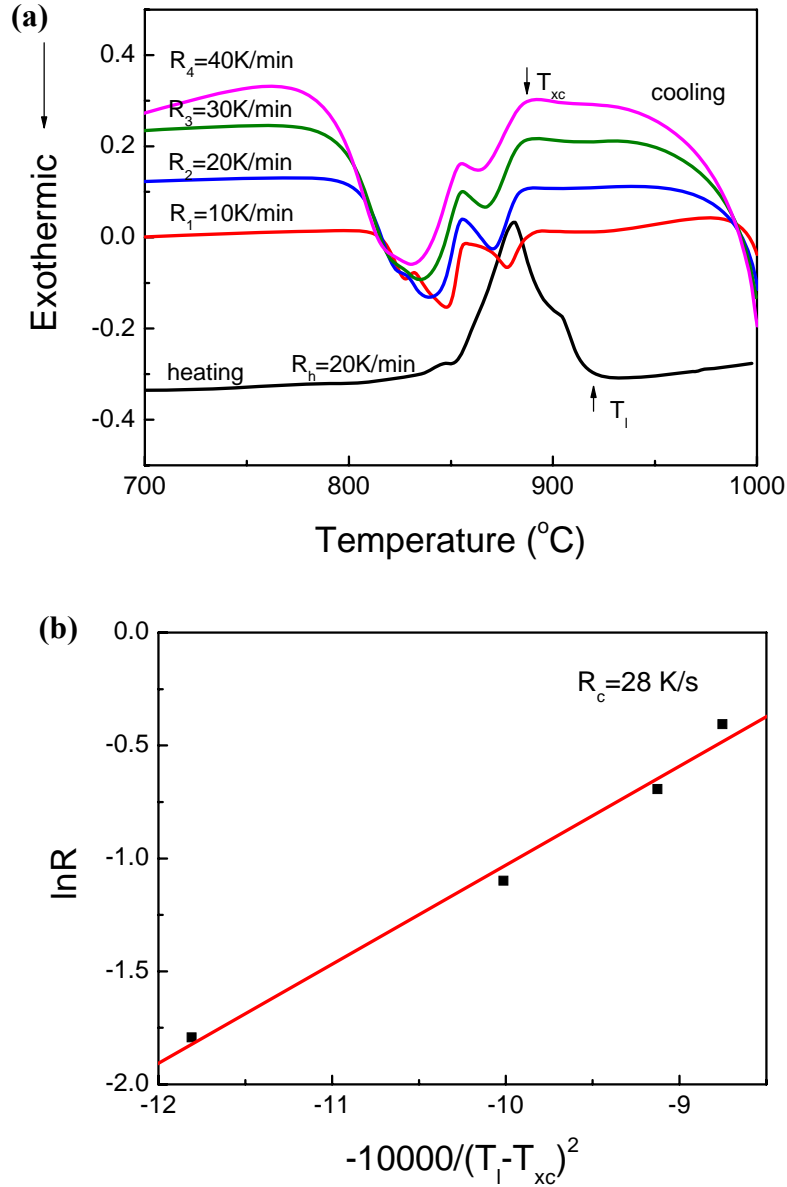


Fig. 2-20 (a) DSC heating and cooling curves of $\text{Ti}_{41.5}\text{Cu}_{37.5}\text{Ni}_{7.5}\text{Zr}_{2.5}\text{Hf}_5\text{Sn}_5\text{Si}_1$ alloy at heating rate of 20 K/min and various cooling rates of 10-40 K/min; (b) the plot of $\ln R$ vs. $-10000 / (T_l - T_{xc})^2$

2.4.2.2 Thermal stability

Knowledge of thermal ability is of importance as well as evaluating the GFA of an alloy. In general, the supercooled liquid region, ΔT_x , is considered as an indicator of thermal stability for glassy alloy. Since the major onset crystallization temperature corresponds to effective nucleation and growth of crystals [Shao et al., 2005], T_{x1} can also be considered as a useful indicator of thermal stability for a metallic glass. In contrast to the $\text{Ti}_{40}\text{Zr}_{25}\text{Ni}_8\text{Cu}_9\text{Be}_{18}$ glassy alloy, the $\text{Ti}_{41.5}\text{Cu}_{37.5}\text{Ni}_{7.5}\text{Zr}_{2.5}\text{Hf}_5\text{Sn}_5\text{Si}_1$ alloy presents a distinct glass transition, the wide supercooled liquid region and the higher onset crystallization temperature, T_{x1} , revealing the higher thermal stability of the $\text{Ti}_{41.5}\text{Cu}_{37.5}\text{Ni}_{7.5}\text{Zr}_{2.5}\text{Hf}_5\text{Sn}_5\text{Si}_1$ BMG than that of $\text{Ti}_{40}\text{Zr}_{25}\text{Ni}_8\text{Cu}_9\text{Be}_{18}$ BMG.

Since the activation energy for crystallization, reflecting the magnitude of energy barrier which

the atoms should overcome when they are rearranged from disorder to order states, is a reference for measuring the thermal stability of a metallic glass, i.e., the higher the value of the activation energy of crystallization, the higher is the thermal stability of an amorphous alloy, activation energy for crystallization is an effective parameter for evaluating the thermal stability of glassy alloys, which is commonly deduced from Kissinger equation [Kissinger, 1957]:

$$\frac{\beta}{(T_p)^2} = v_x \exp\left(\frac{-E_x}{RT_p}\right) \quad (2-2)$$

where β is the heating rate, v_x a pre-exponential factor, E_x the activation energy for crystallization, R the gas constant and T_p is the temperature of maximum energy release of each peak in the DSC scan which can be measured at selected heating rates β . And this equation can be converted to the expression:

$$\ln\left(\frac{\beta}{T_p^2}\right) = C - \frac{E_x}{RT_p} \quad (2-3)$$

where C is a constant ($=\ln v_x$). By plotting $\ln(\beta/T_p^2)$ vs. $1/T_p$, a straight line will be obtained. The slope of the straight line is just the apparent activation energy for crystallization identified by Kissinger equation.

Fig. 2-21 (a) and Fig. 2-22 (a) show the DSC traces of $\text{Ti}_{40}\text{Zr}_{25}\text{Ni}_8\text{Cu}_9\text{Be}_{18}$ and $\text{Ti}_{41.5}\text{Cu}_{37.5}\text{Ni}_{7.5}\text{Zr}_{2.5}\text{Hf}_5\text{Sn}_5\text{Si}_1$ BMGs performed at various heating rates in the range of 5-40 K/min, respectively. The peak temperatures of crystallization at different heating rates for these two alloys are given in Table 2-11 and 2-12. It can be seen that besides the strengthening of the peak intensity, each exothermic peak shifts to higher temperature with increase in heating rate, indicating a dependence of the characteristic temperatures on the heating rate. The typical Kissinger plots for both $\text{Ti}_{40}\text{Zr}_{25}\text{Ni}_8\text{Cu}_9\text{Be}_{18}$ and $\text{Ti}_{41.5}\text{Cu}_{37.5}\text{Ni}_{7.5}\text{Zr}_{2.5}\text{Hf}_5\text{Sn}_5\text{Si}_1$ BMGs are shown in Fig. 2-21 (b) and Fig. 2-22 (b), respectively. The crystallization activation energies, E_{Tp1} and E_{Tp2} , for $\text{Ti}_{40}\text{Zr}_{25}\text{Ni}_8\text{Cu}_9\text{Be}_{18}$ alloy are determined from Fig. 2-21 (b) to be 235.2 and 628.4 kJ/mol, respectively, while for $\text{Ti}_{41.5}\text{Cu}_{37.5}\text{Ni}_{7.5}\text{Zr}_{2.5}\text{Hf}_5\text{Sn}_5\text{Si}_1$ alloy are determined from Fig. 2-22 (b) to be 319.4 and 304.1 kJ/mol. Since the activation energy for crystallization reflects the magnitude of energy barrier which the atoms should overcome when they are rearranged from disorder to order states, one can conclude that the thermal stability of $\text{Ti}_{41.5}\text{Cu}_{37.5}\text{Ni}_{7.5}\text{Zr}_{2.5}\text{Hf}_5\text{Sn}_5\text{Si}_1$ glassy alloy is higher than that of $\text{Ti}_{40}\text{Zr}_{25}\text{Ni}_8\text{Cu}_9\text{Be}_{18}$ glassy alloy, also in good agreement with the former evaluation by considering the value of T_{x1} and ΔT_x as well as the nature of initial microstructure. According to the study by Kim et al., the primary crystallization product for $\text{Ti}_{40}\text{Zr}_{25}\text{Ni}_8\text{Cu}_9\text{Be}_{18}$ glassy alloy is icosahedral quasicrystals [Kim et al., 2004]. Recently, evidence of predominance of icosahedral cluster in the undercooled liquid has been established through X-ray scattering experiments using a synchrotron [Kelton et al., 2003]. It is believed that quasicrystals have low surface energy with the glass due to these icosahedral clusters, leading to a nucleation advantage, resulting in the easy formation of quasicrystals, as is in accordance with the relatively lower activation energy for the first crystallization of $\text{Ti}_{40}\text{Zr}_{25}\text{Ni}_8\text{Cu}_9\text{Be}_{18}$ glassy alloy.

In addition, we found that the activation energy for the first crystallization reaction, E_{Tp1} , of $\text{Ti}_{40}\text{Zr}_{25}\text{Ni}_8\text{Cu}_9\text{Be}_{18}$ alloy is much lower than E_{Tp2} , which indicated that the remaining amorphous phase after completing the first crystallization reaction is much more stable to bypass the second crystallization reaction.

Table 2-11

Peak temperatures of crystallization for $\text{Ti}_{40}\text{Zr}_{25}\text{Ni}_8\text{Cu}_9\text{Be}_{18}$ BMG.

β (K/min)	T_{p1} ($^{\circ}\text{C}$)	T_{p2} ($^{\circ}\text{C}$)
10	387.6	504.6
20	395.1	507.1
30	402.7	512.7
40	408.4	514.4

Table 2-12

Peak temperatures of crystallization for $\text{Ti}_{41.5}\text{Cu}_{37.5}\text{Ni}_{7.5}\text{Zr}_{2.5}\text{Hf}_5\text{Sn}_5\text{Si}_1$ BMG.

β (K/min)	T_{p1} ($^{\circ}\text{C}$)	T_{p2} ($^{\circ}\text{C}$)
5	471.6	535.6
10	478.7	548.7
20	488.6	563.6
40	501.2	571.2

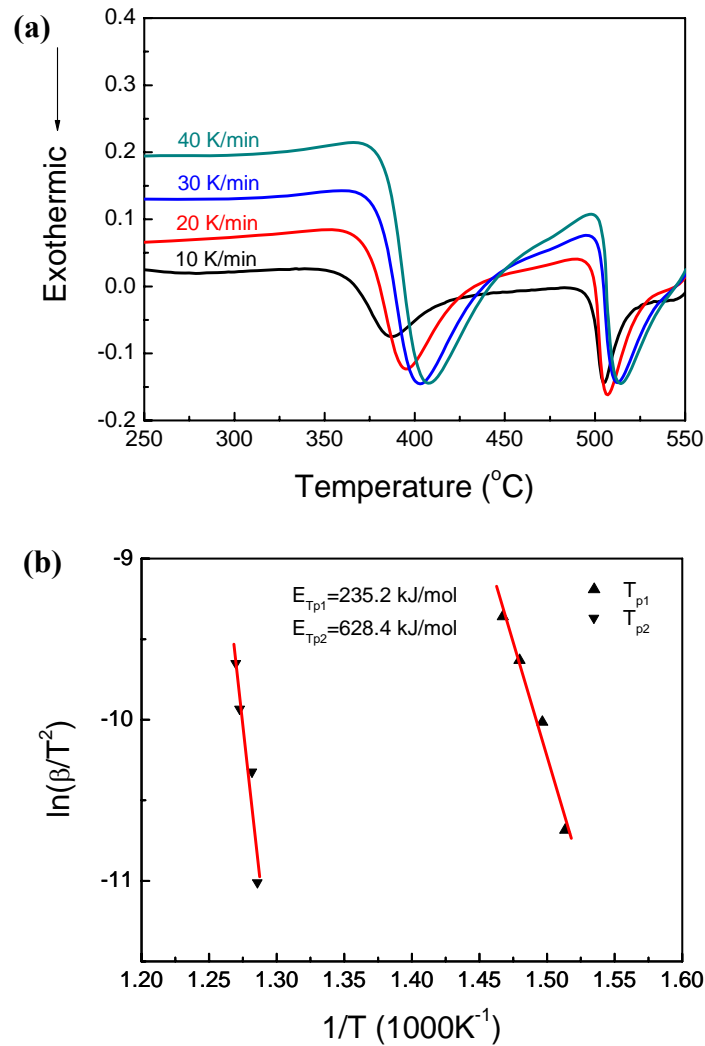


Fig. 2-21 (a) DSC curves of $\text{Ti}_{40}\text{Zr}_{25}\text{Ni}_8\text{Cu}_9\text{Be}_{18}$ BMG at various heating rates and (b) Kissinger plots

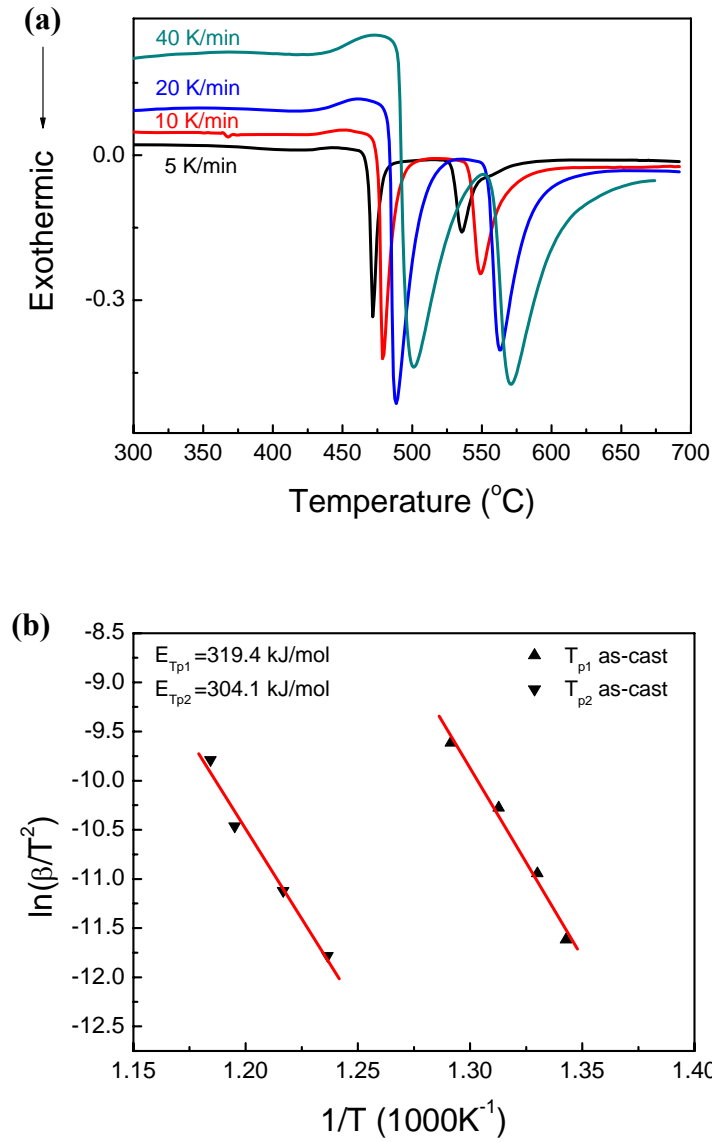


Fig. 2-22 (a) DSC curves of Ti_{41.5}Cu_{37.5}Ni_{7.5}Zr_{2.5}Hf₅Sn₅Si₁ BMG at various heating rates and (b) Kissinger plots

2.5 Discussion on the Identification of Microstructure and the Structural Stability

Although the HRTEM observation, a featureless homogeneous contrast and a series of diffuse halo rings, revealed the nature of monolithic glassy state for Ti₄₀Zr₂₅Ni₈Cu₉Be₁₈ alloy with a diameter of 2 mm, however, the fact that no obvious structural relaxation and glass transition were observed upon heating in the DSC measurement prompted us to rethink about the real nature of as-cast Ti₄₀Zr₂₅Ni₈Cu₉Be₁₈ alloy. On the other hand, HRTEM observation on Ti_{41.5}Cu_{37.5}Ni_{7.5}Zr_{2.5}Hf₅Sn₅Si₁ BMG with 2 mm in diameter revealed a phase separation-like structure. These results push us to do more experiments to identify the microstructure of glassy alloy and find the correlation between the nature of glassy alloy and their properties. In regard to

the relation between the microstructure and the properties, we will discuss in the following chapters. In this section, we focus on the microstructure identification for $\text{Ti}_{40}\text{Zr}_{25}\text{Ni}_8\text{Cu}_9\text{Be}_{18}$ as well as $\text{Ti}_{41.5}\text{Cu}_{37.5}\text{Ni}_{7.5}\text{Zr}_{2.5}\text{Hf}_5\text{Sn}_5\text{Si}_1$ BMG with 2 mm in diameter.

To our knowledge, metallic glass crystallizes on heating, yielding both stable and metastable phases. The process of crystallization is of first order and follows a nucleation and growth process. Although the crystallization of glassy alloy undergoing a nucleation and growth event in the DSC, is not a necessary and sufficient condition to prove the amorphous state, isothermal DSC measurement was performed to check if there exist quenched-in nuclei in the initial state of as-cast glassy alloy.

The DSC traces obtained from $\text{Ti}_{40}\text{Zr}_{25}\text{Ni}_8\text{Cu}_9\text{Be}_{18}$ and $\text{Ti}_{41.5}\text{Cu}_{37.5}\text{Ni}_{7.5}\text{Zr}_{2.5}\text{Hf}_5\text{Sn}_5\text{Si}_1$ BMGs during isothermal holding at 340 °C, 30 K below the onset crystallization temperature and at 440 °C, 45 K below T_{x1} , are shown in Fig. 2-23 (a) and (b), respectively. The DSC trace of $\text{Ti}_{41.5}\text{Cu}_{37.5}\text{Ni}_{7.5}\text{Zr}_{2.5}\text{Hf}_5\text{Sn}_5\text{Si}_1$ glassy alloy showed an exothermic peak, indicating that phase formation occurs by nucleation and growth mechanism in the glass matrix. However, no exothermic peak was observed, but the calorimetric signal decreased monotonically during isothermal treatment in the isothermal DSC trace of $\text{Ti}_{40}\text{Zr}_{25}\text{Ni}_8\text{Cu}_9\text{Be}_{18}$ BMG. Several possible origins are responsible for this signal [Yang et al., 2006]: (i) DSC instrumental transients; (ii) grain coarsening or growth of quenched-in nuclei; (iii) relaxation of the glass. The first and the third possibilities can be ignored because of the precipitation of large quantities of nanocrystals obtained from the annealed sample under this condition which is not shown here. So, this monotonically decreasing calorimetric signal during isothermal treatment provides the evidence that the crystallization process involves only the grain coarsening or growth of quenched-in nuclei. For grain coarsening or growth of the existing nuclei, the kinetics of the two processes is fundamentally different although they may exhibit similar calorimetric behavior. Growth of the existing nuclei in metallic glasses involves a solid state transformation from an amorphous state to a crystalline state, while grain coarsening occurs in micro-crystalline or nanocrystalline materials just corresponding to the reduction in interface enthalpy due to the annihilation of grain boundaries. For the present $\text{Ti}_{40}\text{Zr}_{25}\text{Ni}_8\text{Cu}_9\text{Be}_{18}$ BMG, clearly, there is no sign of crystals that can be detected using XRD, neutron diffraction and even HRTEM in the as-cast sample, which confirms the growth of the quenched-in nuclei as the origins for the decreasing calorimetric signal. In summary, the original microstructure of the $\text{Ti}_{40}\text{Zr}_{25}\text{Ni}_8\text{Cu}_9\text{Be}_{18}$ BMG consists of large quantities of quenched-in nuclei, and the quenched-in nuclei are not stable and easy to grow directly.

on the contrary, although the occurrence of exothermic reaction which is corresponding to a nucleation and growth event, in the isothermal DSC trace of $\text{Ti}_{41.5}\text{Cu}_{37.5}\text{Ni}_{7.5}\text{Zr}_{2.5}\text{Hf}_5\text{Sn}_5\text{Si}_1$ alloy can not provide a necessary and sufficient condition to prove the glassy state of $\text{Ti}_{41.5}\text{Cu}_{37.5}\text{Ni}_{7.5}\text{Zr}_{2.5}\text{Hf}_5\text{Sn}_5\text{Si}_1$, one possible reason could be applied to explain the absence of the monotonic decrease in calorimetric signal during isothermal DSC measurement which is corresponding to the growth of crystals. Unlike the quenched-in nuclei in $\text{Ti}_{40}\text{Zr}_{25}\text{Ni}_8\text{Cu}_9\text{Be}_{18}$ BMG, the phase separation-like structure in the as-cast $\text{Ti}_{41.5}\text{Cu}_{37.5}\text{Ni}_{7.5}\text{Zr}_{2.5}\text{Hf}_5\text{Sn}_5\text{Si}_1$ BMG, may become a heterogeneous nucleus or not and then grow or disappear upon heating (or other input of energies) through atomic diffusion depending on its degree of ordering and the degree of structural similarity between the primary crystallization phase upon heating and this phase separation-like structure. In order to determine the structure thermal stability of the original microstructure in

$\text{Ti}_{41.5}\text{Cu}_{37.5}\text{Ni}_{7.5}\text{Zr}_{2.5}\text{Hf}_5\text{Sn}_5\text{Si}_1$ BMG, annealing treatment was performed on this alloy, which will be present in the Chapter 4 in detail. Fig. 2-24, 2-25, 2-26 show the TEM images obtained from the annealed samples at 397 °C (35 K below T_g) for different time of 15 min to 12 h. We found that the phase separation-like structure can easily disappear upon heating and then new nanocrystals start to nucleate and growth following the typical crystallization process. So, based on the analysis above we can deduce the large structural difference between the quenched-in phase separation-like structure and the primary crystalline phase upon heating. Accordingly, we can obtain a conclusion: the low similarity between the quenched-in phase separation-like structure and the primary phase upon heating leads to the decomposition of the phase separation-like structure through the atomic diffusion. In summary, the original microstructure of the $\text{Ti}_{41.5}\text{Cu}_{37.5}\text{Ni}_{7.5}\text{Zr}_{2.5}\text{Hf}_5\text{Sn}_5\text{Si}_1$ BMG consists of phase separation-like structure, and the phase separation-like are not stable and tending to decompose upon heating.

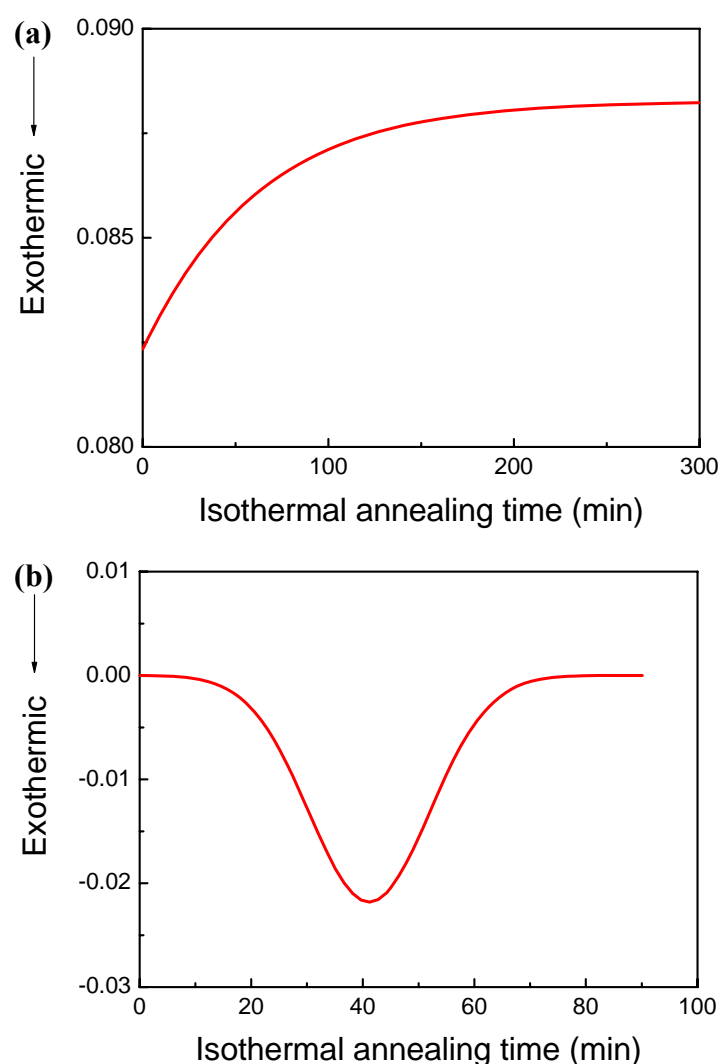


Fig. 2-23 Isothermal annealing DSC curves obtained from as-cast (a) $\text{Ti}_{40}\text{Zr}_{25}\text{Ni}_8\text{Cu}_9\text{Be}_{18}$ and (b) $\text{Ti}_{41.5}\text{Cu}_{37.5}\text{Ni}_{7.5}\text{Zr}_{2.5}\text{Hf}_5\text{Sn}_5\text{Si}_1$ alloys with 2 mm in diameter

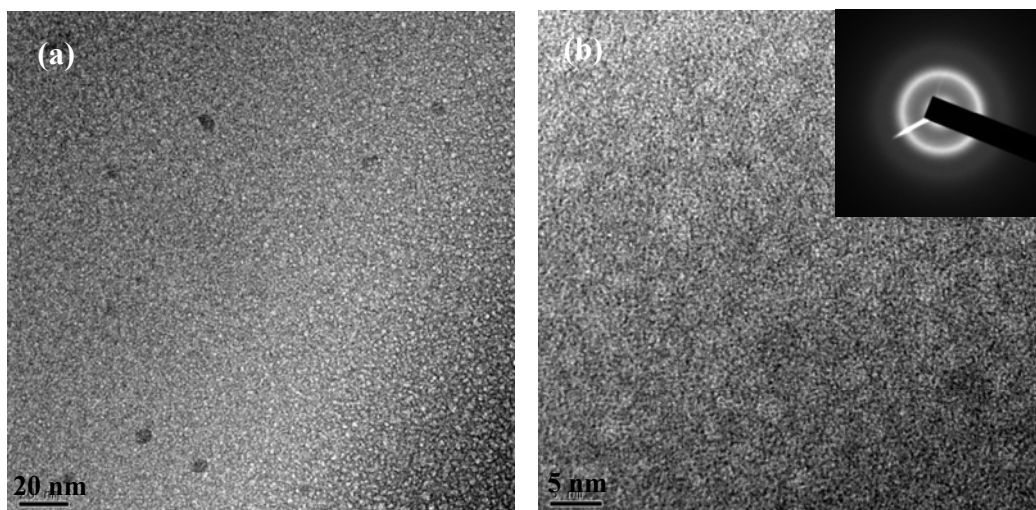


Fig. 2-24 (a) Bright-field TEM image, (b) bright-field HRTEM image and corresponding SADP obtained from the as-cast $\text{Ti}_{41.5}\text{Cu}_{37.5}\text{Ni}_{7.5}\text{Zr}_{2.5}\text{Hf}_5\text{Sn}_5\text{Si}_1$ sample annealed at 397 °C for 15 min

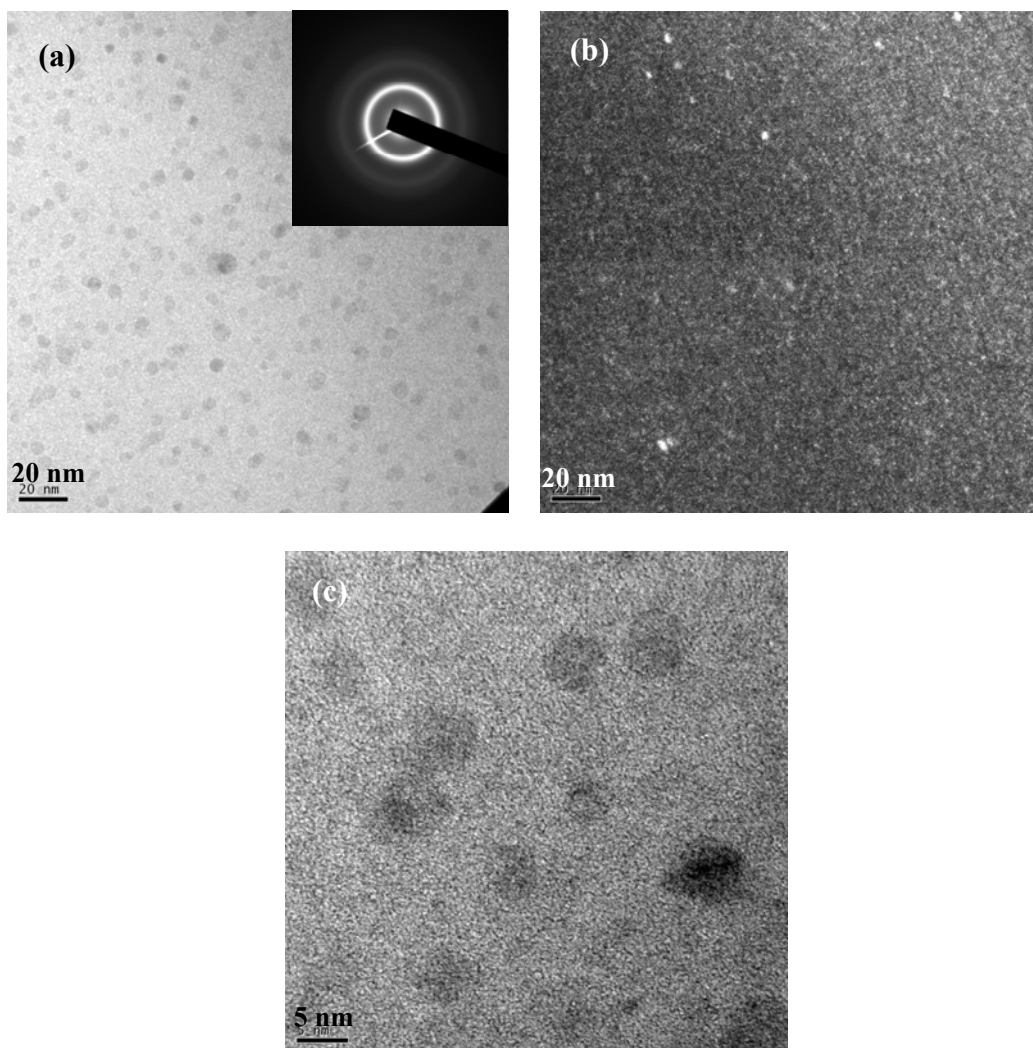


Fig. 2-25 (a) Bright-field TEM image and corresponding SADP, (b) dark-field TEM image, (c) HRTEM image obtained from the as-cast $\text{Ti}_{41.5}\text{Cu}_{37.5}\text{Ni}_{7.5}\text{Zr}_{2.5}\text{Hf}_5\text{Sn}_5\text{Si}_1$ sample annealed at 397 °C for 8 h

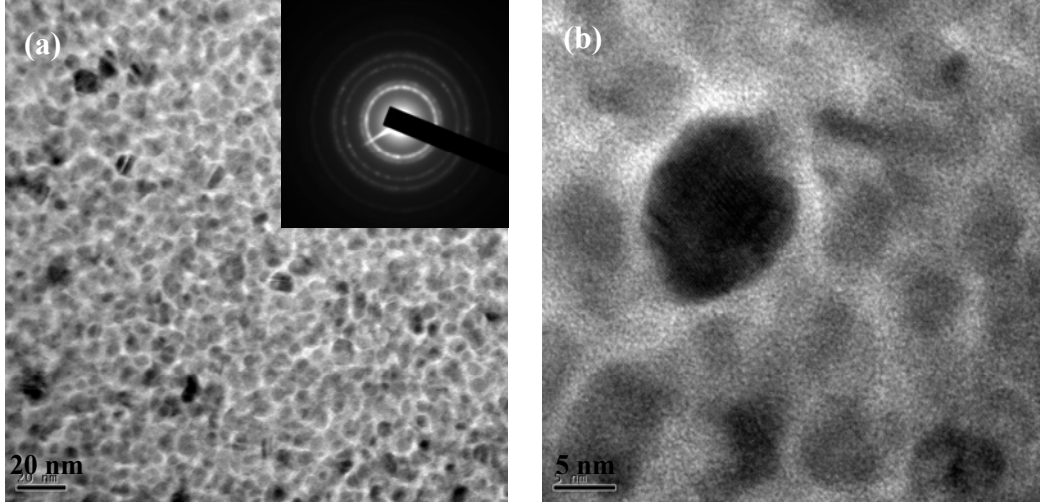


Fig. 2-26 (a) Bright-field TEM image and corresponding SADP, (b) HRTEM image obtained from the as-cast $\text{Ti}_{41.5}\text{Cu}_{37.5}\text{Ni}_{7.5}\text{Zr}_{2.5}\text{Hf}_5\text{Sn}_5\text{Si}_1$ sample annealed at 397 °C for 12 h

The kinetic transition from crystalline products to an amorphous phase is a common structural change that occurs during solidification with increasing cooling rate and liquid undercooling. The two main strategies to synthesize amorphous alloys are based upon nucleation control and growth control as depicted in Fig. 2-27 [Perepezko et al., 2007]. With nucleation control, the undercooling that is achieved during cooling bypasses the nucleation reaction and the nucleation size distribution, $C(n)$, that may be retained by the cooling does not overlap with the critical nucleation size, n^* , at the crystallization temperature, T_x . These kinetic conditions are the basis for bulk glass formation during slow cooling. Further studies by Cahn [Cahn, 1983], Jones [Jones, 1982], and a comprehensive review by Boettinger and Perepezko [Boettinger et al., 1985] elucidate the important role of applying melt undercooling, a measure of liquid metastability, as a common underlying link between advanced processing methods and the development of novel solidification structures. During isothermal annealing at T_x , the heat evolution rate \dot{Q} exhibits a clear delay before the onset of the nucleation reaction and a peak maximum associated with the completion of nucleation and continued growth. On the other hand, under growth control conditions the cooling rate is insufficient to bypass the nucleation onset completely so that some small fraction of crystallites may form initially, but the rapidly rising viscosity and falling growth rate with continued cooling near T_g prevents rapid cluster growth. In this case, upon reheating a sample, rapid crystallization of quenched-in structures, as well as additional nucleation, ensues at T_x , which essentially coincides with T_g . Many of the early metallic glass alloys were synthesized under growth controlled conditions (i.e. marginal glass formers) [Cochrane et al., 1999]. In our study, the formation of $\text{Ti}_{40}\text{Zr}_{25}\text{Ni}_8\text{Cu}_9\text{Be}_{18}$ and $\text{Ti}_{41.5}\text{Cu}_{37.5}\text{Ni}_{7.5}\text{Zr}_{2.5}\text{Hf}_5\text{Sn}_5\text{Si}_1$ glassy alloys are considered to be growth controlled and nucleation controlled, respectively.

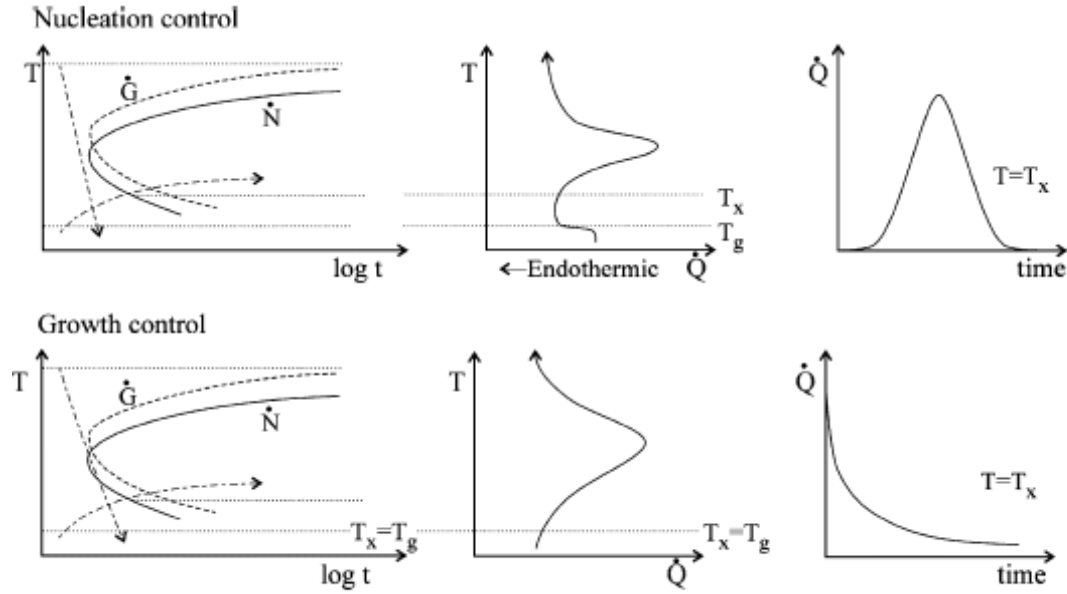


Fig. 2-27 Principal forms of kinetic control for metallic glass formation [Perepezko et al., 2007]

2.6 Conclusion

Two Ti-based bulk metallic glasses, with the nominal composition of $\text{Ti}_{40}\text{Zr}_{25}\text{Ni}_8\text{Cu}_9\text{Be}_{18}$ and $\text{Ti}_{41.5}\text{Cu}_{37.5}\text{Ni}_{7.5}\text{Zr}_{2.5}\text{Hf}_5\text{Sn}_5\text{Si}_1$, as the typical representation of Ti-Zr-Ni and Ti-Cu-Ni system, respectively, were selected for investigation in this study. The characteristic of the original structure, thermal stability and glass forming ability were studied in this chapter. The following conclusions can be obtained:

1. $\text{Ti}_{40}\text{Zr}_{25}\text{Ni}_8\text{Cu}_9\text{Be}_{18}$ bulk metallic glass with a diameter up to 4 mm can be synthesized based on growth control, resulting in quenched-in nuclei that are formed in the glass matrix. Isothermal DSC measurement indicated the priority of quenched-in nuclei growth as a result of monotonically decreasing calorimetric signal during isothermal treatment.
2. $\text{Ti}_{41.5}\text{Cu}_{37.5}\text{Ni}_{7.5}\text{Zr}_{2.5}\text{Sn}_5\text{Hf}_5\text{Si}_1$ bulk metallic glass with diameter of 2 mm can be synthesized based on nucleation control. Phase separation-like structure was formed which exhibited the bright grey and dark grey region in the HRTEM observation. However, due to the low similarity between the phase separation-like structure and the primary crystallization phase, the phase separation-like structure tends to decompose upon heating through atomic diffusion. XRD pattern and neutron diffraction reveal the existence of some particles corresponding to $\text{Ti}_5\text{Sn}_3\text{Cu}$ and $\text{TiNi}(\text{Cu})$ phases in the amorphous matrix for 4 mm sample.
3. The high values of ΔT_x , T_{rg} , γ and δ for both $\text{Ti}_{40}\text{Zr}_{25}\text{Ni}_8\text{Cu}_9\text{Be}_{18}$ and $\text{Ti}_{41.5}\text{Cu}_{37.5}\text{Ni}_{7.5}\text{Zr}_{2.5}\text{Sn}_5\text{Hf}_5\text{Si}_1$ BMGs reveal a high thermal stability and high GFA for these two alloys. The critical cooling rate R_c of $\text{Ti}_{40}\text{Zr}_{25}\text{Ni}_8\text{Cu}_9\text{Be}_{18}$ and $\text{Ti}_{41.5}\text{Cu}_{37.5}\text{Ni}_{7.5}\text{Zr}_{2.5}\text{Sn}_5\text{Hf}_5\text{Si}_1$ BMGs, are 1.5 and 28 K/s, respectively, indicating the higher GFA of $\text{Ti}_{40}\text{Zr}_{25}\text{Ni}_8\text{Cu}_9\text{Be}_{18}$ BMG. In addition, the activation energies for the first crystallization reaction for these two alloys are 235.2 and 319.4 kJ/mol, respectively, revealing the higher thermal stability of $\text{Ti}_{41.5}\text{Cu}_{37.5}\text{Ni}_{7.5}\text{Zr}_{2.5}\text{Sn}_5\text{Hf}_5\text{Si}_1$ BMG.

CHAPTER 3

LOW-TEMPERATURE PHYSICAL PROPERTIES FOR TI-BASED BULK METALLIC GLASSES

3.1 Background and Motivation

The structure of amorphous materials is significantly different from that of ordered crystalline materials. They exhibit properties of solid as well as liquid, and are often viewed as a frozen liquid. Amorphous materials exhibit significantly different low-temperature physical properties, such as specific heat, thermal conductivity and electrical resistivity etc., compared with crystalline materials. As we know, the characteristic and properties of crystalline solids can be generally explained based on the periodicity theory; however, so far, no developed fundamental theory was constructed based on disordered structure. Due to the weakness of thermal motion, some physical phenomenon may occur at low temperature which can not be observed at ambient temperature. So, it is of significance to study the low-temperature physical properties of amorphous materials from the view of science, and it is one of the important branches of condensed matter physics.

The investigation of low-temperature physical properties on amorphous materials is far behind that on crystalline materials. With the development of amorphous materials, people started to carry out extensive work in this field based on atom and free electron behaviors etc.

Previous study on the low-temperature physical properties of amorphous materials was only restricted within the aspect of atomic structure of insulated materials due to the limitation of amorphous materials development, although large quantity of work has been done based on the low-temperature thermal properties during the last four decades.

Fortunately, the study on the low-temperature physical properties of amorphous materials has been extended into the aspect of electrical structure since the discovery of metallic glasses, not only the physical properties mentioned above have been investigated, but also the electrical transport properties were studied by electrical resistivity, thermal potential, and Hall coefficient measurements, which also provided a chance of investigation on amorphous materials based on the electronic structure. In other words, the discovery of a series of new bulk metallic glasses in recent years broadened the research field of amorphous materials not only within the amorphous dielectric or semiconductor.

So far, several theoretical models have been constructed to explain the abnormal low-temperature physical properties of amorphous materials. In regard to thermal properties, two-level systems model (or tunneling state model) was successfully applied to interpret the abnormal low-temperature ($T < 1$ K) specific heat of amorphous materials which deviated from the Debye dependence. Based on two-level systems model, soft potential model was successfully developed to explain the low-temperature specific heat of amorphous materials under the

temperature of 10 K. It means that soft potential model can not be applied to explain the abnormal so-called “boson peak” in some extent. And, the low-temperature specific heat in a broader temperature range, for example, several tens of Kelvin, can not be interpreted efficiently. So it is necessary to construct an available universal theoretical model to interpret the thermal properties of materials in a broad temperature range. Besides that, the correlation between “boson peak” and abnormal low-temperature thermal properties is still in debate. On the other hand, the different transport properties compared with crystalline materials, such as large magnitude of resistivity, rather small and even negative temperature coefficient of resistivity and the minimum of resistivity generally occur at low temperature for amorphous alloys, which are of interest to construct relevant theory to explain these abnormal phenomena. Ziman liquid metal scattering of electron theory [Ziman, 1961] was extended to explain the scattering of electron originated from the disordered structure in metallic glasses. Nagel [Nagel, 1977] successfully obtained the resistivity-temperature dependence of amorphous conductor and evaluated the magnitude of temperature coefficient of resistivity by applying free electron model, which was in good agreement with the experimental results. Besides that, Mott s-d scattering of electron model [Mott, 1964], two-level systems scattering theory [Vladár et al., 1983-a, b, c], etc., also could explain some phenomena of the variation of resistivity with temperature in amorphous alloys in some extent [Tang, 2006].

Although bulk metallic glasses are a kind of glasses which have the simplest structure, the existence of a large quantity of free electrons which act as conduction-electron in them leads to their absolutely different thermal and electrical transport properties compared with crystalline metallic alloys. So far, related to bulk metallic glasses, extensive work has been carried out on GFA, thermal stability, phase transformation kinetics, structural characteristic, mechanical properties and corrosion resistance properties etc., however, limited work has been done about their low-temperature physical properties under the condition of considering the effects of free electron-assisted, and the effects of disordered structure on the low-temperature scattering of electron, electron states and density of states.

Low-temperature physical properties of amorphous materials include low-temperature thermal properties, electrical transport properties, magnetic properties and superconductivity, etc. We just focus our study on low-temperature thermal properties and electrical transport properties by considering the existence of group of free electrons.

3.1.1 Low-temperature Specific Heat

Metallic glasses have long represented an intriguing class of materials. The recent discovery of a new family of bulk metallic glasses offers excellent opportunities for the understanding of the metallic glassy state and investigation of the physical properties of the metallic glasses by using various physical methods. It is well known that the glass forming ability and unique properties are closely related to its microstructural features. But not much information is known so far on the microstructure, especially electronic structure, of BMGs due to the complicated multiple components. The study on low-temperature specific heat of BMGs offers an effective way to understand atomic and electronic structural characteristics of BMG, since electron and lattice vibration behaviors can be distinguished from specific heat at low temperature. Up to now, a few studies have been done on low-temperature specific heats of BMGs, although much research has

been carried out on insulating amorphous alloys, binary or ternary metallic glasses, such as Zr-Pd [Graebner et al., 1977], Ti-Si [Rogatchev et al., 2000] and Pd-Si-Cu [Golding et al., 1972].

The differences between glassy and crystalline states in heat capacities have significance for understanding of the unique microstructural characteristics and nature of the BMGs.

3.1.1.1 Anomalies and theoretical model

It has been well known that the low-temperature physical properties, thermal, vibrational, acoustic and electrical transport etc. of amorphous solids differ distinctly from those of crystalline solids and seem to be universal for various glasses irrespective of either the type of chemical bonding or other structural details continue to be one of the major unsolved and debated issues in the field of condensed matter physics [Zeller et al., 1971].

In regard to the thermal properties, two features are nearly universally observed in the specific heat C_p and thermal conductivity k , of amorphous materials. First, at very low temperature typically $T < 1$ K, the specific heat C_p depends approximately linearly on temperature ($C_p \propto T$) and the thermal conductivity k almost quadratically ($k \propto T^2$) on temperature, deviating from Debye's theory, which is expected to be cubic dependent as observed in crystals at low temperature. This is due to the existence of low-energy excitations, which are commonly interpreted by two-level systems model (TLS) (or tunneling states model (TM)) proposed by Phillips [Phillips, 1972] and Anderson et al. [Anderson et al., 1972] which postulated the ubiquitous existence of atoms or small groups of atoms in amorphous solids which can tunnel between two nearly degenerate local energy minima.

The second is a broad peak or bump which is so-called boson peak in C_p/T^3 vs. T and the corresponding plateau in k at the same higher temperature $T > 1$ K. The universal feature is related to a difference or excess in the density of relatively low-energy vibrational states over the crystalline Debye behavior, however, the physical origin of the scaling behavior is not yet well understood. The most accepted, phenomenological models to explain this behavior of glasses in the whole range of low-frequency excitations is the phenomenological soft-potential model (SPM) [Karpov et al., 1983] (it can be regarded as an extension of the tunneling states model which is based on the idea that besides two-level systems (TLS) there also exist quasi harmonic soft localized modes (SLM)) which postulates the coexistence in glasses of acoustic phonons (crystalline-like, extended lattice vibrations) with quasilocalized low-frequency (soft) modes. Nevertheless, the specific nature of the low-frequency vibrations is still a matter of intense debate. In the SPM, the potential of these soft modes is assumed to have a uniform stabilizing fourth-order term W , an energy scale which is the basic parameter of the model [Karpov et al., 1983; Gurevich et al., 1993; Ramos et al., 1997]. In addition, each mode has its own first-order (asymmetry D_1) and second-order (restoring force D_2) terms, which can be either positive or negative, hence giving rise to a distribution of double-well potentials (tunneling states) and more or less harmonic single-well ones (soft vibrations). The parameter W marks the crossover from the tunneling-states region at the lowest temperatures to the soft-modes region above it. Indeed, W can be approximately determined either from the minimum T_{\min} in C_p/T^3 ($W \approx 1.8-2k_B T_{\min}$) or from the position of the maximum $T_{k,\max}$ in a k/T vs k plot ($W \approx 1.6k_B T_{k,\max}$) [Ramos et al., 1997]. Similarly to the TM, a random distribution of potentials is assumed: $P(D_1, D_2) = P_s$ [Ramos et al., 2002]. For a more detailed description of the SPM, the reader is referred to the reviews of Refs. [Ramos et al., 1998; Parshin, 1994]. Recently, there has been some success explaining these phenomena within

the general concept of a soft potential and/or interacting defect model, which attempts to fit the C_p/T^3 peak, the k plateau and the $T < 2$ K tunneling states together in a single model. These modeling efforts are still controversial and the details of the models and the underlying microscopic mechanisms are not yet universally accepted.

3.1.1.2 Critical review

The long history of research on thermal properties of amorphous solids details remarkably similar behavior for a wide range of disordered materials but no comprehensive picture of the physical origins of these similarities.

The well known two-level systems model as well as soft-potential model can be applied within the restriction of a particular temperature range, generally lower than 10 K. What is missing, however, is an explanation of the glassy anomalies at still higher temperatures, namely, the broad peak in C_p/T^3 and the second rise of the thermal conductivity. In terms of the low-energy vibrational density of states $g(\omega)$ (VDOS) and the frequency ω , the general observation of the peak in C_p/T^3 is due to an anomalous VDOS having the shape of a peak when reported as $g(\omega)/\omega^2$, observed universally in Raman and neutron scattering. The maximum appears at a frequency at which the corresponding crystals still have only sound waves with a wavelength of the order of ten to twenty interatomic spacings. In glasses, the soft vibrational modes of the maximum coexist with sound waves of that wavelength. They are more numerous by 2 to 3 orders of magnitude than the tunneling states which dominate the properties below 1 K [Gil et al., 1993]. Consequently, differences in the excess specific heats are assumed to be due to variations in the magnitude of the excess VDOS. $g(\omega)$ is affected by the complex vibrational properties of a disordered topology and it has been shown that, in the low-frequency region, $g(\omega)$ has a maximum in a number of glasses. The boson peak is mainly due to the excess density of low-energy vibrational modes, and gives a low temperature excess specific heat [Bartolotta et al., 2001]. A better understanding of these modes is highly desirable, and a unified model is needed which would allow a low-temperature thermal properties of glasses to be described within a wide temperature range.

3.1.1.3 Theoretical model applying in metallic glasses

Low-temperature thermal properties are very important for understanding the nature and properties of low-energy excitations in glasses. The tunneling states observed below 1 K for the most cases are studied widely and systemically, especially in insulating glasses where the specific heat C_p is due to vibrational excitations. The situation in metallic glasses is not so simple because of the electronic degrees of freedom. Their contribution, however, can be separated in amorphous superconductors with high enough large transition temperature T_c . In such materials, at low temperature, electronic degrees of freedom freeze out and the remainder is due to vibrational excitations. According to the results of numerous experiments at low temperatures the vibrational contribution to the specific heat is virtually linear with the temperature T . This has been explained in the framework of the well-known model of two-level systems. At higher temperatures the situation becomes more complicated. Along with the contribution of conduction electrons there exists an extra temperature-dependent contribution which is natural to ascribe to common vibrational degrees of freedom [Gey et al., 1993]. Namely, the specific heat of both electrons and tunneling states are linear T -dependent at low temperature; it is difficult to distinguish the contributions to specific heat between electrons and tunneling states and to determine the density

of tunneling states in metallic glasses. Fortunately, there are some superconductive metallic glasses where the conduction electrons can be ignored and the tunneling states have been studied below the superconductive temperature in the metallic glasses [Graebner et al., 1977; Samwer et al., 1982; Surgers et al., 1989]. However, few investigations have been carried out on the tunneling states above the superconductive temperature except the investigation of electron-assisted tunneling states in CuZr and Zr-Ti-Ni-Cu-Be bulk metallic glasses reported by Tang et al. [Tang et al., 2005-a; Tang et al., 2005-b]. Tang et al. have successfully distinguished the tunneling states contribution to specific heat by calculating specific heat in the different temperature ranges, respectively, and they indicated that compared with insulating glasses, the electron-assisted tunneling states have much larger entropy and higher density in the metallic glass. Furthermore, the previous work involved mainly about the properties in the narrow temperature range (below 10 K). It is of significance to research the specific heat in a wide temperature range.

3.1.2 Transport Properties

In 1973, Mooij [Mooij, 1973] discovered an interesting correlation between the temperature coefficient of resistivity (TCR) and the resistivity of random metal alloys. Mooij found that metals with resistivities less than $\rho^* \simeq 150 \mu\Omega \text{ cm}$ tend to have the usual positive TCR while most alloys with resistivities exceeding ρ^* have anomalous negative TCRs. This correlation is quite universal, holding for both glassy and crystalline metals. Similar anomalies have been reported for the magnetoresistance and the thermopower.

Due to the limitation of amorphous materials development, previous studies on the low-temperature physical properties of amorphous materials were limited in the aspect of atomic structure of insulated materials. However, the investigation of low-temperature physical properties on amorphous materials has been extended into the electronic structure since the discovery of metallic glasses. Electrical transport properties were generally investigated based on the measurements of electrical resistivity, thermal potential, and Hall coefficient etc., amongst which electrical resistivity measurement was performed in this study.

The investigation of ρ for metallic glasses has been reported by several researchers [Maitrepierre, 1970; Boucher, 1972]. They found that the transport properties of metallic glasses were significantly different from their crystalline counterparts [Korn et al., 1972; Matsuda et al., 1984; Howson et al., 1988]. The magnitude of the electrical resistivity in amorphous state is generally to be 100-300 $\mu\Omega \text{ cm}$, which is 10-100 times greater than that in crystalline state. In

addition, the temperature coefficient of resistivity (TCR) defined as $\alpha = \frac{1}{\rho} \frac{d\rho}{dT}$ is rather small

and sometimes negative for some metallic glasses. And sometimes a minimum T_{\min} appears in the resistivity at low temperatures. The metallic glasses have higher concentration of conduction electrons up to 10^{22} cm^{-3} , and the electrical resistivity of metallic glasses is originated from the disordered structure due to the scattering of electrons. In general, metallic glasses exhibit complex electrical resistivity-temperature dependence, so a systematic study in this field can provide us valuable informations about the scattering of electron mechanism.

Several theories have been developed to explain the greater magnitude of the resistivity ρ and

the rather small or negative temperature coefficient of resistivity at high temperature ($\geq \theta_D$, the Debye temperature) as well as low temperature ($\leq \theta_D$) [Mizutani, 1983]: Faber-Ziman scattering of electron model, Mott s-d scattering of electron model, two-level systems model etc. which will be introduced in detail as follow:

1. Faber-Ziman scattering of electron model

One of the early theories, proposed by Faber and Ziman in 1965 [Faber et al., 1965], was based on the assumptions that the glass is composed of rigidly fixed ions (nuclei and core electrons) with a nearly free electron gas consisting of valence electrons, and that each ion interacts with the conduction electrons through a localized pseudopotential. Unfortunately, actual resistivity measurements revealed that this assumption of electrons scattering elastically with ions was inadequate. As a result, a ‘generalized’ Faber-Ziman theory was constructed which incorporates electron-phonon interactions into the original theory [Mizutani, 1983].

According to the generalized Faber-Ziman theory [Mizutani, 1983], the resistivity, ρ , may be expressed by the following equation:

$$\rho = (\rho_0 + \Delta\rho) \exp[-2W(T)] \quad (3-1)$$

where ρ_0 is the residual resistivity at 0 K, $\Delta\rho$ the contribution due to inelastic electron-phonon interaction, and the exponential term is the Debye-Waller factor. At low temperatures, $T \geq 20$ K, expansion of the Debye-Waller factor yields

$$\frac{\rho}{\rho_0} = 1 - \beta T^2 \quad (3-2)$$

This temperature dependence of ρ is characteristic of metallic glasses with sp electrons at the Fermi energy level, E_F . Moreover, it is assumed to be due to the interaction of the sp conduction electrons with the lattice vibrations.

The temperature dependence of the resistivity in the Faber-Ziman model comes from the temperature dependence of the structure factor. For amorphous alloys containing transition metal at E_F (in this study), a strong s-d scattering results in $K_F l \cong l$, K_F being the Fermi vector and l the mean free path of the electrons. In this situation, the generalized Faber-Ziman theory is not adequate and multiple scattering events become important, giving rise to weak localization or quantum interference effects [Gupta, et al., 2001], and the d-electron contribution to the scattering mechanism needs to be considered.

It has been proposed by Mizutani [Mizutani, 1985] that this unique temperature dependence of the resistivity (for the glasses which contain a number of d electrons at the Fermi energy level, E_F) in the range 30-300 K is given by the following empirical equation:

$$\frac{\rho}{\rho_{300}} = A + B \exp\left(\frac{-T}{\Delta}\right) \quad (3-3)$$

where A , B and Δ are the fitting parameters. The characteristic temperature, Δ , was found to be related to the Debye temperature, θ_D , and the parameter B to be consistent with the electronic specific heat coefficient, γ by Dikeakos et al. [Dikeakos et al., 1999].

The temperature dependence of the electrical resistivity arises from the interaction of conduction electrons with lattice vibrations. At low temperature (< 30 K), superconductivity and quantum interference effects come into play.

2. Mott s-d electron scattering model [Mott, 1964; Mott, 1972]

S-d electron scattering model was proposed by Mott to interpret the electrical transport properties of transition metal containing alloys. The electronic structure of transition metals contains d band which is not fully filled with electrons as well as s band outside of d band, and superposition occurring between d and s bands. As we know, d band shows high density of states as well as unhomogeneous distribution; s band, however, is in the contrary. Moreover, both d and s bands are unfilled, and the spacing of d band is smaller than that of s band and voids are in it. Mott model was constructed based on this two bands model which supposed that two different characteristic of electrons, sp band electrons and d band electrons, coexisted at Fermi surface. The electrical resistivity of transition metals is attributed to two contributions: sp band contribution and d band contribution. It is generally believed that the effective mass of d electrons is too large to conduct electricity efficiently, so carriers are mainly acting as by sp band electrons. The Mott s-d electron scattering model was constructed based on the following assumption: when the mean free path of the electrons is short enough comparable to the interatomic separation, the resistance is mainly originated from the d voids contribution to the scattering of sp electrons. The number of d voids is proportional to the density of states near the Fermi surface, the electrical conductivity can be expressed by the equation $\sigma \approx \sigma_s \propto N_s(E_F) / N_d(E_F)$.

Mott s-d electron scattering model provides a simple explanation for Mooij correlation. For the transition metals which have large electrical resistivity, s-d electron scattering plays an important role, and Fermi energy level will move and broaden with increase in temperature, finally leading to the decrease of electrical resistivity. The resistivity-temperature dependence can be expressed by equation:

$$\rho_{s-d}(T) = \rho_0 \left[1 - \frac{\pi^2}{6} (k_B T)^2 (E_0 - E_F)^{-2} \right] \equiv \rho_0 (1 - cT^2) \quad (3-4)$$

where $-T^2$ is negative term, ρ_0 is the residual resistivity, E_0 is top energy level.

Mott s-d electron scattering model was applied in crystalline transition metals and alloys during the early time, later one found that this model was also available in amorphous metals and alloys containing transition metals.

3. Two-level systems model

Two-level system scattering is originated from structure factor. The existence of two-level system scattering is evidenced in the measurements of low-temperature specific heat which has been mentioned in the above section, thermal conductivity and ultrasonic on metallic glasses as well as insulating glasses [Phillips, 1972; Anderson et al., 1972]. Two-level system scattering is a typical excitation in glasses, and it generally correlates with large atomic volume. In amorphous materials, some atoms or group of atoms may possess two local energy minima which can be regarded as double-well potential due to the disordered structure of amorphous materials, some atoms or electrons can tunnel through the two energy minima barriers, resulting in the change of energy level. In the two-level systems, atoms possess a high degree of unharmonic vibration states and can emit as well as absorb phonons, leading to the occurrence of low-temperature low-energy excitation. Based on this TLS electron scattering model, the electrical resistivity is given by equation:

$$\rho(T) = -c \ln(k_B^2 T^2 + \Delta^2) \quad (3-6)$$

where c is a constant with a magnitude of 0.1; Δ represents the difference between two energy minima of double-well potential. Theoretically, Δ is limited within the energy corresponding to 1 K.

Cochrane et al. [R.W. Cochrane et al., 1975] found that two-level systems were similar with the spin orientation of the Kondo effect, and supposed that the low-temperature resistivity minima observed in magnetic or nonmagnetic metallic glasses may arise from the two-level systems scattering to the quasi Kondo effect. Tsuei et al. [Tsuei, 1978] developed two-level systems scattering model (structural Kondo model) to a wide temperature range, and interpreted the negative temperature coefficient of resistivity of metallic glasses. The total electrical resistivity can be expressed as:

$$\rho(T) = a + b\rho_N(T) - c \ln(k_B^2 T^2 + \Delta^2) \quad (3-7)$$

where a , b and c are constants, $\rho_N(T)$ represents the general electron-phonon term. However, fitting the experimental data with this equation brings a large value of Δ which equals the energy corresponding to 30-60 K, and fails to give a theoretic explanation. By studying the ultrasonic and specific heat, some researches reported that the contribution of two-level systems on the resistance may be undetectable due to its rather low value [Black et al., 1978; Vladár et al., 1982].

The motion of electrons in disordered systems is one of the most fundamental problems in solid state physics. Both theoretical and experimental studies of the low temperature behavior of electrical resistivity of disordered electronic systems have led to quantum corrections to the Boltzmann contribution. It has been shown that the diffusive motion of electrons in two-dimensional as well as in three-dimensional disordered systems entails quantum corrections to the electrical resistivity and the magnetoresistivity. There are two principal sources of quantum corrections, arising from weak localization and the Coulomb interaction. Both of these corrections are important when the mean free path becomes short so that electron propagation between scattering events is no longer free-electron-like but diffusive. At low enough temperatures, where the elastic scattering time is a few orders of magnitude shorter than the inelastic scattering time, the quantum corrections arising from the interference of the electronic partial waves are very important. It has been shown that constructive interference of the electronic waves can only be expected in a back-scattering geometry. This quantum interference effect will produce an increase of the sample resistivity. The magnitude of this additional contribution at given temperature is reduced by the presence of the inelastic electron-phonon, spin-orbit or spin-flip scattering, since they destroy the constructive interference [Kokanović, 2006].

3.1.3 Motivation

In this study, we performed the low-temperature specific heat and electrical resistivity measurements in a wide temperature range from ambient temperature down to 4.2 K on the representative Ti-based $\text{Ti}_{41.5}\text{Cu}_{37.5}\text{Ni}_{7.5}\text{Zr}_{2.5}\text{Hf}_5\text{Sn}_5\text{Si}_1$ bulk metallic glass which is nonmagnetic and nonsuperconductive within the experimental temperature range. The main purposes of this study can be stated as follows: (i) observation of the low-temperature anomaly in such BMGs; (ii) explanation of these abnormal phenomena within the framework of existing classical theoretical model; (iii) try to correlate these anomalies with fragility and GFA.

The deviation of specific heat-temperature dependence from Debye dependence, a broad hump

in C_p/T^3 vs. T , the large magnitude of resistivity and the negative temperature coefficient of resistivity, were successfully observed in our measurements, which confirm the universality of the low-temperature thermal and electrical transport properties of glasses. The abnormal thermal properties were explained by the recently developed soft potential model (SPM), in the frames of which, supposing a coexistence of acoustic phonons with electrons, soft (low-frequency) localized harmonic oscillators modes and describing low-energy excitations, and it can fit well with the experimental data in a wide low-temperature range. On the other hand, the abnormal electrical resistivity was interpreted by applying the ‘generalized’ Faber-Ziman theory.

3.2 Experiment

The rod samples in diameter of 2 mm used for measurement of the physical properties (specific heat, electrical resistivity) were cut into proper dimensions. The specific heat and resistivity measurements were performed in a wide temperature range, $4.2 \text{ K} < T < 300 \text{ K}$, with a highly sensitive DC-current method using a four probes technique in the Institut Néel in Grenoble, France. The transport measurements were carried out in resistance ranges from a few $\mu\Omega$ to a few $\text{m}\Omega$ and the voltage across the junction was of the order of a nanovolt. The sample exhibits nonmagnetic property in the temperature range.

3.3 Results and Discussion

3.3.1 Specific Heat at Low Temperature

The temperature-dependent specific heat, C_p , of the $\text{Ti}_{41.5}\text{Cu}_{37.5}\text{Ni}_{7.5}\text{Zr}_{2.5}\text{Hf}_5\text{Sn}_5\text{Si}_1$ bulk metallic glass in the temperature range from 4.2 to 100 K is shown in [Fig. 3-1](#), and it can be seen that the temperature-dependence specific heat of this metallic glass is similar with that of other amorphous materials [[Mizutani et al., 1978](#); [Gil, et al., 1993](#); [Gey et al., 1993](#); [Tang et al., 2005-a](#); [Tang et al., 2005-b](#); [S.N. Zhang et al., 2009](#); [Amakai et al., 2007](#); [Salamatov, 1996](#); [Jäckel et al., 2002](#); [Astrath et al., 2006](#); [Ramos et al., 2002](#); [Talón et al., 2000](#); [Zhou et al., 2006](#); [H.Y. Bai et al., 2001](#); [H.Y. Bai et al., 2002](#); [Terziyska et al., 2009](#)].

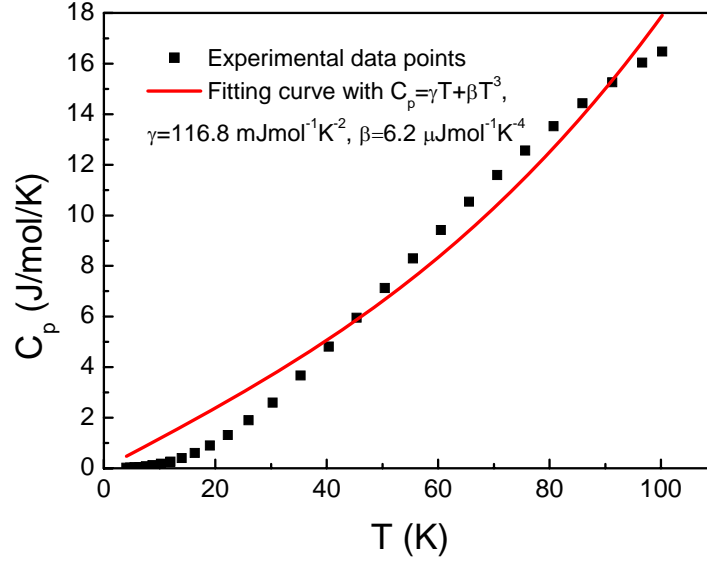


Fig. 3-1 The specific heat C_p of $\text{Ti}_{41.5}\text{Cu}_{37.5}\text{Ni}_{7.5}\text{Zr}_{2.5}\text{Hf}_5\text{Sn}_5\text{Si}_1$ alloy in the temperature range from 4.2 to 100 K. The solid line is a fitting of the specific heat data based on $C_p = \gamma T + \beta T^3$

For the metallic glass, we must consider its long-range disordered atomic structure and large quantity of free electrons that may affect its specific heat. It is well known that, similar with other solids, the low-temperature specific heat of amorphous solids consists of electron, phonon and low-energy excitation contributions, which can be expressed as

$$C_p = C_{\text{Electron}} + C_{\text{Phonon}} + C_{\text{Excitation}} \quad (3-8)$$

where C_{Electron} , C_{Phonon} and $C_{\text{Excitation}}$ represent the contributions of electrons, phonons and low-energy excitations (arising from magnetism, superconductor, etc.) to the specific heat, respectively. As we know, the metallic glass studied in this work is nonmagnetic, and no superconductivity occurs within the experimental temperature range of 4.2-100 K, so the contributions of low-energy excitations arising from magnetism, superconductor to C_p should not be taken into consideration. To our knowledge, the low-energy excitation, tunneling states effects (two-level systems effects), generally come out below 1 K for amorphous solids; however, in regard to metallic glass, the tunneling states effects maybe can be observed at even higher temperature (but below several Kelvin). Accordingly, the contributions to the low-temperature specific heat for the metallic glass are dependent on different temperature ranges. Therefore, at extremely low temperature, C_p is the sum of three terms: electronic specific heat C_{Electron} , phonon specific heat C_{Phonon} and the contribution of tunneling states to specific heat C_{TS} , which can be expressed as

$$C_p = C_{\text{Electron}} + C_{\text{Phonon}} + C_{\text{TS}} \quad (3-9)$$

while at higher temperature, only electron and phonon contribute to specific heat, which can be expressed as

$$C_p = C_{\text{Electron}} + C_{\text{Phonon}} \quad (3-10)$$

So, the analysis of low-temperature specific heat of metallic glass should be focused on: (i) distinguish the contributions of tunneling states and electrons at the extremely low temperature

below several Kelvin for the same linear temperature dependence, (ii) determine the electron and phonon contributions to the specific heat correctly in the moderately low temperature, (iii) construct a theoretical model to describe the low-temperature specific heat of metallic glass in a wide temperature range. In the following study, we first calculate the electron and phonon contributions to the specific heat by fitting the moderately low temperature specific heat, then try to find the contributions of tunneling states at extremely-low temperature, finally discuss a theoretical model used for describing the specific heat within a broad temperature range.

3.3.1.1 Electron and phonon contributions to specific heats

Numerous experiments reveal that at low temperatures the vibrational contribution to the specific heat is virtually linear T -dependent [Löhneysen, 1981]. It means that the specific heat of both electrons and tunneling states are linear T -dependent, therefore the linear term in specific heat at extremely low temperature originates from two contributions, tunneling states and electronic contributions, which makes the situation more complicated. Especially for metallic glass, the research on the electron-assisted tunneling states above the superconductor transition temperature is significant. So, to determine the contribution of tunneling states to specific heat of metallic glass, the principal work we should do is to distinguish the contributions between tunneling states and electrons.

It is well known that the low-temperature specific heat of amorphous materials can be generally fitted by the expression:

$$C_p = \gamma T + \beta T^3 \quad (3-11)$$

where the parameters γ and β are the coefficients corresponding to electron and phonon contributions to the specific heat, respectively, and the first term represents C_{Electron} and the second term stands for C_{Phonon} based on Debye model, at extremely low temperature, the specific heat can be fitted by the expression as

$$C_p = \gamma_{TS} T + \gamma_{\text{Electron}} T + \beta T^3 \quad (3-12)$$

The tunneling states contribute weakly to specific heat near 10 K [Anderson et al., 1972; Phillips, 1972], so we can determine the electron and phonon contributions to specific heat near 10 K by least-square fitting the experimental specific heat data with $C_p = \gamma T + \beta T^3$. Traditionally,

we fit the specific heat experimental data with the $C_p / T = \gamma + \beta T^2$ by using a least-square linear fit method, to determine the electronic and phonon specific heat coefficients. The γ (the value of intercept on the axis of ordinates) can be simply obtained to extrapolate the fitting curve to 0 K, and the β can be derived from the slope of $C_p/T-T^2$ curve.

In Fig. 3-2 (a) and (b), the specific heat of $\text{Ti}_{41.5}\text{Cu}_{37.5}\text{Ni}_{7.5}\text{Zr}_{2.5}\text{Hf}_5\text{Sn}_5\text{Si}_1$ BMG in the temperature range of 4-15 K are displayed both in C_p versus T and a typical C_p/T versus T^2 plots. The solid lines in Fig. 3-2 (a) and (b) are the corresponding fitting curves obtained based on the $C_p = \gamma T + \beta T^3$ expression. It is clear that the specific heat of this metallic glass in the temperature range of 4-15 K is well fitted by the expression $C_p = \gamma T + \beta T^3$ with $\gamma=3.51\text{-}3.58$

$\text{mJ mol}^{-1} \text{K}^{-2}$ and $\beta=130.0 \text{ } \mu\text{J mol}^{-1} \text{K}^{-4}$ values, the uncertainties are $\Delta\gamma=\pm 0.13 \text{ mJ mol}^{-1} \text{K}^{-2}$, $\Delta\beta=\pm 0.97 \text{ } \mu\text{J/mol K}^{-4}$. It should be noted that (i) the different values of γ parameter obtained from fitting curves of C_p versus T and C_p/T versus T^2 is ascribed from the calculation error, (ii) the typical expression, $C_p = \gamma T + \beta T^3$, can be only applied for fitting rather low-temperature specific heat, however, this is not available at higher temperature, as can be confirmed by the large deviation of the fitting curve from the experimental data in the temperature range of 4-100 K (see Fig. 3-1).

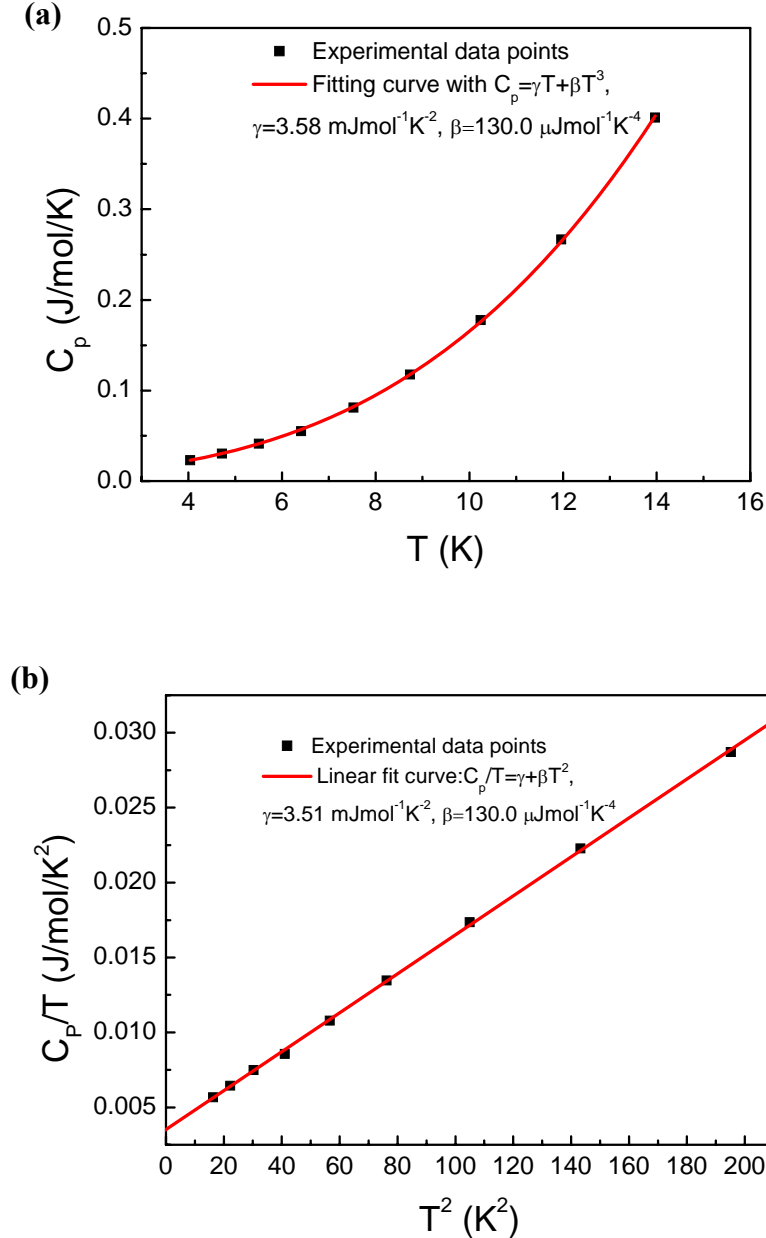


Fig. 3-2 Specific heat C_p of $\text{Ti}_{41.5}\text{Cu}_{37.5}\text{Ni}_{7.5}\text{Zr}_{2.5}\text{Hf}_5\text{Sn}_5\text{Si}_1$ BMG in the temperature range from 4 to 15 K, shown as (a) C_p vs. T and (b) C_p/T vs. T^2 , respectively. The solid lines are obtained from

fitting the specific heat data based on the typical expression $C_p = \gamma T + \beta T^3$

3.3.1.2 Tunneling states effects

Further observation was performed on the linear relationship of C_p/T versus T^2 in the temperature range of 4-15 K in Fig. 3-3, and more detailed information was obtained. The data points are well fitted in a $C_p/T = \gamma + \beta T^2$ form with $\gamma^A = 3.42 \text{ mJ mol}^{-1} \text{ K}^{-2}$, and $\beta^A = 130.6 \text{ } \mu\text{J mol}^{-1} \text{ K}^{-4}$ over a wider temperature range, $30 \text{ K}^2 < T^2 < 195 \text{ K}^2$ (see the fitting curve marked A in Fig. 3-3), while in the lower temperature range $16 \text{ K}^2 < T^2 < 30 \text{ K}^2$, the data points are a little deviated from the fitting curve A obtained above and also well fitted in the same polynomial form, but with different parameters, $\gamma^B = 3.83 \text{ mJ mol}^{-1} \text{ K}^{-2}$, $\beta^B = 117.1 \text{ } \mu\text{J mol}^{-1} \text{ K}^{-4}$ (see the fitting curve marked B). So, at temperature below $T^2 \approx 30 \text{ K}^2$, like other BMGs [Mizutani et al., 1978; Tang et al., 2005-a; Tang et al., 2005-b], a clear positive deviation from the straight line A is evident. We can define this deviation as an “excess” specific heat ΔC_p , which could be ascribed to the ferromagnetic impurity contributions [Chen, et al., 1972] or the glassy-state effects (tunneling states effects or two-level system effects) [Zeller et al., 1971]. We believe that in the present case such an anomaly is attributed to the glassy-state effects in the BMG. However, the common phenomenon in BMGs has not been paid much attention before. It should be pointed out that the tunneling states effects occur at higher temperature for metallic glasses compared with that for other amorphous solids which exhibit the tunneling states effects at temperature below 1 or 2 K, as also provides us an opportunity to study it even under the liquid He temperature 4.2 K.

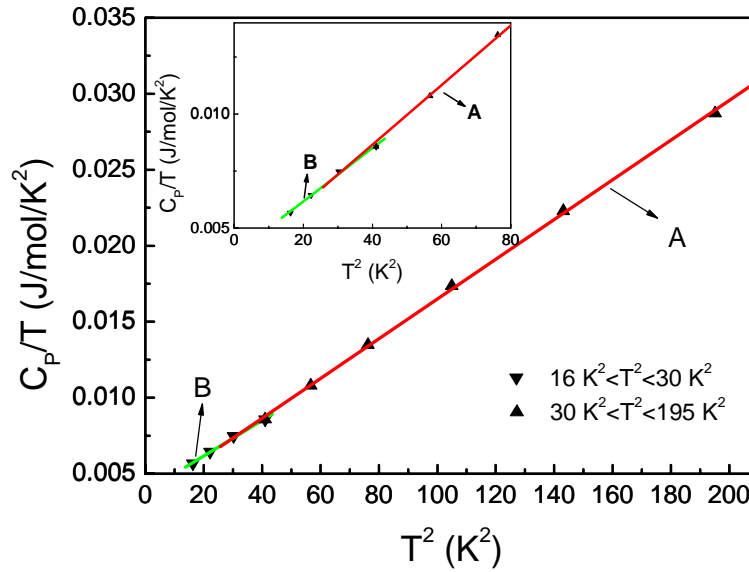


Fig. 3-3 The specific heat C_p of $\text{Ti}_{41.5}\text{Cu}_{37.5}\text{Ni}_{7.5}\text{Zr}_{2.5}\text{Hf}_5\text{Sn}_5\text{Si}_1$ BMG in the temperature range from 4 to 15 K, shown as C_p/T vs. T^2 , the solid lines are obtained from fitting the specific heat data based on the expression $C_p/T = \gamma + \beta T^2$. Inset showing the enlarged image when $T^2 < 80 \text{ K}^2$

The “excess” specific heat ΔC_p can be obtained from the expression as

$$\Delta C_p = C_p - \gamma^A T - \beta^A T^3 \quad (3-13)$$

It means that the ΔC_p can be obtained by subtracting the contributions of electrons and phonons to

the specific heat which are determined based on $C_p = \gamma T + \beta T^3$ expression using the specific heat coefficients of γ^A and β^A at temperatures below $T^2 \approx 30$ K from the experimental specific heat C_p . The obtained excess specific heat, ΔC_p , should be corresponding to the contribution of the tunneling states. The calculated data points of ΔC_p are shown in Fig. 3-4 (a) and (b) as ΔC_p - T and $\Delta C_p/T$ - T forms, respectively.

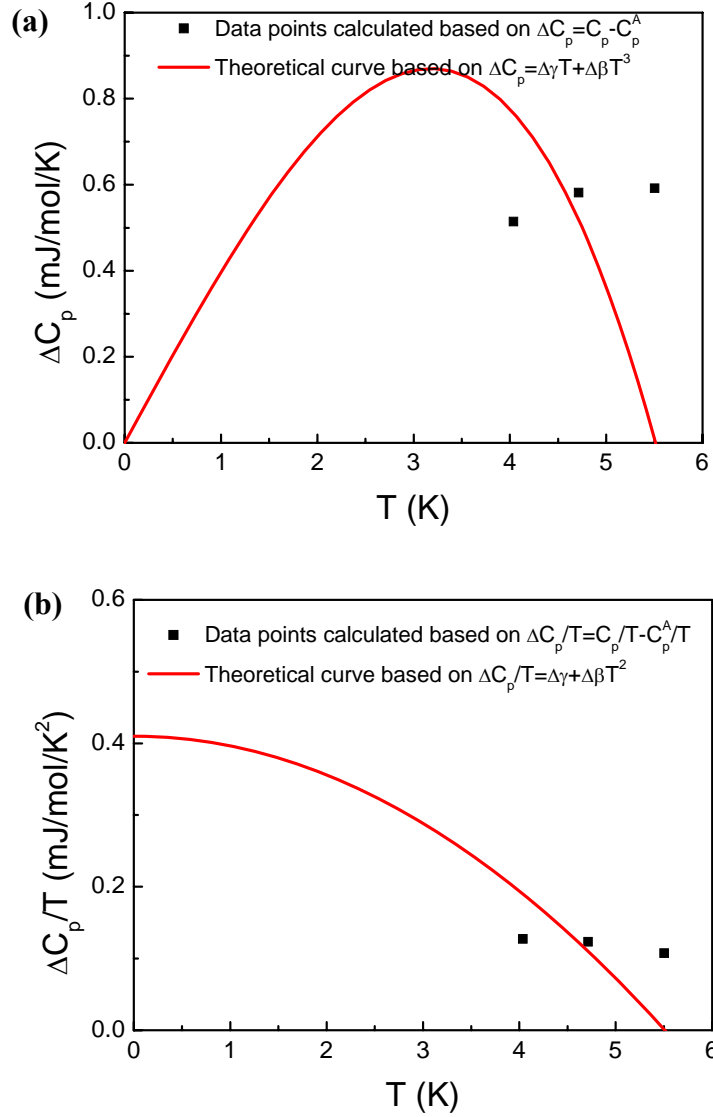


Fig. 3-4 The excess specific heat of Ti_{41.5}Cu_{37.5}Ni_{7.5}Zr_{2.5}Hf₅Sn₅Si₁ BMG is shown as (a) ΔC_p vs. T and (b) $\Delta C_p/T$ vs. T . The solid lines are the theoretical curves calculated based on expression the

$$\Delta C_p = \Delta\gamma T + \Delta\beta T^3$$

Unfortunately, the lowest temperature performed in this study is 4.2 K, which is relatively too high for researching the tunneling states. However, we can evaluate the ΔC_p dependent on T at extremely low temperature down to 0 K through an obtained theoretical prediction curve under the condition of neglecting the difference between the real value and theoretical value around the intersection of two linear fitting curves, A and B , in the linear C_p/T - T^2 dependent curves. The theoretical prediction value of ΔC_p can be obtained based on the typical expression:

$$\Delta C_p = C_p^B - C_p^A = \Delta\gamma T + \Delta\beta T^3 \quad (3-14)$$

where $\Delta\gamma = \gamma^B - \gamma^A$, $\Delta\beta = \beta^B - \beta^A$. In Fig. 3-4 (a) and (b), the solid lines correspond to the evaluation results. We found the difference between the data points calculated based on $\Delta C_p = C_p - \gamma^A T - \beta^A T^3$ and the theoretical predicted curve obtained based on $\Delta C_p = C_p^B - C_p^A = \Delta\gamma T + \Delta\beta T^3$, which is due to the deviation of C_p^B from C_p around the intersection temperature mentioned above. Although the specific heat at even lower temperature than 4.2 K can not be obtained within the restriction of our experimental condition; thanks to the theoretical evaluation, we can get more information about the tunneling states under the extremely low temperature. In addition, the predicted value further approaches the experimental value with decrease in the temperature range down to the absolute 0 K. It should be pointed out that although numerous experiments confirm the linear relationship between the contribution of tunneling states to specific heat C_{TS} and T , namely, $C_{TS} = \gamma_{TS} T$, in our calculation, we adopt

$\Delta C_p = C_p^B - C_p^A = \Delta\gamma T + \Delta\beta T^3$ expression to evaluate the value of ΔC_p just for enhancing the precision; in addition, the value of $\Delta\beta T^3$ term is far too small compared with that of $\Delta\gamma T$ term at extremely low temperature, and with decrease in temperature, the value of $\Delta\beta T^3$ decreases much more rapidly than that of $\Delta\gamma T$ term. So in fact, the value of ΔC_p is mainly dependent on $\Delta\gamma T$ term, which is in accordance with the experimental results which show the linear relationship of C_{TS} vs. T at extremely low temperature. In fact, according to the excess specific heat research for BMGs, we found that the $\Delta C_p/T$ vs. T relation exhibits a parabola characteristic, which indicates the existence of T^2 term, so in the ΔC_p vs. T relation, there exists a T^3 term, as can be confirmed the contribution of phonon to the excess specific heat, especially at higher temperature, several Kelvin, and at the temperature below 1 K, it approximately exhibits a linear ΔC_p vs. T relationship because the contribution of βT^3 term is negligible.

The entropy of the tunneling states is $1.51 \text{ mJ mol}^{-1} \text{ K}^{-1}$ for $\text{Ti}_{41.5}\text{Cu}_{37.5}\text{Ni}_{7.5}\text{Zr}_{2.5}\text{Hf}_5\text{Sn}_5\text{Si}_1$ BMG calculated by $\Delta S = \int_0^{T_{\max}} (\Delta C/T) dT$. Because the problem of the tunneling states is in analogy with that of spin- $\frac{1}{2}$ particles in a magnetic field [Phillips, 1987], the total entropy of the tunneling states can be calculated by $\Delta S = n \cdot R \ln 2$, here n (the density of tunneling states per atom) is constant, and R is the gas constant. So n is calculated to be 2.62×10^{-4} for this BMG. It means that there are 2.62×10^{-4} mol atoms (or groups of atoms) per mole atoms of the BMG in tunneling states.

The tunneling states model (two-levels system model) has been proposed to explain this specific heat anomaly at extremely low temperature. A linear contribution of tunneling states to specific heat is expressed as [Phillips, 1987]

$$C_{TS} = \frac{\pi^2}{6} n_0 k_B^2 T = \gamma_{TS} T \quad (3-15)$$

where $n_0 = n(E)$ is a constant state density. All amorphous substances have approximately the

same density of states of tunneling defects, i.e., the values of γ_{TS} have approximately the same order of magnitude for different amorphous materials. Typically, γ_{TS} is between 10^{-1} – 10^{-2} mJ mol⁻¹ K⁻² and n_0 is about 0.02-0.09 (eV atom)⁻¹. Graebner et al. [Graebner et al., 1977] published the first evidence for a linear specific heat anomaly in a metallic glass of the superconducting Zr_{0.7}Pd_{0.3} with $\gamma_{TS}=1.0 \times 10^{-1}$ mJ mol⁻¹ K⁻², which is very similar to that found in insulating glasses. For Ti_{41.5}Cu_{37.5}Ni_{7.5}Zr_{2.5}Hf₅Sn₅Si₁ BMG, the former research on the contribution of tunneling states to specific heat reveals that the γ_{TS} value is approximately 0.4 mJ mol⁻¹ K⁻² or even smaller, it is estimated that γ_{TS}/γ is about 10%, here, γ is the coefficient of linear specific heat term of the BMG. Therefore, specific heat anomaly from the tunneling effect is only a minor part of the linear term, and electronic contribution dominates the linear specific heat of the BMG. We found that the value of γ_{TS}/γ is larger for this metallic glass than that of other amorphous materials, which is maybe the reason why the obvious tunneling states can be observed at higher temperature, however not for other amorphous materials. By subtracting the part of the tunneling effect, the state density for the BMG is derived to be 1.45 (eV atom)⁻¹.

The above analysis confirms the existence of tunneling states effects at several Kelvin for BMGs. Tang et al. [Tang et al., 2005-a] and Bai et al. [H.Y. Bai et al., 2001] also reported such a conclusion by low-temperature specific heat study on Cu₅₀Zr₅₀ and Vit 1 BMGs, respectively. Especially, Tang et al proved this result by the investigation of low-temperature electrical resistivity. So in the following study, we try to further prove the existence of tunneling states effects at several Kelvin for BMGs by the analysis of electrical resistivity in the low temperature range of 5-30 K. Theoretically, when the temperature is below about 10 K, the electrical resistivity of alloys should mainly be attributed to the residual resistivity and be close to a constant. The resistivity for BMGs, however, increases slowly with decreasing temperature below around 22 K, as is shown in Fig. 3-5. The T -dependent resistivity can be well explained by the Kondo model [R.W. Cochrane et al., 1975]

$$\rho(T) = \rho_0 + A \cdot \rho_N(T) - \lambda \cdot \ln(T^2 + \Delta^2) \quad (3-16)$$

where ρ_0 , A , λ , and Δ are constants, $\rho_N(T)$ is the regular electron-phonon term which is also close to zero at low temperature. The fitting curve based on Kondo model with the fitting parameters of $\rho_0 + A \cdot \rho_N(T) = 268.3$ $\mu\Omega \cdot \text{cm}$, $\lambda = 0.025$, $\Delta = 0.00004$ is shown in Fig. 3-5. It is obvious that the resistivity of this BMG above 15 K, deviates from the Kondo model, which is maybe ascribed from the atoms (or clusters of atoms) assisted tunneling states effects between two sides of a double well potential in the BMG. The analysis of the resistivity reveals the existence of the tunneling states effects in the BMG at the temperature below several Kelvin. It should be pointed out that the tunneling states effects are responsible for the deviation phenomena from the Kondo model; however, the tunneling states effects are not so obvious at the temperature of several

Kelvin, which is believed to be more obvious at the even lower temperature compared with our experimental minimum temperature, as is in accordance with the research results of low-temperature specific heat.

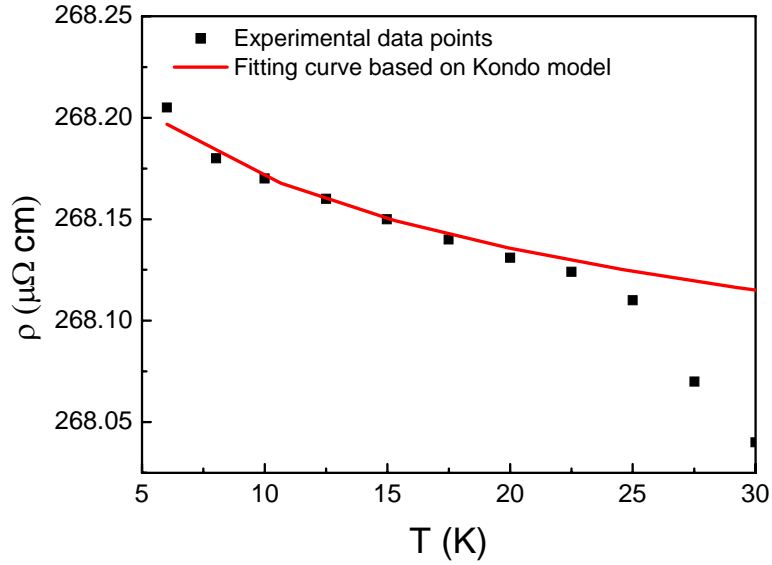


Fig. 3-5 The electrical resistivity of the $\text{Ti}_{41.5}\text{Cu}_{37.5}\text{Ni}_{7.5}\text{Zr}_{2.5}\text{Hf}_5\text{Sn}_5\text{Si}_1$ BMG in the temperature range of 5-30 K. The solid line is the least-squares fitting result by the Kondo model

In summary, the tunneling states effects in bulk metallic glasses were confirmed to be observed below several Kelvin by studying the low-temperature specific heat as well as electrical resistivity, as is significantly different from that in insulating glasses which generally occurs below 1 K. In addition, the density of tunneling states of this BMG at several Kelvin is about 2.62×10^{-4} which is much higher than that of superconductive metallic glasses which is about 10^{-6} order per atom [Tang et al., 2005-a] similar to many insulating glasses, as indicated the large difference of density of tunneling states under the different condition of with and without large quantity of conduction electrons. The high density of tunneling states may be due to the conduction electron-assisted tunneling, as is required by the electrons' dephasing quantum theory [Aleiner et al., 2001].

3.3.1.3 Anomalous Boson peak

Low-temperature anomalies, which were found to be universal for different kinds of glasses, are still a puzzle in the physics of condensed matter. First, they show up at very low temperatures as an anharmonic contribution, producing a linear term in specific heat C_p . Then, at higher temperatures, the so-called excess vibrational contribution appears as a hump in C_p/T^3 . The above investigation was focused on the specific heat in the extremely low temperature range, and the electron-assisted tunneling at several Kelvin was found and studied. In the following study, we focus on the specific heat at rather high temperature in a wide temperature range.

The low-temperature specific heat of $\text{Ti}_{41.5}\text{Cu}_{37.5}\text{Ni}_{7.5}\text{Zr}_{2.5}\text{Hf}_5\text{Sn}_5\text{Si}_1$ BMG from 4.2 to 100 K is shown as C_p/T^3 vs. T in logarithmic scale in Fig. 3-6. As can be seen, the low-temperature data exhibits the usual glassy behavior, however, with a hardly pronounced hump (Boson peak) in C_p/T^3 vs. T plot. According to the expression: $C_p = C_{\text{Electron}} + C_{\text{Phonon}}$, C_{Phonon} is determined by subtracting C_{Electron} ($\gamma = 3.51 \text{ mJ mol}^{-1} \text{ K}^{-2}$ which is determined by fitting the specific heat at low

temperature in Fig. 3-2) from the measured C_p . Fig. 3-7 shows the phonon specific heat C_{Phonon} as well as C_{Phonon}/T^3 plotted as a function of temperature in the range of $4.2 \text{ K} \leq T \leq 100 \text{ K}$. The solid line in Fig. 3-7 is obtained by fitting the phonon specific heat with the aid of the Debye model in the form of

$$\frac{C_{\text{Phonon}}(T)}{3R} = n_D F_D\left(\frac{\theta_D}{T}\right) \quad (3-17)$$

where θ_D is Debye temperature, n_D is a dimensionless constant (usually $n_D = 1$ in solids) and stands for Debye oscillator strength, R is the gas constant, and $F_D\left(\frac{\theta_D}{T}\right)$ is the Debye function defined as

$$F_D(x) = 3\left(\frac{1}{x}\right)^3 \int_0^x \frac{\xi^4 e^\xi}{(e^\xi - 1)^2} d\xi \quad (3-18)$$

The fitting curve gives the parameters of $\theta_D = 279 \text{ K}$ and $n_D = 0.911$. It can be seen from the $C_{\text{Phonon}}-T$ plot that the experimental data of the specific heat are well fitted by the Debye model at low enough temperatures ($4.2 \text{ K} < T < 10 \text{ K}$) and higher temperatures $T > 45 \text{ K}$, however they are not well fitted in the temperature range of 10 to 45 K which shows higher values than the fitted curve, and indicates that the specific heat of BMGs in a wide temperature range cannot be well fitted only by this simplest law Debye model, it cannot quantitatively explain the experimental phonon specific heat data enough in the intermediate temperature range (10-45 K), which suggests the existence of other kinds of vibrational contributions. Different results were obtained by plotting C_{Phonon}/T^3-T curve (Fig. 3-7 (b)), the measured C_{Phonon}/T^3 derived from the fitting curve based on Debye theory not only in the temperature range of 10-45 K but also at temperatures below 10 K, in other words, the phonon specific heat of this BMG calculated based on Debye model is always lower than measured values of C_{Phonon} in the lower temperature range $< 45 \text{ K}$, this excess specific heat is ascribed to the low-energy vibrations which are hard to be explained within the Debye model; based on the Debye model, the value of C_{Phonon}/T^3 should be approximately a constant, however, instead of a constant, a pronounced hump feature centered at $\sim 10 \text{ K}$ emerged; besides that an obvious inflexion was found at temperature around 6 K from which the value of C_{Phonon}/T^3 increases again with decrease in temperature, indicating another contribution to excess specific heat, and is well in accordance with the above study on tunneling states effect at temperature below 6 K.

According to the analysis above, the excess specific heat can be separated into two parts and should arise from some low-frequency vibrations. The first one is at lower temperature below 6 K arising from the tunneling states effects which has been investigated in the last section; the second one is at higher temperature with a feature of broad hump. It is reasonable to think that the broad hump in specific heat around 10 K indicating extra modes corresponds to the boson peak. As in many oxide glasses [Courten et al., 2001] or organic glasses [Ramos et al., 2003], the observed humps similar to our results correspond to the boson-peak contribution. So far, there is a current debate on the possible explanation for the excitation that gives rise to the so called boson peak, since disordered systems, such as glasses, in principle do not allow to derive a quasiparticle and its excitation spectrum. Recent studies revealed that such an excess specific heat is believed to be due to the contribution of Einstein oscillators. An additional quantized Einstein oscillator is required to model the specific heat of the BMG in the wide temperature range.

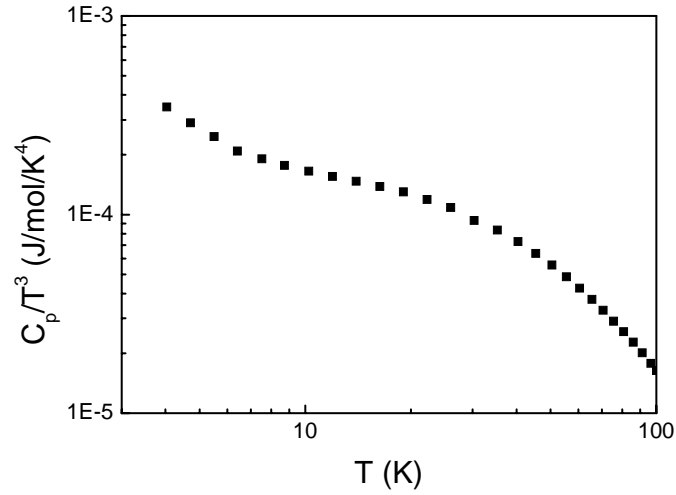


Fig. 3-6 The specific heat of $\text{Ti}_{41.5}\text{Cu}_{37.5}\text{Ni}_{7.5}\text{Zr}_{2.5}\text{Hf}_5\text{Sn}_5\text{Si}_1$ BMG in the temperature range from 4.2 to 100 K plotted as C_p/T^3 vs. T

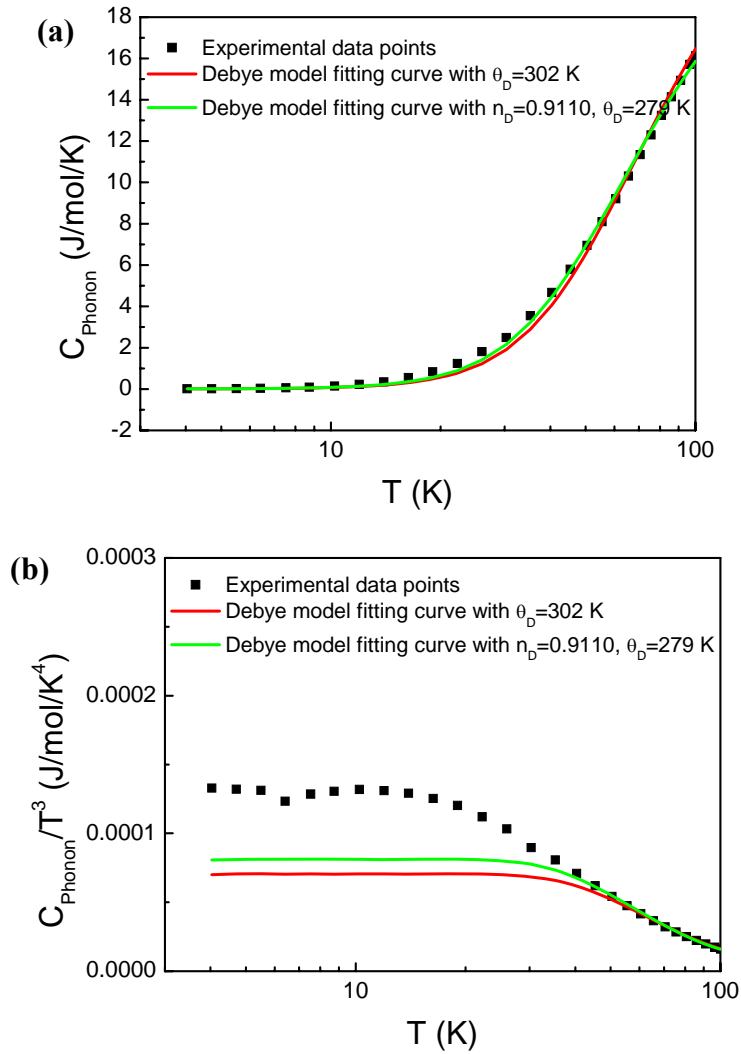


Fig. 3-7 The phonon specific heat C_{Phonon} of $\text{Ti}_{41.5}\text{Cu}_{37.5}\text{Ni}_{7.5}\text{Zr}_{2.5}\text{Hf}_5\text{Sn}_5\text{Si}_1$ BMG in the temperature range from 4.2 to 100 K, shown as (a) C_{Phonon} vs. T and (b) C_{Phonon}/T^3 vs. T . The solid lines are the fitting curves based on Debye model

It is worth further investigating the excess specific heat; however, it is not clear how to do a quantitative comparison in the systems with different chemical composition. One of the ways is the scaling of all parameters with the values expected in the Debye model. If the substances would differ only by density and elastic constant (sound velocities), then after scaling with the Debye values, they should show a similar behavior. The specific heat scaled by the calculated specific heat based on Debye model, C_p/C_{Deb} as well as C_{Phonon}/C_{Deb} , versus temperature for $Ti_{41.5}Cu_{37.5}Ni_{7.5}Zr_{2.5}Hf_5Sn_5Si_1$ BMG are shown in Fig. 3-8. For the effect of the linear term in specific heat, mainly originated from the electronic contribution, no hump can be seen in the C_p/C_{Deb} curve. It is obvious that, without the mask of the electronic specific heat, an additional source of specific heat or a maximum in C_{Phonon}/C_{Deb} which should arise from some low-frequency vibrations can be clearly seen around 10 K, as is in accordance with the above results.

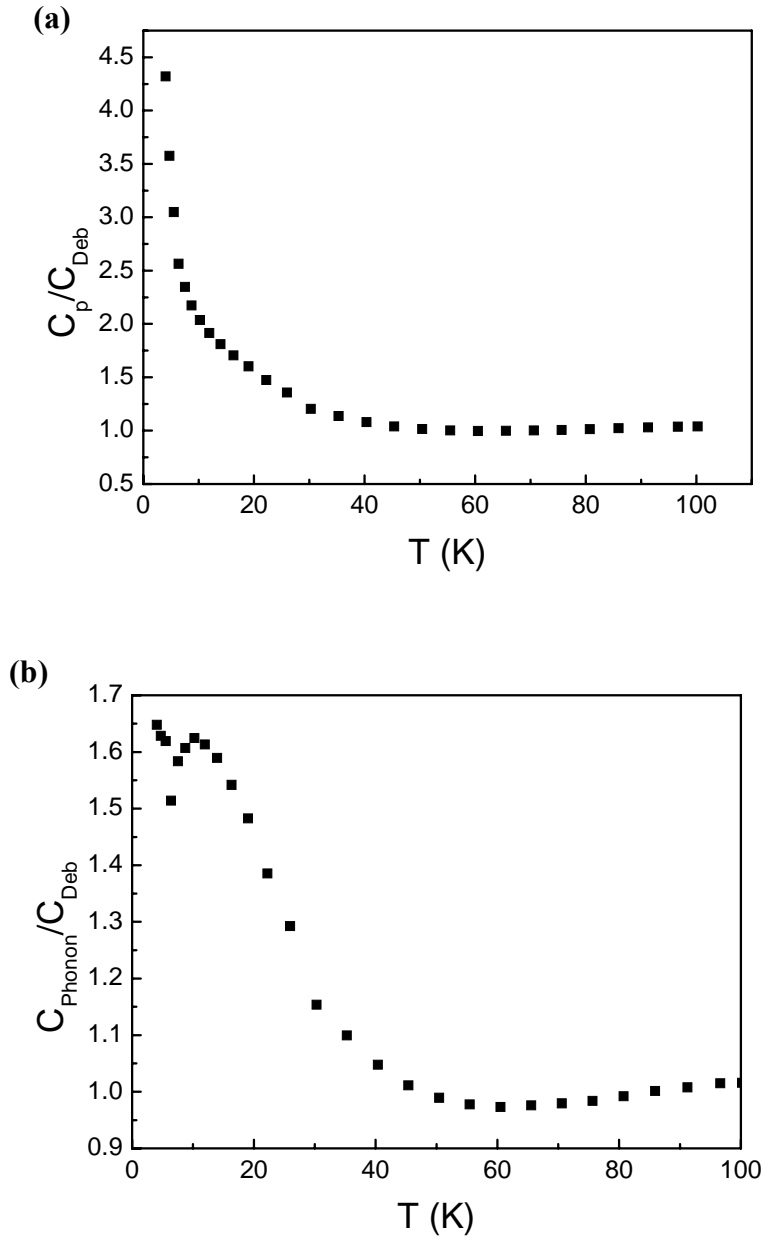


Fig. 3-8 The specific heat (a) C_p and (b) C_{Phonon} scaled by the calculation results vs. temperature for $Ti_{41.5}Cu_{37.5}Ni_{7.5}Zr_{2.5}Hf_5Sn_5Si_1$ BMG

The ratio of excess specific heat $C_{\text{Phonon}} - C_{\text{Deb}}$ to the Debye value C_{Deb} is shown in Fig. 3-9. It indicates that with decreasing temperature the phonon contributions to C_p are more reduced than contributions from low-energy vibrations. The ratio of the excess specific heat to the Debye contribution $(C_{\text{Phonon}} - C_{\text{Deb}})/C_{\text{Deb}}$ around the maximum is 0.62 for the $\text{Ti}_{41.5}\text{Cu}_{37.5}\text{Ni}_{7.5}\text{Zr}_{2.5}\text{Hf}_5\text{Sn}_5\text{Si}_1$ BMG, which should be a fragile system which shows the high value on the fragility scale according to the observation by Sokolov et al. [Sokolov et al., 1997; D.M. Zhu et al., 1998]. The fragility of supercooled liquid determined by the chemical bonds can be correlated with the thermodynamic behavior of glasses, and maybe related to the glass forming ability [D.M. Zhu et al., 1998].

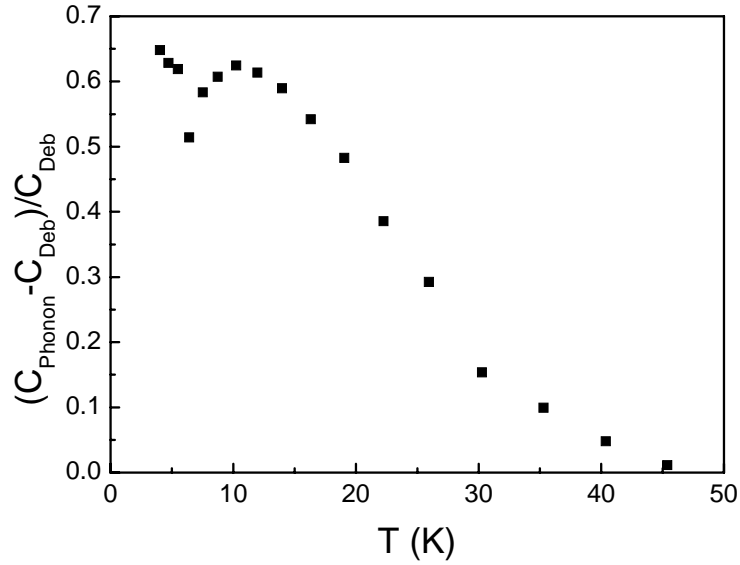


Fig. 3-9 Temperature dependence of specific heat $C_{\text{Phonon}} - C_{\text{Deb}}$ scaled by the Debye value C_{Deb} vs. temperature for $\text{Ti}_{41.5}\text{Cu}_{37.5}\text{Ni}_{7.5}\text{Zr}_{2.5}\text{Hf}_5\text{Sn}_5\text{Si}_1$ BMG

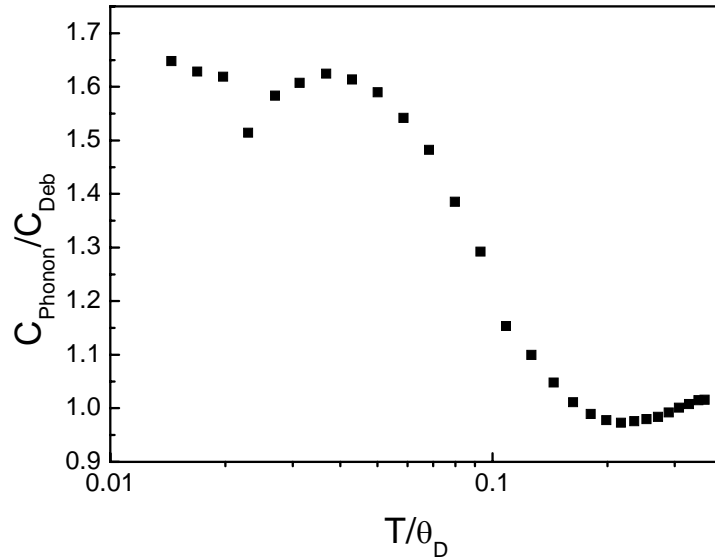


Fig. 3-10 The specific heat of the $\text{Ti}_{41.5}\text{Cu}_{37.5}\text{Ni}_{7.5}\text{Zr}_{2.5}\text{Hf}_5\text{Sn}_5\text{Si}_1$ BMG scaled by Debye values

The so-called “boson peak” which is the excess low-energy vibrational spectra of many glasses deviating in a characteristic way from Debye’s plane-wave density of states, are observed mainly

in nonmetallic glasses. Recent coherent neutron scattering study on metallic glasses [Meyer et al., 1998] confirmed a pronounced boson peak in the vibrational spectra, and the peak position shows no dispersion in wave numbers q , while intensities are strongly correlated with the static structure factor, indicating that the boson peak is related to the intrinsic properties of the metallic glasses. So it is of interest to research it.

Although some interpretations have been proposed for the origin of the excess vibrational density of states (VDOS) found in glasses with respect to the Debye behavior of the corresponding crystals [Foret et al., 1996; Parshin et al., 2001], so far, no explanation is available. The question of whether these additional vibrational modes are related with the unique icosahedral short range ordering (SRO) structures in BMGs is highly debated. Therefore, it will be interesting to find out whether the excess VDOS turns out to be widespread in the metallic glasses, and what sort of modes are involved in the boson peak. Recently, the existence of localized harmonic vibrational modes which will result in an additional Einstein-type vibration (Einstein oscillators) has been confirmed by Tang and Zhou et al. [Tang et al., 2005-b; Zhou et al., 2006]. However, as we know, the Einstein oscillators are uncommon in solids because of strong interatomic coupling. Particularly, in metallic alloys, localized modes are exceedingly rare due to the close-packed microstructure. However, some investigations indicate that the localized vibration modes do exist in some amorphous materials [Caplin et al., 1973; Foret et al., 1996]. So it is necessary to clarify the nature of the additional vibration modes in BMGs since they not only modify the overall vibrational mode distribution but also influence the phonon thermal conductivity of BMGs.

3.3.1.4 Existence of localized harmonic vibrational modes (Einstein oscillators)

The phonon specific heat C_{Phonon} of BMGs can not be only described by the Debye model which has been confirmed by the above analysis, and additional vibrational modes, Einstein oscillators, were proposed to be introduced into the typical Debye model to model the phonon specific heat of BMGs in recent studies [Tang et al., 2005-b; Zhou et al., 2006]. So the low-temperature phonon specific heat C_{Phonon} of $\text{Ti}_{41.5}\text{Cu}_{37.5}\text{Ni}_{7.5}\text{Zr}_{2.5}\text{Hf}_5\text{Sn}_5\text{Si}_1$ BMG in a wide temperature range can be described as follow:

$$\frac{C_{\text{Phonon}}(T)}{3R} = n_D F_D\left(\frac{\theta_D}{T}\right) + n_E F_E\left(\frac{\theta_E}{T}\right) \quad (3-19)$$

Here n_E is dimensionless Einstein-type vibration strength; θ_E is the Einstein temperature and $F_E\left(\frac{\theta_E}{T}\right)$ is the Einstein function expressed as follow:

$$F_E(x) = \frac{x^2 e^x}{(e^x - 1)^2} \quad (3-20)$$

So as shown in Eq. 3-10

$$C_p(T) = C_{\text{Electron}} + C_{\text{Phonon}} = \gamma T + 3R(n_D F_D\left(\frac{\theta_D}{T}\right) + n_E F_E\left(\frac{\theta_E}{T}\right)) \quad (3-21)$$

A model for calculating the low-temperature specific heat of BMGs is constructed which can be regarded as the sum of three components: the electron specific heat and the contributions of one Debye mode and one Einstein mode. By least-square fitting the low-temperature specific heat C_p

data to Eq. 3-21, the values of fitting parameters, θ_D , n_D , θ_E and n_E values of $\text{Ti}_{41.5}\text{Cu}_{37.5}\text{Ni}_{7.5}\text{Zr}_{2.5}\text{Hf}_5\text{Sn}_5\text{Si}_1$ BMG were successfully obtained, they are listed in Table 3-1. As illustrated in Fig. 3-21, electron specific heat γT is shown by the double dash-dotted line ($\gamma=3.51$ mJ mol⁻¹ K⁻²); the contribution of Debye mode is shown in the dashed line with $\theta_D=327$ K and $n_D=0.9004$; the contribution of Einstein mode is marked by dash-dotted line with $\theta_E=89$ K and $n_E=0.0956$. The solid line through the specific heat experimental data represents the calculated fitting specific heat according to Eq. 3-21. It is clear that the experimental specific heat data are well fitted by this fitting curve based on Eq. 3-21 with the fitting parameters of $\theta_D=327$ K, $n_D=0.9004$, $\theta_E=89$ K, and $n_E=0.0956$. Successfully introducing the Einstein mode into the typical Debye model to describe the phonon specific heat indicates the existence of the localized harmonic vibration mode (Einstein oscillators) in the BMG.

With the derived n_D values, the Debye frequency ω_D and sound velocity v_s can be estimated using the following equations [S.N. Zhang et al., 2009]:

$$\omega_D = \frac{k_B \theta_D}{\hbar} \quad (3-22)$$

$$v_s = \frac{\omega_D}{(6\pi^2 \frac{N}{V})^{1/3}} \quad (3-23)$$

where $\hbar = 1.05 \times 10^{-34}$ J s and $k_B = 1.38 \times 10^{-23}$ J/K are reduced Planck constant and Boltzmann constant, respectively; N/V the number of molecular (we assume a $\text{Ti}_{41.5}\text{Cu}_{37.5}\text{Ni}_{7.5}\text{Zr}_{2.5}\text{Hf}_5\text{Sn}_5\text{Si}_1$ is a molecular) per unit volume, which can be deduced from $N_A d/M$, where M is the atomic mass per unit mole, where N_A is the Avogadro's number, d is the density of the alloy. The volume we used here is estimated from the density of each sample. The derived values of ω_D and v_s are 4.30×10^{13} Hz and 2.75×10^3 m/s also listed in Table 3-1.

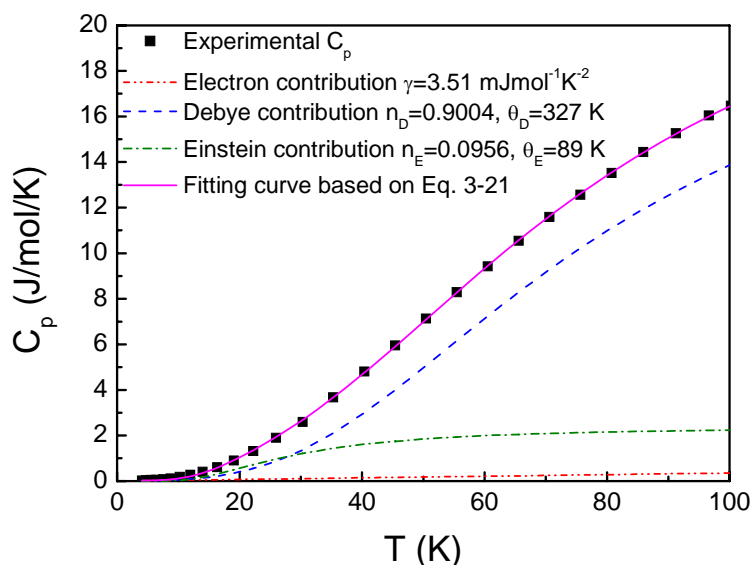


Fig. 3-11 Temperature dependent specific heat of $\text{Ti}_{41.5}\text{Cu}_{37.5}\text{Ni}_{7.5}\text{Zr}_{2.5}\text{Hf}_5\text{Sn}_5\text{Si}_1$ BMG in the temperature range of 4.2-100 K, fitted by Eq. 3-21.

Table 3-1

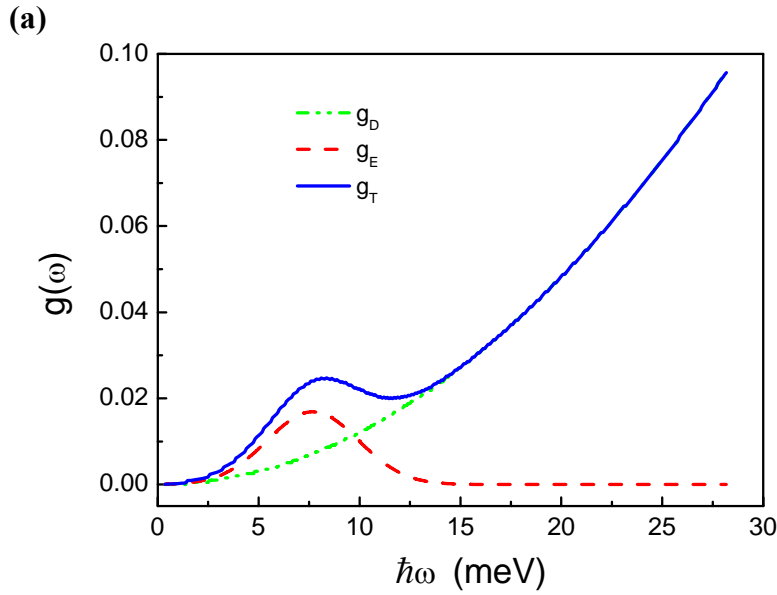
Debye temperature θ_D , Debye-type vibration strength n_D , Einstein temperature θ_E , Einstein-type vibration strength n_E , Debye frequency ω_D , velocity of sound v_s of $\text{Ti}_{41.5}\text{Cu}_{37.5}\text{Ni}_{7.5}\text{Zr}_{2.5}\text{Hf}_5\text{Sn}_5\text{Si}_1$ BMG

θ_D (K)	n_D	θ_E (K)	n_E	ω_D (10^{13} Hz)	v_s (10^3 m/s)
327	0.9004	89	0.0956	4.30	2.75

In order to confirm the existence of localized harmonic vibrational mode, the VDOS of $\text{Ti}_{41.5}\text{Cu}_{37.5}\text{Ni}_{7.5}\text{Zr}_{2.5}\text{Hf}_5\text{Sn}_5\text{Si}_1$ BMG was derived from the low-temperature specific heat. The contribution of Einstein mode to the VDOS is supposed to obey a Gaussian distribution with a main frequency corresponding to the Einstein frequency [Hermann et al., 2003]:

$$g_E = n_E / (\sigma \sqrt{2\pi}) \exp[-(T - \theta_E)^2 / 2\sigma^2] \quad (3-24)$$

where σ is the width of Gaussian distribution (we postulate $\sigma = \theta_E/3.4$), while the contribution of Debye mode to the VDOS obeys ω^2 distribution. The deduced total VDOS in the units of oscillators per mole, g_T , can be obtained from the sum of Debye and Einstein mode's contributions, $g_T = g_D + g_E$. As show in Fig. 3-12 (a), the contributions to the VDOS of Debye mode g_D , and Einstein mode g_E are shown as dash-dotted line and dashed line, respectively, and the total VDOS g_T is shown as solid line. The rescaling $g_T/\omega^2 - \omega$ dependence is shown in Fig. 3-12 (b). It is clear that the maximum value of VDOS is at about 28.19 meV which is corresponding to the Debye temperature θ_D , and the Einstein mode in $\text{Ti}_{41.5}\text{Cu}_{37.5}\text{Ni}_{7.5}\text{Zr}_{2.5}\text{Hf}_5\text{Sn}_5\text{Si}_1$ BMG induces the deviation of the vibrational density of state from the Debye squared-frequency law, and induces a peak at about 5.95 meV shown in the rescaling $g_T/\omega^2 - \omega$ dependence curve which is corresponding to the anomalous boson peak, indicating the boson peak may originate from the Einstein oscillator.



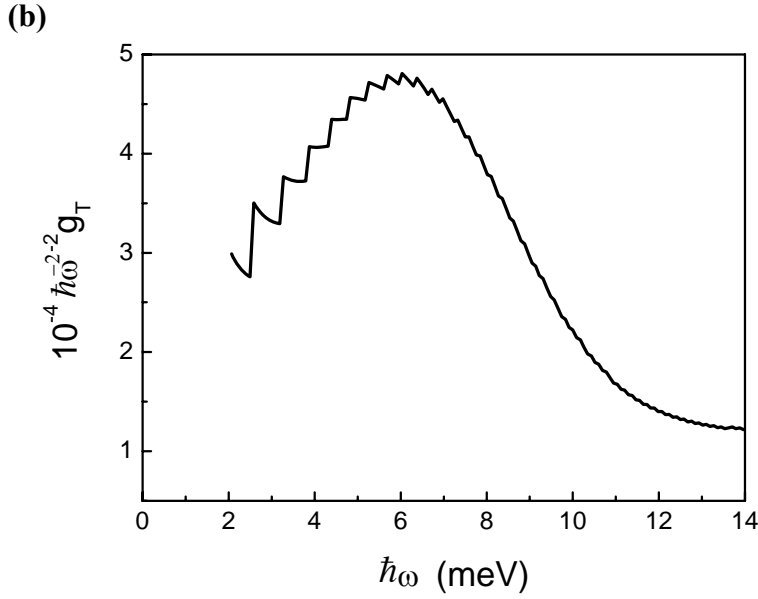


Fig. 3-12 (a) The total VDOS g_T (the solid line), and the VDOS contributed from the Debye g_D (the dash-dotted line) and Einstein g_E (the dashed line) modes, respectively. (b) The derived VDOS of $\text{Ti}_{41.5}\text{Cu}_{37.5}\text{Ni}_{7.5}\text{Zr}_{2.5}\text{Hf}_5\text{Sn}_5\text{Si}_1$ BMG

In regard to the origin of boson peak, two main opinions are widely acceptable so far: the localized vibrational modes and the collective propagating modes. The collective propagating modes persist at high frequency. The boson peak in other glasses, such as glycerol, is induced by the collective propagating mode because the wave number q -independent feature is absent at the energy of the boson peak. The $\text{Ti}_{41.5}\text{Cu}_{37.5}\text{Ni}_{7.5}\text{Zr}_{2.5}\text{Hf}_5\text{Sn}_5\text{Si}_1$ BMG shows the similar characteristic of microstructure, low-temperature specific heat and VDOS with Vit 4 alloy [Tang et al., 2005-b] whose boson peak determined by both neutron scattering [Foret et al., 1996] and specific heat [Tang et al., 2005-b] is ascribed to the localized vibrations. Although we did not perform other measurements, such as neutron scattering measurement to investigate the origin of boson peak, we can deduce that the boson peak in this metallic glass is ascribed to localized vibrations that show no more anharmonicity than any other phonon modes which is the common feature of BMGs.

Tang et al. [Tang et al., 2005-b] reported that the addition of the quantized Einstein oscillator is necessary to provide a good fit to the low-temperature specific heat data of all BMGs studied (including various typical BMGs currently available). So one question is whether and how the Einstein mode correlates with the unique icosahedral SRO (MRO or even cluster) microstructure in BMGs which has been observed and verified by recent investigations. As we know, the Einstein oscillators are uncommon in solids because of strong interatomic coupling; especially in metallic alloys, it is unimaginable that the Einstein oscillator presents in the highly-random-packed microstructure due to the strong interaction between the constituent atoms. However, the former investigations reveal that in metallic compounds with the oversized cage structure or large voids or enough large free volume, some atoms or metallic ions are weakly bound and occupy the oversized cages or voids, and the vibrations of these loose “rattler” atoms are regarded as resulting in the independent localized harmonic modes [Hermann et al., 2003; Caplin et al., 1973; H.Y. Bai et al., 1996]. The localized mode is directly correlated to the density and size of voids. Recently, a

model for the structure of metallic glasses consisting of the closely packed clusters which is efficiently packed solute-centered atomic cluster was proposed [Miracle, 2004] and these interstitial intercluster sites are filled with additional solute component atoms. The model is useful for understanding short and medium range order in BMGs and allows predictions of new glass forming alloy composition [Miracle, 2004]. In metallic glasses' structure, the vibrations of some solute atoms could act as loose or weakly bound atoms in the interstitial intercluster sites, and the vibration of these loose "rattler" atoms are regarded to induce the independent localized modes. Because of the existence of the significant degree of icosahedral SRO, MRO or (oversized) clusters in BMGs, which might contain loose or weakly bound atoms inside. The structure analysis in the last chapter indicates that the $\text{Ti}_{41.5}\text{Cu}_{37.5}\text{Ni}_{7.5}\text{Zr}_{2.5}\text{Hf}_5\text{Sn}_5\text{Si}_1$ BMG does exist such local structure. In addition, $\text{Ti}_{41.5}\text{Cu}_{37.5}\text{Ni}_{7.5}\text{Zr}_{2.5}\text{Hf}_5\text{Sn}_5\text{Si}_1$ BMG consists of seven components with large difference of atomic sizes: Ti (0.145 nm), Cu (0.128 nm), Ni (0.124 nm), Zr (0.160 nm), Hf (0.159 nm), Sn (0.158 nm) and Si (0.134 nm). The smaller atoms could act as loose or weakly bound atoms in the oversized cages or voids. Actually, the components show different diffusion behaviors in the glass. Tracer diffusion measurements in several BMGs have consistently demonstrated that large atoms such as Zr, Hf, Sn and Ti are slow, with diffusion constants that are orders of magnitude smaller than that of smaller atoms such as Ni and Cu whose atoms remain mobile even at temperatures slightly below T_g , where the viscosity increased by several orders of magnitude.

The vibrations of the loose atoms show harmonic Einstein modes in the BMG. In the theoretical view, among various theories, the mode-coupling theory (MCT) [Götze et al., 1992] and the free volume theory [Cohen et al., 1959] are two successful theories that can predict a qualitative change in microscopic dynamics and glass transition in various supercooled liquids. The essence of the MCT deals with the cage effect; that is, in a liquid of densely packed atoms, an atom is temporarily trapped inside the cage formed by neighboring atoms and undergoes vibrations and rattling before escaping the cage. MCT predicts a two-step relaxation process, with α relaxation responsible for viscous flow and a faster β relaxation that can be visualized as a rattling of the atoms in the transient cages. Meyer et al. [Meyer et al., 1998] observed such a fast β relaxation in the Vit 4 liquid, in full accord with MCT, and some metallic glasses showed stronger harmonic behavior than most crystalline solids. The free volume theory also involves the cage effect. The BMGs, which have slow kinetics and are prepared by quick quenching from the liquid state, to some extent can inherit liquid structure and contain a large number of cage structure and free volumes. The atoms sitting in the oversized cage or in sufficiently large free volumes are loose and can vibrate in independent harmonic modes. The assumption is confirmed to some extent by Angell [Angell et al., 2003], who found a much stronger boson peak in hyperquenched glasses [Tang et al., 2005-b].

In this study, we confirm the existence of Einstein oscillator in $\text{Ti}_{41.5}\text{Cu}_{37.5}\text{Ni}_{7.5}\text{Zr}_{2.5}\text{Hf}_5\text{Sn}_5\text{Si}_1$ BMG by analysis of experimental specific heat data in the temperature range of 4.2 to 100 K, in accordance with the results of Tang and Zhou et al. [Tang et al., 2005-a; Tang et al., 2005-b; Zhou et al., 2006], which originates from the unique SRO in BMGs, and finally induces the anomalous boson peak at low temperature obtained from the VDOS calculation. By introducing the localized Einstein vibrational mode into the typical Debye model, the low-temperature specific heat in a wide temperature range can be successfully interpreted. According to the investigation of Zhou et al. [Zhou et al., 2006], the localized oscillators themselves do not contribute to the heat conduction;

however, they do influence phonon transport through anharmonic interactions.

3.3.2 Electrical Resistivity

3.3.2.1 Experimental results analysis

In metallic glasses, scattering from structural disorder is the dominant mechanism responsible for resistivity and hence they have a much higher residual resistivity than similar crystalline materials. The temperature dependence of the resistivity ρ is anomalous over a wide range of temperature and the resistivity decreases with increasing temperature. This is in contrast to the normal behavior for ordered crystalline metals, where the temperature coefficient of resistivity α is large and positive. There have been a number of theories attempting to explain this behavior, Faber-Ziman scattering of electron model, Mott s-d scattering of electron model, two-level systems model, local spin fluctuation model etc.

The electrical resistivity, ρ , versus temperature for $\text{Ti}_{41.5}\text{Cu}_{37.5}\text{Ni}_{7.5}\text{Zr}_{2.5}\text{Hf}_5\text{Sn}_5\text{Si}_1$ BMG from 6 to 280 K is shown in Fig. 3-13. Its room-temperature electrical resistivity, $\rho(280\text{ K})$, is large up to $258.89\text{ }\mu\Omega\cdot\text{cm}$. This is resulting from the following reasons. The resistance is originating from the scattering of electrons, so the resistance is well correlated with the electron mean path; when the electron mean path is large, the resistance is small. It is known that the normal crystalline metals have large electron mean path up to $100\text{-}1000\text{ }\text{\AA}$; while in the disordered amorphous alloys, the electron mean path is rather small, $3\text{-}10\text{ }\text{\AA}$, so the electron is free only within several interatomic distances or even shorter distances, which is believed to be the main reason of leading to the unique characteristic of resistance of amorphous alloys.

In addition, ρ is approximately a constant (ρ decreases slightly with increase in temperature) at low temperature in the range of $6\text{-}30\text{ K}$ and then decreases nearly linearly (with larger $d\rho/dT$ than that in the lower temperature range of $6\text{-}30\text{ K}$) when the temperature increases toward 280 K , so it displays a negative temperature coefficient of resistivity (TCR), α , which is defined as $(1/\rho)d\rho/dT$, throughout the whole experimental temperature range of $6\text{-}280\text{ K}$ which can be observed in TCR- T dependent curve shown in Fig. 3-14, as is in accordance with the TCR characteristic of some other nonmagnetic metallic glasses [Azhazha et al., 2003; Kokanović, 2006; Nagel, 1977], and the value of TCR is calculated to be $-10^{-4}\sim 0\text{ K}^{-1}$, it should be $-1.08\times 10^{-4}\text{ K}^{-1}$ at room temperature. The room temperature coefficient of resistivity of this BMG exhibits large negative value. As regards the room temperature values of both resistivity and temperature coefficient of the resistivity, the studied BMG is similar to those of other BMGs. Mooij [Mooij, 1973] pointed out a remarkable correlation between the resistivity value and the occurrence of negative α for a large number of amorphous as well as other highly disordered metallic conductors, as a result, α is positive for metals with $\rho < 100\text{ }\mu\Omega\cdot\text{cm}$, while for metals with $\rho > 150\text{ }\mu\Omega\cdot\text{cm}$ the observation of negative α is the rule rather than an exception; by confining attention to disordered systems containing d electrons that had a relatively small TCR, he found that the resistivity tends to be larger in systems which have a small value of TCR. We found that the resistivity of the BMG studied here is consistent with the well-known Mooij correlation.

The change in the temperature-dependent electrical resistivity, relative to its value at 280 K , which is defined as $\Delta\rho/\rho(280\text{ K}) = (\rho(T) - \rho(280\text{ K}))/\rho(280\text{ K})$, of $\text{Ti}_{41.5}\text{Cu}_{37.5}\text{Ni}_{7.5}\text{Zr}_{2.5}\text{Hf}_5\text{Sn}_5\text{Si}_1$ BMG within the temperature range of $6\text{-}280\text{ K}$ is shown in Fig. 3-15, it should be pointed out that

the value of $\rho(0)$ is assumed to be the resistivity at very low temperature (6-30 K) for the nearly constant residual resistivity as mentioned above (here we assume $\rho(0) = \rho(6 \text{ K})$). So the change in resistivity over the temperature range of 6-280 K can be evaluated to be only 3.59%, which indicates that the temperature-dependent contribution to the total value of the resistivity is extremely small. The values of $\rho(0)$, $\rho(280 \text{ K})$ and $\alpha(280 \text{ K})$ are listed in Table 3-2. In addition, the resistivity of $\text{Ti}_{40}\text{Zr}_{25}\text{Ni}_8\text{Cu}_9\text{Be}_{18}$ BMG is also measured as a function of temperature, aiming to find the difference in microstructure of these two BMGs by comparing their low-temperature resistivity. In order to shorten the presentation of this work, the results about the $\text{Ti}_{40}\text{Zr}_{25}\text{Ni}_8\text{Cu}_9\text{Be}_{18}$ BMG are not shown here in details, however, they are listed in Table 3-2. It can be seen that these two BMGs exhibit similar characteristic of resistivity. The main feature in these two electrical resistivity data is the rather high residual resistivity, reflecting the high atomic disorder in the samples.

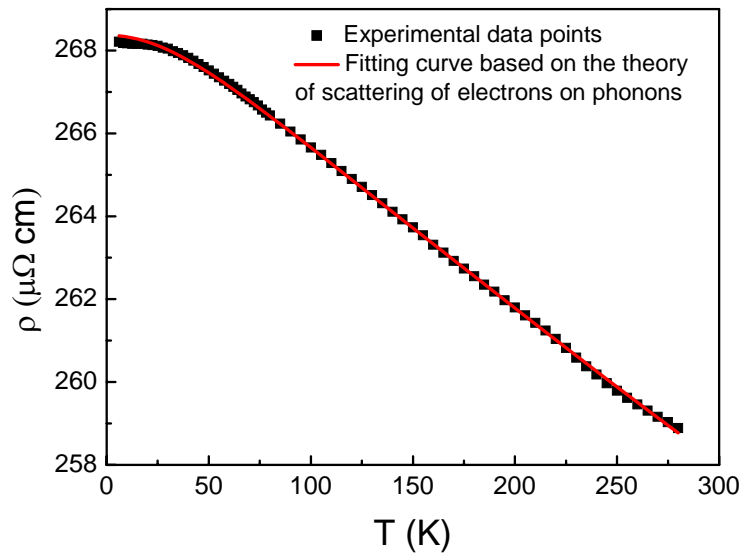


Fig. 3-13 Dependence of ρ - T for $\text{Ti}_{41.5}\text{Cu}_{37.5}\text{Ni}_{7.5}\text{Zr}_{2.5}\text{Hf}_5\text{Sn}_5\text{Si}_1$ BMG in the temperature range of 6-280 K. The solid line represents the fitting result based on free-electron model

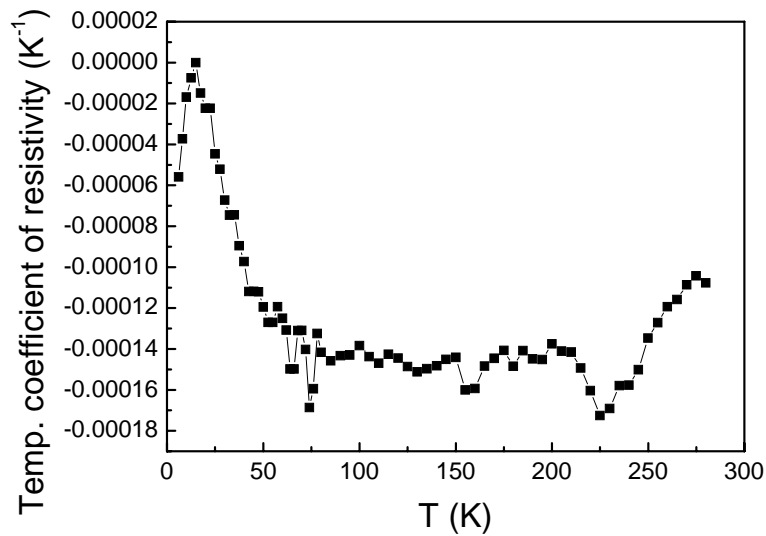


Fig. 3-14 Temperature coefficient of resistivity for $\text{Ti}_{41.5}\text{Cu}_{37.5}\text{Ni}_{7.5}\text{Zr}_{2.5}\text{Hf}_5\text{Sn}_5\text{Si}_1$ BMG as a function of temperature

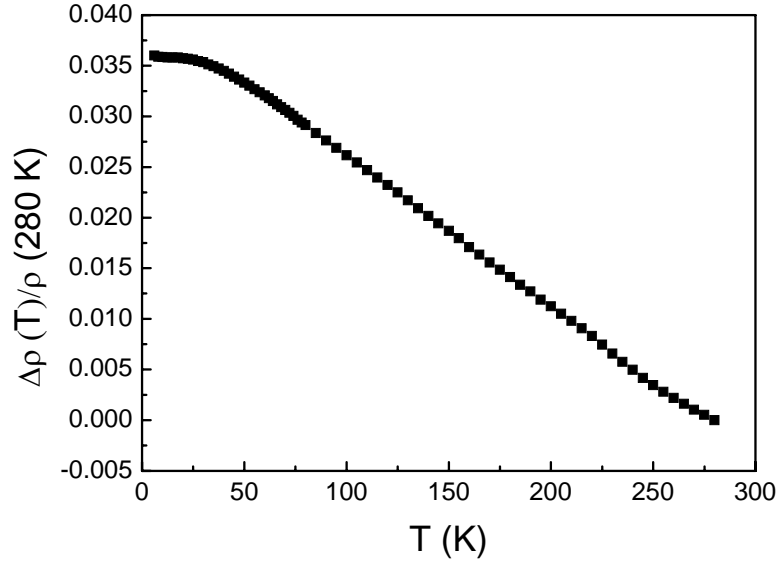


Fig. 3-15 The change in the temperature-dependent part of the electrical resistivity relative to its value at 280 K $\Delta\rho(T)/\rho(280\text{ K})$ of $\text{Ti}_{41.5}\text{Cu}_{37.5}\text{Ni}_{7.5}\text{Zr}_{2.5}\text{Hf}_5\text{Sn}_5\text{Si}_1$ BMG

Table 3-2

The resistivity and temperature coefficient of resistivity for $\text{Ti}_{41.5}\text{Cu}_{37.5}\text{Ni}_{7.5}\text{Zr}_{2.5}\text{Hf}_5\text{Sn}_5\text{Si}_1$ and $\text{Ti}_{40}\text{Zr}_{25}\text{Ni}_8\text{Cu}_9\text{Be}_{18}$ BMGs

Alloy	$\rho(280\text{ K})$ ($\mu\Omega\cdot\text{cm}$)	$(1/\rho)d\rho/dT$ (K^{-1})	$\rho(0\text{ K})$ ($\mu\Omega\cdot\text{cm}$)
$\text{Ti}_{41.5}\text{Cu}_{37.5}\text{Ni}_{7.5}\text{Zr}_{2.5}\text{Hf}_5\text{Sn}_5\text{Si}_1$	258.89	-1.08×10^{-4}	268.21
$\text{Ti}_{40}\text{Zr}_{25}\text{Ni}_8\text{Cu}_9\text{Be}_{18}$	251.46	-1.66×10^{-4}	267.31

3.3.2.2 Discussion about negative TCR

In this part, based on the analysis of temperature dependence of resistivity for $\text{Ti}_{41.5}\text{Cu}_{37.5}\text{Ni}_{7.5}\text{Zr}_{2.5}\text{Hf}_5\text{Sn}_5\text{Si}_1$ BMG, we discuss the negative temperature coefficient of resistivity for nonmagnetic metallic glasses in terms of the existing theories. Ziman [Ziman, 1961] has calculated the temperature dependence of resistivity using a formalism primarily derived for simple liquid crystals. Evans et al. [Evans et al., 1971] have extended this to include liquid transition metals and Sinha [Sinha, 1970] has suggested that this theory could be applied to metallic glasses. In applying this theory to the glass, the temperature dependence is included as in the case of the liquid by taking into account the change in the shape of the structure factor $S(k)$ as T is varied. Nagel [Nagel, 1977] has suggested that in order to get an estimation of the importance of this effect on the resistivity, a calculation must be made starting from a microscopic model of the glass. In a liquid, $S(k)$ will depend quite strongly on temperature and can be calculated using the Percus-Yevick equations. A similar model has been used to describe the glass. However, in the solid, the change in $S(k)$ should be calculated as due to the vibration of ions around their equilibrium positions.

Based on the Ziman theory, Nagel [Nagel, 1977] reported the resistivity as a function of temperature which can be expressed as

$$\rho(T) = \frac{30\pi^3 \hbar^3}{me^2 k_F^2 E_F \Omega} \sin^2[\eta_2(E_F)] \times \{1 + [S_E(2k_F) - 1]e^{-2[W(T) - W(0)]}\} \quad (3-25)$$

where e and m are the electron charge and the mass of the electron, respectively; and k_F and E_F are the Fermi wave vector and energy, respectively; Ω is the average atomic volume, $\eta_2(E_F)$ is the d -wave phase shift describing the scattering of the conduction electrons, of energy E_F , by the ion cores which each carry a muffin-tin potential; $W(T)$ is the Debye-Waller factor, $S_E(2k_F)$ is the equilibrium structure factor at $k=2k_F$, and can be expressed as

$$S_E(k) = \frac{1}{N} \sum_{i,j} e^{i\vec{k}(\vec{r}_i - \vec{r}_j)} \quad (3-26)$$

where \vec{r}_i is the equilibrium position of the i th atom and N is the total number of atoms.

According to the Eq. 3-25, the temperature coefficient of the resistivity can be calculated from the expression:

$$\alpha = \frac{1}{\rho} \frac{\partial \rho}{\partial T} \simeq 2 \left(\frac{1 - S_T(2k_F)}{S_T(2k_F)} \right) \frac{\partial W(T)}{\partial T} \quad (3-27)$$

where $W(T)$ can be obtained from the well-known Debye approximation.

$$W(T) = \frac{3\hbar^2 k^2 T^2}{2Mk_B \theta_D^3} \int_0^{\theta_D/T} \left(\frac{1}{e^z - 1} + \frac{1}{2} \right) z dz, \quad W(0) = \frac{3\hbar^2 k^2 T^2}{8Mk_B \theta^3} \quad (3-28)$$

where θ_D is the Debye temperature, k_B is the Boltzmann constant and M is the average atomic mass. Since $\partial W / \partial T > 0$, α is negative if $S_T(2k_F) > 1$, and positive otherwise. If $2k_F$ is near k_p , the first peak of $S(k)$, then a negative temperature coefficient of the resistivity is expected just as in the case of liquids.

The key point of applying the free-electron model is to find an appropriate effective atomic value, Z , of each constituent, which can favor the expression $2k_F \approx k_p$ as well as

$$\eta = \frac{2k_F - k_p}{k_p} \leq 0.1, \text{ finally leading to the negative TCR. } k_p \text{ can be calculated from the}$$

expression

$$k_p = 4\pi \sin \theta_p / \lambda \quad (3-29)$$

where $2\theta_p$ is the Bragg diffraction angle of the first diffraction peak in XRD curve which is corresponding to the structural factor $S(k)$. The value of the Fermi radius was found within the framework of the free-electron model [Rao, 1983]: $k_F = ((3\pi^2 N_A dZ) / M)^{1/3}$, where N_A is the Avogadro's number, d is the density of the alloy and Z is the effective number of conduction electrons per atom which can be calculated from the expression

$$Z = \sum_i^i w_i Z_i \quad (3-30)$$

where w_i and Z_i represent the atomic percentage and effective atomic value of the i th constituent.

The effective atomic value, Z , of each constituent, k_p , $2k_F$, η for $\text{Ti}_{41.5}\text{Cu}_{37.5}\text{Ni}_{7.5}\text{Zr}_{2.5}\text{Hf}_5\text{Sn}_5\text{Si}_1$ BMG are listed in Table 3-3. At such Z , the value of $2k_F$ is near the first maximum of $S(k)$, so that $S(k)>1$ and according to Eq. 3-27, the resistivity decreases with increase in temperature. By fitting the experimental $\rho(T)$ with Eq. 3-25 in the whole interval of temperatures 6-280 K, the parameters $S(k)$ and θ_D for $\text{Ti}_{41.5}\text{Cu}_{37.5}\text{Ni}_{7.5}\text{Zr}_{2.5}\text{Hf}_5\text{Sn}_5\text{Si}_1$ BMG are obtained and listed in Table 3-3. The best fitting curve is shown in Fig. 3-13. It can be seen from Fig. 3-13, obviously, that the temperature dependence of resistivity of $\text{Ti}_{41.5}\text{Cu}_{37.5}\text{Ni}_{7.5}\text{Zr}_{2.5}\text{Hf}_5\text{Sn}_5\text{Si}_1$ BMG can be well fitted by free-electron model. The obtained $S(2k_F)>1$ can successfully explain the negative TCR.

Table 3-3 Values of the parameters using for calculating resistivity of $\text{Ti}_{41.5}\text{Cu}_{37.5}\text{Ni}_{7.5}\text{Zr}_{2.5}\text{Hf}_5\text{Sn}_5\text{Si}_1$ BMG in Eq. 3-25

Z_{Ti}	Z_{Cu}	Z_{Ni}	Z_{Zr}	Z_{Hf}	Z_{Sn}	Z_{Si}	$k_p (\text{\AA}^{-1})$	$2k_F (\text{\AA}^{-1})$	η	$S(2k_F)$	$\theta_D (\text{K})$
2	1	1	2	2	4	4	2.83	2.941	0.038	1.32	182

It seems that the free-electron model can explain the temperature dependence of resistivity of this BMG. However, we found that the value of Debye temperature, θ_D , is too low compared with the high value of $\theta_D \sim 280\text{--}330$ K for $\text{Ti}_{41.5}\text{Cu}_{37.5}\text{Ni}_{7.5}\text{Zr}_{2.5}\text{Hf}_5\text{Sn}_5\text{Si}_1$ BMG obtained from the low-temperature specific heat measurement, which indicates that the obtained fitting parameter, θ_D , is unreasonable although the experimental error in the determination of θ_D is ± 50 K [Banerjee et al., 1981] because that Eq. 3-25 is more adequate at high temperature [Dolocan et al., 1987]. To the contrary, our data are described by Eq. 3-25 within the whole temperature interval 6-280 K. It is obvious that the Debye temperature is not defined clearly for amorphous solids where there is, rather, a statistic distribution of atomic vibration frequencies. We should give a reasonable explanation on the reason why the value of θ_D obtained from the free-electron model fitting resistivity is unreasonable, however, calculated from the Debye model fitting specific heat is believable. Because the application of Debye model on fitting specific heat is independent on the nature of the materials, amorphous or crystalline; the situation of the application of free-electron model is on the contrary strongly dependent on the nature of materials and can be only used in liquid metal or metallic glasses systems. So, θ_D is obtained, based on the assumption of glassy state nature. We suspect that the unreasonable θ_D value is due to the non-fully amorphous nature of materials. As we know, the formation of local ordering structure will lead to the decrease in resistivity, with not change in the negative TCR. So, if the materials are fully metallic glasses, the resistivity will be higher, which results in the increase in θ_D , as can be seen from the Eq. 3-25. Now, the obtained θ_D is under the condition of the assumption of fully glassy state of this alloy. In addition, the value of θ_D for non-fully amorphous material (even if MRO exists, clusters, etc., local ordering structure or even limited nanocrystals) should be higher than that of fully metallic glasses, so, the real value of θ_D for $\text{Ti}_{41.5}\text{Cu}_{37.5}\text{Ni}_{7.5}\text{Zr}_{2.5}\text{Hf}_5\text{Sn}_5\text{Si}_1$ alloy should be higher than the obtained value and approaches to $\theta_D \sim 280\text{--}330$ K. So, the obtained unreasonable low value of θ_D in terms of free-electron model reveals the non-fully amorphous nature of $\text{Ti}_{41.5}\text{Cu}_{37.5}\text{Ni}_{7.5}\text{Zr}_{2.5}\text{Hf}_5\text{Sn}_5\text{Si}_1$ BMG. About the microstructure of $\text{Ti}_{41.5}\text{Cu}_{37.5}\text{Ni}_{7.5}\text{Zr}_{2.5}\text{Hf}_5\text{Sn}_5\text{Si}_1$ BMG we will give more details.

In summary, the negative TCR of nonmagnetic $\text{Ti}_{41.5}\text{Cu}_{37.5}\text{Ni}_{7.5}\text{Zr}_{2.5}\text{Hf}_5\text{Sn}_5\text{Si}_1$ BMG can be interpreted successfully thanks to the free-electron model proposed by Nagel; however, the temperature dependence of resistivity $\text{Ti}_{41.5}\text{Cu}_{37.5}\text{Ni}_{7.5}\text{Zr}_{2.5}\text{Hf}_5\text{Sn}_5\text{Si}_1$ BMG can not be interpreted by simply using free-electron model due to the special nature of BMG compared with rapidly

quenched-in metallic glasses where there may exist MRO or clusters, etc., local ordering structure or even limited nanocrystals.

3.3.2.3 The microstructure analysis based on resistivity

It is well known that the resistivity is extremely sensitive to the number of crystals in the glassy matrix [Kokanović, 2006]. Besides that, the structural relaxation also leads to electrical transport change drastically [Poon, 1982; Koch et al., 1983]. It is said that the resistivity can reflect even extremely tiny microstructure changes of metallic glasses. Thus, the resistivity measurement provides a rather sensitive tool and effective method for probing the microscopic state of metallic glasses. Also it is an easy technique for studying phase transformations, defects and other structural changes in crystals as well as metallic glasses. So, in our study, we plan to investigate the microstructure of these two BMGs through the analysis of low-temperature resistivity, which will compare with the results obtained in Chapter 2 through the XRD, neutron diffraction and HRTEM analysis. The detail research idea is that by investigating the temperature dependence of resistivity to analyze the scattering mechanism firstly, and then determine the microstructure, finally establish the correlation between resistivity and microstructure of BMGs. In the last section, by analyzing the temperature dependence of resistivity data of $\text{Ti}_{41.5}\text{Cu}_{37.5}\text{Ni}_{7.5}\text{Zr}_{2.5}\text{Hf}_5\text{Sn}_5\text{Si}_1$ BMG, we have found its different microstructures compared with the quenched-in glassy alloys. In this part, we will focus on the determination of exact microstructure of this alloy: local ordering structure or crystals.

In strongly disordered amorphous systems when the electron mean free path becomes comparable with interatomic distance an incipient weak localization shows up and the correction to the Boltzmann conductivity [Howson, 1984] is given by

$$\Delta\sigma = \frac{2e^2}{\pi\hbar L_i(T)} \quad (3-31)$$

where $L_i(T)$ is the inelastic diffusion length and $L_i(T) = (D\tau_i)^{1/2}$ where D is the electronic diffusion constant and τ_i is the inelastic scattering time. This was shown to lead to temperature dependence of electrical resistivity in strongly disordered alloys of the form:

$$\Delta\rho \sim -T, \quad \frac{\theta_D}{10} < T < \frac{\theta_D}{3} \quad (3-32a)$$

$$\Delta\rho \sim -T^{1/2}, \quad \frac{\theta_D}{3} < T < \theta_D \quad (3-32b)$$

We have tried to fit the experimental temperature variation of the electrical resistivity of the $\text{Ti}_{41.5}\text{Cu}_{37.5}\text{Ni}_{7.5}\text{Zr}_{2.5}\text{Hf}_5\text{Sn}_5\text{Si}_1$ BMG based on the theory of weak localization (shown in Fig. 3-16). The best fit yields $\Delta\rho/\rho(280\text{ K}) = 4.08 \times 10^{-2} - 1.50 \times 10^{-4} \times T$ at temperature $< 110\text{ K}$, and $\Delta\rho/\rho(280\text{ K}) = 6.93 \times 10^{-2} - 4.13 \times 10^{-3} \times T^{1/2}$ at temperature $> 110\text{ K}$. It is clear that the experimental data points are not well fitted by the obtained fitting curves. So, the temperature dependence of resistivity for $\text{Ti}_{41.5}\text{Cu}_{37.5}\text{Ni}_{7.5}\text{Zr}_{2.5}\text{Hf}_5\text{Sn}_5\text{Si}_1$ BMG can not be described by simply using the theory of weak localization, which suggests that the microstructure of $\text{Ti}_{41.5}\text{Cu}_{37.5}\text{Ni}_{7.5}\text{Zr}_{2.5}\text{Hf}_5\text{Sn}_5\text{Si}_1$ BMG is not strongly disordered, as has been confirmed through HRTEM in Chapter 2, and in accordance with the results obtained in the last section. Additional scattering mechanism should be considered into interpreting the temperature dependence of resistivity of this BMG, as will be discussed later. It should be pointed out that the nature of one material is the sufficient but not necessary condition

of one model. In other words, if the materials is strongly disordered, the temperature dependence of resistivity should be described by the theory of weak localization; on the contrary, even if the resistivity can be well fitted by the theory of weak localization, it can not confirm the strongly disordered nature of the material; however, at least, we can confirm that if the resistivity can not be fitted by the theory of weak localization, the nature of the material must not be strongly disordered.

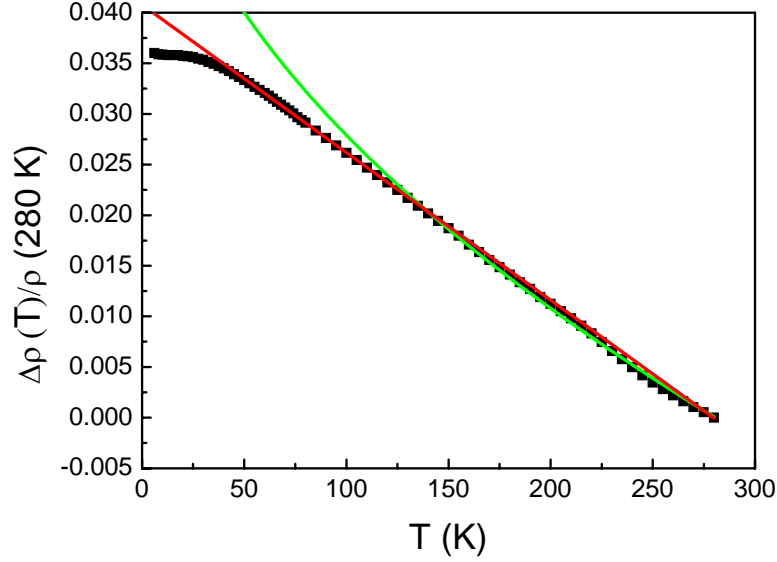
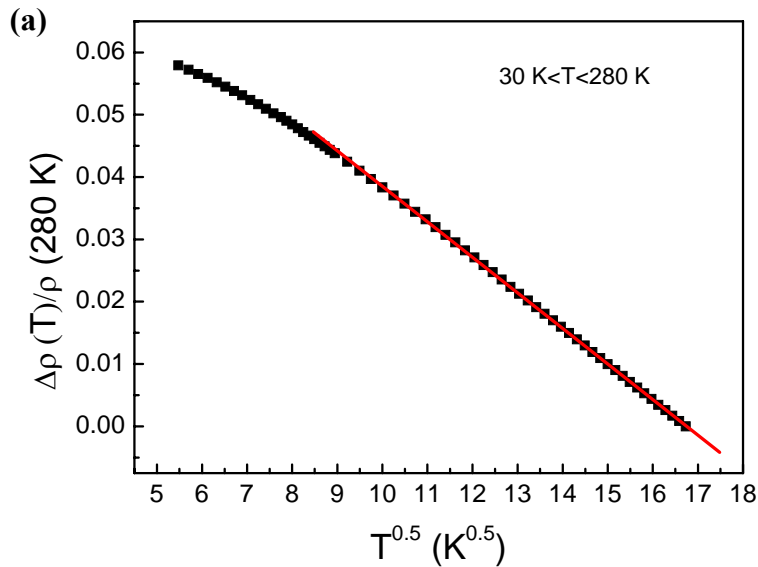


Fig. 3-16 $\Delta\rho/\rho(280\text{ K})$ for $\text{Ti}_{41.5}\text{Cu}_{37.5}\text{Ni}_{7.5}\text{Zr}_{2.5}\text{Hf}_5\text{Sn}_5\text{Si}_1$ BMG as a function of temperature. The solid lines are the fitting curves based on the theory of weak localization

The same fitting was also performed on $\text{Ti}_{40}\text{Zr}_{25}\text{Ni}_8\text{Cu}_9\text{Be}_{18}$ BMG. **Fig. 3-17 (a)** plots the $\Delta\rho/\rho(280\text{ K})$ as a function of the square root of temperature for $\text{Ti}_{40}\text{Zr}_{25}\text{Ni}_8\text{Cu}_9\text{Be}_{18}$ BMG in the temperature range of 30-280 K. The $\Delta\rho/\rho(280\text{ K})$ of the same alloy as a function of temperature between 30 and 80 K is plotted in **Fig. 3-17 (b)**. From the presented results it can be seen that $\Delta\rho/\rho(280\text{ K})$ is indeed linear with temperature in the temperature range of 30-80 K, and the $\Delta\rho/\rho(280\text{ K})$ is linear with the square root of temperature in the temperature range of 80-280 K. The crossover temperature of the character of temperature dependence is about 80 K. It follows that θ_D of the $\text{Ti}_{40}\text{Zr}_{25}\text{Ni}_8\text{Cu}_9\text{Be}_{18}$ BMG is about 240 K. This is, up to our knowledge, the first crude estimate of the Debye temperatures of the $\text{Ti}_{40}\text{Zr}_{25}\text{Ni}_8\text{Cu}_9\text{Be}_{18}$ BMG. Based on the theory of weak localization, the best fit yields $\Delta\rho/\rho(280\text{ K})=6.65\times 10^{-2}-2.83\times 10^{-4}\times T$ in the temperature range 30-80 K. This temperature behavior of the electrical resistivity can be treated within the framework of the weak localization of electrons where the temperature dependence of ρ is determined by temperature dependence of the inelastic scattering time τ_i which is assumed to be equal to βT^2 where β is the inelastic scattering parameter. And $\Delta\rho/\rho(280\text{ K})=9.56\times 10^{-2}-5.70\times 10^{-3}\times T^{1/2}$ at temperature $>80\text{ K}$. The root temperature dependence presumably comes from the weak localization effect which changes over with $\Delta\rho(T)\sim T^{1/2}$ due to the fact that at high temperatures, the τ_i is given by the simple form, $\tau_i\sim T^{-1}$. It is clear that the temperature dependence of resistivity for $\text{Ti}_{40}\text{Zr}_{25}\text{Ni}_8\text{Cu}_9\text{Be}_{18}$ BMG can be well described by the theory of weak localization, which suggests that the microstructure of $\text{Ti}_{40}\text{Zr}_{25}\text{Ni}_8\text{Cu}_9\text{Be}_{18}$ BMG maybe strongly disordered, as in accordance with the observation of disordered features through HRTEM.

By comparing the fitting results of $\text{Ti}_{41.5}\text{Cu}_{37.5}\text{Ni}_{7.5}\text{Zr}_{2.5}\text{Hf}_5\text{Sn}_5\text{Si}_1$ and $\text{Ti}_{40}\text{Zr}_{25}\text{Ni}_8\text{Cu}_9\text{Be}_{18}$ BMGs, we found that the degree of disordering of $\text{Ti}_{40}\text{Zr}_{25}\text{Ni}_8\text{Cu}_9\text{Be}_{18}$ BMG is higher than that of $\text{Ti}_{41.5}\text{Cu}_{37.5}\text{Ni}_{7.5}\text{Zr}_{2.5}\text{Hf}_5\text{Sn}_5\text{Si}_1$ BMG. It is well known that the microstructure of BMGs is different from that of liquid metal and the former metallic glasses obtained from rapidly quench-in method, which consists of large quantities of icosahedral SRO, MRO, clusters or even nanocrystals. Further analysis will be carried out based on the free-electron model proposed by Nagel aiming to clarify the different microstructures between these two BMGs in detail.

So far, we can make a conclusion that the microstructure of $\text{Ti}_{41.5}\text{Cu}_{37.5}\text{Ni}_{7.5}\text{Zr}_{2.5}\text{Hf}_5\text{Sn}_5\text{Si}_1$ BMG must not be strongly disordered. What is the microstructure in it, crystals or just icosahedral SRO, MRO, clusters, etc, local ordering structure? According to the former investigations on the effects of annealing heat treatment on the electrical resistivity of glassy alloys, we confirm that no crystals even if nanocrystals are formed in the amorphous matrix of $\text{Ti}_{41.5}\text{Cu}_{37.5}\text{Ni}_{7.5}\text{Zr}_{2.5}\text{Hf}_5\text{Sn}_5\text{Si}_1$ BMG, so the contribution of reducing the resistivity arises from the local ordering, which is due to the following reason. Large quantities of researches reveal that the temperature dependence of resistivity is extremely sensitive to the microstructure of materials. The TCR for partially crystalline metallic glasses even if for partially nanocrystalline metallic glasses is positive, a positive TCR is often a sign of the presence of quenched-in crystals within glassy matrix, while the TCR for fully metallic glasses (or the glassy alloys with large quantities of SRO or clusters) is negative. For the situation that there exists some icosahedral SRO, MRO, clusters, etc., local ordering structure in the glassy matrix, which is similar with the microstructure of the quenched-in metallic glasses annealed below the crystallization temperature, the TCR will stay negative however, the value of electrical resistivity is lower than that of metallic glasses with the same composition, since the ordering structure increases electron mobility and leads to a resistivity reduction. The electrical resistivity of this kind of materials, similar with the partially crystalline metallic glasses is composed of the structural components of both fractions (amorphous and ordered structure).



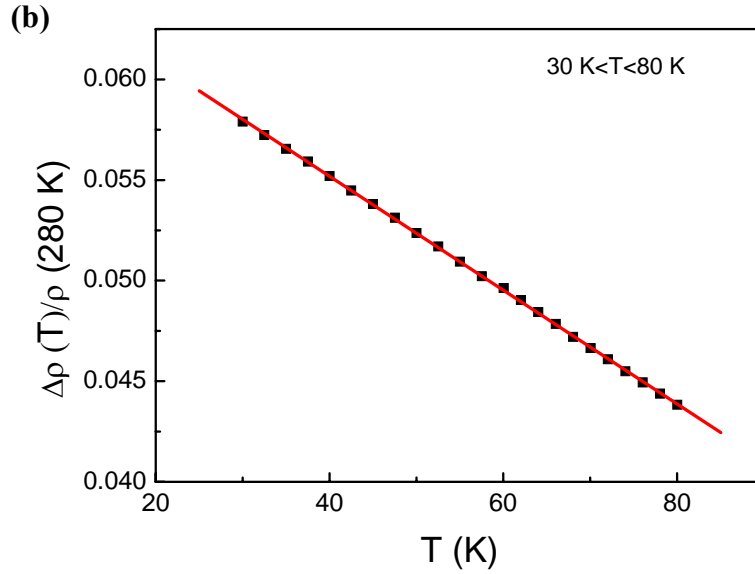


Fig. 3-17 (a) $\Delta\rho/\rho$ (280 K) for $\text{Ti}_{40}\text{Zr}_{25}\text{Ni}_8\text{Cu}_9\text{Be}_{18}$ BMG as a function of the square root of temperature from 30 to 280 K; (b) $\Delta\rho/\rho$ (280 K) for the same BMG as a function of temperature from 30 to 80 K.

3.3.2.4 Scattering mechanism of resistivity

So far, we have confirmed the existence of local ordering structure in the $\text{Ti}_{41.5}\text{Cu}_{37.5}\text{Ni}_{7.5}\text{Zr}_{2.5}\text{Hf}_5\text{Sn}_5\text{Si}_1$ BMG. Actually, it is a common phenomenon for BMGs which is believed to be a unique characteristic compared with the traditional quenched-in metallic glasses. In fact, the so-called BMGs generally consist of some local ordering structure or even a few nanocrystals. So it is of importance to establish a theoretical model to describe the temperature dependence of resistivity for this kind of BMGs. However, to find an adequate model for precisely describing the temperature dependence of resistivity for this kind of BMGs over a wide temperature range from low temperature to ambient temperature is rather difficult, because the resistivity is extremely sensitivity to the microstructure, such as the morphology, size, fraction, etc. Here, we just try to roughly analyze the scattering mechanism according to the $\frac{d\rho}{dT}-T$ dependence based on the existing theories. Although, the resistivity for $\text{Ti}_{41.5}\text{Cu}_{37.5}\text{Ni}_{7.5}\text{Zr}_{2.5}\text{Hf}_5\text{Sn}_5\text{Si}_1$ BMG is originating from two contributions of amorphous matrix and local ordering structure, as we see, the existence of local ordering structure slightly changes the value of resistivity, and changes the temperature dependence of $\frac{d\rho}{dT}$, as can be seen from the comparison of $\frac{d\rho}{dT}$ between $\text{Ti}_{41.5}\text{Cu}_{37.5}\text{Ni}_{7.5}\text{Zr}_{2.5}\text{Hf}_5\text{Sn}_5\text{Si}_1$ and $\text{Ti}_{40}\text{Zr}_{25}\text{Ni}_8\text{Cu}_9\text{Be}_{18}$ BMGs which is believed to be more disordered than $\text{Ti}_{41.5}\text{Cu}_{37.5}\text{Ni}_{7.5}\text{Zr}_{2.5}\text{Hf}_5\text{Sn}_5\text{Si}_1$ BMG, which are shown in Fig. 3-18 and 3-19.

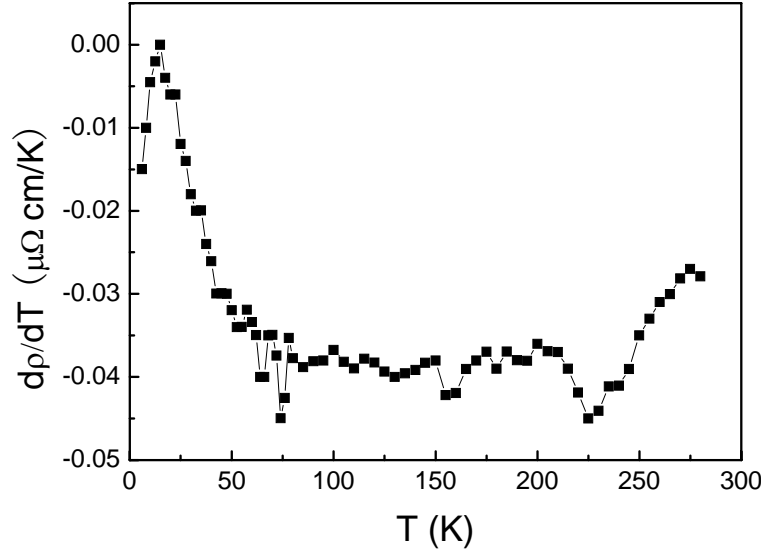


Fig. 3-18 Derivative of resistivity of $\text{Ti}_{41.5}\text{Cu}_{37.5}\text{Ni}_{7.5}\text{Zr}_{2.5}\text{Hf}_5\text{Sn}_5\text{Si}_1$ BMG as a function of temperature

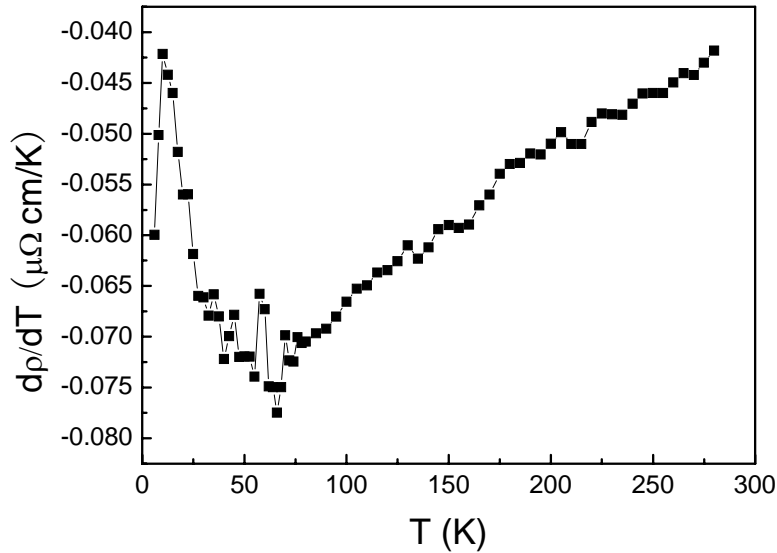


Fig. 3-19 Derivative of resistivity of $\text{Ti}_{40}\text{Zr}_2\text{Ni}_8\text{Cu}_9\text{Be}_{18}$ BMG as a function of temperature

Obviously, the temperature dependences of $\frac{d\rho}{dT}$ for these two BMGs are different, resulting from different scattering mechanism, revealing different nature between these two BMGs. The temperature dependence of $\frac{d\rho}{dT}$ for $\text{Ti}_{40}\text{Zr}_2\text{Ni}_8\text{Cu}_9\text{Be}_{18}$ BMG is in accordance with the normal rule for amorphous metallic metals and the corresponding temperature dependence of resistivity can be roughly separated into four parts: (i) $T < 10$ K, the absolute value of $\frac{d\rho}{dT}$ decreases linearly with increase in temperature, indicating $\rho \propto -\ln T$; (ii) $10 \text{ K} < T < 40 \text{ K}$, the absolute value of $\frac{d\rho}{dT}$ nearly increases linearly with increase in temperature, indicating $\rho \propto -T^2$; (iii) 100

$K < T < 240$ K, there exists a positive linear relation between $\frac{d\rho}{dT}$ and T , and the intercept is negative, it means $\rho \propto -T, +T^2$; (iv) $T > 250$ K (around Debye temperature), the value of $\frac{d\rho}{dT}$ is nearly constant, revealing $\rho \propto -T$. In addition, the temperature corresponding to the minimum value of TCR, T_{\min} , is around 65 K, which is consistent with that of Vit 1 alloy. For $\text{Ti}_{41.5}\text{Cu}_{37.5}\text{Ni}_{7.5}\text{Zr}_{2.5}\text{Hf}_5\text{Sn}_5\text{Si}_1$ BMG, also several temperature regions may be distinguished in the temperature variation of the electrical resistivity. However, the change trend is different. In detail, the first two regions are the same as other typical metallic metals and alloys: the relation of $\rho \propto -\ln T$ at low temperature of 6-15 K and the $\rho \propto -T^2$ dependence at temperature 15-50 K; however in the third region of 80-200 K, the relation of $\rho \propto -T$ exists, and in the fourth region of >230 K, the resistivity obeys the $\rho \propto -T, +T^2$ relation. Based on the analysis above, the temperature dependence of resistivity can be described as a form of piecewise function:

$$\rho = \rho_{01}(1 - a \ln T) \quad T < 15 \text{ K} \quad (3-33a)$$

$$\rho = \rho_{02}(1 - bT^2) \quad 15 \text{ K} < T < 50 \text{ K} \quad (3-33b)$$

$$\rho = \rho_{03}(1 - cT) \quad 80 \text{ K} < T < 200 \text{ K} \quad (3-33c)$$

$$\rho = \rho_{04}(1 - dT + eT^2) \quad T > 230 \text{ K} \quad (3-33d)$$

where ρ represents the electrical resistivity, ρ_{0i} ($i=1-4$) represents the resistivity at 0 K, $a-e$ are fitting parameters which are positive. We have fitted the experimental data points with the piecewise function defined above. The fitting curves are plotted in Fig. 3-20~3-23, and the fitting parameters are listed in Table 3-4.

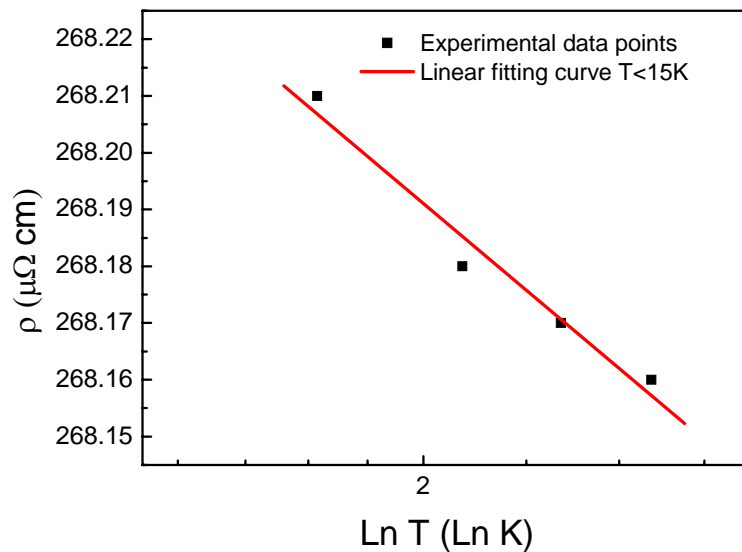


Fig. 3-20 Resistivity of $\text{Ti}_{41.5}\text{Cu}_{37.5}\text{Ni}_{7.5}\text{Zr}_{2.5}\text{Hf}_5\text{Sn}_5\text{Si}_1$ BMG at temperature <15 K as a function of $\ln T$. The solid line is the fitting curve

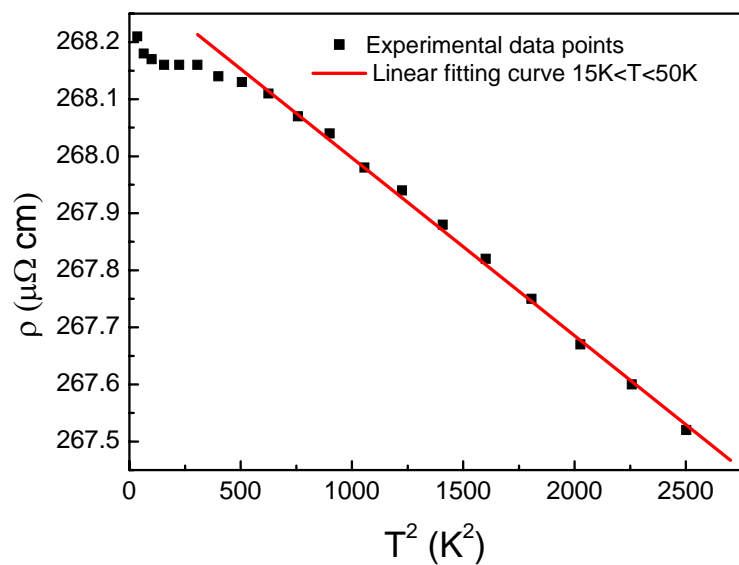


Fig. 3-21 Resistivity of $\text{Ti}_{41.5}\text{Cu}_{37.5}\text{Ni}_{7.5}\text{Zr}_{2.5}\text{Hf}_5\text{Sn}_5\text{Si}_1$ BMG at temperature of 15-50 K as a function of T^2 . The solid line is the fitting curve

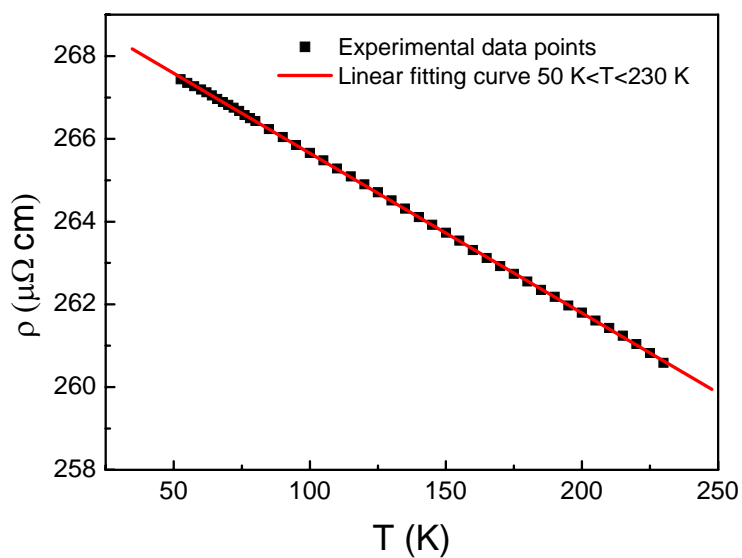


Fig. 3-22 Resistivity of $\text{Ti}_{41.5}\text{Cu}_{37.5}\text{Ni}_{7.5}\text{Zr}_{2.5}\text{Hf}_5\text{Sn}_5\text{Si}_1$ BMG at temperature of 50-230 K as a function of T . The solid line is the fitting curve

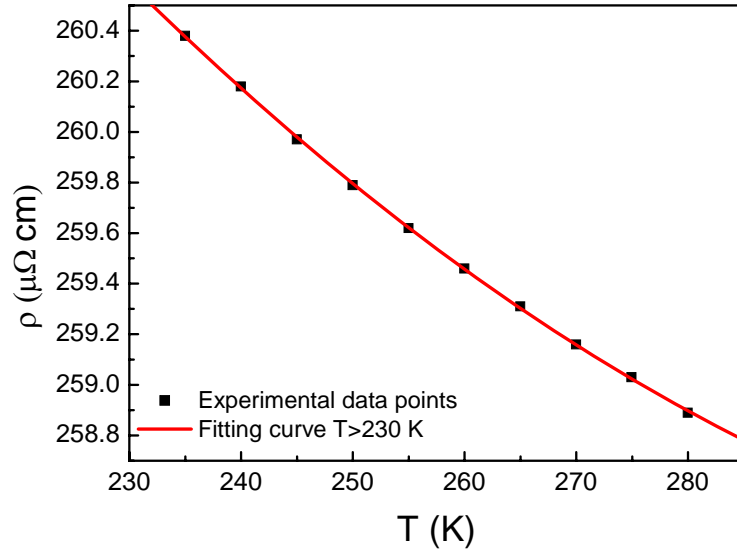


Fig. 3-23 Resistivity of $\text{Ti}_{41.5}\text{Cu}_{37.5}\text{Ni}_{7.5}\text{Zr}_{2.5}\text{Hf}_5\text{Sn}_5\text{Si}_1$ BMG at temperature >230 K as a function of T . The solid line is the fitting curve

Table 3-4

Fitting parameters of resistivity based on piecewise function for $\text{Ti}_{41.5}\text{Cu}_{37.5}\text{Ni}_{7.5}\text{Zr}_{2.5}\text{Hf}_5\text{Sn}_5\text{Si}_1$ BMG

$T < 15$ K	$15 \text{ K} < T < 50$ K	$80 \text{ K} < T < 200$ K	$T > 230$ K
$a = 3.746 \times 10^{-4}$	$b = 1.162 \times 10^{-6} \text{ K}^{-2}$	$c = 1.433 \times 10^{-4} \text{ K}^{-1}$	$d = 4.751 \times 10^{-4} \text{ K}^{-1}$
$\rho_{01} = 268.29157 \mu\Omega \cdot \text{cm}$	$\rho_{02} = 268.30873 \mu\Omega \cdot \text{cm}$	$\rho_{03} = 269.51347 \mu\Omega \cdot \text{cm}$	$e = 0.695 \times 10^{-6} \text{ K}^{-2}$
			$\rho_{04} = 280.95714 \mu\Omega \cdot \text{cm}$

The analysis on the scattering mechanism in this BMG is studied based on the piecewise function above. At low temperature <15 K, the mechanisms of scattering of electrons, such as mechanisms of interference of inelastic electron-electron scattering with elastic scattering on impurities, Kondo-type scattering, scattering on two-level systems, may exist. However, because of the high concentration of magnetic impurities, Ni 7.5at.%, which is much more than 1at.%, the contribution of $-\ln T$ term to resistivity must not be originating from Kondo-type scattering, but originate from the scattering of TLS. As mentioned in the investigation of low-temperature specific heat, TLS is a typical excitation in amorphous materials, and the existence of TLS was confirmed at the temperature below several Kelvin, which is consistent with the observation in resistivity. The existence of TLS scattering also proves the primary glassy state of $\text{Ti}_{41.5}\text{Cu}_{37.5}\text{Ni}_{7.5}\text{Zr}_{2.5}\text{Hf}_5\text{Sn}_5\text{Si}_1$ BMG, because for partially metallic glasses, the TLS scattering at low temperature will be absent, resulting from the change of microstructure of materials leading to the absence of TLS. The theoretical expression is $\rho = \rho_0(1 - C \ln T)$, by fitting the experimental data points, the value of fitting parameter C is obtained to be 3.746×10^{-4} , and the excitation temperature is about 15 K. Then the electron-phonon scattering leads to the resistivity change as a $-T^2$ dependence at temperature of 15-50 K which is far below the Debye temperature; the linear temperature dependence of resistivity in the third temperature region can

be understood as the enhancement of electron-phonon scattering resulting from the enhancement of degree of ordering compared with the strongly disordered metallic glasses, which results in the occurrence of $\rho \propto -T$ relation even at temperature below Debye temperature; similarly, the contribution of $-T$ term also mainly arises from electron-phonon scattering in amorphous matrix. However, the contribution of T^2 term to resistivity may originate from the different local ordering structure which is more effective at high temperature, one evidence that the value of ρ_{04} obtained from the fitting curve in the fourth temperature region is much higher than those obtained from the other three fitting curves, suggests the existence of different contribution to the resistivity.

In summary, the temperature dependences of electrical resistivity of $\text{Ti}_{41.5}\text{Cu}_{37.5}\text{Ni}_{7.5}\text{Zr}_{2.5}\text{Hf}_5\text{Sn}_5\text{Si}_1$ and $\text{Ti}_{40}\text{Zr}_2\text{Ni}_8\text{Cu}_9\text{Be}_{18}$ BMGs have been investigated. They show large resistivity compared with their crystalline duplicates, 258.89 and 251.46 $\mu\Omega\cdot\text{cm}$ for $\text{Ti}_{41.5}\text{Cu}_{37.5}\text{Ni}_{7.5}\text{Zr}_{2.5}\text{Hf}_5\text{Sn}_5\text{Si}_1$ and $\text{Ti}_{40}\text{Zr}_2\text{Ni}_8\text{Cu}_9\text{Be}_{18}$ BMGs, respectively, at 280 K; the temperature coefficient of resistivity, α , is negative over the whole temperature range of 6-280 K, as in good agreement with the characteristic of low-temperature resistivity for nonmagnetic metallic glasses. The negative TCR can be successfully interpreted by free-electron model proposed by Nagel. In addition, the microstructure of $\text{Ti}_{40}\text{Zr}_2\text{Ni}_8\text{Cu}_9\text{Be}_{18}$ BMG could be more disordered than that of $\text{Ti}_{41.5}\text{Cu}_{37.5}\text{Ni}_{7.5}\text{Zr}_{2.5}\text{Hf}_5\text{Sn}_5\text{Si}_1$ BMG which has been verified that there exists local ordering structure in the glassy matrix, resulting in the change of TCR. The electrical resistivity of $\text{Ti}_{41.5}\text{Cu}_{37.5}\text{Ni}_{7.5}\text{Zr}_{2.5}\text{Hf}_5\text{Sn}_5\text{Si}_1$ BMG is composed of the structural components of both fractions (amorphous and ordering structure). Two main scattering mechanisms, TLS scattering, electron-phonon scattering can be applied for interpreting the temperature dependence of electrical resistivity at low temperature and high temperature. In addition, the electron-phonon scattering is enhanced at higher temperature due to the contribution of local ordering structure.

3.4 Conclusion

The low-temperature specific heat and electrical resistivity of Ti-based bulk metallic glasses have been investigated over the temperature range from several Kelvin to ambient temperature, and some results have been obtained.

1. The contributions of electron, phonon and two-level systems to the low-temperature specific heat are successfully distinguished in $\text{Ti}_{41.5}\text{Cu}_{37.5}\text{Ni}_{7.5}\text{Zr}_{2.5}\text{Hf}_5\text{Sn}_5\text{Si}_1$ BMG, the coefficients of electron and phonon specific heat are $\gamma=3.51\text{-}3.58$ $\text{mJ mol}^{-1} \text{K}^{-2}$ and $\beta=130.0$ $\mu\text{J mol}^{-1} \text{K}^{-4}$, respectively.
2. The two-level systems effects in metallic glasses are observed below several Kelvin by studying the low-temperature specific heat as well as electrical resistivity, and is significantly different from that in insulating glasses which generally occurs below 1 K. In addition, the density of tunneling states of $\text{Ti}_{41.5}\text{Cu}_{37.5}\text{Ni}_{7.5}\text{Zr}_{2.5}\text{Hf}_5\text{Sn}_5\text{Si}_1$ BMG at several Kelvin is about 2.62×10^{-4} which is much higher than that of superconductive metallic glasses which is about 10^{-6} order per atom similar to many insulating glasses, as indicates the large difference of density of tunneling states under the different condition of with and without large quantity of conduction electrons. The high density of tunneling states may be due to the conduction electron-assisted tunneling.

-
3. The contribution of phonon to low-temperature specific heat of $\text{Ti}_{41.5}\text{Cu}_{37.5}\text{Ni}_{7.5}\text{Zr}_{2.5}\text{Hf}_5\text{Sn}_5\text{Si}_1$ BMG in a wide temperature range of 4.2-100 K can be successfully described by introducing localized harmonic vibration mode (Einstein oscillator mode) into the typical Debye model, and the VDOS, derived from the specific heat, shows an excess peak at 5.95 meV that corresponds to the boson peak, and indicates that the Einstein oscillator induces the boson peak in BMGs. The presence of an Einstein oscillator suggests the existence of the vibrations of loose atoms in an independent localized harmonic mode in the highly random packed metallic glasses. Debye temperature θ_D and Einstein temperature θ_E are calculated to be 327 and 89 K, respectively.
 4. BMGs show large resistivity compared with their crystalline counterparts, 258.89 and 251.46 $\mu\Omega\cdot\text{cm}$ for $\text{Ti}_{41.5}\text{Cu}_{37.5}\text{Ni}_{7.5}\text{Zr}_{2.5}\text{Hf}_5\text{Sn}_5\text{Si}_1$ and $\text{Ti}_{40}\text{Zr}_2\text{Ni}_8\text{Cu}_9\text{Be}_{18}$ BMGs at 280 K, respectively, and a small negative temperature coefficient of resistivity over the whole temperature range from 6 to 280 K. The negative TCR can be successfully explained by free-electron model proposed by Nagel.
 5. The composite microstructure, local ordered structure/glassy matrix, of $\text{Ti}_{41.5}\text{Cu}_{37.5}\text{Ni}_{7.5}\text{Zr}_{2.5}\text{Hf}_5\text{Sn}_5\text{Si}_1$ BMG, has been found by means of low-temperature resistivity measurement, and the existence of local ordering structure leads to the change of temperature dependence of TCR. However, microstructure of $\text{Ti}_{40}\text{Zr}_2\text{Ni}_8\text{Cu}_9\text{Be}_{18}$ BMG is confirmed to be more disordered than that of $\text{Ti}_{41.5}\text{Cu}_{37.5}\text{Ni}_{7.5}\text{Zr}_{2.5}\text{Hf}_5\text{Sn}_5\text{Si}_1$ BMG, as is consistent with the observation of HRTEM.
 6. The electrical resistivity of $\text{Ti}_{41.5}\text{Cu}_{37.5}\text{Ni}_{7.5}\text{Zr}_{2.5}\text{Hf}_5\text{Sn}_5\text{Si}_1$ BMG is composed of the structural components of two fractions: amorphous and local ordered structure. Two main scattering mechanisms, TLS scattering, electron-phonon scattering can be applied for interpreting the temperature dependence of electrical resistivity at low and high temperature. In addition, the electron-phonon scattering is enhanced at higher temperature due to the contribution of local ordering structure.

CHAPTER 4

THERMALLY INDUCED STRUCTURAL TRANSFORMATIONS

4.1 Background and Motivation

Many desirable properties of amorphous materials including excellent physical, chemical and mechanical properties result from their random atomic structure. However, since a glass can be described as an undercooled melt, this amorphous structure is thermodynamically metastable, so it tends to undergo subtle structural changes (structural relaxation) or transform to an equilibrium crystalline structure by a series of continuous transformations once external energies are supplied either thermally by heat treatments or mechanically by application of external stresses (in this chapter, we will focus on the thermally induced transformations including structural relaxation, glass transition and crystallization). The transformation into a more stable crystalline structure may result in either degradation or upgrade of properties for amorphous materials, which is dependent on the nature of the transformed microstructure of different amorphous materials. So, it makes us to be concerned about the behavior, nature and the mechanism of the thermally induced transformations as well as their effects on the subsequent thermodynamics and kinetics of crystallization and mechanical properties, and finally finding out the correlation between the microscopic mechanisms and the macroscopic properties.

As a result of the supercooling necessary for glass formation, a metallic glass is metastable with respect to the ideal glassy state below the glass formation temperature. During isothermal annealing below T_g , the glass tries to reach the ideal glassy state. This process is designated as structural relaxation [Chen, 1980; Van den Beukel, 1986]. Further annealing leads to crystallization. This latter process represents the tendency of the material to acquire its equilibrium crystalline structure. Such a transformation can be easily observed during an isochronous heating experiment. Fig. 4-1 shows the enlarged drawing of isochronous DSC curve of $\text{Ti}_{41.5}\text{Cu}_{37.5}\text{Ni}_{7.5}\text{Zr}_{2.5}\text{Hf}_5\text{Sn}_5\text{Si}_1$ BMG. Three transformation regions which are marked with different shadows correspond to structural relaxation (exothermic), glass transition (endothermic) and crystallization (exothermic) with increase in temperature. The original amorphous state transforms to ideal amorphous state through structural relaxation, and then the amorphous phase transforms to supercooled liquid by glass transition, followed by transformation to crystals with increase in temperature.

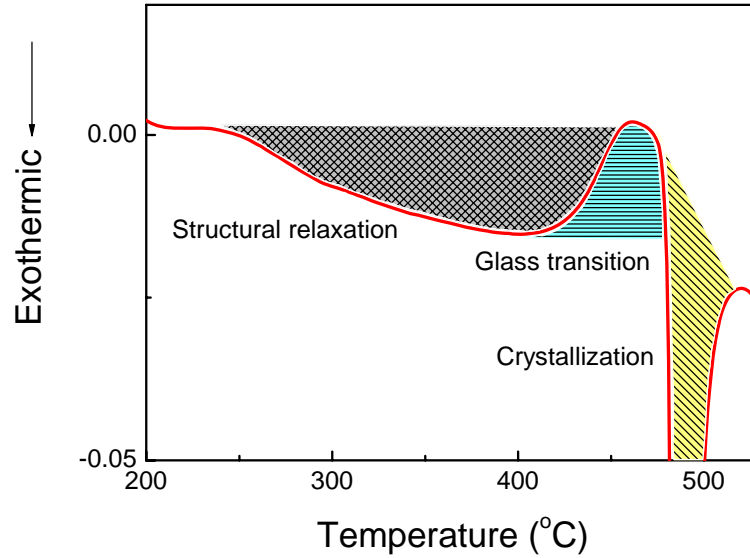


Fig. 4-1 The partial enlarged drawing of isochronous DSC curve of $\text{Ti}_{41.5}\text{Cu}_{37.5}\text{Ni}_{7.5}\text{Zr}_{2.5}\text{Hf}_5\text{Sn}_5\text{Si}_1$ BMG. The shadow regions are corresponding to structural relaxation, glass transition and crystallization

So far, as an elementary and important scientific question, the complex transformation (devitrification process of amorphous materials: structural relaxation, glass transition and crystallization) has already been studied quite extensively by researchers with traditional DSC experiments in order to describe the thermodynamics and kinetics of the transformation, combining with performing ex-situ X-ray diffraction techniques, microstructure observation on the glassy alloys with different heat treatments to obtain the structural information upon devitrification to get a complete picture of thermally induced devitrification behavior, as is crucial for understanding the behavior, essence and the mechanism of the thermally induced transformation of glassy alloys. It should be noted that although extensive work has been done on the thermally induced devitrification, it just focused on a limited field or limited glassy alloys systems, and much work is still needed to be done. In this study, we focus our work not only on the typical fully BMGs but also on the marginal glassy alloys whose microstructure is not fully amorphous phase. Actually the existing BMGs are mostly marginal glassy alloys whose nature are complicated with respect to the typical fully glassy alloys, which may lead to the different thermal induced transformation behavior and the corresponding mechanism for their different nature and the sensitivity of microstructure on the thermal activation. $\text{Ti}_{41.5}\text{Cu}_{37.5}\text{Ni}_{7.5}\text{Zr}_{2.5}\text{Hf}_5\text{Sn}_5\text{Si}_1$ and $\text{Ti}_{40}\text{Zr}_{25}\text{Ni}_8\text{Cu}_9\text{Be}_{18}$ BMGs are typical Ti-based BMGs which show the typical marginal characteristic, phase separation-like structure or quenched-in nuclei, so these two alloys should be a good medium for investigating the unique behavior and mechanism of thermally induced structural transformations and their effects on mechanical properties.

In this chapter, the behavior and mechanisms of thermally induced structural transformations including structural relaxation, glass transition and crystallization will be presented based on the analysis of thermodynamics and kinetics as well as the microstructure observation and phase analysis by in-situ neutron diffraction. Amongst the above work, structural relaxation and glass transition will be described in the framework of the traditional free volume theory; crystallization kinetics of isothermal and isochronous process will be investigated based on the appropriate

application of the well-known JMA model and a modified kinetic model called Starink model here constructed by considering the soft impingement for detecting the possibility of different nucleation and growth mechanism at these two thermal activated conditions. With regard to the effects of thermally induced structural transformations on the thermodynamic and kinetic properties as well as the mechanical properties, they will be discussed in the following chapters.

4.1.1 Structural Relaxation

Metallic glasses produced by rapid quenching from the melted liquid are in a metastable state; if the melted liquid is cooled with a sufficient rapid cooling rate to avoid crystallization, then a glass is formed in which the liquid-like structure is preserved with a solid-like viscosity. Due to the frozen-in disorder, the Gibbs energy of a glass is higher than that of a crystal. This excess energy provides a thermodynamic driving force for spontaneous structural rearrangements generally referred to as structural relaxation which is an intrinsic property of the amorphous state. The notion of structural relaxation in metallic glasses was firstly introduced phenomenologically as the totality of atomic rearrangement processes bringing the amorphous metastable state closer to metastable equilibrium state [Chen, 1976; Srolovitz et al., 1981]. The structural relaxation is generally considered to consist of two types of short-range ordering, namely, chemical short-range ordering (CSRO) and topological short-range ordering (TSRO) [Van den Beukel et al., 1983]. The former α relaxation is a reversible process and represents the changes in local surroundings of a given atom, which is comparable to short-range ordering in crystalline alloys; while the latter called β relaxation is an irreversible process of free volume. The structural relaxation of metallic glasses leads to a decrease of the amount of free volume (TSRO) when the sample was annealed in the temperature range preceding the crystallization, and an increase of the degree of short-range ordering (CSRO) when the sample was annealed in the lower range of temperature and a decrease of the residual stresses [Van den Beukel et al., 1984].

It is generally considered that structural relaxation is mainly irreversible, resulting in irreversible changes of the physical, chemical and mechanical properties. In particular, the loss of the ability to undergo viscous flow leads to severe embrittlement and deterioration of the mechanical properties of metallic glasses [Chen, 1980; Ashby et al., 2006]. The loss of the free volume upon structural relaxation is most often supposed to be the physical origin of embrittlement. It is therefore quite important to clarify the relaxation phenomenon not only for technical application of the amorphous alloys but also for understanding the nature of amorphous structure.

Structural relaxation can be detected by atom probe, DSC, XRD, electrical resistivity, density, acoustic emission, Mössbauer technique and positron annihilation spectroscopy (PAS), etc. Amongst these methods, with PAS it is possible to gain insight into changes in the size and/or concentration of open volume regions, for example those associated with plastic deformation [Flores et al., 2007]. Although PAS provides information about the distribution of free volume at the nano-scale, it is currently not possible to make quantitative measurements. Conversely, DSC has been used to characterize free volume changes in metallic glasses after structural relaxation, with several efforts focused on quantifying free volume differences [Van den Beukel et al., 1990; Slipenyuk et al., 2004; Launey et al., 2007]. So investigation on recovery enthalpy by using DSC is the most popular and simplest way to study the structural relaxation.

Structural relaxation in metallic glasses is of high scientific interest from a fundamental scientific and engineering point of view not only because it has profound influences on the physical, chemical and mechanical properties but also because it can yield information on materials processes governing the glassy kinetics. Although extensive investigation has been performed on the structural relaxation in metallic glasses, so far, some scientific questions about structural relaxation are still in debate and some are still needed to be answered. Especially for the marginal bulk metallic glasses, the investigation on whose relaxation structural is vacant since the previous study on the structural relaxation was generally performed on the fully amorphous materials and avoiding on the marginal metallic.

4.1.1.1 Theory model

There are many types of glasses (including oxide, organic polymer, chalcogenide and metallic) and their structural relaxation has been followed by many types of “relaxation anomaly” of their physical properties. Examples include exponential saturation time dependency, linear or sigmoidal log-time dependency, overshooting, one maximum, one minimum or even combination of such time and complex temperature dependency following specific heat treatment.

Many models have been established to explain the various observed structural relaxation effects for different types of glasses, including Tool's, Kissinger, entropic, Narayanaswamy, Moynihan, Kovacs-Aklonis-Hutchinson-Ramox, activation energy spectrum, free volume, distribution of non-linear relaxations and stretched exponential, etc. As an effective theory which can quantitatively describe the kinetics of structural relaxation, the free volume theory will be adopted in this study, and its relevant theory will be shown as follow.

The notion of free volume was firstly proposed by Beuche, Turnbull and Cohen. They believed that the large fluidity of liquid was due to the existence of ‘vacancy’ in the liquid. The ‘vacancy’ can be described as the difference between the average volume of each molecule in the liquid and the actual volume of each molecule, namely, $\Delta V^* = V/N - V_1$. When ΔV^* is larger than a certain critical value, namely, when the size of the ‘vacancy’ can be comparable to an atom, it can be rearranged in the liquid without needing any energy, this excess volume is defined as free volume.

Free volume theory indicates that the motion of atom or molecule in the liquid is the process that atoms move to the neighboring vacancy, namely, is the process where the free volume is rearranged. The free volume in the liquid is dependent on the temperature and pressure, and decreases with increase in pressure and decrease in temperature. The free volume in the liquid can move continuously and is free-distributed. When the liquid is cooled, the free volume will be reduced, and the glass can be formed when the free volume is reduced to a certain critical value.

The structural relaxation kinetics of metallic glass has been explained by free volume theory, which has formulated by Cohen and Turnbull [Cohen et al., 1959], thereafter established by Cohen and Grest [Cohen et al., 1979], and developed by Spaepen [Spaepen, 1977] to describe the mechanical properties of amorphous alloys. Van den Beukel et al. have done extensive outstanding work related to the free volume [Van den Beukel et al, 1983, 1984, 1990; Van den Beukel, 1986]. They have successfully interpreted the glass transition and relaxation of glass during the thermal analysis measurement, and described the temperature dependence of some physical behaviors of metallic glasses, viscosity, electrical resistivity, modulus, etc.

The free volume model (FVM) describes the atomic mobility of amorphous solids in terms of the free volume available for the atoms. Atoms being surrounded by a critical free volume v^* can

perform atomic movements in their close neighborhood. The probability for an atom being surrounded by free volume v^* [Cohen et al., 1959; Turnbull et al., 1970] is called the structural defect concentration c_f . The structural relaxation is identified as an approach of the amorphous solid to the quasi-equilibrium defect concentration $c_{f,e}$. By rapid solidification of liquid alloys an excess defect concentration $c_{f,0}$ is frozen into the glassy state. Upon isothermal heating the sample $c_{f,0}$ reduces towards $c_{f,e}$. By subsequent heating of the sample to a higher temperature, the defect concentration increases until equilibrium has again been established. These processes of annihilation and creation of free volume can experimentally be determined directly by measuring the specific heat changes of amorphous alloys under isothermal and non-isothermal conditions.

Fig. 4-2 shows a sketch presenting the free volume history of a glass during its production by rapid quenching and a subsequent warming up until crystallization occurs [Van den Beukel et al., 1990]. The quantity plotted on the ordinate is the so called “reduced free volume” $x = v_f / v^*$;

v_f =free volume per atomic volume; v^* =constant of order 0.1. The straight line AB has the equation

$$x_{eq} = \frac{T - T_0}{B} \quad (4-1)$$

and represents an approximation to the reduced free volume in thermodynamic equilibrium. This equation is based on the observation that in a (rather narrow) region around the glass temperature T_g the equilibrium viscosity of glasses can be described by

$$\eta_{eq} = \eta_0 \exp\left(\frac{B}{T - T_0}\right) = \eta_0 \exp\left(\frac{1}{x_{eq}}\right) \quad (4-2)$$

The first equality represents the well known phenomenological Fulcher-Vogel equation; the second equality represents the interpretation of viscosity in terms of the free volume model [Cohen et al., 1959; Spaepen, 1977]: the viscosity should be inversely proportional to the “flow defect concentration” $c_f = \exp\left(-\frac{1}{x}\right)$. Then Eq. 4-1 follows directly from Eq. 4-2. It is noted that, according to a study by Cohen and Grest [Cohen et al., 1979], Eq. 4-1 has to be considered as an approximation which is valid in a limited temperature range.

During the rapid quench which produces the glass from the melt, in the high temperature region (AB) the kinetics of free volume annihilation is fast enough for equilibrium to be maintained. At lower temperatures (BC) this is no longer the case and an excess (non equilibrium) amount of free volume x_0 is frozen in. x_0 corresponds to the equilibrium value of x at temperature T_f , the so called “fictive temperature”. When subsequently the specimen is put into a DSC and warmed up at a constant heating rate, the excess free volume anneals out and x will move into the direction of the equilibrium line (CD). This yields a release of energy and the process is often called topological short range ordering, which is a part of the structural relaxation of the glass.

At D, x crosses the equilibrium line AB because the kinetics is too slow to follow the increase of x_{eq} due to the continuous increase of temperature. From now on x is smaller than the equilibrium value. This means that from D a new free volume must be produced in order to attain equilibrium; this is an endothermic process. This is what happens in the range DEF. At E, equilibrium is attained. On EF the kinetics of free volume production is fast enough to keep up

with the linearly increasing $x_{eq}(T)$. Finally, in F at temperature T_x , crystallization occurs.

As annealing out of free volume yields a release of energy, production of free volume will require energy. Therefore we put for the change in energy due to the change in free volume $(\Delta U)_{fv} = \beta \Delta x$. It follows that the contribution to the specific heat is given by

$$(\Delta c)_{fv} = \left(\frac{d\Delta U}{dT} \right)_{fv} = \beta \frac{dx}{dT} \quad (4-3)$$

In Fig. 4-2, dx/dT in the course of an experiment at constant heating rate (CDEF) is plotted vs T (dashed curve). It shows the structural relaxation ($dx/dT < 0$) followed by the glass transition. The result is very similar to the observed $\Delta C_p(T)$ in DSC experiments.

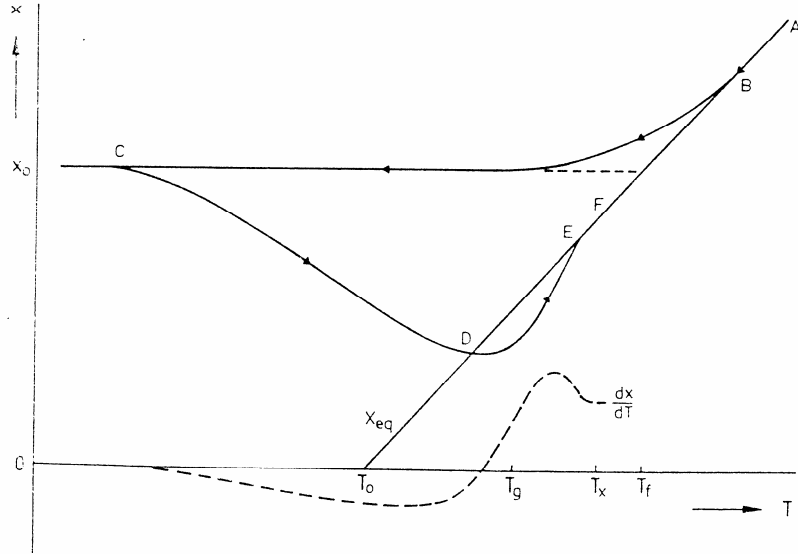


Fig. 4-2 Free volume vs. temperature of a glass during rapid quenching and subsequent continuous heating [Van den Beukel et al, 1990]

In order to make this picture more quantitative, the kinetics of free volume annihilation and production must be known. It has been shown that the approach to equilibrium during structural relaxation of metallic glasses caused by annealing can be described by annihilation and/or production of structural defects. The proper differential equation describing the change of the structural defect concentration c_f at a constant temperature T with the time t of relaxation for both as-quenched or pre-annealed samples is proposed by Tsao and Spaepen and given by [Tsao et al., 1985; Duine et al., 1992]

$$\frac{dc_f}{dt} = -k_r c_f (c_f - c_{f,e}) \quad (4-4)$$

where $k_r = \nu_r \exp(-Q_r / RT)$ is the rate constant of relaxation, Q_r is the activation energy for relaxation, ν_r is the attempt frequency and $c_{f,e}$ the equilibrium defect concentration at the temperature of isothermal annealing.

Under non-isothermal structural relaxation conditions at a constant heating rate θ , c_f is described by

$$\frac{dc_f}{dT} = -k_r c_f (c_f - c_{f,e}) / \theta \quad (4-5)$$

4.1.1.2 Mechanism of structural relaxation

Since the structural relaxation is the process of atomic rearrangement, the mode of the atomic rearrangement can reflect the mechanism of structural relaxation. Many investigations indicate that two mechanisms may be the governing mechanism for the structural relaxation process: local rearrangement through the single atomic motion governed by the solid-state short-range diffusion mechanism, and the complete rearrangement of the backbone of the structure through the collective hopping mechanism, as is still in debate. For example, Ehmler et al. [Ehmler et al., 1998] found that the atomic rearrangements during the structural relaxation involved the collective hopping mechanism for the small and medium size atoms in the $\text{Zr}_{46.75}\text{Ti}_{8.25}\text{Cu}_{7.5}\text{Ni}_{10}\text{Be}_{27.5}$ BMG through isotope effect measurements, whereas, Gallino et al. [Gallino et al., 2007-a] reported that the activation energy obtained from the Arrhenius fit was comparable to the activation energy required for the diffusion of the medium size atoms, suggesting that solid-state diffusion is the governing mechanism for the enthalpy relaxation process of the $\text{Zr}_{58.5}\text{Cu}_{15.6}\text{Ni}_{12.8}\text{Al}_{10.3}\text{Nb}_{2.8}$ BMG.

4.1.2 Crystallization

The properties of materials are believed to be determined by their microstructure, namely, the nature, perfection, and spatial distribution of their component phases. For metallic glass, it is of significance to know the crystallization behavior and its corresponding mechanism for realizing the control of the microstructure of precipitates and finally expanding their engineering applications. The crystallization of metallic glasses upon heating yield both stable and metastable phases, is of first order phase transformation and follows a nucleation and growth process.

4.1.2.1 Kinetics of crystallization

The crystallization kinetics of metallic glasses is a typical solid-state reaction for the solid-state reaction is characterized by the existence of a specialized zone of locally enhanced reactivity at the reaction interface. The shape of thermal analysis (TA) curve is characterized by a kinetic model function $f(\alpha)$ derived from the physico-geometric assumption of the reaction interface movement. The rate of the kinetic process can be expressed as a product of temperature dependent rate constant $K(T)$ and α dependent kinetic model function $f(\alpha)$:

$$\frac{d\alpha}{dt} = f(\alpha)K(T) \quad (4-6)$$

where t and $K(T)$ are the time and temperature dependent rate constant, respectively. The kinetic model function $f(\alpha)$ should be invariable with respect to procedural parameters such as sample mass and heating rate (non-isothermal conditions) or temperature (isothermal conditions).

Generally, $K(T)$ is described assuming Arrhenius form:

$$K(T) = K_0 \exp\left(-\frac{E_a}{RT}\right) \quad (4-7)$$

where the apparent activation enthalpy E_a and pre-exponential factor K_0 are the kinetic parameters that should not depend on the temperature T and the fractional conversion α . In addition, the rate

of the kinetic process $d\alpha/dt$ is proportional to the measured specific heat flow ϕ , normalized per sample mass (W/g):

$$\frac{d\alpha}{dt} = \frac{\phi}{\Delta H_c} \quad (4-8)$$

where ΔH_c corresponds to the total enthalpy change associated with the solid-state reaction process. The fractional conversion α can be easily obtained by partial integration of isothermal or non-isothermal TA curve. So the TA curve can be described as

$$\phi = \Delta H_c K_0 \exp\left(-\frac{E_a}{RT}\right) f(\alpha) \quad (4-9)$$

The aim of the kinetics analysis is to find out the “two kinetic parameters”, E_a and K_0 , and the kinetic model function $f(\alpha)$.

The Johnson-Mehl-Avrami (JMA) model [Avrami, 1939; Avrami, 1940; Avrami, 1941], standard nucleation-growth model, is widely accepted for the analysis of isothermal crystallization kinetics for metallic glasses, whose expression is:

$$\alpha = 1 - \exp[-(Kt)^n] \quad (4-10)$$

where n is the well-known Avrami exponent relating to the nucleation and growth mechanism, whose values and the corresponding physical meanings are summarized in Table 4-1. This model describes the time dependence of the fractional crystallization α . The rate equation can be obtained from Eq. 4-10 by differentiation with respect to time:

$$\frac{d\alpha}{dt} = Kn(1-\alpha)[- \ln(1-\alpha)]^{1-\frac{1}{n}} \quad (4-11)$$

So the kinetic model function of the JMA model can be expressed as

$$f(\alpha) = n(1-\alpha)[- \ln(1-\alpha)]^{1-\frac{1}{n}} \quad (4-12)$$

The kinetic equation for the JMA model can be written as

$$\phi = \Delta H_c Kn(1-\alpha)[- \ln(1-\alpha)]^{1-\frac{1}{n}} \quad (4-13)$$

It should be emphasized that the validity of the JMA equation is based on the following assumptions [Henderson, 1979; Shepilov et al., 1994; Málek, 2000]:

- (i) Isothermal crystallization conditions,
- (ii) Homogeneous nucleation or heterogeneous nucleation at randomly dispersed second-phase particles,
- (iii) Growth rate of new phase is controlled by temperature and is independent of time,
- (iv) Low anisotropy of growing crystals.

Table 4-1

Physical meaning of Avrami exponent n in JMA equation [Christian, 2003]

(a) Polymorphic changes, discontinuous precipitation, eutectoid reactions, interface controlled growth, etc

Conditions	n
Increasing nucleation rate	>4
Constant nucleation rate	4
Decreasing nucleation rate	3-4
Zero nucleation rate (saturation of point sites)	3
Grain edge nucleation after saturation	2
Grain boundary nucleation after saturation	1

(b) Diffusion controlled growth

Conditions	n
All shapes growing from small dimensions, increasing nucleation rate	>2.5
All shapes growing from small dimensions, constant nucleation rate	2.5
All shapes growing from small dimensions, decreasing nucleation rate	1.5~2.5
All shapes growing from small dimensions, zero nucleation rate	1.5
Growth of particles of appreciable initial volume	1~1.5
Needles and plates of finite long dimensions, small in comparison with their separation	1
Thickening of long cylinders (needles) (e.g. after complete end impingement)	1
Thickening of very large plates (e.g. after complete edge impingement)	0.5
Precipitation on dislocations (very early stages)	$\sim 2/3$

It is well-known that the crystallization mechanism can be determined in terms of the calculated Avrami exponent. If the Avrami exponent satisfies the linear JMA equation, keeping a constant over wide volume fraction, the nucleation and growth of precipitates are basically controlled by a certain crystallization mode. However, the Avrami exponent often deviates from the linear JMA mode, which means the mechanism of crystallization is beyond the assumptions of JMA equation and becomes more complicated [Holzer et al., 1991; Bakai et al., 2002]. Thanks to the local Avrami exponent n_{loc} proposed by Calka [Calka et al., 1988], which describes the Avrami exponent as a function of the transformed volume fraction of precipitates, the mechanism of the overall phase transformation processes can be successfully explained, especially for those involving the complicated stages depending on the transformed volume fraction. The local Avrami exponent can be calculated by the following equation [Calka et al., 1987]:

$$n_{loc}(\alpha) = \frac{\partial \ln(-\ln(1-\alpha))}{\partial \ln(t-t_0)} \quad (4-14)$$

However, it should be noted that the appropriate application of the kinetic model is essential for the calculation of Avrami exponent and further influences the determination of crystallization mechanism. Our recent study reveals that deriving the changeable kinetic exponent by the local Avrami exponent may lead to errors if an inappropriate kinetic model is chosen, resulting in the misinterpretation of phase transformation mechanism, as will be shown and verified in this study.

So we emphasize that the applicability of JMA model should be test before use, and other kinetic models should be in use in case of the invalidity of JMA model.

In regard to the problem that how to test the application of JMA model, a reliable test is based on the properties of the $y(\alpha)$ and $z(\alpha)$ functions [Málek, 2000]. In isothermal conditions these functions are defined as

$$y(\alpha) = \phi \quad (4-15a)$$

$$z(\alpha) = \phi t \quad (4-15b)$$

In non-isothermal conditions these functions are defined as follows:

$$y(\alpha) = \phi \exp\left(-\frac{E_a}{RT}\right) \quad (4-16a)$$

$$z(\alpha) = \phi T^2 \quad (4-16b)$$

For practical reasons the $y(\alpha)$ and $z(\alpha)$ functions are normalized within the (0 1) range. These functions exhibit maxima at α_M and α_p^∞ , respectively. The maximum of the $y(\alpha)$ function for the JMA model depends on the value of the kinetic exponent:

$$\alpha_M = 0 \quad \text{for } n \leq 1 \quad (4-17a)$$

$$\alpha_M = 1 - \exp\left(\frac{1}{n} - 1\right) \quad \text{for } n > 1 \quad (4-17b)$$

The latter is a constant for the JMA model

$$\alpha_p^\infty = 0.632 \quad (4-18)$$

The validity of the JMA can easily be verified by checking the maximum α_p^∞ of the $z(\alpha)$ function. If the maximum falls into the $0.61 \leq \alpha_p^\infty \leq 0.65$ range then the experimental data probably correspond to the JMA model. If the maximum is shifted to lower values of fractional conversion ($\alpha_p^\infty < 0.6$), the conditions of validity of the JMA model are not fulfilled. Such a displacement indicates increasing complexity of the process and can be caused, for example, by the influence of surface nucleation. Nevertheless, the complex behavior can also be observed when the temperature distribution within the sample is affected considerably by liberation of the crystallization heat at the growth interface. If the dimensions of the crystallized phase are small, the rate of the process is controlled by nucleation in assemblage of similar particles, and the kinetic exponent is $n = 1$. The maximum of the $y(\alpha)$ function is then close to zero, i.e. $\alpha_M = 0$. However, if the maximum of the $y(\alpha)$ function is shifted to higher values, it clearly indicates an increasing influence of the product (i.e. crystallized phase) to the overall crystallization kinetics. A typical example is spherulite crystal growth morphology where the spatial constraints in highly viscous media play an important role and the crystallized phase further increases the rate of the process in the preferred direction.

The deviations from the JMA for describing the crystallization kinetics in amorphous materials have been reported [Xing et al., 1999; Málek, 2000; Starink, 2001]. Reasons of such deviations have been attributed to the breakdown of the assumptions required for the JMA model. Some researchers proposed that the deviations might come from three reasons: the capillarity effect, the vacancy annihilation and the blocking due to the anisotropic growth [Starink, 2001]. Furthermore, in diffusion-controlled phase transformations such as the nanocrystallization of amorphous alloys, the overlap of diffusion fields surrounding the growing particles (soft impingement) should also be considered [F. Liu et al., 2007], however, only the strong impingement is believed to be responsible for the termination of growth for crystals in JMA theory. Actually, beside strong impingement, soft impingement also plays an important role in the termination of growth for crystals at the late stage [Pradell et al., 1997]. So introducing the soft impingement into the kinetics model is necessary and effective to solve the deviations from the JMA model. Based on the analysis above, Starink [Starink, 1997; Starink, 2001, Starink, 2004] proposed a theoretical model by introducing an impingement factor, λ , to solve the invalidity of JMA model in some cases, which can be expressed as:

$$\alpha = 1 - (1 + (\lambda - 1)(Kt)^n)^{-\frac{1}{\lambda-1}} \quad (4-19)$$

where λ ($\lambda > 1$) is the impingement factor. If $\lambda = 1$, Eq. 4-19 can be reduced to Eq. 4-10.

The kinetics model function, $f(\alpha)$, can be deduced as the following function:

$$f(\alpha) = n(1 - \alpha)^\lambda \left(\frac{(1 - \alpha)^{-(\lambda-1)} - 1}{\lambda - 1} \right)^{1-\frac{1}{n}} \quad (4-20)$$

The theoretical DSC heat flow functions for the phase transformations based on the modified kinetics model can be written as:

$$\phi = \Delta H_c K n (1 - \alpha)^\lambda \left[\frac{(1 - \alpha)^{-(\lambda-1)} - 1}{\lambda - 1} \right]^{1-\frac{1}{n}} \quad (4-21)$$

In addition, an empirical kinetics function with two parameters which was proposed by Sestak and Berggren [Sestak et al., 1971], and later simplified by Gorbachev [Gorbachev, 1980], was successfully used to give a quantitative description of the crystallization of amorphous alloy. It can be written as

$$f(\alpha) = \alpha^m (1 - \alpha)^n \quad (4-22)$$

which is usually named as SB(m, n) kinetic model, where the parameters m and n are defined as the relative contributions of acceleratory and decay regions of the kinetic process and they are also taken as kinetic parameters describing the shape of measured TA curve. The SB kinetic model can be used for a quantitative description of more complex crystallization processes involving partially overlapping nucleation and growth phases. The kinetic exponents, m and n , are characteristic of a particular crystallization process, however it is rather problematic to find their real physical meaning. The more information related to the SB(m, n) kinetic model is shown in reference [Gorbachev, 1980].

Henderson [Henderson, 1979] has shown that the validity of the JMA equation can be extended in non-isothermal conditions if the entire nucleation process takes place during the early stages of the transformation, and it becomes negligible afterward. The crystallization rate is defined only by

temperature and does not depend on the previous thermal history. The kinetic equation for the JMA model in the non-isothermal condition can be written as

$$\phi = \Delta H_c K_0 \exp\left(-\frac{E_a}{RT}\right) n(1-\alpha) [-\ln(1-\alpha)]^{1-\frac{1}{n}} \quad (4-23)$$

and the kinetic equation for the Starink model in the non-isothermal condition can be expressed as

$$\phi = \Delta H_c K_0 \exp\left(-\frac{E_a}{RT}\right) n(1-\alpha)^\lambda \left[\frac{(1-\alpha)^{-(\lambda-1)} - 1}{\lambda - 1} \right]^{1-\frac{1}{n}} \quad (4-24)$$

The original establishment of JMA model is based on the isothermal heating process, extending the JMA model and the Starink model into the non-isothermal condition can realize the determination of phase transformation mechanism in the non-isothermal condition through the calculation of Avrami exponent n .

4.1.2.2 Mechanism of nano-crystallization

Nano-crystalline alloys generally exhibit excellent properties which are hard to be realized in conventional crystalline and glassy alloys. And it is well known that annealing glassy alloy precursors is an effective way to prepare nano-crystalline alloys. Inoue [Inoue, 1994] indicated that the formation of a nano-crystalline structure from a glassy alloy should satisfy the following criteria: (i) multistage crystallization processes; (ii) high nucleation frequency; (iii) low growth rate; and (iv) enhancement of the thermal stability of the remaining glassy phase caused by the redistribution of a solute element at the nano-crystalline/glassy interface. In addition, the direct growth of the quenched-in nuclei in the glassy matrix is another way to form nano-crystalline alloys, and with regard to this, the general criteria indicated by Inoue mentioned above (item (i), (iii) and (iv)) should also be followed. It has been shown recently that a class of Ti and Zr glasses crystallizes to form nanometer size quasicrystals. Evidence of predominance of icosahedral cluster in the undercooled liquid has been established through X-ray scattering experiments using a synchrotron. It is argued that quasicrystals have low surface energy with the glass due to these icosahedral clusters. This leads to a nucleation advantage, resulting in the observed nano-quasicrystallization of these glasses [Chang et al., 2006].

4.1.3 Motivation

The development of superplastic precise forming technology, utilizing viscous flowing property exhibited by BMGs in the supercooled liquid region, leads to fabricating the products of BMGs and the wider applications of these alloys. However, during the process of superplastic forming of BMGs at high temperature, relaxation is inevitable and crystallization will occur if the unsuitable forming process is adopted. So it is meaningful to know the nature of the thermal induced transformations including structural relaxation, glass transition and crystallization, and their influences on the thermodynamics and kinetics of crystallization and the mechanical properties. In this chapter, only the relaxation and crystallization behaviors and their kinetics will be presented.

The structure of this chapter is as follows: (i) kinetics of structural relaxation; (ii) kinetics of crystallization and (iii) thermally induced structure transformations.

1. In the first section, structural relaxation of BMGs were realized through the samples annealed at

different temperature below T_g for different time approaching the metastable equilibrium state, however avoiding crystallization. The kinetics of structural relaxation was investigated through the enthalpy recovery method in the framework of free volume theory.

2. In the second section, detailed investigations were performed on the kinetics of crystallization for $\text{Ti}_{41.5}\text{Cu}_{37.5}\text{Ni}_{7.5}\text{Zr}_{2.5}\text{Hf}_5\text{Sn}_5\text{Si}_1$ and $\text{Ti}_{40}\text{Zr}_{25}\text{Ni}_8\text{Cu}_9\text{Be}_{18}$ BMGs under the condition of both isochronous and isothermal heating. Appropriate kinetics model was adopted after discussing the applicability of JMA model utilizing the method proposed by Malek to determine the mechanism of crystallization.

3. In the third section, the thermally induced phase transformations and the microstructural changes under the condition of isochronous and isothermal heating were detected.

4.2 Experiment

(1) Enthalpy relaxation

A schematic representation of the entire temperature program is shown in Fig. 4-3. To erase the thermal history of metallic glasses, each sample was heated from room temperature to a certain temperature (about 20 °C above T_g) at a heating rate of 20 K/min (since in this scan the material reaches its equilibrium state), and then immediately cooled to room temperature at a cooling rate of 50 K/min, then heat the sample to the isothermal annealing temperature (387, 397, 412 and 422 °C for $\text{Ti}_{41.5}\text{Cu}_{37.5}\text{Ni}_{7.5}\text{Zr}_{2.5}\text{Hf}_5\text{Sn}_5\text{Si}_1$, 273, 283, 293 and 303 °C for $\text{Ti}_{40}\text{Zr}_{25}\text{Ni}_8\text{Cu}_9\text{Be}_{18}$) at a heating rate of 30 K/min and anneal for different period of time (5 min-12 h). After each isothermal annealing, the sample was heated up to high temperature to complete the crystallization (700 and 600 °C for $\text{Ti}_{41.5}\text{Cu}_{37.5}\text{Ni}_{7.5}\text{Zr}_{2.5}\text{Hf}_5\text{Sn}_5\text{Si}_1$ and $\text{Ti}_{40}\text{Zr}_{25}\text{Ni}_8\text{Cu}_9\text{Be}_{18}$, respectively) at a heating rate of 20 K/min and then immediately cooled down to room temperature at a heating rate of 50 K/min for the following calculation of recovery enthalpy. Finally, this heating and cooling cycle was repeated using the same procedure as before for baseline correction. In all experiments, three replicates were analyzed. The relaxation enthalpy ΔH_{relax} was determined by measuring the overshoot endothermic enthalpy around T_g of an annealed sample with respect to the as-cast sample, as indicated on the heating curves shown in Fig. 4-4. The DSC was calibrated using Indium and Zinc for temperature and heating flow (melting point and ΔH_m are 156.6 °C and 3.26 kJ/mol for Indium, are 419.5 °C and 7.35 kJ/mol for Zinc).

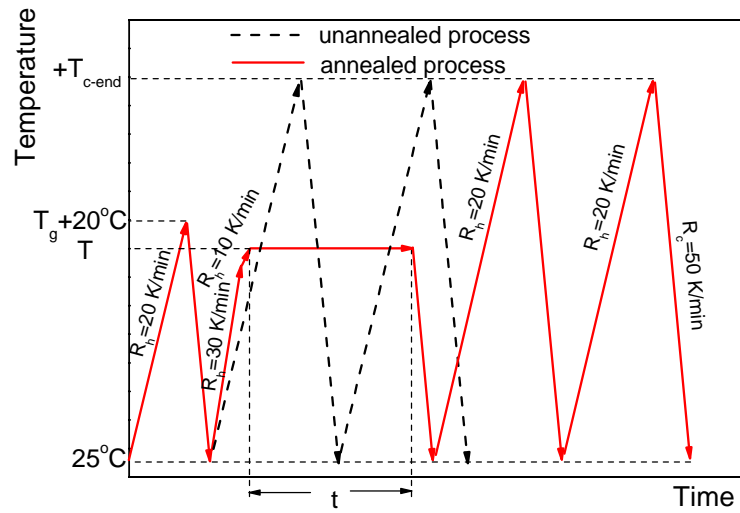


Fig. 4-3 Schematic representation of DSC temperature profile used to measure the enthalpy relaxation of the glass

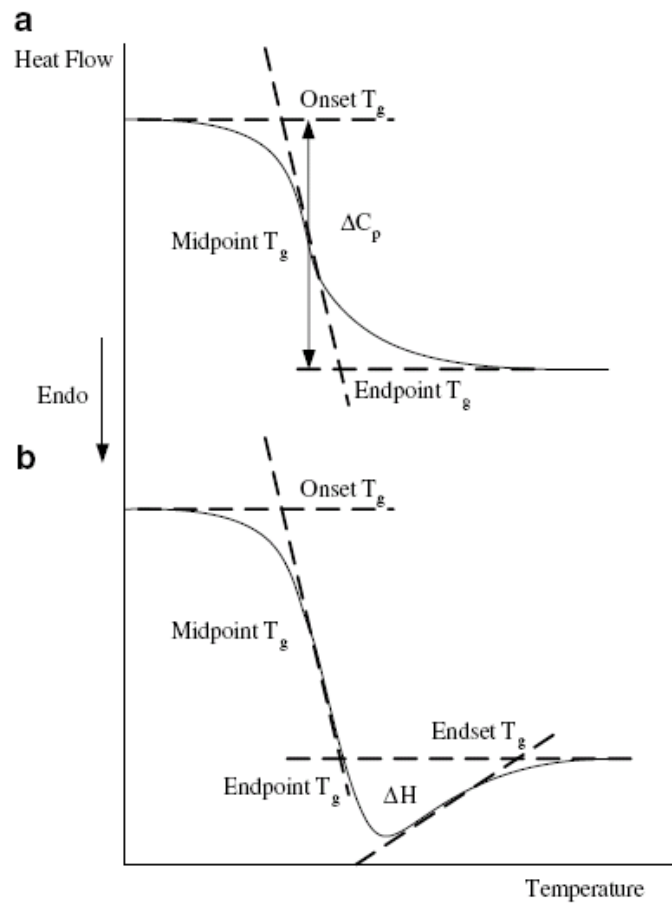


Fig. 4-4 Glass transition measured using DSC for an unannealed sample showing the locations of the onset, midpoint, endpoint T_g values and change of heat capacity ΔC_p at T_g ; (b) an annealed sample where the area under the endotherm associated with T_g is defined as enthalpy recovery ΔH ([Y. Liu et al., 2007])

(2) Crystallization kinetics

Isothermal and isochronous DSC measurements were performed on the as-cast samples to investigate the crystallization kinetics. For $\text{Ti}_{41.5}\text{Cu}_{37.5}\text{Ni}_{7.5}\text{Zr}_{2.5}\text{Hf}_5\text{Sn}_5\text{Si}_1$ BMG, heating rates of 5 to 40 K/min were selected for the non-isothermal DSC analysis, while several temperatures (430, 435, 438, 440 °C) between real T_g and T_x were selected for the isothermal DSC analysis. While for $\text{Ti}_{40}\text{Zr}_{25}\text{Ni}_8\text{Cu}_9\text{Be}_{18}$ BMG, only the isochronous heating with 10-40 K/min was performed on this sample.

(3) Phase and microstructure transformations

Phase transformations were identified by in-situ neutron diffraction. In-situ neutron diffraction was studied on the D1B-CRG diffractometer at Institute Laue Langevin in Grenoble at the 2.518 or 2.524 Å wavelength, spectra during continuous heating at 2 K/min under vacuum were recorded every 5 minutes using a position sensitive detector covering 80° in 2-theta. The sample was heated in the bulk form and during the heating treatment was continuously under high secondary vacuum, so that no oxidation mechanism could interfere with crystallization. Post-mortem X-ray diffraction studies have also been performed on the samples after neutron diffraction experiments. Data reduction was done with the LAMP and FULLPROF programs of ILL. Microstructure transformations were observed by SEM and TEM on the annealed samples which were annealed at different crystallization stages for the same time and isothermally annealed at the same temperature between T_g and T_x for different time.

4.3 Kinetics for Structural relaxation

Structural relaxation occurring in amorphous materials is recognized as an important factor related to changes in physical properties, which is due to atomic (molecular) cooperative rearrangements that lead to changes in free volume or configurational entropy. Relaxation phenomena have been widely studied in polymeric, molecular and inorganic glasses by a variety of techniques, particularly enthalpy relaxation [Hammond et al., 2003]. In contrast, only a few studies of structural enthalpy relaxation of metallic glasses have been reported. Due to limited information on the enthalpy relaxation kinetics of metallic glasses, especially for BMGs which consist of large quantities of short-range ordering structure or even quenched-in nuclei, its relationship to atomic mobility and thermal stability is largely unexplored. On the other hand, the glass transition temperature has been proven to be an effective indicator for thermal stability. Consequently, the glass transition and enthalpy relaxation studies of metallic glasses are suggested to have practical use in the prediction of thermal stability, and the knowledge of the relationship between enthalpy relaxation and annealing temperature obtained in the current study may help us to prevent the undesired changes during application of the BMGs.

The investigation on the relaxation recovery enthalpy by using DSC provides a direct way to study the structural relaxation of glass, and finally being correlated with the GFA, thermal stability of metallic glasses and the structural relaxation behavior.

4.3.1 Theory of Enthalpy Relaxation

The enthalpy recovery theory will be presented as follows [Y. Liu et al., 2007]. Fig. 4-5 shows an illustration of the enthalpy change during unannealing and annealing experiments. Line AB is

the liquid line (melt), and Line BC is the supercooled melt line (the melting without crystallization at temperature below melting temperature T_m). Line BL is the isothermal crystallization process at T_m . Line ML is the crystal line. Path ABCDE represents the cooling process after melting at cooling rate R_c . Path EDFCBA represents reheating process at heating rate R_h , through which T_g and ΔC_p of unannealed sample were determined. Path DG represents the isothermal annealing process at annealing temperature T_a , where ΔH is the released enthalpy through relaxation. H_i and H_t are the enthalpies at the beginning of annealing and at the annealing point for time t , respectively. Then:

$$\Delta H = H_i - H_t \quad (4-25)$$

Path HGJKBA represents the reheating process at heating rate R_h after annealing, through which an endothermic overshoot is observed in the glass transition range (Fig. 4-4). This overshoot is due to the rapid recovery of the lost enthalpy ΔH or the extra entropy through the annealing. The values of the lost enthalpy ΔH in this study were obtained from the experimental values by the method described in the experimental section. The equilibrium enthalpy at annealing temperature T_a is assumed to be H_{∞} , which is presented as point N on the extrapolated equilibrium liquids line CFJNM at annealing temperature T_a . Assume C_{pl} is the specific heat of the equilibrium liquid and C_{pg} is that of the glass. The following equations could be derived:

$$\delta_H = H_i - H_{\infty} = (C_{pl} - C_{pg}) \cdot (T_g - T_a) = \Delta C_p \cdot (T_g - T_a) \quad (4-26)$$

where δ_H is the maximum relaxation enthalpy that a glass can release during relaxation at that annealing time. But δ_H is never achieved during relaxation because a glass never reaches its true equilibrium state H_{∞} during practice.

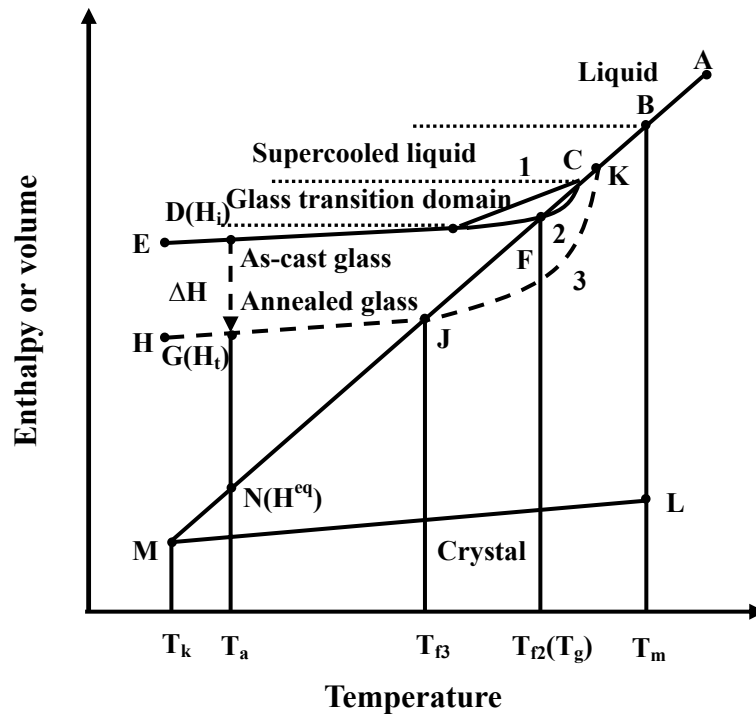
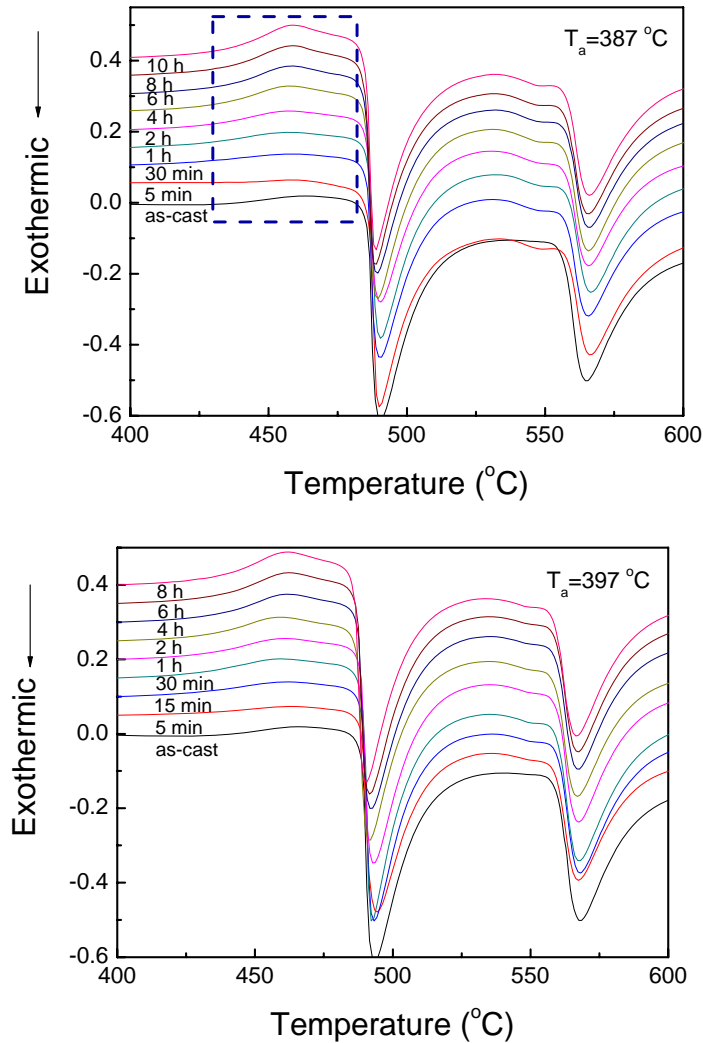


Fig. 4-5 Schematic diagram of the change in enthalpy of a glass with isothermal annealing and without annealing [Y. Liu et al., 2007]

4.3.2 Experimental Results of Enthalpy Relaxation

The enthalpy of a glass at a certain temperature T may deviate from its equilibrium value H_T^{eq} , since some additional enthalpy can be trapped when the glass forms. Long-time annealing of the glass at that temperature (10 or 20 K below the calorimetric glass transition) will result in the loss of this additional enthalpy and the glass gradually relaxes into the equilibrium supercooled liquid state. The enthalpy of the glass that was lost during the isothermal annealing can be recovered by a subsequent DSC scan of the annealed sample, resulting in an overshoot in the DSC signal in reference to the unrelaxed sample. The enthalpy recovery $\Delta H_T(t)$ during the DSC scan is equal to the enthalpy relaxed during the isothermal annealing experiment.

The enthalpy relaxation of $\text{Ti}_{41.5}\text{Cu}_{37.5}\text{Ni}_{7.5}\text{Zr}_{2.5}\text{Hf}_5\text{Sn}_5\text{Si}_1$ and $\text{Ti}_{40}\text{Zr}_{25}\text{Ni}_8\text{Cu}_9\text{Be}_{18}$ BMGs was investigated by isothermal annealing the as-cast samples at temperatures T_a below T_g for different times, t_a , and then heating with heating rate of $R_h=20$ K/min, through the subsequent glass transition to recover the enthalpy lost during the previous isothermal annealing experiments. The obtained continuous heating DSC curves of the isothermally annealed (relaxed) as well as the as-cast (unrelaxed) $\text{Ti}_{41.5}\text{Cu}_{37.5}\text{Ni}_{7.5}\text{Zr}_{2.5}\text{Hf}_5\text{Sn}_5\text{Si}_1$ and $\text{Ti}_{40}\text{Zr}_{25}\text{Ni}_8\text{Cu}_9\text{Be}_{18}$ samples are shown in Fig. 4-6 and 4-7, respectively.



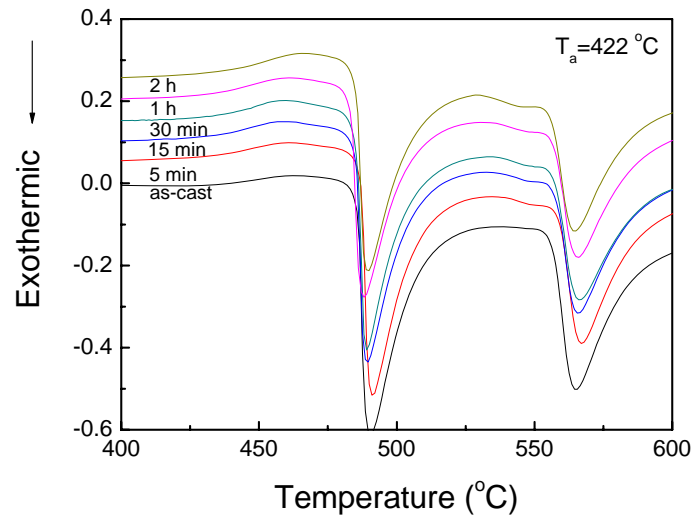
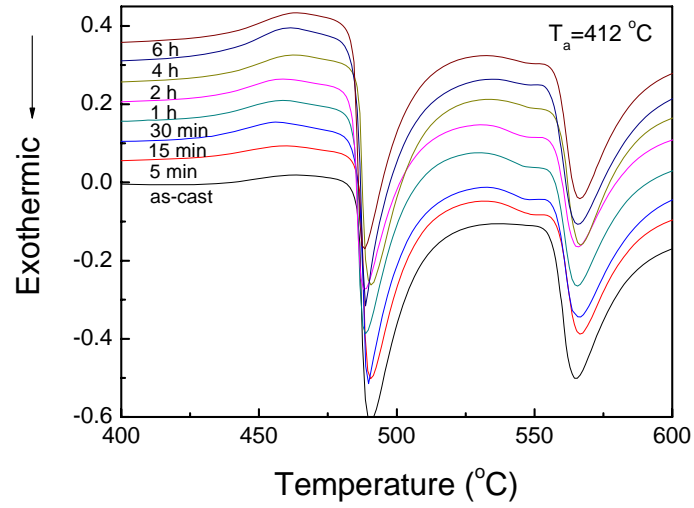
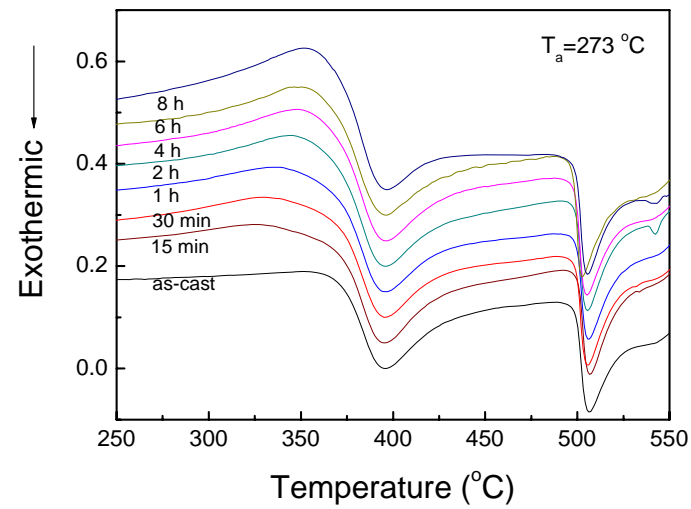


Fig. 4-6 Enthalpy recovery measurements of $\text{Ti}_{41.5}\text{Cu}_{37.5}\text{Ni}_{7.5}\text{Zr}_{2.5}\text{Hf}_5\text{Sn}_5\text{Si}_1$ BMG after isothermal relaxation from the amorphous into the supercooled liquid state at different temperatures (387, 397, 412, 422 $^{\circ}\text{C}$) for different time. In addition the measurement for an unrelaxed sample is shown



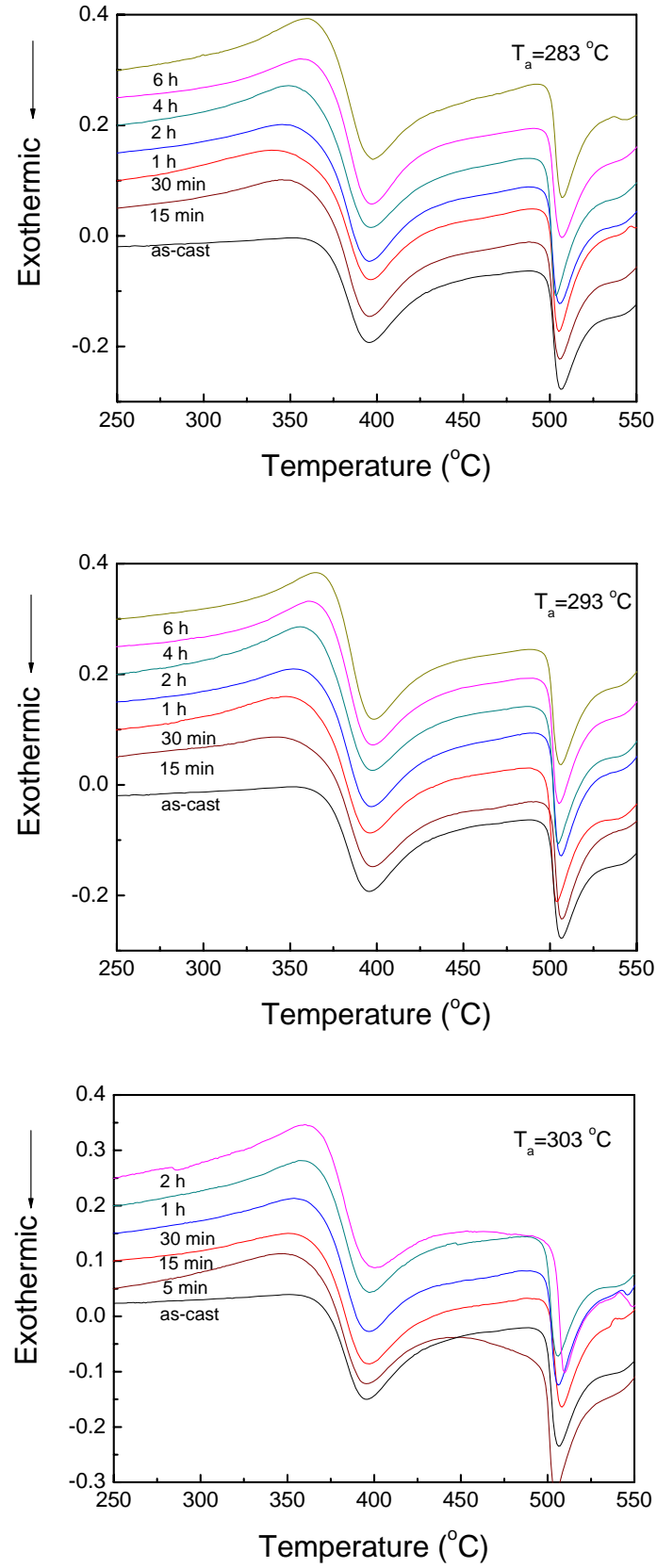


Fig. 4-7 Enthalpy recovery measurements of $\text{Ti}_{40}\text{Zr}_{25}\text{Ni}_8\text{Cu}_9\text{Be}_{18}$ BMG after isothermal relaxation from the amorphous into the supercooled liquid state at different temperatures (273, 283, 293, 303 $^{\circ}\text{C}$) for different time. In addition the measurement for an unrelaxed sample is shown

It is clear that the amount of enthalpy that was recovered during reheating the samples is what was released during the prior isothermal annealing. An overshoot at the vicinity of glass transition in the DSC heat flow signal, depending on t , can be clearly observed. A measure of this recovered enthalpy is the area between the curves of the relaxed and unrelaxed samples as mentioned in the last section. Seen from the Fig. 4-6 and 4-7, the relaxed samples show a large endothermic heat recovery in the calorimetric glass transition region, whereas an unrelaxed reference does not exhibit this effect. The sharpness and heat release of the endothermic reaction increased with increasing in the annealing temperatures and times. In addition, the recovery enthalpy increases with decreasing annealing temperature, meanwhile the relaxation time prolongs with decreasing annealing temperature, as is attributed to the slowdown of the relaxation kinetics with decrease in isothermal annealing temperature T_a . On the other hand, the amorphous samples relax towards lower enthalpic states with increasing t and eventually towards the equilibrium state after a long time of annealing. Consequently, the relaxation process is time and temperature dependent. The reduction of the enthalpy during relaxation can be understood as the result of local rearrangements of the atoms causing the reduction of the free volume that has been frozen-in during cooling throughout the glass transition. This equilibration towards the supercooled liquid state is associated with decrease in free volume and a further increase in short-range ordering and thus with a reduction in the entropy of the alloy.

Structural relaxation and the glass transition in the multicomponent metallic glasses is significantly more complicated than in the simple binary or ternary metallic glasses due to the many variables of atomic bonds between the constituent elements and their interaction forces [K.B. Kim et al., 2007]. So far there is few detailed investigation on the structural relaxation and glass transition of such complex metallic glasses.

Before further analysis, it is necessary to discuss the nature of these two BMG because of their special original microstructure and its possible effects on the structural relaxation behavior. As we know, the general structural relaxation investigation requires avoiding the occurrence of any phase separation or nanocrystallization to ensure that all the changes in chemical, physical or other properties (in this study is the recovery enthalpy) are only originating from the structural relaxation during the process of structural relaxation measurement, it is the most important thing in the study of structural relaxation theory. However, because of the wide existence of margin metallic glasses, it is also important to know the structural relaxation about such metallic glasses. For example, whether the structural relaxation of margin metallic glasses exists, whether their structural relaxation follows the general characteristic as the traditional metallic glasses and whether the existing structural relaxation model still works on the margin metallic glasses.

In this study, $\text{Ti}_{40}\text{Zr}_{25}\text{Ni}_8\text{Cu}_9\text{Be}_{18}$ BMG is a margin metallic glass for the existence of quenched-in nuclei in the amorphous matrix. The quench-in nuclei tend to grow through an exothermic reaction. They may influence on the structural relaxation or not, which depends on the stability of the quenched-in nuclei. Namely, if the incubation time for crystallization τ_{inc} is far longer than the average relaxation time τ , it means that these two events, structural relaxation and growth of quench-in nuclei will not be simultaneous, in this case the structural relaxation will not be disturbed by the existence of quenched-in nuclei, so their enthalpy relaxation behavior should be similar and even the same as other typical metallic glasses; or else, the enthalpy relaxation behavior must be different because of the concurrence of structural relaxation and crystallization. For $\text{Ti}_{40}\text{Zr}_{25}\text{Ni}_8\text{Cu}_9\text{Be}_{18}$ BMG, in the study of the effects of low temperature annealing on the

consequent crystallization which will be presented in the next chapter, we found that the enthalpy for the crystallization of the as-cast sample annealed even at relatively high temperature of 308 °C (5 °C below T_g) for a long time of 2 h changes very slightly because of the limited thermal induced growth of the quenched-in nuclei, which indicates that under the experimental condition (annealing temperature and time) used in this study, the overshoot of the endothermic reaction in the vicinity of glass transition of the pre-annealed samples with respect to the as-cast samples is mainly ascribed from the structural relaxation and the growth of quenched-in nuclei is so limited that it can be ignored, especially under the condition of low annealing temperature and short annealing time, the quenched-in nuclei are stable enough to avoid growing, so it seems that for this alloy, the incubation time for crystallization τ_{inc} is longer than the average relaxation time τ , its structural relaxation could occur without the disturbance of the growth of the quenched-in nuclei, at least in some extent, the quenched-in is stable enough. For the $Ti_{41.5}Cu_{37.5}Ni_{7.5}Zr_{2.5}Hf_5Sn_5Si_1$ BMG, it is another case because of the existence of the phase separation-like structure in the amorphous matrix. As discussed in the chapter 2, the phase separation-like structure is unstable, however not tending to crystallize but tending to decompose through the atomic rearrangement upon heating. So the enthalpy relaxation behavior of $Ti_{41.5}Cu_{37.5}Ni_{7.5}Zr_{2.5}Hf_5Sn_5Si_1$ BMG should follow the general law as that of typical metallic glasses.

Although the enthalpy relaxation behavior of these two BMGs may follow the general law according to the above analysis, differences must exist due to the different nature of these two BMGs. It is said that, through the investigation on the enthalpy relaxation of these two BMGs, we can compare their different nature. First, we compared the structural relaxation upon continuous heating between as-cast $Ti_{41.5}Cu_{37.5}Ni_{7.5}Zr_{2.5}Hf_5Sn_5Si_1$ and $Ti_{40}Zr_{25}Ni_8Cu_9Be_{18}$ BMGs, and found that there is obvious exothermic structural relaxation reaction in the DSC traces of the as-cast $Ti_{41.5}Cu_{37.5}Ni_{7.5}Zr_{2.5}Hf_5Sn_5Si_1$ BMG (Fig. 4-1) although the heat release associated with the broad exothermic reaction is difficult to be quantified, and the peak size decreases significantly with increase in the annealing temperature or time; however, no obvious exothermic structural relaxation reaction can be observed for the as-cast $Ti_{40}Zr_{25}Ni_8Cu_9Be_{18}$ BMG, as implies that the as-received $Ti_{41.5}Cu_{37.5}Ni_{7.5}Zr_{2.5}Hf_5Sn_5Si_1$ BMG is farther deviated from the metastable equilibrium of the supercooled liquid than the $Ti_{40}Zr_{25}Ni_8Cu_9Be_{18}$ BMG, and confirmed the more relaxed property of the $Ti_{40}Zr_{25}Ni_8Cu_9Be_{18}$ BMG than the $Ti_{41.5}Cu_{37.5}Ni_{7.5}Zr_{2.5}Hf_5Sn_5Si_1$ BMG, as can be verified through the quantitative calculation which will be shown later. Further observations of the glass transition were performed on the relaxed samples as well as on the as-cast samples, it is found that the endothermic glass transition reaction in the continuous heating DSC curves for the $Ti_{41.5}Cu_{37.5}Ni_{7.5}Zr_{2.5}Hf_5Sn_5Si_1$ alloy shows the general picture for the typical metallic glasses: obvious glass transition, onset and end glass transition temperature. For $Ti_{40}Zr_{25}Ni_8Cu_9Be_{18}$ alloy, although the glass transition can be observed, and the corresponding endothermic peak becomes larger and sharper with increase in annealing time for a certain annealing temperature which is believed to be resulted from the relaxation enthalpy recovery, the onset glass transition temperature is blurry and no end glass transition temperature can be observed, which indicates that the supercooled liquid is so unstable that the later stage of the glass transition and the beginning stage of the crystallization overlap each other. As we know, the structural relaxation behavior can reflect the thermal stability of the BMG in some extent, so the different nature between the $Ti_{41.5}Cu_{37.5}Ni_{7.5}Zr_{2.5}Hf_5Sn_5Si_1$ and $Ti_{40}Zr_{25}Ni_8Cu_9Be_{18}$ BMGs must be shown in the characteristic investigation on the structural relaxation.

The characteristic of enthalpy relaxation for $\text{Ti}_{41.5}\text{Cu}_{37.5}\text{Ni}_{7.5}\text{Zr}_{2.5}\text{Hf}_5\text{Sn}_5\text{Si}_1$ and $\text{Ti}_{40}\text{Zr}_{25}\text{Ni}_8\text{Cu}_9\text{Be}_{18}$ BMGs will be presented in the next section based on the existing enthalpy relaxation model, and the correlation between the structural relaxation properties and the thermal stability will also be shown.

4.3.3 Characteristics of Enthalpy Relaxation

Fig. 4-8 (a) shows the enthalpy recovery $\Delta H_T(t)$ upon different annealing times at $T_a=387, 397, 412, 422$ °C for $\text{Ti}_{41.5}\text{Cu}_{37.5}\text{Ni}_{7.5}\text{Zr}_{2.5}\text{Hf}_5\text{Sn}_5\text{Si}_1$ BMG. $\Delta H_T(t)$ increases rapidly as a function of t in an initial stage of relaxation, and then saturates till a certain annealing time t . For example, for the samples annealed at $T_a=387$ °C, the rate of enthalpy relaxation is very large in an initial stage of relaxation, however, beyond about 1.5×10^4 s, it becomes very slow. It can be seen that the process of enthalpy relaxation is non-linear. Further investigation by changing the x-axis or y-axis to logarithmic scale indicates that the enthalpy relaxation is non-exponential. The enthalpy relaxation process cannot be described by a simple exponential relaxation function, due to the microstructural heterogeneities of the sample, and suggests that the enthalpy relaxation of the $\text{Ti}_{41.5}\text{Cu}_{37.5}\text{Ni}_{7.5}\text{Zr}_{2.5}\text{Hf}_5\text{Sn}_5\text{Si}_1$ liquid does not involve a single Debye relaxation event, as is in accordance with the previous report related to amorphous materials. So the enthalpy relaxation of BMGs also has the characteristics of non-exponentiality and non-linearity, which follows an stretched exponential relaxation function, known as Kohlrausch-Williams-Watts (KWW) expression ([Vilgis et al., 1993; Busch et al., 1998-a; Fan et al., 2004]).

$$\phi(t) = \exp\left[-\left(\frac{t}{\tau}\right)^\beta\right] \quad (4-27)$$

where t is the annealing time and τ is the characteristic structural relaxation time, β is the Kohlrausch exponent whose value is between zero and unity $0 < \beta \leq 1$, reflecting the width of relaxation time distribution spectrum originating from the inhomogeneity of the supercooled liquid. The value of $\beta=1$ corresponds to a single relaxation time with exponential behavior. The smaller the value of β , the more the distribution of atomic motions deviates from a single exponential behavior. So, if the relaxation time distribution becomes broader, the value of β will be reduced, and the enthalpy recovery curve will be spread out over a wider temperature range.

The time dependence of $\Delta H_T(t)$ at a given temperature can be well fitted by stretched exponential relaxation function

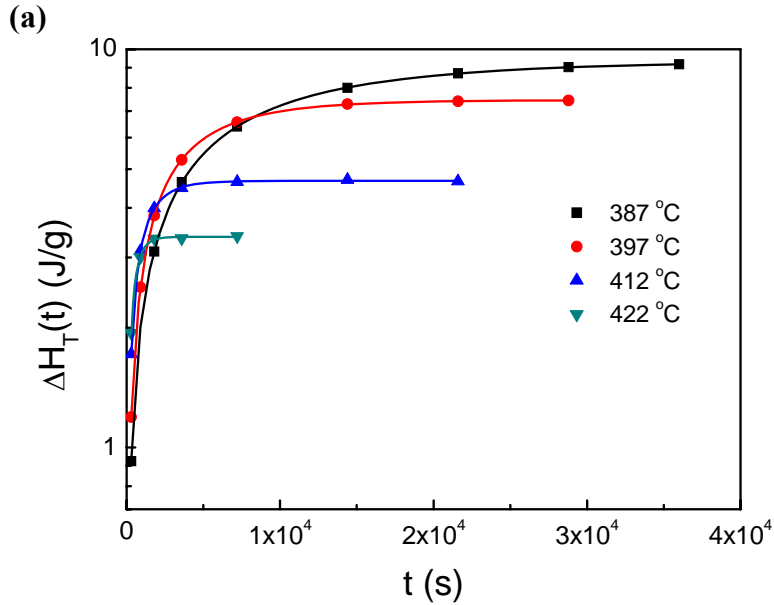
$$\Delta H_T(t) = \Delta H_T^{eq} \left\{1 - \exp\left[-\left(\frac{t}{\tau}\right)^\beta\right]\right\} \quad (4-28)$$

where ΔH_T^{eq} is the equilibrium value of $\Delta H_T(t)$ for $t \rightarrow \infty$ at the annealing temperature T_a .

By fitting the data of recovery enthalpy vs. annealing time with Eq. 4-28, the values of ΔH_T^{eq} , τ and β , at different annealing temperatures, $T=387, 397, 412$ and 422 °C, were obtained and listed in Table 4-2. It is found that the values of ΔH_T^{eq} , τ and β were strongly dependent on the annealing temperature, and the higher T_a temperature, the lower the values of ΔH_T^{eq} , τ and higher of β , which is attributed to the fact that the glass completely relaxes into the supercooled liquid on

a short timescale, indicating that the enthalpy recovery is determined by the annealing temperatures. It should be pointed out that Wang et al. [X.D. Wang et al., 2007] reported that the enthalpy recovery is also determined by the thermal history of samples treated above T_g besides the annealing temperature below T_g . The difference in the values of ΔH_T^{eq} , τ and β is mainly ascribed to the degree of the amorphous phase deviating from its equilibrium state at each T_a temperature.

It is found that the stretching exponent β of $\text{Ti}_{41.5}\text{Cu}_{37.5}\text{Ni}_{7.5}\text{Zr}_{2.5}\text{Hf}_5\text{Sn}_5\text{Si}_1$ BMG is around 0.8. The values of β for some typical multicomponent BMGs as well as some other amorphous materials have been reported in the literatures. Busch and Johnson [Busch et al., 1998-a] reported that the isothermal relaxation of viscosity just below glass transition temperature in a $\text{Zr}_{46.75}\text{Ti}_{8.25}\text{Cu}_{7.5}\text{Ni}_{10}\text{Be}_{27.5}$ BMG is described well by the stretched exponential relaxation function with a Kohlrausch exponent of about 0.8. Fan et al. [Fan et al., 2004] performed the thermodynamic approach to the kinetics of isothermal structural relaxation for a $\text{Pd}_{43}\text{Cu}_{27}\text{Ni}_{10}\text{P}_{20}$ BMG. They found that the enthalpy relaxation just below glass transition temperature is fitted well by the stretched exponential relaxation function with a Kohlrausch exponent of about 0.7. Böhmer et al. [Böhmer et al., 1993] reviewed the structural relaxation process of about 70 covalent glass formers, ionic melt, supercooled liquids, amorphous polymers and glassy crystals and concluded that the isothermal relaxation process is described well by the stretched exponential function with Kohlrausch exponent over the range from about 0.3 to 1. So, the value of stretching exponent β for $\text{Ti}_{41.5}\text{Cu}_{37.5}\text{Ni}_{7.5}\text{Zr}_{2.5}\text{Hf}_5\text{Sn}_5\text{Si}_1$ BMG is rather large and comparable with that of other typical BMGs, indicating a narrow distribution of relaxation time or a less exponential response, which is also the characteristic of structural relaxation of BMGs.



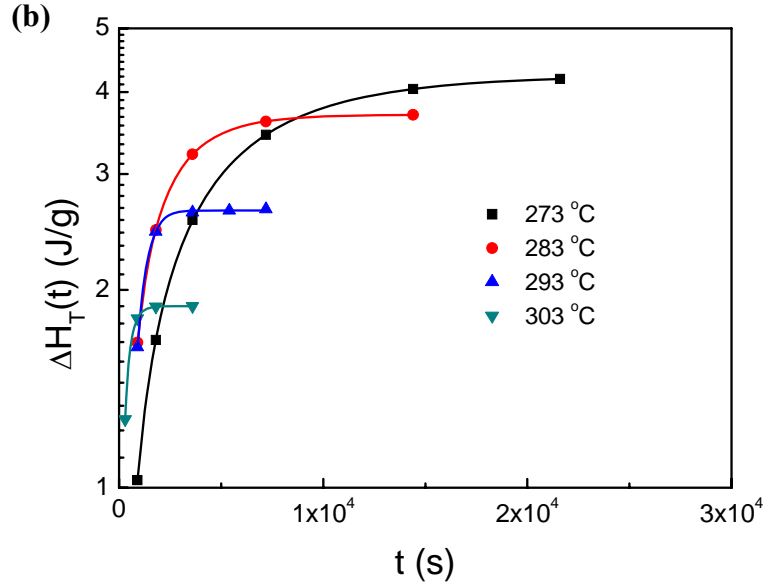


Fig. 4-8 Experimental relaxation recovery enthalpy $\Delta H_T(t)$ as a function of annealing time t at various temperatures for (a) $\text{Ti}_{41.5}\text{Cu}_{37.5}\text{Ni}_{7.5}\text{Zr}_{2.5}\text{Hf}_5\text{Sn}_5\text{Si}_1$ and (b) $\text{Ti}_{40}\text{Zr}_{25}\text{Ni}_8\text{Cu}_9\text{Be}_{18}$ BMGs, and fitted with stretched exponential function

Table 4-2

The values of ΔH_T^{eq} , τ and β at various temperatures for $\text{Ti}_{41.5}\text{Cu}_{37.5}\text{Ni}_{7.5}\text{Zr}_{2.5}\text{Hf}_5\text{Sn}_5\text{Si}_1$ and $\text{Ti}_{40}\text{Zr}_{25}\text{Ni}_8\text{Cu}_9\text{Be}_{18}$ BMGs determined from the $\Delta H_T(t)$ vs. t curves fitted with the stretched exponential relaxation function.

T_a (°C)	ΔH_T^{eq} (J/g)	τ (s)	β
387	9.4	5988	0.7537
397	7.4	2753	0.787
412	4.7	800	0.79528
422	3.4	361	0.87624

T_a (°C)	ΔH_T^{eq} (J/g)	τ (s)	β
273	4.2	3997	0.86201
283	3.7	1616	0.87987
293	2.6	624	0.91135
303	1.9	266	0.93578

In literature, Vogel-Fulcher-Tammann (VFT) equation is used to describe the non-Arrhenius behavior of the mean relaxation time τ [Y. Liu et al., 2006]

$$\tau = \tau_0 \exp\left(\frac{D^* T_0}{T - T_0}\right) \quad (4-29)$$

where τ_0 is the pre-exponential factor related to relaxation time constant, D^* is the fragility parameter and T_0 is the VFT temperature at which barriers with respect to flow would go to

infinity. The value of T_0 in VFT equation is believed to correspond to the theoretical Kauzmann temperature T_k . The Kauzmann temperature T_k is the critical temperature to mark the lower limit of the experimental glass transition and at T_k the configurational entropy of the system reaches zero. In most enthalpy relaxation studies, T_0 in VFT equation is assumed to be 0 and the temperature dependence of τ is assumed to be Arrhenius-like [Y. Liu et al., 2006]

$$\tau = \tau'_0 \exp\left(\frac{E_a}{RT_a}\right) \quad (4-30)$$

where τ'_0 is the pre-exponential factor, R is the ideal gas constant, E_a is the apparent activation energy. It must be pointed out that actually T_0 is not equal to 0 for glasses and T_0 is approximately several tens of Kelvins below T_g . However, the effect of T_0 in VTF equation could be ignored when considering the temperature dependence of τ in the experimental annealing temperature range for glasses, as has been verified by many researchers in the field of amorphous materials.

The temperature dependence of the relaxation time τ is shown in an Arrhenius plot in Fig. 4-9. The data can be well fitted by a straight line, indicating that the assumption of Arrhenius behavior of the relaxation time τ for the enthalpy relaxation from the glass into the supercooled liquid state within the experimental temperature range in this study could be accepted. The relaxation time increases exponentially with decreasing temperature, making the equilibrium inaccessible at even lower annealing temperatures. Other researchers also reported such an Arrhenius behavior of the relaxation time τ [Y. Liu et al., 2007; Gallino et al., 2007-a; Gallino et al., 2007-b; Fan et al., 2004], and by fitting the enthalpy relaxation data it is found that they are best described by an Arrhenius equation rather than the VFT equation. In this study, we also obtain the similar result that we failed to describe the temperature dependency of the enthalpy relaxation times by the VFT equation. The fitted curve based on the Arrhenius equation yields a τ'_0 of 2.96×10^{-20} s and a E_a of 294 kJ/mol or 3.06 eV, as is shown in Fig. 4-9.

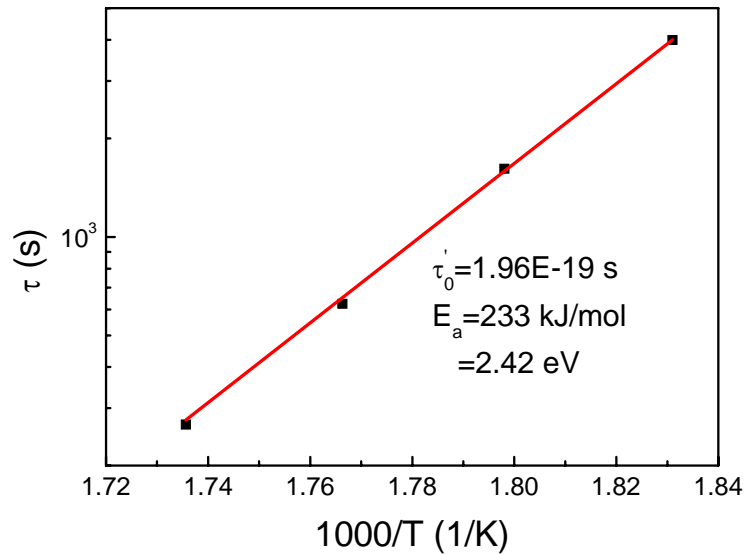


Fig. 4-9 Enthalpy relaxation times for the $\text{Ti}_{41.5}\text{Cu}_{37.5}\text{Ni}_{7.5}\text{Zr}_{2.5}\text{Hf}_5\text{Sn}_5\text{Si}_1$ BMG as a function of inverse temperature fitted with the Arrhenius equation

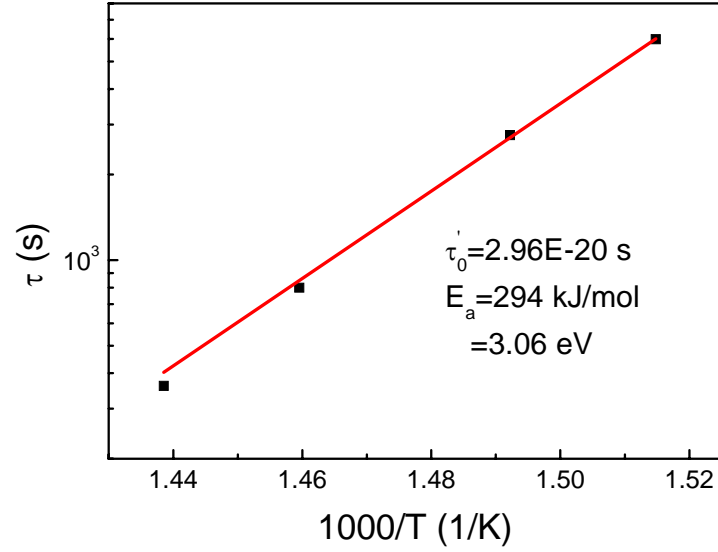


Fig. 4-10 Enthalpy relaxation times for the $\text{Ti}_{40}\text{Zr}_{25}\text{Ni}_8\text{Cu}_9\text{Be}_{18}$ BMG as a function of inverse temperature fitted with the Arrhenius equation

4.3.4 Mechanism of Enthalpy Relaxation

The mechanism of enthalpy relaxation is associated with the atomic rearrangement, so it is necessary to investigate the mobility of the different atoms in multicomponent metallic glasses during the process of relaxation. Masuhr et al. [Masuhr et al., 1999] has analyzed the characteristic diffusion times for the different atoms around the glass transition for Zr-Ti-Cu-Ni-Be alloy. It is found that these times show Arrhenius behavior for the small and medium size atoms, while follow VTF law for the large size atoms. In addition, the activation energies for diffusion of the small size atoms such as Ni, Cu are about 2 eV, whereas the medium size atoms such as Ti have activation energies of about 3 eV, however, the activation energies for diffusion of the large size atoms such as Zr are much bigger with respect to the small and medium size atoms. So for the $\text{Zr}_{58.5}\text{Cu}_{15.6}\text{Ni}_{12.8}\text{Al}_{10.3}\text{Nb}_{2.8}$ (Vit106a) alloy whose apparent activation energy for the enthalpy relaxation is 2.97 eV, local rearrangements of the medium size atoms Al and Nb as well as the small atoms Cu and Ni are sufficient to cause complete relaxation into the enthalpic state of the supercooled liquid without involving the complete rearrangement of the backbone of the structure made of large atoms like Zr [Gallino et al., 2007-a]. In the case of $\text{Ti}_{41.5}\text{Cu}_{37.5}\text{Ni}_{7.5}\text{Zr}_{2.5}\text{Hf}_5\text{Sn}_5\text{Si}_1$ alloy whose activation energy of 3.06 eV for the enthalpy relaxation, different from Vit106a alloy, although the local rearrangements of the medium size atoms Ti as well as the small atoms Cu, Ni and Si are sufficient to cause complete relaxation into the enthalpic state of the supercooled liquid without involving the motion of the large size atoms Zr, Hf and Sn, the complete rearrangement of the backbone of the structure is necessary because that the medium size atom Ti can be regarded as constituting the backbone of the amorphous structure, so the rearrangement involving the collective hopping mechanism for the small and medium size atoms is the governing mechanism for the enthalpy relaxation process of this alloy, as is in agreement with the case of $\text{Zr}_{46.75}\text{Ti}_{8.25}\text{Cu}_{7.5}\text{Ni}_{10}\text{Be}_{27.5}$ alloy [Ehmler et al., 1998].

4.3.5 Discussion on the Comparison of Enthalpy Relaxation between $\text{Ti}_{41.5}\text{Cu}_{37.5}\text{Ni}_{7.5}\text{Zr}_{2.5}\text{Hf}_5\text{Sn}_5\text{Si}_1$ and $\text{Ti}_{40}\text{Zr}_{25}\text{Ni}_8\text{Cu}_9\text{Be}_{18}$ BMGs

Besides $\text{Ti}_{41.5}\text{Cu}_{37.5}\text{Ni}_{7.5}\text{Zr}_{2.5}\text{Hf}_5\text{Sn}_5\text{Si}_1$, the characteristic of enthalpy relaxation behavior for $\text{Ti}_{40}\text{Zr}_{25}\text{Ni}_8\text{Cu}_9\text{Be}_{18}$ BMG was also investigated. The corresponding results are shown together with those of $\text{Ti}_{41.5}\text{Cu}_{37.5}\text{Ni}_{7.5}\text{Zr}_{2.5}\text{Hf}_5\text{Sn}_5\text{Si}_1$. It is found that characteristic of the enthalpy relaxation of the $\text{Ti}_{40}\text{Zr}_{25}\text{Ni}_8\text{Cu}_9\text{Be}_{18}$ BMG also follows a general law: the stretched exponential relaxation function and the Arrhenius relaxation time, which indicates that the incubation time for crystallization τ_{inc} is indeed longer than the average relaxation time τ for $\text{Ti}_{40}\text{Zr}_{25}\text{Ni}_8\text{Cu}_9\text{Be}_{18}$ BMG, the enthalpy relaxation occurs almost without the disturbance of the growth of the quenched-in nuclei as we predicted at the beginning of this chapter.

The characteristic parameters Kohlrausch exponent β and average structural relaxation τ derived from the stretched exponential relaxation function are essential for the analysis of enthalpy relaxation, which are believed to be correlated with the GFA and thermal stability of metallic glasses, respectively. However, the stretching exponent β and the average structural relaxation τ shows the characteristic of the temperature dependence, it is not possible to construct the correlation between the stretching exponent and GFA of metallic glasses; at the same time, the average structural relaxation τ is also dependent on the annealing temperature, it is difficult to get the relationship between the average structural relaxation and thermal stability of metallic glasses. In this study, two parameters, β_g and τ_g , representing the stretching exponent and the average structural relaxation time at the calorimetric glass transition temperature, respectively, will be proposed to evaluate the enthalpy relaxation properties and finally construct the correlation with the GFA and thermal stability.

The problem is how to construct the relation between parameter β_g and the GFA of metallic glasses. It has been reported that the stretching exponent β has a relation with the fragility index m . The fragility index m is an indicator of the fragility of supercooled liquid; furthermore, it is well known that the fragility of liquid is correlated with the GFA of glasses, so the relation between β_g and the GFA could be successfully constructed.

Angell [Angell, 1991] classified supercooled liquids as strong or fragile by the temperature sensitivity of the viscosity or relaxation time. Strong liquids are characterized by a small jump in specific heat combined with a low activation energy near T_g . In contrast, fragile liquids have a large jump in specific heat and high activation energy. The larger value of m corresponds to the fragile liquid behavior. For example, SiO_2 and GeO_2 are the typical strong liquids whose fragility index are around 20 [Böhmer et al., 1993; Sipp et al., 2001], while $\text{Au}_{53.2}\text{Pb}_{27.6}\text{Sb}_{19.2}$ shows the typical fragile liquid behavior whose fragility index is up to around 120 [Klose et al., 1994]. The strong liquid is generally related to the good GFA. Most of the bulk metallic glasses show strong liquid behavior, as is attributed from the existence of large quantities of free volume. The fragility index m for Vit 1 alloy [Busch et al., 2001], Vit 4 alloy [Busch et al., 2001], $\text{Mg}_{65}\text{Cu}_{25}\text{Y}_{10}$ [Busch et al., 1998-b] and $\text{Pd}_{40}\text{Ni}_{40}\text{P}_{20}$ [Flores et al., 2002] are 50, 44, 45 and 51, respectively. Such strong liquids typically have a fragility index m of less than 50.

There appears to be a correlation between the Kohlrausch exponent β and the fragility index m in glass-forming liquids. Early studies of enthalpy relaxation and recovery were focused on organic and inorganic glassy materials. In metallic glass systems, enthalpy relaxation phenomena

were investigated by Chen [Chen, 1981] in $\text{Pd}_{48}\text{Ni}_{32}\text{P}_{20}$, Sommer et al. [Sommer et al., 1984] in $\text{Cu}_{67}\text{Ti}_{33}$ and other binary systems, and Koebrugge et al. [Koebrugge et al., 1992] in $\text{Pd}_{40}\text{Ni}_{40}\text{P}_{20}$. The enthalpy relaxation and recovery near T_g was also studied recently in bulk metallic glass forming liquids [Busch et al., 1998-a]. It is found that the more fragile liquid has a low Kohlrausch exponent. Such a correlation is also suitable for the covalent, ionic, and polymeric glasses near the glass transition [Böhmer et al., 1993]. Bendler [Bendler et al., 2003] proposed a relation between the fragility m and Kohlrausch exponent β based on the defect diffusion model, which can be expressed as

$$m = - \frac{0.65 T_c^{1.5\gamma} L^3 \ln(1-c)\gamma}{\beta d_0^3 T_g^{1.5\gamma} \left(1 - \frac{T_c}{T_g}\right)^{1+1.5\gamma}} \quad (4-31)$$

Assuming that all the parameters in the Eq. 4-31 are constant except β , the above equation can be reduced as $m = \frac{42}{\beta}$. This expression can successfully describe the relation between the

fragility index m and Kohlrausch exponent β for polymeric, alcoholic and metallic glasses. Since the strong liquid is generally related to a good GFA, and the strong liquids typically have a fragility index m of less than 50, the value of Kohlrausch exponent β for the glasses who exhibit a good GFA should be larger than 0.84.

Fig. 4-11 shows the stretching exponent β as a function of annealing temperature T_a for $\text{Ti}_{41.5}\text{Cu}_{37.5}\text{Ni}_{7.5}\text{Zr}_{2.5}\text{Hf}_5\text{Sn}_5\text{Si}_1$ and $\text{Ti}_{40}\text{Zr}_{25}\text{Ni}_8\text{Cu}_9\text{Be}_{18}$ BMGs. It is found that the stretching exponent β of $\text{Ti}_{41.5}\text{Cu}_{37.5}\text{Ni}_{7.5}\text{Zr}_{2.5}\text{Hf}_5\text{Sn}_5\text{Si}_1$ as well as $\text{Ti}_{40}\text{Zr}_{25}\text{Ni}_8\text{Cu}_9\text{Be}_{18}$ BMG shows an approximately linear increase with annealing temperature. The values of β_g for $\text{Ti}_{41.5}\text{Cu}_{37.5}\text{Ni}_{7.5}\text{Zr}_{2.5}\text{Hf}_5\text{Sn}_5\text{Si}_1$ and $\text{Ti}_{40}\text{Zr}_{25}\text{Ni}_8\text{Cu}_9\text{Be}_{18}$ BMGs are calculated to be 0.884 and 0.962, respectively, and higher than 0.84, lower than 1, which indicates that both of these two alloys show relatively strong liquid behavior and accordingly relatively good GFA. Gallino et al. reported that the stretching exponent of the $\text{Zr}_{58.5}\text{Cu}_{15.6}\text{Ni}_{12.8}\text{Al}_{10.3}\text{Nb}_{2.8}$ BMG increases linearly with temperature and approaches unity close to T_g . The β_g value of $\text{Ti}_{40}\text{Zr}_{25}\text{Ni}_8\text{Cu}_9\text{Be}_{18}$ BMG is between that of $\text{Ti}_{41.5}\text{Cu}_{37.5}\text{Ni}_{7.5}\text{Zr}_{2.5}\text{Hf}_5\text{Sn}_5\text{Si}_1$ and $\text{Zr}_{58.5}\text{Cu}_{15.6}\text{Ni}_{12.8}\text{Al}_{10.3}\text{Nb}_{2.8}$ BMGs, which indicates that the $\text{Ti}_{40}\text{Zr}_{25}\text{Ni}_8\text{Cu}_9\text{Be}_{18}$ BMG should exhibit better GFA than $\text{Ti}_{41.5}\text{Cu}_{37.5}\text{Ni}_{7.5}\text{Zr}_{2.5}\text{Hf}_5\text{Sn}_5\text{Si}_1$ BMG, however worse than $\text{Zr}_{58.5}\text{Cu}_{15.6}\text{Ni}_{12.8}\text{Al}_{10.3}\text{Nb}_{2.8}$ BMG, and in accordance with the fact, thus it further confirms that this relation between the structural relaxation and the GFA of metallic glass is reasonable and the proposed parameter β_g can be used in roughly evaluating the supercooled liquid properties and GFA.

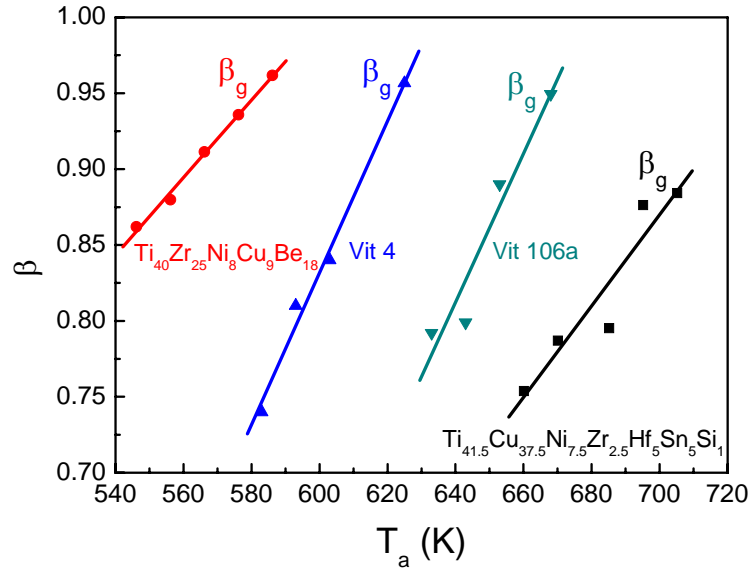


Fig. 4-11 Stretching exponent β as a function of annealing temperature T for $\text{Ti}_{41.5}\text{Cu}_{37.5}\text{Ni}_{7.5}\text{Zr}_{2.5}\text{Hf}_5\text{Sn}_5\text{Si}_1$, $\text{Ti}_{40}\text{Zr}_{25}\text{Ni}_8\text{Cu}_9\text{Be}_{18}$, Vit 4 and Vit 106a BMGs

The structural relaxation time τ should be related to the thermal stability of metallic glasses, in this study the parameter τ_g was introduced to construct the correlation between structural relaxation behavior and the thermal stability. In general, the long structural relaxation time corresponds to a good thermal stability.

There exists a linear relationship between the logarithmic relaxation time $\ln \tau$ and the difference between the glass transition temperature and annealing temperature ΔT_a , which can be written as

$$\ln \tau = \ln \tau_g + A \Delta T_a \quad (4-32)$$

Fig. 4-12 shows the $\ln \tau$ vs. ΔT_a curves of $\text{Ti}_{41.5}\text{Cu}_{37.5}\text{Ni}_{7.5}\text{Zr}_{2.5}\text{Hf}_5\text{Sn}_5\text{Si}_1$ and $\text{Ti}_{40}\text{Zr}_{25}\text{Ni}_8\text{Cu}_9\text{Be}_{18}$ BMGs, and the values of τ_g for these two alloys as well as the other three typical BMGs are listed in **Table 4-3**. It is generally believed that the structural relaxation time at glass transition temperature is around 100 s. It is found that the τ_g value of $\text{Ti}_{41.5}\text{Cu}_{37.5}\text{Ni}_{7.5}\text{Zr}_{2.5}\text{Hf}_5\text{Sn}_5\text{Si}_1$ alloy is much lower than that of $\text{La}_{55}\text{Al}_{25}\text{Ni}_{10}\text{Cu}_{10}$ BMG (up to 1720 s), however, is comparable with $\text{Pd}_{43}\text{Ni}_{10}\text{Cu}_{27}\text{P}_{20}$ and $\text{Zr}_{58.5}\text{Cu}_{15.6}\text{Ni}_{12.8}\text{Al}_{10.3}\text{Nb}_{2.8}$ BMGs, which indicates that the thermal stability of $\text{Ti}_{41.5}\text{Cu}_{37.5}\text{Ni}_{7.5}\text{Zr}_{2.5}\text{Hf}_5\text{Sn}_5\text{Si}_1$ alloy is comparable with the well-known typical BMGs. In regards to the $\text{Ti}_{40}\text{Zr}_{25}\text{Ni}_8\text{Cu}_9\text{Be}_{18}$ BMG, the value of τ_g is much smaller than the other four alloys, which suggests that $\text{Ti}_{40}\text{Zr}_{25}\text{Ni}_8\text{Cu}_9\text{Be}_{18}$ BMG is more relaxed and only need short relaxation time to reach the internal equilibrium state, which may be due to the smaller activation energy for structural relaxation and free volume, as confirms the worse thermal stability of $\text{Ti}_{40}\text{Zr}_{25}\text{Ni}_8\text{Cu}_9\text{Be}_{18}$ BMG than the other four BMGs. This result is in good agreement with the fact which indicates that the parameter τ_g is efficient in roughly evaluating the supercooled liquid properties and thermal stability.

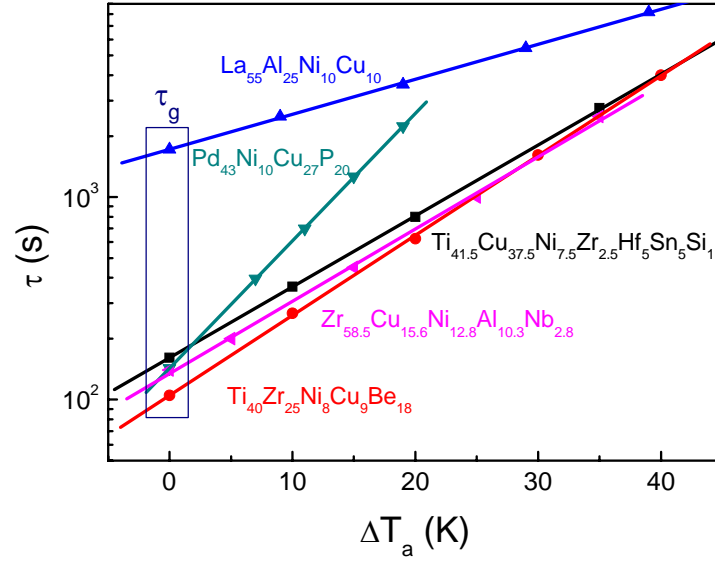


Fig. 4-12 Mean structural relaxation time τ as a function of ΔT for $\text{Ti}_{41.5}\text{Cu}_{37.5}\text{Ni}_{7.5}\text{Zr}_{2.5}\text{Hf}_5\text{Sn}_5\text{Si}_1$, $\text{Ti}_{40}\text{Zr}_{25}\text{Ni}_8\text{Cu}_9\text{Be}_{18}$ as well as other typical BMGs. The solid lines are the linear fitting curves

$$\text{based on } \ln \tau = \ln \tau_g + A\Delta T_a$$

Table 4-3

The calculated A and τ_g for $\text{Ti}_{41.5}\text{Cu}_{37.5}\text{Ni}_{7.5}\text{Zr}_{2.5}\text{Hf}_5\text{Sn}_5\text{Si}_1$ and $\text{Ti}_{40}\text{Zr}_{25}\text{Ni}_8\text{Cu}_9\text{Be}_{18}$ as well as the typical BMGs

Composition	A	τ_g (s)	Ref.
$\text{Ti}_{41.5}\text{Cu}_{37.5}\text{Ni}_{7.5}\text{Zr}_{2.5}\text{Hf}_5\text{Sn}_5\text{Si}_1$	0.08059	161	This work
$\text{Ti}_{40}\text{Zr}_{25}\text{Ni}_8\text{Cu}_9\text{Be}_{18}$	0.09071	105	This work
$\text{La}_{55}\text{Al}_{25}\text{Ni}_{10}\text{Cu}_{10}$	0.04	1720	[T. Zhang, 2007]
$\text{Pd}_{43}\text{Ni}_{10}\text{Cu}_{27}\text{P}_{20}$	0.14478	143	[Fan et al., 2004]
$\text{Zr}_{58.5}\text{Cu}_{15.6}\text{Ni}_{12.8}\text{Al}_{10.3}\text{Nb}_{2.8}$	0.08074	~140	[Gallino et al., 2007-a]

4.4 Kinetics of Crystallization

The analysis of the crystallization kinetics for isothermal as well as isochronous heating of metallic glasses is the elementary work from the standpoint of scientific research. Especially for the isothermal crystallization process, it is of significance from the technological point of view. The obtained TTT curves can quantify the resistance against crystallization of the supercooled liquid and finally optimize the process parameters for the following net-shape-forming in the supercooled liquid region.

The crystallization of metallic glasses under the different heating condition, isothermal and isochronous, may be consistent or inconsistent, and the corresponding crystallization mechanism also may be consistent or inconsistent, so the complete picture for the investigation of crystallization kinetics should be performed under both conditions, isothermal and isochronous, and is significant to be known for the crystallization control under a certain condition.

Additionally, the appropriate application of kinetics model in the analysis of crystallization

behavior is essential to ensure the correctness of the following kinetics analysis. The inappropriate application of kinetics model must lead to the wrong results.

4.4.1 Comparison of Theoretical kinetics Analysis based on the JMA and Starink Kinetics Models

In the section of background and motivation, we have mentioned that our recent study reveals that deriving the changeable kinetic exponent by the local Avrami exponent may lead to errors if an inappropriate kinetic model is chosen, resulting in the misinterpretation of phase transformation mechanism, as will be shown in this section.

To clarify the deviation from the JMA model, we design four transformations based on the JMA and Starink models with the same kinetic parameters except different values of λ from 1 to 4 (1, 1.2, 2, 4), $n=3$, $T=700$ K, $E_a=350$ kJ/mol. The calculated heat flow and transformed volume fraction as a function of time are shown in Fig. 4-13 and 4-14. Compared with the situation of typical JMA transformation, a large λ (>1) value leads to the transformation rate decrease and finally prolongs the transformed time, even if the four transformations have the same 4 other parameters, n , T , E_a and k_0 , which indicates that the value of λ can be used to describe the degree of deviation from the typical JMA transformation.

Through the calculation of two parameter autocatalytic model, one can obtain the same results. Fig. 4-15 (a) and (b) show the calculated $y(\alpha)$ and $z(\alpha)$ as a function of α for the four transformations mentioned above, respectively. With increase in λ value, the value of α_p^∞ decreases and deviates from the typical value of 0.632 for JMA phase transformation, and also the value of α_M deviates from $\alpha_M = 1 - \exp(\frac{1}{n} - 1)$. For example, the values of α_p^∞ at $\lambda=1.2$ and 4, are 0.604 and 0.375, respectively.

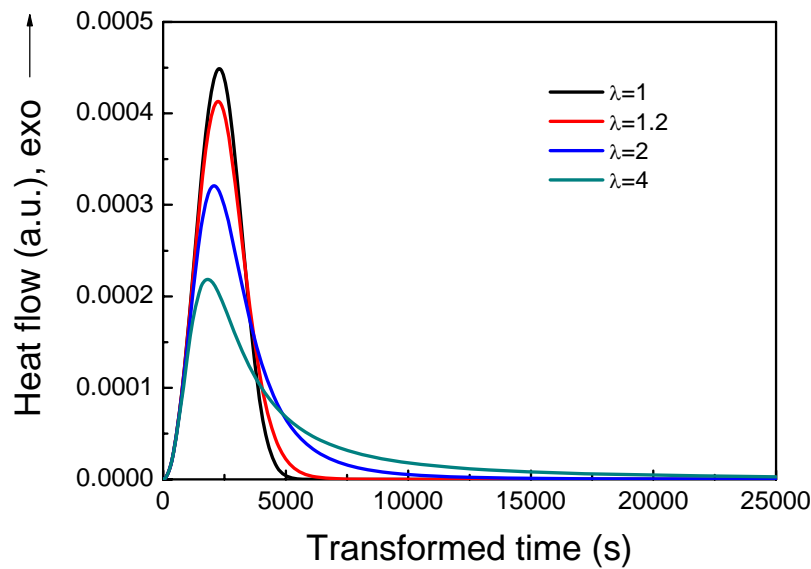


Fig. 4-13 Theoretical thermal analysis curves with different impingement factors (JMA and Starink models). The kinetic parameters used are $T=700$ K, $n=3$, $E=350$ kJ/mol, $K_0=5e22$ s⁻¹, $\lambda=1$, 1.2, 2, 4

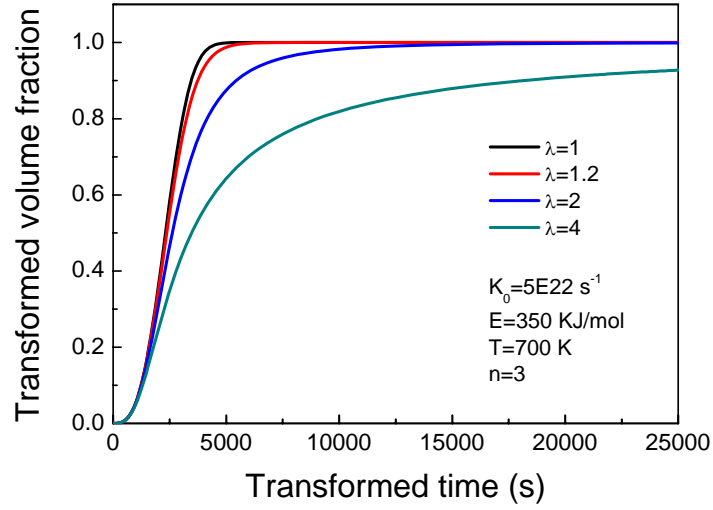


Fig. 4-14 Transformed fraction as function of time at different impingement factors (JMA and Starink models). The kinetic parameters used are $T=700$ K, $n=3$, $E=350$ kJ/mol, $K_0=5e22$ s⁻¹, $\lambda=1, 1.2, 2, 4$

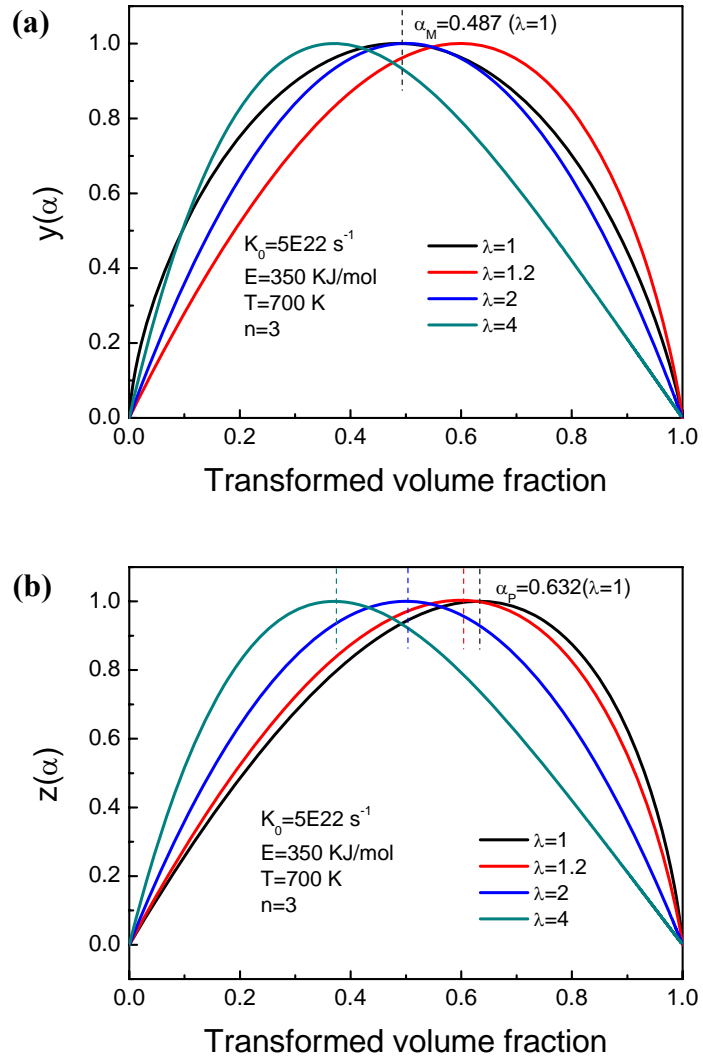


Fig. 4-15 Normalized $y(\alpha)$ and $z(\alpha)$ functions obtained from the theoretical JMA model and kinetics considered impingement effect.

The JMA plots of the four transformations are shown in Fig. 4-16. It is found that the three transformations ($\lambda=1.2, 2, 4$) deviate from the typical linear characteristic of JMA plot ($\lambda=1$), which starts from the very beginning $\alpha=0.01$ and deviates significantly at $\alpha=0.10$. The local Avrami exponent n_{loc} was then calculated according to Eq. 4-14 and plotted as a function of α in Fig. 4-17. It is found that for $\lambda=1$, the local Avrami exponent remains at a constant value of 3 in the whole transformed volume fraction range, as is consistent with the kinetic exponent value we set, however, in the case of $\lambda>1$, the local Avrami exponent decreases monotonously. From the definition of local Avrami exponent, the mechanisms of the overall transformation should be described by a changing kinetic exponent. However, as we know, the Avrami exponent n for these four transformations should be a constant of 3 during the whole phase transformation range as the value we set, so, for the phase transformations with $\lambda>1$, a low value of the Avrami exponent will be obtained by the wrong application of JMA model in calculating n , and the calculated value of n is not a constant, which decreases with the time, as is similar with the local Avrami exponent which is widely used in interpreting the non-constant characteristic of Avrami exponent: change dependent with the time or transformed volume fraction. However, here, it is resulting from the failed application of kinetic model, not using the real change of phase transformation mechanism for the value of n , was assumed to be a constant of 3 for these four phase transformations. In addition, the larger λ is, the smaller value of n is. So the wrong evaluated value of Avrami exponent will be obtained as long as the inappropriate kinetic model is applied.

Based on the Starink model, the Avrami exponent can be determined from the slope of a

$\ln \frac{(1-\alpha)^{-(\lambda-1)} - 1}{\lambda - 1}$ vs. $\ln t$ plot (Fig. 4-18) and the corresponding local Avrami exponent n_{loc} is

modified to be

$$n_{loc} = \frac{\partial \ln \frac{(1-\alpha)^{-(\lambda-1)} - 1}{\lambda - 1}}{\partial \ln t}. \text{ It is seen that the slope of the } \ln \frac{(1-\alpha)^{-(\lambda-1)} - 1}{\lambda - 1} \text{ vs. } \ln t \text{ plots}$$

for four phase transformations is consistent and equal to 3. So the appropriate use of kinetic model is essential for the determination of nucleation and growth mechanism.

Actually, the JMA model can be obtained from the Starink model under the condition of $\lambda=1$. In this case, Starink model can be regarded as a general expression for describing the kinetics of phase transformations, which is effective for solving the common problems which is not strictly in accordance with the JMA theory.

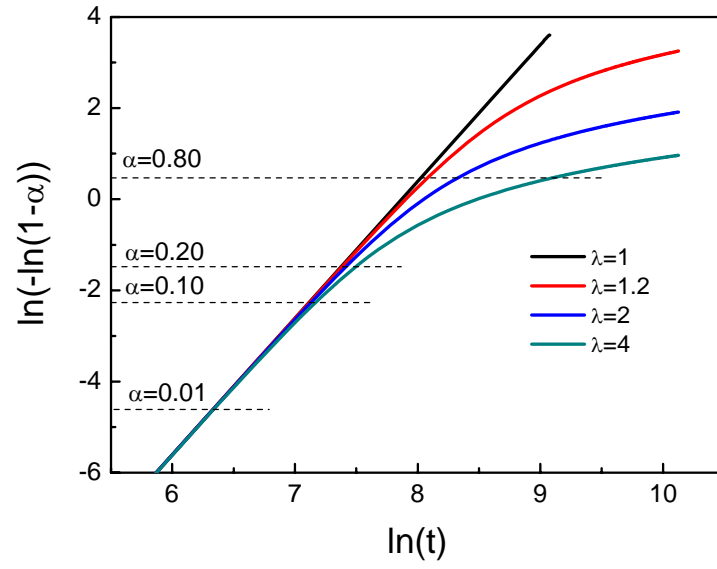


Fig. 4-16 Avrami plot calculated based on JMA model

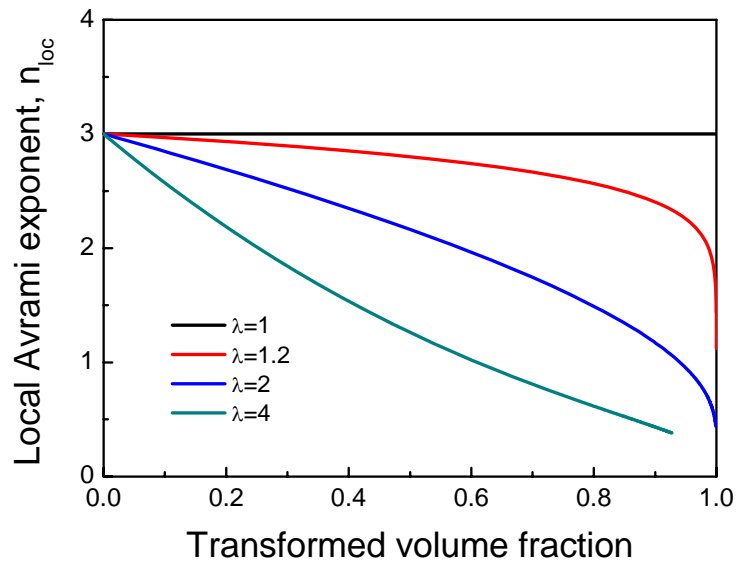


Fig. 4-17 The local Avrami exponents calculated from Eq. 4-14 as a function of the transformed fraction for different transformations

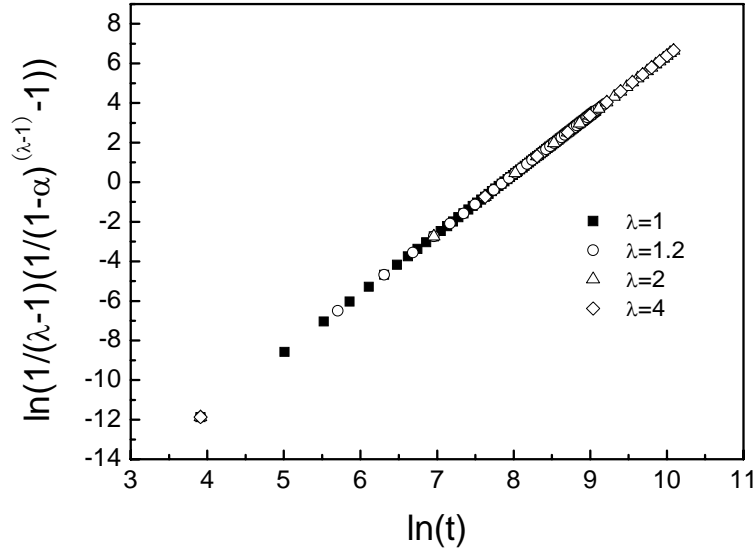


Fig. 4-18 Avrami plots assuming to the right kinetic model

4.4.2 Kinetics Analysis of Crystallization for

$\text{Ti}_{41.5}\text{Cu}_{37.5}\text{Ni}_{7.5}\text{Zr}_{2.5}\text{Hf}_5\text{Sn}_5\text{Si}_1$ BMG

As shown in chapter 2, the crystallization of $\text{Ti}_{41.5}\text{Cu}_{37.5}\text{Ni}_{7.5}\text{Zr}_{2.5}\text{Hf}_5\text{Sn}_5\text{Si}_1$ as well as $\text{Ti}_{40}\text{Zr}_{25}\text{Ni}_8\text{Cu}_9\text{Be}_{18}$ BMGs is multistage, only the kinetics analysis for the first crystallization stage will be presented in this chapter for their rather important effects.

4.4.2.1 Isothermal kinetics analysis for the crystallization of

$\text{Ti}_{41.5}\text{Cu}_{37.5}\text{Ni}_{7.5}\text{Zr}_{2.5}\text{Hf}_5\text{Sn}_5\text{Si}_1$ BMG

The experimental isothermal DSC curves for the crystallization of $\text{Ti}_{41.5}\text{Cu}_{37.5}\text{Ni}_{7.5}\text{Zr}_{2.5}\text{Hf}_5\text{Sn}_5\text{Si}_1$ BMG annealed at different temperatures between 430 and 440 °C are shown in Fig. 4-19 (solid lines). Each DSC curve exhibits an incubation period followed by an exothermic peak, which corresponds to the crystallization of the amorphous phase. The incubation time for the exothermic reaction at different temperatures are listed in Table 4-5. It can be seen that the incubation time as well as the whole isothermal crystallization time increases as the annealing temperatures decrease, and the enthalpy for the crystallization at each annealing temperature keeps the same value, indicating a typical nucleation/growth crystallization mode.

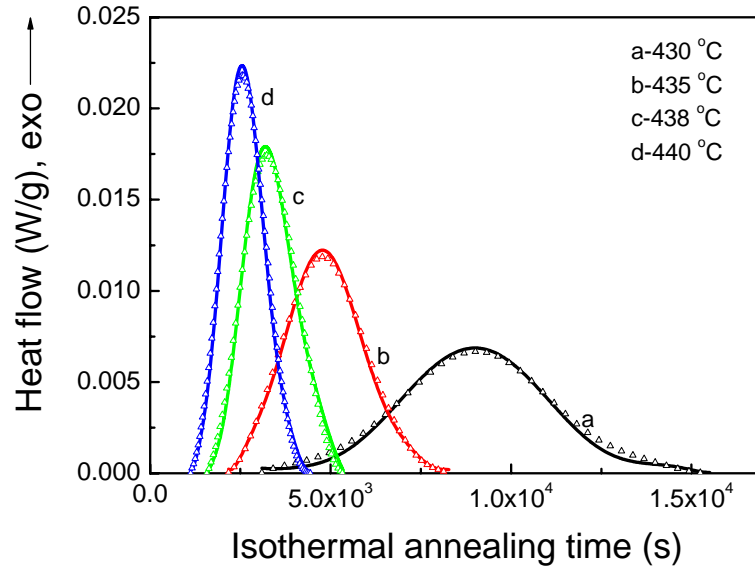
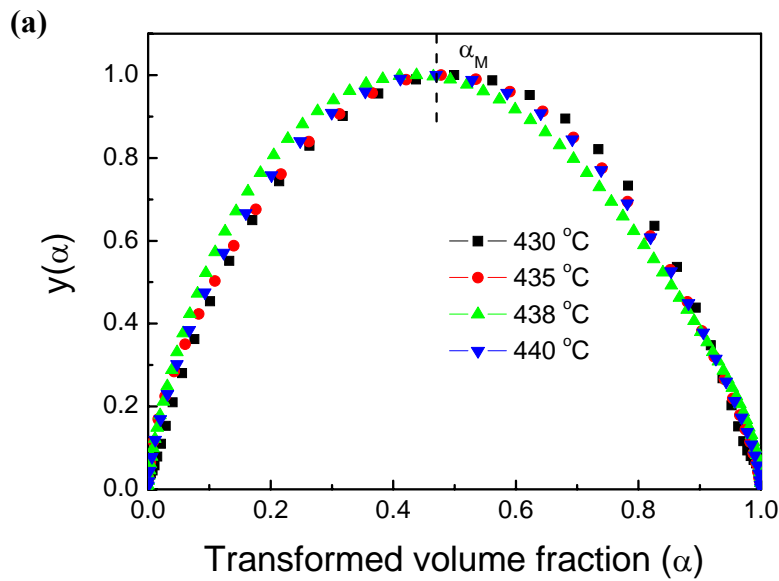


Fig. 4-19 Comparison of the experimental DSC curves (solid lines) and the DSC data calculated based on JMA model (symbols) for the first crystallization stage of $\text{Ti}_{41.5}\text{Cu}_{37.5}\text{Ni}_{7.5}\text{Zr}_{2.5}\text{Hf}_5\text{Sn}_5\text{Si}_1$ BMG

As discussed above, the appropriate kinetic model must be determined before studying the transformation kinetics. **Fig. 4-20 (a)** and **(b)** show the calculated $y(\alpha)$ and $z(\alpha)$ as a function of α at different annealing temperatures. The values of α_p^∞ for the samples annealed at all the annealing temperatures are consistent within the 0.61-0.65 range, indicating that the kinetic isothermal crystallization of $\text{Ti}_{41.5}\text{Cu}_{37.5}\text{Ni}_{7.5}\text{Zr}_{2.5}\text{Hf}_5\text{Sn}_5\text{Si}_1$ BMG can be described by the JMA model. Based on the JMA model, the average value of Avrami exponent can be deduced from the α_M value in the $y(\alpha)$ - α plot, and should be approximately 2.75.



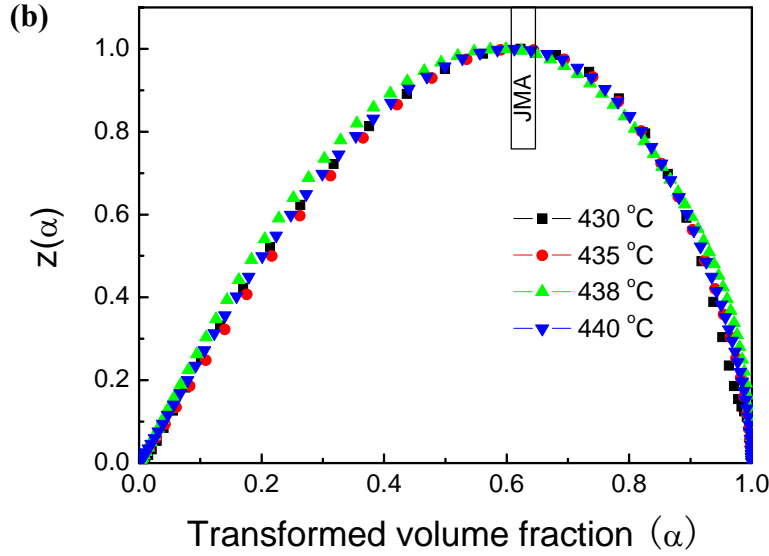


Fig. 4-20 Normalized (a) $y(\alpha)$ and (b) $z(\alpha)$ as a function of transformed volume fraction obtained from the isothermal DSC curves of $\text{Ti}_{41.5}\text{Cu}_{37.5}\text{Ni}_{7.5}\text{Zr}_{2.5}\text{Hf}_5\text{Sn}_5\text{Si}_1$ BMG for the first crystallization stage. The dash line in (a) shows the α_M value, the solid lines in (b) show the typical interval of

α_p^∞ values for the JMA model

The kinetic parameters, the reaction rate constant K_0 and Avrami exponent n , can be calculated by fitting the experimental DSC curves with the Eq. 4-13 based on the JMA model, and are summarized in Table 4-4. The JMA fitting curves are shown in Fig. 4-19 (symbols) for comparison, it is clear that the experimental DSC curves (solid lines) of the isothermal crystallization can be successfully described by the JMA model with the kinetic parameters listed in Table 4-5. In order to get the whole picture of the Avrami exponent n , the change of Avrami exponent as a function of transformed volume fraction of precipitates at different isothermal temperature was obtained by the calculation of local Avrami exponent n_{loc} according to Eq. 4-14, which is shown in Fig. 4-21. It is found that Avrami exponents n basically keep constant in the middle range ($0.2 < x < 0.8$) at a certain annealing temperature, and is in the range of 2.5-3.0 except at the lower temperature of 430 °C, which is coincident with the typically JMA model. Some reports related to the isothermal crystallization kinetics reported that the phase transformation mechanism may depend on temperature during isothermal annealing. Further analysis makes us think about whether the Avrami exponent is dependent on the annealing temperature or not, however, due to the absence of much enough experimental data, we can only make the conclusion that it is not reliable. In regard to the sensitivity of the Avrami exponent n dependence of annealing temperature, it should be discussed in a large annealing temperature range and perform more experiments, as will be realized in a future work.

Table 4-4

Kinetic parameters obtained from the first crystallization reaction of the $\text{Ti}_{41.5}\text{Cu}_{37.5}\text{Ni}_{7.5}\text{Zr}_{2.5}\text{Hf}_5\text{Sn}_5\text{Si}_1$ samples using the JMA model

Isothermal temperature ($^{\circ}\text{C}$)	K_0 (s^{-1})	n	Incubation time τ (s)
430	2.934e20	3.37	3082
435	4.145e20	2.92	2166
438	5.523e20	2.56	1570
440	5.509e20	2.85	1114

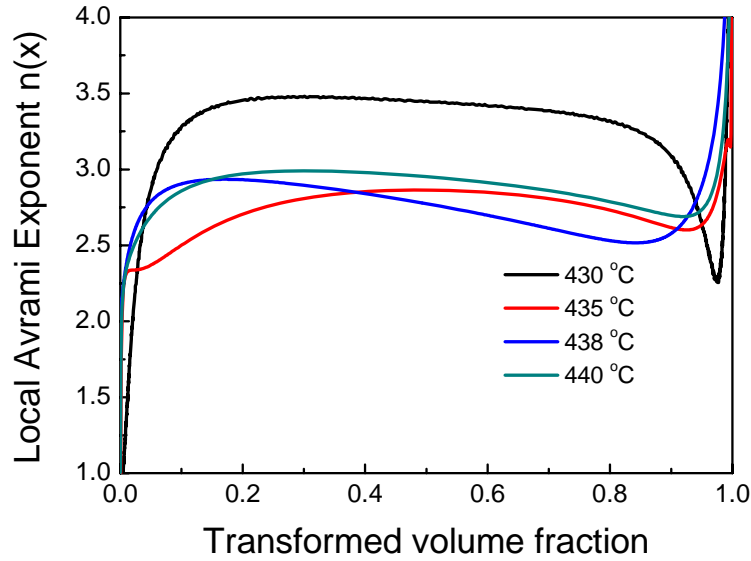


Fig. 4-21 Local Avrami exponent for the first crystallization stage of $\text{Ti}_{41.5}\text{Cu}_{37.5}\text{Ni}_{7.5}\text{Zr}_{2.5}\text{Hf}_5\text{Sn}_5\text{Si}_1$

By using the Ranganathan and Heimandahl model [Ranganathan et al., 1981] suggesting that the Avrami exponent n can be expressed as

$$n = a + bc \quad (4-33)$$

where a is the nucleation index, ($a=0$ for a nucleation rate of zero, $0 < a < 1$ for a decreasing nucleation rate with time, $a=1$ for a constant nucleation rate and $a > 1$ for an increasing nucleation rate), and b is the dimension of the growth (with values 1, 2, or 3 for one-, two-, three-dimensional growth, respectively), and c is the growth index ($c=1$ for interface-controlled growth and $c=0.5$ for diffusion-controlled growth).

For $\text{Ti}_{41.5}\text{Cu}_{37.5}\text{Ni}_{7.5}\text{Zr}_{2.5}\text{Hf}_5\text{Sn}_5\text{Si}_1$ metallic glass annealed in the temperature range between 430 and 440 $^{\circ}\text{C}$, it is found that the value of the index a is between 1.35 and 1.42, meaning an ‘increasing nucleation rate’ (except at 430 $^{\circ}\text{C}$), that of the index b was equal to 3 corresponding to a ‘sphere-type growth’, and the value of the index c was equal to 0.5 meaning a ‘diffusion-controlled growth’. This suggests that the crystallization for the first stage crystallization reaction of the $\text{Ti}_{41.5}\text{Cu}_{37.5}\text{Ni}_{7.5}\text{Zr}_{2.5}\text{Hf}_5\text{Sn}_5\text{Si}_1$ metallic glass occurred with an increasing nucleation rate with time and is mainly governed by a three dimensional diffusion-controlled growth. In the case of isothermal annealing temperature below 430 $^{\circ}\text{C}$, the value of Avrami exponent n is larger than 3, assuming this value is believable, it suggests that the growth mechanism may change from the diffusion-controlled three-dimensional growth to the interface-controlled three-dimensional growth with decreasing nucleation rate.

4.4.2.2 Isochronal kinetics analysis

Fig. 2-22 (a) (in chapter 2) shows the DSC curves of $\text{Ti}_{41.5}\text{Cu}_{37.5}\text{Ni}_{7.5}\text{Zr}_{2.5}\text{Hf}_5\text{Sn}_5\text{Si}_1$ BMG measured at various heating rates of 5-40 K/min. At each heating rate, two crystallization events can be identified, corresponding to two crystallization stages. However, only under the condition of low heating rate, the two crystallization events can be well-separated, while the high heating rate can lead to the merge of two crystallization events. So in this study, only the isochronous heating process at heating rates of 5 and 10 K/min were chosen to be investigated.

As previously, the kinetic model was determined before studying the transformation kinetics through the calculation of $z(\alpha)$. Fig. 4-22 shows the calculated $z(\alpha)$ as a function of α for the first crystallization event at different heating rates of 5 and 10 K/min. It is clear that the values of α_p^∞ are significantly smaller than the 0.61-0.65 values of the JMA model, indicating that the crystallization event of this alloy deviates from the JMA theory. The value of α_p^∞ exhibits strong heating rate dependence. When the heating rate increases from 5 to 10 K/min, the value of α_p^∞ decreases approximately from 0.325 to 0.258 for the first crystallization event. So the Starink model considering the impingement (λ) is believed to be more applicable for describing the isochronal crystallization kinetics of $\text{Ti}_{41.5}\text{Cu}_{37.5}\text{Ni}_{7.5}\text{Zr}_{2.5}\text{Hf}_5\text{Sn}_5\text{Si}_1$ BMG in this study.

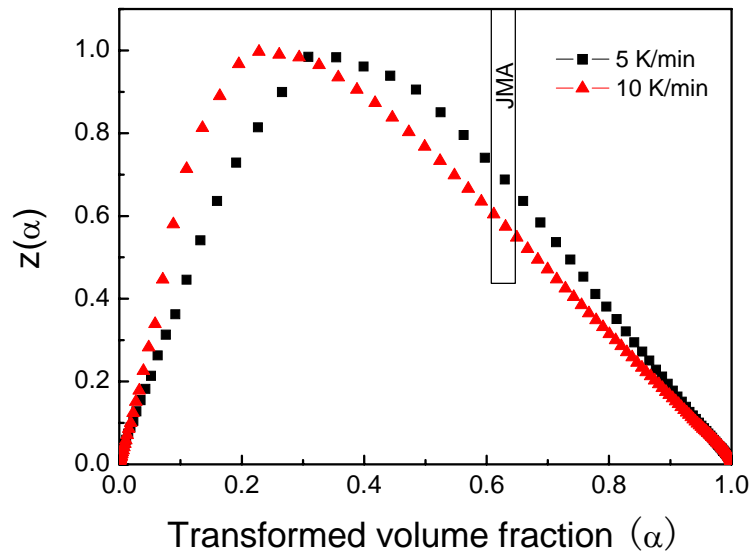


Fig. 4-22 Normalized $z(\alpha)$ function obtained by transformation of non-isothermal DSC data for the first crystallization stage of $\text{Ti}_{41.5}\text{Cu}_{37.5}\text{Ni}_{7.5}\text{Zr}_{2.5}\text{Hf}_5\text{Sn}_5\text{Si}_1$ BMG. Solid lines show the typical

interval of α_p^∞ values for the JMA model

Besides the theoretical DSC curves calculated based on the Starink model, we have also calculated theoretical DSC curves based on the JMA model for comparison. The corresponding theoretical DSC curves based on both JMA and Starink models are shown in Fig. 4-23 and 4-24, respectively, the experimental DSC curves (baseline corrected) are also shown in these two figures for comparison. For the DSC curves calculated using the JMA model, obvious difference exists between the calculated and experimental data even if using low heating rate, and the deviation

from the JMA model increases remarkably with increase in heating rate. The DSC curves calculated based on Starink model, however, fit well with the experimental data, suggesting that the isochronal crystallization kinetics of the $\text{Ti}_{41.5}\text{Cu}_{37.5}\text{Ni}_{7.5}\text{Zr}_{2.5}\text{Hf}_5\text{Sn}_5\text{Si}_1$ BMG could be successfully described by the Starink model through considering the impingement. The kinetic parameters, K_0 , n , E_a as well as λ calculated from both JMA and Starink curves are summarized in Table 4-5.

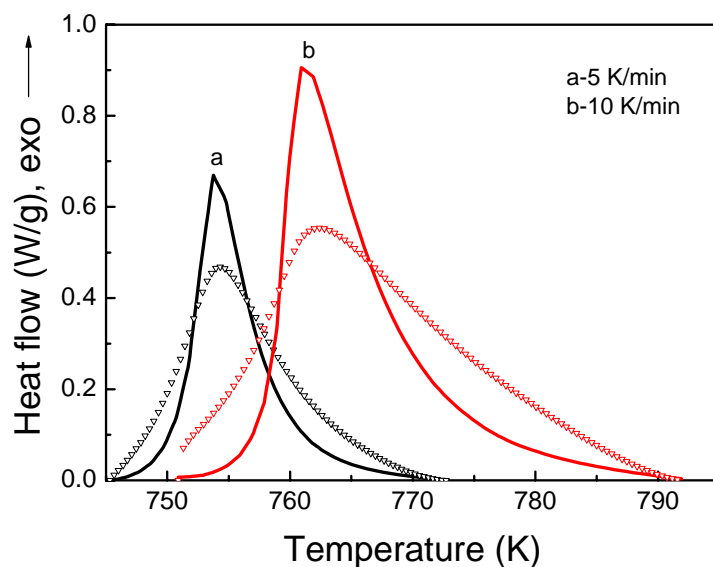


Fig. 4-23 Comparison of the experimental DSC curves (solid lines) and the DSC data calculated based on JMA model (symbols) for the first crystallization stage of $\text{Ti}_{41.5}\text{Cu}_{37.5}\text{Ni}_{7.5}\text{Zr}_{2.5}\text{Hf}_5\text{Sn}_5\text{Si}_1$ BMG under the condition of non-isothermal heating

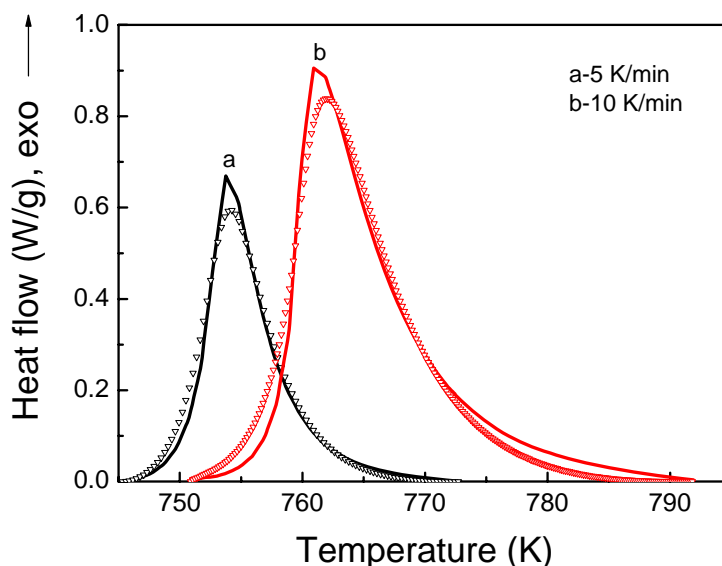


Fig. 4-24 Comparison of the experimental DSC curves (solid lines) and the DSC data calculated based on the Starink model (symbols) for the first crystallization stage of $\text{Ti}_{41.5}\text{Cu}_{37.5}\text{Ni}_{7.5}\text{Zr}_{2.5}\text{Hf}_5\text{Sn}_5\text{Si}_1$ BMG under the condition of non-isothermal heating

Table 4-5

Kinetic parameters determined using JMA and Starink models for the first crystallization stage of $\text{Ti}_{41.5}\text{Cu}_{37.5}\text{Ni}_{7.5}\text{Zr}_{2.5}\text{Hf}_5\text{Sn}_5\text{Si}_1$ BMG with heating rate of 5 and 10 K/min

Heat rate (K/min)	K_0 (s^{-1})		n		λ	E_a (kJ/mol)	
	JMA	Starink	JMA	Starink	Starink	JMA	Starink
5	2.89e20	6.23e19	1.62	3.68	2.29	323	313
10	6.46e19	1.58e20	1.32	3.26	3.08	315	318

It is found that the fitting parameters calculated from the JMA model and Starink model are quite different, especially the Avrami exponent n who determines the crystallization mechanism. Based on the JMA model, the calculated Avrami exponent is in the range of 1.3-1.6 at the experimental heating rates, implying that the first crystallization process is basically a diffusion-controlled three dimensional growth of pre-existing nuclei, and is inconsistent with the truth for the fully amorphous nature of the as-cast samples. On the contrary, if the first crystallization process is governed by a growth of pre-existing nuclei, this process should be well described by JMA model, at least at low heating rate. On the other hand, the value of Avrami exponent obtained from fitting the experimental data with the Starink model is in the range of 3.2-3.6 is also reasonable, suggesting that it is governed by an interface-controlled three dimensional growth process. Furthermore, it is found that the kinetic parameters are strongly sensitive to the heating rate, for example, the Avrami exponent n decreases and the impingement factor λ increases with increase in heating rate. So increasing the heat rate may lead to the continuous decrease of Avrami exponent, and finally lead to the change in crystallization mechanism. From this viewpoint, the mechanism for isothermal and isochronal crystallization is consistent.

It should be pointed out that the isothermal crystallization process can be well fitted by the JMA model, while in the case of isochronal crystallization event it is far deviating from the JMA theory, as may be due to (i) the limited application of JMA model in isochronal crystallization, (ii) the enhancement of the soft impingement effect resulting from the thermal activation in continuous heating, or (iii) the fast increase of the initial crystallization rate due to a secondary nucleation induced by the crystal growth or associated with the adiabatic temperature drift in the metallic glass as the crystallization heat is released in the isochronal crystallization process. Strictly speaking, the JMA model can be extended to non-isothermal conditions only provided that a new crystalline phase grows from a constant number of nuclei and all nucleation is completed before the macroscopic crystal growth started. The so-called “site saturation” assumption is an important condition for the isokinetic crystallization process where the crystallization rate is defined only by temperature and does not depend on the previous thermal history [Henderson, 1979]. In light of the above requirement, the considerable deviation from JMA model for the isochronal crystallization of this alloy may be due to the overlapping of the nucleation and growth processes. On the other hand, in order to understand the different crystallization behavior in the isothermal and isochronal process (obey JMA model or not), we should consider the different degree of soft impingement effects in these two processes because in the study of another metallic glass, $\text{Ti}_{40}\text{Zr}_{25}\text{Ni}_8\text{Cu}_9\text{Be}_{18}$, we found that even if the “site saturation” assumption for the application of JMA model in isochronal crystallization is fulfilled, the isochronal crystallization may still deviates from the JMA theory, and the higher the heating rate, the larger deviation from

the JMA model will be, consequently, the different degree of the soft impingement effects resulting from the thermal activation associated with the heating rate should be responsible for the deviation from the JMA model. Pradell et al. [Pradell et al., 1997] reported that the soft impingement effect, especially in the late stage of the phase transformation process, could cause similar deviation from the JMA kinetics equation for a FINEMET amorphous alloy. It is generally believed that the soft impingement effect should be obvious at the late stage of crystallization for the single step crystallization reaction. In regard to the multi-step crystallization process, the degree of the soft impingement effect is associated with the detailed crystallization behavior. For $\text{Ti}_{41.5}\text{Cu}_{37.5}\text{Ni}_{7.5}\text{Zr}_{2.5}\text{Hf}_5\text{Sn}_5\text{Si}_1$ metallic glass, the soft impingement plays an important effect even for the first crystallization process because of its special crystallization behavior which will be presented later: large quantities of nanocrystals are formed during the first crystallization process. From another point of view, the isothermal process can be regarded as the limit when the heating rate is small enough in the isochronal process, during the process of isochronal crystallization, with increase in heating rate, the soft impingement effect increases from a very limited degree to a large degree, so for the isothermal crystallization (regarded as an isochronal process with small enough heating rate), the soft impingement can be neglected and the JMA model is valid, while for the isochronal process it is the contrary.

Comparing the isothermal and isochronal crystallization processes, the crystallization for the isochronal process is significantly influenced by the soft impingement while not in the isothermal process, which indicates the more complicated crystallization process for the isochronal process with respect to the isothermal process; however, the calculated Avrami exponent reveals that the crystallization mechanisms of these two processes are almost consistent.

4.4.3 Kinetics Analysis of Crystallization for $\text{Ti}_{40}\text{Zr}_{25}\text{Ni}_8\text{Cu}_9\text{Be}_{18}$ BMG

The crystallization kinetics for isothermal as well as isochronal process for the $\text{Ti}_{40}\text{Zr}_{25}\text{Ni}_8\text{Cu}_9\text{Be}_{18}$ BMG were investigated using the same method applied in the crystallization kinetics study for the $\text{Ti}_{41.5}\text{Cu}_{37.5}\text{Ni}_{7.5}\text{Zr}_{2.5}\text{Hf}_5\text{Sn}_5\text{Si}_1$ BMG above.

4.4.3.1 Isothermal kinetics analysis

The isothermal crystallization for the $\text{Ti}_{40}\text{Zr}_{25}\text{Ni}_8\text{Cu}_9\text{Be}_{18}$ BMG has been presented in the chapter 2. The isothermal DSC curves at any annealing temperature in the supercooled liquid region show the characteristic of the monotonic calorimetric signal instead of exothermic peak, indicates that the isothermal crystallization mechanism for $\text{Ti}_{40}\text{Zr}_{25}\text{Ni}_8\text{Cu}_9\text{Be}_{18}$ BMG is governed by the quenched-in nuclei growth with zero nucleation rate.

4.4.3.2 Isochronal kinetics analysis

The DSC curves of the as-cast $\text{Ti}_{40}\text{Zr}_{25}\text{Ni}_8\text{Cu}_9\text{Be}_{18}$ BMG isochronal heated with heating rates of 10, 20, 30 and 40 K/min have been shown in Fig. 2-21 (a) in the chapter 2. As we have shown, the crystallization process exhibits three steps, as usual, only the kinetics of the first crystallization event will be investigated in this study. The value of α_p^∞ shown in the $z(\alpha)$ - α plot (Fig. 4-25) is about 0.4, obviously deviating from that of JMA model (0.61-0.65), suggesting that the JMA model is not applicable to describe the crystallization process of this alloy, as can be seen from the

larger difference between the theoretical JMA fitting curves and the experimental data shown in Fig. 4-26. By considering the soft impingement effect, the Starink model is successful in describing this crystallization process (Fig. 4-27), the obtained kinetic parameters at different heating rates are summarized in Table 4-6. The Avrami exponents obtained at different heating rates are around 1.5, implying that the isochronal crystallization process is governed by a diffusion-controlled three dimensional growth of the quenched-in nuclei, which is in accordance with the isothermal crystallization process.

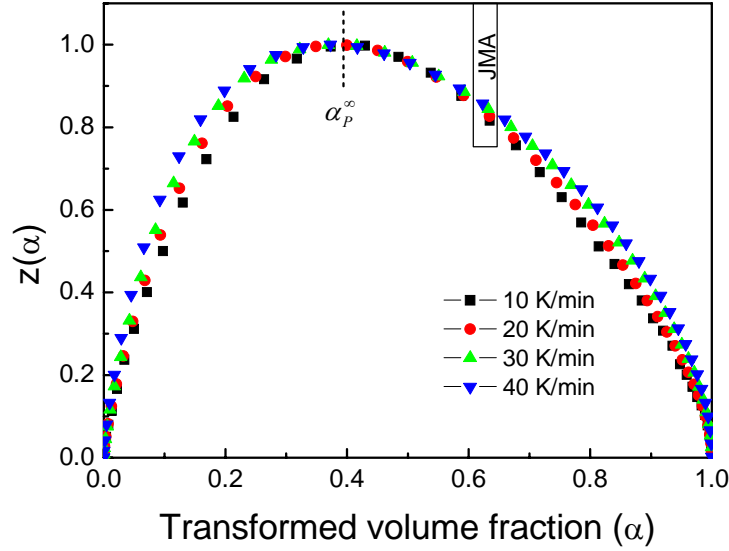


Fig. 4-25 Normalized $z(\alpha)$ function obtained by transformation of non-isothermal DSC data for the first crystallization stage of $\text{Ti}_{40}\text{Zr}_{25}\text{Ni}_8\text{Cu}_9\text{Be}_{18}$ BMG

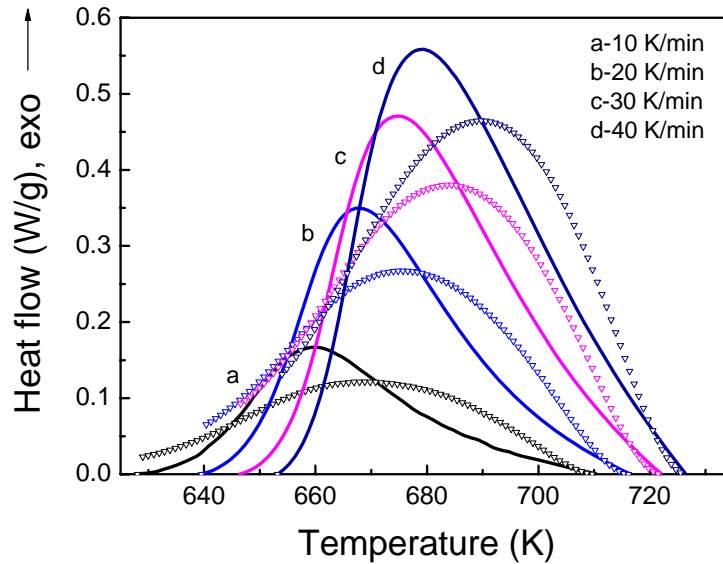


Fig. 4-26 Comparison of the experimental DSC curves (solid lines) and the DSC data calculated based on JMA model (symbols) for the first crystallization stage of $\text{Ti}_{40}\text{Zr}_{25}\text{Ni}_8\text{Cu}_9\text{Be}_{18}$ BMG under the condition of non-isothermal heating

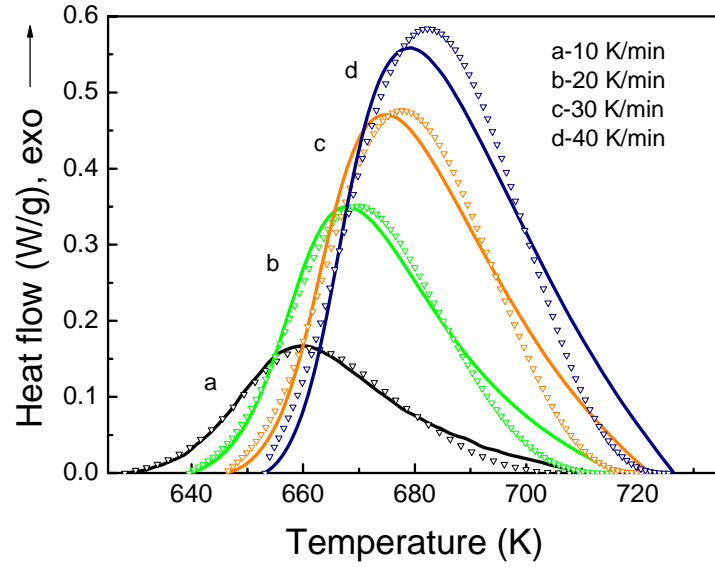


Fig. 4-27 Comparison of the experimental DSC curves (solid lines) and the DSC data calculated based on the impingement model (symbols) for the first crystallization stage of $\text{Ti}_{40}\text{Zr}_{25}\text{Ni}_8\text{Cu}_9\text{Be}_{18}$ BMG under the condition of non-isothermal heating

Table 4-6

Normalized $z(\alpha)$ function obtained by transformation of non-isothermal DSC data for the first crystallization stage of $\text{Ti}_{40}\text{Zr}_{25}\text{Ni}_8\text{Cu}_9\text{Be}_{18}$ BMG

Heat rate (K/min)	$K_0 \text{ (s}^{-1}\text{)}$		n		λ
	JMA	Starink	JMA	Starink	Starink
10	2.16e16	4.12e16	1.00	1.60	1.95
20	2.70e16	4.74e16	1.00	1.66	2.03
30	2.53e16	4.25e16	0.996	1.53	2.21
40	2.47e16	4.32e16	1.00	1.41	2.21

4.5 Thermally Induced Structural Transformations

It is believed that the characteristics of the microstructure, morphology, grain size and distribution, etc., determine the final properties of the materials. So the investigation on the microstructure evolution upon isochronal heating as well as isothermal heating is an important and elementary research. It is necessary to investigate the phase transformation under the isothermal and isochronal conditions because the phase transformation process via different caloric inputting mode may be different, as has been reported in some metallic glasses. In this section, the thermally induced (the caloric inputting mode: isothermal and isochronal) structural transformations (the phase transformations and microstructure evolution during the process of structural relaxation to crystallization) of $\text{Ti}_{41.5}\text{Cu}_{37.5}\text{Ni}_{7.5}\text{Zr}_{2.5}\text{Hf}_5\text{Sn}_5\text{Si}_1$ and $\text{Ti}_{40}\text{Zr}_{25}\text{Ni}_8\text{Cu}_9\text{Be}_{18}$ BMGs have been investigated and will be presented.

4.5.1 Thermally Induced Structural Transformations for $\text{Ti}_{41.5}\text{Cu}_{37.5}\text{Ni}_{7.5}\text{Zr}_{2.5}\text{Hf}_5\text{Sn}_5\text{Si}_1$ BMG

4.5.1.1 Phase transformation

$\Phi 4$ samples have been heated in the DSC apparatus at 716 K, slightly above T_g ($T_g=698\text{K}$) at a constant heating rate (20 K/min) then maintained at this temperature for annealing at different times then quenched in air. In order to study the crystallization process by an ex-situ method, two $\Phi 4$ samples were heated at the same heating rate: one was maintained 5 min at 769 K, this temperature being at the end of the first crystallization DSC peak, and the other one was maintained at 873 K, this temperature being at the end of the second crystallization DSC peak. X-ray patterns of these samples show broad amorphous peak with the cubic $\text{TiNi}(\text{Cu})$ phase peak intensities increasing with time and the hexagonal $\text{Ti}_5\text{Sn}_3\text{Cu}$ phase appearing more clearly, the pattern recorded after the first crystallization peak (769 K) having the same properties, the cell parameter of this cubic phase ($a=0.3090(2)$ nm) is not evolving with crystallization in all these samples (Fig. 4-28). The sample recorded after the second DSC event at 800 K can be indexed with two main phases, the tetragonal $\gamma\text{-TiCu}$ phase with parameters $a=0.3120(1)$ nm and $c=0.5920(3)$ nm and the hexagonal $\text{Ti}_5\text{Sn}_3\text{Cu}$ phase with parameters $a=0.8020(3)$ nm and $c=0.5583(2)$ nm (Fig. 4-28). The $\gamma\text{-TiCu}$ phase replacing the cubic $\text{TiNi}(\text{Cu})$ phase with close cell parameters ($a(\gamma\text{-TiCu})=a(\text{TiNi})$; $c(\gamma\text{-TiCu})=2a(\text{TiNi})$), it is suggested that the second peak in the DSC scan is the transformation of the metastable cubic $\text{TiNi}(\text{Cu})$ phase in tetragonal $\gamma\text{-TiCu}$ phase. The $\beta\text{-Ti}$ phase is bcc with space group $\text{Im}\bar{3}\text{m}$ and implies no ordering between the atoms at the 0,0,0 position and the centered $1/2, 1/2, 1/2$ ones. X-ray is not able to show this ordering for contiguous elements among the 3d metal series. We will see in the following experiments with neutron diffraction studies that titanium occupies mainly the 0,0,0 position and Cu and Ni, the centered $1/2, 1/2, 1/2$ one, so that the (100) and (111) peaks are present, leading to the $\text{Pm}\bar{3}\text{m}$ space group.

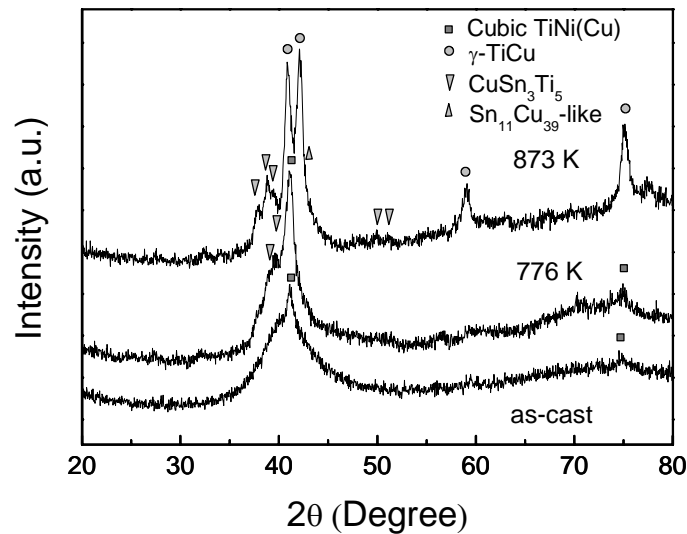


Fig. 4-28 XRD patterns obtained from the as-cast $\text{Ti}_{41.5}\text{Cu}_{37.5}\text{Ni}_{7.5}\text{Zr}_{2.5}\text{Hf}_5\text{Sn}_5\text{Si}_1$ specimen with 4 mm in diameter and the annealed specimens at 769 and 873 K, respectively.

However, simply applying the X-ray technique to determine the phase transformation is not believable. Especially for the determination of phase evolution in the complex multi-component metallic glasses whose phase transformation is complicated, in which generally metastable phases will occur as a inter-process upon heating, and the intensity of diffraction peak is generally to be weak and less diffraction peaks can be observed resulting from the small grain size and incomplete crystallization; in addition, the relative diffraction peak will be changed due to the orientation in solid materials which is absent in powder materials; solid solution is common to be formed during the crystallization of metallic glasses resulting in the change of lattice parameter finally changing the d value which is related to the position of diffraction peak. For example, during the phase analysis of X-ray diffraction, it is difficult to identify the existence of metastable cubic TiNi(Cu) and γ -TiCu phase because of the similar position of main diffraction peaks, leading to fail in getting the exact information about the phase transformation upon heating. Based on the analysis above, it is necessary to combine other experiments to identify the phase transformation upon heating. In this study, in-situ neutron diffraction was performed. In addition, SEM with EDS and TEM observation were applied for getting information about the microstructure evolution as well as for determining the phase structure, in order to clarify the crystallization behavior of this alloy.

Neutron diffraction patterns have been recorded on $\Phi 4$ samples. The constant heating rate at 2 K/min up to 920 K and after a plateau at this temperature is presented in Fig. 4-31 as a 3D plot with 2θ along the x-axis, the temperature (or time) along the y-axis and the intensity of the neutron counts along the z-axis. Neutron diffraction technique measures the whole volume of the sample, so it is possible to observe three different components of diffraction, a bump centered at $2\theta=73^\circ$ corresponding to the amorphous part of the sample, small lines around $2\theta=22$ and 42° and indexed as the $\text{Ti}_5\text{Sn}_3\text{Cu}$ phase and 3 stronger lines indexed as (100), (110) and (111) of a cubic phase. The neutron diffraction pattern at the beginning of the experiment (without any thermal treatment) (see Fig. 4-29) and the corresponding X-ray diffraction pattern have been both refined with a model of two phases, $\text{Ti}_5\text{Sn}_3\text{Cu}$ (SP= $P6_3/mmc$; $a=0.8117(7)$ nm, $c=0.5605(8)$ nm) and TiNi(Cu) (SP= $Pm-3m$; $a=0.3117(1)$ nm) with Ti at the 0,0,0 position and Ni, Cu at the $\frac{1}{2}, \frac{1}{2}, \frac{1}{2}$ position. The result of these refinements gives a good refinement with the 3 peaks (100), (110) and (111) and X-ray diffraction pattern with the (110) peak only. Copper, nickel and titanium have a too close number of electrons to observe this ordering by X-ray, but the high neutron contrast between scattering lengths of titanium (-0.34) compared to copper (0.77) and nickel (1.03) evidences this ordering. During the heating at 2 K/min, two transformations of phases occur, the first at $T_{x1}=737$ K with the appearance of a new set of lines indexed as the γ -TiCu phase and a $\text{Sn}_{11}\text{Cu}_{39}$ -like phase at 803 K. From T_{x1} , the diffraction intensity of the three strongest lines corresponding to metastable cubic TiNi(Cu) phase decreases with increase in temperature until the temperature around T_{x2} where the three strongest lines originated from the nature of the as-cast $\Phi 4$ sample disappear; meanwhile in the same temperature range, three new lines which are corresponding to the new phase γ -TiCu phase come out, indicating that the cubic TiNi(Cu) phase transforms into the γ -TiCu phase via the first exothermic event upon heating. Above T_{x2} , the intensity of the three diffraction peaks located at $2\theta=24.5^\circ, 54^\circ, 75^\circ$ corresponding to γ -TiCu phase increases with increase in temperature, in addition, two new diffraction peaks also corresponding to γ -TiCu phase located at $2\theta=69.4^\circ, 71.5^\circ$ occur, indicating that more γ -TiCu phase forms resulting from the transformation from amorphous phase into γ -TiCu phase. The lines

corresponding to the $\text{Ti}_5\text{Sn}_3\text{Cu}$ phase don't change during this heating process and have the same intensity at the end of the experiment as at the beginning. As previously done, the neutron diffraction pattern at the end of the neutron diffraction experiment recorded at room temperature which is shown in Fig. 4-30 and the sample measured by X-ray diffraction have been refined with a model of 3 phases: $\gamma\text{-TiCu}$ (SG=P4/nmm; $a=0.3153(2)$ nm, $c=0.5972(3)$ nm), $\text{Ti}_5\text{Sn}_3\text{Cu}$ (SP=P6₃/mmc; $a=0.8125(7)$ nm, $c=0.5631(8)$ nm) and $\text{Sn}_{11}\text{Cu}_{39}$ (SP=F-43m; $a=1.8086(5)$ nm).

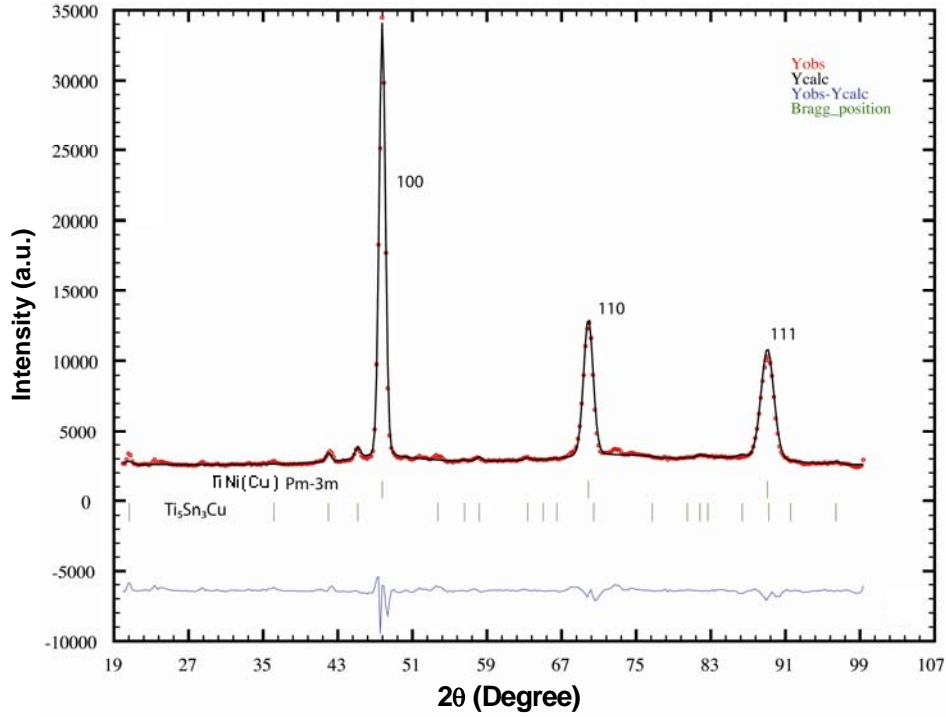


Fig. 4-29 Neutron diffractogram recorded at $\lambda=0.2518$ nm of the $\text{Ti}_{41.5}\text{Cu}_{37.5}\text{Ni}_{7.5}\text{Zr}_{2.5}\text{Hf}_5\text{Sn}_5\text{Si}_1$ alloy with 4 mm in diameter

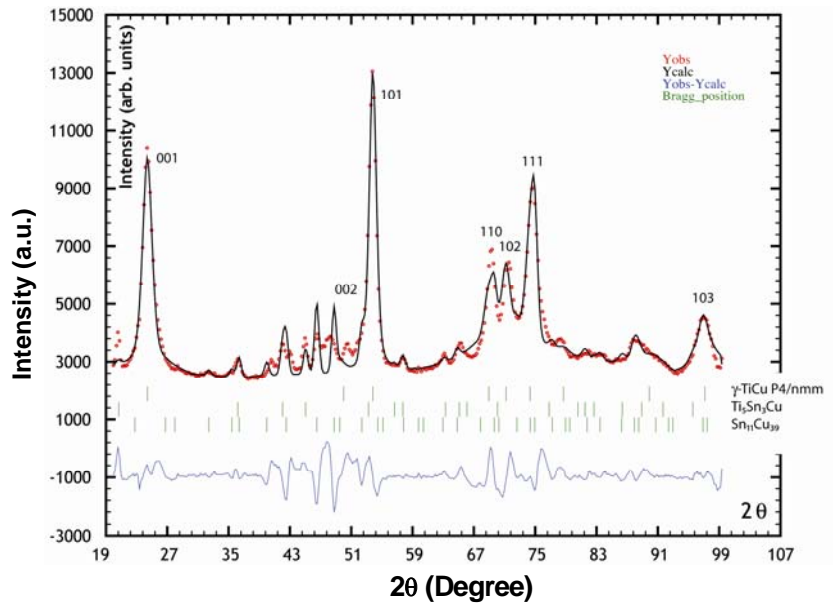


Fig. 4-30 Neutron diffraction pattern of the $\text{Ti}_{41.5}\text{Cu}_{37.5}\text{Ni}_{7.5}\text{Zr}_{2.5}\text{Hf}_5\text{Sn}_5\text{Si}_1$ alloy with 4 mm in diameter after full crystallization upon continuous heating

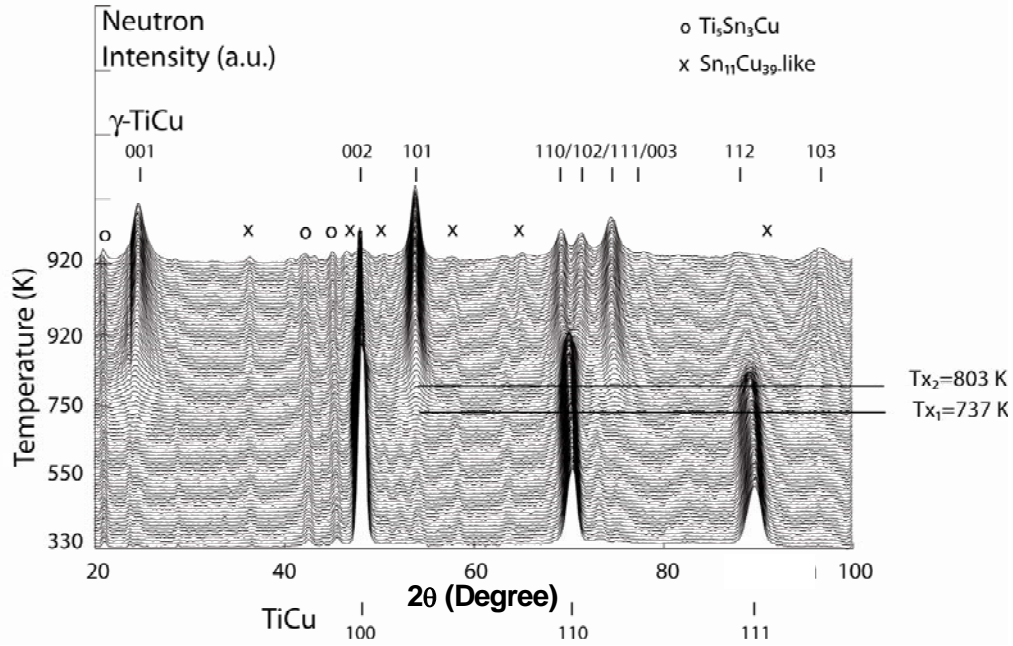


Fig. 4-31 3D Neutron thermodiffractogram recorded at $\lambda=0.2518$ nm during a constant heating at 2 K/min of the $\Phi 4$ mm sample of $\text{Ti}_{41.5}\text{Cu}_{37.5}\text{Ni}_{7.5}\text{Zr}_{2.5}\text{Hf}_5\text{Sn}_5\text{Si}_1$ alloy

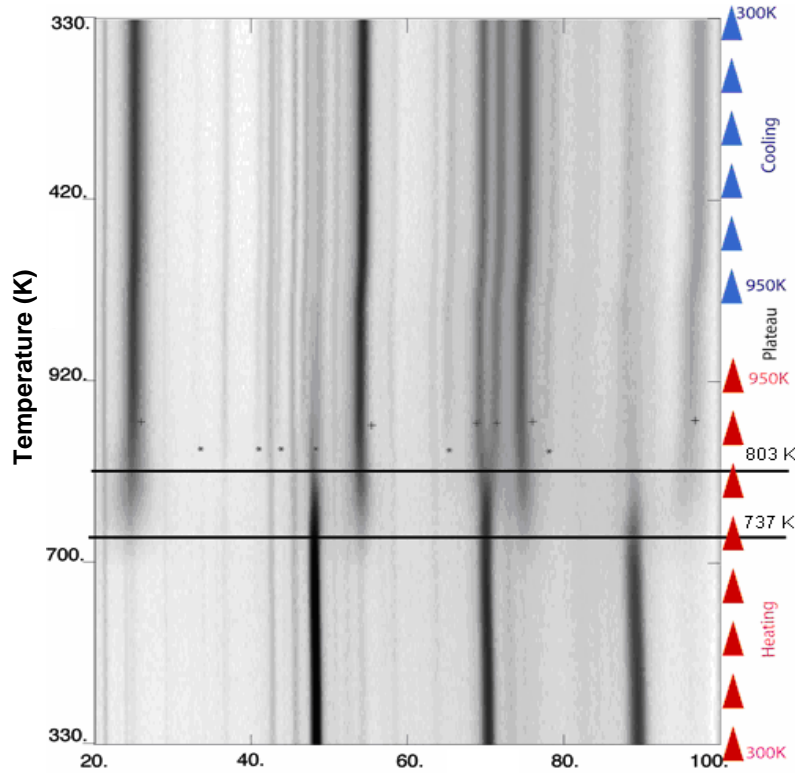


Fig. 4-32 Planform of the 3D Neutron thermodiffractogram, 2-theta along the x-axis, the temperature along the y-axis, and the neutron counts intensity along the z-axis, recorded at $\lambda=0.2518$ nm during a constant heating at 2 K/min of the $\Phi 4$ mm sample of $\text{Ti}_{41.5}\text{Cu}_{37.5}\text{Ni}_{7.5}\text{Zr}_{2.5}\text{Hf}_5\text{Sn}_5\text{Si}_1$ alloy

Now, we summarize the information obtained by ex-situ crystallization in the DSC furnace then described by X-ray and in-situ neutron diffraction experiments as a function of annealing

temperature. The first phase to crystallize in this system is a cubic non-centered phase of TiNi(Cu) formula with space group Pm-3m presenting an ordering between titanium and the other 3d metals. By heating the sample above $T_{x1}=737$ K, the cubic TiNi(Cu) phase transforms to tetragonal γ -TiCu(Ni), the transformation is finished at $T_{x2}=803$ K when no more peaks of the cubic phase are visible. When the temperature is higher than T_{x2} , the remaining amorphous phase transforms into γ -TiCu phase, and a cubic phase with the $\text{Sn}_{11}\text{Cu}_{39}$ -like phase appears with a low intensity. However, the $\text{Ti}_5\text{Sn}_3\text{Cu}$ phase shown since the glass formation does not evolve during the heat treatment, which indicates the stable nature of this phase, because that the nucleation and growth of $\text{Ti}_5\text{Sn}_3\text{Cu}$ phase require the diffusion and motion of more Sn atom, however, on one hand, the percentage of Sn atom is only 5 at.% in the nominal composition of this alloy; on the other hand, the Sn atom is difficult to move due to its large atomic radius. So we should consider that if the $\text{Ti}_5\text{Sn}_3\text{Cu}$ phase can be only occurring as a solidification phase not crystallization phase upon heating in this BMG, as will be verified by investigating the microstructure of samples obtained by controlling different solidification rate.

Fig. 4-35 and 4-38 show the microstructure of annealed samples after the different heat treatment conditions: isochronous and isothermal, respectively, to investigate the microstructure evolution including the morphology, size, volume fraction and distribution upon heating which is essential for the following mechanical properties study.

For as-cast sample in diameter of 4 mm, only less bright grains with morphology of equiax crystal can be observed in the SEM image (Fig. 4-33). However, according to the investigation of X-ray diffraction and neutron diffraction, one more type of grain should exist in the as-cast glass former. Further observation by TEM reveals that another spherical grain with average size of 30 nm distributes in the amorphous matrix (Fig. 4-34), as is accordance with the X-ray diffraction which shows a broad hump at around $2\theta=40^\circ$ as well as a broad peak superimposes on it which suggests the coexistence of amorphous phase and nanocrystals. EDS results reveal the higher percentage of Sn content in it than that in the matrix. Three morphologies coexist in Fig. 4-36: bright equiax crystal, feather-like microstructure and amorphous matrix. EDS was performed to get the chemical composition of these microstructures. In this study, two points for each type of microstructure were chosen for performing EDS in order to ensure the reliability. For an instance, one group of the chemical compositions of the bright grain and the grey matrix are shown in Table 4-7, which verifies the fact that the bright grain is rich in Sn and is determined to be $\text{Ti}_5\text{Sn}_3\text{Cu}$ phase. We also found that the grain size with large difference between 1 and 10 μm and the grain number for the bright microstructure in the annealed sample almost do not change with respect to the as-cast glassy former, as also can be confirmed by the observation of isothermal annealed samples at 443 $^\circ\text{C}$ for different time which is shown in Fig. 4-38. The SEM observation is in good agreement with the X-ray and neutron diffraction measurements.

With increase in temperature or annealing time, the feather-like grain precipitated continuously, as can be confirmed by the observation of SEM obtained from isochronous and isothermal DSC annealed samples. Finally, after completing the both crystallization events, the microstructure mainly consists of less $\text{Ti}_5\text{Sn}_3\text{Cu}$ phase with morphology of bright equiax grain and large quantities of γ -TiCu phase with feather-like morphology.

In addition, by analyzing the chemical composition of the bright equiax grain which is listed in Table 4-8 (corresponding to the bright equiax grain in Fig. 4-37) we found that the grain size is dependent on the Sn content, namely, the more Sn content, the larger grain size is. When the grain

size is $<2\ \mu\text{m}$, the chemical composition with lower percentage of Sn content is similar with that of the matrix, while the grain size is $>2\ \mu\text{m}$, the chemical composition rich-in Sn and poor-in Cu compared with the matrix, however, the percentage of Ti atom in $\text{Ti}_5\text{Sn}_3\text{Cu}$ particles is constant which is similar with that in the matrix. See Table 4-8, for instance, the percentage of Sn in the small grain ($\sim 2\ \mu\text{m}$) and large grain ($\sim 8\ \mu\text{m}$) is 5.82% and 21.43%, respectively, as indicates that the growth of $\text{Ti}_5\text{Sn}_3\text{Cu}$ particles need destroy the original crystal lattice, and the Sn atoms in the matrix surrounding the $\text{Ti}_5\text{Sn}_3\text{Cu}$ particles move towards the $\text{Ti}_5\text{Sn}_3\text{Cu}$ particles, while on the contrary, the excess Cu atoms in the $\text{Ti}_5\text{Sn}_3\text{Cu}$ particles move towards the matrix, so the mechanism of grain growth for $\text{Ti}_5\text{Sn}_3\text{Cu}$ particles may not simply accord with the Oswald growth mechanism, it need much more atomic thermal motion to form the $\text{Ti}_5\text{Sn}_3\text{Cu}$ phase with the exact atomic ratio.

It is interesting that the chemical compositions of $\text{Ti}_5\text{Sn}_3\text{Cu}$ phase ($<2\ \mu\text{m}$), cubic non-centered phase of $\text{TiNi}(\text{Cu})$ and $\gamma\text{-TiCu}(\text{Ni})$ are similar with that of amorphous phase (nominal composition of the sample). Considering the solidification process, the supercooled liquid can easily transform into these three phases directly bypassing other processes, actually, we found three phases in the solidification microstructure obtained by controlling slow down the solidification rate, while by improving the solidification rate, the microstructure with only phase separation-like structure in the amorphous matrix can be obtained. Consequently, the order of phase precipitation during the solidification is $\gamma\text{-TiCu}(\text{Ni})$ phase, $\text{Ti}_5\text{Sn}_3\text{Cu}$ phase and then cubic non-centered phase $\text{TiNi}(\text{Cu})$. As we know, the final microstructure of alloys is very sensitive to the solidification rate, especially for this alloy, because of the similar chemical composition of the precipitation phases with that of the amorphous phase, so the most important problem is how to control the solidification rate to ensure the good nature of the as-cast sample. On the contrary process, namely the crystallization events upon heating, the $\text{Ti}_5\text{Sn}_3\text{Cu}$ phase with large difference of the chemical composition compared with the amorphous phase is difficult to precipitate from the matrix. We also found that the distribution of $\text{Ti}_5\text{Sn}_3\text{Cu}$ phase is not widespread and homogenously distributed in the matrix, and the $\gamma\text{-TiCu}(\text{Ni})$ phase develops around the $\text{Ti}_5\text{Sn}_3\text{Cu}$ nucleus, leading to the final unhomogeneous distribution of $\gamma\text{-TiCu}(\text{Ni})$ phase, as can be confirmed by observation of microstructure through SEM (Fig. 4-38).

The above analysis confirms the formation of $\text{Ti}_5\text{Sn}_3\text{Cu}$ phase during the solidification process; however, it may not precipitate from the amorphous phase during crystallization upon heating. We can deduce that if $\text{Ti}_5\text{Sn}_3\text{Cu}$ phase can be obtained from the amorphous phase during the crystallization, more and more $\text{Ti}_5\text{Sn}_3\text{Cu}$ phase should form during the crystallization process, however, the number and the size of $\text{Ti}_5\text{Sn}_3\text{Cu}$ particles are independent of the temperature and annealing time, so the $\text{Ti}_5\text{Sn}_3\text{Cu}$ phase is believed to be absent during the crystallization process.

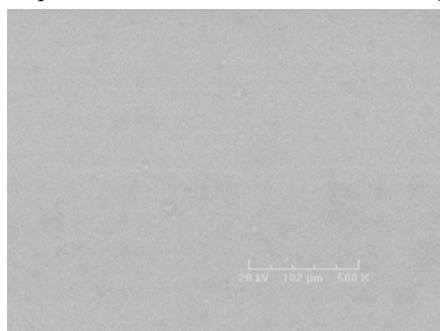


Fig. 4-33 SEM of as-cast sample with 4 mm in diameter

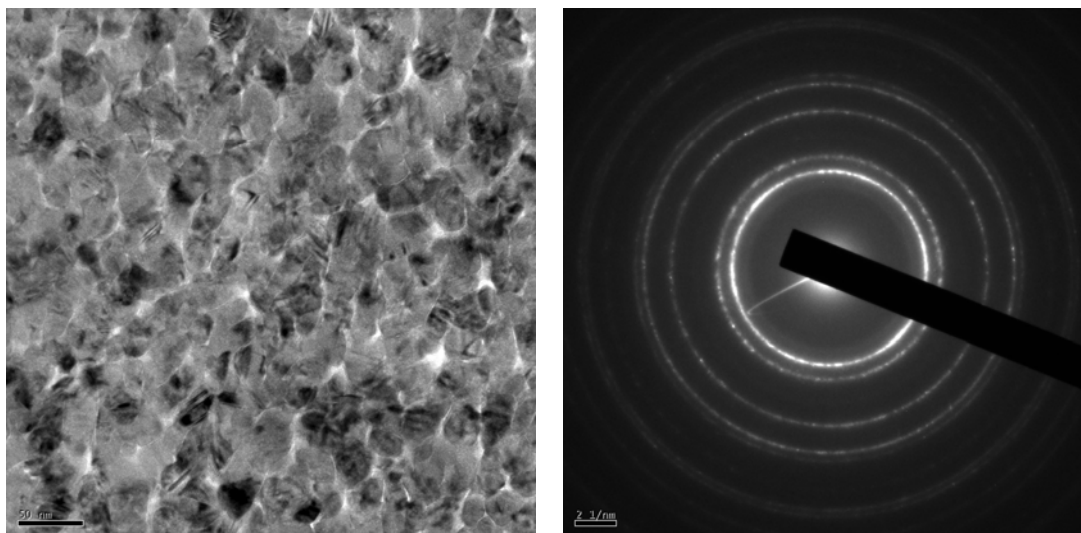


Fig. 4-34 TEM of the matrix of as-cast sample with 4 mm in diameter

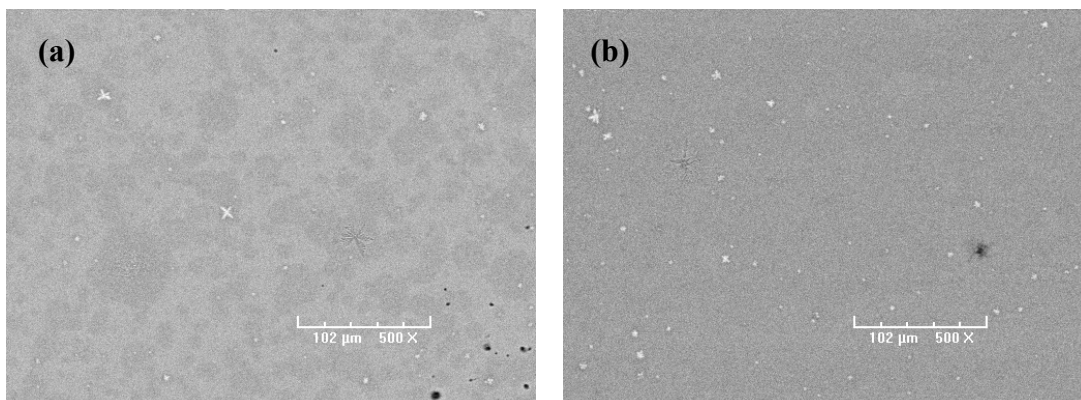


Fig. 4-35 SEM of annealed samples at (a) 496 °C and (b) 600 °C which are corresponding to complete the first and second crystallization event, respectively

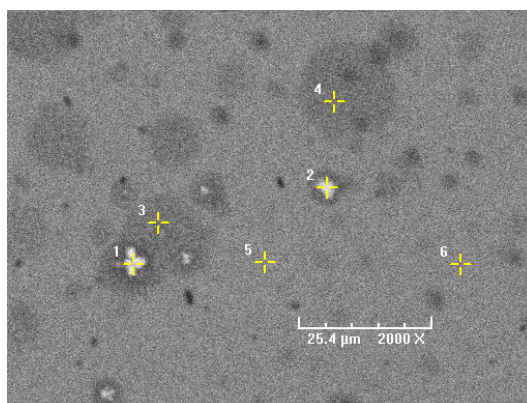


Fig. 4-36 Microstructure and numbering of the points where EDS was performed

Table 4-7

Chemical composition of different microstructure in Fig. 4-36 marked with cross cursor obtained from EDS measurement

No.	Ti	Cu	Ni	Zr	Hf	Sn	Si
1	42.98	24.19	3.88	4.65	2.81	16.53	4.97
2	41.07	34.46	6.76	3.10	2.49	8.07	4.06
3	43.56	35.13	7.14	2.76	2.25	5.42	3.75
4	42.66	36.27	6.70	2.78	2.75	5.32	3.52
5	42.70	36.37	6.57	2.61	2.93	5.48	3.32
6	42.50	35.36	6.57	2.67	4.05	5.40	3.45

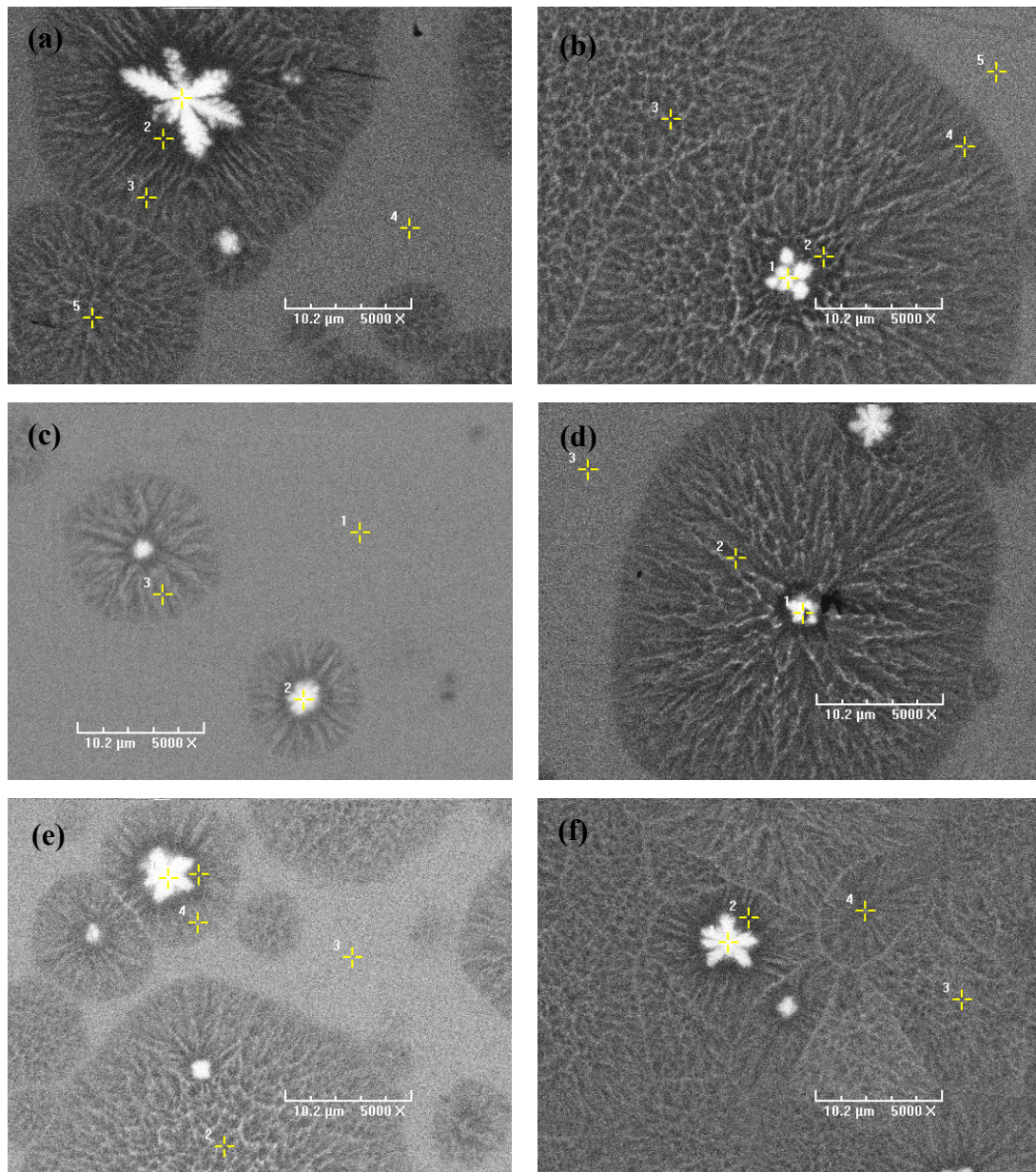


Fig. 4-37 Showing the bright equiax grain performed EDS

Table 4-8

Chemical composition of the bright grain obtained from different grain with different grain size, the point performed EDS were shown in Fig. 4-37 marked with cross cursor

No.	Ti	Cu	Ni	Zr	Hf	Sn	Si	Grain size (μm)
1 (Fig. 4-37 (a))	43.03	16.34	2.69	7.49	4.43	21.43	4.59	~ 8
1 (Fig. 4-37 (b))	43.28	19.55	3.52	6.15	4.85	18.37	4.27	~ 4
2 (Fig. 4-37 (c))	42.82	29.76	5.89	4.67	5.48	8.16	3.22	< 3
1 (Fig. 4-37 (d))	43.11	32.87	6.20	4.06	5.28	5.82	2.66	~ 2
1 (Fig. 4-37 (e))	43.85	17.96	3.04	6.80	4.10	20.16	2.79	< 5
1 (Fig. 4-37 (f))	43.95	19.23	3.18	6.41	4.76	18.33	4.13	< 5
1 (Fig. 4-36)	42.98	24.19	3.88	4.65	2.81	16.53	4.97	< 4
2 (Fig. 4-36)	41.07	34.46	6.76	3.10	2.49	8.07	4.06	< 3

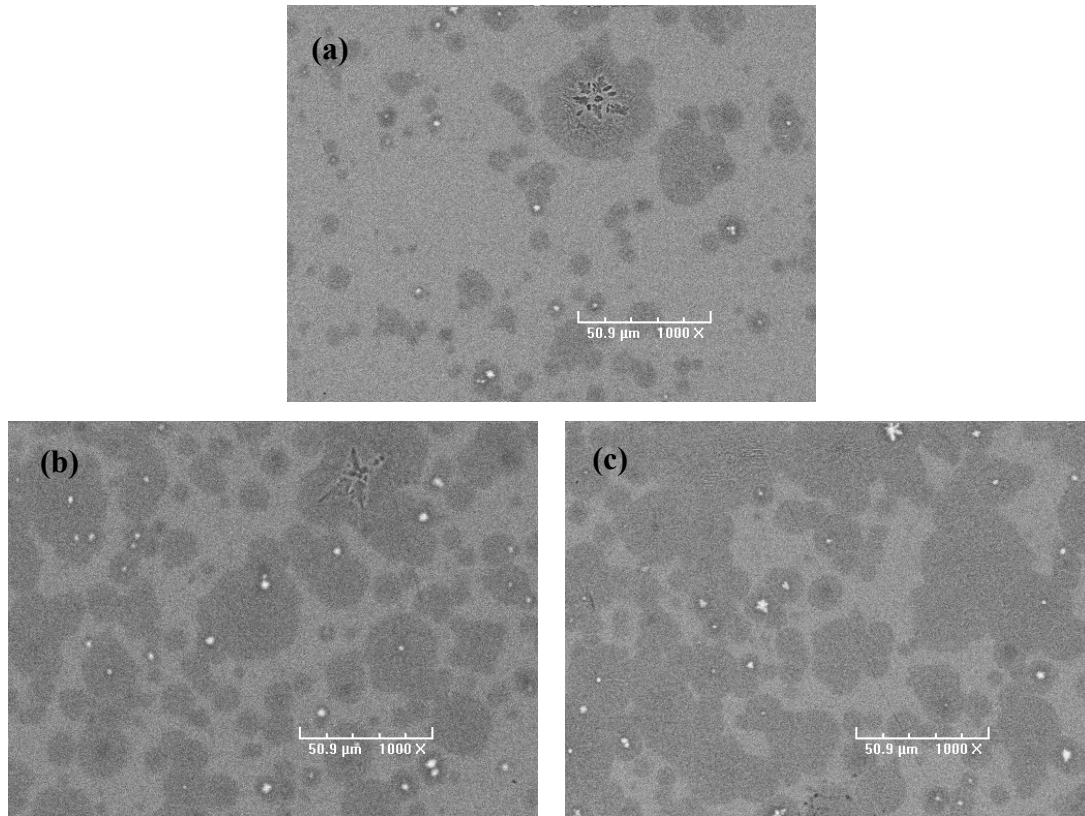


Fig. 4-38 SEM of as-cast sample annealed at 443 °C for different (a) 16 min, (b) 26 min and (c) 44 min which are corresponding to complete 20%, 50% and 100% of the first crystallization event, respectively

In summary, the phase transformation upon heating for $\text{Ti}_{41.5}\text{Cu}_{37.5}\text{Ni}_{7.5}\text{Zr}_{2.5}\text{Sn}_5\text{Hf}_5\text{Si}_1$ with 4 mm in diameter can be described as: metastable cubic $\text{TiNi}(\text{Cu})$ phase with space group $\text{Pm}\bar{3}\text{m}$ transforms to tetragonal $\gamma\text{-TiCu}(\text{Ni})$ phase corresponding to the first exothermal event in continuous heating DSC curve; followed by the remaining amorphous phase transforming into $\gamma\text{-TiCu}$ phase and a cubic $\text{Sn}_{11}\text{Cu}_{39}$ -like phase corresponding to the second crystallization event. For the 2 mm sample with the same nominal composition, the crystallization can be deduced to be similar with that of 4 mm sample: the amorphous phase transforms to the cubic $\text{TiNi}(\text{Cu})$ phase at

the first crystallization stage, and then the cubic TiNi(Cu) phase transforms to γ -TiCu phase and the remaining amorphous phase transforms into γ -TiCu phase and a cubic Sn₁₁Cu₃₉-like phase through the second crystallization stage.

4.5.1.2 Microstructure evolution

Isothermal annealing is an effective way to get nanocrystal/amorphous composite to develop the physical and chemical properties of amorphous materials. On the other hand, the net-shape forming in the supercooled liquid region is also an isothermal annealing process. Consequently, study on the microstructure evolution under the condition of isothermal annealing is essential for realizing the controlling of microstructure. It is obvious that, the mixture of two or three types of microstructures in the as-cast or annealed sample, especially the existence of γ -TiCu(Ni) phase with large difference in grain size and unhomogeneous distribution, will lead to the drastically decrease in mechanical properties. Previous study in Chapter 2 has presented the microstructure evolution of the sample with 2 mm in diameter at low annealing temperature of 397 °C below T_g 35 K for different time from 15 min to 12 h (Fig. 2-25 in chapter 2). It is found the annihilation of the phase separation-like structure when the sample was annealed for 15 min followed by a development of less nanocrystals when the sample was annealed for 8 h, finally, large quantities of nanocrystals with the average grain size of 5-10 nm until annealing up to 12 h, indicating that nanocrystalline/amorphous composite can be obtained by choosing appropriate heat treatment condition: annealing temperature and annealing time, to prevent from the transformation from metastable cubic TiNi(Cu) phase to tetragonal γ -TiCu(Ni) phase.

It is known that the sample annealed at low temperature below T_g should follow structural relaxation and crystallization. It is clear that the precipitation of nanocrystals is corresponding to the crystallization process. While during the process of structural relaxation, the supercooled liquid tends to reach the thermodynamic metastable equilibrium state through the atomic rearrangement; at the same time, the fine scale atomic clusters may be formed promoted by the annihilation of the free volume defects which are generally shown as the regions of fine scale lattice ordering. Such tiny changes within the atomic scale in the structure can not be easily detected even by HRTEM; however, at least, the microstructure changes from the as-received phase separation-like structure to the annihilation of such a structure when the sample was annealed at 397 °C can confirm the atomic motion during the structural relaxation.

4.5.2 Thermally Induced Structural Transformations for Ti₄₀Zr₂₅Ni₈Cu₉Be₁₈ BMG

The phase transformation upon heating for Ti₄₀Zr₂₅Ni₈Cu₉Be₁₈ BMG has been obtained in the reference [Kim et al., 2004] only by ex-situ crystallization in the DSC furnace then described by X-ray diffraction experiment as a function of annealing temperature. The two step crystallization of Ti₄₀Zr₂₅Ni₈Cu₉Be₁₈ BMG upon heating was reported as follow: primary icosahedral phase precipitation from amorphous matrix, followed by the remaining amorphous phase crystallizing into the hexagonal Laves phase. The icosahedral phase transformed into a Laves phase at high temperature through an endothermic reaction. In this study, we present the different results obtained by in-situ neutron diffraction on amorphous bulk samples and compared with DSC

studies performed at the same heating rate as the neutron diffraction study, annealing at low temperature has also been done by in-situ neutron diffraction. Electron microscopies analysis (SEM and TEM equipped with energy-dispersive X-ray spectrometry (EDS)) have been used to characterize the samples before and after annealing steps.

4.5.2.1 Phase transformation

The typical temperatures obtained from the continuous heating DSC and in-situ neutron diffraction at heating rate of 2 K/min are summarized in Table 4-9. Fig. 4-39 shows the DSC trace recorded at 2 K/min, the glass transition temperature is not well marked and there is a continuous endothermic reaction starting around 555 K. A first crystallization event (exothermic) appears at $T_{x1}=608$ K with low intensity and a broad temperature range. A second crystallization event (exothermic) appears at $T_{x2}=749$ K with a sharper peak. A first endothermic reaction occurs at $T_{m1}=810$ K (low intensity), a second endothermic event occurs at $T_{m2}=845$ K and the full melting at $T_m=955$ K. In the previous studies [Kim et al., 2004], the T_{x1} and T_{x2} were observed, but T_{m1} was also considered as a crystallization event, full melting was observed at 948 K.

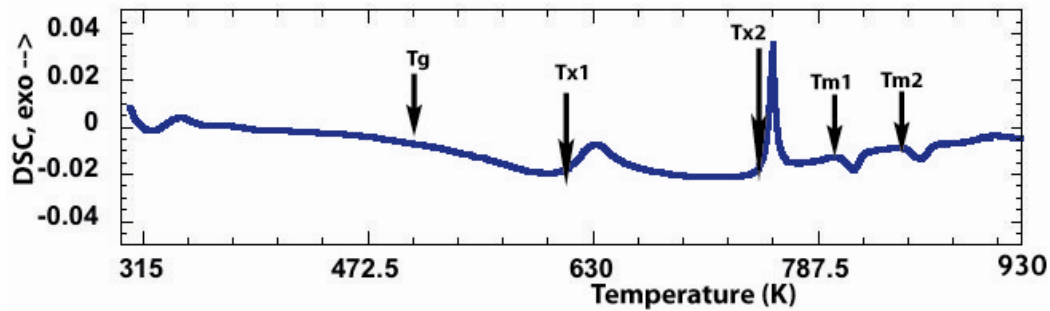


Fig. 4-39 DSC curve of $\text{Ti}_{40}\text{Zr}_{25}\text{Ni}_8\text{Cu}_9\text{Be}_{18}$ BMG obtained at heating rate of 2 K/min

Table 4-9

Typical temperatures obtained from isochronal DSC and in-situ neutron diffraction measurements at heating rate of 2 K/min

Sample	T_g (K)	T_{x1} (K)	T_{x2} (K)	T_{m1} (K)	T_{m2} (K)	T_m (K)
DSC (2 K/min)	555	608	749	810	845	955
Neutron (2 K/min)		610	724	814		

In-situ neutron diffraction experiments have been done on 2 samples of the same batch and with 2 heating profiles. The first heating treatment was done at a constant speed of 2 K/min and a diffraction pattern was recorded continuously during the temperature change every 5 minutes (each neutron pattern has a mean temperature value during a 10 K change) up to 930 K, then cooling down at room temperature. The second heating treatment was a constant heating at 2 K/min up to T_g+30 , then a dwell at this temperature until crystallization was not evolving, then cooling down at room temperature.

The Fig. 4-40 shows the constant heating experiment such as the x-axis is the 2-theta diffraction angle, y-axis is the time (during temperature change) and the z-axis is the neutron counts intensity. At the beginning of the experiment, the characteristic diffraction pattern of an amorphous compound with short range order (bump maximum at 2-theta=68°; $d=2.514$ Å) is observed. At 610 K (608 K in DSC experiment), some new peaks appear at 2-theta=39.34° and 65.54° corresponding to d spacings 3.785 and 2.340 Å, respectively, these peaks are diffuse at the

beginning corresponding certainly to very tiny crystals, then sharper with time and temperature increasing. With only 2 peaks it is difficult to ascertain a phase, but we can exclude some hypothesis, in particular α - or β -Ti, which did not present a peak at $d=3.785 \text{ \AA}$. In the same way the icosahedral phase often observed in phases with beryllium presents a double peak around $d=2.34 \text{ \AA}$. In simple binary phases, only the TiBe_2 (cfc, $a=6.45 \text{ \AA}$) phase presents 2 peaks close to the observed peaks, by refining the cell parameter, the value $a=6.603 \text{ \AA}$ has been determined. It could be explained by a partial replacement of Ti by a bigger atom such as zirconium. However the ZrBe_2 compound is hexagonal, so only partial replacement must be assumed.

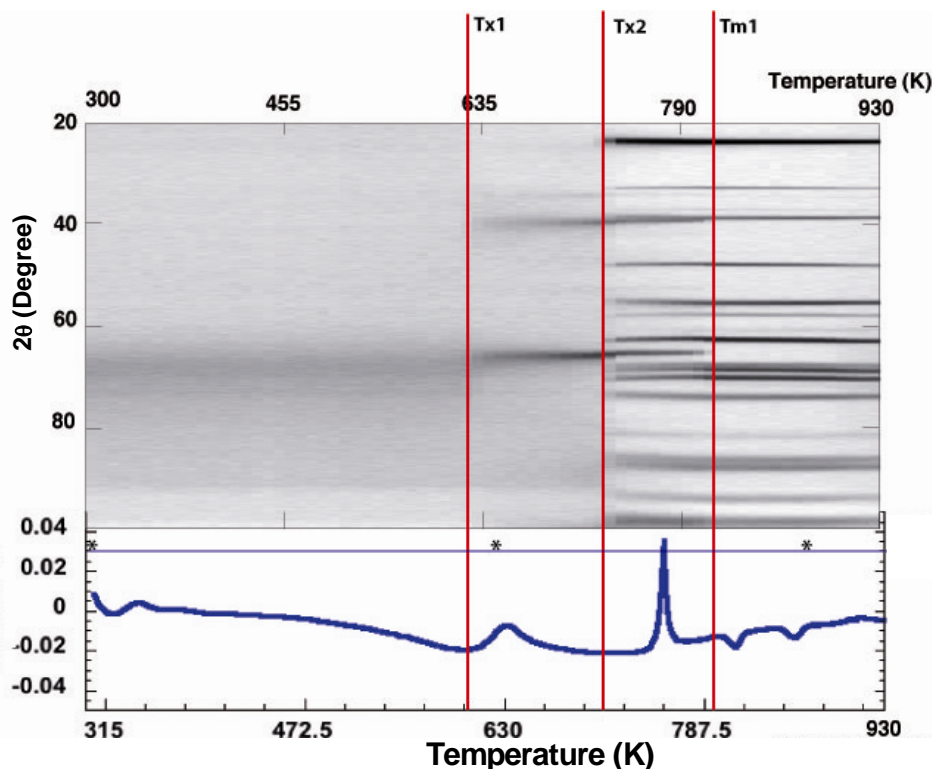


Fig. 4-40 Planform of the 3D Neutron thermodiffractogram, the temperature along the x-axis, 2-theta along the y-axis, and the neutron counts intensity along the z-axis, recorded at $\lambda=0.2518 \text{ nm}$ during a constant heating at 2 K/min of the $\text{Ti}_{40}\text{Zr}_{25}\text{Ni}_8\text{Cu}_9\text{Be}_{18}$ BMG

At $T=724 \text{ K}$, new peaks appear and the main phases agreeing with peak positions are an hexagonal C14 phase with cell parameters $a=5.25 \text{ \AA}$ and $c=8.65 \text{ \AA}$ at high temperature, and a cubic Zr_2Ni phase with $a=11.00 \text{ \AA}$ at high temperature. These phases are present at all temperatures up to 930 K and also after cooling at room temperature. The temperature of the crystallization event is observed well below the temperature observed during the DSC experiment (749 K). We have no explanation for this temperature difference.

The last observation of this constant speed experiment is the disappearance of the primary crystallization phase at $T_{m1}=814 \text{ K}$, which is in agreement with the DSC experiment ($T_{m1}=810 \text{ K}$). After heating at 930 K (just before melting), no other phenomenon is observed, so the sample was cooled at room temperature and these data used to perform a profile refinement. This data refinement is reported in [Table 4-10](#) and [Fig. 4-41](#), using a C14 hexagonal model for one phase and the big cube phase model for the other one. Cell parameters, occupation factors of the various sites and their atomic positions when variables were refined and the result reported in [Fig. 4-41](#). The refinement quality factors were respectively 6.7%, 8.9% and 3.5% for C14 phase, cubic phase

and full profile. For the C14 phase, it corresponds to the formula $Zr_{1.0}Ti_{1.08}Ni_{0.82}Cu_{0.10}$ or $Zr(Ti,Ni,Cu)_2$ or $Zr_{33.3}Ti_{35.9}Ni_{27.3}Cu_{3.4}$ and it represents 92% of phase quantity. This phase has been previously described by R.M. Waterstrat [Waterstrat, 1992] as $ZrTiNi$ with $a=5.205 \text{ \AA}$ and $c=8.476 \text{ \AA}$. The cell parameters as measured in this experiment are slightly bigger due to a different site occupation. For the “Big cube” phase, it corresponds to the formula $Ti_{1.536}Zr_{0.464}Ni_{0.364}Cu_{0.636}$ or $(Ti,Zr)_2(Ni,Cu)$ or $Ti_{51.2}Zr_{15.5}Ni_{12.1}Cu_{21.2}$ and it represents 8% of phase quantity. This phase has often been reported in Zr-based BMG as the primary crystallization phase with cell parameter in the range 11.95\AA - 12.09\AA [Baricco et al., 2001]. All lines are indexed and calculated with a fairly good agreement.

The Fig. 4-42 shows the static heating experiment at 713 K (before the second crystallization event). At the beginning of the experiment, the characteristic diffraction pattern of an amorphous compound with short range order (bump maximum at $2\text{-theta}=68^\circ$; $d=2.514\text{\AA}$) is observed, like in the first experiment. At 610 K the new peaks of the cubic $Ti(Zr)Be_2$ phase appear and are becoming finer with time evolution, meaning growth of crystals. After 150 minutes at this temperature, new peak appears close to $2\text{-theta}=24^\circ$, corresponding to the main line of the big cube phase. The big cube phase is the second crystallization product to be formed after the $Ti(Zr)Be_2$ phase.

An annealed sample at $T=790 \text{ K}$ for 5 minutes has been studied by HRTEM and is presented in Fig. 4-43. Three different kinds of crystals are observed: crystals (A) have a regular shape with 200 nm size, they appear in black or grey color, crystals (B) have also a regular shape with 50 nm size, they appear in a white color, crystals (C) have a “flower-” or “feather-” like shape, very irregular and 250 nm in size. The chemical mean analysis is reported in Table 4-11. There is a good agreement between neutron chemical analysis and EDS chemical analysis concerning the elements phase content. For the $(Ti,Zr)Be_2$ structure, beryllium is not analyzed by EDS as it has a too low number of electrons and the chemical formula is calculated on the elements that are observed. But we can consider it is the good phase as there is no copper or nickel inside and that the peaks of the α -Ti or β -Ti phase are not observed. The formation of the $(Ti,Zr)Be_2$ phase as primary crystallization phase (PCP) is in agreement with previous primary crystallization studies of BMG containing beryllium phase. We have observed during the crystallization of $Zr_{46.75}Ti_{8.25}Cu_{7.5}Ni_{10}Be_{27.5}$ phase the formation of $ZrBe_2$ and a quasicrystalline phase [Van de Moortèle et al., 2004] as PCP and whose HRTEM images are very similar in shape and size. Depending on the history of the glass formation (sample diameter, cooling technique, oxygen presence), different phases can be formed because of the different atomic structures (short range order) possible in the glass state. It is why the observations of Kim [Kim et al., 2004] and Kou [Kou et al., 2009] of a quasicrystalline phase as PCP may be also the result of the BMG synthesis process, different from our samples.

In summary, by coupled experiments by in-situ neutron diffraction, DSC and HRTEM/EDS, we have evidenced the phases formed during heating or annealing the $Ti_{40}Zr_{25}Ni_8Cu_9Be_{18}$ bulk metallic glass. During the primary crystallization, a cubic $(Ti,Zr)Be_2$ phase is formed, this phase is unstable and decomposes at higher temperature. The second crystallization products, which are very stable up to full melting, are at 92% a C14 hexagonal Laves phase $Zr_{1.0}Ti_{1.08}Ni_{0.82}Cu_{0.10}$ or $Zr(Ti,Ni,Cu)_2$, and at 8% a big cube phase, $Ti_{1.536}Zr_{0.464}Ni_{0.364}Cu_{0.636}$ or $(Ti,Zr)_2(Ni,Cu)$. We have not evidenced the formation of an icosahedral phase as in previous studies, but this may due to a different synthesis process. Further measurements of mechanical properties are done on these materials and will be compared to other

materials prepared with a different process to see if the PCP has an influence on mechanical properties.

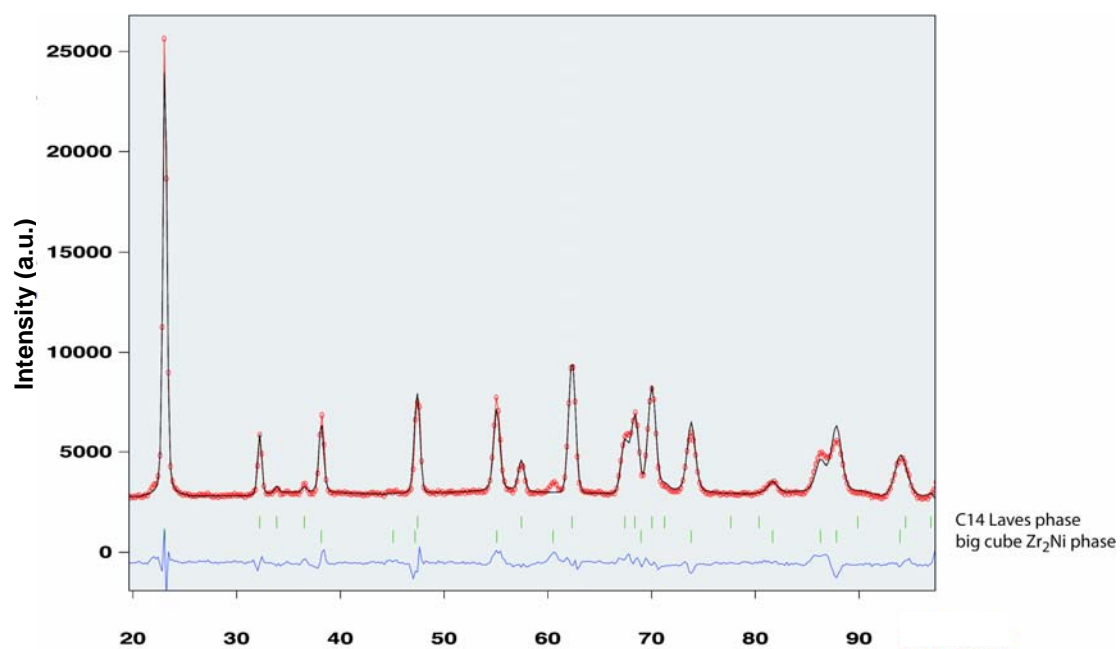


Fig. 4-41 Neutron diffraction curve for the fully crystallized $\text{Ti}_{40}\text{Zr}_{25}\text{Ni}_8\text{Cu}_9\text{Be}_{18}$ BMG. The data refinement results using a C14 hexagonal model for one phase and the big cube phase model for the other one

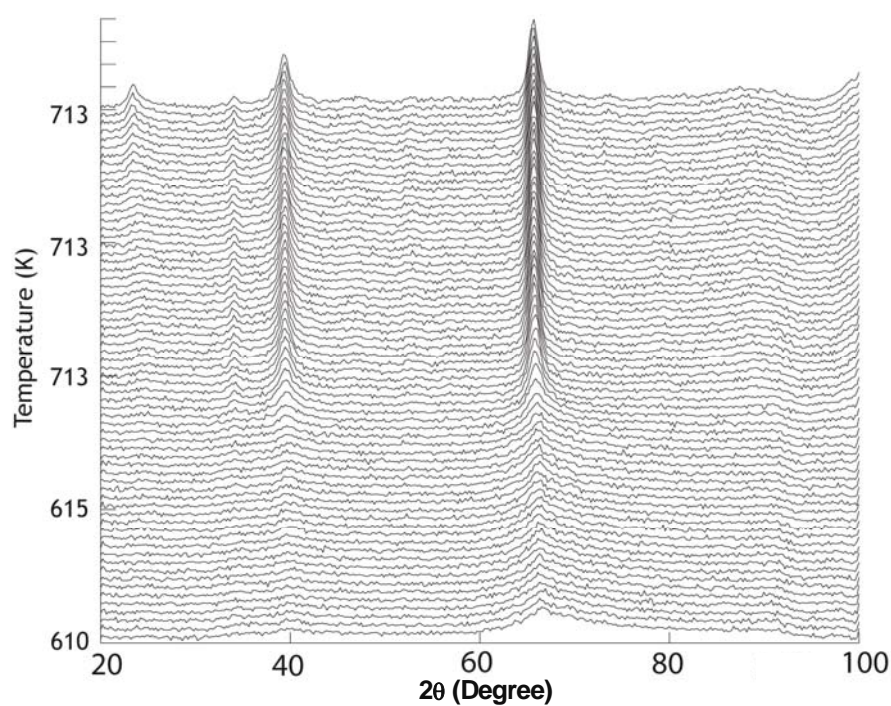


Fig. 4-42 Neutron diffraction patterns for $\text{Ti}_{40}\text{Zr}_{25}\text{Ni}_8\text{Cu}_9\text{Be}_{18}$ BMG isothermally annealed at 713 K

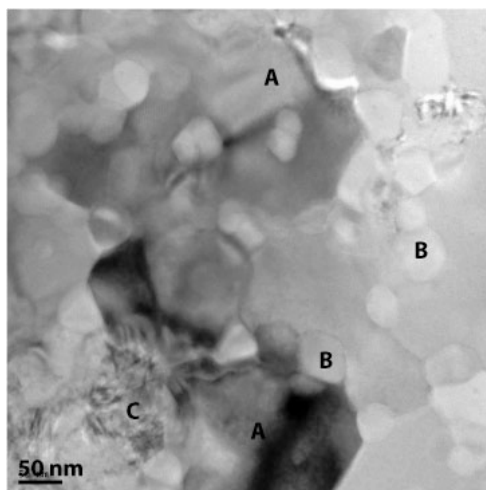


Fig. 4-43 TEM image of the $\text{Ti}_{40}\text{Zr}_{25}\text{Ni}_8\text{Cu}_9\text{Be}_{18}$ BMG isothermally annealed at 790 K for 5 minutes

Table 4-10

Data refinement using the C14 hexagonal model and the big cube phase model. Cell parameters, occupation factors of the various sites and their atomic positions when variables were refined and listed in this table.

Atom	C14 Laves phase, Hexagonal P63/mmc, $a=5.228(1) \text{ \AA}$, $c=8.629(2) \text{ \AA}$			
Zr (4f)	1/3	2/3	$Z=0.065(1)$	0.1666
Ti (2a)	0	0	0	0.067
Cu (2a)				0.067
Ti (6h)	$x=0.836(3)$	x	x	0.113
Ni (6h)				0.137
Atom	Big cube phase, Cubic Fd3m, $a=10.871(1) \text{ \AA}$			
Zr (48f)	$x=0.192(1)$	0	0	0.027
Ti (48f)				0.223
Zr (16d)	5/8	5/8	5/8	0.051
Ti (16d)				0.033
Cu (32e)	$x=0.943(1)$	x	x	0.106
Ni (32e)				0.061

Table 4-11

The chemical composition for the different microstructures in the $\text{Ti}_{40}\text{Zr}_{25}\text{Ni}_8\text{Cu}_9\text{Be}_{18}$ sample isothermally annealed at 790 K for 5 min.

Elements	Zr (at.%)	Ti (at.%)	Cu (at.%)	Ni (at.%)	Be (at.%)
Crystals (A) (EDS)	36.9	34.6	15.2	13.2	
C14 Laves Phase	33.3	35.9	3.4	27.3	
Crystals (B) (EDS)	20.4	60.9	8.3	10.4	
Big cube phase	15.5	51.2	21.2	12.1	
Crystals (C) (EDS)	54.2	45.0	0.5	0.3	
Ti(Zr)Be ₂ cubic phase	16.6	16.6	0	0	66.6

4.5.2.2 Microstructure evolution

Low temperature isothermal annealing was performed on the as-cast $\text{Ti}_{40}\text{Zr}_{25}\text{Ni}_8\text{Cu}_9\text{Be}_{18}$ BMG at 293 °C with 20 K below T_g for different time from 15 min to 6 h to investigate the microstructure evolution during the structural relaxation and crystallization process. Fig. 4-44 and 4-45 show the TEM image and corresponding SADP obtained from the samples annealed at 293 °C for 2 h and 6 h, respectively. It is clear that no crystals are formed until the sample is annealed for 6 h. The nano-scaled particles in the Fig. 4-45 are corresponding to the primary cubic $(\text{Ti,Zr})\text{Be}_2$ phase. It indicates that a nanocrystals/amorphous matrix composite structure can be obtained as a result of the first crystallization reaction.

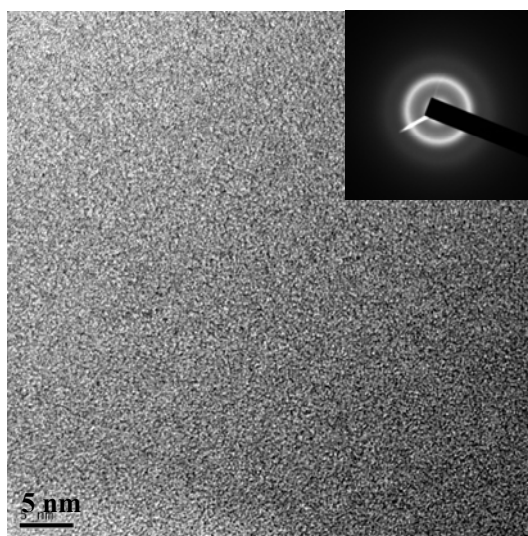


Fig. 4-44 HRTEM image and corresponding SADP obtained from the $\text{Ti}_{40}\text{Zr}_{25}\text{Ni}_8\text{Cu}_9\text{Be}_{18}$ alloys annealed at 293 °C for 2 h

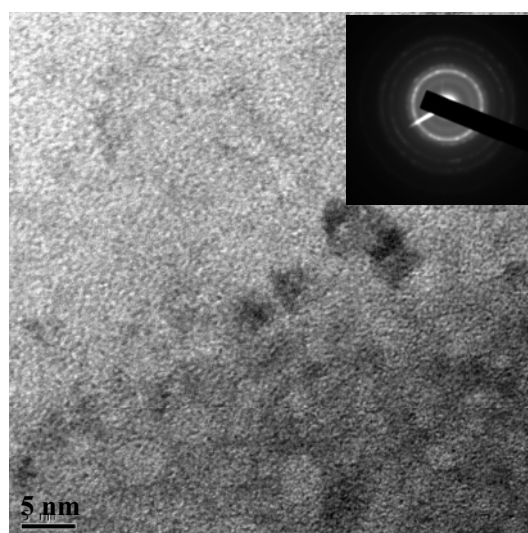


Fig. 4-45 HRTEM image and corresponding SADP obtained from the $\text{Ti}_{40}\text{Zr}_{25}\text{Ni}_8\text{Cu}_9\text{Be}_{18}$ alloys annealed at 293 °C for 6 h

4.6 Conclusion

The thermally induced structural transformations including structural relaxation and crystallization for $\text{Ti}_{41.5}\text{Cu}_{37.5}\text{Ni}_{7.5}\text{Zr}_{2.5}\text{Hf}_5\text{Sn}_5\text{Si}_1$ and $\text{Ti}_{40}\text{Zr}_{25}\text{Ni}_8\text{Cu}_9\text{Be}_{18}$ BMGs have been investigated in detail in this chapter. The following results were obtained:

- (1) Although the $\text{Ti}_{40}\text{Zr}_{25}\text{Ni}_8\text{Cu}_9\text{Be}_{18}$ BMG can be regarded as a margin alloy for the existence of quenched-in nuclei in the amorphous matrix, it is found that, like $\text{Ti}_{41.5}\text{Cu}_{37.5}\text{Ni}_{7.5}\text{Zr}_{2.5}\text{Hf}_5\text{Sn}_5\text{Si}_1$ BMG, the enthalpy relaxation of $\text{Ti}_{40}\text{Zr}_{25}\text{Ni}_8\text{Cu}_9\text{Be}_{18}$ BMG from the amorphous state into the equilibrium supercooled liquid state also follows the characteristic of enthalpy relaxation for glasses: a stretched exponential function with the relaxation time obeying an Arrhenius law, which indicates that the incubation time for crystallization τ_{inc} is longer than the average relaxation time τ for $\text{Ti}_{40}\text{Zr}_{25}\text{Ni}_8\text{Cu}_9\text{Be}_{18}$ BMG and the enthalpy relaxation occurs almost without the disturbance of the growth of the quenched-in nuclei.
- (2) The rearrangement involving the collective hopping mechanism for the small and medium size atoms is the governing mechanism for the enthalpy relaxation process for both $\text{Ti}_{41.5}\text{Cu}_{37.5}\text{Ni}_{7.5}\text{Zr}_{2.5}\text{Hf}_5\text{Sn}_5\text{Si}_1$ and $\text{Ti}_{40}\text{Zr}_{25}\text{Ni}_8\text{Cu}_9\text{Be}_{18}$ BMGs.
- (3) Two parameters, β_g and τ_g , representing the stretching exponent and the average structural relaxation time at the calorimetric glass transition temperature, respectively, were proposed to evaluate the enthalpy relaxation properties and their correlations with the GFA and thermal stability, respectively, have been constructed. The high value of $\beta_g > 0.84$ corresponds to a good GFA, and the high value of τ_g corresponds to a good thermal stability. The high value of β_g up to 0.962 for $\text{Ti}_{40}\text{Zr}_{25}\text{Ni}_8\text{Cu}_9\text{Be}_{18}$ BMG confirms its better GFA than $\text{Ti}_{41.5}\text{Cu}_{37.5}\text{Ni}_{7.5}\text{Zr}_{2.5}\text{Hf}_5\text{Sn}_5\text{Si}_1$ BMG whose β_g value is 0.884; however, the value of τ_g for $\text{Ti}_{40}\text{Zr}_{25}\text{Ni}_8\text{Cu}_9\text{Be}_{18}$ BMG is 105, much smaller than 161 for $\text{Ti}_{41.5}\text{Cu}_{37.5}\text{Ni}_{7.5}\text{Zr}_{2.5}\text{Hf}_5\text{Sn}_5\text{Si}_1$ BMG, indicating a better thermal stability of $\text{Ti}_{41.5}\text{Cu}_{37.5}\text{Ni}_{7.5}\text{Zr}_{2.5}\text{Hf}_5\text{Sn}_5\text{Si}_1$ BMG than $\text{Ti}_{40}\text{Zr}_{25}\text{Ni}_8\text{Cu}_9\text{Be}_{18}$ BMG.
- (4) The JMA model and Starink model in which the effects of soft impingement are introduced are proposed to investigate the crystallization kinetics depending on whether the crystallization behavior is deviating from the JMA theory or not. Theoretical calculation reveals that the selection of the appropriate kinetics model is crucial for the following kinetics analysis. For example, the wrong application of JMA model (it means that the crystallization does not satisfy some assumptions of the JMA theory) will lead to an error result: changeable kinetic exponent depending on the transformed volume fraction described by the local Avrami exponent, finally lead to the misinterpretation of phase transformation mechanism.
- (5) The first isothermal crystallization reaction of the $\text{Ti}_{41.5}\text{Cu}_{37.5}\text{Ni}_{7.5}\text{Zr}_{2.5}\text{Hf}_5\text{Sn}_5\text{Si}_1$ BMG can be described by JMA model, however, the isochronal process not, which indicates that the isochronal crystallization process is significantly influenced by the soft impingement, and the more complicated crystallization process for the isochronal process with respect to the isothermal process. The crystallization mechanisms for the isothermal and isochronal processes are almost consistent: from a diffusion-controlled three-dimensional growth with an increasing nucleation rate to an interface-controlled three-dimensional growth with decrease in the isothermal annealing temperature or decrease in heating rate.
- (6) By considering the soft impingement effect, the Starink model is successful in describing the

first isochronal crystallization process of $\text{Ti}_{40}\text{Zr}_{25}\text{Ni}_8\text{Cu}_9\text{Be}_{18}$ BMG, the Avrami exponents obtained at different heating rates are around 1.5, implying that the isochronal crystallization process is governed by a diffusion-controlled three dimensional growth of the quenched-in nuclei, as is in accordance with the monotonic calorimetric signal in the isothermal crystallization DSC curve.

- (7) The phase transformation upon heating for $\text{Ti}_{41.5}\text{Cu}_{37.5}\text{Ni}_{7.5}\text{Zr}_{2.5}\text{Sn}_5\text{Hf}_5\text{Si}_1$ with 4 mm in diameter can be described as: metastable cubic $\text{TiNi}(\text{Cu})$ phase with space group Pm-3m transforms to tetragonal $\gamma\text{-TiCu}(\text{Ni})$ phase corresponding to the first exothermal event in continuous heating DSC curve; followed by the remaining amorphous phase transforming into $\gamma\text{-TiCu}$ phase and a cubic $\text{Sn}_{11}\text{Cu}_{39}$ -like phase corresponding to the second crystallization event. For the 2 mm sample with the same nominal composition, the crystallization can be deduced to be similar with that of 4 mm sample: the amorphous phase transforms to the cubic $\text{TiNi}(\text{Cu})$ phase at the first crystallization stage, and then the cubic $\text{TiNi}(\text{Cu})$ phase transforms to $\gamma\text{-TiCu}$ phase and the remaining amorphous phase transforms into $\gamma\text{-TiCu}$ phase and a cubic $\text{Sn}_{11}\text{Cu}_{39}$ -like phase through the second crystallization stage.
- (8) The BMG samples isothermal annealed at low temperature below T_g follow the structural relaxation and crystallization. For $\text{Ti}_{41.5}\text{Cu}_{37.5}\text{Ni}_{7.5}\text{Zr}_{2.5}\text{Sn}_5\text{Hf}_5\text{Si}_1$ BMG, the annihilation of the phase separation-like structure when the sample was annealed at 397 °C for 15 min is due to the atomic motion during the structural relaxation, the following development of nanocrystals when the sample was annealed for 8 h indicates that nanocrystalline/amorphous composite can be obtained by choosing appropriate heat treatment condition.
- (9) The phase evolution upon heating of $\text{Ti}_{40}\text{Zr}_{25}\text{Cu}_9\text{Ni}_8\text{Be}_{18}$ BMG proceeds by two complicated crystallization reactions: during the primary crystallization, a cubic $(\text{Ti,Zr})\text{Be}_2$ phase is formed at 608 K ($a=6.603\text{Å}$), this phase is unstable and decomposes at higher temperature 810 K. The second crystallization products, which are formed at 749 K and very stable up to full melting, are at 92% a C14 hexagonal Laves phase $\text{Zr}_{1.0}\text{Ti}_{1.08}\text{Ni}_{0.82}\text{Cu}_{0.10}$ or $\text{Zr}(\text{Ti,Ni,Cu})_2$, and at 8% a big cube phase, $\text{Ti}_{1.536}\text{Zr}_{0.464}\text{Ni}_{0.364}\text{Cu}_{0.636}$ or $(\text{Ti,Zr})_2(\text{Ni,Cu})$. When the sample is heated at 2 K/min then hold at $T_g+158=713$ K (before $T_{x2}=749$ K) the $(\text{Ti,Zr})\text{Be}_2$ phase develops. After 60 minutes, the big cube phase starts to appear, an important amorphous bump being still present. We have not evidenced the formation of an icosahedral phase as in previous studies, as may be due to a different history of the glass formation (sample diameter, cooling technique and oxygen presence). The nanocrystals/amorphous matrix composite structure can be obtained through the first isothermal crystallization reaction at low temperature below T_g .

CHAPTER 5

EFFECTS OF PRE-ANNEALING NEAR GLASS TRANSITION TEMPERATURE ON THE THERMODYNAMICS AND KINETICS OF THE FOLLOWING GLASS TRANSITION AND CRYSTALLIZATION

5.1 Background and Motivation

5.1.1 Background

The applications of glassy alloys are to some extent restrained due to their thermodynamically metastability, which is linked to the nature and nucleation kinetics of the crystalline phases. Structural relaxation and crystallization are two of the most important and intensively investigated topics in metallic glasses, so far, many investigations were focused on them [Taub et al., 1980; Thompson et al., 1983; Angell et al, 2000; L. Liu et al., 2002]. However, from the applicable point of view, the effects of thermally induced transformations, especially structural relaxation and slight crystallization, much attention should be paid, since the net-shape-forming technique is generally performed in the SLR and only the structural relaxation or slightly partial crystallization occurs for the glassy alloys within the forming time under the condition of keeping homogeneous deformation. From another point of view, studying the effects of thermally induced transformations is of significance for knowing the properties of the final products after forming in the SLR and further evaluating their usability. Although its significance in science and application, limited work has been done in this field, and the relationship between structural relaxation or slight crystallization and following crystallization is unclear. The annealing-induced local atomic structural development is considered to have significant influence on the subsequent crystallization [Wang et al., 1998], which is attributed to atomic rearrangement in the amorphous state that continuously lowers the free energy of the glass. In general, the thermal stability will be decreased due to the increase of T_g , and decrease of T_x , and the crystallization will be accelerated due to the decrease of activation energy E_p for the annealed samples. However, up to now the effects of structural relaxation on subsequent glass transition and crystallization have been a

controversial question, for instance, for $\text{Zr}_{41}\text{Ti}_{14}\text{Cu}_{12.5}\text{Ni}_{10}\text{Be}_{22.5}$, $\text{Zr}_{62}\text{Al}_8\text{Ni}_{13}\text{Cu}_{17}$ and $\text{Co}_{43}\text{Fe}_{20}\text{Ta}_{5.5}\text{B}_{31.5}$ BMGs [Zhuang et al., 2000; X.D. Wang et al., 2006; Yuan et al., 2007], pre-annealing enhanced the activation energy for the following crystallization, which suggests that the effects of pre-annealing may be dependent on the nature and kinetic of nucleation of BMGs. So it is worthwhile clarifying the relationship between the effects of pre-annealing and the nature and kinetics of glass transition and crystallization for the glassy alloys.

5.1.2 Motivation

The detailed studies on the structural relaxation, glass transition and crystallization of as-cast $\text{Ti}_{41.5}\text{Cu}_{37.5}\text{Ni}_{7.5}\text{Zr}_{2.5}\text{Hf}_5\text{Sn}_5\text{Si}_1$ and $\text{Ti}_{40}\text{Zr}_{25}\text{Ni}_8\text{Cu}_9\text{Be}_{18}$ BMGs have been presented in the last chapter. From the applicable point of view, it is also of importance to study the effects of pre-annealing at the temperature in the supercooled liquid region on the subsequent thermodynamics and kinetics of glass transition and crystallization, because it can reflect the thermodynamic and kinetic properties and evaluate the usability of the net-shape-forming products. In this chapter, the glass transition and crystallization kinetics of the pre-annealed $\text{Ti}_{41.5}\text{Cu}_{37.5}\text{Ni}_{7.5}\text{Zr}_{2.5}\text{Hf}_5\text{Sn}_5\text{Si}_1$ and $\text{Ti}_{40}\text{Zr}_{25}\text{Ni}_8\text{Cu}_9\text{Be}_{18}$ BMGs at different pre-annealing conditions were investigated by DSC under the isochronous and isothermal conditions, aiming to clarify the effects of thermally induced transformations, especially the structural relaxation and slightly partial crystallization, on the thermodynamics and kinetics of glass transition and crystallization. And the relationship between the effects of structural relaxation and the nature and kinetics of crystallization was explored.

The main part of this chapter includes the following two parts: (i) effects of thermally induced transformations on the thermodynamic properties of glass transition and crystallization; (ii) effects of pre-annealing on the kinetics properties of glass transition and crystallization. In the second part, for the $\text{Ti}_{41.5}\text{Cu}_{37.5}\text{Ni}_{7.5}\text{Zr}_{2.5}\text{Hf}_5\text{Sn}_5\text{Si}_1$ BMG, we focus on the effects of structural relaxation induced by pre-annealing; while for the $\text{Ti}_{40}\text{Zr}_{25}\text{Ni}_8\text{Cu}_9\text{Be}_{18}$ BMG, we focus on the slightly partial crystallization induced by pre-annealing for its crystallization mechanism: saturation of point sites with zero nucleation rate.

5.2 Experiment

(1) Pre-annealing were performed in a broad temperature range for a certain period of time in order to get the annealed samples with different microstructure (structural relaxation structure and crystallization), to investigate the effects of different thermal induced transformations on the thermodynamic properties. As shown in Fig. 5-1, annealing temperature was selected in the range of 397-432 °C and the annealing time was chosen as 1 h for $\text{Ti}_{41.5}\text{Cu}_{37.5}\text{Ni}_{7.5}\text{Zr}_{2.5}\text{Hf}_5\text{Sn}_5\text{Si}_1$ BMG. While for $\text{Ti}_{40}\text{Zr}_{25}\text{Ni}_8\text{Cu}_9\text{Be}_{18}$ BMG, the annealing temperature and annealing time are 278-340 °C and 1 h, respectively. After each annealing in the DSC, the isochronous heating at heating rate of 20 K/min was performed sequentially.

(2) Isochronous (at different heating rates) and isothermal (at different temperature) DSC (see Fig. 5-1) were performed on the annealed samples in order to investigate the effects of structural relaxation and slightly partial crystallization on the kinetics of glass transition and crystallization.

For $\text{Ti}_{41.5}\text{Cu}_{37.5}\text{Ni}_{7.5}\text{Zr}_{2.5}\text{Hf}_5\text{Sn}_5\text{Si}_1$ BMG, pre-annealing was performed at 430 °C for 30 min, the continuous heating with the rates of 5-40 K/min and isothermal heating at temperatures of 425-440 °C were then adopted to heat the annealed samples till full crystallization. While for $\text{Ti}_{40}\text{Zr}_{25}\text{Ni}_8\text{Cu}_9\text{Be}_{18}$ BMG, pre-annealing was performed at temperature of 308 °C for 2 h and the following isochronous heatings with 10-40 K/min.

(3) In the case of phase analysis, X-ray diffraction was performed.

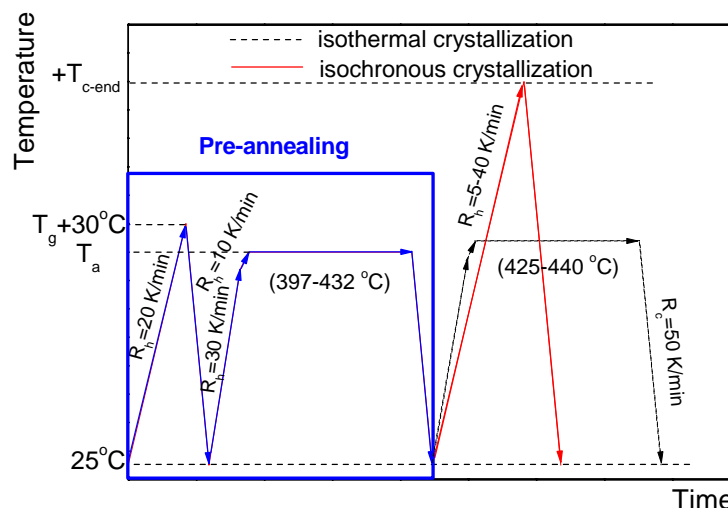


Fig. 5-1 Diagram of experimental method used in investigating the thermodynamics and kinetics of glass transition and crystallization for the annealed samples. The typical temperatures in the diagram are those for the $\text{Ti}_{41.5}\text{Cu}_{37.5}\text{Ni}_{7.5}\text{Zr}_{2.5}\text{Hf}_5\text{Sn}_5\text{Si}_1$ BMG

5.3 Effects of Thermally Induced Transformation of BMGs on Their Thermodynamic Properties of Glass Transition and Crystallization

Fig. 5-2 shows the DSC curves obtained from the annealed $\text{Ti}_{41.5}\text{Cu}_{37.5}\text{Ni}_{7.5}\text{Zr}_{2.5}\text{Hf}_5\text{Sn}_5\text{Si}_1$ samples which were annealed at wide temperature range of 397-432 °C for 1 h. As we expected, the annealed samples with different microstructure were obtained by means of the above pre-annealing. During the process of annealing at 397 and 412 °C for 1 h, only structural relaxation occurred while the crystallization was avoided. The detailed studies about the structural relaxation have been presented in chapter 4. The atom diffusion and rearrangement originating from the structural relaxation result in the annihilation of free volume and the decrease in the free energy of the glasses, finally influencing their corresponding thermodynamic properties. In addition, annealing at temperature higher than 432 °C for 1 h leads to crystallization, which can be seen from the decrease of the crystallization enthalpy with respect to that of the as-cast sample as well as the slight diffraction peak corresponding to the crystalline phase (see **Fig. 5-3**). It should be noted that for the sample annealed at 427 °C for 1 h, no crystals were precipitated from the amorphous phase which can be confirmed from the isothermal DSC curve (not shown here), so the changes of the thermodynamic parameters were believed to be attributed to the structural

relaxation and slight nucleation.

So the effects of thermally induced transformations on the thermodynamic properties can be simply obtained through comparing the typical thermodynamic parameters. The thermodynamic parameters including T_g , T_{x1} , T_{p1} and ΔT_x determined by the DSC curves are gathered in Table 5-1. It can be seen that structural relaxation leads to increasing in T_g , while the values of T_{x1} and T_{p1} do not change, which results in the decrease of ΔT_x . In case of crystallization, the values of T_g , T_{x1} and T_{p1} decrease, and the values of calculated ΔT_x decrease, which is due to the change of the composition of the remaining glassy matrix through the long range order diffusion of the atoms. The remaining glassy matrix is more metastable compared with the as-cast BMG. The low values of T_g , T_{x1} , T_{p1} and ΔT_x can be used to verify this point.

It should be noted that the values of T_g , T_{x1} and T_{p1} for the as-cast sample are higher than for the structural relaxation samples, while its value of ΔT_x is lower, indicating the decrease of thermal stability of the structural relaxation samples with respect to the as-cast sample, as is attributed to the transformation from the phase separation-like structure of the as-cast sample to the metastable equilibrium state through the thermally induced atomic diffusion. The increased value of ΔT_x for the structural relaxation samples compared with that of as-cast sample suggests the more stable state of the structural relaxed glasses than the as-cast state.

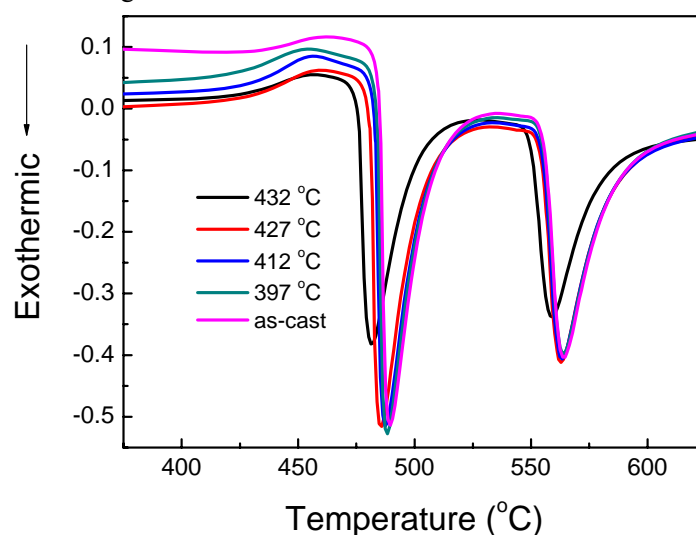


Fig. 5-2 DSC curves obtained from the annealed $\text{Ti}_{41.5}\text{Cu}_{37.5}\text{Ni}_{7.5}\text{Zr}_{2.5}\text{Hf}_5\text{Sn}_5\text{Si}_1$ samples which were annealed at different temperature, 397-432 °C for 1 h and as-cast sample, at heating rate of 20 K/min

Table 5-1

Thermodynamic parameters obtained from the DSC curves of annealed $\text{Ti}_{41.5}\text{Cu}_{37.5}\text{Ni}_{7.5}\text{Zr}_{2.5}\text{Hf}_5\text{Sn}_5\text{Si}_1$ samples at heating rate of 20 K/min

Annealing temperature (°C)	T_g (°C)	T_{x1} (°C)	T_{p1} (°C)	ΔT_x (°C)
As-cast	432	485	489	53
397	425	484	488	59
412	428	484	488	56
427	428	481	486	53
432	426	477	482	51

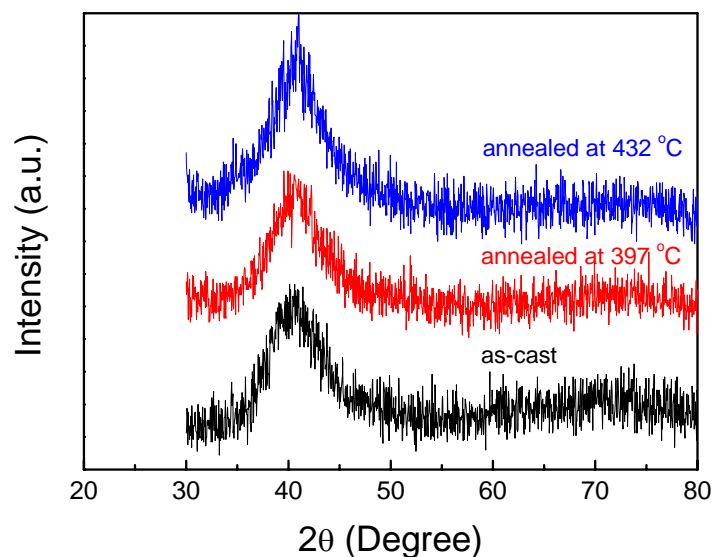


Fig. 5-3 X-ray diffraction patterns obtained from the $\text{Ti}_{41.5}\text{Cu}_{37.5}\text{Ni}_{7.5}\text{Zr}_{2.5}\text{Hf}_5\text{Sn}_5\text{Si}_1$ samples annealed at 397 and 432 °C for 1 h as well as the as-cast sample

Similar experiments were performed on $\text{Ti}_{40}\text{Zr}_{25}\text{Ni}_8\text{Cu}_9\text{Be}_{18}$ BMG. **Fig. 5-4** shows the DSC curves obtained from their annealed samples which were annealed at 278-340 °C for 1 h. And the corresponding XRD patterns are shown in **Fig. 5-5**. No distinct crystalline phases were detected within the sensitivity of XRD for the samples annealed at 278-308 °C, while the crystalline diffraction peaks, however, not obvious, can be detected for the samples annealed at higher temperature 340 °C, as is in accordance with the DSC results. The small and broaden crystalline peaks in the XRD pattern obtained from the samples annealed at 340 °C confirmed the coexistence of nanocrystals and amorphous phase. For its different mechanism of crystallization (growth of the quenched-in nuclei) compared with $\text{Ti}_{41.5}\text{Cu}_{37.5}\text{Ni}_{7.5}\text{Zr}_{2.5}\text{Hf}_5\text{Sn}_5\text{Si}_1$ BMG, the effects of structural relaxation may not be distinguished for the simultaneous development of structural relaxation and the growth of crystals. Based on the structural relaxation study in the last chapter, the structural relaxation is dominant under the condition of low temperature and short time, while the crystallization becomes more and more dominant with increase in temperature and time. It is found that the effects of structural relaxation and crystallization are in consistent, which lead to the monotonic increase in T_g , T_{x1} and T_{p1} . The rapid increase of T_g and the slow increase of T_{x1} are responsible for the final decrease of ΔT_x , which indicates that the thermal stability decreases with thermally induced transformation. It is of interest that the pre-annealing leads to the delay of the crystallization for the annealed samples and for the change of the chemical composition caused by pre-annealing, as can be confirmed from the increase of T_g , T_{x1} and T_{p1} , however, the sequent crystallization reaction will be accelerated.

From the viewpoint of cluster model [Oguni, 1997], the annihilation of free volume during structural relaxation could be a process for clusters to be formed. The lower the free volume, the more the clusters generate in a sample. Enthalpy recovery can be considered as the destruction of the formed clusters. Within the incubation time, no critical clusters can be formed. Consequently, no obvious difference in the following crystallization is expected. Once critical clusters are formed after long-time annealing, they cannot be destroyed during reheating and can act as nuclei for the following crystallization. Therefore, the structural relaxation and following crystallization are two

independent processes. However, the different characteristics of crystallization usually come from the changes in short-range ordering affected by structural relaxation.

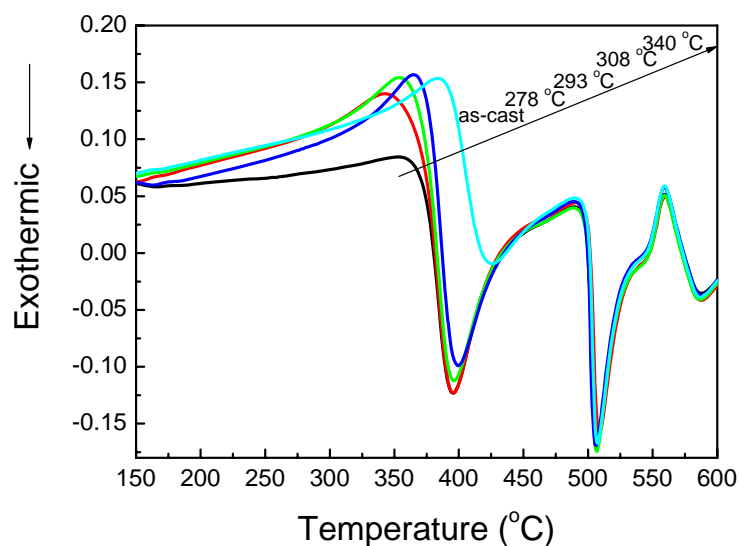


Fig. 5-4 Continuous heating DSC curves obtained from the $\text{Ti}_{40}\text{Zr}_{25}\text{Ni}_8\text{Cu}_9\text{Be}_{18}$ samples annealed at various different temperatures of 278-340 °C for 1 h as well as the as-cast sample, at a heating rate of 20 K/min

Table 5-2

Typical temperature parameters obtained from the annealed as well as the as-cast $\text{Ti}_{40}\text{Zr}_{25}\text{Ni}_8\text{Cu}_9\text{Be}_{18}$ samples

Annealing temperature (°C)	T_g (°C)	T_{x1} (°C)	T_{p1} (°C)	ΔT_x (°C)
As-cast	313	372	395	59
278	300	367	395	67
293	308	369	395	61
308	321	374	399	53
340	340	390	425	50

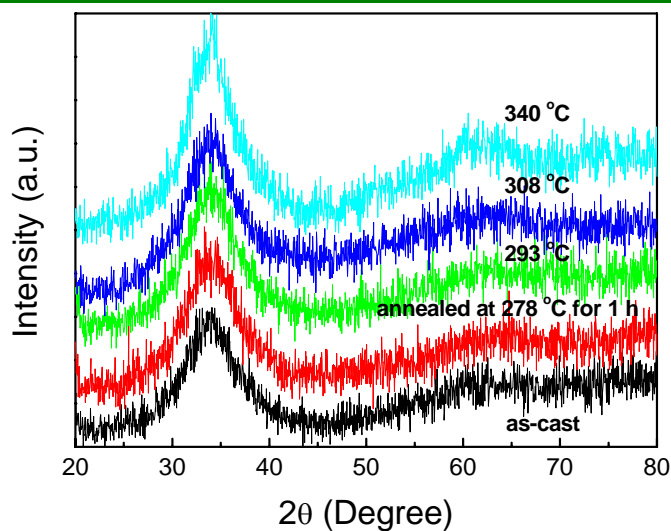


Fig. 5-5 X-ray diffraction patterns obtained from the annealed as well as as-cast $\text{Ti}_{40}\text{Zr}_{25}\text{Ni}_8\text{Cu}_9\text{Be}_{18}$ samples

The good choice of the appropriate pre-annealing temperature and time provides an opportunity to compare the effects of pre-annealing between $\text{Ti}_{41.5}\text{Cu}_{37.5}\text{Ni}_{7.5}\text{Zr}_{2.5}\text{Hf}_5\text{Sn}_5\text{Si}_1$ and $\text{Ti}_{40}\text{Zr}_{25}\text{Ni}_8\text{Cu}_9\text{Be}_{18}$ BMGs. The annealing temperatures applied in this study for the two alloys are both 5, 20 and 35 °C below T_g . Compared with $\text{Ti}_{41.5}\text{Cu}_{37.5}\text{Ni}_{7.5}\text{Zr}_{2.5}\text{Hf}_5\text{Sn}_5\text{Si}_1$ BMG, pre-annealing for the $\text{Ti}_{40}\text{Zr}_{25}\text{Ni}_8\text{Cu}_9\text{Be}_{18}$ BMG has more apparent effects on the thermodynamic parameters, T_g , T_{x1} and T_{p1} , which indicates that the thermodynamic properties of $\text{Ti}_{40}\text{Zr}_{25}\text{Ni}_8\text{Cu}_9\text{Be}_{18}$ BMG are more sensitive than that of $\text{Ti}_{41.5}\text{Cu}_{37.5}\text{Ni}_{7.5}\text{Zr}_{2.5}\text{Hf}_5\text{Sn}_5\text{Si}_1$ BMG. In addition, the opposite influence on the typical thermodynamic parameters suggests the different crystallization behavior and mechanism for the annealed samples, which makes us be interested in investigating the effects of pre-annealing on the kinetics of glass transition and crystallization, as will be shown in the next section.

5.4 Effects of Pre-annealing of BMGs on Their Kinetics Properties of Glass Transition and Crystallization

The pre-annealing of BMGs near T_g or in the SLR may induce structural relaxation, nucleation and growth of nuclei in the BMG, and finally influence the kinetics of the glass transition and crystallization. During the process of forming, crystallization is generally avoided by applying the appropriate temperature and time, so only structural relaxation and slight nucleation may occur during this period of time. In this section, we focus on the effects of pre-annealing near T_g on the kinetics of the subsequent glass transition and crystallization. For $\text{Ti}_{41.5}\text{Cu}_{37.5}\text{Ni}_{7.5}\text{Zr}_{2.5}\text{Hf}_5\text{Sn}_5\text{Si}_1$ BMG, it was pre-annealed at 430 °C for 30 min, then isochronous as well as isothermal DSC measurements were both performed on the annealed samples; while for $\text{Ti}_{40}\text{Zr}_{25}\text{Ni}_8\text{Cu}_9\text{Be}_{18}$ BMG, only isochronous DSC measurement was performed on the annealed samples at 308 °C for 2 h for its crystallization mechanism of growth of quenched-in nuclei.

5.4.1 Non-isothermal Kinetics of Glass Transition and Crystallization

Fig. 5-6 (a) shows the isochronous DSC traces for the pre-annealed $\text{Ti}_{41.5}\text{Cu}_{37.5}\text{Ni}_{7.5}\text{Zr}_{2.5}\text{Hf}_5\text{Sn}_5\text{Si}_1$ BMG at different heating rates of 5-40 K/min. In order to clarify the effects of pre-annealing on the kinetics of glass transition and crystallization, the isochronous DSC scans for the as-cast samples at the same heating rates were also presented in **Fig. 5-6 (a)** for comparison. Similar with the as-cast samples, the DSC traces obtained from the annealed samples exhibit the endothermic characteristics of a glass transition followed by two-step exothermic crystallization events at higher temperature, and they exhibit the kinetic characteristic of both the glass transition and the crystallization because that the typical thermodynamic parameters, T_g , T_x and T_p , shift to a higher temperature with increase in heating rate, as indicates that the pre-annealing does not change the kinetic nature of the glass transition and the crystallization.

The values of T_g and T_p obtained from the DSC curves at different heating rates are listed in **Table 5-3**. It is clear that the glass transition and crystallization are markedly affected by the pre-annealing. The activation energies for the crystallization of the annealed samples were

evaluated using the well-known Kissinger's equation, which are shown in Fig. 5-6 (b). The activation energy for the first crystallization event increased from 319.4 to 475.6 kJ/mol, while those for the second crystallization event did not change within the experimental error, after pre-annealing at temperature near T_g , as is similar to the previous reports for $Zr_{41}Ti_{14}Cu_{12.5}Ni_{10}Be_{22.5}$ [Zhuang et al., 2000], $Zr_{62}Al_8Ni_{13}Cu_{17}$ [X.D. Wang et al., 2006] and $Co_{43}Fe_{20}Ta_{5.5}B_{31.5}$ [Yuan et al., 2007] BMGs. It should be noted that there may exist a contradiction between the lower crystallization temperature and the larger activation energy for the crystallization, in regards to this point, detailed discussion will be presented later with the help of analysis on mechanism of crystallization.

In summary, the effects of pre-annealing near T_g on the kinetics of glass transition and crystallization can be summarized as follow: the glass transition and crystallization are accelerated, followed by a sluggish crystallization reaction.

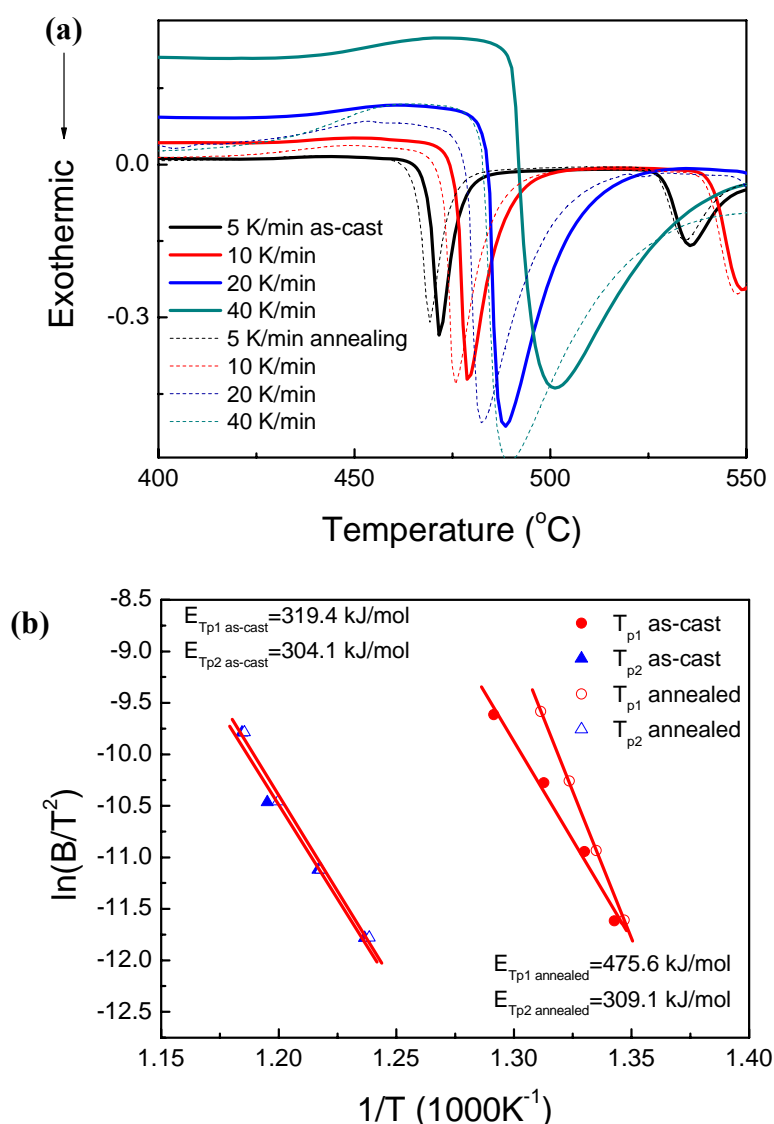


Fig. 5-6 (a) Isochronal DSC scans of as-cast (solid lines) and pre-annealed at 430 °C for 30 min (dashed lines) $Ti_{41.5}Cu_{37.5}Ni_{7.5}Zr_{2.5}Hf_5Sn_5Si_1$ BMG at different heating rates of 5-40 K/min and (b) activation energies evaluated by Kissinger's equation according to T_p temperature of as-cast and pre-annealed samples

CHAPTER 5 EFFECTS OF PRE-ANNEALING NEAR GLASS TRANSITION
TEMPERATURE ON THE THERMODYNAMICS AND KINETICS OF THE FOLLOWING
GLASS TRANSITION AND CRYSTALLIZATION

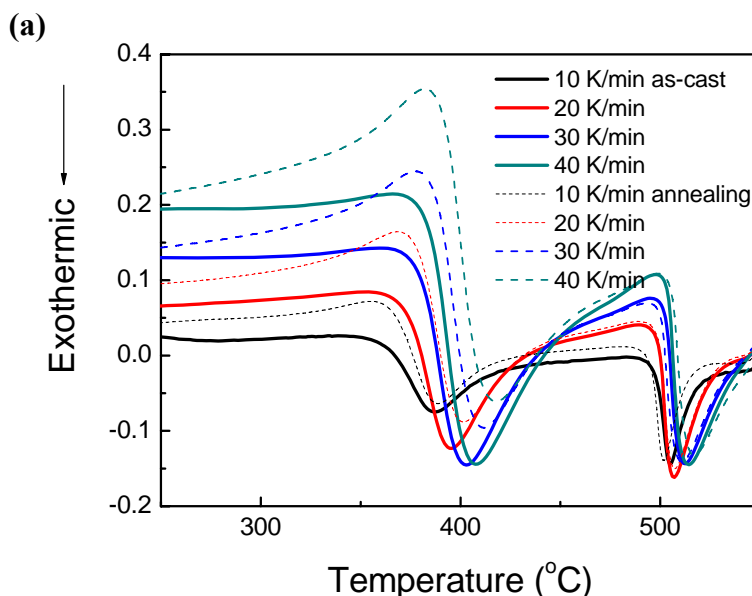
Table 5-3

Comparison of values of T_g and T_p determined at different heating rates and the calculated values E_p for annealed and as-cast $\text{Ti}_{41.5}\text{Cu}_{37.5}\text{Ni}_{7.5}\text{Zr}_{2.5}\text{Hf}_5\text{Sn}_5\text{Si}_1$ samples

B (K/min)	T_g (°C)		T_{p1} (°C)		T_{p2} (°C)		E_{p1} (kJ/mol)		E_{p2} (kJ/mol)	
	As-cast	Annealed	As	An	As	An	As	An	As	An
5	421	415	471.6	469.3	535.6	534.3				
10	427	419	478.7	475.9	548.7	547.9	319.4	475.6	304.1	309.1
20	432	422	488.6	482.4	563.6	560.4				
40	438	424	501.2	489.4	571.2	570.4				

Similar experiments were performed on $\text{Ti}_{40}\text{Zr}_{25}\text{Ni}_8\text{Cu}_9\text{Be}_{18}$ BMG, and the obtained isochronous DSC traces for the pre-annealed and as-cast samples were shown in Fig. 5-7 (a), the linear fitting Kissinger's curves for determining the activation energies for crystallization were shown in Fig. 5-7 (b). The thermodynamic parameters and the calculated activation energies are gathered in Table 5-4. It is found that, different from $\text{Ti}_{41.5}\text{Cu}_{37.5}\text{Ni}_{7.5}\text{Zr}_{2.5}\text{Hf}_5\text{Sn}_5\text{Si}_1$ BMG, the activation energies for the first and second crystallization events of $\text{Ti}_{40}\text{Zr}_{25}\text{Ni}_8\text{Cu}_9\text{Be}_{18}$ BMG decreased from 235.2 to 172.2 kJ/mol, and from 628.4 to 451.9 kJ/mol, respectively, after pre-annealing at temperature near T_g , indicating that the crystallization reactions are accelerated, which may be due to the secondary nucleation induced by the crystal growth. In regard to the lower typical thermodynamic parameters of the annealed samples than those of the as-cast samples, it can be attributed to the change of chemical composition of the glass matrix caused by growth of nuclei.

In summary, the effects of pre-annealing near T_g on the kinetics of glass transition and crystallization can be summarized as follow: the glass transition and crystallization are delayed, followed by an accelerated crystallization reaction.



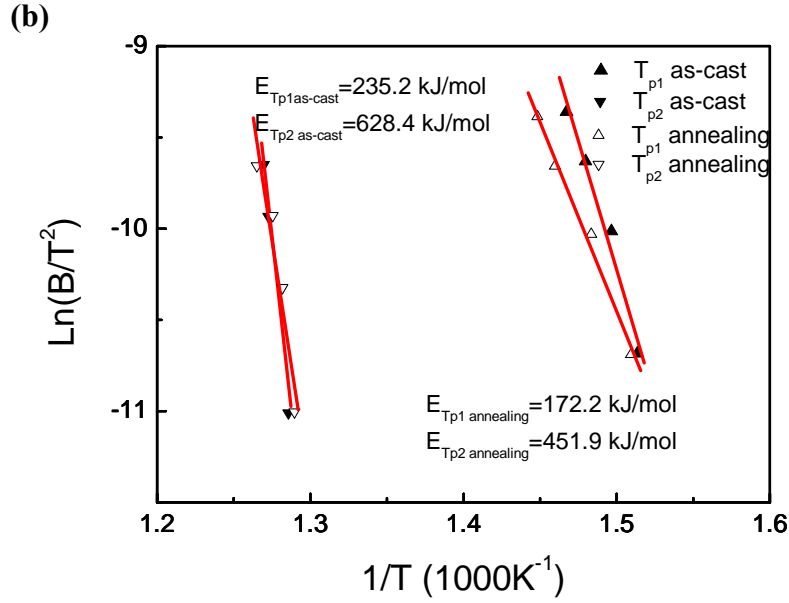


Fig. 5-7 (a) Isochronal DSC scans of as-cast (solid lines) and pre-annealed at 308 °C for 2 h (dashed lines) $\text{Ti}_{40}\text{Zr}_{25}\text{Ni}_8\text{Cu}_9\text{Be}_{18}$ BMG at different heating rates of 10–40 K/min and (b) activation energies evaluated by Kissinger's equation according to T_p temperatures of as-cast and pre-annealed samples

Table 5-4

Comparison of values of T_p determined at different heating rates and the calculated values of E_p for annealed and as-cast $\text{Ti}_{40}\text{Zr}_{25}\text{Ni}_8\text{Cu}_9\text{Be}_{18}$ samples

B (K/min)	T_{p1} (°C)		T_{p2} (°C)		E_{p1} (kJ/mol)		E_{p2} (kJ/mol)	
	As	An	As	An	As	An	As	An
10	387.6	389.2	504.6	502.3	235.2	172.2	628.4	451.9
20	395.1	401.0	507.1	507.0				
30	402.6	411.8	512.6	510.8				
40	408.4	417.3	514.4	517.3				

5.4.2 Isothermal Kinetics of Crystallization

Isothermal DSC measurements were also performed on the annealed $\text{Ti}_{41.5}\text{Cu}_{37.5}\text{Ni}_{7.5}\text{Zr}_{2.5}\text{Hf}_5\text{Sn}_5\text{Si}_1$ samples to further investigate the effects of pre-annealing on the kinetics of crystallization. Isothermal DSC curves of the annealed samples at different temperatures between 425 and 440 °C are shown in Fig. 5-8, those of the as-cast samples are also added in Fig. 5-8 for comparison. It is clear that the pre-annealing has obvious effects on the crystallization of bulk metallic glasses, which can be seen from the decreased incubation time, as is in accordance with the isochronous DSC results.

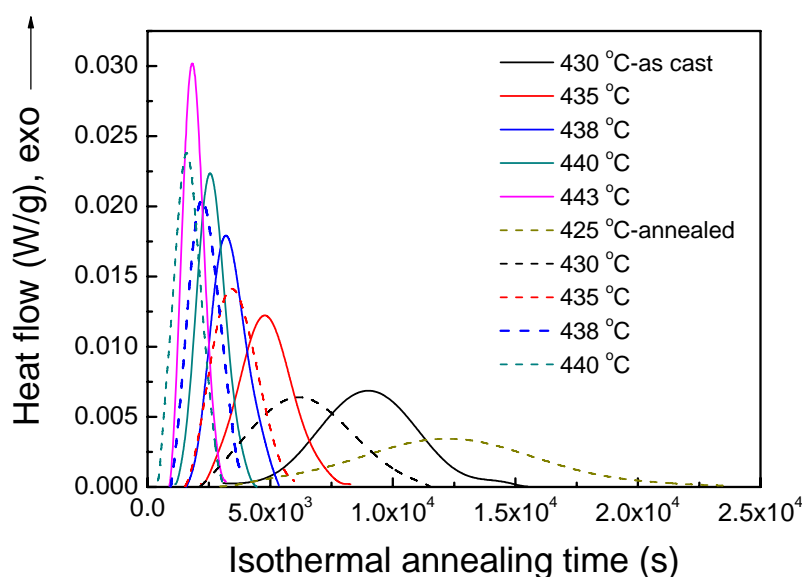


Fig. 5-8 Isothermal DSC curves of as-cast (solid lines) and pre-annealed (dashed lines) $\text{Ti}_{41.5}\text{Cu}_{37.5}\text{Ni}_{7.5}\text{Zr}_{2.5}\text{Hf}_5\text{Sn}_5\text{Si}_1$ BMG for the first crystallization stage

In order to further clarify the effects of pre-annealing on the kinetics of crystallization, the mechanism of crystallization was determined based on the isothermal DSC curves by applying the kinetics model. The values of α_p^∞ in $z(\alpha)$ - α curves (**Fig. 5-9**) are located in the interval of 0.61-0.65, which confirms the applicability of the JMA model in the kinetics analysis on the annealed $\text{Ti}_{41.5}\text{Cu}_{37.5}\text{Ni}_{7.5}\text{Zr}_{2.5}\text{Hf}_5\text{Sn}_5\text{Si}_1$ samples. **Fig. 5-10** shows a good fitting between the calculated curves based on JMA model and the experimental curves. The obtained kinetic parameters are gathered in **Table 5-5**. In addition, local Avrami exponent $n_{\text{loc}}(x)$ and local activation energies were also calculated as a function of transformed volume fraction, which are shown in **Fig. 5-11** and **5-12**. It can be seen that the change in the Avrami exponents for the pre-annealed samples was basically identical to that with the as-cast samples: the Avrami exponents increased rapidly at the beginning of the crystallization, then remained constant within the range of $0.1 < x_v < 0.9$, finally increasing rapidly; the values of kinetics parameters changed: slightly decrease in n and increase in K and E_a . The change of Avrami exponents suggests that the pre-annealing leads to the change of the mechanism of crystallization. In detail, the crystallization of as-cast sample was governed by diffusion-controlled three-dimensional growth of nuclei with increasing nucleation rate; however, the crystallization of pre-annealed sample was governed by diffusion-controlled three-dimensional growth of nuclei with a constant nucleation rate. The change of the thermodynamics and kinetics of crystallization caused by pre-annealing can be interpreted based on the analysis of the microstructure change induced by pre-annealing, as will be discussed as follow.

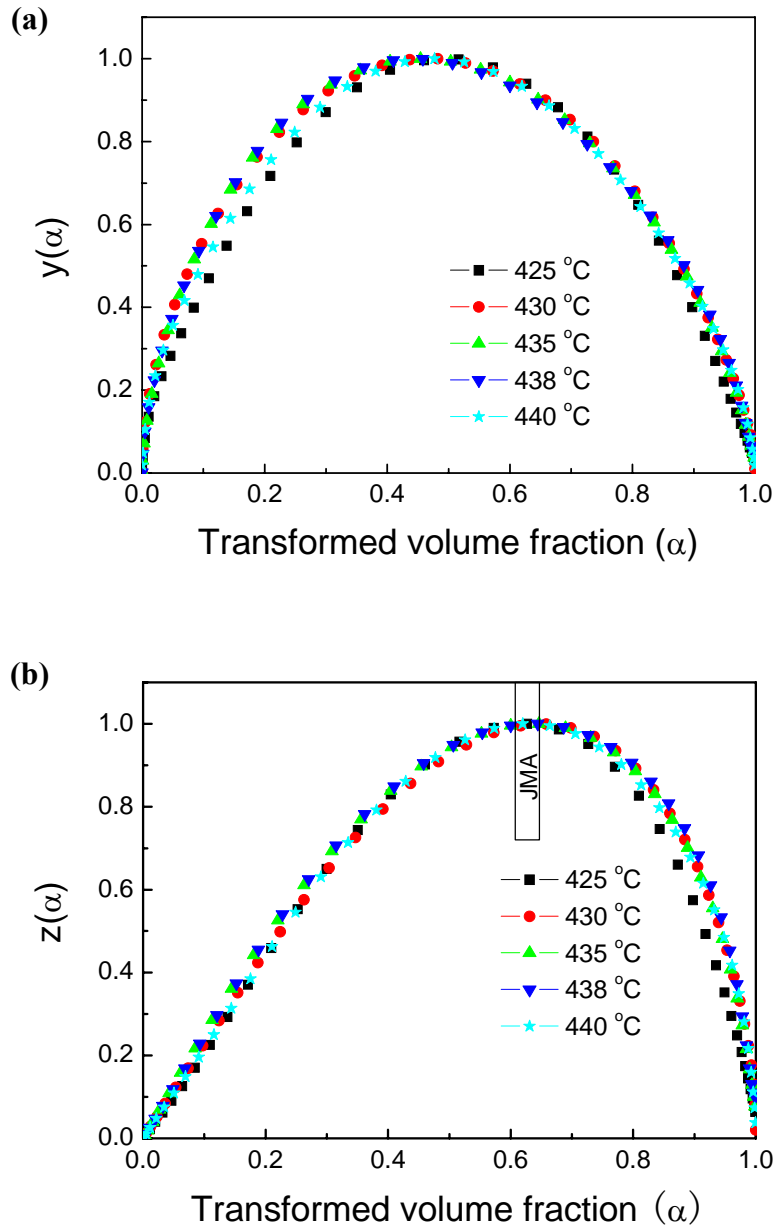


Fig. 5-9 Normalized (a) $y(\alpha)$ and (b) $z(\alpha)$ as a function of transformed volume fraction for the first crystallization of the annealed $\text{Ti}_{41.5}\text{Cu}_{37.5}\text{Ni}_{7.5}\text{Zr}_{2.5}\text{Hf}_5\text{Sn}_5\text{Si}_1$ BMG

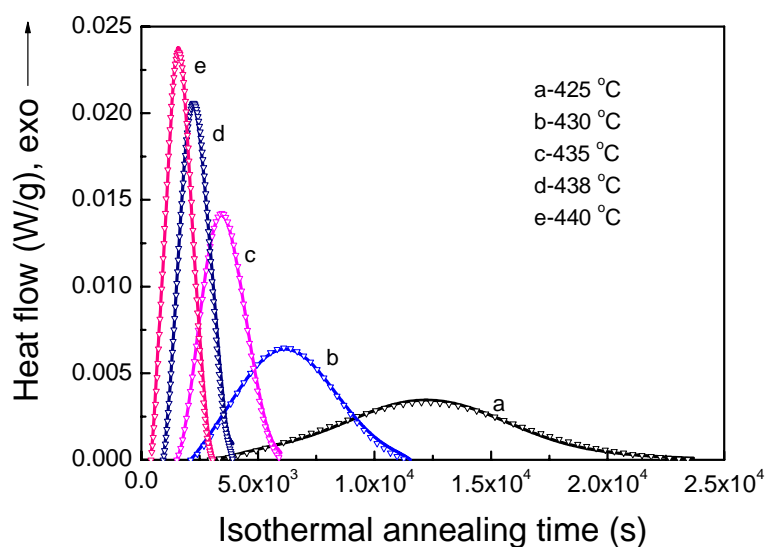


Fig. 5-10 Comparison of the experimental DSC curves (solid lines) and the DSC data calculated based on the JMA model (symbols) for the first crystallization stage of the annealed $\text{Ti}_{41.5}\text{Cu}_{37.5}\text{Ni}_{7.5}\text{Zr}_{2.5}\text{Hf}_5\text{Sn}_5\text{Si}_1$ BMG

Table 5-5

Kinetic parameters obtained from the first crystallization reaction of the annealed $\text{Ti}_{41.5}\text{Cu}_{37.5}\text{Ni}_{7.5}\text{Zr}_{2.5}\text{Hf}_5\text{Sn}_5\text{Si}_1$ samples using the JMA model

Isothermal temperature (°C)	K	n	Incubation time τ (s)
425	8.456e-5	3.14	2950
430	1.880e-4	2.70	2116
435	4.180e-4	2.66	1520
438	6.019e-4	2.68	945
440	6.416e-4	2.91	416

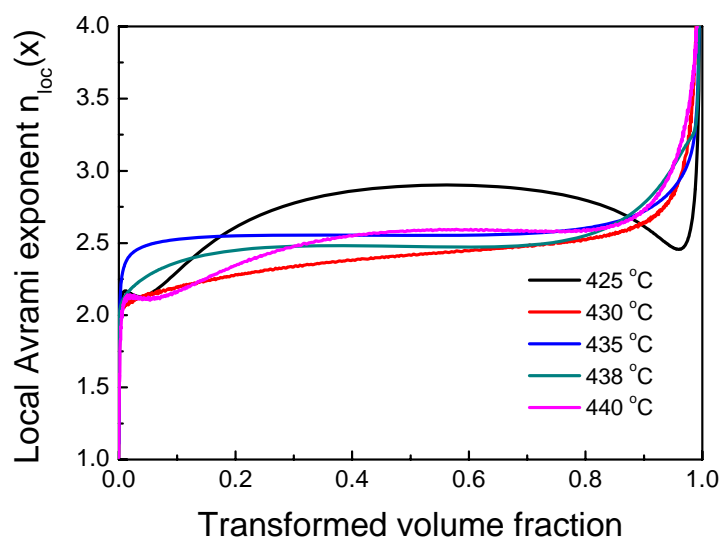


Fig. 5-11 Dependence of Avrami exponent vs. transformed volume fraction for pre-annealed $\text{Ti}_{41.5}\text{Cu}_{37.5}\text{Ni}_{7.5}\text{Zr}_{2.5}\text{Hf}_5\text{Sn}_5\text{Si}_1$ samples at different isothermal temperatures

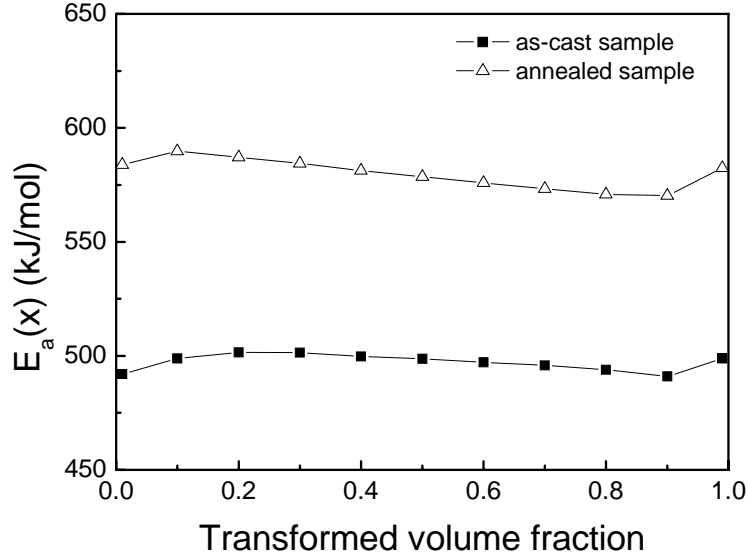


Fig. 5-12 Activation energies E_a as a function of transformed volume fraction for the first crystallization stage of the as-cast and pre-annealed $\text{Ti}_{41.5}\text{Cu}_{37.5}\text{Ni}_{7.5}\text{Zr}_{2.5}\text{Hf}_5\text{Sn}_5\text{Si}_1$ samples

Pre-annealing near T_g will induce structural relaxation, nucleation and growth of nuclei in the BMGs, thus the annealed sample has different microstructure and the subsequent nucleation process. The change of microstructure of $\text{Ti}_{41.5}\text{Cu}_{37.5}\text{Ni}_{7.5}\text{Zr}_{2.5}\text{Hf}_5\text{Sn}_5\text{Si}_1$ BMG in the process of pre-annealing at 430 °C for 30 min was checked by XRD in [Fig. 5-13](#) and isothermal DSC (see [Fig. 5-6 \(a\)](#)). It can be seen that no crystalline peak was detected within the sensitivity of XRD, and no exothermic event occurred, indicating that no crystallization occurred during the process of pre-annealing. Usually, pre-annealing near T_g causes atomic structural rearrangement (CSRO and TSRO) in the local region, which is the so-called structural relaxation discussed in the last chapter. So if the structure of the clusters is similar to that of the primary phase in the crystallization reaction, the crystallization will be promoted; otherwise, it will be delayed. In this study, the lower values of T_{x1} and T_{p1} can be attributed to the clusters formed during the process of pre-annealing has a similar structure with the primary phase, cubic $\text{TiNi}(\text{Cu})$. From another point of view, the nucleation in the as-cast samples is realized through a composition fluctuation from the initial homogeneous alloy with lower density of clusters, while the nucleation in the annealed sample with higher density of cluster is realized by heterogeneous nucleation processes due to the heterogeneous structure and composition. So, the reason why the crystallization reaction of the annealed samples occurred earlier than that of the as-cast samples can be successfully explained.

In regard to the sluggish crystallization reaction, firstly, the possibility of the change of the primary phase should be considered since the higher value of activation energy for the crystallization of the annealed samples generally could be attributed to the change of the primary phase. The identical crystallization products of the annealed and as-cast samples can be obtained in this study, so the sluggish crystallization reaction of the pre-annealed samples was not due to the precipitation of different crystalline products from those in the as-cast samples, other reason should be found.

It is well known that the crystallization process of the glassy alloys comprises the nucleation and growth of nuclei. It was reported that the crystallization peak temperature corresponds to the stage where the crystals start to impinge each other and is more related to the growth process [[H.R. Wang, et al., 2003](#); [Qin et al., 2004](#)], and the activation energy calculated from the crystallization

peak temperatures based on Kissinger equation resembles the activation energy for growth of nuclei [H.R. Wang, et al., 2003]. The activation energies derived from the isothermal DSC based on Arrhenius equation are the integration of the activation energy of nucleation and growth:

$$E_a = aE_n + bE_g, \text{ where } a \text{ and } b \text{ are positive constants related to Avrami exponent and}$$

$a + b = 1$. Assuming the value of activation energy calculated from the crystallization peak temperatures by Kissinger equation is equal to that for growth of nuclei, so subtracting the activation for growth from the total activation energy E_a , the value of activation energy for nucleation of the annealed sample is lower than that of the as-cast sample, as can be used to explain the acceleration of the crystallization of the annealed samples. Then the increase in the total activation energy should be attributed to the increase in the activation energy for growth of nuclei. On one hand, the constituent elements were rearranged to form pairs with strong bonding during the process of pre-annealing. On the other hand, the growth of nuclei requires long-range atomic rearrangement of constituent element, which is closely related to the diffusion of atoms, and the diffusion in the supercooled liquid region of BMGs requires a cooperative motion involving a cluster of neighboring atoms. It has been shown that the diffusion mechanisms and diffusivity in the glassy alloys is sensitive to the relaxation state of the samples, and the diffusivity in the relaxed alloy with an indirect mechanism is smaller than that of the as-prepared alloy with collective mechanism [Frank et al., 1994]. So the pre-annealing induced structural changes in the BMG may change the diffusion mechanism and decrease the diffusivity, and finally changes the nucleation mechanism. Thus, the increase in the activation energy of crystallization and the change in the nucleation mechanism for the $\text{Ti}_{41.5}\text{Cu}_{37.5}\text{Ni}_{7.5}\text{Zr}_{2.5}\text{Hf}_5\text{Sn}_5\text{Si}_1$ BMG after annealing near T_g are due to the decrease of diffusivity caused by pre-annealing induced structural transformations.

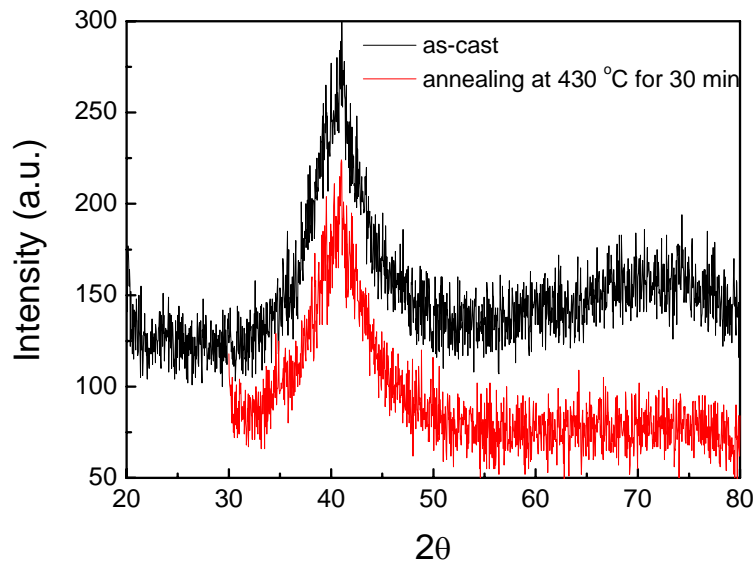


Fig. 5-13 X-ray diffraction patterns obtained from as-cast and annealed $\text{Ti}_{41.5}\text{Cu}_{37.5}\text{Ni}_{7.5}\text{Zr}_{2.5}\text{Hf}_5\text{Sn}_5\text{Si}_1$ samples

5.5 Conclusion

The effects of pre-annealing near T_g on the thermodynamics and kinetics of the subsequent glass transition and crystallization for $\text{Ti}_{41.5}\text{Cu}_{37.5}\text{Ni}_{7.5}\text{Zr}_{2.5}\text{Hf}_5\text{Sn}_5\text{Si}_1$ and $\text{Ti}_{40}\text{Zr}_{25}\text{Ni}_8\text{Cu}_9\text{Be}_{18}$ BMGs have been investigated in detail by isochronous and isothermal DSC. The following results were obtained:

- (1) For both BMGs, pre-annealing does not change the kinetic characteristic of glass transition and crystallization, but changes the thermodynamics and kinetic parameters.
- (2) For the annealed $\text{Ti}_{41.5}\text{Cu}_{37.5}\text{Ni}_{7.5}\text{Zr}_{2.5}\text{Hf}_5\text{Sn}_5\text{Si}_1$ sample, the nucleation was prompted, which is characterized by having lower on-set crystallization temperature in the continuous heating DSC and shorter incubation time in the isothermal DSC, and is due to the similar structure of the clusters in the process of pre-annealing with the primary phase of crystallization; however, the growth of nuclei was sluggish due to the decrease of diffusivity caused by pre-annealing induced structural transformations. Based on JMA model, the annealed $\text{Ti}_{41.5}\text{Cu}_{37.5}\text{Ni}_{7.5}\text{Zr}_{2.5}\text{Hf}_5\text{Sn}_5\text{Si}_1$ BMG was governed by diffusion-controlled three-dimensional growth of nuclei with a constant nucleation rate.
- (3) For the annealed $\text{Ti}_{40}\text{Zr}_{25}\text{Ni}_8\text{Cu}_9\text{Be}_{18}$ sample, the glass transition of BMG was delayed, which is characterized by having higher glass transition temperature and higher on-set crystallization temperature, and is resulting from the change of the chemical composition caused by growth of nuclei, however, the subsequent crystallization reaction was accelerated, which may be due to the secondary nucleation induced by the crystal growth.

CHAPTER 6

EFFECTS OF THERMALLY INDUCED STRUCTURAL TRANSFORMATIONS ON ROOM TEMPERATURE MECHANICAL PROPERTIES OF TI-BASED BMGS

6.1 Background and Motivation

Since the Ti-based BMGs are expected to be potential structural materials, the investigations on their mechanical behavior are of significance. In the last two chapters, we have presented the thermally induced structural transformations (structural relaxation and crystallization) of $\text{Ti}_{41.5}\text{Cu}_{37.5}\text{Ni}_{7.5}\text{Zr}_{2.5}\text{Hf}_5\text{Sn}_5\text{Si}_1$ and $\text{Ti}_{40}\text{Zr}_{25}\text{Ni}_8\text{Cu}_9\text{Be}_{18}$ BMGs and their effects on the thermodynamics and kinetics of the subsequent glass transition and crystallization; in this chapter, we will focus on their effects on the room-temperature mechanical properties, due to the following reasons:

- (1) Extensive work has been done on the deformation behavior and mechanism in many metallic glass systems; however, universal agreement on the deformation mechanism of metallic glasses has not yet been attained [Nieh et al., 2001; H.S. Kim, 2004; Lee et al., 2005-a]. Accordingly, it is necessary to further carry out this work aspect.
- (2) Thermally induced transformations of metallic glasses may provide one way to strengthen and (or) toughen the metallic glasses, since the previous investigation indicates that the microstructure changes caused by structural relaxation or crystallization in some metallic glass systems may lead to the enhancement of mechanical properties [Inoue et al., 2000-b; Han et al., 2001; Hajlaoui et al., 2007].
- (3) It is well known that the superplastic forming in the supercooled liquid region is the most promising way for realizing metallic glass forming [Kawamura et al., 1998; Nieh et al., 1999]. However, during this process, structural relaxation of amorphous phase is inevitable and crystallization will occur if adopting unsuitable forming process [Nieh et al., 2001; J. Lu et al., 2003; J. Shen et al., 2006-a]. So it is very meaningful to know how relaxation and crystallization influence the mechanical properties of BMGs, and check the room-temperature mechanical properties for the samples after hot working, finally to determine if such materials can be used as practical products.

In the following section, the general characteristics and mechanisms for the room-temperature deformation and fracture of metallic glasses as well as the effects of thermally induced structural

transformations on the mechanical properties will be reviewed, to clarify the motivation of this study.

6.1.1 Characteristics and Mechanisms for Room-temperature Deformation and Fracture of Metallic Glasses

The plastic strain energy imposed on crystalline materials can be accommodated through many pathways including slip, twin, phase transformation, heat generation, etc.; however, metallic glasses have fundamentally different deformation characteristics and mechanisms compared with crystalline materials because dislocation networks cannot be created in these alloys to accommodate plastic strains due to the absence of long range atomic ordering:

- (i) The plastic flow in metallic glasses at room temperature and moderate strain rates is typically inhomogeneous and proceeds via formation and propagation of shear bands [Anand et al., 2005; Schuh et al., 2007-a]. In the absence of long range order, there exists no dislocation slip mechanism to explain the origin of these shear bands. The deformation of these glasses generally conforms to elastic-perfectly plastic flow behavior [Mukai et al., 2002-a; Z.F. Zhang et al., 2003]. The inhomogeneous plastic flow in that case is related to a local change in viscosity leading to a softening of the glass and the localization of plastic strain. There exist two hypotheses aimed to explain the local softening of the glass. Spaepen suggests that these shear bands locally nucleate in the regions where the deformation-induced creation of free volume cannot be fully compensated by thermal diffusive relaxation [Spaepen, 1977], followed by the coalescence of excess free volume and significant reduction of viscosity. Consequently, shear bands manifest as sudden load drops in macroscopic compression curves or pop-in events in nanoindentation experiments [Concustell et al., 2005; Schuh et al., 2003-a]. The second model invokes flow softening due to adiabatic heating during shear deformation [Leamy et al., 1972; Bruck et al., 1996]. Although most of the current work conforms to an explanation based on the concept of excess free volume, evidence also points out a substantial temperature rise near the fracture surface [Wright et al., 2001].
- (ii) The yield behavior of metallic glasses cannot be simply described by the classical von Mises or Tresca criteria, as for crystalline metals, since normal stress components acting on the shear plane and/or hydrostatic pressure also play an important role at the onset of plasticity as the shear stress components [Schuh et al., 2004; Ogata et al., 2006]. The dependence of yielding on normal stresses seems to be related to atomic friction and the dilatation events that occur during plastic flow in metallic glasses [Schuh et al., 2003-b]. To account for the normal stress or pressure dependence of the shear stress, the Mohr-Coulomb yield criteria has been used in the literature [Donovan et al., 1989; C.T. Liu et al., 1998; Lowhaphandu et al., 1999], i.e., $\tau_y = \tau_0 - \alpha \sigma_n$, here, τ_y is the effective shear yield stress, τ_0 is a constant, and α is a system specific coefficient (pressure sensitive index). Consequently, for uniaxial deformation the shear plane yielding is slightly deviated from 45° to the tensile or compressive axis that is specific to

the alloy composition.

6.1.2 Effects of Thermally Induced Structural Transformations on Room-temperature Mechanical Properties of Metallic Glasses

For gaining insights into the effects of thermally induced structural transformations on the room-temperature mechanical properties of metallic glasses, extensive work has been done through the tensile, compressive, indentation, etc. measurements in the past two decades. It is found that the mechanical properties of metallic glasses are strongly dependent on various structures originating from structural relaxation or crystallization upon heat treatment; however, it does not follow any universal law for the different structural relaxation and crystallization behavior amongst different metallic glasses.

- (i) Generally, the structural relaxation causes the loss of the ability to undergo viscous flow and leads to severe embrittlement, increase in strength and slight increase in hardness of metallic glasses [Chen, 1980; Mulder et al., 1983; Ashby et al., 2006]. The physical origin of these effects can be attributed to the reduction of free volume causing a lower defect concentration upon structural relaxation [Yan et al., 2004; Murali et al., 2005].
- (ii) The effects of nanocrystals on the shear bands slip in the metallic glass composites are very complicated, they depend on the grain size, volume fraction and the distribution of nanocrystals. As a result, two effects may occur depending on different metallic glass systems after partial crystallization. One is that the precipitation of nanocrystallites deteriorates the mechanical properties with respect to the single amorphous phase alloys, such as strength and plasticity [Nagendra et al., 2000; Ramamurty et al., 2002]. The other one is that both the mechanical strength and plasticity of metallic glasses can be significantly improved by the formation of the nanocrystals [Inoue et al., 2000-b; Han et al., 2001; Hajlaoui et al., 2007]. In addition, it is also found that the hardness and elastic modulus are generally improved by crystallization.

6.1.3 Main Issues Related to Room-temperature Deformation

Although the room-temperature mechanical deformation, fracture and shear bands of metallic glasses and the corresponding composites have been widely investigated in various metallic glass systems during the past three decades, until now there still exist some issues in argument need in further investigations.

- (1) The complete picture of micromechanism for room-temperature deformation and fracture of metallic glasses has not emerged.

Various fracture modes can be observed for metallic glasses. For example, under the condition of compressive testing, several characteristics of fracture may occur: (i) fracture along the only one flat rough (or smooth) plane which is slightly deviated from the maximum shear plane, on the surface of which, well developed vein patterns, river-like patterns or even dimples, generally can be found, as is the most typical feature for the fracture surface of metallic glasses (e.g. Zr-based metallic glasses); (ii) fracture along multi-planes, sometimes the fracture seems to take place in a

normal fracture mode more or less, rather than as a pure shear mode, and one completed fracture surface is separated into two or three or even more fracture planes and sometimes even the samples are damaged into several pieces, in this case, the feature of fracture surface is so complicated that more features (vein patterns, river-like pattern, nanoscaled dimples and nanowaves, ect.) dominate the fracture surface, indicating that the generation and propagation of shear bands (cracks) are very complicated, finally leading to the complicated deformation and fracture mechanism (Fe-, Ni-, Mg-based metallic glasses). Accordingly, the varieties of the morphologies for the fracture surfaces suggest complicated and various deformation and fracture mechanisms of metallic glasses.

Consequently, the above analysis indicates the dissimilar intrinsic plasticity of different existing families of BMGs and accordingly the dissimilar deformation and fracture mode. This phenomenon may be associated with the characteristic of the nature for each material, e.g. the properties of the constituent elements (metallic or nonmetallic, cluster formation), the ratio between the elastic shear modulus and the bulk modulus, μ/B , and the Poisson ratio, ν of metallic glasses, etc. So, a simple investigation on the fracture surface to know the mechanism of deformation and fracture is not sufficient, other micromechanisms should be taken into consideration.

In addition, the deformation induced nanocrystallization either by indentation [J.J. Kim et al., 2002] or uniaxial compression [J.C. Lee et al., 2004; S.W. Lee et al., 2006-a], and the local temperature rise to several thousands degrees resulting in softening are some of the features associated with shear bands, which suggest that shear banding in BMGs may involve complex thermal and structural changes and result in a complex deformation behavior.

(2) The behavior and mechanism of ductile-brittle transition induced by structural relaxation and crystallization are still unclear.

Effects of structural relaxation and crystallization on the mechanical properties of metallic glasses should be studied since as mentioned above, they are the function of the nature of metallic glasses which is correlated with the thermally induced structural transformation behavior. The mechanical properties of the annealed samples may enhance or degenerate. The correlation between the thermally induced structural transformation behavior and the mechanical properties should be constructed.

6.1.4 Motivation

As mentioned before the room temperature mechanical properties of the two compositions, $\text{Ti}_{41.5}\text{Cu}_{37.5}\text{Ni}_{7.5}\text{Zr}_{2.5}\text{Hf}_5\text{Sn}_5\text{Si}_1$ and $\text{Ti}_{40}\text{Zr}_{25}\text{Ni}_8\text{Cu}_9\text{Be}_{18}$ BMGs, have been reported in the literature. For $\text{Ti}_{40}\text{Zr}_{25}\text{Ni}_8\text{Cu}_9\text{Be}_{18}$ BMG, Kim et al. [Kim et al., 2004] reported its high compressive fracture strength of 1810 MPa and large plastic elongation of about 4 % as well as a microhardness of 560 kg/mm²; in addition, Fornell et al. [Fornell et al., 2009] discussed its yielding and intrinsic plasticity in terms of its thermal and elastic properties. However, in regard to $\text{Ti}_{41.5}\text{Cu}_{37.5}\text{Ni}_{7.5}\text{Zr}_{2.5}\text{Hf}_5\text{Sn}_5\text{Si}_1$ BMG, the mechanical deformation investigations are vacant, although Huang et al. [Huang et al., 2007-a] have presented a high compressive fracture strength of 2260 MPa and Vickers hardness of 676 kg/mm², with plastic strain only of about 0.5%. Accordingly, to our knowledge the previous investigations have been restricted to investigation of the mechanical response only in the amorphous state. A systematic and a comprehensive

investigation on the quasi-static mechanical behavior and associated failure mechanisms both in the as-cast and heat-treated states are lacking.

Accordingly, much work related to these two alloys needed to be done. The large differences on compositions, original structures as well as structural transformation behavior between these two typical Ti-based BMGs provide us appropriate mediums to find the intrinsic reasons responsible for their large differences on room-temperature mechanical properties. In addition, due to the restriction of small size of Ti-based metallic glasses, few reports are related to the mechanical deformation of these metallic glasses, especially for the Be-free Ti-based metallic glasses. So, from this standpoint, we hope that our study can provide some relevant data as complementarities to the experimental database for the mechanical deformation of Ti-based metallic glasses. The research work in this chapter will be focused on the following two aspects:

- (i) The room-temperature mechanical deformation and fracture mechanism for these two alloys were clarified by the study of the physical nature of shear bands through the compressive testing and the nanoindentation measurements, combined with the analysis of characteristics of material nature and considering the role of deformation-induced nanocrystals.
- (ii) The mechanical response changes, especially the ductile-brittle transition mechanism, induced by the structural transformations (structural relaxation and crystallization) of these two alloys were investigated, to evaluate the hot workability in the supercooled liquid to provide necessary reference for choosing appropriate superplastic forming process parameters.

6.2 Experiment

(1) Samples with different degrees of thermally induced structural changes (structural relaxation and crystallization) with respect to the as-cast metallic glasses were obtained through annealing treatment in DSC furnace at selected temperatures for selected times based on the isochronous and isothermal DSC curves obtained in the former study.

(2) Uniaxial compression tests for three samples of each condition were performed on cylindrical rods of 2 mm in diameter and 3.5 mm in length by using a MTS 4 M as well as a DY 35 testing machine at room temperature with constant strain rates of 1×10^{-4} - $5 \times 10^{-3} \text{ s}^{-1}$. The sample end surfaces were polished to be parallel to each other and perpendicular to the loading axis. BN powder was used as lubricant to reduce friction between testing samples and the platen of the machine. The fractured samples were observed in a ZEISS Ultra 55 high-resolution scanning electron microscope (HRSEM) as well as a JEOL-JSM6400 SEM.

(3) Nanoindentation experiments were conducted using an XP nanoindenter in load-control mode with load of 200 mN at various loading rates of 1-10 mN/s on the polished cross-section of as-cast and annealed samples. For each sample, 6 points were selected to perform the nanoindentation measurement. The load-displacement curves, including unloading, were analyzed according to [Oliver et al., 1992] to extract the values of hardness and Young's modulus.

(4) Vickers hardness was measured on a SHIMADZU micro-hardness tester applying the load of 500 g for 15 s. The final micro-hardness was determined to be the mean value of 6 points for each as-cast as well as annealed samples.

6.3 Behavior and Mechanism of Deformation and Fracture for Ti-based BMGs

6.3.1 Characteristics of Deformation and Fracture for Ti-based BMGs

6.3.1.1 Mechanical response of Ti-based BMGs

(1) Mechanical properties

Fig. 6-1 shows the typical uniaxial compressive true strain-stress (σ - ϵ) curves corresponding to the as-cast $\text{Ti}_{40}\text{Zr}_{25}\text{Ni}_8\text{Cu}_9\text{Be}_{18}$ and $\text{Ti}_{41.5}\text{Cu}_{37.5}\text{Ni}_{7.5}\text{Zr}_{2.5}\text{Hf}_5\text{Sn}_5\text{Si}_1$ BMGs deformed at room temperature with a constant strain rate of $5 \times 10^{-4} \text{ s}^{-1}$. It is found that these two alloys both showed elasticity up to a strain of $\sim 2\%$, however exhibited significantly different degrees of strength and plasticity, i.e. $\text{Ti}_{40}\text{Zr}_{25}\text{Ni}_8\text{Cu}_9\text{Be}_{18}$ BMG had a maximum strength of 1850 MPa and a considerable plastic strain of 8.0%, while $\text{Ti}_{41.5}\text{Cu}_{37.5}\text{Ni}_{7.5}\text{Zr}_{2.5}\text{Hf}_5\text{Sn}_5\text{Si}_1$ BMG exhibited a maximum strength of 2120 MPa with a slight however appreciable plastic strain of 1.6%. In addition, the Vickers microhardness was measured to be 5.2 and 6.3 GPa for $\text{Ti}_{40}\text{Zr}_{25}\text{Ni}_8\text{Cu}_9\text{Be}_{18}$ and $\text{Ti}_{41.5}\text{Cu}_{37.5}\text{Ni}_{7.5}\text{Zr}_{2.5}\text{Hf}_5\text{Sn}_5\text{Si}_1$ BMGs, respectively, demonstrating the large difference of microhardness between these alloys. The mechanical properties obtained from these two alloys are listed in Table 6-1.

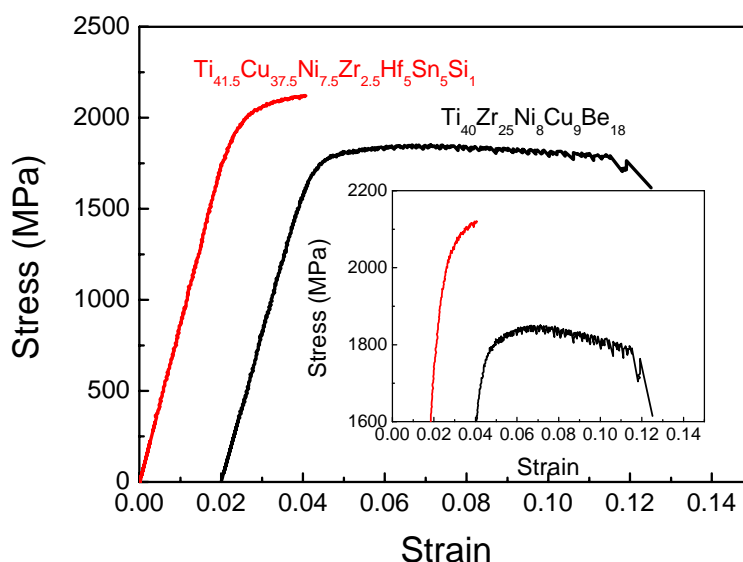


Fig. 6-1 Typical room-temperature compressive stress-strain curves at a constant strain rate of $5 \times 10^{-4} \text{ s}^{-1}$ for $\text{Ti}_{40}\text{Zr}_{25}\text{Ni}_8\text{Cu}_9\text{Be}_{18}$ and $\text{Ti}_{41.5}\text{Cu}_{37.5}\text{Ni}_{7.5}\text{Zr}_{2.5}\text{Hf}_5\text{Sn}_5\text{Si}_1$ BMGs. The inset shows the enlarged image of the serrated flow

Table 6-1

Yielding stress (σ_y), maximum compressive stress (σ_{\max}), elastic strain (ε_e), plastic strain (ε_p) and microhardness (H) of as-cast $\text{Ti}_{40}\text{Zr}_{25}\text{Ni}_8\text{Cu}_9\text{Be}_{18}$ and $\text{Ti}_{41.5}\text{Cu}_{37.5}\text{Ni}_{7.5}\text{Zr}_{2.5}\text{Hf}_5\text{Sn}_5\text{Si}_1$ samples obtained from the compression tests and Vickers hardness measurements.

Composition	σ_y (MPa)	σ_{\max} (MPa)	ε_e (%)	ε_p (%)	H (GPa)
$\text{Ti}_{40}\text{Zr}_{25}\text{Ni}_8\text{Cu}_9\text{Be}_{18}$	1770	1850	2.1	8.0	5.2
$\text{Ti}_{41.5}\text{Cu}_{37.5}\text{Ni}_{7.5}\text{Zr}_{2.5}\text{Hf}_5\text{Sn}_5\text{Si}_1$	1950	2120	2.0	1.6	6.3

The differences in mechanical response can also be detected by nanoindentation measurements. For example, the hardness deduced from the load-displacement (P - h) curves (Fig. 6-2) was 5.5 and 6.2 GPa for $\text{Ti}_{40}\text{Zr}_{25}\text{Ni}_8\text{Cu}_9\text{Be}_{18}$ and $\text{Ti}_{41.5}\text{Cu}_{37.5}\text{Ni}_{7.5}\text{Zr}_{2.5}\text{Hf}_5\text{Sn}_5\text{Si}_1$ BMGs, respectively, which is approximately consistent with the value obtained from the conventional microhardness measurements. In addition, the ratio of the plastic work W_{plast} over the total work W_{tot} , $W_{\text{plast}}/W_{\text{tot}}$, who can indicate the plastic capacity, can be estimated by comparing the final indentation depth with the maximum indentation depth. The relevant parameters deduced from nanoindentation measurements are summarized in Table 6-2. It is found that the value of $W_{\text{plast}}/W_{\text{tot}}$ for $\text{Ti}_{40}\text{Zr}_{25}\text{Ni}_8\text{Cu}_9\text{Be}_{18}$ BMG is of 71%, larger than that for $\text{Ti}_{41.5}\text{Cu}_{37.5}\text{Ni}_{7.5}\text{Zr}_{2.5}\text{Hf}_5\text{Sn}_5\text{Si}_1$ BMG (66%), demonstrating the different plastic capacity between these two alloys. It is worthy to point out that although the plasticity of $\text{Ti}_{41.5}\text{Cu}_{37.5}\text{Ni}_{7.5}\text{Zr}_{2.5}\text{Hf}_5\text{Sn}_5\text{Si}_1$ BMG is very limited in uniaxial compression testing, under the condition of nanoindentation measurement, the plastic deformation is considerably obvious, which confirms that the plastic deformation for metallic glasses is located in the narrow shear bands. Fig. 6-3 shows the SEM images of the indents for $\text{Ti}_{40}\text{Zr}_{25}\text{Ni}_8\text{Cu}_9\text{Be}_{18}$ and $\text{Ti}_{41.5}\text{Cu}_{37.5}\text{Ni}_{7.5}\text{Zr}_{2.5}\text{Hf}_5\text{Sn}_5\text{Si}_1$ BMGs. The morphologies of these two indents are clearly different. In the case of $\text{Ti}_{40}\text{Zr}_{25}\text{Ni}_8\text{Cu}_9\text{Be}_{18}$ BMG, obvious residual pile-up of materials in the manner of stepwise propagation (shear bands) around the indent can be seen, while for $\text{Ti}_{41.5}\text{Cu}_{37.5}\text{Ni}_{7.5}\text{Zr}_{2.5}\text{Hf}_5\text{Sn}_5\text{Si}_1$ BMG, such residual pile-up is smaller compared with $\text{Ti}_{40}\text{Zr}_{25}\text{Ni}_8\text{Cu}_9\text{Be}_{18}$ BMG.

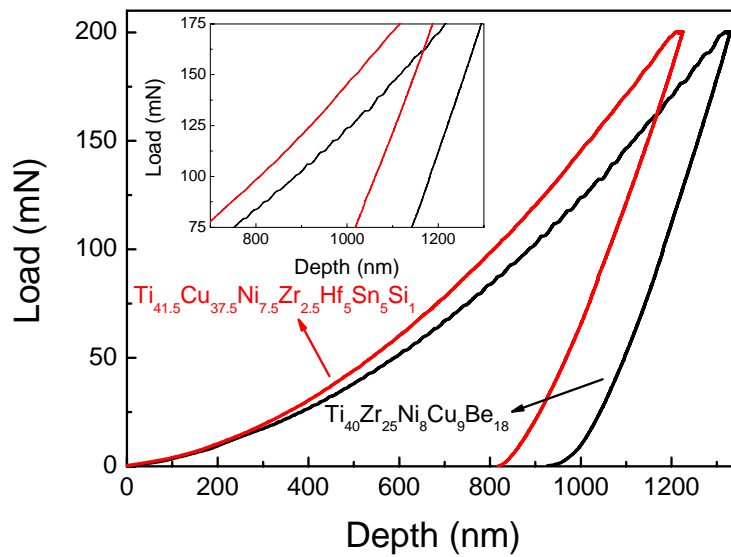


Fig. 6-2 Typical load-displacement curves measured during nanoindentation tests in load control mode at a loading rate of 5 mN/s for as-cast $\text{Ti}_{40}\text{Zr}_{25}\text{Ni}_8\text{Cu}_9\text{Be}_{18}$ and $\text{Ti}_{41.5}\text{Cu}_{37.5}\text{Ni}_{7.5}\text{Zr}_{2.5}\text{Hf}_5\text{Sn}_5\text{Si}_1$ BMGs. The inset shows the enlarged image of the pop-in

Table 6-2

The maximum depth (h_{\max}), Young's modulus (E_y), hardness (H) and ratio $W_{\text{plast}}/W_{\text{tot}}$ calculated from the load-displacement curves of nanoindentation measurements for $\text{Ti}_{40}\text{Zr}_{25}\text{Ni}_8\text{Cu}_9\text{Be}_{18}$ and $\text{Ti}_{41.5}\text{Cu}_{37.5}\text{Ni}_{7.5}\text{Zr}_{2.5}\text{Hf}_5\text{Sn}_5\text{Si}_1$ BMGs

Composition	h_{\max} (nm)	E_r (GPa)	H (GPa)	$W_{\text{plast}}/W_{\text{tot}}$ (%)
$\text{Ti}_{40}\text{Zr}_{25}\text{Ni}_8\text{Cu}_9\text{Be}_{18}$	1328	98	5.5	71
$\text{Ti}_{41.5}\text{Cu}_{37.5}\text{Ni}_{7.5}\text{Zr}_{2.5}\text{Hf}_5\text{Sn}_5\text{Si}_1$	1224	103	6.2	66

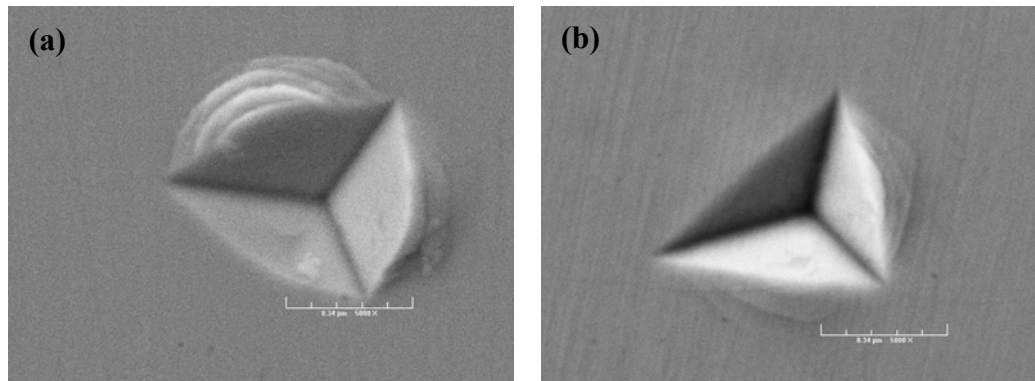


Fig. 6-3 SEM micrographs of indents for as-cast (a) $\text{Ti}_{40}\text{Zr}_{25}\text{Ni}_8\text{Cu}_9\text{Be}_{18}$ and (b) $\text{Ti}_{41.5}\text{Cu}_{37.5}\text{Ni}_{7.5}\text{Zr}_{2.5}\text{Hf}_5\text{Sn}_5\text{Si}_1$ BMGs

(2) Serrated flow

After yielding, obvious serrated flow can be observed in the compressive stress-strain curve for $\text{Ti}_{40}\text{Zr}_{25}\text{Ni}_8\text{Cu}_9\text{Be}_{18}$ BMG (see the enlarged image in [Fig. 6-1](#)). The occurrence of inhomogeneous plastic flow indicates the initiation and propagation of individual shear bands during quasistatic loading [[Schuh et al., 2007-b](#)]. And in these shear bands there is a sudden decrease of viscosity [[Spaepen, 1977](#)], which brings about load drops and a concomitant mechanical softening. However, for $\text{Ti}_{41.5}\text{Cu}_{37.5}\text{Ni}_{7.5}\text{Zr}_{2.5}\text{Hf}_5\text{Sn}_5\text{Si}_1$ BMG, after yielding, no clear serrated flow can be seen on its stress-strain curve, and it appears that the stress increases with strain, indicating a strain hardening behavior. These results suggest different deformation and fracture mechanism between these two alloys, as will be discussed later.

Such serrated flow in compression tests is corresponding to the discrete displacement burst (pop-in) in the P - h curves in the nanoindentation measurements. These pop-ins are associated with the emission of individual shear hands underneath the indenter tip, as has been reported [[Schuh et al., 2003-a](#); [Golovin et al., 2001](#)]. The character of serrated flow appears different between these two alloys. The $\text{Ti}_{40}\text{Zr}_{25}\text{Ni}_8\text{Cu}_9\text{Be}_{18}$ BMG seems to exhibit more pronounced and sharp displacement bursts and these displacement bursts throughout the full loading history of the indent, as is in agreement with the finding of Golovin et al. [[Golovin et al., 2001](#)]; while the $\text{Ti}_{41.5}\text{Cu}_{37.5}\text{Ni}_{7.5}\text{Zr}_{2.5}\text{Hf}_5\text{Sn}_5\text{Si}_1$ BMG shows smoother curves at the same loading rate. As proposed by Liu et al. [[L. Liu et al, 2005](#)], this difference may result from their different microstructures, in terms of free volume, and short and middle-range ordering, as well as their different innate properties, e.g. modulus and hardness.

6.3.1.2 Effects of strain rate on mechanical response

The investigation on the effects of strain rate on the mechanical response was performed on $\text{Ti}_{40}\text{Zr}_{25}\text{Ni}_8\text{Cu}_9\text{Be}_{18}$ BMG who exhibits large plasticity. Typical compressive stress-strain curves of this alloy at various strain rates of 1×10^{-4} – $5 \times 10^{-3} \text{ s}^{-1}$ are shown in Fig. 6-4. All these curves exhibit a clear yield point, followed by a macroscopic plastic strain without strain hardening prior to fracture within the strain rate range applied in this study. The fracture strength is almost independent of strain rate, while the plastic strain is strongly dependent on the strain rate, i.e. its plastic strain drastically decreased from 11.6% at strain rate of $1 \times 10^{-4} \text{ s}^{-1}$ to 3.5% at strain rate of $5 \times 10^{-3} \text{ s}^{-1}$. The serrated flow is apparent at low strain rate and is prone to weaken at high strain rate. Such a rate dependence of serrated flow phenomenon also can be detected from the load-displacement curves measured by nanoindentation testing (see Fig. 6-5). The nature of serrated flow changes from ideal stepwise load-displacement curves (discrete displacement burst) at low loading rate to relatively smooth parabolic curves (as fluctuations or ripples) at high loading rate, i.e. the amount and the degree of the discrete, horizontal displacement bursts (pop-ins) were decreased with increase in loading rates (see the enlarged image in Fig. 6-5). However, the critical applied loading rate, above which the serrated flow is completely suppressed, was not obtained, due to the low value of the highest loading rate applied in this study. Such rate-dependent pop-in phenomenon in metallic glasses is attributed to the transition from deformation being carried by the discrete operation of individual shear bands at low strain rate, to the continuous operation of multiple shear bands at higher strain rate. In addition, it is found that although the nature of serrated flow is loading rate dependent, the general shape of the load-displacement curves are quite similar at all loading rates, suggesting a rate independent hardness or strength, as is in accordance with the results obtained from the compressive testing.

Our results are similar with the investigation on $\text{Ti}_{45}\text{Zr}_{16}\text{Ni}_9\text{Cu}_{10}\text{Be}_{18}$ BMG who has a neighboring composition with $\text{Ti}_{40}\text{Zr}_{25}\text{Ni}_8\text{Cu}_9\text{Be}_{18}$ BMG reported by Zhang et al. [J. Zhang et al., 2007], however, the phenomenon that strength increases with strain rate has not been detected in this study. Such an absence of a strain rate effect on strength has also been found in Vitreloy1 and $\text{Zr}_{59}\text{Cu}_{20}\text{Al}_{10}\text{Ni}_8\text{Ti}_3$ BMGs by Bruck et al. [Bruck et al., 1996] and Subhash et al. [Subhash et al., 2002], and Zhang et al. [Z.F. Zhang et al., 2003], respectively, and is attributed to the fact that the propagation rate of shear bands is faster than the applied strain rate suggested by Mukai et al. [Mukai et al., 2002-b].

In regard to the reason why plastic strain decreases with increase in strain rate, the role of quenched-in nuclei on the slide of shear bands in $\text{Ti}_{40}\text{Zr}_{25}\text{Ni}_8\text{Cu}_9\text{Be}_{18}$ BMG should be considered. It was suggested that [J.M. Park et al., 2005], such inhomogeneous microstructural features may become inhomogeneous energy barriers. A propagating shear band might be forced to be deflected or branched when it reaches the region of the high energy barrier. This would result in the initiation of new shear bands. The increase of the total area of shear bands due to the formation of multiple shear bands and deflection in the individual shear bands leads to appreciable macroscopic plasticity at low strain rate. However, at high strain rate, the strain rate is so fast that there would be insufficient time for shear bands to deflect or branch. The shear bands have to overcome the energy barrier to continue shear flow deformation.

Compared with other relevant investigations on the effects of strain rate on the mechanical response, it is found that the strain rate dependence of mechanical response may be different even in the same alloy. For example, Sergueeva et al. [Sergueeva et al., 2004] reported that the ductility increases while the fracture strength decreases with increase in strain rate in tension for bulk

Vitreloy1 alloy. On the contrary, Bruck et al. [Bruck et al., 1996] and Subhash et al. [Subhash et al., 2002] found that the fracture strength and plastic strain of Vitreloy1 alloy were independent of strain rate. These conflicting results suggest that many factors, such as chemical compositions, degree of amorphization, loading mode, and sample geometry of the metallic glasses, may significantly influence the mechanical response under various strain rates.

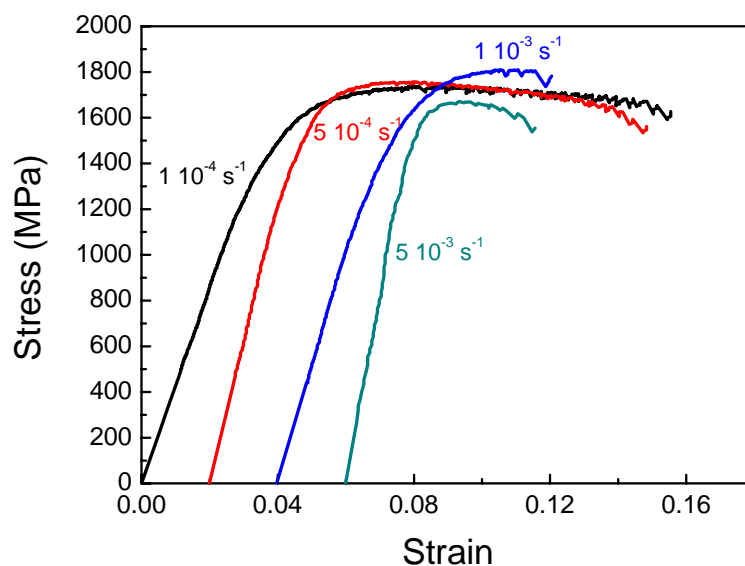


Fig. 6-4 Compressive stress-strain curves of $\text{Ti}_{40}\text{Zr}_{25}\text{Ni}_8\text{Cu}_9\text{Be}_{18}$ BMG at the strain rates of 1×10^{-4} – $5 \times 10^{-3} \text{ s}^{-1}$

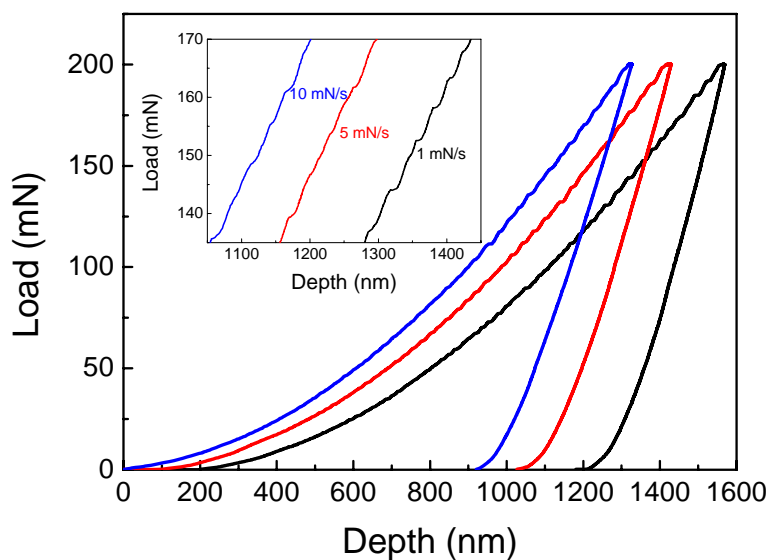


Fig. 6-5 Indentation load-displacement curves at various loading rates for $\text{Ti}_{40}\text{Zr}_{25}\text{Ni}_8\text{Cu}_9\text{Be}_{18}$ BMG

6.3.2 Deformation and Fracture Mechanisms of Ti-based BMGs

As typical marginal metallic glasses, $\text{Ti}_{40}\text{Zr}_{25}\text{Ni}_8\text{Cu}_9\text{Be}_{18}$ and $\text{Ti}_{41.5}\text{Cu}_{37.5}\text{Ni}_{7.5}\text{Zr}_{2.5}\text{Hf}_5\text{Sn}_5\text{Si}_1$

BMGs have unique microstructure nature, i.e. quench-in nuclei/amorphous matrix and phase separation-like structure/amorphous matrix, respectively. Their significant differences in mechanical response presented above, make us be interested in elucidating their different deformation and fracture mechanisms. In this section, the deformation and fracture mechanisms of these two alloys will be investigated based on the analysis of their fractographies.

6.3.2.1 Analysis of fractographies of Ti-based BMGs

Fig. 6-6 and 6-7 show the outer surfaces of the fractured $\text{Ti}_{40}\text{Zr}_{25}\text{Ni}_8\text{Cu}_9\text{Be}_{18}$ and $\text{Ti}_{41.5}\text{Cu}_{37.5}\text{Ni}_{7.5}\text{Zr}_{2.5}\text{Hf}_5\text{Sn}_5\text{Si}_1$ samples deformed at a strain rate of $5 \times 10^{-4} \text{ s}^{-1}$, showing different features of shear bands. Surprisingly, the multiple shear bands (including primary shear bands and branched secondary shear bands (see Fig. 6-6 (b))) are observed over the whole surface of the fractured $\text{Ti}_{40}\text{Zr}_{25}\text{Ni}_8\text{Cu}_9\text{Be}_{18}$ sample, which indicates that shear bands are distributed homogeneously in the whole sample, suggesting the large plasticity during compressive deformation. However, the density of shear bands on the outer surface of $\text{Ti}_{41.5}\text{Cu}_{37.5}\text{Ni}_{7.5}\text{Zr}_{2.5}\text{Hf}_5\text{Sn}_5\text{Si}_1$ BMG is significantly lower compared with that for $\text{Ti}_{40}\text{Zr}_{25}\text{Ni}_8\text{Cu}_9\text{Be}_{18}$ BMG (see Fig. 6-7), and only several primary shear bands which are approximately along the direction of the maximum shear plane (44°) can be observed in the local region near the fracture surface, in addition, no branched secondary shear bands are formed (Fig. 6-7 (b)), which suggests that for $\text{Ti}_{41.5}\text{Cu}_{37.5}\text{Ni}_{7.5}\text{Zr}_{2.5}\text{Hf}_5\text{Sn}_5\text{Si}_1$ BMG, plastic deformation is only located near the fracture surface, demonstrating the small plasticity during compressive deformation.

It should be pointed out that for common BMGs, it is well known that one major shear band dominates the deformation and results in a sudden fracture, in this study we found multiple shear bands on the outer surface of fractured $\text{Ti}_{40}\text{Zr}_{25}\text{Ni}_8\text{Cu}_9\text{Be}_{18}$ BMG, suggesting that a large number of shear bands simultaneously operate during the plastic deformation, and may be due to the contribution of nanocrystals transformed from the quenched-in nuclei during deformation on blocking the propagation of shear bands. More discussion will be presented later.

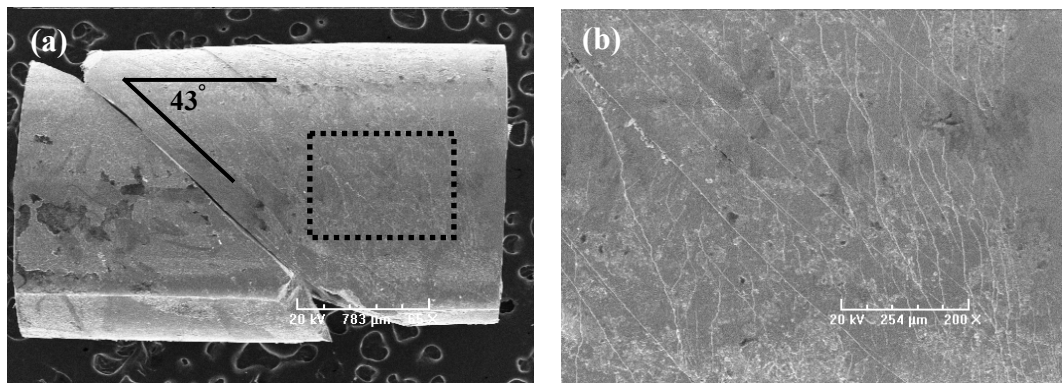


Fig. 6-6 (a) View of side surface of the fractured $\text{Ti}_{40}\text{Zr}_{25}\text{Ni}_8\text{Cu}_9\text{Be}_{18}$ sample and (b) high magnification of shear bands in the rectangle area

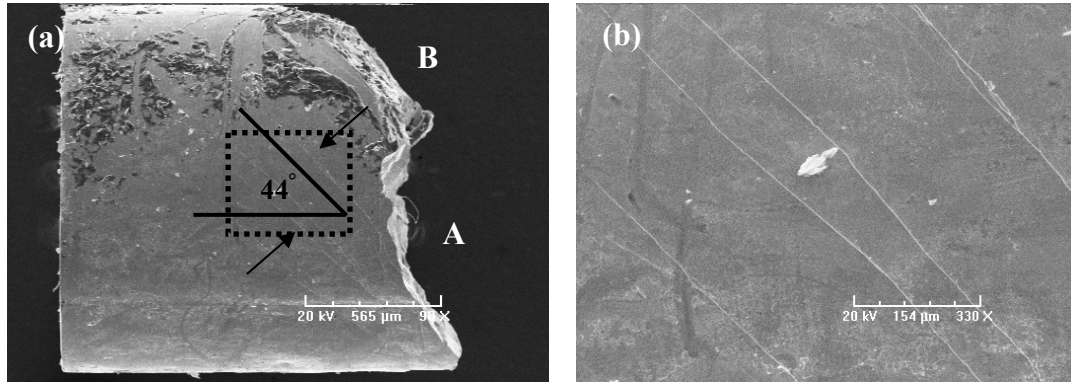
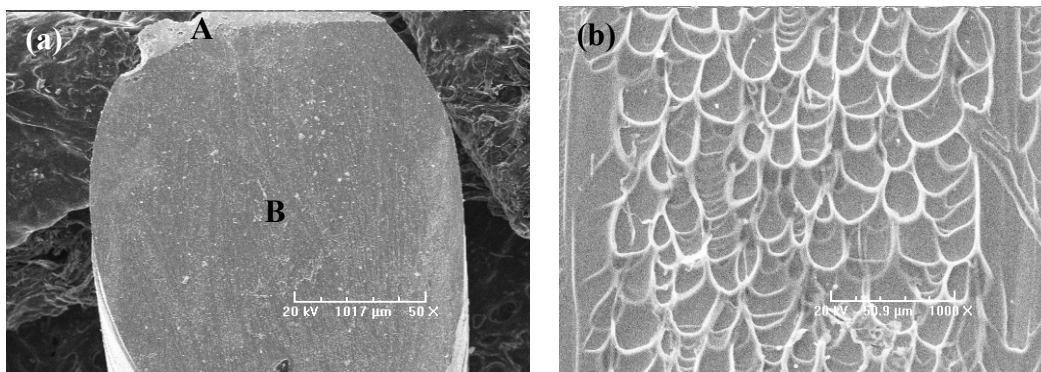


Fig. 6-7 (a) View of side surface of the fractured $\text{Ti}_{41.5}\text{Cu}_{37.5}\text{Ni}_{7.5}\text{Zr}_{2.5}\text{Hf}_5\text{Sn}_5\text{Si}_1$ sample and (b) high magnification of shear bands in the rectangle area

Fig. 6-8 and **6-9** show the corresponding fracture surface for $\text{Ti}_{40}\text{Zr}_{25}\text{Ni}_8\text{Cu}_9\text{Be}_{18}$ and $\text{Ti}_{41.5}\text{Cu}_{37.5}\text{Ni}_{7.5}\text{Zr}_{2.5}\text{Hf}_5\text{Sn}_5\text{Si}_1$ BMGs, respectively. For $\text{Ti}_{40}\text{Zr}_{25}\text{Ni}_8\text{Cu}_9\text{Be}_{18}$ BMG, the fracture surface is clearly separated into two zones as marked A and B, respectively in **Fig. 6-8 (a)** and **(c)**. Zone B dominates the fracture surface which is flat, smooth, nearly along the maximum shear plane (the shear fracture angle is about 43°) and covered by the well-developed vein patterns with the average width (or the wavelength of the vein features) of 10-20 μm produced by the initiation and propagation of local shear bands upon fracture as shown in **Fig. 6-8 (b)**). Such vein patterns are frequently observed in metallic glasses deformed under compression, particularly when they exhibit significant plasticity. In the case of zone A, it shows a more brittle fracture mode with the morphology of rough river-like patterns (see **Fig. 6-8 (c)** and **(d)**). Such cleavage-like fracture morphologies are usually observed at the fracture surface of brittle metallic glasses (Mg- [Xi et al., 2005], Fe- [G. Wang et al., 2006; Z.F. Zhang et al., 2006], Ni- [Liang et al., 2008; J. Shen et al., 2006-b], Co-based [Z.F. Zhang et al., 2006] metallic glasses) and are associated with a much faster fracture.



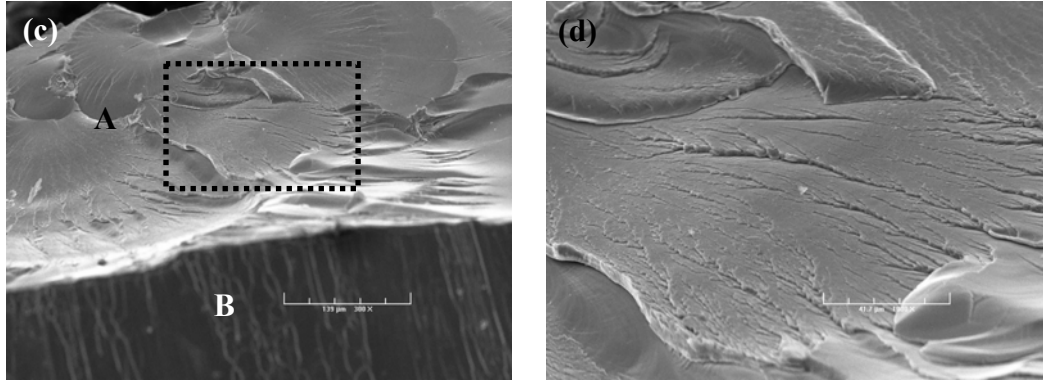


Fig. 6-8 (a) Fracture surface of the $\text{Ti}_{40}\text{Zr}_{25}\text{Ni}_8\text{Cu}_9\text{Be}_{18}$ sample deformed at the strain rate of $5 \times 10^{-4} \text{ s}^{-1}$, (b) higher magnification of vein patterns, (c) enlarged image of the upper region, and (d) enlarged image of the river-like patterns in zone A

$\text{Ti}_{41.5}\text{Cu}_{37.5}\text{Ni}_{7.5}\text{Zr}_{2.5}\text{Hf}_5\text{Sn}_5\text{Si}_1$ BMG displays similar fracture characteristics, except that it displays larger area of cleavage-like zone A than $\text{Ti}_{40}\text{Zr}_{25}\text{Ni}_8\text{Cu}_9\text{Be}_{18}$ BMG, as suggests the similar deformation and fracture mechanism for these two alloys despite large difference in mechanical response. It seems that the plasticity is associated with the proportion of the shear zone, the large proportion of the rough zone is indicative of limited plasticity or even brittle fracture, e.g. $\text{Ti}_{41.5}\text{Cu}_{37.5}\text{Ni}_{7.5}\text{Zr}_{2.5}\text{Hf}_5\text{Sn}_5\text{Si}_1$ BMG in this study. Liang et al. [Liang et al., 2008] also found such phenomenon in compression testing of Ni-based BMG. For $\text{Ti}_{40}\text{Zr}_{25}\text{Ni}_8\text{Cu}_9\text{Be}_{18}$ BMG, since the rough zone only occupies extremely limited proportion ($<5\%$) of the fracture surface, the shear fracture mode is dominant during the process of compressive deformation. However, the situation of $\text{Ti}_{41.5}\text{Cu}_{37.5}\text{Ni}_{7.5}\text{Zr}_{2.5}\text{Hf}_5\text{Sn}_5\text{Si}_1$ BMG is different, the rough zone occupies large proportion of the fracture surface, which indicates that the normal fracture mode plays an important role especially at the later stage of the deformation, provided that the sample fractured initially in a pure shear mode (zone B) and ended up in a normal mode (zone A) with a hysterical failure. In regard to the typical shear fracture mode in metallic glasses, much work has been done; however, rare work related to the rough zone has been done in detail before. Accordingly, a careful observation on the rough zone in the fractured $\text{Ti}_{41.5}\text{Cu}_{37.5}\text{Ni}_{7.5}\text{Zr}_{2.5}\text{Hf}_5\text{Sn}_5\text{Si}_1$ BMG was performed to understand the generation and propagation of cracks and finally clarify the unique deformation and fracture mechanism.

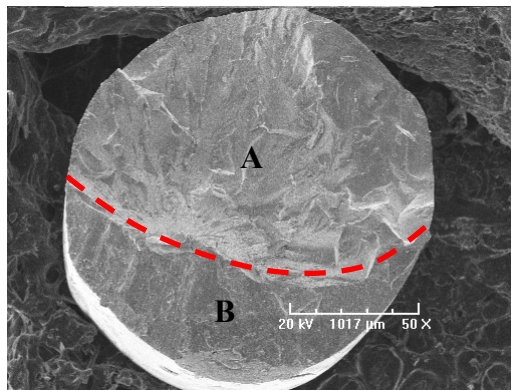


Fig. 6-9 SEM image showing the top view of the fracture surface for $\text{Ti}_{41.5}\text{Cu}_{37.5}\text{Ni}_{7.5}\text{Zr}_{2.5}\text{Hf}_5\text{Sn}_5\text{Si}_1$ BMG

Fig. 6-10 displays the SEM observation of the fracture surface in the vicinity of the boundary between two zones. Interestingly, a transition from the vein-like patterns in shear zone B to the river-like patterns in rough zone A can be obviously observed. And the morphology of rough zone is very complicated, consisting of large areas of river-like pattern regions and limited area of mirror and hackle regions as marked in Fig. 6-10. Such fracture morphologies are rare, and different from those of pure brittle metallic glasses like Mg-, and Fe-based metallic glasses reported by Xi et al. [Xi et al., 2005; Xi et al., 2006] and Zhang et al. [Z.F. Zhang et al., 2006] which consist of three typical regions, i.e. mirror, mist, and hackle regions defined by Johnson and Holloway [J.W. Johnson et al., 1966]; however, they have been found in $\text{Ni}_{42}\text{Cu}_5\text{Ti}_{20}\text{Zr}_{21.5}\text{Al}_8\text{Si}_{3.5}$ BMG subjected to compressive deformation by Shen and Liang et al. [Liang et al., 2008; J. Shen et al., 2006-b] as well as in $\text{Fe}_{73.5}\text{Cu}_1\text{Nb}_3\text{Si}_{13.5}\text{B}_9$ glassy ribbon deformed under a uniaxial tension by Wang. et al [G. Wang et al., 2006].

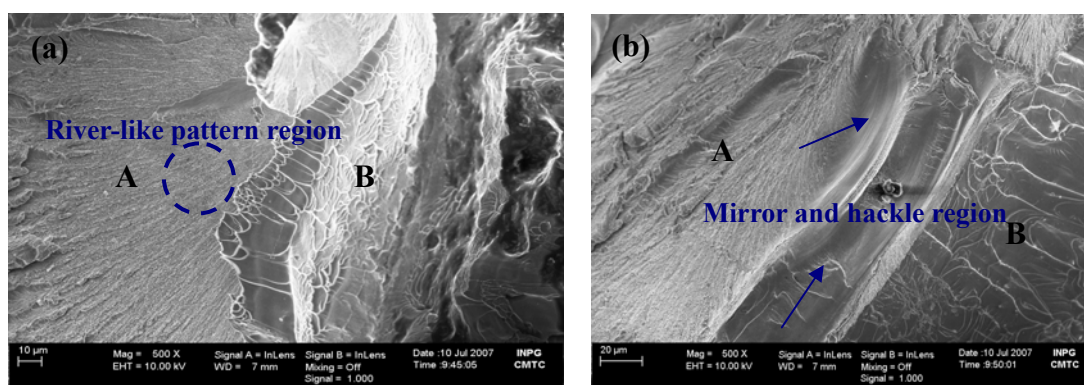


Fig. 6-10 Morphology transition of the fracture surface in the vicinity of the boundary of zone A and zone B for the $\text{Ti}_{41.5}\text{Cu}_{37.5}\text{Ni}_{7.5}\text{Zr}_{2.5}\text{Hf}_5\text{Sn}_5\text{Si}_1$ alloy

Fig. 6-11 display a serial of SEM images of the river-like patterns along the cracking direction to examine the evolution of the morphology upon cracking propagation. It is found that the initial region (circled in Fig. 6-10 (a)) shows the characteristic of homogeneous numerous microdimples, similar to those in the vein patterns, but with much smaller size of about 200-300 nm, as shown in Fig. 6-11 (a). Such phenomenon suggests that the universal local softening mechanism dominates the fracture of metallic glasses in spite of their deformation and fracture mode, but at different length scales [Liang et al., 2008; J. Shen et al., 2006-b; Xi et al., 2005; G. Wang et al., 2006 ; Z.F. Zhang et al., 2006], e.g. the plastic deformation in the rough region is very short-ranged in the local shear bands in $\text{Ti}_{41.5}\text{Cu}_{37.5}\text{Ni}_{7.5}\text{Zr}_{2.5}\text{Hf}_5\text{Sn}_5\text{Si}_1$ BMG and the minor local plasticity has no distinct effect on the global compressive plasticity. In addition, it also indicates that the local tensile stress played a key role in the fracture process [Z.F. Zhang et al., 2003; Flores et al., 2004]. Then, along the cracking propagation direction, the homogeneous microdimples become unstable and gradually transform to river-like patterns with the characteristic of radial strip (or the so-called microbranches) parallel to the cracking propagation direction (see Fig. 6-11 (b) and marked by arrows) via linkage and coalescence of the adjacent microdimples. Through careful observation on the end part of such river-like patterns in Fig. 6-12, we can see an obvious transition from strip river-like patterns to the well-known parallel periodic nanowaves. In Fig. 6-12 (b), we can see the microbranches consisting of well-aligned microdimples with the size of several tens of nanometer and very shallow depth. They continue linking and coalescing again, however perpendicular to the cracking propagation direction, which indicates the branching and healing mechanisms

contributing to plasticity. And in Fig. 6-12 (c), we can see clearly that at the end of the microbranches, early-stage nanowaves have been formed between the microbranches, however not parallel to each other; then they continue propagating along their own direction and developing and interacting to form largely extended, dense waves, finally reach parallel to each other at the position where the microbranches disappear completely. The highly intensive and parallel periodic nanowaves with the average wavelength of 60 nm are shown in Fig. 6-12 (d). Accordingly, such nanowaves are believed to be formed due to the increase in cracking energy caused by crack microbranching, this is consistent with the theoretical predictions and experimental observations which confirm that in rapid fracture of brittle amorphous materials, a propagating crack becomes unstable to facilitate crack branching when its velocity exceeds a critical value (approximately 0.4 times of the Rayleigh wave speed in glass) which leads to large oscillations in the crack velocity and roughening of the fracture surface [J. Shen et al., 2006-b].

Fig. 6-13 summaries a sketch of periodic morphology evolution in the river-like pattern region on the compressive fracture surface of $\text{Ti}_{41.5}\text{Cu}_{37.5}\text{Ni}_{7.5}\text{Zr}_{2.5}\text{Hf}_5\text{Sn}_5\text{Si}_1$ BMG, consisting of microdimple, river-like pattern and mirror zones with crack propagation. Such periodic fracture patterns are dominating the fracture surface in the rough zone for this alloy.

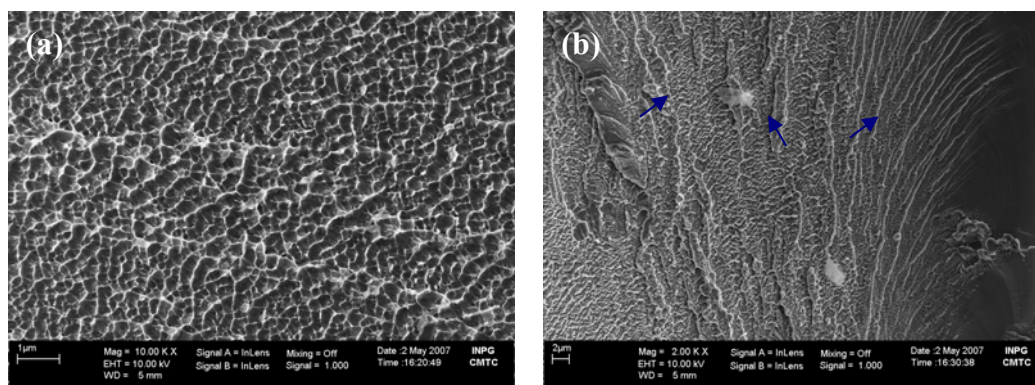
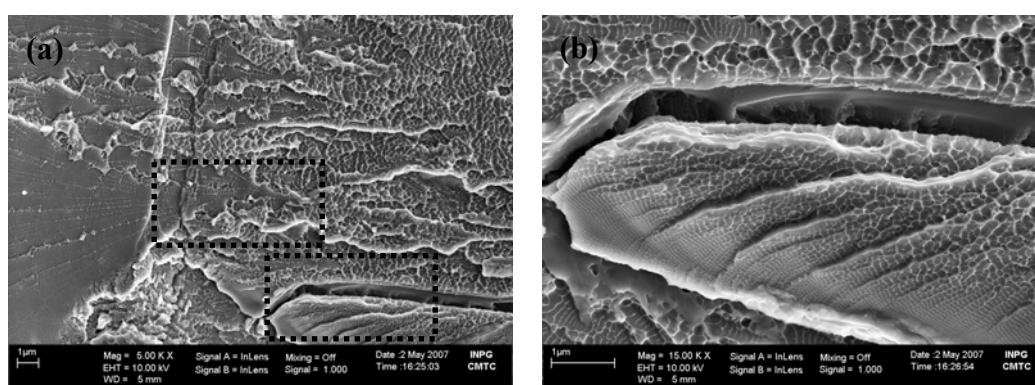


Fig. 6-11 (a) SEM image showing the initial region of the river-like patterns (circled in Fig. 6-10 (a)) and (b) developed radial microbranches



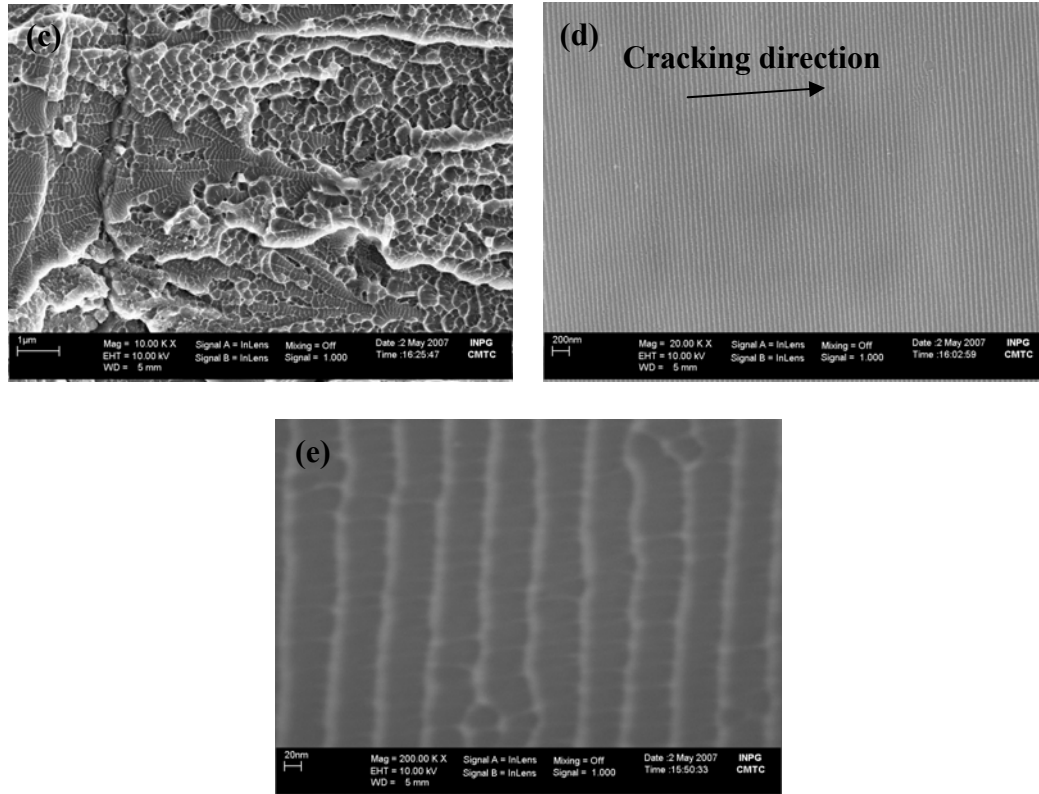


Fig. 6-12 (a) SEM image of the end part of the microbranches, (b) and (c) enlarged images corresponding to the area circled in (a) showing the transition from the microbranches to periodic nanowaves, (d) highly parallel periodic nanowaves, and (e) enlarged image of periodic nanowaves

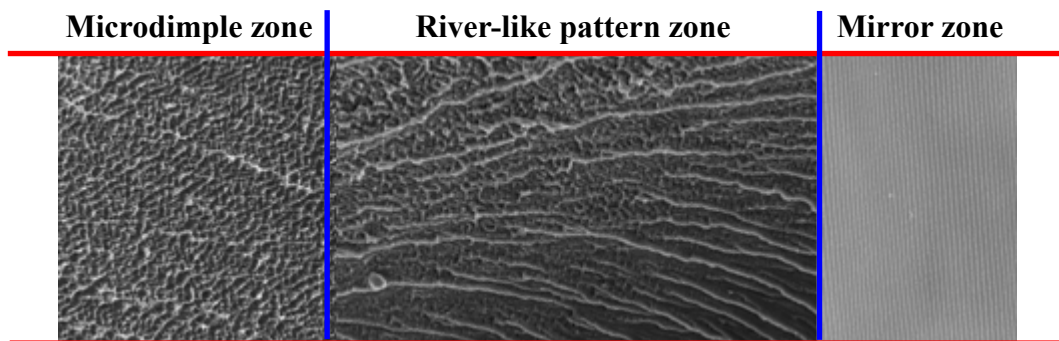


Fig. 6-13 Schematic drawing of the main periodic morphology evolution on the compressive fracture surface of $\text{Ti}_{41.5}\text{Cu}_{37.5}\text{Ni}_{7.5}\text{Zr}_{2.5}\text{Hf}_5\text{Sn}_5\text{Si}_1$ BMG

Actually, besides the periodic morphology evolution mentioned above, the typical three-region transition which has been confirmed to be generally occurring on the typical cleavage fracture surface, i.e. from the mirror, mist to hackle region, were also observed in this study (see the smooth cleavage fracture region in [Fig. 6-14](#)), however, such transition zone is limited on the fracture surface of this alloy. [Fig. 6-15](#) shows the enlarged image of the smooth region circled in [Fig. 6-14](#). The characteristics of such typical transition can be observed clearly, as will not be repeated here since such transition has been studies in references [[Xi et al., 2005](#); [Xi et al., 2006](#); [Z.F. Zhang et al., 2006](#)].

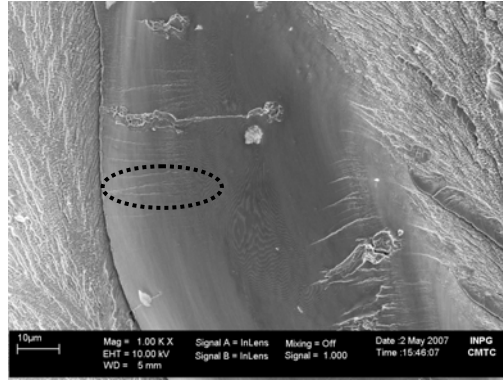


Fig. 6-14 SEM image showing the smooth region in rough zone on the fracture surface of $\text{Ti}_{41.5}\text{Cu}_{37.5}\text{Ni}_{7.5}\text{Zr}_{2.5}\text{Hf}_5\text{Sn}_5\text{Si}_1$ BMG

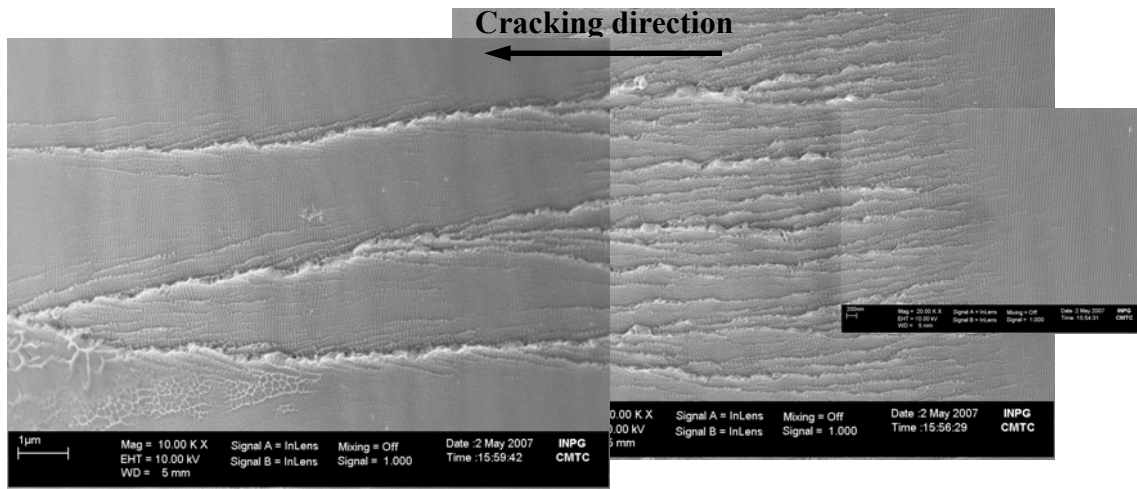


Fig. 6-15 Enlarged image circled in Fig. 6-14

6.3.2.2 Universal deformation and fracture mechanisms of Ti-based BMGs

Based on the analysis above, we confirm that the plastic flow of metallic glasses is located within narrow shear bands, and the universal local softening mechanism dominates the fracture of metallic glasses in spite of their deformation and fracture mode, but at different length scales. However, the fact that Ti-based BMGs fracture initially in a pure shear mode ($<45^\circ$), and end up along the maximum normal stress plane (90°), suggests that a rather complex stress state was existing and leads to obvious crack bifurcation prior to failure, demonstrating a complex deformation and fracture mechanism.

Fig. 6-16 displays the schematic illustration showing the changes of stress state during compressive fracture. At the initial stage, cracking starts from the surface of the sample, and the fracture follows a pure shear mode. The compressive loading, σ , can be disassembled as the normal stress, σ_θ^c , exerting on the fracture plane, and the shear stress, τ_θ^c , driving the crack to propagate along the fracture plane (see Fig. 6-16 (a), where θ denotes the angle between the shear stress and the compressive loading direction). As the main crack propagates, the crack-induced

gap between the upper and lower parts of the sample yields the building-up of tensile stress and moment, M , ahead of the crack tip, and the local stress state changes accordingly (see Fig. 6-16 (b)). As the energy input upon loading accumulates, the main crack becomes unstable due to the rapid increase in cracking velocity, leading to microbranching and final failure (see Fig. 6-16 (c)).

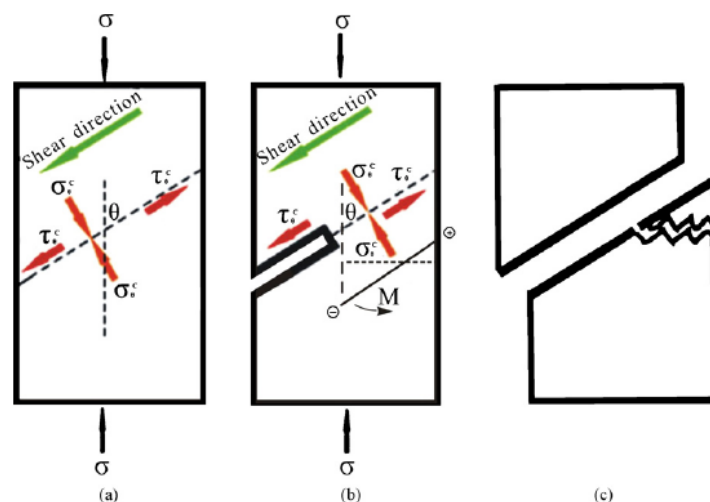


Fig. 6-16 Schematic illustration showing the changes of stress state during compressive fracture: (a) crack propagating approximately along the maximum shear direction (45°); (b) tensile stress and moment formation due to loading direction deviation from the center axis of the sample; (c) final fracture. The counter-clockwise bending moment as indicated represents the bending moment of the upper part of the sample [Liang et al., 2008]

As reported, the classic Mohr-Coulomb criterion can reasonably explain the slight deviation of BMGs' compressive fracture angles from the maximum shear planes owing to normal compressive stress; however, it fails to interpret the unique fracture process occurring in this study, i.e. the compressive fracture proceeds via a transition from shear mode to normal mode. Here we consider that the ellipse criterion which is originally proposed by Zhang et al. [Z.F. Zhang et al., 2005-a] for describing the tensile fracture mechanism can also be used for interpreting the change of fracture angles from $<45^\circ$ to 90° during the compressive fracture process of BMGs. The ellipse criterion unifies the classical fracture criteria, and can be expressed as

$$\frac{\sigma^2}{\sigma_0^2} + \frac{\tau^2}{\tau_0^2} \geq 1 \quad (6-1)$$

where σ_0 is the critical normal fracture stress, τ_0 the critical shear fracture stress, σ the normal fracture stress, and τ the shear fracture stress. When $\tau_0 / \sigma_0 \rightarrow 0$, the fracture angle should be quite close to 45° , which follows the shear fracture mode, agreeing with Tresca criterion. On the other hand, when $\tau_0 / \sigma_0 \geq \sqrt{2}/2$, the fracture angle should be 90° , which means that the compressive fracture occurs along the plane perpendicular to the compressive axis, according with the maximum normal stress criterion. Accordingly, the unique fracture behavior of Ti-based BMGs can be successfully interpreted by the ellipse criterion combined with the analysis of the changes of stress state during the compressive fracture process mentioned above.

6.3.3 Discussion on Intrinsic Plasticity or Brittleness Ti-based BMGs

The dissimilar intrinsic plasticity or brittleness in different BMG systems is essentially due to their different nature, e.g. (i) properties of constituent elements and composition, (ii) and structural configurations. It was reported that the high metalloid content as well as the presence in major quantities of a metallic constituent that has a body centered cubic structure in its crystalline state (e.g. Mg-based metallic glasses), leads to intrinsic brittleness [Ramamurty et al., 2002]. Spaepen [Spaepen, 1977] proposed for the first time that shear bands are initiated as a result of coalescence of the free volume, which was later confirmed by HRTEM [J. Li et al., 2002]. Sung et al. [Sung et al., 2004] argued that alloys with a low melting temperature usually exhibit large plastic strain. In addition, the elastic moduli are apparently important parameters as a chain to understand the correlation between the structural characteristics and relevant mechanical properties. Lewandowski et al. [Lewandowski et al., 2005] have pointed out that the intrinsic plasticity or brittleness of metallic glasses is correlated with their Poisson's ratio, ν . The larger the ν is, the more ductile the metallic glasses become. Metallic glasses with a high Poisson's ratio $\nu > 0.31$ -0.32 or, equivalently, a ratio of elastic shear modulus to bulk modulus, μ/B less than 0.41-0.43, are ductile. The value of Poisson's ratio for $\text{Ti}_{40}\text{Zr}_{25}\text{Ni}_8\text{Cu}_9\text{Be}_{18}$ metallic glass is measured to be 0.358, higher than 0.32. And its μ/B value is 0.314, which is higher than that for Pd-based and Pt-based metallic glasses ($\mu/B > 0.18$) but lower than that for some (more brittle) rare earth-based metallic glasses ($\mu/B > 0.43$ for Mg-based and Ce-based metallic glasses) or oxide glasses ($\mu/B > 0.7$) [Fornell et al., 2009], and indicates its moderate plasticity.

In addition, in an attempt to understand the reason for the dissimilar intrinsic plasticity of different BMGs, besides the properties of constituent elements and the structural configurations mentioned above, thermal stability and properties of primary phase should also be considered, since the deformation-induced crystallization may occur and the obtained nanocrystals may significantly affect their relevant mechanical properties through the interaction with shear bands in addition that the atoms can change their position easily under uniaxial compression in metallic glasses with low activation energy and accordingly the free volumes can nucleate in many localized regions including nanocrystallites, which can lead to the formation of multiple shear bands and then enhancement in plasticity. Accordingly, activation energy was introduced to evaluate the intrinsic plasticity of metallic glasses [S.W. Lee et al., 2006-b].

The TEM image for the fractured $\text{Ti}_{40}\text{Zr}_{25}\text{Ni}_8\text{Cu}_9\text{Be}_{18}$ BMG is shown in Fig. 6-17. The nanocrystals with an average size of 4 nm are homogeneously embedded in the amorphous matrix, demonstrating the precipitation of nanocrystals during compressive deformation for this alloy. The formation of the nanocrystals is possibly due to the effects of adiabatic heating and (or) shear flow stress. And the deformation-induced nanocrystals may affect the deformation behavior and the corresponding mechanical response. For example, it was reported recently that the as-cast $\text{Cu}_{50}\text{Zr}_{50}$ BMGs exhibited a compressive plastic strain of more than 50% at room temperature due to a dispersion of embedded nanocrystals, which was explained by the suppression of shear softening through nanocrystal coalescence [Inoue et al., 2005]. However, the microstructures observed from the fractured $\text{Ti}_{41.5}\text{Cu}_{37.5}\text{Ni}_{7.5}\text{Zr}_{2.5}\text{Hf}_5\text{Sn}_5\text{Si}_1$ sample are almost identical to those observed from the as-cast sample, which indicates that no appreciable deformation-induced microstructure changes occur during compressive deformation for this alloy. The supply of the mechanical energy during compression can promote the precipitation of nanocrystals in

$\text{Ti}_{40}\text{Zr}_{25}\text{Ni}_8\text{Cu}_9\text{Be}_{18}$ however not in $\text{Ti}_{41.5}\text{Cu}_{37.5}\text{Ni}_{7.5}\text{Zr}_{2.5}\text{Hf}_5\text{Sn}_5\text{Si}_1$ BMG, which is associated with their different thermal stability (activation energy for crystallization).

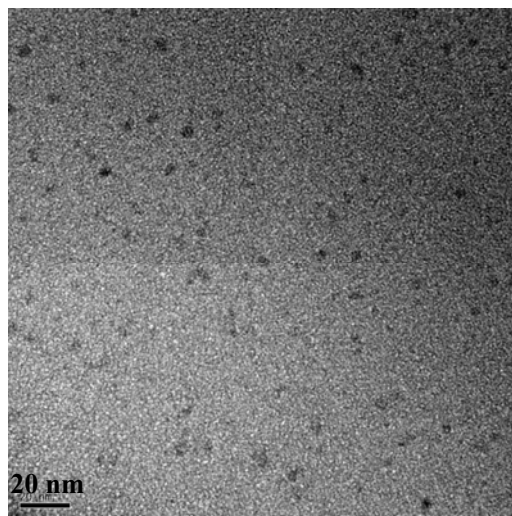


Fig. 6-17 TEM image of the fractured $\text{Ti}_{40}\text{Zr}_{25}\text{Ni}_8\text{Cu}_9\text{Be}_{18}$ BMG

Based on the analysis above, the large plasticity for $\text{Ti}_{40}\text{Zr}_{25}\text{Ni}_8\text{Cu}_9\text{Be}_{18}$ BMG may result from its high value of Poisson's ratio as well as homogeneous precipitation of nanocrystals during deformation which can disperse the strain localization upon compressive loading, resulting in the generation of multiple shear bands (see the outer surface of fractured $\text{Ti}_{40}\text{Zr}_{25}\text{Ni}_8\text{Cu}_9\text{Be}_{18}$ sample in Fig. 6-6 (b)), in turn, leading to the enhanced plasticity.

There are many reports related to the enhancement of plasticity due to the inhomogeneous microstructures in amorphous alloys, such as phase separation or medium-range order (structure on the 1-2 nm scale) [Park et al., 2006; Park et al., 2007]. Similar to nanocrystals, such inhomogeneous microstructures become inhomogeneous energy barriers, and a propagating shear band might be forced to be deflected or branched when it reaches the high energy barrier region. This would result in the initiation of new shear bands. The increase of the total area of shear bands due to the formation of multiple shear bands and deflection in the individual shear bands leads to appreciable macroscopic plasticity at low strain rate. However, it is clear that the dispersion of phase separation-like structure in the amorphous $\text{Ti}_{41.5}\text{Cu}_{37.5}\text{Ni}_{7.5}\text{Zr}_{2.5}\text{Hf}_5\text{Sn}_5\text{Si}_1$ alloy plays an effective role in strengthening, however, not in toughening, as may be associated with the properties of such phase separation-like structure. It may have similar properties with brittle intermetallic compounds which generally strongly degrade the toughness and the plasticity of materials. In addition, the size and volume fraction of the phase separation-like structure may also significantly affect their function during deformation. Since the existing contradiction between our study and the previous reports, the effects of phase separation-like structure in the metallic glasses deserve further investigation in order to understand fully the deformation nature.

In summary, the macroscopic plasticity or brittleness for metallic glasses is not only associated with the properties of constituent elements and structural nature but also related to the structural changes upon compression and their interaction with shear bands during deformation.

6.4 Effects of Thermally Induced Structural Transformations on the Mechanical Properties

6.4.1 Structurally Relaxed and Crystallized States

To study the effects of structural relaxation and crystallization on the mechanical properties of $\text{Ti}_{40}\text{Zr}_{25}\text{Ni}_8\text{Cu}_9\text{Be}_{18}$ and $\text{Ti}_{41.5}\text{Cu}_{37.5}\text{Ni}_{7.5}\text{Zr}_{2.5}\text{Hf}_5\text{Sn}_5\text{Si}_1$ BMGs, nanoindentation measurements as well as room temperature compression tests were performed on the annealed samples with different states, different extent of structural relaxation and crystallized states of these two BMGs in this study.

The annealing conditions were carefully designed according to the investigation results on the structural relaxation and crystallization of these two BMGs in chapter 4. Nanoindentation measurements were performed on the samples annealed according to the annealing condition listed in Table 6-3. The $\text{Ti}_{41.5}\text{Cu}_{37.5}\text{Ni}_{7.5}\text{Zr}_{2.5}\text{Hf}_5\text{Sn}_5\text{Si}_1$ samples annealed at 430 °C for 30 min and 98 min are corresponding to the relaxed and crystallized ($V_{\text{cry}}=5\%$) states, respectively, similar with the two annealing conditions for $\text{Ti}_{40}\text{Zr}_{25}\text{Ni}_8\text{Cu}_9\text{Be}_{18}$ BMG listed in Table 6-3. In addition, room-temperature compression tests were performed on the samples annealed according to the annealing condition listed in Table 6-4. The continuous DSC curves and the XRD patterns of the $\text{Ti}_{40}\text{Zr}_{25}\text{Ni}_8\text{Cu}_9\text{Be}_{18}$ alloy annealed at 278-340 °C for 1 h have been shown in Fig. 5-4 and 5-5 in chapter 5. Fig. 6-18 displays the XRD patterns for the $\text{Ti}_{41.5}\text{Cu}_{37.5}\text{Ni}_{7.5}\text{Zr}_{2.5}\text{Hf}_5\text{Sn}_5\text{Si}_1$ samples annealed at 430 °C for 60-284 min. No crystallization but structural relaxation occurs when it is annealed at 430 °C below T_g for short time, and the crystallization can be confirmed when the sample was annealed for more than 60 min, in accordance with the result obtained from isothermal DSC presented in chapter 4.

Table 6-3

Annealing conditions for the samples used for nanoindentation measurements.

Composition	Annealing conditions (structural relaxation)	Annealing conditions (crystallization)
$\text{Ti}_{40}\text{Zr}_{25}\text{Ni}_8\text{Cu}_9\text{Be}_{18}$	278 °C for 1 h	308 °C for 1 h
$\text{Ti}_{41.5}\text{Cu}_{37.5}\text{Ni}_{7.5}\text{Zr}_{2.5}\text{Hf}_5\text{Sn}_5\text{Si}_1$	430 °C for 30 min	430 °C for 98 min

Table 6-4

Annealing conditions for the samples used for room-temperature compression tests.

Composition	Annealing conditions (structural relaxation)	Annealing conditions (crystallization)
$\text{Ti}_{40}\text{Zr}_{25}\text{Ni}_8\text{Cu}_9\text{Be}_{18}$	278 °C for 1 h 293 °C for 1 h	308 °C for 1 h 340 °C for 1 h
$\text{Ti}_{41.5}\text{Cu}_{37.5}\text{Ni}_{7.5}\text{Zr}_{2.5}\text{Hf}_5\text{Sn}_5\text{Si}_1$	430 °C for 10 min for 30 min for 60 min	430 °C for 98 min ($V_{\text{cry}}=5\%$) for 108 min (10%) for 122 min (20%) for 133 min (30%) for 150 min (50%) for 284 min (100%)

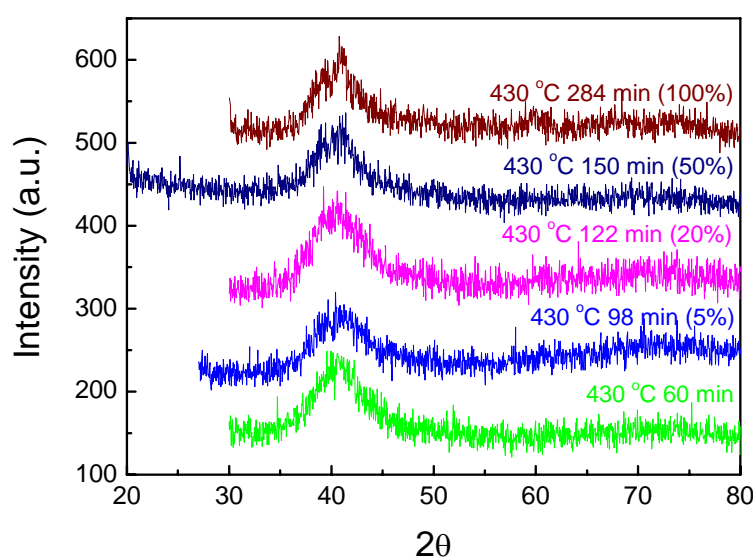


Fig. 6-18 XRD patterns obtained from $\text{Ti}_{41.5}\text{Cu}_{37.5}\text{Ni}_{7.5}\text{Zr}_{2.5}\text{Hf}_5\text{Sn}_5\text{Si}_1$ BMG annealed at 430 °C for various time

6.4.2 Effects of Structural Relaxation and Crystallization on Mechanical Properties

6.4.2.1 Mechanical response under nanoindentation measurements

Fig. 6-19 (a) and (b) display the nanoindentation load-displacement curves for the annealed $\text{Ti}_{40}\text{Zr}_{25}\text{Ni}_8\text{Cu}_9\text{Be}_{18}$ and $\text{Ti}_{41.5}\text{Cu}_{37.5}\text{Ni}_{7.5}\text{Zr}_{2.5}\text{Hf}_5\text{Sn}_5\text{Si}_1$ BMGs, respectively. The load-displacement curves for the as-cast samples are also shown in **Fig. 6-19** for comparison. The variations of the hardness and $W_{\text{plast}}/W_{\text{tot}}$ with structural transformations are given in **Table 6-5**. It is found that for $\text{Ti}_{40}\text{Zr}_{25}\text{Ni}_8\text{Cu}_9\text{Be}_{18}$ alloy, the hardness slightly increases from 5.5 to 6.0 GPa and the value of $W_{\text{plast}}/W_{\text{tot}}$ tends to decrease from 71% to 62% due to the structure changes from amorphous state to partially crystallized state. Such variation of mechanical response with structural transformations is in accordance with the previous reports. However, different results were

obtained for $\text{Ti}_{41.5}\text{Cu}_{37.5}\text{Ni}_{7.5}\text{Zr}_{2.5}\text{Hf}_5\text{Sn}_5\text{Si}_1$ BMG, i.e. the hardness firstly significantly decreases from 6.2 to 5.5 GPa accompanied by the significant decrease of Young's modulus when the sample was annealed for 30 min and then significantly increases to 6.5 GPa for the sample annealed for a long time of 98 min. Such abnormalities are associated with the structural changes of $\text{Ti}_{41.5}\text{Cu}_{37.5}\text{Ni}_{7.5}\text{Zr}_{2.5}\text{Hf}_5\text{Sn}_5\text{Si}_1$ BMG upon isothermal annealing at temperature below T_g . In chapter 4, the microstructure evolution for the sample annealed below T_g has been reported and follows the transition process that from phase separation-like structure (as-cast sample) to amorphous structure (relaxed state) and finally to nanocrystals/amorphous structure (crystallized state). The unique phase separation-like structure in the as-cast sample may lead to increase in hardness, Young's modulus and plasticity compared with the relaxed state sample, and the consequent precipitation of crystals leads to significant increase in hardness however with decrease in plasticity. The corresponding SEM observations of these indents are shown in Fig. 6-20. For each alloy, the morphology changes of three imprints are clearly observed. In the case of $\text{Ti}_{40}\text{Zr}_{25}\text{Ni}_8\text{Cu}_9\text{Be}_{18}$ alloy, different from $\text{Ti}_{41.5}\text{Cu}_{37.5}\text{Ni}_{7.5}\text{Zr}_{2.5}\text{Hf}_5\text{Sn}_5\text{Si}_1$ alloy, the residual pile-up still can be obviously observed even when the sample was crystallized (annealed at 308 °C for 1 h), which indicates its relatively good plasticity.

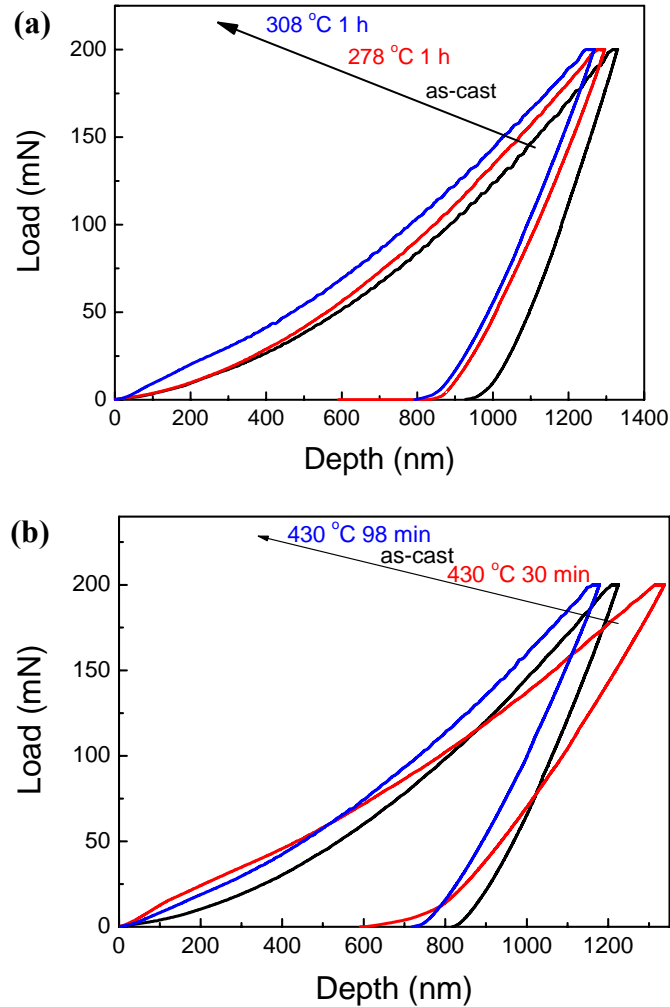


Fig. 6-19 Load-displacement curves measured during nanoindentation tests in load control mode at loading rate of 5 mN/s for annealed as well as as-cast (a) $\text{Ti}_{40}\text{Zr}_{25}\text{Ni}_8\text{Cu}_9\text{Be}_{18}$ and (b) $\text{Ti}_{41.5}\text{Cu}_{37.5}\text{Ni}_{7.5}\text{Zr}_{2.5}\text{Hf}_5\text{Sn}_5\text{Si}_1$ samples

Table 6-5

The maximum depth (h_{\max}), Young's modulus (E_y), hardness (H) and ratio $W_{\text{plast}}/W_{\text{tot}}$ calculated from the load-displacement curves of nanoindentation measurements for annealed as well as as-cast $\text{Ti}_{40}\text{Zr}_{25}\text{Ni}_8\text{Cu}_9\text{Be}_{18}$ and $\text{Ti}_{41.5}\text{Cu}_{37.5}\text{Ni}_{7.5}\text{Zr}_{2.5}\text{Hf}_5\text{Sn}_5\text{Si}_1$ samples

Composition	State	h_{\max} (nm)	E_y (GPa)	H (GPa)	$W_{\text{plast}}/W_{\text{tot}}$ (%)
$\text{Ti}_{40}\text{Zr}_{25}\text{Ni}_8\text{Cu}_9\text{Be}_{18}$	As-cast	1328	98	5.5	71
	At 278 °C for 1 h	1294	100	5.7	64
	At 308 °C for 1 h	1267	103	6.0	62
$\text{Ti}_{41.5}\text{Cu}_{37.5}\text{Ni}_{7.5}\text{Zr}_{2.5}\text{Hf}_5\text{Sn}_5\text{Si}_1$	As-cast	1224	103	6.2	66
	At 430 °C for 30 min	1337	84	5.5	54
	At 430 °C for 98 min	1178	107	6.5	52

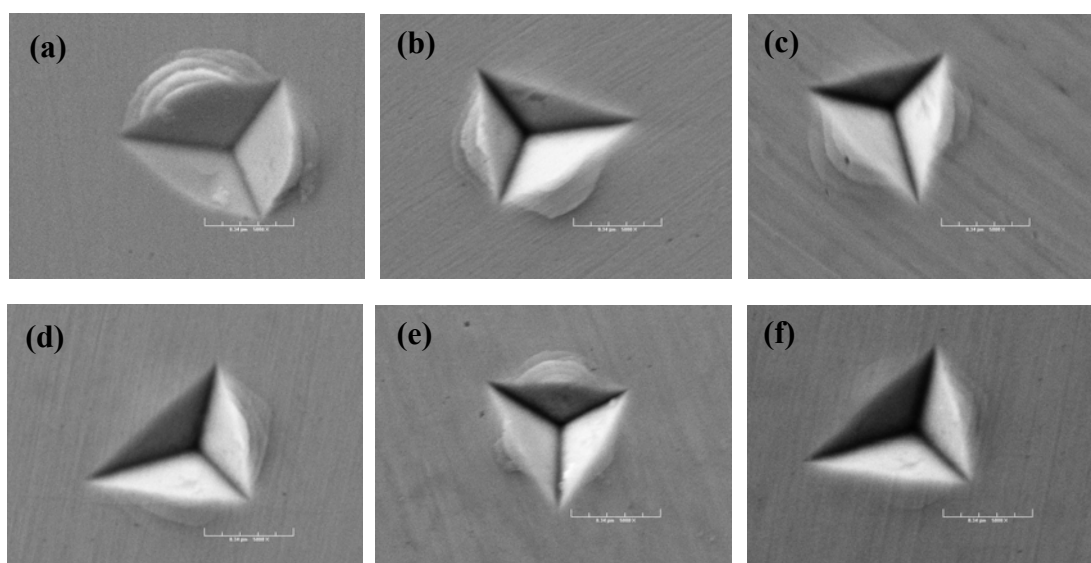


Fig. 6-20 SEM micrographs of indents for as-cast and annealed (a-c) $\text{Ti}_{40}\text{Zr}_{25}\text{Ni}_8\text{Cu}_9\text{Be}_{18}$ and (d-e) $\text{Ti}_{41.5}\text{Cu}_{37.5}\text{Ni}_{7.5}\text{Zr}_{2.5}\text{Hf}_5\text{Sn}_5\text{Si}_1$ samples

In order to obtain more information about the effects of structural transformations on the mechanical response of these two metallic glasses, Vickers hardness was measured on the more annealed samples which are corresponding to the compression tests. **Fig. 6-21** displays the micro-hardness of these two alloys under various annealing conditions. It is found that the micro-hardness increases slowly due to the structural relaxation caused by annealing at a temperature lower than T_g and the crystallization makes the micro-hardness increase rapidly. The increase in the hardness with precipitation of nanocrystals can be explained as follow [Baldwin et al., 2008]. The precipitation of nanocrystals results in incoherent interphase boundaries and because of lattice mismatch among various constituents causing misfit strains at the boundaries. With increase in crystalline volume fraction, the average strain across the boundaries increases and causes the hardening effect. However, there may exist an optimum value of crystalline volume fraction and size of the precipitates which can provide maximum hardness, beyond which, hardness values start to decrease as a result of coarsening of the precipitates and reduction in the lattice mismatch strains, this is the reason why, with increase in volume fraction of crystals, the hardness for $\text{Ti}_{41.5}\text{Cu}_{37.5}\text{Ni}_{7.5}\text{Zr}_{2.5}\text{Hf}_5\text{Sn}_5\text{Si}_1$ alloy increases slowly. Similar observations were

reported in Zr-[Das et al., 2005] and Hf-based [Baldwin et al., 2008] metallic glasses.

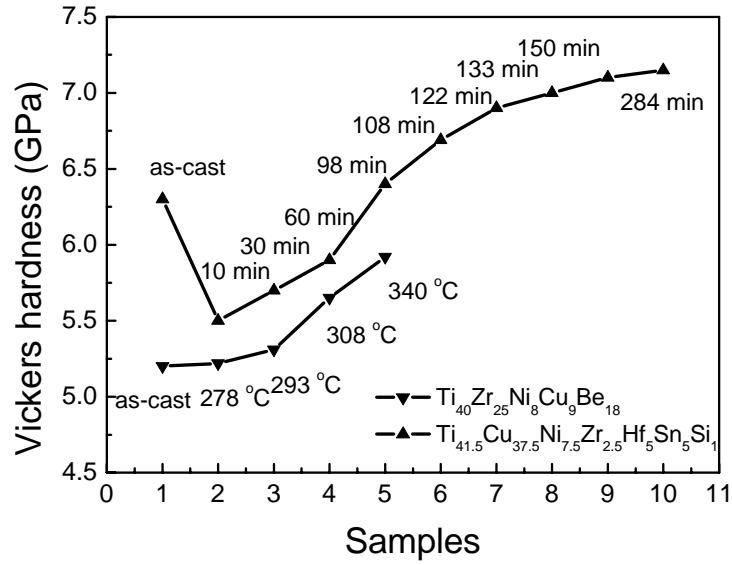
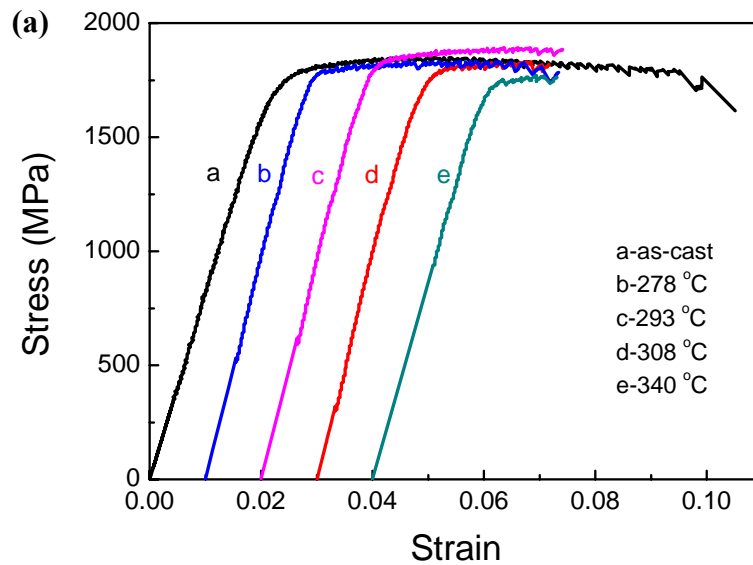


Fig. 6-21 Vickers hardness as a function of annealing conditions for $\text{Ti}_{40}\text{Zr}_{25}\text{Ni}_8\text{Cu}_9\text{Be}_{18}$ and $\text{Ti}_{41.5}\text{Cu}_{37.5}\text{Ni}_{7.5}\text{Zr}_{2.5}\text{Hf}_5\text{Sn}_5\text{Si}_1$ alloys

6.4.2.2 Mechanical response under compression tests

The room-temperature compressive stress-strain curves at a constant strain rate of $5 \times 10^{-4} \text{ s}^{-1}$ for the annealed as well as the as-cast $\text{Ti}_{40}\text{Zr}_{25}\text{Ni}_8\text{Cu}_9\text{Be}_{18}$ and $\text{Ti}_{41.5}\text{Cu}_{37.5}\text{Ni}_{7.5}\text{Zr}_{2.5}\text{Hf}_5\text{Sn}_5\text{Si}_1$ alloys are shown in Fig. 6-22 (a) and (b), respectively. In the case of $\text{Ti}_{40}\text{Zr}_{25}\text{Ni}_8\text{Cu}_9\text{Be}_{18}$ alloy, the compressive strength always keeps a value of about 1850 MPa, independent of structural state (as-cast, relaxed or crystallized state) within the annealing condition in this study; however, the plastic strain decreases from 8.0% for the as-cast sample to 1.0% for the sample annealed at 340 °C for 1 h which consists of large quantities of crystals.



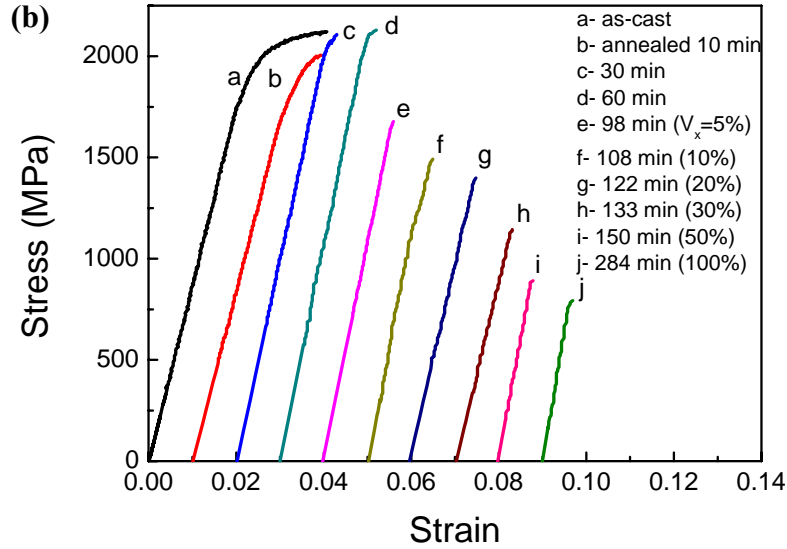
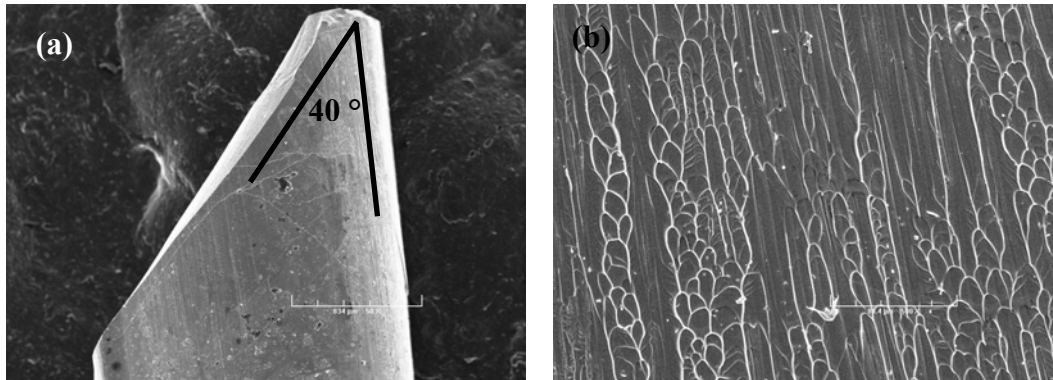


Fig. 6-22 Room-temperature compressive stress-strain curves at a constant strain rate of $5 \times 10^{-4} \text{ s}^{-1}$ for the annealed as well as the as-cast (a) $\text{Ti}_{40}\text{Zr}_{25}\text{Ni}_8\text{Cu}_9\text{Be}_{18}$ and (b) $\text{Ti}_{41.5}\text{Cu}_{37.5}\text{Ni}_{7.5}\text{Zr}_{2.5}\text{Hf}_5\text{Sn}_5\text{Si}_1$ samples

Similar with the as-cast sample, the samples annealed at 293 and 308 °C which are corresponding to the relaxed state and a slightly crystallized state fractures in two pieces. Fracture angles were measured to be 40 and 37 ° for the samples annealed at 293 and 308 °C, respectively, as shown in Fig. 6-23 (a) and (c). Recently some researches demonstrated that the closer to 45 ° the shear fracture angle, the higher the plastic strain would be [Inoue et al., 2005; Z.F. Zhang et al., 2005-b]. Our observations confirm this relationship between fracture angle and plasticity. In addition, some shear bands were also found near the fracture surface for the sample annealed at 293 °C. SEM observations of the fractured surface revealed extensive veins patterns similar to those observed on the fracture surface of as-cast $\text{Ti}_{40}\text{Zr}_{25}\text{Ni}_8\text{Cu}_9\text{Be}_{18}$ sample, which confirmed the occurrence of the plastic flow before failure (Fig. 6-23 (b) and (d)). However, when the sample consists of large volume fraction of crystals (the sample annealed at 340 °C), the sample fractures to multiple fragments, as shown in Fig. 6-23 (e), indicating a ductile-brittle transition and a change in fracture mode from shear fracture to typical cleavage fracture with the failure mechanism of void formation and coalescence (Fig. 6-23 (f)).



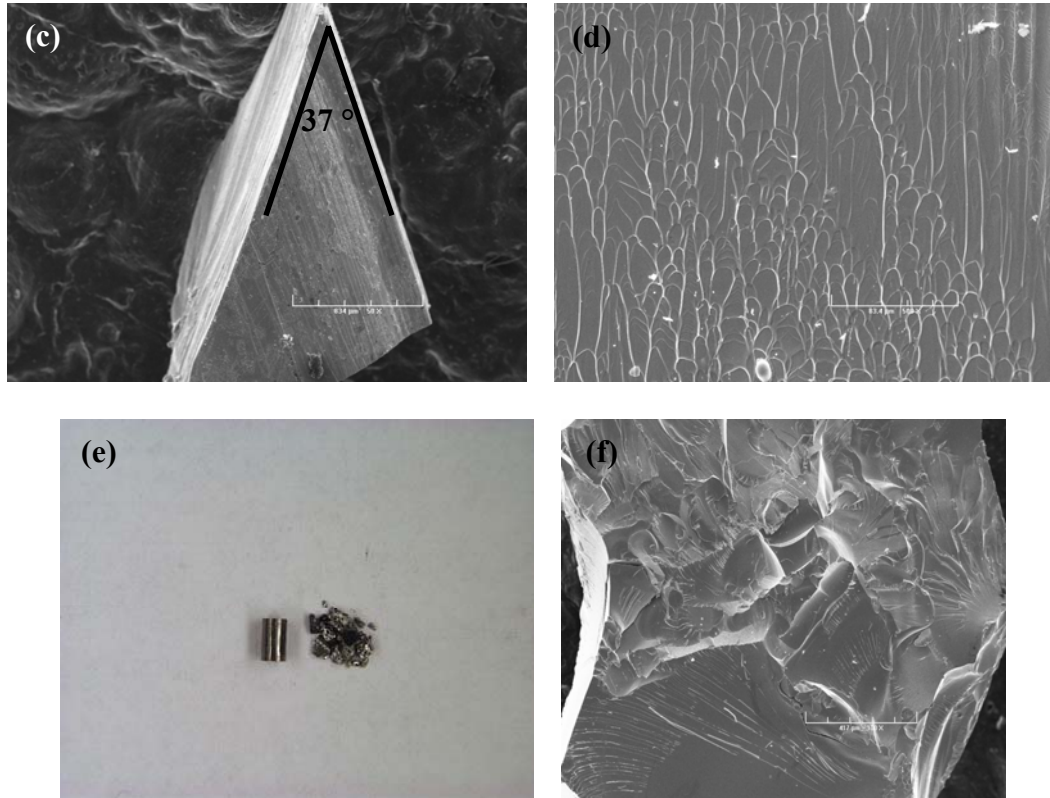


Fig. 6-23 Fracture surfaces for the $\text{Ti}_{40}\text{Zr}_{25}\text{Ni}_8\text{Cu}_9\text{Be}_{18}$ samples annealed at (a-b) 293 °C, (c-d) 308 °C and (e-f) 340 °C for 1 h, deformed at the strain rate of $5 \times 10^{-4} \text{ s}^{-1}$

The variations of compressive properties for $\text{Ti}_{41.5}\text{Cu}_{37.5}\text{Ni}_{7.5}\text{Zr}_{2.5}\text{Hf}_5\text{Sn}_5\text{Si}_1$ alloy with the structural transformations are shown in **Fig. 6-22 (b)**. It is found that the compressive strength as well as plastic strain decreases slightly when the samples is annealed at 430 °C for 10 min, followed by a slight increase in strength which is comparable with that of as-cast sample and complete degeneration of plasticity with increase in annealing time up to 60 min. And then the continuous prolongation of annealing time leads to the drastic decrease in fracture strength, finally, when the sample completes the first crystallization event which is corresponding to the annealing time of 284 min, the fracture is measured to be about 800 MPa.

To understand such variations of compressive properties with the structural transformations, the structural transformations during annealing must be taken into account. The decrease in strength and plasticity at the beginning of annealing (10 min) is due to the structural changes from the phase separation-like structure to amorphous structure through atomic diffusion and rearrangement at temperature below T_g . In other words, the unique phase separation-like structure causes the increase in strength and plasticity with respect to the amorphous structure. The following increase in strength to a high value and embrittlement (30 min and 60 min) is associated with the structural relaxation. However, whatever the degree of crystallization, macroscopically brittle behaviors are obtained, which are associated with the morphology, distribution and the innate properties of the crystals. SEM observations of the fractured samples confirm the cleavage fracture mode with the characteristic of multiple fracture fragments, even dust, as shown in **Fig. 6-24** caused by the existence of crystals.

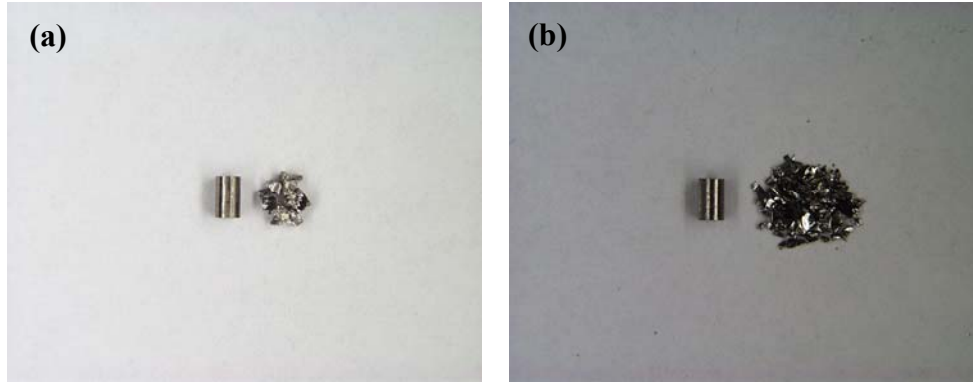


Fig. 6-24 Observation of the fracture surfaces for the $\text{Ti}_{41.5}\text{Cu}_{37.5}\text{Ni}_{7.5}\text{Zr}_{2.5}\text{Hf}_5\text{Sn}_5\text{Si}_1$ samples annealed at 430 °C for (a) 98 min and (b) 284 min

In summary, the increasing relaxation of the amorphous matrix and the precipitation of nanocrystals during annealing may influence the mechanical properties, for example, structural relaxation of the metallic glasses produces a slight increase in hardness, Young's modulus and fracture strength in addition to embrittlement; moreover, the precipitation of nanocrystals of the metallic glasses leads to a rapid increase in hardness and Young's modulus, however indicating a significant decrease in fracture strength and plasticity. The ductile-brittle transition during annealing is attributed to the loss of free volume which can accommodate plastic deformation as a result of structural relaxation and crack initiation at weak points such as the intermetallic precipitates and/or pores. Accordingly, we emphasize that crystallization should be avoided during the superplastic forming in the supercooled liquid region and as long as the flow stress meets the demand of superplastic forming, it is necessary to select a temperature as close to T_g of the metallic glass as possible since the degeneration of mechanical properties caused by structural relaxation and especially crystallization.

6.5 Conclusion

In this chapter, the mechanical properties and the mechanism for deformation and fracture of the as-cast $\text{Ti}_{40}\text{Zr}_{25}\text{Ni}_8\text{Cu}_9\text{Be}_{18}$ and $\text{Ti}_{41.5}\text{Cu}_{37.5}\text{Ni}_{7.5}\text{Zr}_{2.5}\text{Hf}_5\text{Sn}_5\text{Si}_1$ alloys were investigated, in addition, the influences of structural transformations (structural relaxation and crystallization) on the mechanical response were also presented. The results can be summarized as follows:

- (1) The as-cast $\text{Ti}_{40}\text{Zr}_{25}\text{Ni}_8\text{Cu}_9\text{Be}_{18}$ and $\text{Ti}_{41.5}\text{Cu}_{37.5}\text{Ni}_{7.5}\text{Zr}_{2.5}\text{Hf}_5\text{Sn}_5\text{Si}_1$ alloys deformed at room temperature with a constant strain rate of $5 \times 10^{-4} \text{ s}^{-1}$ both exhibit high value of compressive strength of 1850 and 2120 MPa, respectively, however with significantly different plastic strain, 8.0% and 1.6%, respectively. The macroscopic plasticity or brittleness for metallic glasses is not only associated with the properties of constituent elements and structural nature but also related to the structural changes upon compression and their interaction with shear bands during deformation.
- (2) It is confirmed that the plastic flow of metallic glasses is located within narrow shear bands, and the universal local softening mechanism dominates the fracture of metallic glasses in spite of their deformation and fracture mode, but at different length scales. For these two alloys, the compressive fracture surfaces both consist of a shear zone and a rough zone, accompanying the

fracture angles changing from <45 to 90° . Such unique deformation and fracture behavior can be successfully interpreted by the ellipse criterion combined with the analysis on the changes of stress state during the compressive fracture process.

(3) The structural relaxation of the metallic glasses produces a slight increase in hardness, Young's modulus and fracture strength in addition to embrittlement; moreover, the precipitation of nanocrystals of the metallic glasses leads to a rapid increase in hardness and Young's modulus however with a significant decrease in fracture strength and plasticity. Accordingly, the crystallization should be avoided during the superplastic forming in the supercooled liquid region and as long as the flow stress meets the demand of superplastic forming, it is necessary to select a temperature as close to T_g of the metallic glass as possible since the degeneration of mechanical properties is caused by structural relaxation and especially crystallization.

CHAPTER 7

HOMOGENEOUS DEFORMATION BEHAVIOR IN THE SUPERCOOLED LIQUID REGION

7.1 Background and Motivation

Ti-based BMGs, as promising structure materials, their mechanical properties should be paid more attention besides their other elementary properties: glass forming ability, thermal stability and structural transformation, etc. which have been investigated in detail and presented in this study. In chapter 6, we have reported the excellent mechanical properties at ambient temperature such as high strength and high elastic strain limit for as-cast $\text{Ti}_{41.5}\text{Cu}_{37.5}\text{Ni}_{7.5}\text{Zr}_{2.5}\text{Hf}_5\text{Sn}_5\text{Si}_1$ and $\text{Ti}_{40}\text{Zr}_{25}\text{Ni}_8\text{Cu}_9\text{Be}_{18}$ BMGs; however, it does not mean these two alloys are good enough to be used because the absence of informations about the formability and workability. From the application point of view, the formability and workability should be taken into account. In regard to the forming of complex components, for their high strength, high hardness, very limited room temperature plasticity and structural instability of BMGs, the mechanical machining is not possible to be applied during the manufacturing process. To date, the achievable geometries produced with BMGs have been quite limited, and only two fundamentally different processing routes are used. The first method, direct casting, involves the fast cooling of molten BMG so that crystallization during solidification can be avoided. During the cooling process, the entire mold cavity must be simultaneously filled. This requirement makes casting complex shape, for example, thin sections with a high aspect ratio particularly challenging. Only a careful balance of processing parameters allows this path to be commercially viable for some geometries. Other processing paths take advantage of BMGs softening in the supercooled liquid region to form complex components. This good formability in the SLR enables near-net-shape forming of BMGs products such as micro-gears, diffraction grating, micro- and nano-pyramid, and micro-devices through a conventional mold casting followed by hot homogeneous deformation in the undercooled liquid state. The ability to homogeneously deform the BMG alloy in the SLR at a low forming pressure and temperature has been used for a wide range of applications, including net shape processing, micro- and nano-replication, surface smoothening proces extrusion, synthesis of amorphous metallic foams, blow molding and synthesis of BMG composites [Lee et al., 2003; Martinez et al., 2008; X.L. Guo et al., 2009].

The excellent properties together with formability in viscous state promise an application in the field of near-net-shape fabrication of structure components. This potential application has raised a growing interest in detailed investigations of the plastic deformation behavior of many types of BMGs (Pd-, La-, Zr-, Cu-, Mg-based) in the SLR over the past few years [Busch et al., 1998-c; Kawamura et al., 1998; Kawamura et al., 1999; Chu et al., 2002; J. Lu et al., 2003; Bletry et al.,

2004; Nieh et al., 2006; Gun et al., 2007]. The optimization of such technologies requires detailed informations on the stress relaxation, deformation mechanism as well as the structural stability. So, in order to improve the formability of BMGs, further investigation on the high temperature flow behavior of BMGs is necessary for both fundamental science and engineering applications.

In regard to the investigation on the formability and workability of BMGs, three aspects of work should be carried out: (i) the deformation behavior and the corresponding mechanism; (ii) deformation technology and (iii) the thermal stability and mechanical properties of the post-deformed materials. Our study just focus on the (i) and (iii) items mentioned above for the limitation of experimental conditions. The uniaxial compressive test was adopted to investigate the formability in this study. It should be pointed out that, although the stress state in the industrial superplastic manufacture processes are much more complex compared with a simple uniaxial tensile or compressive stress, the uniaxial compressive test in the lab also can provide some information about the deformation behavior and mechanism from the scientific and experimental viewpoints, finally to guide the manufacture of production. The research on the thermal stability and mechanical properties of the post-deformed materials is related to the workability of BMGs, and actually it can be transformed to the investigation on the thermal stability and mechanical properties of the annealed samples which exhibit different microstructures induced by structural relaxation or crystallization, as has been reported in chapter 5 and chapter 6, respectively. Since the drastic degradation of mechanical properties due to the precipitation of crystalline phase, during the deformation time must be carefully controlled to be as short as possible to avoid the crystallization during the deformation in the supercooled liquid region. So our investigation in this chapter will be focused on the characteristic and mechanism of high-temperature deformation of Ti-based BMGs.

In the following section, the motivation of this study will be clarified through the critical review on the high-temperature deformation behavior of BMGs, and finally determined the investigation content.

7.1.1 Review on the High-temperature Deformation Behavior of BMGs

The mechanical deformation of metallic glasses can be generally classified into two modes, namely, homogeneous and inhomogeneous deformation [Kawamura et al., 1998]. In spite of their composition and metallic bonding, all the metallic glasses discovered so far exhibit inhomogeneous deformation when being deformed at low temperatures (e.g. room temperature) and are characterized by the formation of localized shear bands where the strain is concentrated, followed by rapid propagation of these bands and catastrophic shear failure immediately, as can be seen in the deformation mechanism map (steady-state strain rate as a function stress and temperature) for a typical metallic glass shown in Fig. 7-1 under the condition of high stress and low temperature. By contrast, at lower stress and elevated temperature, they can be deformed homogeneously (Fig 7-1): each volume element undergoes the same strain, due to a drastic drop in viscosity (usually by several orders of magnitude) during the glass transition process upon heating and exhibit considerable amount of plastic deformation [J. Lu et al., 2003].

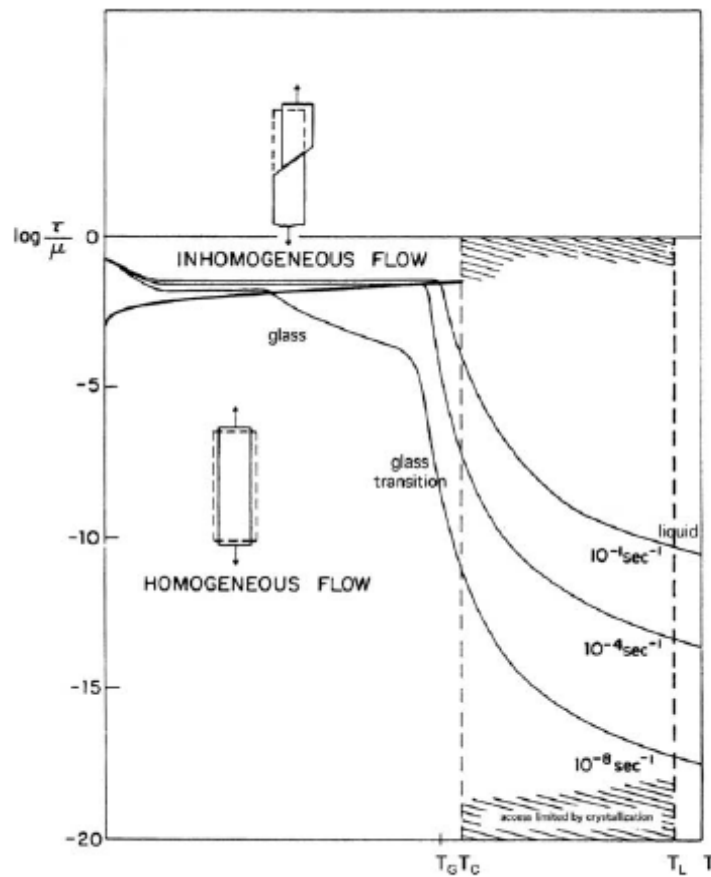


Fig. 7-1 Deformation mechanism map for a metallic glass obtained from the reference [Spaepen, 2006]

7.1.1.1 Development of homogeneous deformation of metallic glasses in the supercooled liquid region

There were only some sporadic studies on the homogeneous deformation of metallic glasses in the supercooled liquid region in the 1980s since the glassy alloys usually had a narrow supercooled liquid region. The tested samples were primarily in ribbon shape, and the experimental results on deformation mechanisms were also in debate. It is worth noting that Khonik and Zelenskiy analyzed available mechanical data from 15 different metallic glasses, and made several empirical observations. The active study on homogeneous deformation of bulk metallic glasses began in the late 1990s, only several years after the materials could be reliably made [Nieh et al., 2006]. Up to date, many bulk metallic glasses with a wide supercooled liquid region and high formability in the supercooled liquid region have been discovered in La-, Pd-, Zr-, Cu-based composition alloys. Some high-temperature deformation data from the typical metallic glasses are summarized in Table 7-1. It is found that the investigation on the high-temperature deformation of metallic glasses were not so extensive and only carried out in a very limited alloy systems like La-, Pd-, Zr-, Cu-based and some typical metallic glasses like $\text{La}_{55}\text{Al}_{25}\text{Ni}_{20}$, $\text{Pd}_{40}\text{Ni}_{40}\text{P}_{20}$, $\text{Zr}_{41.2}\text{Ti}_{13.8}\text{Ni}_{10}\text{Cu}_{12.5}\text{Be}_{22.5}$, $\text{Zr}_{55}\text{Cu}_{30}\text{Al}_{10}\text{Ni}_5$, etc. which exhibit good GFA and thermal stability. In addition, uniaxial tensile testing was the dominant way to study the

CHAPTER 7 HOMOGENEOUS DEFORMATION BEHAVIOR IN THE SUPERCOOLED LIQUID REGION

high-temperature deformation. Consequently, it is necessary to carry out the homogeneous behavior study in more metallic glass systems and more alloy compositions for obtaining more data about the homogeneous deformation in the supercooled liquid region of the metallic glasses, to complement the corresponding database.

Table 7-1

Deformation data of some typical metallic glasses in the supercooled liquid region

Alloy (in at.%)	T_g (K)	T_{x1} (K)	m value	Ductility*	Reference
La ₅₅ Al ₂₅ Ni ₂₀	480	520	1	200 (T)	[Kawamura et al., 1999]
La ₆₀ Al ₂₀ Ni ₁₀ Co ₅ Cu ₅	451	523	1	-	[Saotome et al., 2001]
Pd ₄₀ Ni ₄₀ P ₂₀	578-597	651	0.4-1	12.6 (T)	[Kawamura et al., 1997]
Pd ₄₀ Ni ₄₀ P ₂₀	589	670	0.5-1	0.94 (C)	[Chu et al., 2002]
Zr _{41.5} Ti _{13.75} Ni ₁₀ Cu _{12.5} Be _{22.5}	614	698	0.4-1	16.24 (T)	[G. Wang et al., 2005]
Zr _{41.2} Ti _{13.8} Ni ₁₀ Cu _{12.5} Be _{22.5}	624	713	N/A	0.4 (C)	[X.L. Guo et al., 2009]
Zr _{41.2} Ti _{13.8} Ni ₁₀ Cu _{12.5} Be _{22.5}	628	729		5 (T)	[Lee et al., 2003]
Zr ₅₅ Cu ₃₀ Al ₁₀ Ni ₅	683	775	0.4-0.9	5.5 (T)	[Chan et al., 2007]
Zr ₅₅ Cu ₃₀ Al ₁₀ Ni ₅	680	762	0.5-0.9	5.6 (T)	[Shin et al., 2007-a]
Zr ₅₅ Cu ₃₀ Al ₁₀ Ni ₅	670	768	0.45-0.95	8.0 (T)	[Shin et al., 2007-b]
Zr ₆₅ Al ₁₀ Ni ₁₀ Cu ₁₅	652	757	0.8-1	3.4 (T)	[Kawamura et al., 1998]
Zr ₆₅ Al ₁₀ Ni ₁₀ Cu ₁₅	652	757	0.83	7.5 (T)	[W.J. Kim et al., 1993]
Zr ₆₅ Al ₁₀ Ni ₁₀ Cu ₁₅				13.5 (T)	[W.J. Kim et al., 2006-a]
Zr _{52.5} Al ₁₀ Ti ₅ Cu _{17.9} Ni _{14.6}	358	456	0.45-0.55	6.5 (T)	[Nieh et al., 1999]
Zr _{52.5} Al ₁₀ Cu ₂₂ Ti _{2.5} Ni ₁₃	659	761	0.5-1	~1.0 (C)	[Bletry et al., 2006]
Cu ₆₀ Zr ₂₀ Hf ₁₀ Ti ₁₀	721	766	0.3-0.6	0.77 (C)	[Chiang et al., 2004]
Cu ₅₄ Ni ₆ Zr ₂₂ Ti ₁₈	712	769	1	6.5 (T)	[W.J. Kim et al., 2006-b]
Cu ₄₇ Ti ₃₃ Zr ₁₁ Ni ₆ Sn ₂ Si ₁				6.0 (T)	[Bae et al., 2002]
Mg ₆₅ Cu ₂₅ Y ₁₀	423	493	1	>13 (T)	[Gun et al., 2007]
Ce ₇₀ Al ₁₀ Cu ₂₀	366	427	0.3-1	0.89 (C)	[Chu et al., 2006]
Ca ₆₅ Mg ₁₅ Zn ₂₀	378	413	1	>8.5 (T)	[Law et al., 2008]
Ti ₄₅ Zr ₂₄ Ni ₇ Cu ₈ Be ₁₆	601	648	-	1.0 (T)	[Bae et al., 2004]

* “T” and “C” stand for tension and compression, respectively.

7.1.1.2 Main issues related to homogeneous deformation

Since the beginning of the active study on homogeneous deformation of bulk metallic glasses in the late 1990s, much work has been focus on (i) the characteristic of deformation behavior and (ii) the rheological behavior: the transition between Newtonian flow and non-Newtonian flow. Some significant results have been obtained, in which some are in agreement; however, others are still in argument, which will be shown in detail as follows:

1. The characteristic of homogeneous deformation in the supercooled liquid region

The bulk metallic glasses exhibit thermal instability at high temperatures, and accordingly display different mechanical behaviors. Extensive investigations demonstrated that the deformation of BMGs is strongly dependent on strain rate and temperature. Three different types of deformation behaviors were observed when the metallic glasses were deformed near or in the supercooled liquid region. Firstly, the stress overshoot phenomena and some plastic deformation

after elastic deformation were observed, and the stress overshoot induced drastically increased free volume and atomic redistributions at temperature near the glass transition temperature or with high strain rate. Secondly, superplastic deformations and extremely low stable stress deformations were observed in the temperature range from above the stress overshoot temperatures to below the crystallization temperature with lower strain rate by homogeneous viscous flows. Thirdly, above the crystallization temperature or after a long deformation time even at temperature below the crystallization temperature, strain hardening was observed with the characteristic of monotonic increment in the stress level, which is believed to be associated with microstructural instability, namely, the concurrent formation of nanocrystals in the amorphous matrix during deformation [Choi et al., 2007].

2. The rheological behavior: transition from Newtonian flow to non-Newtonian flow

Newtonian behavior was usually observed in the low strain rate regime, while deformation became non-Newtonian in the high strain rate regime. It has been observed in many BMGs systems, including Zr-, Pd- and Cu-based. It appears to be a general phenomenon for metallic glasses deformed in the supercooled liquid region [Nieh et al., 2006]. A typical example showing the transition between Newtonian and non-Newtonian flow is shown in Fig. 7-2. m is the strain rate sensitivity index defined as $m = \frac{\partial \sigma}{\partial \dot{\epsilon}}$ and its value approaching to unity represents the Newtonian flow, while lower than unity suggests the deviation from the Newtonian flow. From both the theoretical and practical point of view, the better understanding of the rheological behavior of metallic glasses is quite important. For Newtonian flow behavior, the plastic shear strain rate, $\dot{\epsilon}_s$ is directly proportional to the applied shear stress, σ_s , while in the case of the non-Newtonian flow behavior, the stress-strain rate relationship is non-linear.

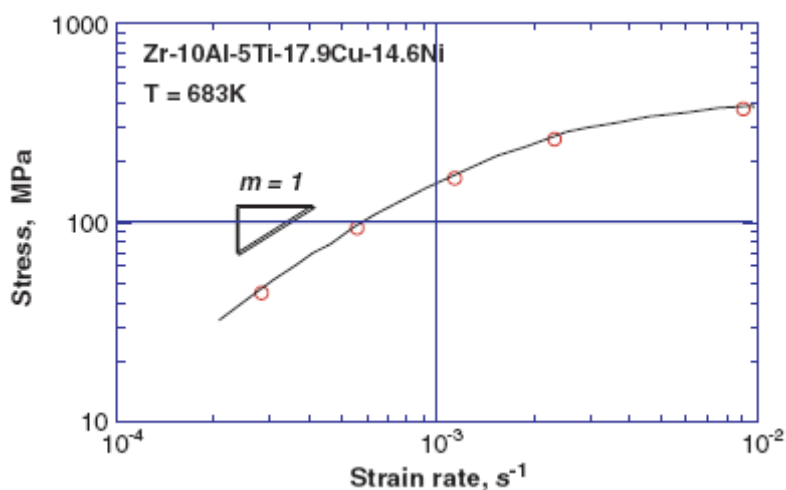


Fig. 7-2 Stress-strain rate curve for a Zr-10Al-5Ti-17.9Cu-14.6Ni metallic glass shows Newtonian flow at low strain rates but non-Newtonian flow at high strain rate [Nieh et al., 1999]

Two possible explanations were proposed to clarify the non-Newtonian behavior [L. Liu et al., 2007; Chan et al., 2007]. The first one associates the non-Newtonian behavior with the stress overshoot, which involves a structural disordering caused by a rapid increment of stress-induced free volumes, as has been verified recently by an important finding of structural disordering in Pd₄₀Ni₄₀P₂₀ BMG during plastic deformation at high temperatures [De Hey et al., 1998]. The other

one was suggested by Nieh et al. [Nieh et al., 1999; Nieh et al., 2001] based on the microstructure examination of the different parts of the deformed $\text{Zr}_{52.5}\text{Ti}_5\text{Al}_{7.5}\text{Cu}_{17.9}\text{Ni}_{14.6}$ BMGs in the supercooled liquid region, they argued that non-Newtonian deformation observed at high strain rates was attributed to the concurrent nanocrystallization of the amorphous phase during deformation.

The understanding of the transition mechanism between Newtonian and non-Newtonian viscous flow is very important, and it has been investigated by many researchers. The most acceptable theory was introduced by Spaepen called “transition state theory” based on two competing processes of stress-driven free volume creation and diffusion-controlled free volume annihilation [Spaepen, 1977]. Both Reger-Leonhard et al. [Reger-Leonhard et al., 2000] and Bletry et al. [Bletry et al., 2004] invoked the transition state theory to explain the departure from Newtonian flow. They indicated that at higher strain rate a transition to partially inhomogeneous flow occurs along with the homogeneous flow ($m=1$) causing a deviation from the linearity in the $\dot{\epsilon}-\sigma$ relation. The non-Newtonian data were well correlated with Newtonian ones using the equation from transition state theory:

$$\dot{\epsilon} = \dot{\epsilon}_0 \sinh \frac{\sigma \gamma_0 \Omega_f}{M k_B T} \quad (7-1)$$

where $\dot{\epsilon}_0$ is the reference strain rate, γ_0 is the local strain produced by the shear site of volume

Ω_f , $M = \sqrt{3}$, k_B and T have their usual meanings. However, it should be pointed out that the transition state theory is essentially thermomechanical, independent of the material’s microstructure.

Although we have obtained many significant results about the homogeneous deformation behavior of metallic glasses in the supercooled liquid region, a number of basic problems are still in argument and not satisfactorily solved, which are needed to be further investigated in the future research work.

1. The quantitative description of the deformation of metallic glasses at high temperature

The nature of the physical process of the deformation of BMGs in the supercooled liquid region is not well understood, and unraveling this behavior constitutes one of the main scientific challenges. De Hey et al. [De Hey et al., 1998] have used the free volume model proposed by Spaepen [Spaepen, 1977], which is a continuum-level one-dimensional model and has long been used to represent the inelastic response of metallic glasses to analyze the high-temperature deformation of $\text{Pd}_{40}\text{Ni}_{40}\text{P}_{20}$ metallic glass. Bletry et al. [Bletry et al., 2006; Bletry et al., 2007] also have proposed a model based on the free volume theory, and successfully described the high-temperature deformation of $\text{Zr}_{52.5}\text{Al}_{10}\text{Cu}_{27}\text{Ti}_{2.5}\text{Ni}_8$ and $\text{Zr}_{52.5}\text{Al}_{10}\text{Cu}_{22}\text{Ti}_{2.5}\text{Ni}_{13}$ BMGs. Very recently, Anand and Su [Anand et al., 2007] introduced a elastic-viscoplastic constitutive theory which is quite different from the free volume theory of Spaepen, and it was successfully extended to the high homologous temperature regime and applied in describing the stress-strain response of $\text{Pd}_{40}\text{Ni}_{40}\text{P}_{20}$ metallic glass at high temperature. However, unlike oxide glasses in which phase transformation kinetics are sluggish, structures of BMGs are generally unstable. It is, therefore, difficult to develop the quantitative description of the mechanical response of BMG in the supercooled liquid region. The equation would be kinematical in nature and must be in real-time.

2. Whether the stress induces the change of structure or not?

This question also can be regarded as whether the crystallization will be accelerated through deforming in the supercooled liquid region. Since metallic glasses are not in thermodynamic equilibrium, phase transformations from the amorphous phase to the more stable crystalline phase can occur with the supply of external energy. Heating and deformation (or stress) are the principal origins of driving forces affecting this transformation during the high-temperature deformation.

The most popular standpoint is that the nonlinear viscous flow induces the crystallization during the deformation of BMGs in the supercooled liquid region, which is due to the fact that the strain energy caused by plastic deformation can complement the thermal energy required for crystallization at these temperatures, suggested by Nieh et al. [Nieh et al., 1999, Nieh et al., 2001] and Lee et al. [Lee et al., 2003]. However, there are also sporadic reports indicating the significant suppression of the precipitation of nanocrystals when the metallic glasses are subjected to the non-Newtonian viscous flow at a condition where a structural disorder is created, for example, Saida et al. [Saida et al., 2002] found the suppression of quasicrystallization by nonlinear viscous flow in Zr-Al-Ni-Cu-Pd metallic glasses, and they argued that the seemingly contradictory results may be due to the precipitation of the metastable quasicrystalline phase as the primary phase, are suppressed for the icosahedral atomic configurations and are destroyed by the mechanically induced disorder. This finding suggests that the effects of deformation on the structural changes may be inconsistent for different metallic glasses and associated with the structure and stability of the primary phase, and also may associate with the different viscosity flow, Newtonian flow or non-Newtonian flow. So, the investigation on the effects of the deformation on the structural changes during the homogeneous deformation in the supercooled liquid region, whether it induces the crystallization or not, or even has no influence, is vital for optimizing the conditions to minimize the crystallization. Accordingly, much experimental data obtained from different kinds of metallic glasses are needed, and also the possible reason which can be explained such phenomenon.

7.1.2 Motivation

As reviewed in Table 7-1, some metallic glasses in La-, Pd-, Zr-, Cu-, etc. alloy systems exhibit superplasticity by behaving like Newtonian fluids in the supercooled liquid region. This superplastic property allows complicated near-net shape manufacturing of metallic glasses. Ti-based metallic glasses have special advantages over other metallic glasses for their high specific strength and relatively low cost. Thus, the development of Ti-based BMGs is prone to expand their commercial applications. However, within our knowledge, there is only one report on the high-temperature deformation in Ti-based BMGs which has presented the small elongation of 100% to failure of $\text{Ti}_{45}\text{Zr}_{24}\text{Ni}_7\text{Cu}_8\text{Be}_{16}$ BMG. So it is necessary to extend the high-temperature deformation investigation into the Ti-based metallic glasses, and try to find their characteristic of deformation and give a reasonable explanation.

In regard to the $\text{Ti}_{41.5}\text{Cu}_{37.5}\text{Ni}_{7.5}\text{Zr}_{2.5}\text{Hf}_5\text{Sn}_5\text{Si}_1$ and $\text{Ti}_{40}\text{Zr}_{25}\text{Ni}_8\text{Cu}_9\text{Be}_{18}$ BMGs studied in this study, for their different structural nature, the deformation behavior in the supercooled liquid region may be different. Especially for $\text{Ti}_{40}\text{Zr}_{25}\text{Ni}_8\text{Cu}_9\text{Be}_{18}$ BMG, as a margin metallic glass, its thermal instability may lead to a different plastic deformation at elevated temperature compared with other typical metallic glasses.

In this chapter, the deformation behavior of Ti-based BMGs with significant different nature in the supercooled liquid region will be investigated in detail from the following aspects:

- (1) Characteristic and mechanism of high-temperature deformation of Ti-based BMGs will be reported as a function of stress (σ), strain rate ($\dot{\epsilon}$), temperature (T), phase/microstructure (Ω), and corresponding viscosity (η), namely, $f(\sigma, \dot{\epsilon}, T, \Omega, \eta)$, and will compare with other typical BMGs;
- (2) The effects of deformation (stress) on the structural changes will be investigated under the conditions of Newtonian flow and non-Newtonian flow deformation, to clarify the correlation between the effect of deformation on the structural changes and the viscosity flow mode, and give a possible explanation in terms of the structure of the primary phase;
- (3) A systemic and effective way to optimize the processing conditions will be proposed, and the hot workability will be evaluated, based on the homogeneous deformation behavior investigation combined with the systemic investigation on the thermal stability, microstructure and mechanical properties for the as-cast and deformed samples.

7.2 Experiment

The compressive tests were performed to investigate the deformation behavior of $\text{Ti}_{41.5}\text{Cu}_{37.5}\text{Ni}_{7.5}\text{Zr}_{2.5}\text{Hf}_5\text{Sn}_5\text{Si}_1$ and $\text{Ti}_{40}\text{Zr}_{25}\text{Ni}_8\text{Cu}_9\text{Be}_{18}$ BMGs at elevated temperature.

The compressive test samples with 2 mm in diameter and 4 mm in length were sliced directly from the as-cast rods. Two ends of the samples were ground and polished to ensure the parallelism, and the two end surfaces were perpendicular to the longitudinal axis of the sample, as is to minimize the possible artificial effect caused by sample misalignment. BN powder was used as lubricant to minimize friction between test samples and the compression platform.

The compressive tests were conducted using an MTS 4M testing machine which was equipped with a high temperature heating furnace capable of maintaining a temperature fluctuation within ± 0.5 °C without any protection of the inert gases, to investigate the deformation behavior of the $\text{Ti}_{41.5}\text{Cu}_{37.5}\text{Ni}_{7.5}\text{Zr}_{2.5}\text{Hf}_5\text{Sn}_5\text{Si}_1$ and $\text{Ti}_{40}\text{Zr}_{25}\text{Ni}_8\text{Cu}_9\text{Be}_{18}$ BMGs at elevated temperature. Fig. 7-3 shows the apparatus used for high-temperature compressive testing. The test samples were inserted between two die-plates in the machine, and heated up to the temperature of 20 K below the testing temperature at a heating rate of 20 K/min followed by a continuous heating to the testing temperature at a heating rate of 10 K/min, and then maintained for ~5 min at the testing temperature for thermal equilibration prior to the beginning of the compressive test. After the completion of each test, the sample was immediately moved out and cooled by water to maintain the structure of the compressed sample. Two types of compressive tests were carried out: (i) constant strain rate testing at constant temperature, and (ii) strain-rate-change (SRC) testing (where the change in flow stress brought about by a change in strain rate is recorded) at constant temperature. In this work, the samples were repeated up twice with each testing condition for consistency.

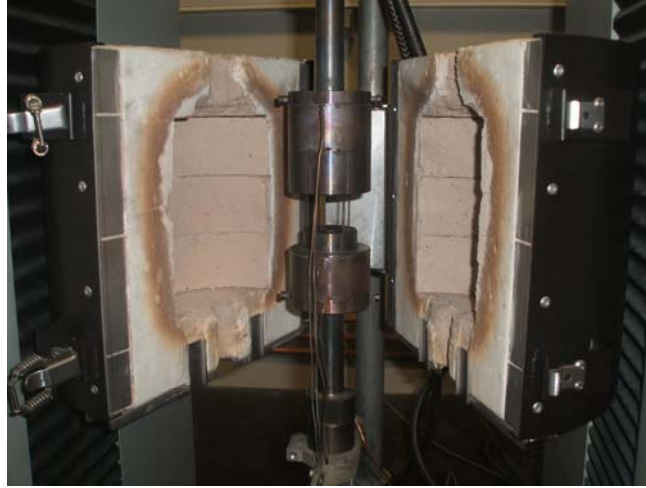


Fig. 7-3 The apparatus used for high-temperature compressive testing

1. Characteristic of deformation behavior at elevated temperature

For $\text{Ti}_{41.5}\text{Cu}_{37.5}\text{Ni}_{7.5}\text{Zr}_{2.5}\text{Hf}_5\text{Sn}_5\text{Si}_1$ BMG, in order to study the effects of temperature, constant strain rate ($5 \times 10^{-4} \text{ s}^{-1}$) compressive tests were conducted at temperatures of 392, 412, 422, 432 and 440 °C; while in order to study the effects of strain rate, the samples were compressed at 440 °C with different strain rates of 2.5×10^{-4} , 5×10^{-4} , 1×10^{-3} and $8 \times 10^{-3} \text{ s}^{-1}$.

2. Plastic flow regime in the supercooled liquid region

A strain-rate-change method was used to determine the strain-rate sensitivity value m which is determined based on the equation of $\sigma = K\dot{\epsilon}^m$ by measuring the change in flow stress σ brought about by a change in strain rate $\dot{\epsilon}$, finally to clarify the plastic flow regime in the supercooled liquid region. SRC test is an effective way in order to get more information from one test. However, it should be pointed out that the selection of strain rate as well as the duration (or strain interval) for each strain rate is important to realize the SRC test, the SRC test should be completed in a possible short time because the crystallization during the deformation in the supercooled liquid region is thermal and mechanical controlled which should be avoided during the SRC test. The time-temperature-transformation (TTT) curve (Fig. 7-4) obtained from the isothermal crystallization analysis of the $\text{Ti}_{41.5}\text{Cu}_{37.5}\text{Ni}_{7.5}\text{Zr}_{2.5}\text{Hf}_5\text{Sn}_5\text{Si}_1$ BMG demonstrated that the incubation period for isothermal crystallization can provide a large time scale for conducting the SRC deformation test. According to the TTT curve, the SRC testing condition was determined and summarized in Table 7-2. The last step is used to check if the deformation is accompanied by crystallization. During the compressive testing, dynamic crystallization was characterized by an eventual increase in the flow stress from a low steady-state value with increasing strain.

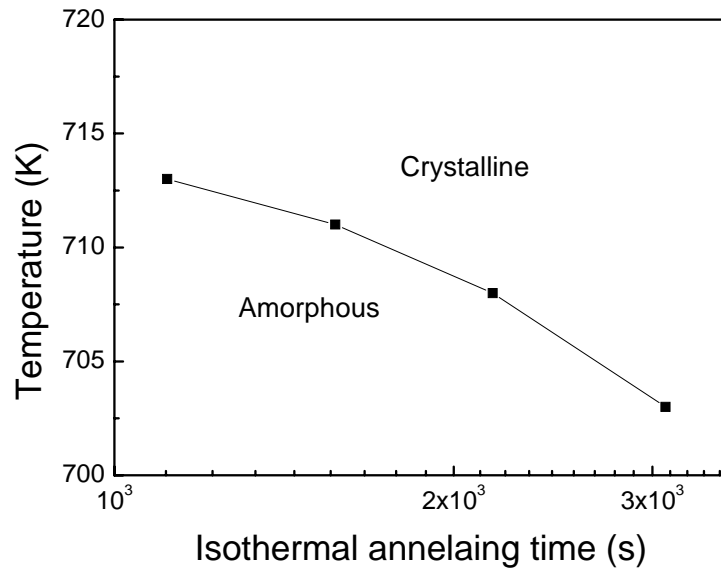


Fig. 7-4 Time-temperature-transformation curve for the $\text{Ti}_{41.5}\text{Cu}_{37.5}\text{Ni}_{7.5}\text{Zr}_{2.5}\text{Hf}_5\text{Sn}_5\text{Si}_1$ BMG determined by using a rod with a 2 mm diameter

Table 7-2

Testing condition for SRC tests for $\text{Ti}_{41.5}\text{Cu}_{37.5}\text{Ni}_{7.5}\text{Zr}_{2.5}\text{Hf}_5\text{Sn}_5\text{Si}_1$ BMG at temperatures of 430-450 °C in increments of 5 K

Temperature (°C)	Step 1 $\dot{\epsilon}$ ($\times 10^{-4}$ s^{-1})	Step 2 $\dot{\epsilon}$ ($\times 10^{-4}$ s^{-1})	Step 3 $\dot{\epsilon}$ ($\times 10^{-4}$ s^{-1})	Step 4 $\dot{\epsilon}$ ($\times 10^{-4}$ s^{-1})	Step 5 $\dot{\epsilon}$ ($\times 10^{-4}$ s^{-1})	Step 6 $\dot{\epsilon}$ ($\times 10^{-4}$ s^{-1})	Step 7 $\dot{\epsilon}$ ($\times 10^{-4}$ s^{-1})	Time (exclude the last step) (s)
430	1	2.5	5	10	20	40	5	1291
435	2.5	5	10	20	40	5		545
440	2.5	5	10	20	40	5		666
445	2.5	5	10	20	40	5		497
450	2.5	5	10	20	40	5		301

Temperature (°C)	Step 1 ϵ	Step 2 ϵ	Step 3 ϵ	Step 4 ϵ	Step 5 ϵ	Step 6 ϵ	Step 7 ϵ	Time (exclude the last step) (s)
430	0.063	0.07	0.117	0.08	0.08	0.11	0.14	1291
435	0.058	0.073	0.104	0.09	0.075	0.4		545
440	0.095	0.06	0.08	0.112	0.123	0.078		666
445	0.063	0.055	0.058	0.09	0.13	0.05		497
450	0.03	0.046	0.037	0.055	0.1	0.04		301

7.3 Characteristics of High-temperature Deformation of Ti-based BMGs

Since the characteristics and mechanism of high-temperature deformation of BMGs is a function of stress (σ), strain rate ($\dot{\epsilon}$), temperature (T), phase/microstructure (Ω), and corresponding viscosity (η), the characteristics of high-temperature deformation of Ti-based BMGs in this study will be discussed based on the effects of the above five parameters on the deformation.

7.3.1 $\text{Ti}_{41.5}\text{Cu}_{37.5}\text{Ni}_{7.5}\text{Zr}_{2.5}\text{Hf}_5\text{Sn}_5\text{Si}_1$ BMG

The high-temperature deformation behavior was investigated as the function of temperature and strain rate. Fig. 7-5 and Fig. 7-6 show the compressive true stress-strain (σ - ϵ) curves of $\text{Ti}_{41.5}\text{Cu}_{37.5}\text{Ni}_{7.5}\text{Zr}_{2.5}\text{Hf}_5\text{Sn}_5\text{Si}_1$ BMG obtained at a constant strain rate of $5 \times 10^{-4} \text{ s}^{-1}$ for various temperatures ranging from 392 to 440 °C and at temperature of 440 °C for different strain rates ranging from 2.5×10^{-4} to $8 \times 10^{-3} \text{ s}^{-1}$, respectively. It is found that, similar with typical metallic glasses, its high-temperature deformation behavior was highly temperature and strain rate dependent. Two typical σ - ϵ curves can be observed: first, at low deformation temperatures (below T_g) or high strain rates ($> 1 \times 10^{-3} \text{ s}^{-1}$), the stress overshoot and yield drop phenomena can be observed followed by a large plastic deformation at low steady-state flow with a stress plateau, and the stress-overshoot peak increased gradually along with decrease in temperature and increase in strain rate; second, the increase in test temperature to T_g as well as the decrease in strain rate to $1 \times 10^{-3} \text{ s}^{-1}$ causes a drastic decrease in the steady state plastic flow stress without stress overshoot and yield drop phenomena, for example, from 591 MPa at 412 °C, decreases to 185 MPa at T_g . In addition, after a long time deformation, a gradual increase in stress in the later stage of deformation was observed, which was verified by XRD and believed to be associated with the concurrent formation of nanocrystals in the amorphous matrix in the extended process of deformation. However, a typical linear type of σ - ϵ curve with a brittle fracture at a maximum stress has not been observed due to the load limitation of the MTS 4M testing machine on which the maximum stress was controlled within 800 MPa in this study. Furthermore, a large plastic deformation ($\epsilon \approx 1.0$) can be reached without any strain hardening. It should be pointed out that even the sample deformed at the high temperature of 440 °C with a low strain rate of $5 \times 10^{-4} \text{ s}^{-1}$ (may be close to Newtonian flow), the plastic deformation can reach 0.8, indicating the excellent compressibility of this alloy.

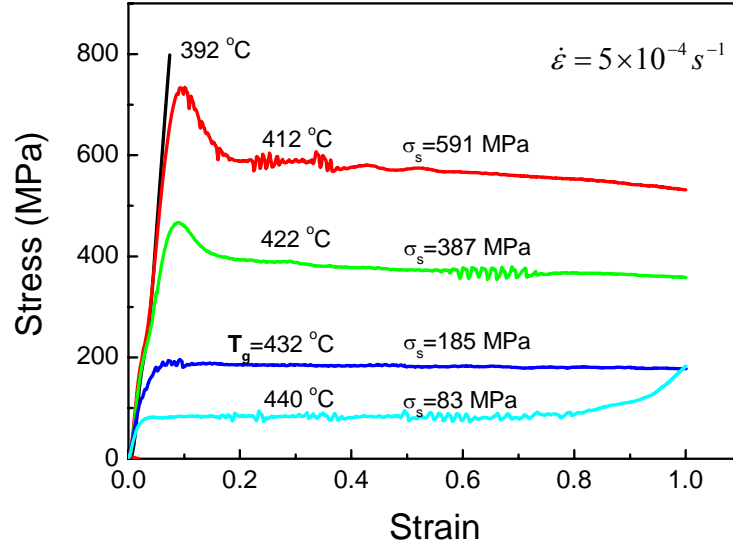


Fig. 7-5 Flow stress vs. strain for different temperatures of 392-440 °C at constant strain rate of $5 \times 10^{-4} \text{ s}^{-1}$ for $\text{Ti}_{41.5}\text{Cu}_{37.5}\text{Ni}_{7.5}\text{Zr}_{2.5}\text{Hf}_5\text{Sn}_5\text{Si}_1$ BMG

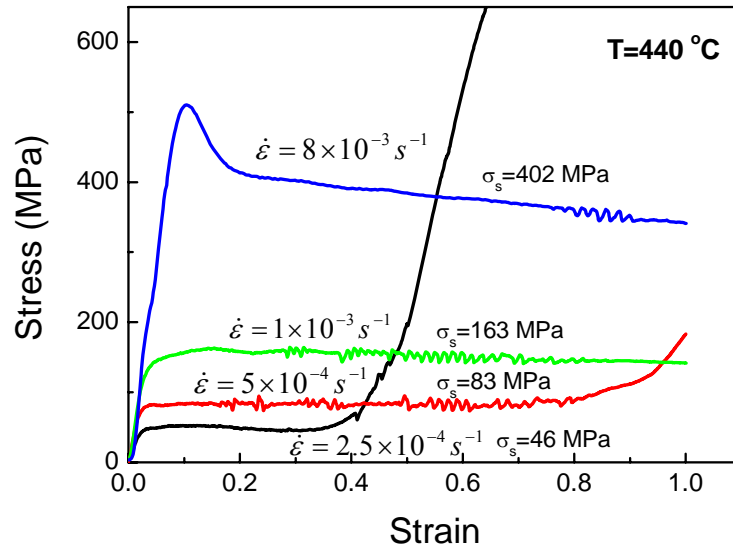


Fig. 7-6 Flow stress vs. strain for different strain rates of 2.5×10^{-4} - $8 \times 10^{-3} \text{ s}^{-1}$ at 440 °C for $\text{Ti}_{41.5}\text{Cu}_{37.5}\text{Ni}_{7.5}\text{Zr}_{2.5}\text{Hf}_5\text{Sn}_5\text{Si}_1$ BMG

Fig. 7-7 displays the macrographs of the $\text{Ti}_{41.5}\text{Cu}_{37.5}\text{Ni}_{7.5}\text{Zr}_{2.5}\text{Hf}_5\text{Sn}_5\text{Si}_1$ metallic glass samples before and after compressive testing at different temperatures of 430, 435 and 440 °C. It is found that the surface of post-deformed samples becomes brown-black, as could be attributed to the oxidation formed on the surface of the samples in the experimental temperature range without the protection of inert gases. It can be seen that all samples exhibited significant plastic deformation. Especially for the sample deformed at 435 °C which exhibits good compressive ability, it shows the characteristic of homogeneous deformation where each volume element of the material undergoes the same strain (see Fig. 7-7 (b)). However, homogeneous deformation only occurred at temperatures higher than 430 °C; when the deformation temperature was slightly below T_g , plastic deformation started to deviate from the homogeneous deformation with the characteristic of shear deformation (deformation mode is probably a mixture of inhomogeneous plus homogeneous

deformation) (see Fig. 7-7 (a)). When the sample was subjected to a long time deformation at high temperature, the post-deformed samples was cracked due to the strain hardening (see Fig. 7-7 (c)). Homogenous deformation only occurred at high temperature and low strain rate.

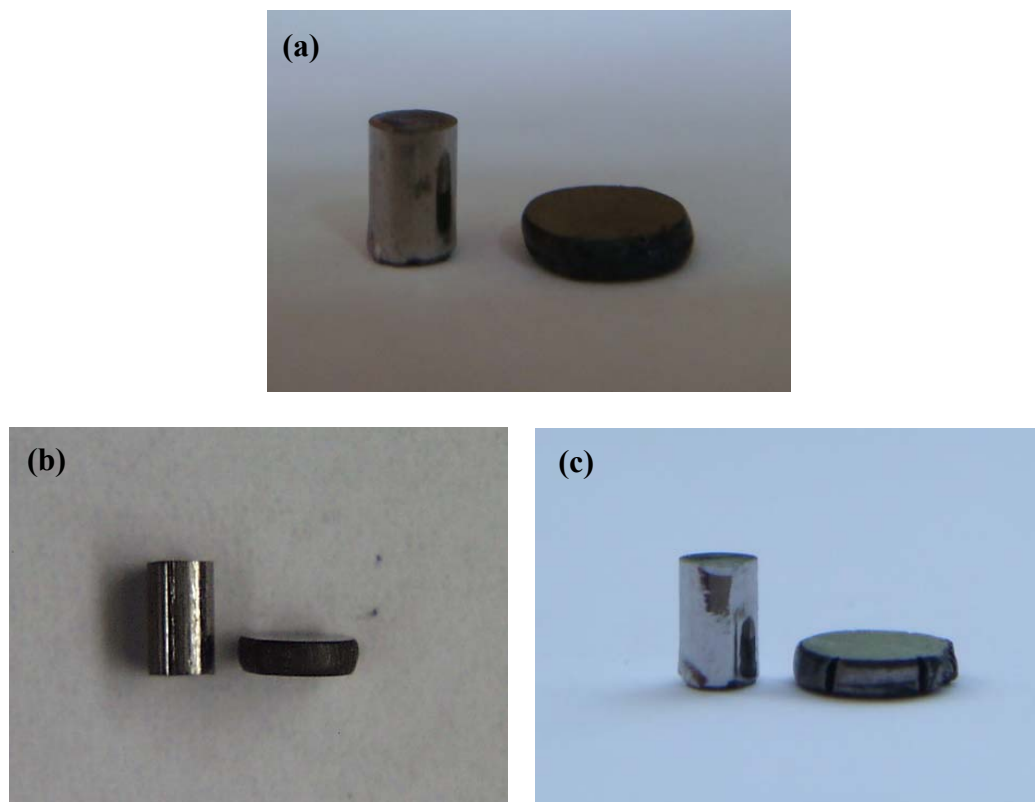


Fig. 7-7 Edge views of $\text{Ti}_{41.5}\text{Cu}_{37.5}\text{Ni}_{7.5}\text{Zr}_{2.5}\text{Hf}_5\text{Sn}_5\text{Si}_1$ BMG samples before (left) and after (right) compressive deformation at (a) 430 °C, (b) 435 °C and (c) 440 °C

The temperature and strain rate dependence on the deformation behavior has been well known through the investigation above, and the effects of temperature on the crystallization are also clear through the isothermal crystallization kinetics analysis in chapter 4; however, the effects of strain rate on the crystallization is still unclear. In this study, the effects of strain rate on the crystallization were investigated by comparing the compressive deformation stress-strain curves of the two samples deformed at 430 °C with two strain rates of 2.5×10^{-4} and $5 \times 10^{-4} \text{ s}^{-1}$. It should be pointed out that the as-cast samples were annealed for 1 h before loading in order to shorten the compressive displacement. Fig. 7-8 displays the corresponding σ - ϵ curves. Assuming the tangential point of the steady-state flow deformation stage and the following strain hardening stage represents the onset of crystallization, it can be seen that the incubation time is consistent to be 27 min for these two conditions, indicating that the crystallization is independent on the strain rate. Based on the above investigation we can deduce that the deformation behavior is independent on the strain rate applying history. This can be verified by the following experiment.

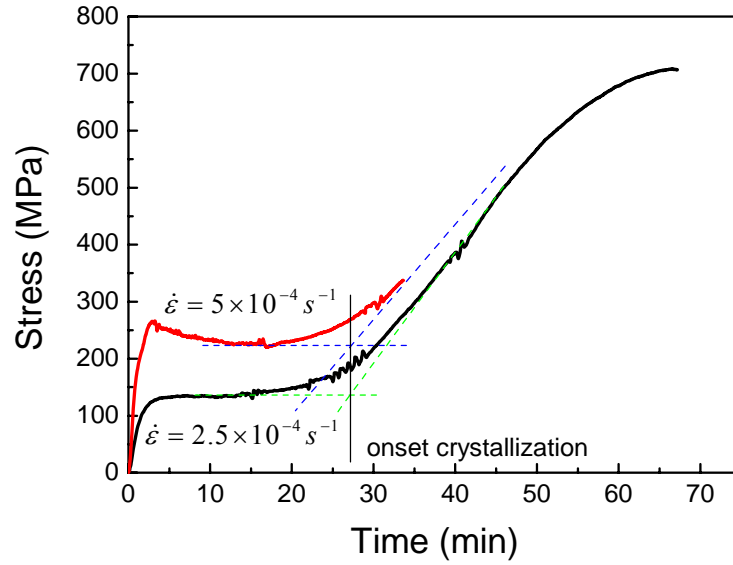


Fig. 7-8 Compressive stress-strain curves obtained from the samples deformed at 430 °C with the strain rates of 2.5×10^{-4} and $5 \times 10^{-4} \text{ s}^{-1}$, before loading, the samples were annealed for 1 h

Fig. 7-9 presents the σ - ϵ curve obtained from the strain-rate change test at 430 °C with successively increasing and decreasing steps. In addition, a constant strain rate testing was also performed and compared with the strain-rate change σ - ϵ curve. It can be seen that when the strain rate decreases finally to $5 \times 10^{-4} \text{ s}^{-1}$ after several jumps, the stress reaches the same level as that measured for the sample continuously deformed at this constant strain rate, indicating that the steady-state flow stress is not dependent on the strain-rate applying history (past mechanical history). This finding is the base of the strain-rate change testing.

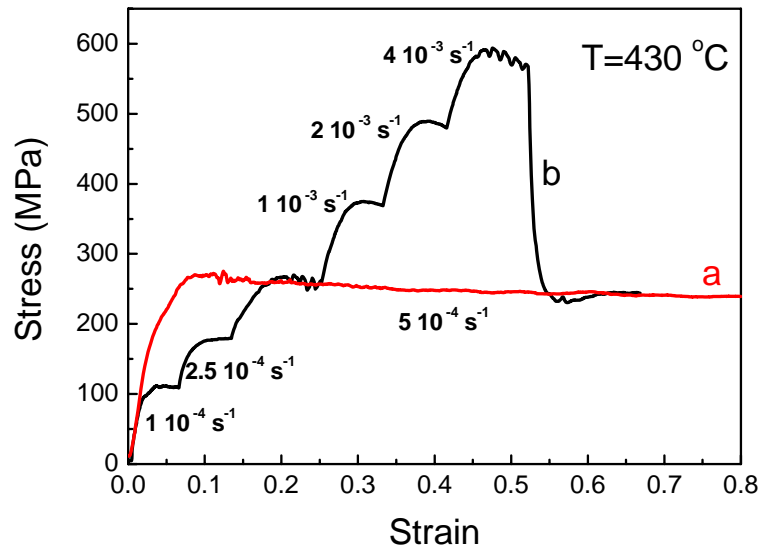


Fig. 7-9 Stress-strain curves obtained from constant strain rate of $5 \times 10^{-4} \text{ s}^{-1}$ (curve a) and strain-rate jump (curve b) compressive measurements at 430 °C for $\text{Ti}_{41.5}\text{Cu}_{37.5}\text{Ni}_{7.5}\text{Zr}_{2.5}\text{Hf}_5\text{Sn}_5\text{Si}_1$ BMG

7.3.2 Ti₄₀Zr₂₅Ni₈Cu₉Be₁₈ BMG

It has been referenced for various BMGs that an increase in stress is caused by the temperature-time induced crystallization, which can be verified through the analysis of the relation between true stress-testing time (σ - t) curve and T-T-T diagram combined with the XRD and TEM observations. The presence of nanocrystalline phases is expected to increase the viscosity according to the equation [Waniuk et al., 1998]

$$\eta_{eff} = \eta(1 + 2.5V_f) \quad (7-2)$$

where η_{eff} is the viscosity of the mixture, η is the viscosity of the surrounding medium, and V_f is the volume fraction of particles. According to the Eq. 7-2, the viscosity of the deformed alloy increases with increasing the crystal fraction, thus the strength and strain hardening are promoted due to primary crystallization of the glassy matrix. This conclusion also can be obtained in this study that crystallization occurred apparently at strains after the steady-state stress plateau for the compressive sample deformed at 440 °C with the constant strain rate of $2.5 \times 10^{-4} \text{ s}^{-1}$. This finding reminds us that the deformation behavior as well as deformability is associated with the microstructure, especially for metallic glasses, it is associated with the microstructure changes caused by thermal instability. The Ti₄₀Zr₂₅Ni₈Cu₉Be₁₈ BMG, as a margin alloy, may exhibit special deformation behavior due to its thermal instability, so the effects of microstructure evolution upon heating should be taken into account in the analysis of high-temperature deformation behavior of Ti₄₀Zr₂₅Ni₈Cu₉Be₁₈ BMG.

Significantly different characteristics of the high-temperature deformation of Ti₄₀Zr₂₅Ni₈Cu₉Be₁₈ BMG can be observed in Fig. 7-10. Three characteristics of the deformation of this alloy in the supercooled liquid region can be summarized as: (i) an initial rapid hardening followed by a gradual increase in flow stress was found in the supercooled liquid region; (ii) further observation on the stress-strain curves, we can see that actually there exists a short-time steady-state plateau before the gradual increase in stress (strain hardening), and the steady-state stress is almost deformation temperature independent which keeps a high constant value of 620 MPa at relatively high deformation temperature compared with T_g (340 -360 °C); however, at lower temperature near T_g (314 °C), the steady-state stress may be higher than 620 MPa (within the limitation of the maximum load of the testing machine, the stress-strain curve at 314 °C did not reach the steady-state stress stage yet until unloading); (iii) it is also found that the strain hardening rate for Ti₄₀Zr₂₅Ni₈Cu₉Be₁₈ BMG is much more sluggish than Ti_{41.5}Cu_{37.5}Ni_{7.5}Zr_{2.5}Hf₅Sn₅Si₁ BMG. According to the above analysis of crystalline phases in the BMGs on the deformation behavior, such a serial of phenomena are believed to be associated with the thermal instability upon heating of Ti₄₀Zr₂₅Ni₈Cu₉Be₁₈ BMG for the structural nature of quenched-in nuclei.

These findings can be well explained combined with the crystallization analysis: (i) since the grain size of the crystals is limited to nanoscale in the Ti₄₀Zr₂₅Ni₈Cu₉Be₁₈ BMG at the beginning stage of the deformation (crystallization), it is expected to behave like ordinary fine crystalline grains during mechanical deformation. This would be similar to the case of conventional superplastic deformation occurring in fine-grained materials [Chiang et al., 2004]. That is the reason why a short-time steady-state plateau occurred before the strain hardening stage. (ii) in regard to why the stress is temperature independent, inconsistent with the general rule of the

inverse proportional temperature dependence, this can also be well understood based on the microstructure evolution analysis at different temperature. Since the grain growth rate is sensitive to the temperature, and that the high growth rate can be obtained at higher temperature, leading to larger grain size for the samples deformed at higher temperature, finally leading to the increase in volume fraction of crystals. So the larger volume fraction of the crystals in the $\text{Ti}_{40}\text{Zr}_{25}\text{Ni}_8\text{Cu}_9\text{Be}_{18}$ BMG at higher temperature results in the increase in viscosity and accordingly enhancing the strength. That is the reason why there exists no temperature dependence of the steady-state stress. (iii) the sluggish strain hardening for this alloy can confirm the sluggish grain growth process, as has been verified in the crystallization analysis in chapter 4.

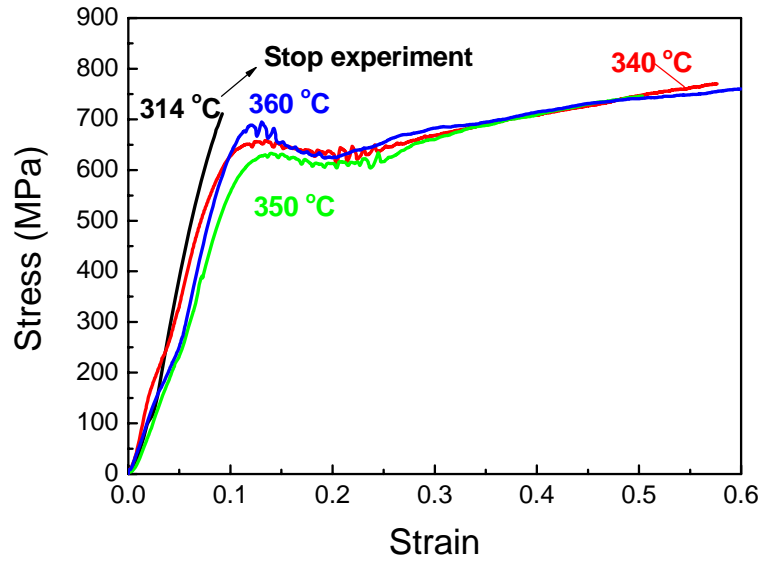


Fig. 7-10 Compressive stress-strain curves obtained from as-cast $\text{Ti}_{40}\text{Zr}_{25}\text{Ni}_8\text{Cu}_9\text{Be}_{18}$ BMG deformed at various temperatures of 314-360 °C at a constant strain rate of $2.5 \times 10^{-4} \text{ s}^{-1}$

7.4 Rheology Behavior of $\text{Ti}_{41.5}\text{Cu}_{37.5}\text{Ni}_{7.5}\text{Zr}_{2.5}\text{Hf}_5\text{Sn}_5\text{Si}_1$ BMG Deformed in the SLR

The transition behavior and mechanism from Newtonian flow to non-Newtonian flow during the homogeneous deformation of metallic glasses are attractive to be investigated due to their practical significance for guiding the net-shape forming technique in addition to their scientific significance. In this section, the mechanism of homogeneous plastic deformation for $\text{Ti}_{41.5}\text{Cu}_{37.5}\text{Ni}_{7.5}\text{Zr}_{2.5}\text{Hf}_5\text{Sn}_5\text{Si}_1$ BMG was discussed in terms of the transition state theory based on the free volume as well as the stretched exponential function.

7.4.1 Transition from Newtonian Flow to Non-Newtonian Flow

The strain-rate change method was performed to obtain the stress-strain curves with various strain rates at various temperatures. In order to minimize the experimental error, the deformed samples were sliced from the same rod. Fig. 7-12 depicts the logarithmic relationship between the

compressive flow stress vs. strain rate at various temperatures of 430, 435, 440, 445 and 450 °C for the $\text{Ti}_{41.5}\text{Cu}_{37.5}\text{Ni}_{7.5}\text{Zr}_{2.5}\text{Hf}_5\text{Sn}_5\text{Si}_1$ BMG. The flow stress was determined based on the method proposed by Kawamura [Kawamura et al., 1996]. It can be seen that the flow stress increased monotonously with the increase of strain rate and the decrease of temperature, as is in accordance with the results of the compressive testing at a constant strain rate. The curves exhibit a sigmoidal-like shape at low temperatures, and the sigmoidal-like shape gradually changes into a nearly straight line at high temperatures, e.g. 450 °C. It is well known that the slope reflects the value of the strain rate sensitivity, m , according to the definition of $m = \partial \log \sigma_{\text{flow}} / \partial \log \dot{\epsilon}$. The calculated strain rate sensitivities as a function of strain rate at various temperatures are displayed in Fig. 7-13. At low temperature, the m shows a small value and considerably decreases with increase in strain rate, for example, at 430 °C, the value of strain rate sensitivity decreases from 0.57 at strain rate of $2.5 \times 10^{-4} \text{ s}^{-1}$ to 0.28 at strain rate of $4 \times 10^{-3} \text{ s}^{-1}$; while at high temperature ($>440 \text{ °C}$), the m exhibits high value, especially at low strain rate, it was measured to be larger than 0.8 being close to 1, for example, at 450 °C, the value of strain rate sensitivity is approximately 0.97 at low strain rate, and even when the strain rate is as high as $4 \times 10^{-3} \text{ s}^{-1}$, m still keeps a high level of 0.8. The value of m being close to unity implies that Newtonian viscous flow governs the plastic flow for the BMG deformed in the low strain rate regime, while the value of m significantly deviating from the unity indicates that the deformation of the BMG follows a non-Newtonian flow in the high strain rate regime. Accordingly, the high m value (>0.8) exists only within a narrow strain rate range for a certain temperature. There must exist a critical strain rate, $\dot{\epsilon}_c$, at a certain deformation temperature, where the Newtonian flow transforms to the non-Newtonian flow, and the $\dot{\epsilon}_c$ shifts to a high value as the increase of temperature. Detailed analysis on the transition from Newtonian flow to non-Newtonian flow will be presented in the following part based on the viscosity analysis.

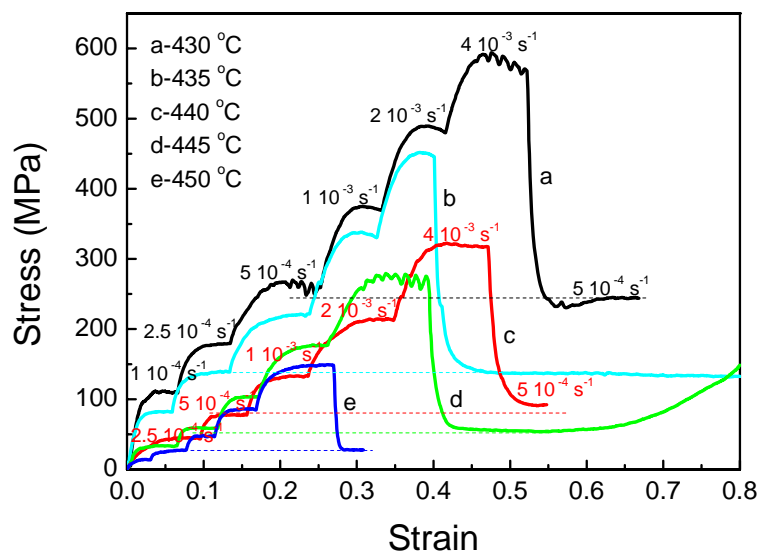


Fig. 7-11 Stress-strain curves obtained from the strain-rate jump test at the temperature range of 430-450 °C for $\text{Ti}_{41.5}\text{Cu}_{37.5}\text{Ni}_{7.5}\text{Zr}_{2.5}\text{Hf}_5\text{Sn}_5\text{Si}_1$ BMG

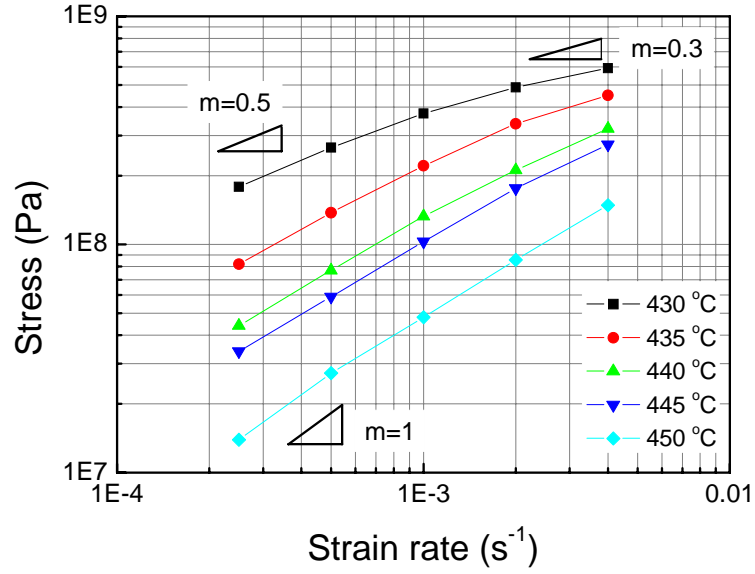


Fig. 7-12 The logarithmic relationship between the compressive flow stress and the strain rate at various temperatures of 430-450 °C for $\text{Ti}_{41.5}\text{Cu}_{37.5}\text{Ni}_{7.5}\text{Zr}_{2.5}\text{Hf}_5\text{Sn}_5\text{Si}_1$ BMG

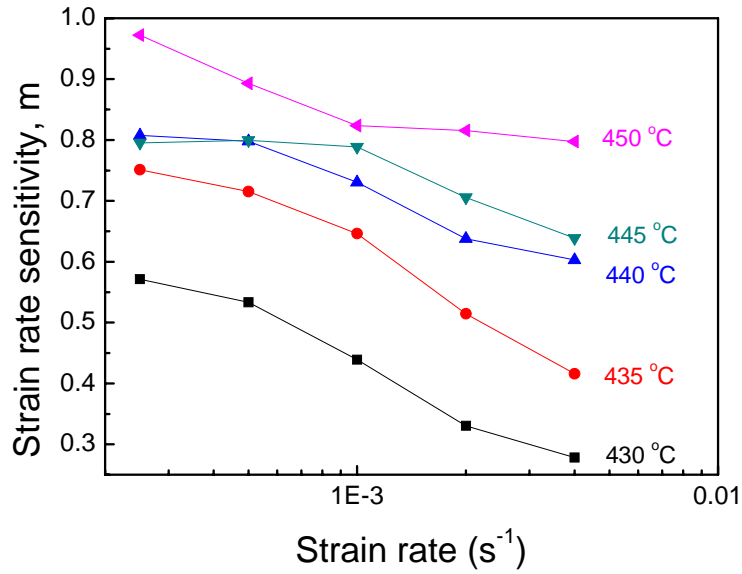


Fig. 7-13 Variation of strain rate sensitivity (m) with strain-rate for $\text{Ti}_{41.5}\text{Cu}_{37.5}\text{Ni}_{7.5}\text{Zr}_{2.5}\text{Hf}_5\text{Sn}_5\text{Si}_1$ BMG deformed at 430-450 °C

To further elucidate the strain rate effect, a plot of the apparent viscosity, calculated based on the equation of [Kawamura et al., 1998]

$$\eta_{app} = \sigma_{flow} / 3\dot{\epsilon} \quad (7-3)$$

where σ_{flow} is the deviatoric stress in the uniaxial test; $\dot{\epsilon}$ is the corresponding strain rate, is shown in Fig. 7-14 as a function of measured strain rate in the temperature range of 430-450 °C, which can characterize the rheologic behavior of the BMG alloy over the range of viscosities and strain rates as shown. Newtonian flow has the simplest constitutive behavior, in which the strain

rate is directly proportional to the stress, while the non-Newtonian flow responds to shearing stress. It is found that the $\text{Ti}_{41.5}\text{Cu}_{37.5}\text{Ni}_{7.5}\text{Zr}_{2.5}\text{Hf}_5\text{Sn}_5\text{Si}_1$ BMG shows nearly Newtonian behavior with weak strain-rate dependence in viscosity at the low strain rate regime. However, at a high strain rate regime, the viscosity is strongly dependent on the strain rate that rapidly decreases as the strain rate increases, demonstrating a non-Newtonian flow at the high strain rate regime. The above analysis suggests that the deformation of the $\text{Ti}_{41.5}\text{Cu}_{37.5}\text{Ni}_{7.5}\text{Zr}_{2.5}\text{Hf}_5\text{Sn}_5\text{Si}_1$ BMG exhibited a transition from Newtonian flow to non-Newtonian flow as the strain rate increases. It seems to be a general phenomenon for BMGs deformed in the supercooled liquid region that has been found in many BMG systems, i.e. $\text{Pd}_{40}\text{Ni}_{40}\text{P}_{20}$ [Chu et al., 2002], $\text{Zr}_{52.5}\text{Al}_{10}\text{Cu}_{17.9}\text{Ni}_{14.6}\text{Ti}_5$ [Nieh et al., 2001], $\text{Zr}_{41.5}\text{Ti}_{13.5}\text{Cu}_{12.5}\text{Ni}_{10}\text{Be}_{22.5}$ [Johnson et al., 2002], $\text{Cu}_{60}\text{Zr}_{20}\text{Hf}_{10}\text{Ti}_{10}$ [Chiang et al., 2004] etc.

It is apparent to see that the deformation temperature affects the critical strain rate. At the low temperature of $<440^\circ\text{C}$, a high strain rate leads to a decrease in the viscosity. At $>440^\circ\text{C}$, the negative strain rate dependence of viscosity is weaker in the low strain rate region, showing a transition from Newtonian flow to non-Newtonian flow. It is easy to obtain the Newtonian viscosity, η_N , at high temperature since its Newtonian flow mode at low strain rate. At low temperature, the determination of η_N is not easy, however it can be realized by extrapolation method. For example, the Newtonian viscosities at 450°C , 430°C for $\text{Ti}_{41.5}\text{Cu}_{37.5}\text{Ni}_{7.5}\text{Zr}_{2.5}\text{Hf}_5\text{Sn}_5\text{Si}_1$ BMG are approximately 1.838×10^{10} and 4.02×10^{11} Pa·s, respectively.

In order to investigate the critical strain rate dependence with temperature, namely, determine the critical strain rate, the normalized viscosity, $\tilde{\eta}$, which is defined as $\tilde{\eta} = \eta_f / \eta_N$, was calculated at each temperature and strain rate, which is summarized in Table 7-3. In general, $\dot{\epsilon}_c$ was defined as the intersection of $\eta_f(\dot{\epsilon})$ lines in the low and high $\dot{\epsilon}$ regions. However, the intersection can not easily be located in the viscosity-strain rate curves for the limited experimental data points. Accordingly, one quantitative analysis was introduced: assuming $\tilde{\eta} > 0.9$ corresponds to the Newtonian flow, accordingly, the $\dot{\epsilon}_c$ can be defined as the strain rate at which the normalized viscosity is larger than 0.9 and approaches to 1. It is clear that the value of $\dot{\epsilon}_c$ is located between 5×10^{-4} – $1 \times 10^{-3} \text{ s}^{-1}$ at high temperature of 450°C , then decreases to $2.5 \times 10^{-4} \text{ s}^{-1}$ at 440°C , finally drastically decreases to a strain rate far below $1 \times 10^{-4} \text{ s}^{-1}$ at low temperature of 430°C .

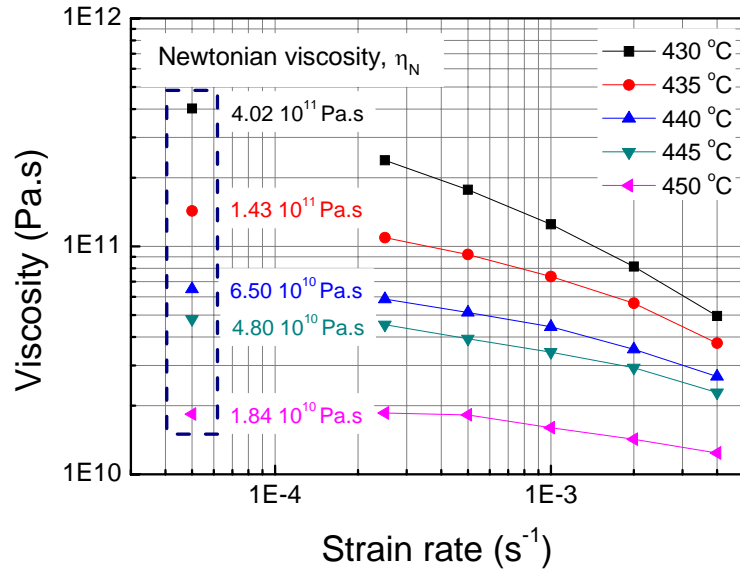


Fig. 7-14 Strain rate dependence of the apparent viscosity at various temperatures of 430-450 °C for $\text{Ti}_{41.5}\text{Cu}_{37.5}\text{Ni}_{7.5}\text{Zr}_{2.5}\text{Hf}_5\text{Sn}_5\text{Si}_1$ BMG

Table 7-3

Newtonian viscosity, η_N and the steady-state flow viscosity, η_f , of $\text{Ti}_{41.5}\text{Cu}_{37.5}\text{Ni}_{7.5}\text{Zr}_{2.5}\text{Hf}_5\text{Sn}_5\text{Si}_1$ samples subjected to various strain rates, $\dot{\epsilon}$, and temperatures, T . (a) 430 °C, (b) 435 °C, (c) 440 °C, (d) 445 °C and (e) 450 °C

(a)

T (°C)	430				
η_N (Pa s)	4.02×10^{11}				
$\dot{\epsilon}$ (s^{-1})	2.5×10^{-4}	5×10^{-4}	1×10^{-3}	2×10^{-3}	4×10^{-3}
η_f (Pa s)	2.39×10^{11}	1.77×10^{11}	1.25×10^{11}	8.15×10^{10}	4.94×10^{10}
$\eta_N \dot{\epsilon}$ (Pa)	1.01×10^8	2.01×10^8	4.02×10^8	8.04×10^8	1.61×10^9
$\tilde{\eta} (= \eta_f / \eta_N)$	0.59	0.44	0.31	0.20	0.12

(b)

T (°C)	435				
η_N (Pa s)	1.43×10^{11}				
$\dot{\epsilon}$ (s^{-1})	2.5×10^{-4}	5×10^{-4}	1×10^{-3}	2×10^{-3}	4×10^{-3}
η_f (Pa s)	1.09×10^{11}	9.20×10^{10}	7.37×10^{10}	5.63×10^{10}	3.76×10^{10}
$\eta_N \dot{\epsilon}$ (Pa)	3.58×10^7	7.15×10^7	1.43×10^8	2.86×10^8	5.72×10^8
$\tilde{\eta} (= \eta_f / \eta_N)$	0.76	0.64	0.52	0.39	0.26

(c)

T (°C)	440				
η_N (Pa s)	6.5×10^{10}				
$\dot{\epsilon}$ (s ⁻¹)	2.5×10^{-4}	5×10^{-4}	1×10^{-3}	2×10^{-3}	4×10^{-3}
η_f (Pa s)	5.87×10^{10}	5.13×10^{10}	4.43×10^{10}	3.53×10^{10}	2.68×10^{10}
$\eta_N \dot{\epsilon}$ (Pa)	1.63×10^7	3.25×10^7	6.5×10^7	1.30×10^8	2.60×10^8
$\tilde{\eta}(=\eta_f/\eta_N)$	0.90	0.79	0.70	0.54	0.41

(d)

T (°C)	445				
η_N (Pa s)	4.8×10^{10}				
$\dot{\epsilon}$ (s ⁻¹)	2.5×10^{-4}	5×10^{-4}	1×10^{-3}	2×10^{-3}	4×10^{-3}
η_f (Pa s)	4.53×10^{10}	3.93×10^{10}	3.43×10^{10}	2.93×10^{10}	2.28×10^{10}
$\eta_N \dot{\epsilon}$ (Pa)	1.20×10^7	2.40×10^7	4.80×10^7	9.60×10^7	1.92×10^8
$\tilde{\eta}(=\eta_f/\eta_N)$	0.94	0.82	0.71	0.61	0.48

(e)

T (°C)	450				
η_N (Pa s)	1.838×10^{10}				
$\dot{\epsilon}$ (s ⁻¹)	2.5×10^{-4}	5×10^{-4}	1×10^{-3}	2×10^{-3}	4×10^{-3}
η_f (Pa s)	1.84×10^{10}	1.82×10^{10}	1.60×10^{10}	1.43×10^{10}	1.24×10^{10}
$\eta_N \dot{\epsilon}$ (Pa)	4.60×10^6	9.19×10^6	1.84×10^7	3.68×10^7	7.35×10^7
$\tilde{\eta}(=\eta_f/\eta_N)$	1.00	0.99	0.87	0.78	0.67

The apparent activation energy of deformation, Q_{app} , can be calculated according to the Arrhenius equation:

$$\eta_N = \eta_0 \exp\left(\frac{Q_{app}}{kT}\right) \quad (7-4)$$

where η_0 is a constant, Q_{app} represents the apparent activation energy. The apparent activation energy of deformation for $\text{Ti}_{41.5}\text{Cu}_{37.5}\text{Ni}_{7.5}\text{Zr}_{2.5}\text{Hf}_5\text{Sn}_5\text{Si}_1$ BMG was obtained to be 6.4 eV by linear fitting the $\ln \eta_N - 1/T$ plot (Fig. 7-15), which is much larger than $\text{Pd}_{40}\text{Ni}_{10}\text{Cu}_{30}\text{P}_{20}$, $\text{Zr}_{41.2}\text{Ti}_{13.8}\text{Cu}_{12.5}\text{Ni}_{10}\text{Be}_{22.5}$, $\text{Mg}_{65}\text{Cu}_{25}\text{Gd}_{10}$, $\text{Mg}_{65}\text{Cu}_{25}\text{Y}_{10}$ etc. typical metallic glasses (Table 7-4). The theoretical explanation for the physical essence of the high value of apparent activation energy for $\text{Ti}_{41.5}\text{Cu}_{37.5}\text{Ni}_{7.5}\text{Zr}_{2.5}\text{Hf}_5\text{Sn}_5\text{Si}_1$ BMG is unclear. As we know, for crystalline materials, Q_{app} is often interpreted as the activation energy for bulk/lattice diffusion of certain species of atoms in the matrix. The value of 6.4 eV for $\text{Ti}_{41.5}\text{Cu}_{37.5}\text{Ni}_{7.5}\text{Zr}_{2.5}\text{Hf}_5\text{Sn}_5\text{Si}_1$ BMG is about more than twice the value for self-diffusion of Ti or Cu (2.00-3.138 eV for Ti, 2.08 eV for Cu [Neumann et al., 2009]) in the crystalline lattice. The high value of Q_{app} frequently reported for

deformation of BMGs in the SCL region is often interpreted as flow occurring by the collective migration of small groups of atoms [Bletry et al., 2004]. On the other hand, taking into account its special composition constituents, it also may result from the large bonding force originating from the electrovalent bond or covalent bond between the nonmetallic element Si and other metallic elements in $\text{Ti}_{41.5}\text{Cu}_{37.5}\text{Ni}_{7.5}\text{Zr}_{2.5}\text{Hf}_5\text{Sn}_5\text{Si}_1$ BMG.

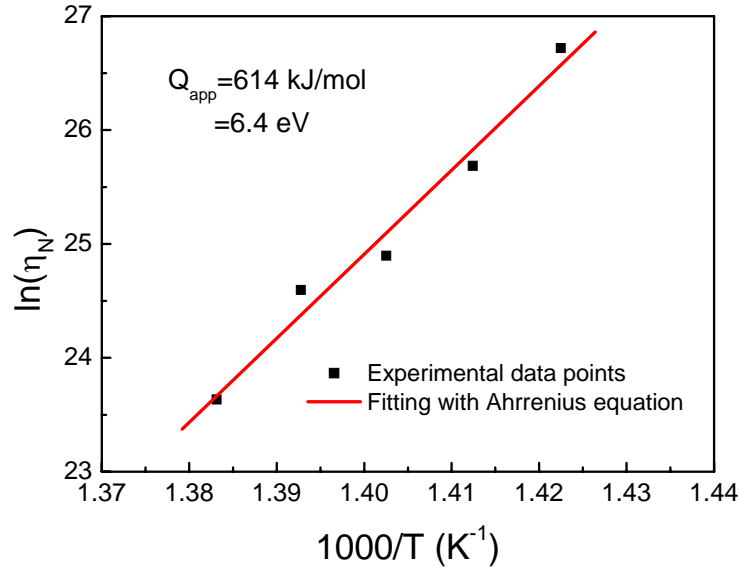


Fig. 7-15 Arrhenius relationship between $\ln(\eta_N)$ and $1/T$ for calculating the apparent activation energy of deformation, Q_{app} , for $\text{Ti}_{41.5}\text{Cu}_{37.5}\text{Ni}_{7.5}\text{Zr}_{2.5}\text{Hf}_5\text{Sn}_5\text{Si}_1$ BMG

Table 7-4

The apparent activation energies for typical metallic glasses

Alloy	Apparent activation energy (eV)	Ref.
$\text{Ti}_{41.5}\text{Cu}_{37.5}\text{Ni}_{7.5}\text{Zr}_{2.5}\text{Hf}_5\text{Sn}_5\text{Si}_1$	6.4	This study
$\text{Pd}_{40}\text{Ni}_{10}\text{Cu}_{30}\text{P}_{20}$	5.0	[Bletry et al., 2004]
$\text{Zr}_{41.2}\text{Ti}_{13.8}\text{Cu}_{12.5}\text{Ni}_{10}\text{Be}_{22.5}$	4.8	[Q. Wang et al., 2005]
$\text{Zr}_{55}\text{Al}_{10}\text{Ni}_5\text{Cu}_{30}$	5.1	[Chen et al., 2001]
$\text{Mg}_{65}\text{Cu}_{25}\text{Gd}_{10}$	3.5	[Puech, 2008]
$\text{Mg}_{65}\text{Cu}_{25}\text{Y}_{10}$	2.9	[Gun et al., 2006]

7.4.2 Analysis on the Transition from Newtonian Flow to Non-Newtonian Flow

The above results show that the deformation behavior of Ti-based BMG in the supercooled liquid region strongly depends on the strain rate and temperature. The alloy exhibited Newtonian-like behavior in the low strain rate regime, then transformed to non-Newtonian behavior in the high strain rate regime. So far, some empirical or theoretical models, e.g. stretched exponential function and transition state theory based on free volume theory [Spaepen, 1977; Argon, 1979; Taub et al., 1981], have been proposed to make a qualitative or quantitative analysis

on the transition from a Newtonian flow to a non-Newtonian flow.

The normalized viscosity, $\tilde{\eta}$, plotted against the product, $\eta_N \dot{\epsilon}$, is shown in Fig. 7-16. A master curve thus can be constructed. It is fitted with the expression

$$\frac{\eta_f}{\eta_N} = 1 - \exp\left[-\left(\frac{B}{\eta_N \dot{\epsilon}}\right)^\beta\right] \quad (7-5)$$

with a Kohlrausch-Williams-Watts stretched exponent $\beta=0.56$ and a constant $B=78$ MPa. The small value of KWW exponent β indicates the large degree of deviation from the Newtonian flow, and the mechanism of plastic deformation is more complex compared with the other typical metallic glasses: $\text{La}_{55}\text{Al}_{25}\text{Ni}_{20}$, $\text{Zr}_{65}\text{Al}_{10}\text{Cu}_{15}\text{Ni}_{10}$, $\text{Zr}_{55}\text{Al}_{10}\text{Ni}_5\text{Cu}_{30}$ and $\text{Zr}_{41.2}\text{Ti}_{13.8}\text{Cu}_{12.5}\text{Ni}_{10}\text{Be}_{22.5}$ etc. whose KWW exponents β are higher than 0.7. Although the mechanical behavior characteristic during the transition from Newtonian flow to non-Newtonian flow can be well described by the stretched exponential function, the physical nature of the deformation mechanisms responsible for the transition from Newtonian flow to non-Newtonian flow is still unclear. Further analysis will be performed in the terms of the well-known transition state theory.

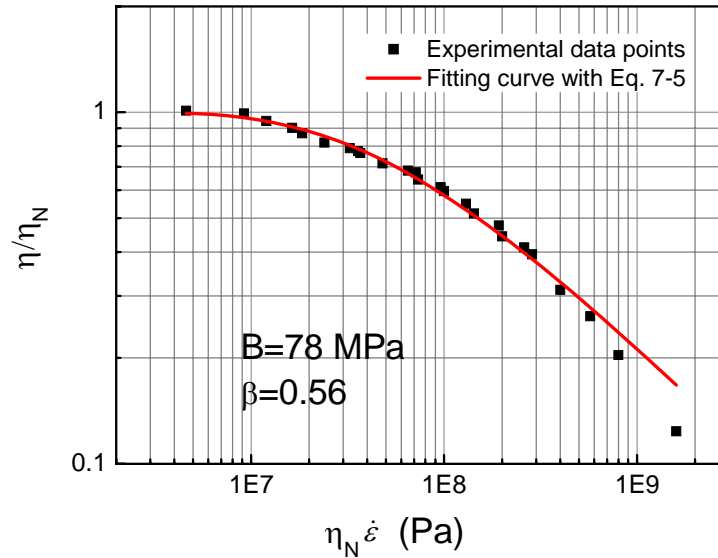


Fig. 7-16 The normalized viscosity, η_f / η_N vs. the product of the Newtonian viscosity and strain rate, $\eta_N \dot{\epsilon}$, at various temperatures of 430, 435, 440, 445 and 450 °C

Transition state theory, which can predict the correlation between strain rate and flow stress of a material and is extensively used to explain the transition from a Newtonian flow to a non-Newtonian flow in various BMGs, is constructed on the basic concept of free volume in an amorphous structure developed initially for liquids by Cohen and Turnbull [Cohen et al., 1959] and extended by Spaepen [Spaepen, 1977] for plastic flow of metallic glasses. Free volume is defined as the excess volume compared to an ideal disordered atomic configuration of maximum density. Based on the free volume theory, the plastic deformation is attributed to uncorrelated atoms jumping into neighboring local large enough holes or flow defects that exceed a critical size, to induce the strain [Spaepen, 1977].

Such so-called flow defects have a concentration c_f given, according to the free volume theory,

by

$$c_f = \exp\left(-\frac{\gamma v^*}{v_f}\right) \quad (7-6)$$

where γ is a geometric factor that corrects the overlap between holes ($0.5 \leq \gamma \leq 1$), v_f is the mean free volume per atom at a given temperature, and v^* is the critical size for which an atomic jump can occur. Spaepen [Spaepen, 1977] suggested describing the plastic flow of metallic glasses in relation to the diffusion of atoms in the glass and the effect of stress on this diffusion. This leads to a relation between the flow stress and the plastic strain rate given by

$$\dot{\epsilon} = 2c_f v_D \exp\left(-\frac{\Delta G^m}{kT}\right) \sinh\left(\frac{\sigma V_{act}}{2\sqrt{3}kT}\right) \quad (7-7)$$

where V_{act} is the activation volume which is equal to the atomic volume if the flow defect is an isolated atom, or a few atomic volumes if several atoms participate in the local flow event.

Uniaxial deformation implies the introduction of the Von Mises factor, $\sqrt{3}$, in the hyperbolic sine term. In this approach, the plastic strain rate results from the product of four terms: the atomic vibration frequency (Debye frequency, v_D), the concentration of defects (c_f), an Arrhenius equation including an activation free energy of flow defect migration (ΔG^m), and an hyperbolic sine term which takes into account the effect of the applied stress on the energy barrier.

If a small variation of the flow defect concentration with strain is assumed, the defect concentration depends only on temperature. Since experiments were carried out in the region of the glass transition, the defect concentration when deformation starts is supposed to be equal to its equilibrium value. In such a framework, Eq. 7-7 can be simplified and rewritten as Eq. 7-8, which is the expression of the transition state theory:

$$\dot{\epsilon} = \dot{\epsilon}_0 \sinh\left(\frac{\sigma V_{act}}{2\sqrt{3}kT}\right) \quad (7-8)$$

where $\dot{\epsilon}_0$ is a frequency factor ($\dot{\epsilon}_0(T) = 2c_f v_D \exp\left(-\frac{\Delta G^m}{kT}\right)$), defined as a measure of the effective number of attempts per unit time to overcome a particular energy barrier, and is expected to be constant at a given temperature. V_{act} and $\dot{\epsilon}_0$ are fitting parameters for fitting the experimental $\dot{\epsilon} - \sigma$ data. The activation volume is the volume of matter involved in each elementary defect jump. In this work, V_{act} is calculated with the value of the peak stress (when there is one) in order to minimize both the variation in defect concentration under a given strain rate and the elastic contribution (at the peak stress, the elastic strain rate $\dot{\sigma}/E = 0$).

Both the activation volume and frequency factor for given deformation temperatures were calculated from fitting the experimental values of peak stresses and strain rates using the Eq. 7-8. Fig. 7-17 shows the good fits of transition state theory model with the experimental results, and the obtained fitting parameters, activation volume V_{act} and the frequency factor $\dot{\epsilon}_0$, are listed in

Table 7-5.

Activation volume V_{act} between 200-299 \AA^3 , and the frequency factor $\dot{\epsilon}_0$ ranging from 1.8×10^{-4} to $2.4 \times 10^{-3} \text{ s}^{-1}$ were obtained depending on various temperatures. It is found that the values of activation volume are higher than the previously reported data for other typical metallic glasses, e.g. $V_{act} \approx 160 \text{ \AA}^3$ for $\text{Zr}_{41.2}\text{Ti}_{13.8}\text{Cu}_{12.5}\text{Ni}_{10}\text{Be}_{22.5}$ BMG [Q. Wang et al., 2005], $V_{act} \approx 120 \text{ \AA}^3$ for $\text{Zr}_{55}\text{Cu}_{30}\text{Al}_{10}\text{Ni}_5$ BMG [Reger-Leonhard et al., 2000] and $V_{act} \approx 200 \text{ \AA}^3$ in the case of $\text{Zr}_{52.5}\text{Al}_{10}\text{Cu}_{22}\text{Ti}_{2.5}\text{Ni}_{13}$ BMG [Bletry et al., 2006], however, are comparable with $V_{act} \approx 280\text{-}380 \text{ \AA}^3$ for $\text{Mg}_{65}\text{Cu}_{25}\text{Gd}_{10}$ BMG [Puech, 2008] and $V_{act} \approx 268\text{-}331 \text{ \AA}^3$ for $\text{Mg}_{65}\text{Cu}_{25}\text{Y}_{10}$ BMG [Gun et al., 2007]. It is known that free volume model postulates that atoms jump from their site into a nearby vacancy-like hole, which implies an activation volume of about one atomic volume [Bletry et al., 2006]. Providing the mean atomic volume of the glass is $\Omega = 13 \text{ \AA}^3$, the measured activation volume concerning high-temperature deformation corresponds to the displacement of 10-30 atoms. This result is indicative of the idea of a cooperative aspect of the diffusion process which takes place during the high-temperature deformation of BMG, similar results are found during the investigation on the mechanism of structural relaxation below the glass transition temperature shown in chapter 4. Bletry et al. [Bletry et al., 2006] also found this phenomenon in $\text{Zr}_{52.5}\text{Al}_{10}\text{Cu}_{22}\text{Ti}_{2.5}\text{Ni}_{13}$ BMG, he reported that atoms do not jump without correlated displacements of their neighbors, and the measured activation volume corresponds to the volume of matter in which atoms are displaced during the elementary shear event, multiplied by the corresponding mean atomic strain. In addition, the higher value of activation volume compared with that of other metallic glasses may suggest the existence of higher defect concentration in $\text{Ti}_{41.5}\text{Cu}_{37.5}\text{Ni}_{7.5}\text{Zr}_{2.5}\text{Hf}_5\text{Sn}_5\text{Si}_1$ BMG which is in favor of an increase in the diffusion constant facilitating the movement of atoms, thus enhancing plastic flow, during the deformation process.

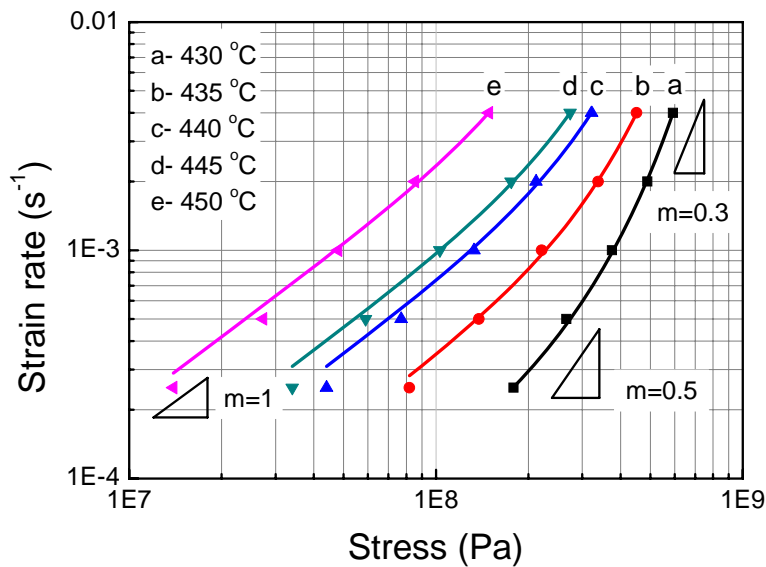


Fig. 7-17 The logarithmic relationship of strain rate vs. compressive flow stress at temperatures ranging of 430-450 °C for $\text{Ti}_{41.5}\text{Cu}_{37.5}\text{Ni}_{7.5}\text{Zr}_{2.5}\text{Hf}_5\text{Sn}_5\text{Si}_1$ BMG, fit of Eq. (7-8) (solid lines) with experimental data points (symbols)

Table 7-5

Activation volume V_{act} and frequency factor $\dot{\epsilon}_0$ obtained from the strain rate-stress curves fitted with Eq. 7-8

$T(^{\circ}\text{C})$	$V_{\text{act}}(\text{\AA}^3)$	$\dot{\epsilon}_0 (\text{s}^{-1})$
430	215.8	0.00018
435	199.8	0.00056
440	209.5	0.00113
445	223.2	0.00139
450	299.0	0.0024

Viscosity can be defined in terms of the free-volume model by combining Eq. 7-3 with Eq. 7-8 to give:

$$\eta = \frac{\sigma}{3\dot{\epsilon}_0 \sinh(\sigma V / 2\sqrt{3}kT)} \quad (7-9)$$

Newtonian viscosity, η_N , is expected at high temperatures and low stresses, thus it can be obtained according to the Eq. 7-9:

$$\eta_N = \frac{2\sqrt{3}kT}{3\dot{\epsilon}_0 V} \quad (7-10)$$

Through a combination of Eqs. 7-9 and 7-10, a viscosity master curve can be derived to gather the variations of the viscosity with strain rate at different temperatures. Based on the work of Bletry et al. [Bletry et al., 2004; Bletry et al., 2006], the normalized viscosity, η/η_N , is given as

$$\frac{\eta}{\eta_N} = \frac{\sigma V / 2\sqrt{3}kT}{\sinh(\sigma V / 2\sqrt{3}kT)} = \frac{x}{\sinh(x)} \quad (7-11)$$

where $x = \sigma V / 2\sqrt{3}kT$, provided that $\dot{\epsilon}_0$ depends only on temperature (implying that c_f does not vary with strain and strain rate, as assumed in this analysis). Fig. 7-18 shows the experimental data points of the normalized viscosity η/η_N as a function of $\sigma V / 2\sqrt{3}kT$. It is found that the experimental data points obtained at various temperatures and strain rates approximately superimpose on a so-called viscosity master curve, although the degree of fitting is not good enough. The rather low degree of fitting of the experimental normalized viscosity with the Eq. 7-11 may be attributed from the following two reasons: (i) experimental and calculation errors, and (ii) the invalidation of the assumption in Eq. 7-11 that $\dot{\epsilon}_0$ depends only on temperature. Anyway, the master curve successfully demonstrates Newtonian flow in the supercooled state at low strain rates where normalized viscosity is unity. Conversely, high strain rates result in a decrease in viscosity, showing a transition state from Newtonian flow to non-Newtonian flow.

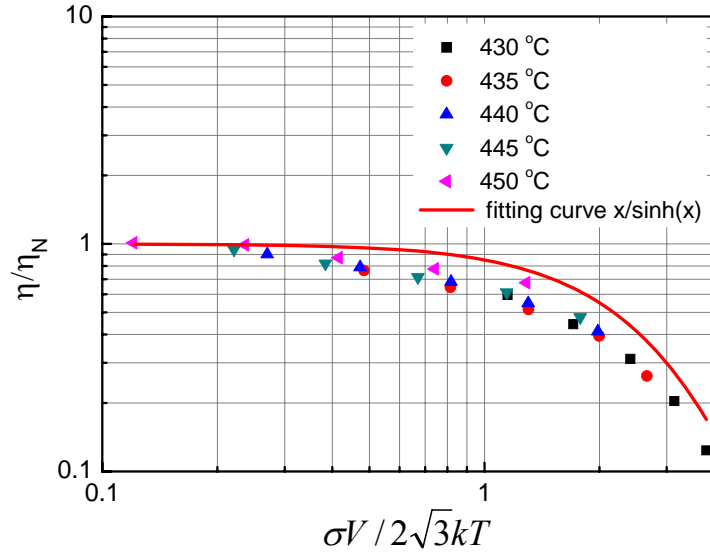


Fig. 7-18 Master curve of the normalized viscosity according to Eq. 7-11

7.5 Effects of Deformation on the Structural Stability of Ti-based BMGs

The structural instability during deformation of metallic glasses in the supercooled liquid region is commonly found; however, there still exists the opposite findings, e.g. $Zr_{65}Al_{7.5}Ni_{10}Cu_{12.5}Pd_5$ and $Ca_{65}Mg_{15}Zn_{20}$ BMGs, when the metallic glasses were deformed in a non-Newtonian regime. This finding suggests that the effects of deformation on the structural changes may be inconsistent in different metallic glasses and associated with the structure and stability of the primary phase, and also may be associated with the different viscosity flow, Newtonian flow or non-Newtonian flow.

In this section, the effects of deformation (stress) on the structural stability of $Ti_{41.5}Cu_{37.5}Ni_{7.5}Zr_{2.5}Hf_5Sn_5Si_1$ BMG subjected to deform at high temperature were investigated. Two experimental conditions (listed in Table 7-6), deformation temperature T and strain rate $\dot{\epsilon}$, which are corresponding to the Newtonian flow and non-Newtonian flow behavior, respectively, were carefully selected according to the above rheology behavior investigation. In order to get the information about the effects of deformation on the structural stability, the comparison of the microstructure must be performed between the post-deformed samples and the undeformed samples (annealed at the same temperature for the same time as the deformed samples). The easy way is to reheat the post-deformed samples as well as the undeformed samples to crystallization through the DSC measurements, and then compare these two continuous heating DSC curves. It should be noted that the deformation time (annealing time) should be long enough to ensure the occurrence of the obvious strain hardening.

Table 7-6

Experimental conditions including temperature T , strain rate $\dot{\epsilon}$ and time t for compression tests as well as isothermal annealing tests.

Deformation mode	T (°C)	$\dot{\epsilon}$ (s^{-1})	t (min)
Non-Newtonian flow	430	2.5×10^{-4}	113
Newtonian flow	440	2.5×10^{-4}	55

Fig. 7-19 displays the variation of the flow stress with deformation time for $Ti_{41.5}Cu_{37.5}Ni_{7.5}Zr_{2.5}Hf_5Sn_5Si_1$ BMG deformed at 430 and 440 °C with a constant strain rate of $2.5 \times 10^{-4} s^{-1}$. At 430 °C, the σ - t curve exhibits a stress overshoot followed by a steady state flow, and it follows the non-Newtonian flow behavior; however, at 440 °C, no stress overshoot can be observed in the σ - t curve, the Newtonian flow behavior dominates its viscoplastic deformation. The onset time for strain hardening which is believed to be associated with the crystallization is marked with an arrow in Fig. 7-19.

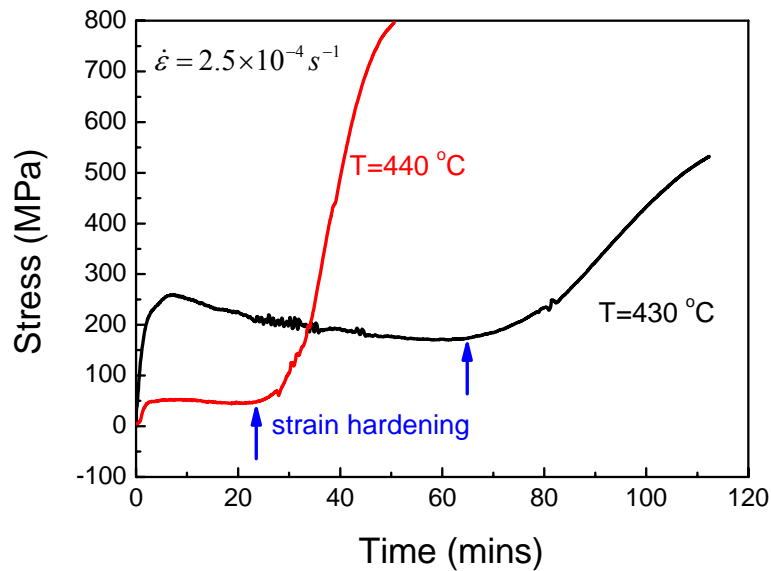


Fig. 7-19 Compressive stress-deformation time curves for the $Ti_{41.5}Cu_{37.5}Ni_{7.5}Zr_{2.5}Hf_5Sn_5Si_1$ BMG at 430 and 440 °C with a constant strain rate of $2.5 \times 10^{-4} s^{-1}$, the arrows locate the onset of strain hardening

At 430 °C, given the fact that the exothermic enthalpy for the crystallization in the reheating DSC curve for the post-deformed sample is smaller than that for the undeformed sample (see Fig. 7-20), one may conclude that the deformation accelerates the crystallization of the amorphous phase. The additional XRD measurements performed on the post-deformed and undeformed samples also confirm this conclusion, since the obvious Bragg peaks appear for the post-deformed sample while not for the undeformed sample (see Fig. 7-21).

The above experiment results demonstrate that under the non-Newtonian flow behavior, the deformation has a significant effect on the structural and thermal stability of $Ti_{41.5}Cu_{37.5}Ni_{7.5}Zr_{2.5}Hf_5Sn_5Si_1$ BMG: the plastic deformation reduces the thermal stability of BMG, and accelerates the crystallization of amorphous phase. It is suggested that the rapid increment of free volume induced by plastic deformation, which in turn, decreased the viscosity and increased

the atom mobility of supercooled liquid, should account for the acceleration of crystallization [L. Liu et al., 2007]. On the other hand, it is possibly due to the strain energy caused by plastic deformation, which is believed to complement the thermal energy required for crystallization and thus accelerates the crystallization, as is suggested by Nieh et al. [Nieh et al., 1999]. Saida et al. [Saida et al., 2002] and Laws et al. [Law et al., 2008] have reported two inconsistent results with the present result in Zr-Al-Ni-Cu-Pd and Ca-Mg-Zn BMGs, respectively. Laws et al. did not give us a reasonable explanation on this phenomenon. Saida et al. argued that it may be determined by the primary phase. If the primary phase is stable, the nonlinear viscous flow accelerates the nanocrystallization; on the contrary, if the primary is metastable, the nanocrystallization will be suppressed [Saida et al., 2002]. However, it is worthy to note that the primary phase in $\text{Ti}_{41.5}\text{Cu}_{37.5}\text{Ni}_{7.5}\text{Zr}_{2.5}\text{Hf}_5\text{Sn}_5\text{Si}_1$ BMG is a metastable phase which will transform to a stable phase at higher temperature, suggesting that other mechanism may be responsible for this deformation-induced stability or instability. Although the mechanism is still unclear, here we give a possible explanation on it. The crystallization is accelerated or suppressed by the deformation may be determined by the crystal lattice of primary phase or the corresponding similar atomic configurations in the supercooled liquid. In the report of Saida et al. [Saida et al., 2002], the icosahedral atomic configurations which are expected to be the main factor for the formation of icosahedral phase as a primary phase are tending to be destroyed by the mechanically induced disorder; however, in our case, the cubic-like atomic configurations which are related to the primary metastable cubic TiNi(Cu) phase may tend to form more ordered configurations by the deformation. This opinion is still needed to be confirmed in the future work.

The acceleration of crystallization process during the high-temperature deformation leads to shorten the incubation time for crystallization. For $\text{Ti}_{41.5}\text{Cu}_{37.5}\text{Ni}_{7.5}\text{Zr}_{2.5}\text{Hf}_5\text{Sn}_5\text{Si}_1$ BMG, it has been verified that the crystallization leads to (i) the drastic degradation of room-temperature mechanical properties, (ii) reducing superplasticity by decreasing the strain rate sensitivity exponent m , (iii) enhancing the flow stress, and (iv) finally increasing in production cost and promotion of die wear. Accordingly, it is vital to optimize the conditions to avoid the crystallization during the superplastic forming of $\text{Ti}_{41.5}\text{Cu}_{37.5}\text{Ni}_{7.5}\text{Zr}_{2.5}\text{Hf}_5\text{Sn}_5\text{Si}_1$ BMG.

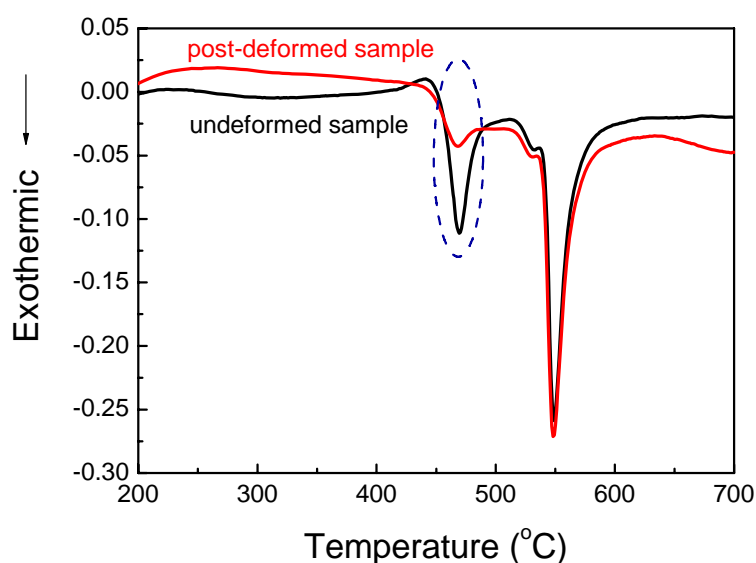


Fig. 7-20 DSC curves obtained from the post-deformed as well as undeformed samples (deformed (annealed) at 430 °C for 113 min), with a heating rate of 10 K/min

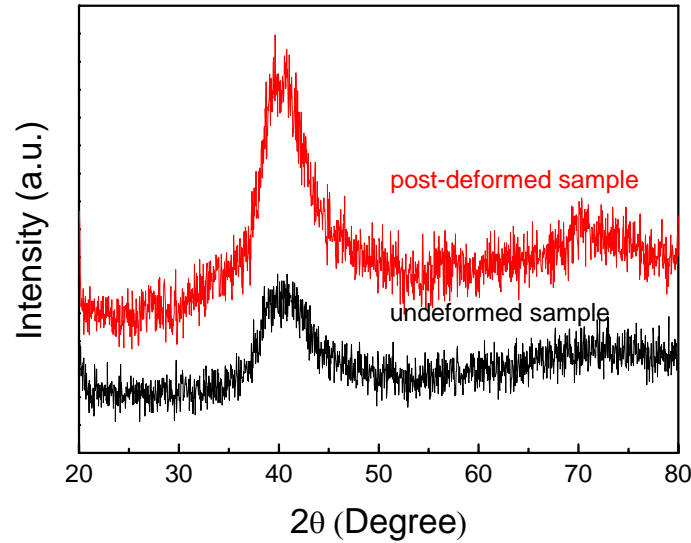


Fig. 7-21 XRD patterns obtained from the post-deformed as well as undeformed samples (deformed (annealed) at 430 °C for 113 min)

Fig. 7-22 compares DSC curves obtained at a constant heating rate of 10 K/min for samples deformed and undeformed (annealed with the same temperature and time) at 440 °C for 55 min. Since the DSC curves for the post-deformed and undeformed samples appear as quite similar profiles as well as the exothermic crystallization enthalpies (see **Fig. 7-22**); meanwhile, the corresponding XRD patterns in **Fig. 7-23** are also consistent, one can consequently conclude that the effects of deformation on the structural stability is limited when $\text{Ti}_{41.5}\text{Cu}_{37.5}\text{Ni}_{7.5}\text{Zr}_{2.5}\text{Hf}_5\text{Sn}_5\text{Si}_1$ BMG is deformed at 440 °C with a constant strain rate of $2.5 \times 10^{-4} \text{ s}^{-1}$. Such limited stress-induced structural changes are attributed to the Newtonian character of the deformation in the investigated experimental domain. Indeed, in the Newtonian regime, the rate of stress-induced defect creation is expected to be negligible in comparison to the relaxation effects. The situation may be different in the non-Newtonian regime for which deformation may increase the defect level and consequently not only decrease the flow stress but also promote crystallization [Q. Wang et al., 2006].

The above results attest that the deformation-induced structural instability is very limited in the Newtonian flow regime, thus, the structural changes during the deformation are still controlled by the annealing time. Accordingly, the incubation time determined in the T-T-T curve can be regarded as the maximum value for avoiding the crystallization during the superplastic forming, unnecessary to taken into account the acceleration effect caused by deformation.

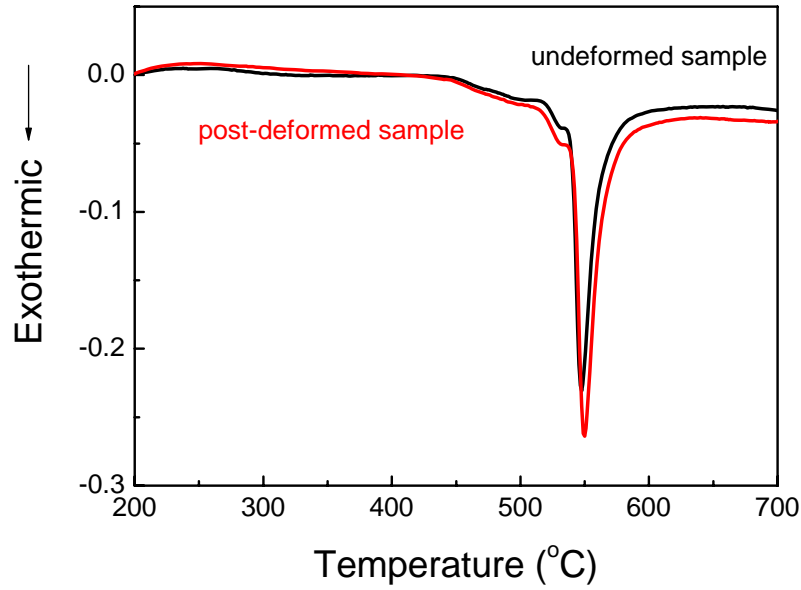


Fig. 7-22 DSC curves obtained from the post-deformed as well as undeformed samples (deformed (annealed) at 440 °C for 55 min), with a heating rate of 10 K/min

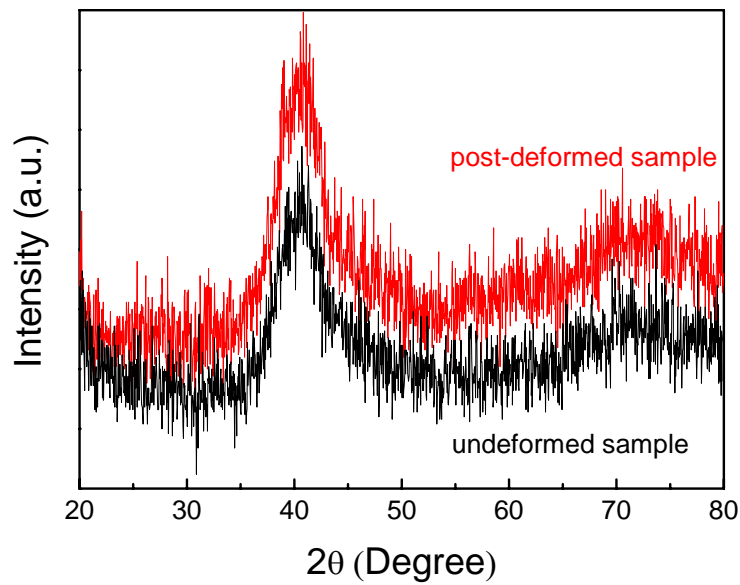


Fig. 7-23 XRD patterns obtained from the post-deformed as well as undeformed samples (deformed (annealed) at 440 °C for 55 min), with a heating rate of 10 K/min

7.6 Evaluation of Hot Workability and Optimization of Processing Conditions

The evaluation of hot workability and the optimization of processing conditions for metallic glasses should be performed based on the detailed analysis of the characteristic of deformation and rheology behavior of metallic glasses in the supercooled liquid region. In this section, we first summarize the characteristics of deformation of $\text{Ti}_{41.5}\text{Cu}_{37.5}\text{Ni}_{7.5}\text{Zr}_{2.5}\text{Hf}_{5}\text{Sn}_{5}\text{Si}_1$ BMG in the

supercooled liquid region and compare them with some typical metallic glasses for evaluating the hot workability of this alloy, and then the beneficial domain (deformation temperature and strain rate) for optimum hot workability will be determined through the constructions of deformation map and power dissipation map.

7.6.1 Characteristic of Deformation of $\text{Ti}_{41.5}\text{Cu}_{37.5}\text{Ni}_{7.5}\text{Zr}_{2.5}\text{Hf}_5\text{Sn}_5\text{Si}_1$ BMG

Although the high-temperature deformation of $\text{Ti}_{41.5}\text{Cu}_{37.5}\text{Ni}_{7.5}\text{Zr}_{2.5}\text{Hf}_5\text{Sn}_5\text{Si}_1$ BMG obeys the general law as other typical metallic glasses: (i) strongly dependent on temperature and strain rate, and (ii) the transition from Newtonian flow to non-Newtonian flow with increase in strain rate, besides that the deformation (stress) induces the structural changes, it is still necessary to compare its properties including steady-state flow stress and strain limit with other typical BMGs to further understand its characteristics of deformation and evaluate its hot workability.

For a direct comparison, the relationship between compressive flow stress and strain rate for $\text{Ti}_{41.5}\text{Cu}_{37.5}\text{Ni}_{7.5}\text{Zr}_{2.5}\text{Hf}_5\text{Sn}_5\text{Si}_1$ BMG as well as other typical BMGs including $\text{Pd}_{40}\text{Ni}_{40}\text{P}_{20}$ [Chu et al., 2002], $\text{Zr}_{41.2}\text{Ti}_{13.8}\text{Ni}_{10}\text{Cu}_{12.5}\text{Be}_{22.5}$ [Gravier, 2006], $\text{Zr}_{52.5}\text{Al}_{10}\text{Cu}_{22}\text{Ti}_{2.5}\text{Ni}_{13}$ [Bletry et al., 2006], $\text{Cu}_{60}\text{Zr}_{20}\text{Hf}_{10}\text{Ti}_{10}$ [Chiang et al., 2004] and $\text{Ce}_{70}\text{Al}_{10}\text{Cu}_{20}$ [Chu et al., 2006] is shown in Fig. 7-24. For each BMG, the strain rate and temperature shown in Fig. 7-24 correspond to the optimum processing conditions reported in the literature. The optimum processing conditions means low cost as well as high efficiency, namely, low flow stress and high strain rate. It is worthwhile to note that a flow stress less than 402 MPa is enough for plastic deformation up to close to 1 strain without fracture for the case of deforming within a high strain rate of $8 \times 10^{-3} \text{ s}^{-1}$ at 440 °C which is only 8 K (15.1% of ΔT_x) higher than the glass transition temperature. The alloy shows an especially easy plastic deformation with extremely low flow stress, around 40 MPa, and a compressive strain up to 0.4, in case of applying the low strain rate down to $2.5 \times 10^{-4} \text{ s}^{-1}$ at the same temperature (see Fig. 7-24). Within our investigation, the optimum processing condition for $\text{Ti}_{41.5}\text{Cu}_{37.5}\text{Ni}_{7.5}\text{Zr}_{2.5}\text{Hf}_5\text{Sn}_5\text{Si}_1$ BMG may locate at 440 °C with the strain rate of $5 \times 10^{-4} \text{ s}^{-1}$, where the flow stress is only 83 MPa and the maximum compressive strain can reach 0.8. However, we found that for $\text{Ce}_{70}\text{Al}_{10}\text{Cu}_{20}$ BMG, the maximum flow stress is lower than 10 MPa and large compressive strain up to 0.89 can be obtained even though the sample is deformed at a high strain rate of $7 \times 10^{-2} \text{ s}^{-1}$ at 420 °C. So it is necessary to compare the flow stress as well as the compressive strain limit of $\text{Ti}_{41.5}\text{Cu}_{37.5}\text{Ni}_{7.5}\text{Zr}_{2.5}\text{Hf}_5\text{Sn}_5\text{Si}_1$ BMG with other typical BMGs to evaluate the formability of this alloy.

In order to evaluate the formability of $\text{Ti}_{41.5}\text{Cu}_{37.5}\text{Ni}_{7.5}\text{Zr}_{2.5}\text{Hf}_5\text{Sn}_5\text{Si}_1$ BMG, three parameters should be considered: flow stress, strain rate and maximum compressive strain. The coexistence of low stress, high strain rate and large compressive strain limit is believed to be corresponding to the good workability. The information about the compressive strain limit for these six BMGs is listed in Table 7-7. It is found that all the BMGs can reach a large compressive strain than 0.7 at high strain rate. However, the flow stresses of $\text{Ti}_{41.5}\text{Cu}_{37.5}\text{Ni}_{7.5}\text{Zr}_{2.5}\text{Hf}_5\text{Sn}_5\text{Si}_1$, $\text{Zr}_{52.5}\text{Al}_{10}\text{Cu}_{22}\text{Ti}_{2.5}\text{Ni}_{13}$ and $\text{Cu}_{60}\text{Zr}_{20}\text{Hf}_{10}\text{Ti}_{10}$ BMGs are much higher than those of $\text{Pd}_{40}\text{Ni}_{40}\text{P}_{20}$, $\text{Ce}_{70}\text{Al}_{10}\text{Cu}_{20}$ and $\text{Zr}_{41.2}\text{Ti}_{13.8}\text{Ni}_{10}\text{Cu}_{12.5}\text{Be}_{22.5}$ BMGs, when they are deformed at the same strain rate, indicating that the formability of $\text{Ti}_{41.5}\text{Cu}_{37.5}\text{Ni}_{7.5}\text{Zr}_{2.5}\text{Hf}_5\text{Sn}_5\text{Si}_1$ BMG in the SLR is comparable with

Zr_{52.5}Al₁₀Cu₂₂Ti_{2.5}Ni₁₃ and Cu₆₀Zr₂₀Hf₁₀Ti₁₀ BMGs, however much worse than Ce-, Pd-based and Zr_{41.2}Ti_{13.8}Ni₁₀Cu_{12.5}Be_{22.5} BMG. The high flow stress in the Ti-based BMG appears to be intrinsic since the compressive strength of the Ti-based BMG at ambient temperature is also comparable with that of Cu- and Zr-based BMGs which is much higher than that of Pd- and Ce-based BMGs.

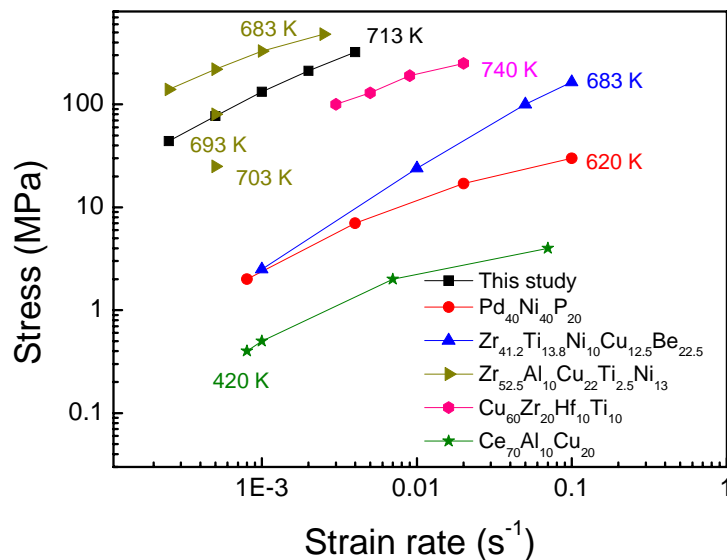


Fig. 7-24 Typical compressive stress-strain rate curves for the typical BMGs when deformed in the supercooled liquid region

Table 7-7

Compressive deformation data of typical BMGs in the supercooled liquid region

Alloy	T_g (K)	T_{x1} (K)	$(T-T_g)/\Delta T_x$ (%)	$\dot{\epsilon}$ (s ⁻¹)	σ (MPa)	ϵ	Reference
Pd ₄₀ Ni ₄₀ P ₂₀	589	670	48.1	8×10^{-4}	1-2	0.94	[Chu et al., 2002]
Zr _{41.2} Ti _{13.8} Ni ₁₀ Cu _{12.5} Be _{22.5}	623	705	73.2	0.1	~165	>0.8	[Gravier, 2006]
Zr _{52.5} Al ₁₀ Cu ₂₂ Ti _{2.5} Ni ₁₃	659	761	43.1	5×10^{-4}	25	~1.0	[Bletry et al., 2006]
Cu ₆₀ Zr ₂₀ Hf ₁₀ Ti ₁₀	721	766	42.2	3×10^{-3}	~110	0.77	[Chiang et al., 2004]
Cu ₆₀ Zr ₂₀ Hf ₁₀ Ti ₁₀	721	766	42.2	2×10^{-2}	~220	-	[Chiang et al., 2004]
Ce ₇₀ Al ₁₀ Cu ₂₀	366	427	88.5	8×10^{-4}	~0.4	0.89	[Chu et al., 2006]
Ce ₇₀ Al ₁₀ Cu ₂₀	366	427	55.7-88.5	7×10^{-2}	<10	-	[Chu et al., 2006]
Ti _{41.5} Cu _{37.5} Ni _{7.5} Zr _{2.5} Hf ₅ Sn ₅ Si ₁	705	758	15.1	5×10^{-4}	83	0.8	This study
Ti _{41.5} Cu _{37.5} Ni _{7.5} Zr _{2.5} Hf ₅ Sn ₅ Si ₁	705	758	15.1	1×10^{-3}	163	~1	This study

7.6.2 Deformation Map of Ti_{41.5}Cu_{37.5}Ni_{7.5}Zr_{2.5}Hf₅Sn₅Si₁ BMG

To generate reliable deformation processing maps of the SCL region, it is necessary to delineate regions of homogeneous and inhomogeneous plastic flow.

The deformation map of Ti_{41.5}Cu_{37.5}Ni_{7.5}Zr_{2.5}Hf₅Sn₅Si₁ BMG in the supercooled liquid region can be generated using the information derived from the viscosity master curve in Fig. 7-18 combined with the experimental observations of the compressive behavior of each sample, which

is displayed in Fig. 7-25. The dominant deformation mechanism is indicated in the deformation map for various temperatures and strain rates, where the boundary between Newtonian flow and non-Newtonian flow is shown (red line), however, the boundary between the homogeneous deformation and inhomogeneous deformation is fictive since no brittle fracture was observed when the samples were subjected to deform at the temperatures and strain rates applied in this study. It is found that, under the experimental conditions (temperatures and strain rates), the homogeneous non-Newtonian deformation dominates a large range of temperature and strain rate window, however, homogeneous Newtonian deformation only occurs in a very narrow temperature and strain rate window which is higher than 435 °C and below the strain rate of $1 \times 10^{-3} \text{ s}^{-1}$. Further analysis will be performed on the basis of power dissipation map of this alloy.

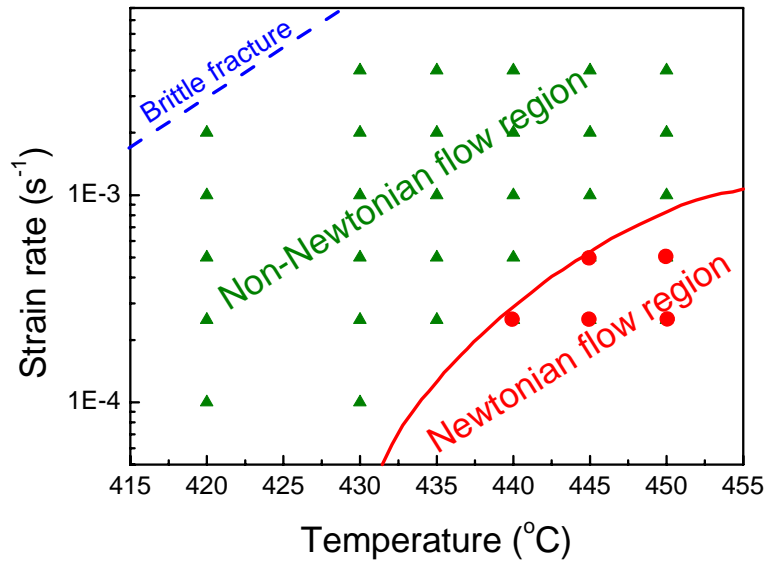


Fig. 7-25 Deformation map showing the regions of Newtonian and non-Newtonian flow for $\text{Ti}_{41.5}\text{Cu}_{37.5}\text{Ni}_{7.5}\text{Zr}_{2.5}\text{Hf}_5\text{Sn}_5\text{Si}_1$ BMG

7.6.3 Power Dissipation Map of $\text{Ti}_{41.5}\text{Cu}_{37.5}\text{Ni}_{7.5}\text{Zr}_{2.5}\text{Hf}_5\text{Sn}_5\text{Si}_1$ BMG

Power dissipation map is generally believed to be an efficient way to predict and evaluate the hot workability of materials as it reflects the relationship between the power dissipation efficiency η and the processing conditions (temperature and strain rate). The power dissipation efficiency η , defined as

$$\eta = 2m/(m+1) \quad (7-12)$$

where m has the general meaning (strain rate sensitivity), reflects the comparison of the non-linear dissipative properties of the deformed workpiece with that of a linear dissipater, namely, the portion of power for the metallurgical change of the structure divided by the total power provided to the workpiece. Accordingly, the region in the power dissipation map with high value of η indicates the superior formability where dynamic microstructural changes such as structural rearrangements in the BMGs or dynamic recrystallization in some crystalline materials are predicted with least thermal dissipation during hot working [Lee et al., 2007].

A three-dimension power dissipation efficiency map (contour plot) of

Ti_{41.5}Cu_{37.5}Ni_{7.5}Zr_{2.5}Hf₅Sn₅Si₁ BMG was constructed with η as a function of temperature as well as strain rate and shown in Fig. 7-26. The number on each contour represents the power dissipation efficiency η . It is found that the region with high power dissipation efficiency above 0.8 covers the high temperature regime, especially when the temperature is above 445 °C, the power dissipation efficiency keeps larger than 0.8 within the strain rate range applied in this study. In addition, comparing the dissipation map with the deformation map, the region of high η not only covers the Newtonian flow domain but also occupies a part of the non-Newtonian flow domain (however Newtonian-like) at high temperature and high strain rate regime which can be seen in the right part of the red line in Fig. 7-26. As we know, during the hot deformation of the bulk metallic glass, most of the input power is used for structural rearrangements assisting viscous flow with least thermal dissipation when the maximum efficiency of power dissipation is over 0.8 [Lee et al., 2005-b; Lee et al., 2007]. So the region in power dissipation map where $\eta > 0.8$ and Newtonian or Newtonian-like viscous flow dominates the deformation behavior, can be considered as a beneficial domain for optimum hot workability of this BMG.

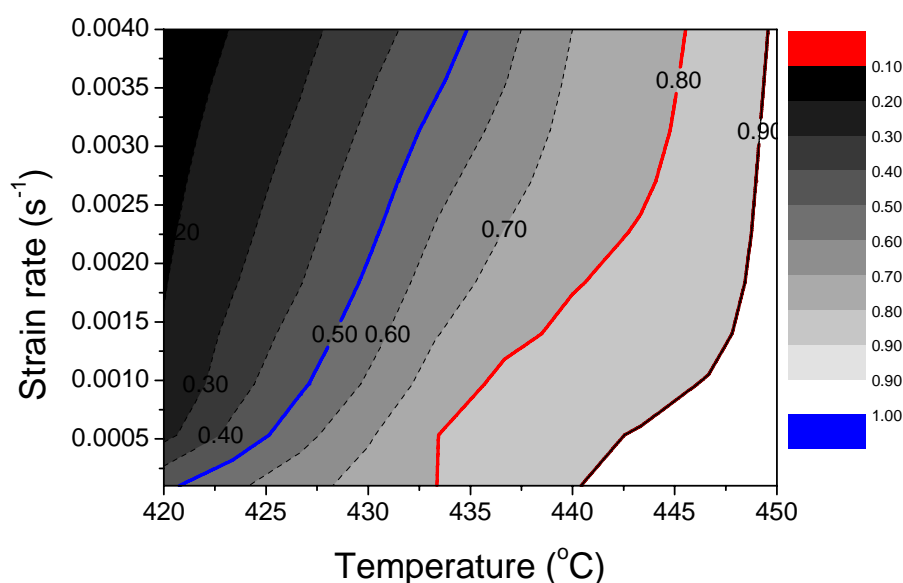


Fig. 7-26 Power dissipation map for Ti_{41.5}Cu_{37.5}Ni_{7.5}Zr_{2.5}Hf₅Sn₅Si₁ BMG at temperatures ranging of 420-450 °C (the number on each contour represents the power dissipation efficiency η)

It should be noted that the powder dissipation map just help us to locate a beneficial domain (temperature and strain rate) for optimum hot workability of this BMG, however, during the industrial manufacture, deformation time must be taken into account. For Ti_{41.5}Cu_{37.5}Ni_{7.5}Zr_{2.5}Hf₅Sn₅Si₁ BMG, the deformation time must be within the upper limit for avoiding crystallization, since the investigation in the last chapter has shown that the crystallization of this alloy will lead to the drastic degradation of mechanical properties. In addition, the acceleration of crystallization when the sample is deformed in the non-Newtonian flow regime will lead to shorten the upper limit of the deformation time, as should be considered. Accordingly, determination of the processing condition must be based on the analysis of the deformation characteristics, rheology behavior and the effects of deformation (stress) on the structural changes.

7.7 Conclusion

The high-temperature deformation behavior of two typical Ti-based BMGs, $\text{Ti}_{41.5}\text{Cu}_{37.5}\text{Ni}_{7.5}\text{Zr}_{2.5}\text{Hf}_5\text{Sn}_5\text{Si}_1$ and $\text{Ti}_{40}\text{Zr}_{25}\text{Ni}_8\text{Cu}_9\text{Be}_{18}$, was investigated under uniaxial compression. The following results were obtained:

(1) The high-temperature deformation of $\text{Ti}_{41.5}\text{Cu}_{37.5}\text{Ni}_{7.5}\text{Zr}_{2.5}\text{Hf}_5\text{Sn}_5\text{Si}_1$ BMG is dependent on the strain rate and temperature. The high strain rate and low temperature lead to the increase in flow stress. The flow stress of this alloy is comparable with that of Zr- and Cu-based BMGs, however, much higher than that of Pd- and Ce-based BMGs, it is believed to be intrinsic which is in accordance with the high strength at room temperature. It exhibits a compressive strain limit of 0.8 at 440 °C and at $5 \times 10^{-4} \text{ s}^{-1}$ with a low flow stress of 83 MPa, suggesting a good superplasticity and workability of this alloy. The formability of this alloy is worse than that of Ce- and Pd-based BMGs.

(2) There exists a transition from Newtonian flow to non-Newtonian flow by increase in strain rate, and can be explained in the framework of transition state theory. High values of activation volume V_{act} between 200-299 Å³ can be obtained, they are comparable with those of Mg-based BMGs. In addition, the high value of apparent activation energy Q_{app} of 6.4 eV can be calculated from the linear fitting of the $\ln \eta_N - 1/T$ plot. The high value of V_{act} as well as Q_{app} is the evidence of collective migration of atomic group (10-30 atoms) during the high-temperature deformation.

(3) $\text{Ti}_{40}\text{Zr}_{25}\text{Ni}_8\text{Cu}_9\text{Be}_{18}$ BMG exhibits different characteristic of high-temperature deformation compared with the typical metallic glasses, the flow stress keeps a high value when the deformation temperature is increased in the supercooled liquid region, this is attributed to the thermal instability caused by the quenched-in nuclei in the amorphous matrix.

(4) The homogeneous non-Newtonian viscous flow accelerates the nanocrystallization in $\text{Ti}_{41.5}\text{Cu}_{37.5}\text{Ni}_{7.5}\text{Zr}_{2.5}\text{Hf}_5\text{Sn}_5\text{Si}_1$ BMG, while the effects of homogeneous Newtonian viscous flow on the structural changes are very limited. Under the non-Newtonian flow regime, whether the deformation accelerates or suppresses the structural changes may be essentially determined by the crystal lattice of primary phase or the corresponding similar atomic configurations in the supercooled liquid. The cubic-like atomic configurations which are related to the primary metastable cubic TiNi(Cu) phase may tend to form more ordered configurations by the deformation for $\text{Ti}_{41.5}\text{Cu}_{37.5}\text{Ni}_{7.5}\text{Zr}_{2.5}\text{Hf}_5\text{Sn}_5\text{Si}_1$ BMG.

(5) A beneficial domain (temperature and strain rate) for optimum hot workability of BMG can be roughly located by constructing the power dissipation efficiency map, where the power dissipation efficiency η is larger than 0.8; however, during the industrial manufacture, deformation time must be taken into account to avoid crystallization since the crystallization leads to drastic degradation of mechanical properties for $\text{Ti}_{41.5}\text{Cu}_{37.5}\text{Ni}_{7.5}\text{Zr}_{2.5}\text{Hf}_5\text{Sn}_5\text{Si}_1$ BMG.

CONCLUSIONS

Two Ti-based bulk metallic glasses, with the nominal composition of $\text{Ti}_{40}\text{Zr}_{25}\text{Ni}_8\text{Cu}_9\text{Be}_{18}$ and $\text{Ti}_{41.5}\text{Cu}_{37.5}\text{Ni}_{7.5}\text{Zr}_{2.5}\text{Hf}_5\text{Sn}_5\text{Si}_1$, as the typical representation of Ti-Zr-Ni and Ti-Cu-Ni system, respectively, were selected for investigation in this study. Our studies focus on thermally induced structural transformations (structural relaxation and crystallization) behavior and their effects on the thermodynamics and kinetics of the subsequent glass transition and crystallization as well as room-temperature mechanical response in addition to homogeneous deformation in the supercooled liquid region and low-temperature physical properties. The following conclusions were obtained:

1. The as-cast $\text{Ti}_{40}\text{Zr}_{25}\text{Ni}_8\text{Cu}_9\text{Be}_{18}$ and $\text{Ti}_{41.5}\text{Cu}_{37.5}\text{Ni}_{7.5}\text{Zr}_{2.5}\text{Hf}_5\text{Sn}_5\text{Si}_1$ alloys with 2 mm in diameter exhibit unique different structural nature: quenched-in nuclei/amorphous structure and phase separation-like structure, respectively, as also can be confirmed by low-temperature electrical resistivity measurement. The critical cooling rates R_c for $\text{Ti}_{40}\text{Zr}_{25}\text{Ni}_8\text{Cu}_9\text{Be}_{18}$ and $\text{Ti}_{41.5}\text{Cu}_{37.5}\text{Ni}_{7.5}\text{Zr}_{2.5}\text{Hf}_5\text{Sn}_5\text{Si}_1$ BMGs, are 1.5 and 28 K/s, respectively, indicating the higher GFA of $\text{Ti}_{40}\text{Zr}_{25}\text{Ni}_8\text{Cu}_9\text{Be}_{18}$ BMG; while the activation energies for the first crystallization reaction for these two alloys are 235.2 and 319.4 kJ/mol, respectively, revealing the higher thermal stability of $\text{Ti}_{41.5}\text{Cu}_{37.5}\text{Ni}_{7.5}\text{Zr}_{2.5}\text{Hf}_5\text{Sn}_5\text{Si}_1$ BMG.
2. The two-level system effects in $\text{Ti}_{41.5}\text{Cu}_{37.5}\text{Ni}_{7.5}\text{Zr}_{2.5}\text{Hf}_5\text{Sn}_5\text{Si}_1$ BMG are observed below several Kelvin by studying the low-temperature specific heat as well as electrical resistivity, and are significantly different from those in insulating glasses which generally occur below 1 K, indicating the conduction electron-assisted tunneling. The contribution of phonon to low-temperature specific heat of $\text{Ti}_{41.5}\text{Cu}_{37.5}\text{Ni}_{7.5}\text{Zr}_{2.5}\text{Hf}_5\text{Sn}_5\text{Si}_1$ BMG in a wide temperature range of 4.2-100 K can be successfully described by introducing localized harmonic vibration mode (Einstein oscillator mode) into the typical Debye model, and the VDOS, derived from the specific heat, shows an excess peak at 5.95 meV that corresponds to the boson peak, and indicates that the Einstein oscillator induces the boson peak in BMGs. Debye temperature θ_D and Einstein temperature θ_E are calculated to be 327 and 89 K, respectively. It shows large resistivity of 258.89 $\mu\Omega\cdot\text{cm}$ at 280 K and a small negative temperature coefficient of resistivity.
3. The enthalpy relaxation of $\text{Ti}_{40}\text{Zr}_{25}\text{Ni}_8\text{Cu}_9\text{Be}_{18}$ and $\text{Ti}_{41.5}\text{Cu}_{37.5}\text{Ni}_{7.5}\text{Zr}_{2.5}\text{Hf}_5\text{Sn}_5\text{Si}_1$ BMG from the amorphous state into the equilibrium supercooled liquid state both follow the characteristic of enthalpy relaxation for glasses: a stretched exponential function with the relaxation time obeying an Arrhenius law. The rearrangement involving the collective hopping mechanism for the small and medium size atoms is the governing mechanism for the enthalpy relaxation process for both two alloys. Two parameters, β_g and τ_g , representing the stretching exponent and the average structural relaxation time at the calorimetric glass transition temperature, respectively, were proposed to evaluate the enthalpy relaxation properties and their correlations with the GFA and thermal stability, respectively, have been constructed. The high value of β_g up to 0.962 for $\text{Ti}_{40}\text{Zr}_{25}\text{Ni}_8\text{Cu}_9\text{Be}_{18}$ BMG confirms its better GFA than $\text{Ti}_{41.5}\text{Cu}_{37.5}\text{Ni}_{7.5}\text{Zr}_{2.5}\text{Hf}_5\text{Sn}_5\text{Si}_1$ BMG whose β_g value is 0.884; however, the value of

- τ_g for $\text{Ti}_{40}\text{Zr}_{25}\text{Ni}_8\text{Cu}_9\text{Be}_{18}$ BMG is 105, much smaller than 161 for $\text{Ti}_{41.5}\text{Cu}_{37.5}\text{Ni}_{7.5}\text{Zr}_{2.5}\text{Hf}_5\text{Sn}_5\text{Si}_1$ BMG, indicating a better thermal stability of $\text{Ti}_{41.5}\text{Cu}_{37.5}\text{Ni}_{7.5}\text{Zr}_{2.5}\text{Hf}_5\text{Sn}_5\text{Si}_1$ BMG than $\text{Ti}_{40}\text{Zr}_{25}\text{Ni}_8\text{Cu}_9\text{Be}_{18}$ BMG.
4. The JMA model and Starink model in which the effects of soft impingement are introduced are proposed to investigate the crystallization kinetics depending on whether the crystallization behavior is deviating from the JMA theory or not. Theoretical calculation reveals that the selection of the appropriate kinetics model is crucial for the following kinetics analysis. For example, the wrong application of JMA model (it means that the crystallization does not satisfy some assumptions of the JMA theory) will lead to an error result: changeable kinetic exponent depending on the transformed volume fraction described by the local Avrami exponent, finally lead to the misinterpretation of phase transformation mechanism.
 5. The phase transformation upon heating for $\text{Ti}_{41.5}\text{Cu}_{37.5}\text{Ni}_{7.5}\text{Zr}_{2.5}\text{Sn}_5\text{Hf}_5\text{Si}_1$ BMG can be described as: the amorphous phase transforms to the cubic $\text{TiNi}(\text{Cu})$ phase with space group Pm-3m at the first crystallization stage; followed by the cubic $\text{TiNi}(\text{Cu})$ phase transforms to γ -TiCu phase and the remaining amorphous phase transforms into γ -TiCu phase and a cubic $\text{Sn}_{11}\text{Cu}_{39}$ -like phase through the second crystallization stage. The crystallization mechanism for the first crystallization reaction is that from a diffusion-controlled three-dimensional growth with an increasing nucleation rate to an interface-controlled three-dimensional growth with decrease in the isothermal annealing temperature or decrease in heating rate.
 6. The phase evolution upon heating of $\text{Ti}_{40}\text{Zr}_{25}\text{Cu}_9\text{Ni}_8\text{Be}_{18}$ BMG proceeds by two complicated crystallization reactions: during the primary crystallization, a cubic $(\text{Ti,Zr})\text{Be}_2$ phase is formed at 608 K ($a=6.603 \text{ \AA}$), this phase is unstable and decomposes at higher temperature 810 K; the second crystallization products, which are formed at 749 K and very stable up to full melting, are at 92% a C14 hexagonal Laves phase $\text{Zr}_{1.0}\text{Ti}_{1.08}\text{Ni}_{0.82}\text{Cu}_{0.10}$ or $\text{Zr}(\text{Ti,Ni,Cu})_2$, and at 8% a big cube phase, $\text{Ti}_{1.536}\text{Zr}_{0.464}\text{Ni}_{0.364}\text{Cu}_{0.636}$ or $(\text{Ti,Zr})_2(\text{Ni,Cu})$. The first crystallization reaction is governed by a diffusion-controlled three dimensional growth of the quenched-in nuclei.
 7. For both BMGs, pre-annealing does not change the kinetic characteristics of glass transition and crystallization, but changes the thermodynamic and kinetic parameters. For the annealed $\text{Ti}_{41.5}\text{Cu}_{37.5}\text{Ni}_{7.5}\text{Zr}_{2.5}\text{Hf}_5\text{Sn}_5\text{Si}_1$ sample, the nucleation was prompted, due to the similar structure of the clusters in the process of pre-annealing with the primary phase of crystallization; however, the growth of nuclei was sluggish due to the decrease of diffusivity caused by pre-annealing induced structural transformations. For the annealed $\text{Ti}_{40}\text{Zr}_{25}\text{Ni}_8\text{Cu}_9\text{Be}_{18}$ sample, the glass transition of BMG was delayed, resulting from the change of the chemical composition caused by growth of nuclei, however, the subsequent crystallization reaction was accelerated, which may be due to the secondary nucleation induced by the crystal growth.
 8. The as-cast $\text{Ti}_{40}\text{Zr}_{25}\text{Ni}_8\text{Cu}_9\text{Be}_{18}$ and $\text{Ti}_{41.5}\text{Cu}_{37.5}\text{Ni}_{7.5}\text{Zr}_{2.5}\text{Hf}_5\text{Sn}_5\text{Si}_1$ alloys deformed at room temperature with a constant strain rate of $5 \times 10^{-4} \text{ s}^{-1}$ both exhibit high value of compressive strength of 1850 and 2120 MPa, respectively, however with significantly different plastic strain, 8.0% and 1.6%, respectively. The macroscopic plasticity or brittleness for metallic glasses is not only associated with the properties of constituent elements and structural nature but also related to the structural changes upon compression and their interaction with shear

bands during deformation. It is confirmed that the plastic flow of metallic glasses is located within narrow shear bands, and the universal local softening mechanism dominates the fracture of metallic glasses in spite of their deformation and fracture mode, but at different length scales. For these two alloys, the compressive fracture surfaces both consist of a shear zone and a rough zone, accompanying the fracture angles changing from <45 to 90° . Such unique deformation and fracture behavior can be successfully interpreted by the ellipse criterion combined with the analysis on the changes of stress state during the compressive fracture process.

9. The structural relaxation of the metallic glasses produces a slight increase in hardness, Young's modulus and fracture strength in addition to embrittlement; moreover, the precipitation of nanocrystals of the metallic glasses leads to a rapid increase in hardness and Young's modulus however with a significant decrease in fracture strength and plasticity. Accordingly, the crystallization should be avoided during the superplastic forming in the supercooled liquid region and as long as the flow stress meets the demand of superplastic forming, it is necessary to select a temperature as close to T_g of the metallic glass as possible since the degeneration of mechanical properties is caused by structural relaxation and especially crystallization.
10. The high-temperature deformation of $\text{Ti}_{41.5}\text{Cu}_{37.5}\text{Ni}_{7.5}\text{Zr}_{2.5}\text{Hf}_5\text{Sn}_5\text{Si}_1$ BMG is dependent on the strain rate and temperature. The flow stress of this alloy is comparable with that of Zr- and Cu-based BMGs, however, much higher than that of Pd- and Ce-based BMGs, it is believed to be intrinsic which is in accordance with the high strength at room temperature. It exhibits a compressive strain limit of 0.8 at 440°C and at $5 \times 10^{-4} \text{ s}^{-1}$ with a low flow stress of 83 MPa, suggesting a good superplasticity and workability of this alloy. The formability of this alloy is worse than that of Ce- and Pd-BMGs. However, $\text{Ti}_{40}\text{Zr}_{25}\text{Ni}_8\text{Cu}_9\text{Be}_{18}$ BMG exhibits different characteristic of high-temperature deformation compared with the typical metallic glasses, the flow stress keeps a high value when the deformation temperature is increased in the supercooled liquid region, this is attributed to the thermal instability caused by the quenched-in nuclei in the amorphous matrix.
11. The homogeneous non-Newtonian viscous flow accelerates the nanocrystallization in $\text{Ti}_{41.5}\text{Cu}_{37.5}\text{Ni}_{7.5}\text{Zr}_{2.5}\text{Hf}_5\text{Sn}_5\text{Si}_1$ BMG, while the effects of homogeneous Newtonian viscous flow on the structural changes are very limited. Under the non-Newtonian flow regime, whether the deformation accelerates or suppresses the structural changes may be essentially determined by the crystal lattice of primary phase or the corresponding similar atomic configurations in the supercooled liquid. The cubic-like atomic configurations which are related to the primary metastable cubic $\text{TiNi}(\text{Cu})$ phase may tend to form more ordered configurations by the deformation for $\text{Ti}_{41.5}\text{Cu}_{37.5}\text{Ni}_{7.5}\text{Zr}_{2.5}\text{Hf}_5\text{Sn}_5\text{Si}_1$ BMG.
12. A beneficial domain (temperature and strain rate) for optimum hot workability of $\text{Ti}_{41.5}\text{Cu}_{37.5}\text{Ni}_{7.5}\text{Zr}_{2.5}\text{Hf}_5\text{Sn}_5\text{Si}_1$ BMG can be roughly located by constructing the power dissipation efficiency map, where the power dissipation efficiency η is larger than 0.8; however, during the industrial manufacture, deformation time must be taken into account to avoid crystallization since the crystallization leads to drastic degradation of mechanical properties for $\text{Ti}_{41.5}\text{Cu}_{37.5}\text{Ni}_{7.5}\text{Zr}_{2.5}\text{Hf}_5\text{Sn}_5\text{Si}_1$ BMG.

REFERENCES

- [Aleiner et al., 2001] I. L. Aleiner, B. L. Altshuler and Y. M. Galperin, Experimental tests for the relevance of two-level systems for electron dephasing, *Phys. Rev. B* 2001, 63: 201401.
- [Amakai et al., 2007] Y. Amakai, S. Murayama, H. Takano, M. Mizutani, K. Asano, Y. Obi and K. Takanashi, Specific heat of amorphous $\text{Ce}_x\text{Ru}_{100-x}$ alloys, *J. Mag. Mag. Mater.* 2007, 310: 416~418.
- [Anand et al., 2005] L. Anand and C. Su, A theory for amorphous viscoplastic materials undergoing finite deformations, with application to metallic glasses, *J. Mech. Phys. Solids*, 2005, 53: 1362~1396.
- [Anand et al., 2007] L. Anand and C. Su, A constitutive theory for metallic glasses at high homologous temperatures, *Acta Mater.* 2007, 55: 3735~3747.
- [Anderson et al., 1972] P.W. Anderson, B.I. Halperin and C.M. Varma, Anomalous low temperature thermal properties of glasses and spin-glasses, *Philos. Mag.* 1972, 25: 1~9.
- [Angell, 1991] C.A. Angell, Relaxation in liquids, polymers and plastic crystal-strong/fragile patterns and related problems, *J. Non-Cryst. Solids*. 1991, 13: 131~133.
- [Angell et al, 2000] C.A. Angell, K.L. Ngai, G.B. McKenna, P.F. McMillan and S.W. Martin, Relaxation in glassforming liquids and amorphous solids, *J. Appl. Phys.* 2000, 88: 3113~3157.
- [Angell et al., 2003] C. A. Angell, Y. Yue, J. D. Copley, S. Borick and S. Mossa, Potential energy, relaxation, vibrational dynamics and the boson peak, of hyperquenched glasses, *J. Phys.: Condens. Matter* 2003, 15, S1051~1068.
- [Argon, 1979] A.S. Argon, Plastic deformation in metallic glasses, *Acta Metall.* 1979, 27: 47~58.
- [Argon et al., 1980] A.S. Argon and H.Y. Kuo, Free energy spectra for inelastic deformation of five metallic glass alloys, *J. Non-Cryst. Solids*. 1980, 37: 241~266.
- [Ashby et al., 2006] M.F. Ashby and A.L. Greer, Metallic glasses as structural materials, *Scripta Mater.* 2006, 54: 321~326.
- [Asoka-Kumar et al., 2000] P. Asoka-Kumar, J. Hartley, R. Howell, P.A. Sterne and T.G. Nieh, Chemical ordering around open-volume regions in bulk metallic glass $\text{Zr}_{52.5}\text{Ti}_5\text{Al}_{10}\text{Cu}_{17.9}\text{Ni}_{14.6}$, *Appl. Phys. Lett.* 2000, 77: 1973~1975.
- [Astrath et al., 2006] N.G.C. Astrath, A. Steimacher, A.N. Medina, J.H. Rohling, J.R.D. Pereira, A.C. Bento, M.L. Baesso, L.M. da Silva and F.G. Gandra, Low temperature specific heat of doped and undoped glasses, *J. Non-Cryst. Solids*. 2006, 352: 3572~3576.
- [Avrami, 1939] M. Avrami, Kinetics of phase change, *J. Chem. Phys.* 7 (1939) 1103~1112.
- [Avrami, 1940] M. Avrami, Kinetics of phase change, *J. Chem. Phys.* 8 (1940) 212~224.
- [Avrami, 1941] M. Avrami, Kinetics of phase change, *J. Chem. Phys.* 9 (1941) 177~184.
- [Azhazha et al., 2003] V. Azhazha, A. Grib, G. Khadzhay, B. Merisov and A. Pugachov, Influence of hydrogen on electrical resistivity of $\text{Ti}_{66}\text{Ni}_{20}\text{Cu}_{10}\text{Si}_4$ amorphous alloy, *Hydrogen Energy*, 2003, 28: 415~418.
- [Bae et al., 2002] D.H. Bae, H.K. Lim, S.H. Kim, D.H. Kim and W.T. Kim. Mechanical behavior of a bulk Cu-Ti-Zr-Ni-Si-Sn metallic glass forming nano-crystal aggregate bands during deformation in the supercooled liquid region, *Acta Mater.* 2002, 50: 1749~1759.
- [Bae et al., 2004] D.H. Bae, J.M. Park, J.H. Na, D.H. Kim, Y.C. Kim and J.K. Lee, Deformation behavior of Ti-Zr-Ni-Cu-Be metallic glass and composite in the supercooled liquid region, *J. Mater. Res.* 2004, 19: 937~942.
- [Bai et al., 2008] L. Bai, C.X. Cui, Q.Z. Wang, S.J. Bu and Y.M. Qi, Ti-Zr-Fe-Si system amorphous alloys with excellent biocompatibility, *J. Non-Cryst. Solids*. 2008, 354: 3935~3938.
- [H.Y. Bai et al., 1996] H. Y. Bai, J. L. Luo, D. Jin and J. R. Sun, Particle size and interfacial effect on the specific heat of nanocrystalline Fe, *J. Appl. Phys.* 1996, 79: 361~364.
- [H.Y. Bai et al., 2001] H.Y. Bai, J.L. Luo, Z.J. Chen and W.H. Wang, Low temperature specific heat of bulk glassy and crystalline $\text{Zr}_{41}\text{Ti}_{14}\text{Cu}_{12.5}\text{Ni}_{10}\text{Be}_{22.5}$ alloys, *Appl. Phys. Lett.* 2001, 78: 2697~2699.
- [H.Y. Bai et al., 2002] H.Y. Bai, J.L. Luo, J. Zhang and Z.J. Chen, Low temperature specific heat of typical glass forming alloy, *J. Appl. Phys.* 2002, 91: 9123~9127.

- [Bakai et al., 2002] A.S. Bakai, H. Hermann and N.P. Lazarev, Diffusion-limited crystallization of heterogeneous glasses, *Philos. Magn. A* 2002, 82: 1521~1539.
- [Baldwin et al., 2008] F. Baldwin, N.V. Ravi Kumar, K. Das, A. Bandyopadhyay and Y.M. Gupta, Effect of hafnium incorporation on the crystallization and mechanical behavior of a Zr-based bulk amorphous alloy, *Mater. Sci. Eng. A* 2008, 477: 233~242.
- [Banerjee et al., 1981] N. Banerjee, R. Roy, A.K. Majumdar and R. Hasegawa, Electrical resistivity in the $\text{Fe}_{100-x}\text{B}_x$ series ($13 \leq x \leq 26$), *Phys. Rev. B* 1981, 24: 6801~6806.
- [Barandiaran et al., 1981] J.M. Barandiaran and J. Colmenero, Continuous cooling approximation for the formation of a glass, *J. Non-Cryst. Solids* 1981, 46: 277~287.
- [Baricco et al., 2001] M. Baricco, S. Spriano, I. Chang, M.I. Petrzlik and L. Battezzati, "Big cube" phase formation in Zr-based metallic glasses, *Mater. Sci. Eng. A* 2001, 304-306: 305~310.
- [Bartolotta et al., 2001] A. Bartolotta, G. Carini, G. D'Angelo, M. Ferrari, A. Fontana, M. Montagna, F. Rossi and G. Tripodo, A study of Raman spectroscopy and low-temperature specific heat in gel-synthesized amorphous silica, *J. Non-Cryst. Solids* 2001, 280: 249~254.
- [Bendler et al., 2003] J.T. Bendler, J.J. Fontanella and M.F. Shlesinger, Physical basis of fragility, *J. Chem. Phys.* 2003, 118: 6713~6716
- [Black et al., 1978] J.L. Black and B.L. Gyorffy, Interaction of the conduction electrons with tunneling states in metallic glasses, *Phys. Rev. Lett.* 1978, 41: 1595~1598.
- [Bletry et al., 2004] M. Bletry, P. Guyot, Y. Brechet, J.J. Blandin and J.L. Soubeyroux, Homogeneous deformation of bulk metallic glasses in the supercooled liquid state, *Mater. Sci. Eng. A* 2004, 387-389: 1005~1011.
- [Bletry et al., 2006] M. Bletry, P. Guyot, J.J. Blandin and J.L. Soubeyroux, Free volume model: high-temperature deformation of a Zr-based bulk metallic glass, *Acta Mater.* 2006, 54: 1257~1263.
- [Bletry et al., 2007] M. Bletry, P. Guyot, Y. Bréchet, J.J. Blandin and J.L. Soubeyroux, Transient regimes during high-temperature deformation of a bulk metallic glass: a free volume approach, *Acta Mater.* 2007, 55: 6331~6337.
- [Boettinger et al., 1985] W.J. Boettinger, J.H. Perepezko, in: *Rapidly Solidified Crystalline, Alloys*, Morristown, New Jersey, 1985, pp. 21-58.
- [Böhmer et al., 1993] R. Böhmer, K.L. Ngai, C.A. Angell and D.J. Plazek, Non-exponential relaxations in strong and fragile glass formers, *J. Chem. Phys.* 1993, 99: 4201~4209.
- [Boucher, 1972] B.Y. Boucher, Influence of phosphorus on the electrical properties of Pd-Ni-P amorphous alloys, *J. Non-Cryst. Solids* 1972, 7: 277~284.
- [Bruck et al., 1996] H.A. Bruck, A.J. Rosakis and W.L. Johnson, The dynamic compressive behavior of beryllium bearing bulk metallic glasses, *J. Mater. Res.* 1996, 11: 503-511.
- [Busch et al., 1998-a] R. Busch and W.L. Johnson, The kinetic glass transition of the $\text{Zr}_{46.75}\text{Ti}_{8.25}\text{Cu}_{7.5}\text{Ni}_{10}\text{Be}_{27.5}$ bulk metallic glass former supercooled liquids on a long time scale, *Appl. Phys. Lett.* 1998, 72: 2695~2697.
- [Busch et al., 1998-b] R. Busch, W. Liu and W.L. Johnson, thermodynamics and kinetics of the MgCuY metallic glass forming liquid, *J. Appl. Phys.* 1998, 83: 4134~4141.
- [Busch et al., 1998-c] R. Busch, W. Liu and W.L. Johnson, Thermodynamics and kinetics of the $\text{Mg}_{65}\text{Cu}_{25}\text{Y}_{10}$ bulk metallic glass forming liquid, *J. Appl. Phys.* 1998, 83: 4134~4141.
- [Busch et al., 2001] R. Busch, A. Masuhr and W.L. Johnson, Thermodynamics and kinetics of Zr-Ti-Cu-Ni-Be bulk metallic glass forming liquids, *Mater. Sci. Eng. A* 2001, 304-306: 97~102.
- [Cahn, 1983] R.W. Cahn, *Physical Metallurgy*, 3rd ed., North Holland, Amsterdam, 1983, p. 1780.
- [Calka et al., 1987] A. Calka and A.P. Radinski, The local value of the Avrami exponent: a new approach to devitrification of glassy metallic ribbons, *Mater. Sci. Technol.* 1987, 97: 241~246.
- [Calka et al., 1988] A. Calka and A.P. Radinski, Decoupled bulk and surface crystallization in $\text{Pd}_{85}\text{Si}_{15}$ glassy metallic alloys: description of isothermal crystallization by a local value of the Avrami exponent, *J. Mater. Res.* 1988, 3: 59~66.
- [Calin et al., 2007] M. Calin, L.C. Zhang and J. Eckert, Tailoring of microstructure and mechanical properties of a Ti-based bulk metallic glass-forming alloy, *Scripta Mater.* 2007, 57: 1101-1104.
- [Cao et al., 2006] Q.P. Cao, H.F. Li, Y.H. Zhou, A. Horsewell and J.Z. Jiang, Effect of rolling deformation on the microstructure of bulk $\text{Cu}_{60}\text{Zr}_{20}\text{Ti}_{20}$ metallic glass and its crystallization, *Acta Mater.* 2006, 54: 4373~4383.

- [Caplin et al., 1973] A. D. Caplin, G. Grüner and J. B. Dunlop, Al_{10}V : an Einstein solid, *Phys. Rev. Lett.* 1973, 30: 1138~1140.
- [Chan et al., 2007] K.C. Chan, L. Liu and J.F. Wang, Superplastic deformation of $\text{Zr}_{55}\text{Cu}_{30}\text{Al}_{10}\text{Ni}_5$ bulk metallic glass in the supercooled liquid region, *J. Non-Cryst. Solids*, 2007, 353: 3758~3763.
- [Chang et al., 2006] H.J. Chang, D.H. Kim, Y.M. Kim, Y.J. Kim and K. Chattopadhyay, On the origin of nanocrystals in the shear band in a quasicrystal forming bulk metallic glass $\text{Ti}_{40}\text{Zr}_{29}\text{Cu}_9\text{Ni}_8\text{Be}_{14}$, *Scripta Mater.* 2006, 55: 509~512.
- [Chen, et al., 1972] H.S. Chen and W.H. Haemmerle, Excess specific heat of a glassy $\text{Pd}_{0.775}\text{Cu}_{0.06}\text{Si}_{0.165}$ alloy at low temperature, *J. Non-Cryst. Solids*, 1972, 11: 161~169.
- [Chen, 1976] H.S. Chen and E. Coleman, Structural relaxation in metallic glasses, *Appl. Phys. Lett.* 1976, 28: 245~247.
- [Chen, 1980] H.S. Chen, Glassy metals, *Rep. Prog. Phys.* 1980, 43: 353~432.
- [Chen, 1981] H.S. Chen. On the mechanisms of structural relaxation in a $\text{Pd}_{48}\text{Ni}_{32}\text{P}_{20}$ glass, *J. Non-Cryst. Solids*. 1981, 46: 289~305.
- [Chen et al., 2001] H.S. Chen, H. Kato, A. Inoue, J. Saida and N. Nishiyama, Thermal evidence of stress-induced structural disorder of a $\text{Zr}_{55}\text{Al}_{10}\text{Ni}_5\text{Cu}_{30}$ glassy alloy in the non-Newtonian region, *Appl. Phys. Lett.* 2001, 79: 60~62.
- [Q.J. Chen et al., 2005] Q.J. Chen, J. Shen, H.B. Fan, J.F. Sun, Y.J. Huang, and D.G. McCartney, Glass-forming ability of an Iron-based alloy enhanced by Co addition and evaluated by a new criterion, *Chin. Phys. Lett.* 2005, 22: 1736~1738.
- [Chiang et al., 2004] C.L. Chiang, J.P. Chu, C.T. Liu, T.G. Nieh, Z.X. Wang and W.H. Wang, Homogeneous plastic deformation in a Cu-based bulk amorphous alloy, *Intermetallics*. 2004, 12: 1057~1061.
- [Choi et al., 2007] Y.C. Choi and S.I. Hong, High-temperature deformation behavior and stress relaxation of Zr-Ti-Cu-Ni-Be bulk metallic glass extracted from commercial golf club heads, *Mater. Sci. Eng. A* 2007, 449-451: 130~133.
- [Christian, 2003] J. Christian, *Rhe theory of transformations in metals and alloys*, Pergamon, 2003, (3rd edition).
- [Chu et al., 2002] J.P. Chu, C.L. Chiang, T.G. Nieh and Y. Kawamura, Superplasticity in a bulk amorphous $\text{Pd}_{40}\text{Ni}_{20}\text{P}$ alloy: a compression study, *Intermetallics*. 2002, 10: 1191~1195.
- [Chu et al., 2003] J.P. Chu, C.L. Chiang, T. Mahalingam and T.G. Nieh, Plastic flow and tensile ductility of a bulk amorphous $\text{Zr}_{55}\text{Al}_{10}\text{Cu}_{30}\text{Ni}_5$ alloy at 700 K, *Scripta Mater.* 2003, 49: 435~440.
- [Chu et al., 2006] J.P. Chu, C.L. Chiang, H. Wijaya, R.T. Huang, C.W. Wu, B. Zhang, W.H. Wang and T.G. Nieh, Compressive deformation of a bulk Ce-based metallic glass, *Scripta Mater.* 2006, 55: 227~230.
- [R.W. Cochrane et al., 1975] R.W. Cochrane, R. Harris, J.O. Ström-Olson and M.J. Zuckermann, Structural manifestations in amorphous alloys: resistance minima, *Phys. Rev. Lett.* 1975, 35: 676~679.
- [Cochrane et al., 1999] R.F. Cochrane, P. Schumacher and A.L. Greer, Crystallization of amorphous $\text{Al}_{85}\text{Ni}_{10}\text{Ce}_5$ alloy, *Mater. Sci. Eng. A* 1999, 133: 367~370.
- [Cohen et al., 1959] M.H. Cohen and D. Turnbull, Molecular transport in liquids and glasses, *J. Chem. Phys.* 1959, 31: 1164~1169.
- [Cohen et al., 1979] M. H. Cohen and G. S. Grest, Liquid-glass transition, a free-volume approach, *Phys. Rev. B* 1979, 20: 1077~1098.
- [Concustell et al., 2005] A. Concustell, J. Sort, G. Alcalá, S. Mato, A. Gebert, J. Eckert and M.D. Baró, Plastic deformation and mechanical softening of $\text{Pd}_{40}\text{Cu}_{30}\text{Ni}_{10}\text{P}_{20}$ bulk metallic glass during nanoindentation, *J. Mater. Res.* 2005, 20: 2719~2725.
- [Courten et al., 2001] E. Courtens, M. Foret, B. Hehlen and R. Vacher, The vibrational modes of glasses, *Solid State Commun.* 2001, 117: 187~200.
- [Das et al., 2005] K. Das, A. Bandyopadhyay and Y.M. Gupta, Effect of crystallization on the mechanical properties of $\text{Zr}_{56.7}\text{Cu}_{15.3}\text{Ni}_{12.5}\text{Nb}_{5.0}\text{Al}_{10.0}\text{Y}_{0.5}$ bulk amorphous alloy, *Mater. Sci. Eng. A* 2005, 394: 302~311.
- [De Hey et al., 1998] P. De Hey, J. Sietsma and A. Van den Beukel, Structural disordering in amorphous $\text{Pd}_{40}\text{Ni}_{40}\text{P}_{20}$ induced high temperature deformation, *Acta Mater.* 1998, 46: 5873~5882
- [Dikeakos et al., 1999] M. Dikeakos and Z. Altounian, Temperature dependence of the resistivity of amorphous Fe-Co-Zr alloys, *J. Non-Cryst. Solids*, 1999, 250-252: 786~790.

- [H.M. Chen et al., 2009] H.M. Chen, X.H. Du, J.C. Huang, J.S.C. Jang and T.G. Nieh, Analysis of plastic strain and deformation mode of a Zr-based two-phase bulk metallic glass in compression, *Intermetallics*. 2009, 17: 330~335.
- [L.Y. Chen et al., 2008] L.Y. Chen, Q. Ge, S. Qu, Q.K. Jiang, X.P. Nie and J.Z. Jiang, Achieving large macroscopic compressive plastic deformation and work-hardening-like behavior in a monolithic bulk metallic glass by tailoring stress distribution, *Appl. Phys. Lett.* 2008, 92: 211905.
- [Cheney et al., 2009] J. Cheney, H. Khalifa and K. Vecchio, Modeling the amorphous forming ability of Ti-based alloys with wide supercooled liquid regions, high hardness, *Mater. Sci. Eng. A* 2009, 506: 94~100.
- [Dolocan et al., 1987] V. Dolocan and E. Dolocan, Electrical resistivity and crystallization of glassy $\text{Fe}_{100-x}\text{B}_x$; $\text{Fe}_{80-x}\text{Co}_x\text{B}_{20}$; $\text{Fe}_{78}\text{B}_{22-x}\text{Si}_x$ and $\text{Fe}_{100-x}\text{B}_{x-y}\text{Si}_y$ alloys, *Rev. Roum. Phys.* 1987, 32: 1077~1090.
- [Donovan et al., 1989] P.E. Donovan, A yield criterion for $\text{Pd}_{40}\text{Ni}_{40}\text{P}_{20}$ metallic glass, *Acta Metall.* 1989, 37: 445~456.
- [Drehman et al., 1982] A.J. Drehman, A.L. Greer and D. Turnbull, Bulk formation of a metallic glass: $\text{Pd}_{40}\text{Ni}_{40}\text{P}_{20}$, *Appl. Phys. Lett.* 1982, 41: 716~717.
- [Duan et al., 2008] G. Duan, A. Wiest, M.L. Lind, A. Kahl and W.L. Johnson, Lightweight Ti-based bulk metallic glasses excluding late transition metals, *Scripta Mater.* 2008, 58: 465~468.
- [Duine et al., 1992] P.A. Duine, J. Sietsma, A. Van den. Beukel, Defect production and annihilation near equilibrium in amorphous $\text{Pd}_{40}\text{Ni}_{40}\text{P}_{20}$ investigated from viscosity data, *Acta Metall. Mater.* 1992, 40: 743~751.
- [Egami et al., 1984] T. Egami and Y. Waseda, Atomic size effect on the formability of metallic glasses, *J. Non-Cryst. Solids*. 1984, 64: 113~134.
- [Egami, 1996] T. Egami, The atomic structure of aluminum based metallic glasses and universal criterion for glass formation, *J. Non-Cryst. Solids*. 1996, 205~207: 575~582.
- [Egami, 1997] T. Egami, Universal criterion for metallic glass formation, *Mater. Sci. Eng. A* 1997, 226~228: 261~267.
- [Ehmler et al., 1998] H. Ehmler, A. Heesemann, K. Rätzke, F. Faupel and U. Geyer, Mass dependence of diffusion in a supercooled metallic melt, *Phys. Rev. Lett.* 1998, 80: 4919~4922.
- [Evans et al., 1971] R. Evans, D.A. Greenwood and P. Lloyd, Calculations of the transport properties of liquid transition metals, *Phys. Lett. A* 1971, 35: 57~58.
- [Faber et al., 1965] T.E. Faber and J.M. Ziman, A theory of the electrical properties of liquid metals III. The resistivity of binary alloys, *Philos. Mag.* 1965, 11: 153~173.
- [Fan et al., 2004] G.J. Fan, J.F. Löffler, R.K. Wunderlich and H.J. Fecht, Thermodynamics, enthalpy relaxation, and fragility of $\text{Pd}_{43}\text{Ni}_{10}\text{Cu}_{27}\text{P}_{20}$ bulk metallic glass-forming liquid, *Acta Mater.* 2004, 52: 667~674.
- [Flores et al., 2002] K.M. Flores, D. Suh, R.H. Dauskardt, P. Asoka-Kumar, P.A. Sterne and R.H. Howell, Characterization of free volume in a bulk metallic glass using positron annihilation spectroscopy, *J. Mater. Res.* 2002, 17: 1153~1161.
- [Flores et al., 2004] K. M. Flores and R. H. Dauskardt, Fracture and deformation of bulk metallic glasses and their composites, *Intermetallics*. 2004, 12, 1025~1029.
- [Flores et al., 2007] K.M. Flores, B.P. Kanungo, S.C. Glade and P. Asoka-Kumar, Characterization of plasticity –induced structural changes in a Zr-based bulk metallic glass using positron annihilation spectroscopy, *J. Non-cryst. Solids*. 2007, 353: 1201~1207.
- [Foret et al., 1996] M. Foret, E. Courtens, R. Vacher and J. Suck, Scattering investigation of acoustic localization in fused silica, *Phys. Rev. Lett.* 1996, 77: 3831~3834.
- [Fornell et al., 2009] J. Fornell, A. Concustell, S. Suriñach, W.H. Li, N. Cuadrado, A. Gebert and M.D. Baró and J. Sort, Yielding and intrinsic plasticity of Ti-Zr-Ni-Cu-Be bulk metallic glass, *Int. J. Plasticity*. 2009, 25: 1540~1559.
- [Frank et al., 1994] W. Frank, A. Hörner, P. Scharwaechter and H. Kronmüller, Diffusion in amorphous metallic alloys, *Mater. Sci. Eng., A* 1994, 179-180: 36~40.
- [Gallino et al., 2007-a] I. Gallino, M.B. Shah and R. Busch, Enthalpy relaxation of the $\text{Zr}_{58.5}\text{Cu}_{15.6}\text{Ni}_{12.8}\text{Al}_{10.3}\text{Nb}_{2.8}$ bulk metallic glass forming alloy, *J. Alloy. Compd.* 2007, 434-435: 141~144.
- [Gallino et al., 2007-b] I. Gallino, M.B. Shah and R. Busch, Enthalpy relaxation and its relation to the thermodynamics and crystallization of the $\text{Zr}_{58.5}\text{Cu}_{15.6}\text{Ni}_{12.8}\text{Al}_{10.3}\text{Nb}_{2.8}$ bulk metallic

- glass-forming alloy, *Acta Mater.* 2007, 55: 1367~1376.
- [Gebert et al., 2008] A. Gebert, V. Haehnel, E.S. Park, D.H. Kim and L. Schultz, Corrosion behavior of $\text{Mg}_{65}\text{Cu}_{7.5}\text{Ni}_{7.5}\text{Ag}_5\text{Zn}_5\text{Gd}_5\text{Y}_5$ bulk metallic glass in aqueous environments, *Electrochimica Acta.* 2008, 53, 3403~3411.
- [Gey et al., 1993] W. Gey and W. Eschner, Low-temperature specific heat of Zr-Rh-Pd metallic glasses, *Phys. Rev. B* 1993, 48: 15666~15671.
- [Gil et al., 1993] L. Gil, M.A. Ramos, A. Bringer and U. Buchenau, Low-temperature specific heat and thermal conductivity of glasses, *Phys. Rev. Lett.* 1993, 70: 182~185.
- [Golding et al., 1972] B. Golding, B. G. Bagley and F. S. L. Hsu, Soft transverse phonons in a metallic glass, *Phys. Rev. Lett.* 1972, 29: 68~72.
- [Gorbachev, 1980] V.M. Gorbachev, Some aspect of Sestak's generalized kinetic equation in thermal analysis, *J. Therm. Anal. Cal.* 1980, 18: 193~197.
- [Golovin et al., 2001] Y.I. Golovin, V.I. Ivolgin, V.A. Khonik, K. Kitagawa and A.I. Tyurin, Serrated plastic flow during nanoindentation of a bulk metallic glass, *Scripta Mater.* 2001, 45: 947~952.
- [Götze et al., 1992] W. Götze and L. Sjögren, Relaxation processes in supercooled liquids, *Rep. Prog. Phys.* 1992, 55: 241~376.
- [Graebner et al., 1977] J. E. Graebner, B. Golding, R. J. Schutz, F. S. L. Hsu and H. S. Chen, Low-temperature properties of a superconducting disordered metal, *Phys. Rev. Lett.* 1977, 39: 1480~1483.
- [Gravier, 2006] S. Gravier, Effect of partial crystallization on the mechanical behavior of bulk metallic glasses, thesis Institut National Polytechnique de Grenoble, 2006.
- [Gun et al., 2006] B. Gun, K.J. Laws and M. Ferry, Superplastic flow of a Mg-based bulk metallic glass in the supercooled liquid region, *J. Non-Crys. Solids.* 2006, 352: 3896~3902.
- [Gun et al., 2007] B. Gun, K.J. Laws and M. Ferry, Elevated temperature flow behavior of a Mg-based bulk metallic glass, *Mater. Sci. Eng. A* 2007, 471: 130~134.
- [Guo et al., 2005] F.Q. Guo, H.J. Wang, S.J. Poon and G.J. Shiflet, Ductile titanium-based glassy alloy ingots, *Appl. Phys. Lett.* 2005, 86: 091907.
- [J. Guo et al., 2007] J. Guo, X.F. Bian, T. Lin, Y. Zhao, T.B. Li, B. Zhang and B.A. Sun, Formation and interesting thermal expansion behavior of novel, *Intermetallics*, 2007, 15: 929~933.
- [X.L. Guo et al., 2009] X.L. Guo, K.C. Chan, L. Liu, D.B. Shan and B. Guo, Stress-induced structural change during superplastic deformation of bulk Zr-based metallic glass, *Mater. Sci. Eng.* 2009, 499: 534~539.
- [Gupta, et al., 2001] R. Gupta, A. Gupata, A.K. Nigam and G. Chandra, Effect of induced disorder on low temperature resistivity of some non-magnetic and magnetic metallic glasses, *J. Alloy. Compd.* 2001, 326: 275~279.
- [Gurevich et al., 1993] V.L. Gurevich, D.A. Parshin, J. Pelous and H.R. Schober, Theory of low-energy Raman scattering in glasses, *Phys. Rev. B* 1993, 48: 16318~16331.
- [Hajlaoui et al., 2007] K. Hajlaoui, A.R. Yavari, A. LeMoulec, W.J. Botta, F.G. Vaughan, J. Das, A.L. Greer and Å. Kvick, Plasticity induced by nanoparticle dispersions in bulk metallic glasses, *J. Non-Cryst. Solids.* 2007, 353: 327~331.
- [Han et al., 2001] T.K. Han, T. Zhang, A. Inoue, Y.S. Yang, I.B. Kim and Y.H. Kim, Thermal and mechanical properties of amorphous $\text{Zr}_{65}\text{Al}_{7.5}\text{Ni}_{10}\text{Cu}_{12.5}\text{Ag}_5$ alloy containing nanocrystalline compound particles, *Mater. Sci. Eng. A* 2001, 304-306: 892~896.
- [Hammond et al., 2003] V.H. Hammond, M.D. Houtz and J.M. O'Reilly, Structural relaxation in a bulk metallic glass, *J. Non-Cryst. Solids.* 2003, 325: 179~186.
- [He et al., 2003-a] G. He, J. Eckert, W. Löser and L. Schultz, Novel Ti-base nanostructure-dendrite composite with enhanced plasticity, *Nature Mater.* 2003, 2: 33~37.
- [He et al., 2003-b] G. He, J. Eckert, W. Löser and L. Schultz, Ductile dendritic phase reinforced Ti-based bulk metallic glass-forming alloys, *Mat. Res. Soc. Symp. Proc.* 2003, 754: CC11.12.
- [Henderson, 1979] D.W. Henderson, Thermal analysis of non-isothermal crystallization kinetics in glass forming liquids, *J. Non-Cryst. Solids.* 1979, 30: 301~315.
- [Hermann et al., 2003] R. P. Hermann, R. Jin, W. Schweika, F. Grandjean, D. Mandrus, B. C. Sales and G. J. Long, Einstein oscillators in thallium filled antimony, *Phys. Rev. Lett.* 2003, 90: 135505.

-
- [Holzer et al., 1991] J.C. Holzer and K.F. Kelton, Kinetics of the amorphous to icosahedral phase transformation in Al-Cu-V alloy, *Acta Metall. Mater.* 1991, 39: 1833~1843.
- [Howson, 1984] M.A. Howson, Incipient localization and electron-electron correlation effects in metallic glass alloys, *J. Phys. F* 1984, 14: L25-L31.
- [Howson et al., 1988] M.A. Howson and B.L. Gallagher, The electron transport properties of metallic glasses, *Phys. Rep.* 1988, 170: 265~324.
- [Huang et al., 2007-a] Y.J. Huang, J. Shen, J.F. Sun and X.B. Yu, A new Ti-Zr-Hf-Cu-Ni-Si-Sn bulk amorphous alloy with high glass-forming ability, *J. Alloy. Comp.* 2007, 427: 171~175.
- [Huang et al., 2007-b] Y.J. Huang, J. Shen and J.F. Sun, Bulk metallic glasses: smaller is softer, *Phys. Lett.* 2007, 90: 081919.
- [Huang et al., 2008-a] Y.J. Huang, J. Shen, J.F. Sun and Z.F. Zhang, Enhanced strength and plasticity of a Ti-based metallic glass at cryogenic temperatures, *Mater. Sci. Eng. A* 2008, 498: 203~207.
- [Huang et al., 2008-b] Y.J. Huang, J. Shen and J.F. Sun, Formation, thermal stability and mechanical properties of $\text{Ti}_{42.5}\text{Zr}_{7.5}\text{Cu}_{40}\text{Ni}_5\text{Sn}_5$ bulk metallic glass, *Sci China Ser G-Phys Mech Astron.* 2008, 51: 372~378.
- [L.J. Huang et al., 2008] L.J. Huang, L. Li, G.Y. Liang, Y.L. Guo and D.C. Wu, Crystallization kinetics of $\text{Mg}_{65}\text{Cu}_{25}\text{Nd}_{10}$ amorphous alloy, *J. Non-Cryst. Solids.* 2008, 354: 1048~1053.
- [Hufnagel et al., 2003] T.C. Hufnagel and S. Brennan, Short- and medium-range order in $(\text{Zr}_{70}\text{Cu}_{20}\text{Ni}_{10})_{90-x}\text{Ta}_x\text{Al}_{10}$ bulk amorphous alloys, *Phys. Rev. B* 2003, 67: 014203.
- [Inoue, 1994] A. Inoue, Fabrication and novel properties of nanostructured Al base alloys, *Mater. Sci. Eng. A* 1994, 179~180: 57~61.
- [Inoue et al., 1994] A. Inoue, N. Nishiyama, K. Amiyam, T. Zhang and T. Masumoto, Ti-based amorphous alloys with a wide supercooled liquid region, *Mater. Lett.* 1994, 19: 131~135.
- [Inoue et al., 1998-a] A. Inoue, T. Zhang and A. Takeuchi, Ferrous and nonferrous bulk amorphous alloys, *Mater. Sci. Forum.* 1998, 269~272: 855~864.
- [Inoue, 1999] A. Inoue, Synthesis and properties of Ti-based bulk amorphous alloys with a large supercooled liquid region, *J. Meta. Nano. Mater.* 1999, 2-6: 307~314.
- [Inoue, 2000] A. Inoue, Stabilization of metallic supercooled liquid and bulk amorphous alloys, *Acta Mater.* 2000, 48: 279~306.
- [Inoue et al., 2000-a] A. Inoue, T. Zhang, J. Saida and M. Matsushita, Mater. Enhancement of strength and ductility in Zr-based bulk amorphous alloys, *Trans. JIM* 2000, 41: 1511~1520.
- [Inoue et al., 2000-b] A. Inoue, C. Fan, J. Saida and T. Zhang, High-strength Zr-based bulk amorphous alloys containing nanocrystalline and nanoquasicrystalline particles, *Sci. Technol. Adv. Mater.* 2000, 1: 73~86.
- [Inoue et al., 2001] A. Inoue, W. Zhang, T. Zhang, and K. Kurosaka, High-strength Cu-based bulk glassy alloys in Cu-Zr-Ti and Cu-Hf-Ti ternary systems, *Acta Mater.* 2001, 49: 2645~2652.
- [Inoue et al., 2002] A. Inoue, W. Zhang, T. Zhang and K. Kurosaka, Cu-based bulk glassy alloys with high tensile strength of over 2000 MPa, *J. Non-Cryst. Solids.* 2002, 304: 200~209.
- [Inoue et al., 2004] A. Inoue, W. Zhang, and J. Saida: Synthesis and fundamental properties of Cu-based bulk glassy alloys in binary and multicomponent systems. *Mater. Trans.* 2004, 45: 1153~1162.
- [Inoue et al., 2005] A. Inoue, W. Zhang, T. Tsurui, A.R. Yavari and A.L. Greer, Unusual room-temperature compressive plasticity in nanocrystal-toughened bulk copper-zirconium glass, *Phil. Mag. Lett.* 2005, 85: 221~237.
- [Ishimaru et al., 2005] M. Ishimaru, Y. Hirotsu, S. Hata, C. Ma, N. Nishiyama, K. Amiya and A. Inoue, Structural characterization of Cu-Ti-based bulk metallic glass by advanced electron microscopy, *Phil. Mag. Lett.* 2005, 85: 125~133.
- [Jiang et al., 2003] J.Z. Jiang, J. Saida, H. Kato, T. Ohsuna and A. Inoue, Is $\text{Cu}_{60}\text{Ti}_{10}\text{Zr}_{30}$ a bulk glass-forming alloy? *Appl. Phys. Lett.* 2003, 82: 4041~4043.
- [Law et al., 2008] K.J. Laws, B. Gun and M. Ferry, Mechanical stability of $\text{Ca}_{65}\text{Mg}_{15}\text{Zn}_{20}$ bulk metallic glass during deformation in the supercooled liquid region, *Mater. Sci. Eng. A* 2008, 480: 198~204.
- [Löffler et al., 2000] J.F. Löffler and W.L. Johnson, Model for decomposition and nanocrystallization of deeply undercooled $\text{Zr}_{41.2}\text{Ti}_{13.8}\text{Cu}_{12.5}\text{Ni}_{10}\text{Be}_{22.5}$, *Appl. Phys. Lett.* 2000, 76: 3394.

- [Jäckel et al., 2002] M. Jäckel, R. Geilenkeuser and A. Gladun, Influence of high pressure on the specific heat of amorphous polymers at low temperatures, *Physica B*. 2002, 316-317: 535~538.
- [Johnson, 1999] W.L. Johnson, Bulk glass-forming metallic alloys: science and technology, *MRS Bull* 1999, 24: 42~56.
- [Johnson et al., 2002] W.L. Johnson, J. Lu and M.D. Demetriou, Deformation and flow in bulk metallic glasses and deeply undercooled glass forming liquids-a self consistent dynamic free volume model, *Intermetallics*. 2002, 10: 1039~1046.
- [J.W. Johnson et al., 1966] J. W. Johnson and D. G. Holloway, On the shape and size of the fracture zones on glass fracture surface, *Philos. Mag.* 1966, 14: 731~743.
- [Jones, 1982] H. Jones, *Rapid Solidification of Metals and Alloys*, Monograph #8, Institution of Metallurgists, London, 1982.
- [Karpov et al., 1983] V.G. Karpov, M.I. Klinger and F.N. Ignat'ev, Theory of the low-temperature anomalies in the thermal properties of amorphous structures, *Zh. Eksp. Teor. Fiz.* 1983, 84: 760 (Sov. Phys. JETP 1983, 57: 439).
- [Kawamura et al., 1996] Y. Kawamura, T. Shibata, A. Inoue and T. Masumoto, Newtonian to non-Newtonian master flow curves of a bulk glass alloy $\text{Pd}_{40}\text{Ni}_{10}\text{Cu}_{30}\text{P}_{20}$, *Appl. Phys. Lett.* 1998, 73: 3665~3667.
- [Kawamura et al., 1997] Y. Kawamura, T. Shibata, A. Inoue and T. Masumoto, Superplastic deformation of $\text{Zr}_{65}\text{Al}_{10}\text{Ni}_{10}\text{Cu}_{15}$ metallic glass, *Scripta Mater.* 1997, 37: 431~436.
- [Kawamura et al., 1998] Y. Kawamura, T. Nakamura and A. Inoue. Superplasticity in $\text{Pd}_{40}\text{Ni}_{40}\text{P}_{20}$ metallic glass, *Scripta Mater.* 1998, 39: 301~306.
- [Kawamura et al., 1999] Y. Kawamura, T. Nakamura, A. Inoue and T. Masumoto, High-strain-rate superplasticity due to Newtonian viscous flow in $\text{La}_{55}\text{Al}_{25}\text{Ni}_{20}$ metallic glass, *Mater Trans JIM*. 1999, 40: 794~803.
- [Kawamura et al., 2001] Y. Kawamura, T. Nakamura, H. Kato, H. Mano and A. Inoue, Newtonian and non-Newtonian viscosity of supercooled liquid in metallic glasses, *Mater. Sci. Eng. A* 2001, 304~306: 674~678.
- [Kelton et al., 2003] K.F. Kelton, G.W. Lee, A.K. Gangopadhyay, R.W. Hyers, T.J. Rathz, J.R. Rogers, M.B. Robinson and D.S. Robinson, First X-ray scattering studies on electrostatically levitated metallic liquids: demonstrated influence of local icosahedral order on the nucleation barrier, *Phys. Rev. Lett.* 2003, 90: 195504.
- [Kissinger, 1957] H.E. Kissinger, Reaction kinetics in differential thermal analysis, *Anal. Chem.* 1957, 29: 1702~1706.
- [Klement et al., 1960] W. Klement, R.H. Willens and P. Duwez, Non-crystalline structure in solidified gold-silicon alloys, *Nature*. 1960, 187: 869~870.
- [Kim et al., 2003] Y.C. Kim, J.H. Na, J.M. Park, D.H. Kim, Y.H. Lee and W.T. Kim, Role of nanometer-scale quasicrystals in improving the mechanical behavior of Ti-based bulk metallic glasses, *Appl. Phys. Lett.* 2003, 83: 3093~3095.
- [Kim et al., 2004] Y.C. Kim, W.T. Kim and D.H. Kim, A development of Ti-based bulk metallic glass, *Mater. Sci. Eng. A* 2004, 375-377: 127~135.
- [H.S. Kim, 2004] H.S. Kim, Fictive stress model based finite element analysis for bulk metallic glasses at an elevated temperature, *Met. Mater. Int.* 2004, 10: 461~466.
- [J.J. Kim et al., 2002] J.J. Kim, Y. Choi, S. Suresh and A.S. Argon, Nanocrystallization during nanoindentation of a bulk amorphous metal alloy at room temperature, *Science*. 2002, 295: 654~657.
- [K.B. Kim et al., 2006-a] K.B. Kim, J. Das, X.D. Wang, X. Zhang, J. Eckert and S. Yi, Effect of Sn on microstructure and mechanical properties of (Ti-Cu)-based bulk metallic glasses, *Philos. Mag. Lett.* 2006, 86: 479~486.
- [K.B. Kim et al., 2006-b] K.B. Kim, J. Das, F. Baier, M.B. Tang, W.H. Wang and J. Eckert, Heterogeneity of a $\text{Cu}_{47.5}\text{Zr}_{47.5}\text{Al}_5$ bulk metallic glass, *Appl. Phys. Lett.* 2006, 88: 051911.
- [K.B. Kim et al., 2007] K.B. Kim, P.J. Warren and B. Cantor, Structural relaxation and glass transition behavior of novel $(\text{Ti}_{33}\text{Zr}_{33}\text{Hf}_{33})_{50}(\text{Ni}_{50}\text{Cu}_{50})_{40}\text{Al}_{10}$ alloy developed by equiatomic substitution, *J. Non-Cryst. Solids*, 2007, 353: 3338~3341.
- [K.B. Kim et al., 2008] K.B. Kim, X.F. Zhang, S. Yi, M.H. Lee, J. Das and J. Eckert, Effect of local chemistry, structure and length scale of heterogeneities on the mechanical properties of a $\text{Ti}_{45}\text{Cu}_{40}\text{Ni}_{7.5}\text{Zr}_5\text{Sn}_{2.5}$ bulk metallic glass, *Philos. Mag. Lett.* 2008, 88: 75~81.

- [W.J. Kim et al., 1993] W.J. Kim, D.S. Ma and H.G. Jeong, Superplastic flow in a $Zr_{65}Al_{10}Ni_{10}Cu_{15}$ metallic glass crystallized during deformation in a supercooled liquid region, *Scripta Mater.* 2003, 49: 1067~1073.
- [W.J. Kim et al., 2006-a] W.J. Kim, Y.K. Sa, J.B. Lee and H.G. Jeong, High-strain-rate superplasticity of $Zr_{65}Al_{10}Ni_{10}Cu_{15}$ sheet fabricated by squeeze casting method, *Intermetallics*. 2006, 14: 377~381.
- [W.J. Kim et al., 2006-b] W.J. Kim, Y.K. Sa, J.B. Lee and H.G. Jeong, Superplastic deformation and crystallization behavior of $Cu_{54}Ni_6Zr_{22}Ti_{18}$ metallic-glass sheet, *Intermetallics*. 2006, 14: 1391~1396.
- [Klose et al., 1994] G. Klose and H.J. Fecht, Vitrification close to the Kauzmann point of eutectic Au-Pb-Sb alloy, *Mater. Sci. Eng. A* 1994, 179-180:77~80.
- [Koch et al., 1983] C.C. Koch, D.M. Kroeger, J.S. Lin, J.O. Scarbrough, W.L. Johnson and A.C. Anderson, Effect of annealing on the structure of an amorphous $(Mo_{0.6}Ru_{0.4})_{82}B_{18}$ alloy, *Phys. Rev. B* 1983, 27: 1586~1595.
- [Koebrugge et al., 1992] G.W. Koebrugge, J. Sietsma, A. Van den Beukel. Structural relaxation in amorphous $Pd_{40}Ni_{40}P_{20}$, *Acta. Metall. Mater.* 1992, 40: 753~760.
- [Kokanović, 2006] I. Kokanović, Effect of disorder on the electrical resistivity in the partially crystalline $Zr_{76}Ni_{24}$ metallic glasses, *J. Alloy. Compd.* 2006, 421: 12~18.
- [Korn et al., 1972] D. Korn, W. Mürer and G. Zibold, Electrical resistivity of amorphous Sn-Cu alloys, *Phys. Lett. A* 1972, 47: 117~118.
- [Kou et al., 2009] H.C. Kou, J. Wang, B. Tang, X.F. Gu, R. Hu, J.S. Li, L. Zhou, *J. Alloy. Compd.* 2009, 479: L22~L25.
- [Kramer et al., 2004] M.J. Kramer, M.F. Besser, E. Rozhkova and D.J. Sordellet, Influence of short-range order on devitrification in $Zr_{70}Pd_{20}Cu_{10}$ metallic glasses, *Intermetallics*. 2004, 12: 1119~1124.
- [Kui et al., 1984] H. W. Kui, A. L. Greer and D. Turnbull, Formation of bulk metallic glass by fluxing, *Appl. Phys. Lett.* 1984, 45: 615~616.
- [Kündig et al., 2004] A.A. Kündig, M. Ohnuma, D.H. Ping, T. Ohkubo and K. Hono, In situ formed two-phase metallic glass with surface fractal microstructure, *Acta Mater.* 2004, 52: 2441~2448.
- [Launey et al., 2007] M.E. Launey, J.J. Kruzic, C. Li and R. Busch. Quantification of free volume differences in a $Zr_{44}Ti_{11}Ni_{10}Cu_{10}Be_{25}$ bulk amorphous alloy, *Appl. Phys. Lett.* 2007, 91: 051913.
- [Leamy et al., 1972] H.J. Leamy, H.S. Chen and T.T. Wang, Plastic flow and fracture of metallic glass, *Metall. Trans.* 1972, 3: 699~708.
- [Lee et al., 2003] K.S. Lee, T.K. Ha, S. Ahn and Y.W. Chang, High temperature deformation behavior of the $Zr_{41.2}Ti_{13.8}Cu_{12.5}Ni_{10}Be_{22.5}$ bulk metallic glass, *J. Non-Cryst. Solids*. 2003, 317: 193~199.
- [Lee et al., 2005-a] K.S. Lee, Y.W. Chang, Deformation behavior of Zr-based bulk metallic glass in an undercooled liquid state under compressive loading, *Met. Mater. Int.* 2005, 11: 53~57.
- [Lee et al., 2005-b] K.S. Lee and Y.W. Chang, Extrusion formability and deformation behavior of $Zr_{41.2}Ti_{13.8}Cu_{12.5}Ni_{10}Be_{22.5}$ bulk metallic glass in an undercooled liquid state after rapid heating, *Mater. Sci. Eng. A* 2005, 399: 238~243.
- [Lee et al., 2007] K.S. Lee, J. Eckert and Y.W. Chang, Load relaxation behavior of a $Zr_{41.2}Ti_{13.8}Cu_{12.5}Ni_{10}Be_{22.5}$ bulk metallic glass, *J. Non-Cryst. Solids*. 2007, 353: 2515~2520.
- [J.C. Lee et al., 2004] J.C. Lee, Y.C. Kim, J.P. Ahn, H.S. Kim, S.H. Lee and B.J. Lee, Deformation-induced nanocrystallization and its influence on work hardening in a bulk amorphous matrix composite, *Acta Mater.* 2004, 52: 1525~1533.
- [S.W. Lee et al., 2006-a] S.W. Lee, M.Y. Huh, S.W. Chae and J.C. Lee, Mechanism of the deformation-induced nanocrystallization in a Cu-based bulk amorphous alloy under uniaxial compression, *Scripta Mater.* 2006, 54: 1439~1444.
- [S.W. Lee et al., 2006-b] S.W. Lee, M.Y. Huh, E. Fleury and J.C. Lee, Crystallization-induced plasticity of Cu-Zr bulk amorphous alloys, *Acta Mater.* 2006, 54: 349~355.
- [Lewandowski et al., 2005] J.J. Lewandowski, W.H. Wang and A.L. Greer, Intrinsic plasticity of brittleness of metallic glasses, *Phil. Mag. Lett.* 2005, 85: 77~87.
- [H. Li et al., 2003] H. Li, G. Subhash, X.L. Gao, L.J. Kecskes and R.J. Dowding, Negative strain rate sensitivity and compositional dependence of fracture strength in Zr/Hf based bulk metallic

- glasses, *Scripta Mater.* 2003, 49: 1087~1092.
- [H. Li et al., 2006] H. Li, C. Fan, K. Tao, H. Choo and P.K. Liaw, Compressive behavior of a Zr-based metallic glass at cryogenic temperatures, *Adv. Mater.* 2006, 18: 752~754.
- [J. Li et al., 2002] J. Li, Z.L. Wang and T.C. Hufnagel, Characterization of nanometer-scale defects in metallic glasses by quantitative high-resolution transmission electron microscopy, *Phys. Rev. B* 2002, 65:144201.
- [J.F. Li et al., 2007] J.F. Li, Z.H. Huang and Y.H. Zhou, Crystallization of amorphous $Zr_{60}Al_{15}Ni_{25}$ alloy, *Intermetallics*. 2007, 15: 1013~1019.
- [Liang et al., 2008] W.Z. Liang, J. Shen, J.F. Sun, L.Z. Wu and P.K. Liaw, Compressive fracture characteristics of $Ni_{42}Cu_5Ti_{19}Zr_{22.5}Al_8Si_{3.5}$ bulk metallic glass, *Mater. Sci. Eng. A* 2008, 497: 378~382.
- [Liu, 1998] W.S. Liu, Formation and characterization of Mg-based bulk metallic glasses and nanocrystalline materials, thesis California Institute of Technology, 1998.
- [F. Liu et al., 2007] F. Liu, F. Sommer, C. Bos and E.J. Mittemeijer, Analysis of solid state phase transformation kinetics: models and recipes, *Int. Mater. Rev.* 2007, 52: 193~212.
- [C.T. Liu et al., 1998] C.T. Liu, L. Heatherly, D.S. Easton, C.A. Carmichael, J.L. Wright, J.H. Schneibel, M.H. Yoo, C.H. Chen and A. Inoue, Test environment and mechanical properties of Zr-base bulk amorphous alloys, *Metall Mater Trans.* 1998, 29: 1811~1820.
- [L. Liu et al., 2002] L. Liu, Z.F. Wu and J. Zhang, Crystallization kinetics of $Zr_{55}Cu_{30}Al_{10}Ni_5$ bulk amorphous alloy, *J. Alloys Compd.* 2002, 339: 90~95.
- [L. Liu et al., 2005] L. Liu and K.C. Chan, Plastic deformation of Zr-based bulk metallic glasses under nanoindentation, *Mater. Lett.* 2005, 59: 3090~3094.
- [L. Liu et al., 2006] L. Liu, C.L. Qiu, Q. Chen and S.M. Zhang, Corrosion behavior of Zr-based bulk metallic glasses in different artificial body fluids, *J. Alloy. Comp.* 2006, 425: 268~273.
- [L. Liu et al., 2007] L. Liu, Q. Chen, K.C. Chan, J.F. Wang and G.H.K. Pang, The effect of high temperature plastic deformation on the thermal stability and microstructure of $Zr_{55}Cu_{30}Ni_5Al_{10}$ bulk metallic glass, *Mater. Sci. Eng. A* 2007, 449-451: 949~953.
- [Y. Liu et al., 2006] Y. Liu, B. Bhandari and W.B. Zhou, Glass transition and enthalpy relaxation of amorphous food saccharides: a review, *J. Agric. Food Chem.* 2006, 54: 5701~5717.
- [Y. Liu et al., 2007] Y. Liu, B. Bhandari and W.B. Zhou, Study of glass transition and enthalpy relaxation of mixtures of amorphous sucrose and amorphous tapioca starch syrup solid by differential scanning calorimetry (DSC), *J. Food. Eng.* 2007, 81: 599~610.
- [Louzguine et al., 1999] D.V. Louzguine and A. Inoue, Multicomponent metastable phase formed by crystallization of Ti-Ni-Cu-Sn-Zr amorphous alloys, *J. Mater. Res.* 1999, 14: 4426~4430.
- [Louzguine et al., 2005] D.V. Louzguine, L.V. Louzguina, H. Kato and A. Inoue, Investigation of Ti-Fe-Co bulk alloys with high strength and enhanced ductility, *Acta Mater.* 2005, 53: 2009~2017.
- [Löffler et al., 2001] J.F. Löffler and W.L. Johnson, Crystallization pathways of deeply undercooled Zr-Ti-Cu-Ni-Be melts, *Scripta Mater.* 2001, 44: 1251~1255.
- [Löhneysen, 1981] H. Löhneysen, Low energy excitations in amorphous metals, *Phys. Rep.* 1981, 79: 161~212.
- [Lowhaphandu et al., 1999] P. Lowhaphandu, S.L. Montgomery and J.J. Lewandowski, Effects of superimposed hydrostatic pressure on flow and fracture of a Zr-Ti-Ni-Cu-Be bulk amorphous alloy, *Scripta Mater.* 1999, 41: 19~24.
- [Lu et al., 2002] Z.P. Lu and C.T. Liu, A new glass-forming ability criterion for bulk metallic glasses, *Acta Mater.* 2002, 50: 3501~3512.
- [J. Lu et al., 2003] J. Lu, G. Ravichandran and W.L. Johnson, Deformation behavior of the $Zr_{41.2}Ti_{13.8}Cu_{12.5}Ni_{10}Be_{22.5}$ bulk metallic glass over a wide range of strain-rates and temperatures, *Acta Mater.* 2003, 51: 3429~3443.
- [Ma et al., 2002] C.L. Ma and A. Inoue, Deformation and fracture behaviors of Pd-Cu-Ni-P glassy alloys, *Mater. Trans. JIM.* 2002, 43: 3266~3272.
- [Ma et al., 2004-a] C.L. Ma, S. Ishihara, H. Soejima, N. Nishiyama and A. Inoue, Formation of new Ti-based metallic glassy alloys, *Mater. Trans. JIM.* 2004, 45: 1802~1806.
- [Ma et al., 2004-b] C.L. Ma, H. Soejima, S. Ishihara, K. Amiya, N. Nishiyama and A. Inoue, New Ti-based bulk glassy alloys with high glass-forming ability and superior mechanical properties, *Mater. Trans. JIM.* 2004, 45: 3223~3227.

-
- [W.F. Ma et al., 2009] W.F. Ma, H.C. Kou, J.S. Li, H. Chang and L. Zhou, Effect of strain rate on compressive behavior of Ti-based bulk metallic glass at room temperature, *J. Alloy. Comp.* 2009, 472: 214~218.
- [Maitrepierre, 1970] P. Maitrepierre, Electrical resistivity of amorphous Ni-Pd-P alloys, *J. Appl. Phys.* 1970, 41: 498~503.
- [Málek, 2000] J. Málek, Kinetic analysis of crystallization processes in amorphous materials, *Thermochim. Acta.* 2000, 355: 239~253.
- [Martinez et al., 2008] R. Martinez, G. Kumar and J. Schroers, Hot rolling of bulk metallic glass in its supercooled liquid region, *Scripta Mater.* 2008, 59: 187~190.
- [Masuhr et al., 1999] A. Masuhr, T.A. Waniuk, R. Busch and W.L. Johnson, Time scales for viscous flow, atomic transport, and crystallization in the liquid and supercooled liquid state of $\text{Ti}_{41.2}\text{Ti}_{13.8}\text{Cu}_{12.5}\text{Ni}_{10}\text{Be}_{22.5}$, *Phys. Rev. Lett.* 1999, 82: 2290~2293.
- [Matsuda et al., 1984] T. Matsuda, N. Shiotani and V. Mizutani, Electronic properties of $\text{Mg}_{0.7}\text{Zn}_{0.3-x}\text{Ga}_x$ simple metallic glasses, *J. Phys. F* 1984, 14: 1193~1204.
- [Mattern et al., 2002] N. Mattern, U. Kühn, H. Hermann, H. Ehrenberg, J. Neuefeind and J. Eckert, Short-range order of $\text{Zr}_{62-x}\text{Ti}_x\text{Al}_{10}\text{Cu}_{20}\text{Ni}_8$ bulk metallic glasses, *Acta Mater.* 2002, 50: 305~314.
- [Mattern et al., 2005] N. Mattern, U. Kühn, A. Gebert, T. Gemming, M. Zmkerich, H. Wendrock and L. Schultz, Microstructure and thermal behavior of two-phase amorphous Ni-Nb-Y alloy, *Scripta Mater.* 2005, 53: 271~274.
- [Men et al., 2005] H. Men, S. Pang, A. Inoue and T. Zhang, New Ti-based bulk metallic glasses with significant plasticity, *Mater. Trans. JIM* 2005, 46: 2218~2220.
- [Meyer et al., 1998] A. Meyer, J. Wuttke, O. G. Randl and H. Schobe, Slow motion in a metallic liquid, *Phys. Rev. Lett.* 1998, 80: 4454~4457.
- [Miracle et al., 2003] D.B. Miracle and O.N. Senkov, Topological criterion for metallic glass, *Mater. Sci. Eng. A* 2003, 347: 50~58.
- [Miracle, 2004] D.B. Miracle, A structural model for metallic glasses, *Nature Mater.* 2004, 3: 697~702.
- [Mizutani et al., 1978] U. Mizutani, K.T. Hartwig and T.B. Massalski, Low-temperature specific heats of $\text{Pd}_{1-x-y}\text{Si}_x\text{Cu}_y$ alloys, *Phys. Rev. Lett.* 1978, 41: 661~663.
- [Mizutani, 1983] U. Mizutani, Electronic structure of metallic glasses, *Prog. Mater. Sci.* 1983, 28: 97~228.
- [Mizutani, 1985] U. Mizutani, in: S. Steeb, H. Warlimont (Eds.), *Proceedings of the Fifth International Conference on Rapidly Quenched Metals*, Würzburg, Elsevier, Amsterdam, 1985, p. 977.
- [Mooij, 1973] J.H. Mooij, Electrical conduction in concentrated disordered transition metal alloys, *Phys. Stat. Solidi. A* 1973, 17: 521~530.
- [Morrison et al., 2007] M.L. Morrison, R.A. Buchanan, A. Peker, P.K. Liaw and J.A. Horton, Electrochemical behavior of a Ti-based bulk metallic glass, *J. Non-Cryst. Solids.* 2007, 353: 2115~2124.
- [Mott, 1964] N.F. Mott, Electrons in transition metals, *Adv. Phys.* 1964, 13: 325~422.
- [Mott, 1972] N.F. Mott, The electrical resistivity of liquid transition metals, *Phil. Mag.*, 1972, 26: 1249~1261.
- [Mukai et al., 2002-a] T. Mukai, T.G. Nieh, Y. Kawamura, A. Inoue and K. Higashi, Dynamic response of a $\text{Pd}_{40}\text{Ni}_{40}\text{P}_{20}$ bulk metallic glass in tension, *Scripta Mater.* 2002, 46: 43~47.
- [Mukai et al., 2002-b] T. Mukai, T.G. Nieh, Y. Kawamura, A. Inoue and K. Higashi, Effect of strain rate on compressive behavior of a $\text{Pd}_{40}\text{Ni}_{40}\text{P}_{20}$ bulk metallic glass, *Intermetallics.* 2002, 10: 1071~1077.
- [Mulder et al., 1983] A.L. Mulder, S. van der Zwaag and A. van den Beukel, Embrittlement and disembrittlement in amorphous metglas 2826 A., *Scripta Metall.* 1983, 17: 1399~1402.
- [Murali et al., 2005] P. Murali and U. Ramamurty, Embrittlement of a bulk metallic glass due to sub- T_g annealing, *Acta Mater.* 2005, 53: 1467~1478.
- [Murty et al., 1995] B.S. Murty, M.M. Rao and S. Ranganathan, Differences in the glass-forming ability of rapidly solidified and mechanically alloyed Ti-Ni-Cu alloys, *Mater. Sci. Eng. A* 1995, 196: 237~241.
- [Nagel et al., 1975] S.R. Nagel and J. Tauc, Nearly-free-electron approach to the theory of

- metallic glass alloys, *Phys. Rev. Lett.* 1975, 35: 380~383.
- [Nagel, 1977] S.R. Nagel, Temperature dependence of the resistivity in metallic glasses, *Phys. Rev. B.* 1977, 16: 1694~1698.
- [Nagendra et al., 2000] N. Nagendra, U. Ramamurty, T.T. Goh and Y. Li, Effect of crystallinity on the impact toughness of a La-based bulk metallic glass, *Acta Mater.* 2000, 48: 2603~2615.
- [Neumann et al., 2009] G. Neumann and C. Tuijn, Self-diffusion and impurity diffusion in pure metals: handbook of experimental data, Pergamon. 2009, (1st edition)
- [Nieh et al., 1999] T.G. Nieh, T. Mukai, C.T. Liu and J. Wadsworth, Superplastic behavior of Zr-10Al-5Ti-17.9Cu-14.6Ni metallic glass in the supercooled liquid region, *Scripta Materialia* 1999, 40: 1021~1027.
- [Nieh et al., 2001] T.G. Nieh, J. Wadsworth, C.T. Liu, T. Ohkubo and Y. Hirotsu, Plasticity and structural instability in a bulk metallic glass deformed in the supercooled liquid region, *Acta Mater.* 2001, 49: 2887~2896.
- [Nieh et al., 2006] T.G. Nieh and J. Wadsworth, Homogeneous deformation of bulk metallic glasses, *Scripta Mater.* 2006, 54: 387-392.
- [Ogata et al., 2006] S. Ogata, F. Shimizu, J. Li, M. Wakeda and Y. Shibutani, Atomistic simulation of shear localization in Cu-Zr bulk metallic glass, *Intermetallic.* 2006, 14: 1033~1037.
- [Oguni, 1997] M. Oguni, 'intra-cluster rearrangement' model for the α -process in supercooled liquids, as opposed to 'cooperative rearrangement of whole molecules within a cluster', *J. Non-Cryst. Solids.* 1997, 210: 171~177.
- [Ohkubo, et al., 2007] T. Ohkubo, D. Nagahama, T. Mukai and K. Hono, Stress-strain behaviors of Ti-based bulk metallic glass and their nanostructures, *J. Mater. Res.* 2007, 22: 1406~1413.
- [Oliver et al., 1992] W.C. Oliver and G.M. Pharr, An improved technique for determining hardness and elastic modulus using load and displacement sensing indentation experiments. *J. Mater. Res.* 1992, 7: 1564~1583.
- [Park et al., 2006] E.S. Park and D.H. Kim, Phase separation and enhancement of plasticity in Cu-Zr-Al-Y bulk metallic glasses, *Acta Mater.* 2006, 54: 2597~2604.
- [Park et al., 2007] E.S. Park, J.S. Kyeong and D.H. Kim, Phase separation and improved plasticity by modulated heterogeneity in Cu-(Zr,Hf)-(Gd,Y)-Al metallic glasses, *Scripta Mater.* 2007, 37: 49~32.
- [B.J. Park et al., 2004] B.J. Park, H.J. Chang, W.T. Kim and D.H. Kim. In situ formation of two amorphous phases by liquid phase separation in Y-Ti-Al-Co alloy, *Appl. Phys. Lett.* 2004, 85: 6353~6355.
- [J.M. Park et al., 2005] J.M. Park, H.J. Chang, K.H. Han, W.T. Kim and D.H. Kim, Enhancement of plasticity in Ti-rich Ti-Zr-Be-Cu-Ni bulk metallic glasses, *Scripta Mater.* 2005, 53: 1~6.
- [Parshin, 1994] D.A. Parshin, Interactions of soft atomic potentials and universality of low-temperature properties of glasses, *Phys. Rev. B* 1994, 49: 9400~9418.
- [Parshin et al., 2001] D. A. Parshin and C. Laermans, Interaction of quasilocal harmonic modes and boson peak in glasses, *Phys. Rev. B* 2001, 63: 132203.
- [Peker et al., 1993] A. Peker and W.L. Johnson, A highly processable metallic glass: $Zr_{41.2}Ti_{13.8}Cu_{12.5}Ni_{10.0}Be_{22.5}$, *Appl. Phys. Lett.* 1993, 63: 2341~2344.
- [Peker et al, 1994] A. Peker and W.L. Johnson, US Patent 5, 288, 344, 1994.
- [Perepezko et al., 2007] J.H. Perepezko, J. Hamann, R.J. Hebert, H. Rösner and G. Wilde, Amorphization and devitrification reactions in metallic glass alloys, *Mater. Sci. Eng. A* 2007, 449-451: 84~89.
- [Phillips, 1972] W.A. Phillips, Tunneling states in amorphous solids, *J. Low Temp. Phys.* 1972, 7: 351~360.
- [Phillips, 1987] W.A. Phillips, Two-level states in glasses, *Rep. Prog. Phys.* 1987, 50: 1657~1708.
- [Polk et al., 1978] D.E. Polk, A. Calka and B.C. Giessen, The preparation and thermal and mechanical properties of new titanium rich metallic glasses, *Acta Metall.* 1978, 26: 1097~1103.
- [Poon, 1982] S.J. Poon, Thermal-relaxation studies of the stability of amorphous structures in zirconium-based superconducting alloys, *Phys. Rev. B* 1982, 27: 5519~5525.
- [Pradell et al., 1997] T. Pradell, D. Crespo, N. Clavaguera, J. Zhu and M.T. Clavaguera-Mora, Kinetics of microstructural development in nanocrystalline materials, *Nanostruct. Mater.* 1997, 8: 345~357.
- [Puech, 2008] S. Puech, Preparation, structural characterization and formation of magnesium

- glassy alloys, thesis Institut National Polytechnique de Grenoble, 2008.
- [Qin et al., 2006] F.X. Qin, X.M. Wang, S.L. Zhu, A. Kawashima, H. Kimura and A. Inoue, Fabrication and corrosion properties of novel Ti-based bulk glassy alloy without Ni, *Mater Trans.* 2006, 48: 515~518.
- [Qin et al., 2004] F.X. Qin, H.F. Zhang, B.Z. Ding and Z.Q. Hu, Nanocrystallization kinetics of Ni-based bulk amorphous alloys, *Intermetallics*. 2004, 12: 1197~1203.
- [Qin et al., 2007] F.X. Qin, X.M. Wang and A. Inoue, Effect of annealing on microstructure and mechanical properties of a Ti-Zr-Cu-Pd bulk metallic glass, *Intermetallics*. 2007, 15: 1337~1342.
- [Qin et al., 2008] F.X. Qin, X.M. Wang, G.Q. Xie and A. Inoue, Distinct plastic strain of Ni-free Ti-Zr-Cu-Pd-Nb bulk metallic glass with potential for biomedical applications, *Intermetallics*. 2008, 16: 1026~1030.
- [Ramamurty et al., 2002] U. Ramamurty, M.L. Lee, J. Basu and Y. Li, Embrittlement of a bulk metallic glass due to low-temperature annealing, *Scripta Mater.* 2002, 47: 107~111.
- [Ramos et al., 1997] M.A. Ramos and U. Buchenau, Low-temperature thermal conductivity of glasses within the soft-potential model, *Phys. Rev. B* 1997, 55: 5749~5754.
- [Ramos et al., 1998] M.A. Ramos and U. Buchenau, in: P. Esquinazi (Ed.), *Tunneling Systems in Amorphous and Crystalline Solids*, Springer, Berlin, 1998, p. 527 (Chapter 9).
- [Ramos et al., 2002] M.A. Ramos, C. Talón and S. Vieira, The Boson peak in structural and orientational glasses of simple alcohols: specific heat at low temperatures, *J. Non-Cryst. Solids*. 2002, 307-310: 80~86.
- [Ramos et al., 2003] M. A. Ramos, C. Talon, R. J. Jimenez-Rioboo and S. Vieira, Low-temperature specific heat of structural and orientational glasses of simple alcohols, *J. Phys.: Condens. Matter* 2003, 15: S1007~1018.
- [Ranganathan et al., 1981] S. Ranganathan and M.V. Heimendahl, The three activation energies with isothermal transformations: applications to metallic glasses, *J. Mater. Sci.* 1981, 16: 2401~2404.
- [Rao, 1983] K.V. Rao. Electrical transport properties. In: F.E. Luborsky, editor. *Amorphous metallicalloys*. London: Butterworths, 1983. p. 401~31.
- [Reger-Leonhard et al., 2000] A. Reger-Leonhard, M. Heilmaier and J. Eckert, Newtonian flow of $Zr_{55}Cu_{30}Al_{10}Ni_5$ bulk metallic glassy alloys, *Scripta Mater.* 2000, 43: 459~464.
- [Rogatchev et al., 2000] A. Yu. Rogatchev and U. Mizutani, Hopping conductivity and specific heat in insulating amorphous Ti_xSi_{100-x} alloys, *Phys. Rev. B* 2000, 61: 15550~15553.
- [Saida et al., 2002] J. Saida, S. Ishihara, H. Kato, A. Inoue and H.S. Chen, Suppression of quasicrystallization by nonlinear viscous flow in Zr-Al-Ni-Cu-Pd glassy alloys, *Appl. Phys. Lett.* 2002, 80: 4708~4710.
- [Sakamoto et al., 1996] H. Sakamoto, T. Yanada, N. Okumura and T. Sato, Improvement in brittleness of amorphous Fe-Si-B-C alloy ribbons by controlling casting conditions, *Mater. Sci. Eng. A* 1996, 206: 150~153.
- [Salamatov, 1996] R.I. Salamatov, Vibrational spectrum and temperature behavior of thermal conductivity and specific heat in amorphous dielectrics, *J. Non-Cryst. Solids*, 1996, 202: 128~136.
- [Samwer et al., 1982] K. Samwer and H.v. Löhneysen, Amorphous superconducting Zr_xCu_{1-x} : electronic properties, stability, and low-energy excitations, *Phys. Rev. B* 1982, 26: 107~123.
- [Saotome et al., 2001] Y. Saotome, T. Hatori, T. Zhang and A. Inoue, Superplastic micro/nano-formability of $La_{60}Al_{20}Ni_{10}Co_5Cu_5$ amorphous alloy in supercooled liquid state, *Mater. Sci. Eng. A* 2001, 304: 716~720.
- [Schuh et al., 2003-a] C.A. Schuh and T.G. Nieh, A nanoindentation study of serrated flow in bulk metallic glasses, *Acta Mater.* 2003, 51: 87~99.
- [Schuh et al., 2003-b] C.A. Schuh, A.C. Lund, Atomistic basis for the plastic yield criterion of metallic glass, *Nature Mater.* 2003, 2: 449~452.
- [Schuh et al., 2004] C.A. Schuh, A.L. Lund and T.G. Nieh, New regime of homogeneous flow in the deformation map of metallic glasses: elevated temperature nanoindentation experiments and mechanistic modeling, *Acta Mater.* 2004, 52: 5879~5891.
- [Schuh et al., 2007-a] C.A. Schuh and T.G. Nieh, A survey of instrumented indentation studies on metallic glasses, *J. Mater. Res.* 2007, 19: 46~57.
- [Schuh et al., 2007-b] C.A. Schuh, T.C. Hufnagel and U. Ramamurty, Mechanical behavior of

- amorphous alloys, *Acta Mater.* 2007, 55: 4067~4109.
- [Sergueeva et al., 2004] A.V. Sergueeva, N.A. Mara, J.D. Kuntz, D.J. Branagan and A.K. Mukherjee, Shear band formation and ductility of metallic glasses, *Mater. Sci. Eng. A* 2004, 383: 219-223.
- [Sestak et al., 1971] J. Sestak and G. Berggren, Study of the kinetics of the mechanism of solid-state reactions at increasing temperatures, *Thermochim. Acta.* 1971, 3: 1~12.
- [Shao et al., 2005] G. Shao, B. Lu, Y.Q. Liu and P. Tsakirooulos, Glass forming ability of multi-component metallic systems, *Intermetallics.* 2005, 13: 409~414.
- [Shen et al., 1999] T.D. Shen and R.B. Schwarz, Bulk ferromagnetic glasses prepared by flux melting and water quenching, *Appl. Phys. Lett.* 75 (1999) 49~51.
- [J. Shen et al., 2006-a] J. Shen, G. Wang, J.F. Sun, Z.H. Stachurski, C. Yan, L. Ye and B.D. Zhou, Superplastic deformation behavior of $Zr_{41.25}Ti_{13.75}Ni_{10}Cu_{12.5}Be_{22.5}$ bulk metallic glass in the supercooled liquid region, *Intermetallics.* 2005, 13: 79~85.
- [J. Shen et al., 2006-b] J. Shen, W.Z. Liang and J.F. Sun, Formation of nanowaves in compressive fracture of a less-brittle bulk metallic glass, *Appl. Phys. Lett.* 2006, 89: 121908.
- [Sheng et al., 2006] H.W. Sheng, W.K. Luo, F.M. Alamgir, J.M. Bai and E. Ma, Atomic packing and short-to-medium-range order in metallic glasses, *Nature.* 2006, 439: 419~425.
- [Shepilov et al., 1994] M.P. Shepilov and D.S. Baik, Computer simulation of crystallization kinetics for the model with simultaneous nucleation of randomly-oriented ellipsoidal crystals, *J. Non-Cryst. Solids.* 1994, 171: 141~156.
- [Shin et al., 2007-a] H.S. Shin, Y.J. Jeong, H.Y. Choi and A. Inoue, Influence of crystallization on the deformation behavior of $Zr_{55}Al_{10}Ni_5Cu_{30}$ bulk metallic glass in the supercooled liquid region, *Mater. Sci. Eng. A* 2007, 449-451: 243~247.
- [Shin et al., 2007-b] H.S. Shin, Y.J. Jeong and J.H. Ahn, Strain rate dependence of deformation behavior in Zr-based bulk metallic glasses in the supercooled liquid region, *J. Alloys. Compd.* 2007, 434-435: 40~43.
- [Sinha, 1970] A.K. Sinha, Electrical resistivity, thermoelectric power, and X-ray interference function of amorphous Ni-Pt-P alloys, *Phys. Rev. B.* 1970, 1: 4541~4546.
- [Sipp et al., 2001] A. Sipp, Y. Bottinga and P. Richet, New high viscosity data for 3D network liquids and new correlations between old parameters, *J. Non-Cryst. Solids,* 2001, 288: 166~174.
- [Slipenyuk et al., 2004] A. Slipenyuk and J. Eckert, Correlation between enthalpy change and free volume reduction during structural relaxation of $Zr_{55}Cu_{30}Al_{10}Ni_5$ metallic glass, *Scripta Mater.* 2004, 50: 39~44.
- [Sokolov et al., 1997] A. P. Sokolov, R. Calemczuk, B. Salce, A. Kisliuk, D. Quitmann and E. Duval, Low-temperature anomalies in strong and fragile glass formers, *Phys. Rev. Lett.* 1997, 78: 2405~2408.
- [Sommer et al., 1984] F. Sommer, H. Haas and B. Predel. Microcalorimetric investigations of structural relaxation phenomena in glassy binary transition-metal alloys, *J. Non-Cryst. Solids.* 1984, 61-62: 793~798.
- [Spaepen, 1977] F. Spaepen, A microscopic mechanism for steady state inhomogeneous flow in metallic glasses, *Acta Mater.* 1977, 23: 407~415.
- [Spaepen, 2006] F. Spaepen, Homogeneous flow of metallic glasses: a free volume perspective, *Scripta Mater.* 2006, 54: 363~367.
- [Srolovitz et al., 1981] D. Srolovitz, T. Egami and V. Vitek, Radial distribution function and structural relaxation in amorphous solid, *Phys. Rev. B* 1981, 24: 6936~6944.
- [Starink, 1997] M. Starink, Kinetic equations for diffusion-controlled precipitation reactions, *J. Mater. Sci.* 1997, 32: 4061~4070.
- [Starink, 2001] M.J. Starink, On the meaning of the impingement parameter in kinetic equation for nucleation and growth reactions, *J. Mater. Sci.* 2001, 36: 4433~4441.
- [Starink, 2004] M.J. Starink, Analysis of aluminium based alloys by calorimetry: quantitative analysis of reactions and reaction kinetics, *Int. Mater. Rev.* 2004, 49: 191~226.
- [Subhash et al., 2002] G. Subhash, R.J. Dowding and L.J. Kecskes, Characterization of uniaxial compressive response of bulk amorphous Zr-Ti-Cu-Ni-Be alloy, *Mater. Sci. Eng. A* 2002, 334: 33-40.
- [Suh et al., 2003] D. Suh and R.H. Dauskardt, Effects of open-volume regions on relaxation time scales and fracture behavior of a Zr-Ti-Ni-Cu-Be bulk metallic glass, *J. Non-Cryst. Solids* 2003,

317: 181~186.

[Sun et al., 2006] B.B. Sun, M.L. Sui, Y.M. Wang, G. He, J. Eckert and E. Ma, Ultrafine composite microstructure in a bulk Ti alloy for high strength, strain hardening and tensile ductility, *Acta Mater.* 2006, 54: 1349-1357.

[Sung et al., 2004] D.S. Sung, O.J. Kwon, E. Fleury, K.B. Kim, J.C. Lee, D.H. Kim and Y.C. Kim, Enhancement of the glass forming ability of Cu-Zr-Al alloys by Ag addition, *Met Mater Int.* 2004, 10: 575~579.

[Surgers et al., 1989] C. Surgers, H. v. Löhneysen and L. Schultz, Specific heat of mechanically alloyed amorphous $Zr_{0.7}Ni_{0.3}$, *Phys. Rev. B* 1989, 40: 8787~8790

[Szuëcs et al., 2001] F. Szuëcs, C.P. Kim and W.L. Johnson, Mechanical properties of $Zr_{56.2}Ti_{13.8}Nb_{5.0}Cu_{6.9}Ni_{5.6}Be_{12.5}$ ductile phase reinforced bulk metallic glass composite, *Acta Mater.* 2001, 49: 1507~1513.

[Takeuchi et al., 2000] S. Takeuchi, T. Kakegawa, T. Hashimoto, A.P. Tsai and A. Inoue, Low temperature mechanical properties of bulk metallic glasses, *Mater. Trans.* 2000, 41: 1443~1447.

[Talón et al., 2000] C. Talón, M.A. Ramos and S. Vieira, Low-temperature specific heat of molecular glasses and crystals, *Physica B.* 2000, 284-288: 1155~1156.

[Tang et al., 2005-a] M.B. Tang, H.Y. Bai and W.H. Wang, Tunneling states and localized mode in binary bulk metallic glass, *Phys. Rev. B* 2005, 72: 012202.

[Tang et al., 2005-b] M.B. Tang, H.Y. Bai, M.X. Pan, D.Q. Zhao and W.H. Wang, Einstein oscillator in highly-random-packed bulk metallic glass, *Appl. Phys. Lett.* 2005, 86: 021910.

[Tang, 2006] M.B. Tang, Low-temperature physical properties of bulk metallic glasses: localized mode, tunneling states, and heavy-fermion behavior, thesis Institute of Physics, CAS, 2006.

[Tanner et al., 1977] L.E. Tanner and R. Ray, Physical properties of $Ti_{50}Be_{40}Zr_{10}$ glass, *Scripta Mater.* 1977, 11: 783~789.

[Taub et al., 1980] A.I. Taub and F. Spaepen, The kinetics of structural relaxation of a metallic glass, *Acta Metall.* 1980, 28: 1781~1788.

[Taub et al., 1981] A.I. Taub, F.E. Luborsky, Creep, stress relaxation and structural change of amorphous alloys, *Acta Metall.* 1981, 29: 1939~1948.

[Telford, 2004] M. Telford, The case for bulk metallic glasses, *Mater. Today*, 2004, 7: 36~43.

[Terziyska et al., 2009] B. Terziyska, I. Bivas and K. Nenkov, Modeling of low-temperature specific heat data for $Ge_{27}As_{13}S_{60}$ and $As_{40}S_{60}$ glasses by means of the phenomenologically modified soft potential model, *Cryogenics*. 2009, 49: 171~175.

[Thompson et al., 1983] C.V. Thompson, A.L. Greer and F. Spaepen, Crystal nucleation in amorphous $(Au_{100-y}Cu_y)_{77}Si_9Ge_{14}$ alloys, *Acta Metall.* 1983, 31: 1883~1894.

[Tlomag, 1988] P. Tlomag, Experimental characterization of the surface and near surface transformations during surface biased crystallization of $Fe_{80}B_{20}$ and $Pd_{80}Si_{20}$ amorphous alloys, thesis Southern Illinois University, 1988.

[Tsao et al., 1985] S.S. Tsao and F. Spaepen, Structural relaxation of a metallic glass near equilibrium, *Acta Metall.* 1985, 33: 881~889.

[Tsuei, 1978] C.C. Tsuei, Anomalous electrical conduction in disordered and non-crystalline metallic conductor, *Solid St. Commun.* 1978, 27: 691~695

[Turnbull, 1969] D. Turnbull, Under what conditions can a glass be formed? *Contemp. Phys.* 1969, 10: 473~488.

[Turnbull et al., 1970] D. Turnbull and M.H. Cohen, On the free-volume model of the liquid-glass transition, *J. Chem. Phys.* 1970, 52: 3038~3041.

[Van de Moortèle et al., 2004] B. Van De Moortèle, T. Epicier, J.L. Soubeyroux and J.M. Pelletier, Compositions of different phases appearing during devitrification of $Zr_{46.75}Ti_{8.25}Cu_{7.5}Ni_{10}Be_{27.5}$ bulk metallic glass, *Phil. Mag. Lett.* 2004, 84: 245~256.

[Van den Beukel et al., 1983] A. Van den Beukel and S. Radelaar, On the kinetics of structural relaxation in metallic glasses, *Acta Metall.* 1983, 31: 419~427.

[Van den Beukel et al., 1984] A. Van den Beukel, S. Van der Zwaag and A.L. Mulder, A semi-quantitative description of the kinetics of structural relaxation in amorphous $Fe_{40}Ni_{40}B_{20}$, *Acta Metall.* 1984, 32: 1895~1902.

[Van den Beukel, 1986] A. Van den Beukel, Analysis of chemical short range ordering in amorphous $Fe_{40}Ni_{40}B_{20}$, *J. Non-Cryst. Solids* 1986, 83: 134~140.

[Van den Beukel et al., 1990] A. Van den Beukel and J. Sietsma. The glass transition as a free

- volume related kinetic phenomenon, *Acta Metall Mater.* 1990, 38: 383~389.
- [Vilgis et al., 1993] T.A. Vilgis, Strong and fragile glasses: a powerful classification and its consequences, *Phys. Rev. B* 1993, 47: 2882~2885.
- [Villars et al., 1997] P. Villars, A. Prince and H. Okamoto: *Handbook of Ternary Alloy Phase Diagrams*, (ASM, Materials Park, Ohio, 1997).
- [Vladár et al., 1982] K. Vladár and A. Zawadowski, Theory of resonant electron scattering in amorphous metals, *Solid St. Commun.* 1982, 41: 649~652.
- [Vladár et al., 1983-a] K. Vladár and A. Zawadowski, Noncommutative model Hamiltonian and scaling of first order, *Phys. Rev. B* 1983, 28: 1564~1581.
- [Vladár et al., 1983-b] K. Vladár and A. Zawadowski, Theory of interaction between electrons and the two-level system in amorphous metals. II. Second-order scaling equations, *Phys. Rev. B* 1983, 28: 1582~1595.
- [Vladár et al., 1983-c] K. Vladár and A. Zawadowski, Theory of interaction between electrons and the two-level system in amorphous metals. III. Experimentally observable quantities, *Phys. Rev. B* 1983, 28: 1596~1612.
- [Waterstrat, 1992] R.M. Waterstrat, New ternary Laves phases, *J. Alloy. Compd.* 1992, 179: L33.
- [Wang et al., 1998] W. H. Wang, Q. Wei, and S. Friedrich, Microstructure, decomposition, and crystallization in $Zr_{41}Ti_{14}Cu_{12.5}Ni_{10}Be_{22.5}$ bulk metallic glass, *Phys. Rev. B* 1998, 57: 8211~8217.
- [Wang, 2006] W.H. Wang, Correlations between elastic moduli and properties in bulk metallic glasses, *J. Appl. Phys.* 2006, 99: 093506.
- [G. Wang et al., 2005] G. Wang, J. Shen, J.F. Sun, Y.J. Huang, J. Zou, Z.P. Lu, Z.H. Stachurski and B.D. Zhou, Superplasticity and superplastic forming ability of a Zr-Ti-Ni-Cu-Be bulk metallic glass in the supercooled liquid region, *J. Non-Cryst. Solids.* 2005, 351: 209~317.
- [G. Wang et al., 2006] G. Wang, Y. T. Wang, Y. H. Liu, M. X. Pan, D. Q. Zhao and W. H. Wang, Evolution of nanoscale morphology on fracture surface of brittle metallic glass, *Appl. Phys. Lett.* 2006, 89: 121909.
- [H.R. Wang, et al., 2003] H.R. Wang, Y.L. Gao, G.H. Min, X.D. Hui and Y.F. Ye, Primary crystallization in rapidly solidified $Zr_{70}Cu_{20}Ni_{10}$ alloy from a supercooled liquid region, *Phys. Lett. A* 2003, 314: 81~87.
- [Q. Wang et al., 2005] Q. Wang, J.M. Pelletier, J.J. Blandin and M.L. Suéry, Mechanical properties over the glass transition of $Zr_{41.2}Ti_{13.8}Cu_{12.5}Ni_{10}Be_{22.5}$ bulk metallic glass, *J. Non-Cryst. Solids* 2005, 351: 2224~2231.
- [Q. Wang et al., 2006] Q. Wang, S. Gravier, J.J. Blandin, J.M. Pelletier and J. Lu, Deformation and crystallization of a $Zr_{41.2}Ti_{13.8}Cu_{12.5}Ni_{10}Be_{22.5}$ bulk metallic glass in the supercooled liquid region, *Mater. Sci. Eng. A* 2006, 435-436: 405~411.
- [X.D. Wang et al., 2006] X.D. Wang, H. Lee and S. Yi, Crystallization behavior of preannealed bulk amorphous alloy $Zr_{62}Al_8Ni_{13}Cu_{17}$, *Mater. Lett.* 2006, 60: 935~938.
- [X.D. Wang et al., 2007] X.D. Wang, J.Z. Jiang and S. Yi, Reversible structural relaxation and crystallization of $Zr_{62}Al_8Ni_{13}Cu_{17}$ bulk metallic glass, *J. Non-Cryst. Solids.* 2007, 353: 4157~4161.
- [Waniuk et al., 1998] T.A. Waniuk, R. Busch, A. Masuhr and W.L. Johnson, Equilibrium viscosity of the $Zr_{41.2}Ti_{13.8}Cu_{12.5}Ni_{10}Be_{22.5}$ bulk metallic glass-forming liquid and viscous flow during relaxation, phase separation, and primary crystallization, *Acta Mater.* 1998, 46: 5229~5236.
- [Wen et al., 2003] P. Wen, R.J. Wang, M.X. Pan, D.Q. Zhao and W.H. Wang, Characteristics of microstructure and glass transition of $(Zr_{0.59}Ti_{0.06}Cu_{0.22}Ni_{0.13})_{100-x}Al_x$ bulk metallic glasses, *J. Appl. Phys.* 2003, 93: 759~761.
- [Whang, 1983] S.H. Whang, *Mater. Sci. Eng. A* 1983, 57: 87.
- [Woodcock et al., 2005] T.G. Woodcock, M. Kusy, S. Mato, G. Alcala, J. Thomas, W. Löser, A. Gebert, J. Eckert and L. Schultz, Formation of a metastable eutectic during the solidification of the alloy $Ti_{60}Cu_{14}Ni_{12}Sn_4Ta_{10}$, *Acta Mater.* 2005, 53: 5141-5149.
- [Wright et al., 2001] W.J. Wright, R.B. Schwarz and W.D. Nix, Localized heating during serrated plastic flow in bulk metallic glasses, *Mater. Sci. Eng. A* 2001, 319: 229~232.
- [Wu et al., 2008] Y.F. Wu, W.C. Chiang and J.K. Wu, Effect of crystallization on corrosion behavior of $Fe_{40}Ni_{38}B_{18}Mo_4$ amorphous alloy in 3.5% sodium chloride solution, *Mater. Lett.* 2008, 62: 1554~1556.

-
- [X.F. Wu et al., 2008] X.F. Wu, Z.Y. Su, Y. Si, L.K. Meng and K.Q. Qiu, Bulk metallic glass formation in a ternary Ti-Cu-Ni alloy system, *J. Alloy. Comp.* 2008, 452: 268~272.
- [Xi, 2005] X.K. Xi, Preparation of Mg-based bulk metallic glasses and their fracture behaviors, thesis Institute of Physics, CAS, 2005.
- [Xi et al., 2005] X.K. Xi, D.Q. Zhao, M.X. Pan, W.H. Wang, Y. Wu and J.J. Lewandowski, Fracture of brittle metallic glasses: brittleness or plasticity, *Phys. Rev. Lett.* 2005, 94: 125510.
- [Xi et al., 2006] X.K. Xi, D.Q. Zhao, M.X. Pan, W.H. Wang, Y. Wu and J.J. Lewandowski, Periodic corrugation on dynamic fracture surface in brittle bulk metallic glass, *Appl. Phys. Lett.* 2006, 89: 181911.
- [Xia et al., 2005-a] M.X. Xia, C.L. Ma, H.X. Zheng and J.G. Li, Preparation and crystallization of $\text{Ti}_{53}\text{Cu}_{27}\text{Ni}_{12}\text{Zr}_3\text{Al}_7\text{Si}_3\text{B}_1$ bulk metallic glass with wide supercooled liquid region, *Mater. Sci. Eng. A* 2005, 390: 372~375.
- [Xia et al., 2005-b] M.X. Xia, H.X. Zheng, J. Liu, C.L. Ma and J.G. Li, Thermal stability and glass-forming ability of new Ti-based bulk metallic glasses, *J. Non-Cryst. Solids*, 2005, 351: 3747~3751.
- [Xing et al., 1998] L.Q. Xing, C. Bertrand, J.P. Dallas and M. Cornet, Deformation behavior of partially crystallized $\text{Zr}_{57}\text{Ti}_{15}\text{Al}_{10}\text{Cu}_{20}\text{Ni}_8$ bulk amorphous alloy, *Mater. Lett.* 1998, 34: 90~94.
- [Xing et al., 1999] L.Q. Xing, J. Eckert, W. Loser, L. Schultz and D.M. Herlach, Crystallization behavior and nanocrystalline microstructure evolution of a $\text{Zr}_{57}\text{Cu}_{20}\text{Al}_{10}\text{Ni}_8\text{Ti}_5$ bulk amorphous alloy, *Philos. Mag. A* 1999, 79: 1095~1108.
- [Xing et al., 2000] L.Q. Xing, T.C. Hufnagel, J. Eckert, W. Löser and L. Schultz, Relation between short-range order and crystallization behavior in Zr-based amorphous alloys, *Appl. Phys. Lett.* 2000, 77: 1970~1972.
- [Xu et al., 2004] D.H. Xu, B. Lohwongwatana, G. Duan, W.L. Johnson and C. Garland, Bulk metallic glass formation in binary Cu-rich alloy series $\text{Cu}_{10-x}\text{Zr}_x$ ($x=34, 36, 38.2, 40$ at.%) and mechanical properties of bulk $\text{Cu}_{64}\text{Zr}_{36}$ glass, *Acta Mater.* 2004, 52: 2621~2624.
- [Yan et al., 2004] M. Yan, J.F. Sun and J. Shen, Isothermal annealing induced embrittlement of $\text{Zr}_{41.25}\text{Ti}_{13.75}\text{Ni}_{10}\text{Cu}_{12.5}\text{Be}_{22.5}$ bulk metallic glass, *J. Alloys Comp.* 2004, 381: 86~90.
- [Yang et al., 2006] H.W. Yang and J.Q. Wang, Evidence of structure relaxation prior to nanocrystallization in an Al-based metallic glass, *Scrip Mater.* 2006, 55: 359~362.
- [Yao et al., 2006] K.F. Yao, F. Ruan, Y.Q. Yang, and N. Chen, Superductile bulk metallic glass, *Appl. Phys. Lett.* 2006, 88: 122106.
- [Yu et al., 2007] P. Yu, Y.H. Liu, G. Wang, H.Y. Bai and W.H. Wang, Enhance plasticity of bulk metallic glasses by geometric confinement, *J. Mater. Res.* 2007, 22: 2384~2388.
- [Yuan et al., 2007] Z.Z. Yuan, B.X. Wang, Y.D. Tong and X.D. Chen, Effect of annealing on the kinetics of glass transition and crystallization in Co-Fe-Ta-B amorphous alloy, *J. Alloys. Compd.* 2007, 429: 104~110.
- [Zeller et al., 1971] R. C. Zeller and R. O. Pohl, Thermal conductivity and specific heat of noncrystalline solids, *Phys. Rev. B* 1971, 4: 2029~2041.
- [L.C. Zhang et al., 2007] L.C. Zhang, J. Das, H.B. Lu, C. Duhamel, M. Calin and J. Eckert, High strength Ti-Fe-Sn ultrafine composites with large plasticity, *Scripta Mater.* 2007, 57: 101~104.
- [J. Zhang et al., 2007] J. Zhang, J.M. Park, D.H. and Kim, F.S. Kim, Effect of strain rate on compressive behavior of $\text{Ti}_{45}\text{Zr}_{16}\text{Ni}_9\text{Cu}_{10}\text{Be}_{20}$ bulk metallic glass, *Mater. Sci. Eng. A* 2007, 449-451: 290~294.
- [S.N. Zhang et al., 2009] S.N. Zhang, J. He, T.J. Zhu, X.B. Zhao and T.M. Tritt, Thermal conductivity and specific heat of bulk amorphous chalcogenides $\text{Ge}_{20}\text{Te}_{80-x}\text{Se}_x$ ($x=0,1,2,8$), *J. Non-Cryst. Solids*. 2009, 355: 79~83.
- [T. Zhang et al., 1993] T. Zhang, A. Inoue and T. Masumoto, The effect of atomic size on the stability of supercooled liquid for amorphous $(\text{Ti,Zr,Hf})_{65}\text{Ni}_{25}\text{Al}_{10}$ and $(\text{Ti,Zr,Hf})_{65}\text{Cu}_{25}\text{Al}_{10}$ alloys, *Mater. Lett.* 1993, 15: 379~382.
- [T. Zhang et al., 1994] T. Zhang, A. Inoue and T. Masumoto, Amorphous (Ti,Zr,Hf) -Ni-Cu ternary alloys with a wide supercooled liquid region, *Mater. Sci. Eng. A* 1994, 181-182: 1423~1426.
- [T. Zhang et al., 1998-a] T. Zhang and A. Inoue, Thermal and mechanical properties of Ti-Ni-Cu-Sn amorphous alloys with a wide supercooled liquid region before crystallization, *Mater. Trans. JIM* 1998, 39: 1001~1006.

- [T. Zhang et al., 1998-b] T. Zhang and A. Inoue, Mechanical properties of Zr-Ti-Al-Ni-Cu bulk amorphous sheets prepared by squeeze casting, *Mater. Trans. JIM* 1998, 39: 1230~1237.
- [T. Zhang et al., 1999] T. Zhang and A. Inoue, Preparation of Ti-Cu-Ni-Si-B amorphous alloys with a large supercooled liquid region, *Mater. Trans. JIM* 1999, 40: 301~306.
- [T. Zhang et al., 2001] T. Zhang and A. Inoue, Ti-based amorphous alloys with a large supercooled liquid region, *Mater. Sci. Eng. A* 2001, 304-306: 771~774.
- [T. Zhang, 2007] T. Zhang, Structural relaxation behavior of LaAlNiCu bulk metallic glass, thesis University of Science and Technology of Beijing, 2007.
- [Y. Zhang et al., 2006] Y. Zhang, W.H. Wang and A.L. Greer, Making metallic glasses plastic by control of residual stress, *Nat. Mater.* 2006, 5: 857~860.
- [Z.F. Zhang et al., 2003] Z.F. Zhang, J. Eckert, L. Schultz, Different in compressive and tensile fracture mechanisms of $Zr_{59}Cu_{20}Al_{10}Ni_8Ti_3$ bulk metallic glass, *Acta Mater.* 2003, 51: 1167~1179.
- [Z.F. Zhang et al., 2005-a] Z.F. Zhang and J. Eckert, Unified tensile fracture criterion, *Phys. Rev. Lett.* 2005, 94: 094301.
- [Z.F. Zhang et al., 2005-b] Z.F. Zhang, G. He, H. Zhang and J. Eckert, Rotation mechanism of shear fracture induced by high plasticity in Ti-based nano-structured composites containing ductile dendrites, *Scripta Mater.* 2005, 52: 945~949.
- [Z.F. Zhang et al., 2006] Z. F. Zhang, F. F. Wu, W. Gao, J. Tan and Z. G. Wang, Wavy cleavage fracture of bulk metallic glass, *Appl. Phys. Lett.* 2006, 89: 251917.
- [Zhou et al., 2006] Z.H. Zhou, C. Uher, D.H. Xu, W.L. Johnson, W. Gannon and M.C. Aronson, On the existence of Einstein oscillators and thermal conductivity in bulk metallic glass, *Appl. Phys. Lett.* 2006, 89: 031924.
- [Zhu et al., 2007] S.L. Zhu, X.M. Wang, F.X. Qin and A. Inoue, A new Ti-based bulk glassy alloy with potential for biomedical application, *Mater. Sci. Eng. A* 2007, 459: 233~237.
- [D.M. Zhu et al., 1998] D.M. Zhu and H.W. Chen, Low temperature specific heat and fragility of glasses, *J. Non-Cryst. Solid.* 1998, 224: 97~101.
- [Zhuang et al., 2000] Y.X. Zhuang and W.H. Wang, Effects of relaxation on glass transition and crystallization of $ZrTiCuNiBe$ bulk metallic glass, *J. Appl. Phys.* 2000, 87: 8209~8211.
- [Ziman, 1961] J.M. Ziman, A theory of electrical properties of liquid metals, *Philos. Mag.* 1961, 6: 1013~1034.

Abstract: Two Ti-based bulk metallic glasses, with the nominal composition of $\text{Ti}_{40}\text{Zr}_{25}\text{Ni}_8\text{Cu}_9\text{Be}_{18}$ and $\text{Ti}_{41.5}\text{Cu}_{37.5}\text{Ni}_{7.5}\text{Zr}_{2.5}\text{Hf}_5\text{Sn}_5\text{Si}_1$, who exhibit different structural nature (quenched-in nuclei/amorphous structure and phase separation-like structure, respectively), were investigated. Our studies focus on thermally induced structural transformations (structural relaxation and crystallization) behavior and their effects on thermodynamics and kinetics of the subsequent glass transition and crystallization as well as room-temperature mechanical response in addition to homogeneous deformation in the supercooled liquid region and low-temperature physical properties. As a result, their enthalpy relaxation both follows the general characteristics although their unique structure nature. The latter shows better thermal stability however lower glass forming ability than the former. Phase transformation upon heating was investigated by Neutron diffraction, and JMA as well as Starink model was introduced to study their crystallization kinetics. They both exhibit high value of compressive strength, however with significantly different plastic strain at room temperature. Their unique deformation and fracture behavior whose fracture angles change from $<45^\circ$ to 90° can be interpreted by ellipse criterion. Structural relaxation and crystallization lead to a drastic degradation of plasticity, although the structural relaxation may produce a slight increase in hardness as well as fracture strength. The latter exhibits a good superplasticity and workability, and a beneficial domain for optimum hot workability of this alloy has been located by constructing the power dissipation efficiency map.

Keywords: Bulk metallic glasses, structural characterization, structural relaxation, crystallization, mechanical behaviors, superplasticity.

Résumé: Deux verres métalliques massifs à base de titane, avec les compositions nominales $\text{Ti}_{40}\text{Zr}_{25}\text{Ni}_8\text{Cu}_9\text{Be}_{18}$ et $\text{Ti}_{41.5}\text{Cu}_{37.5}\text{Ni}_{7.5}\text{Zr}_{2.5}\text{Hf}_5\text{Sn}_5\text{Si}_1$, qui montrent des variétés structurales différentes (germes/phase amorphe et séparation de phases, respectivement), ont été étudiés. Nos études se concentrent sur les transformations structurales thermiquement induites (relaxation et cristallisation structurales) et leurs effets sur la thermodynamique et la cinétique de la transition vitreuse et la cristallisation, la réponse mécanique à la température ambiante, la déformation homogène dans la région du liquide surfondu et les propriétés physiques à basse température. En conséquence, leur enthalpie de relaxation suit les caractéristiques générales admises malgré la nature unique de leurs structures. Le deuxième verre présenté montre une meilleure stabilité thermique bien qu'il présente une plus faible capacité à former la structure vitreuse. Les transformations de phases lors du chauffage ont aussi été étudiées par diffraction de neutrons ainsi que par les modèles JMA et de Starink. Ce dernier a été introduit pour étudier leur cinétique de cristallisation. Les deux verres montrent de hautes valeurs de résistance à la compression, toutefois avec des contraintes plastiques sensiblement différentes à température ambiante. Leur déformation et comportement uniques à la rupture, dont les changements d'angles de rupture $< 45^\circ$ à 90° peuvent être interprétés par le critère dit d'ellipse. La relaxation et la cristallisation structurales mènent à une importante dégradation de la plasticité, bien que la relaxation structurale puisse produire une légère augmentation de dureté aussi bien que de la force de rupture. Les verres présentés ont une bonne superplasticité et capacité de mise en forme. Un domaine optimum pour la mise en forme à chaud de cet alliage a été proposé par la construction de carte d'efficacité de dissipation de puissance.

Mots clés: Verres métalliques massifs, caractérisation structurale, relaxation structurale, cristallisation, propriétés mécaniques, superplasticité.